TECHNISCHE UNIVERSITÄT WIEN
Vienna University of Technology

DISSERTATION

Local and Nonlocal Correlations in Interacting Electron Systems

ausgeführt zum Zwecke der Erlangung des akademischen Grades des

Doktors der technischen Wissenschaften (Dr. techn.)

am Institut für Festkörperphysik der

Technischen Universität Wien

unter Anleitung von

Dr. Oleg Janson
Univ.-Prof. Dr. Karsten Held

durch

Dipl.-Ing. Josef Kaufmann

Farberweg 28, 6380 St. Johann i. T.

Matrikelnummer 1026763

Wien, Februar 2021

Die approbierte gedruckte Originalversion dieser Dissertation ist an der TU Wien Bibliothek verfügbar.
The approved original version of this doctoral thesis is available in print at TU Wien Bibliothek.
TU Bibliothek Your knowledge hub

Die approbierte gedruckte Originalversion dieser Dissertation ist an der TU Wien Bibliothek verfügbar.
The approved original version of this doctoral thesis is available in print at TU Wien Bibliothek.

Eidesstattliche Erklärung

Ich erkläre an Eides statt, dass die vorliegende Arbeit nach den anerkannten Grundsätzen für wissenschaftliche Abhandlungen von mir selbstständig erstellt wurde. Alle verwendeten Hilfsmittel, insbesondere die zugrunde gelegte Literatur, sind in dieser Arbeit genannt und aufgelistet. Die aus den Quellen wörtlich entnommenen Stellen, sind als solche kenntlich gemacht.
Das Thema dieser Arbeit wurde von mir bisher weder im In- noch Ausland einer Beurteilerin/einem Beurteiler zur Begutachtung in irgendeiner Form als Prüfungsarbeit vorgelegt.

Datum, Ort | Unterschrift

Affidavit

I declare in lieu of oath, that I wrote this thesis and performed the associated research myself, using only literature cited in this volume. If text passages from sources are used literally, they are marked as such.
I confirm that this work is original and has not been submitted elsewhere for any examination, nor is it currently under consideration for a thesis elsewhere.

Date, Place | Signature

Die approbierte gedruckte Originalversion dieser Dissertation ist an der TU Wien Bibliothek verfügbar.
The approved original version of this doctoral thesis is available in print at TU Wien Bibliothek.
TU Bibliothek WIEN Your knowledge hub

Die approbierte gedruckte Originalversion dieser Dissertation ist an der TU Wien Bibliothek verfügbar.
The approved original version of this doctoral thesis is available in print at TU Wien Bibliothek.

Kurzfassung

Starke Korrelationen in Systemen wechselwirkender Elektronen führen zu einer Vielzahl von faszinierenden physikalischen Phänomenen. Die Berechnung und Simulation des Verhaltens in solchen Systemen stellt uns jedoch vor große Schwierigkeiten. Das Thema dieser Dissertation ist die Entwicklung und Verbesserung von numerischen Methoden für stark korrelierte Elektronensysteme. Nach einer kurzen Einführung in den Formalismus der Greenschen Funktionen für Vielteilchenprobleme wird die analytische Fortsetzung von imaginären auf reelle Frequenzen diskutiert. Insbesondere beschäftigen wir uns mit der Methode der maximalen Entropie, für welche wir auch eine neue Implementierung präsentieren.

Im Folgenden geht es in dieser Dissertation um Methoden zur Berechnung von Greenschen Funktionen. Da diese Berechnung in der vorliegenden Arbeit immer in imaginären Frequenzen geschieht, ist die zuvor abgehandelte analytische Fortsetzung ein fester Bestandteil der nachfolgenden Berechnungen. Zuerst führen wir das Anderson'sche Störstellenproblem ein. Zu dessen numerischer Lösung wurden bereits mehrere Methoden entwickelt, wir konzentrieren uns hier auf Quanten-Monte-Carlo Simulation in kontinuierlicher Zeit. Dieser Algorithmus, erweitert durch das sogenannte Wurm-Sampling, erlaubt es komplizierte Korrelationsfunktionen für das Anderson-Modell zu berechnen. Darauf aufbauend leiten wir neue, symmetrisch verbesserte Schätzer für die Selbstenergie und Vertexfunktionen her und implementieren diese.

Als nächsten Schritt beschreiben wir die dynamische Molekularfeld-Theorie. Diese Methode vermag es lokale Korrelationen im Hubbard-Modell zu erfassen, indem es selbstkonsistent auf ein Anderson-Modell abgebildet wird. Wir untersuchen das Konvergenzverhalten dieser iterativen Prozedur, sowie auch eine Konvergenzbeschleunigung durch Mixing. Danach werden Streuraten von schwach wechselwirkenden Elektronen im Hubbard-Modell auf einem quadratischen Gitter berechnet und mit Ergebnissen aus der Boltzmann'schen Streutheorie verglichen.

Obwohl die dynamische Molekularfeld-Theorie beachtliche Erfolge bei der Vorhersage stark korrelierter Elektronensysteme zu verzeichnen hat, ist es zum Beispiel für die korrekte Beschreibung von Phasenübergängen unerlässlich auch nichtlokale Korrelationen miteinzubeziehen. Dies wird im Rahmen dieser Dissertation mithilfe der Dynamischen Vertex Approximation erreicht, für die wir eine neue, selbstkonsistente Erweiterung entwickeln. Als ersten Anwendungsfall betrachten wir das Hubbard-Modell auf einem Quadratgitter mit schwacher Wechselwirkung, wo wir unsere Methode durch genauen Vergleich mit anderen Methoden genau überprüfen. Darauffolgend zeigen wir auch Ergebnisse für die Fälle von mittlerer bis hin zu starker Wechselwirkung. Weiters untersuchen wir ein lochdotiertes Zweibandmodell, sowie ein Dreiband-Wanniermodell für Strontiumvanadat. Als Anwendungsfall für unsere neue Methode beschäftigen wir uns mit den Auswirkungen der geometrischen Frustration im Hubbard-Modell auf dem Kagome-Gitter und führen auch Vergleiche mit Determinanten-Quanten-Monte-Carlo durch.

Die approbierte gedruckte Originalversion dieser Dissertation ist an der TU Wien Bibliothek verfügbar.
The approved original version of this doctoral thesis is available in print at TU Wien Bibliothek.
TU Bibliothek WIEN Your knowledge hub

Die approbierte gedruckte Originalversion dieser Dissertation ist an der TU Wien Bibliothek verfügbar.
The approved original version of this doctoral thesis is available in print at TU Wien Bibliothek.

Abstract

Strong electronic correlations are the root of many fascinating phenomena of condensed matter physics. However, they also make calculations notoriously difficult. This thesis is concerned with the development and improvement of computational methods for strongly correlated electron systems. After a brief recapitulation of the Green's function formalism, which is the theoretical basis of most such methods, we discuss the analytical continuation from imaginary to real frequencies. Especially the maximum entropy method is explained in detail and an implementation thereof is presented.

The remainder of this thesis deals with methods to compute Green's functions on the imaginary frequency axis. First, the Anderson impurity model (AIM) is considered. It can be solved numerically – a task for which several methods exist. We focus on continuous-time quantum Monte Carlo with worm sampling, through which various kinds of correlation functions can be calculated. On this basis we derive and implement symmetric improved estimators that allow for the computation of the self-energy and vertex functions where the level of stochastic noise is largely reduced with respect to conventional estimators.

As a next step the dynamical mean-field theory (DMFT) is introduced as a method to capture local correlations in the Hubbard model (HM) by self-consistently mapping it onto the AIM. We study the convergence behavior of this iterative procedure and the improvement of convergence due to mixing. Then, we compare electron scattering rates from DMFT in the weak-coupling regime of the square-lattice HM to results from Boltzmann scattering theory.

While local correlations account for many interesting phenomena, such as the Mott-Hubbard metal-insulator transition, they are not sufficient to correctly describe, e.g., the physics of phase transitions in two- or three-dimensional systems. It is thus the final step in this thesis to also include nonlocal correlations by means of the dynamical vertex approximation (DΓA). For this we develop a new self-consistency scheme, which is then applied to several systems: We study the square-lattice HM, where we compare to benchmark methods in the weak-coupling regime, but also present results for intermediate and strong coupling. Furthermore, a two-band model with doping and a three-band Wannier model for strontium vanadate are studied. As an application of our new self-consistent DΓA, we study the effects of geometrical frustration in the kagome lattice, where we also compare our results to determinant quantum Monte Carlo.

Die approbierte gedruckte Originalversion dieser Dissertation ist an der TU Wien Bibliothek verfügbar.
The approved original version of this doctoral thesis is available in print at TU Wien Bibliothek.
TU Bibliothek WIEN Your knowledge hub

Die approbierte gedruckte Originalversion dieser Dissertation ist an der TU Wien Bibliothek verfügbar.
The approved original version of this doctoral thesis is available in print at TU Wien Bibliothek.

Contents

Kurzfassung **v**

Abstract **vii**

List of abbreviations **xii**

1 Introduction and outline **1**

2 Green's functions and analytic continuation **5**
2.1 Brief recapitulation of the Green's function formalism 5
2.1.1 Definition 5
2.1.2 Spatial/momentum dependence 6
2.1.3 Time/frequency dependence 6
2.1.4 Analytic properties 7
2.2 Pade interpolation 8
2.3 Probabilistic approach - Maximum Entropy 9
2.3.1 Formulation of the analytic continuation problem 9
2.3.2 Properties of the kernel 11
2.3.3 Regularization term or prior probability 12
2.4 * Technical aspects of the Maximum Entropy method 13
2.4.1 Choice of α 13
2.4.2 Elimination of unphysical features: Preblur 16
2.4.3 MaxEnt for offdiagonal elements 18
2.5 * Python package for analytic continuation: `ana_cont` 19
2.5.1 Package structure 20
2.5.2 Numerics 20
2.5.3 MaxEnt for susceptibilities 23
2.5.4 MaxEnt for self-energies 24

3 Correlation functions for the Anderson impurity model **27**
3.1 Impurity solvers 29
3.1.1 Exact diagonalization 29
3.1.2 Continuous-time quantum Monte Carlo 30
3.2 * Symmetric improved estimators 38
3.2.1 Derivation 38

An asterisk (*) marks sections that describe the author's original research.

Die approbierte gedruckte Originalversion dieser Dissertation ist an der TU Wien Bibliothek verfügbar.
The approved original version of this doctoral thesis is available in print at TU Wien Bibliothek.
TU Bibliothek WIEN Your knowledge hub

3.2.2 Implementation . . . 44
3.2.3 Validation . . . 45

4 Local correlations in the Hubbard model 49
4.1 Tight-binding model . . . 49
4.1.1 Square lattice . . . 51
4.2 Hubbard model . . . 52
4.3 From Hubbard model to Anderson model: dynamical mean-field theory . . . 52
4.3.1 Limit of infinite dimensions . . . 52
4.3.2 Self-consistent algorithm . . . 53
4.4 * Convergence acceleration . . . 56
4.5 * Quasi-particle scattering rates in DMFT . . . 60
4.5.1 Scattering rates in the Green's function formalism . . . 60
4.5.2 Analytical example . . . 62
4.6 * Comparison of scattering rates in DMFT and Boltzmann transport theory . . . 63
4.6.1 One-band Hubbard model at weak coupling . . . 64
4.6.2 Two-orbital band insulator . . . 68
4.6.3 Strong coupling: Mott-insulator . . . 71
4.7 * Collective modes in excitonic magnets: Dynamical mean-field study . . . 75
4.8 * Topotactic Hydrogen in Nickelate Superconductors . . . 76

5 Nonlocal correlations in the Hubbard model 77
5.1 Dynamical vertex approximation . . . 78
5.1.1 Parquet-DΓA . . . 81
5.1.2 Ladder-DΓA . . . 82
5.1.3 λ-corrected DΓA . . . 83
5.2 * Self-consistent ladder DΓA (sc-DΓA) . . . 83
5.2.1 Implementation . . . 84
5.2.2 Computational effort . . . 87
5.2.3 Relation to p-DΓA . . . 88
5.3 * Statistical error estimates in dynamical mean-field theory and extensions thereof 89
5.4 * Square lattice Hubbard model . . . 90
5.4.1 Weak coupling . . . 92
5.4.2 Intermediate coupling . . . 95
5.4.3 Strong coupling . . . 96
5.5 * Multi-orbital calculations . . . 98
5.5.1 Two-orbital model . . . 98
5.5.2 Strontium vanadate . . . 102
5.6 * Kagome lattice Hubbard model . . . 105
5.6.1 Numerical methods . . . 109
5.6.2 Results . . . 110
5.6.3 Discussion . . . 119

6 Conclusion 125

Die approbierte gedruckte Originalversion dieser Dissertation ist an der TU Wien Bibliothek verfügbar.
The approved original version of this doctoral thesis is available in print at TU Wien Bibliothek.
TU Bibliothek WIEN Your knowledge hub

Appendices **127**

A Properties of Green's functions **129**
A.1 Imaginary-time dependence . . . 129
A.1.1 Time interval . . . 129
A.1.2 Periodicity in imaginary time . . . 130

B Lehmann representations **131**
B.1 Lehmann representations for two-frequency objects . . . 131
B.2 Raman diagram . . . 132
B.3 Eigenbasis representation . . . 132
B.4 Calculation of the integral . . . 133

C Parquet equations in convention-agnostic frequency notation **135**
C.1 Green's functions in AbinitioDΓA . . . 135
C.2 Irreducible vertex . . . 136
C.3 Transition to AbinitioDΓA convention . . . 137
C.4 From four frequencies back to RMP convention . . . 138

D Detailed derivation of symmetric improved estimators **139**
D.1 One-particle Symmetric Improved Estimator . . . 139
D.2 Two-particle Symmetric Improved Estimator . . . 143

Bibliography **151**

Acknowledgments **179**

Curriculum Vitae **181**

Publication list and selected other work **183**
List of publications . . . 183
Collective modes in excitonic magnets [PRL 122, 127601 (2019)] . . . 185
Topotactic hydrogen [PRL 124, 166402 (2020)] . . . 191
AbinitioDΓA code paper [CPC 245, 106847 (2019)] . . . 199
Statistical error estimates [PRB 102, 085124 (2020)] . . . 219

Die approbierte gedruckte Originalversion dieser Dissertation ist an der TU Wien Bibliothek verfügbar.
The approved original version of this doctoral thesis is available in print at TU Wien Bibliothek.
TU Bibliothek WIEN Your knowledge hub

List of abbreviations

Abbreviation	Explanation
AFM	*Antiferromagnetic*
AIM	*Anderson impurity model*
ARPES	*Angular resolved photoemission spectroscopy*
BSE	*Boltzmann scattering equation*
BSE	*Bethe-Salpeter equation*
BZ	*Brillouin zone*
CDMFT	*Cellular DMFT*
CT-QMC	*Continuous-time quantum Monte Carlo*
CT-HYB	*CT-QMC in hybridization expansion*
CT-INT	*CT-QMC in interaction expansion*
DB	*Dual boson approach*
DCA	*Dynamical cluster approximation*
DE	*Dyson equation*
DF	*Dual fermion approach*
DFT	*Density functional theory*
DiagMC	*Diagrammatic Monte Carlo*
DIIS	*Direct inversion in iterative subspace*
DMFT	*Dynamical mean-field theory*
DOS	*Density of states*
DQMC	*Determinant quantum Monte Carlo*
DΓA	*Dynamical vertex approximation*
ED	*Exact diagonalization*
EOM	*Equation of motion*
FF	*Form factor*
FM	*Ferromagnetic*
fRG	*Functional renormalization group*
GF	*Green's function*
GGA	*Generalized gradient approximation*
GS	*Ground state*
HM	*Hubbard model*
IE	*Improved estimators*
KHM	*Kagome lattice Hubbard model*

Die approbierte gedruckte Originalversion dieser Dissertation ist an der TU Wien Bibliothek verfügbar.
The approved original version of this doctoral thesis is available in print at TU Wien Bibliothek.
TU Bibliothek WIEN Your knowledge hub

Abbreviation	Explanation
MaxEnt	*Maximum entropy method*
MC	*Monte Carlo*
MCMC	*Markov chain Monte Carlo*
MIT	*Metal-to-insulator transition*
NP	*Nondeterministic polynomial*
NRG	*Numerical renormalization group*
PA	*Parquet approximation*
p-DΓA	*Parquet DΓA*
PG	*Pseudogap*
QUADRILEX	*Quadruply irreducible local expansion*
QMC	*Quantum Monte Carlo*
sc-DΓA	*self-consistent ladder DΓA*
SDE	*Schwinger-Dyson equation of motion*
SEM	*Standard error of the mean*
SIE	*Symmetric improved estimators*
SVD	*Singular value decomposition*
TB	*Tight binding*
TPSC	*Two-particle self-consistent approach*
TRILEX	*Triply irreducible local expansion*
TUPS	*Truncated unity parquet solver*
1pGF	*One-particle Green's function*
2pGF	*Two-particle Green's function*

Die approbierte gedruckte Originalversion dieser Dissertation ist an der TU Wien Bibliothek verfügbar.
The approved original version of this doctoral thesis is available in print at TU Wien Bibliothek.
TU Bibliothek WIEN Your knowledge hub

Die approbierte gedruckte Originalversion dieser Dissertation ist an der TU Wien Bibliothek verfügbar.
The approved original version of this doctoral thesis is available in print at TU Wien Bibliothek.

Chapter 1

Introduction and outline

The rise of human civilization is closely connected to the utilization of materials by virtue of their properties (Smith, 1965a; b). Earliest attempts to find an explanation for their great variety date back to philosophers of ancient Greece, who proposed that everything consists of indivisibly small *atoms*. Although the ancient atomic hypothesis was not based on experimental evidence, there is a remarkable number of parallels to modern theories. However, it was subsequently disregarded for almost two millennials, and significant progress was only made in modern age, when chemists were able to trace back qualities of materials to their composition. While chemistry already provided the possibility to analyze the fractions in which the various components are contained in a substance, another crucial property of solids was still ignored: the way in which the atoms are arranged determines a large part of the material's macroscopic properties. With X-ray diffraction (Friedrich et al., 1912), a tool to unveil the structure of crystals was finally found in the beginning of the twentieth century.

At the same time quantum theory started to put materials science on rigorous mathematical foundations. Subsequently the key task was formulated as solving the Schrödinger equation for all electrons and nuclei in a crystal – unfortunately a vain endeavor. The main reason for the complete impossibility is rooted in the Coulomb interaction between the electrons. It makes the particles move not independently from each other but instead induces *correlations*. The essence of correlation is illustrated very well by Tolstoy (1869), albeit in a different context: The flow of history is not determined by the decisions of single leaders. Instead it emerges from the interaction of countless individuals that constantly influence each other by actions and reactions. Turning back to physics this means that, as one of the most distinguished condensed matter theoreticians formulated it, "the whole becomes not only more than but very different from the sum of its parts" (Anderson, 1972).

The struggle of physicists to find at least approximate solutions to the quantum mechanical many-body problem has been rewarded by considerable success. Most importantly, the density functional theory (DFT) (Hohenberg and Kohn, 1964; Kohn and Sham, 1965) describes the motion of one electron in a self-consistently determined background charge density. To a certain extent, this density incorporates effects of interaction and correlation. However, it fails to predict the behavior of *strongly* correlated electron systems, in which some of the most intriguing physical phenomena occur, such as Mott metal-insulator transitions (Mott, 1968) or high-temperature superconductivity (Bednorz and Müller, 1986).

Die approbierte gedruckte Originalversion dieser Dissertation ist an der TU Wien Bibliothek verfügbar.
The approved original version of this doctoral thesis is available in print at TU Wien Bibliothek.
TU Bibliothek WIEN Your knowledge hub

Outline. This thesis is concerned with computational methods for strongly correlated electron systems. These are often based on the Green's function formalism (Abrikosov et al., 1975). To enable an efficient numerical treatment we also make use of the Matsubara formalism (Matsubara, 1955) and work in the domain of imaginary time and frequency. However, this requires us to later make the transition back from imaginary to real frequencies in order to obtain physical properties. This procedure, commonly referred to as analytical continuation, is thus used at many points throughout this thesis, justifying a detailed discussion in **Chapter 2**.

Anderson (1961) first put forward a model to explain the formation of magnetic moments in metals with magnetic impurities. It comprises a bath of non-interacting electrons, modeling the conduction band of the host metal, and an impurity site with local interaction between electrons, modeling an impurity atom. The non-interacting bath-electrons are created (annihilated) by second-quantization operators $\hat{c}^\dagger$ ($\hat{c}$) and have a dispersion $\varepsilon_\sigma(\boldsymbol{k})$ for spin orientation σ and crystal momentum $\boldsymbol{k}$. The impurity electrons are created (annihilated) by operators $\hat{d}^\dagger$ ($\hat{d}$) and their repulsion is modeled by a parameter U. Importantly, the impurity and the bath are connected to each other via a hybridization term, where $V(\boldsymbol{k})$ is the hybridization amplitude. Altogether the Hamiltonian reads

$$H_{\mathrm{AIM}} = \sum_{\boldsymbol{k},\sigma} \varepsilon_\sigma(\boldsymbol{k})\hat{c}^\dagger_\sigma(\boldsymbol{k})\hat{c}_\sigma(\boldsymbol{k}) + \sum_{\boldsymbol{k},\sigma} \left(V(\boldsymbol{k})\hat{c}^\dagger_\sigma(\boldsymbol{k})\hat{d}_\sigma + \mathrm{h.c.}\right) + \sum_\sigma \tilde{\varepsilon}_\sigma \hat{d}^\dagger_\sigma \hat{d}_\sigma + U\hat{d}^\dagger_\uparrow \hat{d}^\dagger_\downarrow \hat{d}_\downarrow \hat{d}_\uparrow. \tag{1.1}$$

Through first-order perturbation theory it is possible to arrive at mean-field equations, that already permit a qualitative estimation of the conditions for local moment formation. However, the exact calculation of correlation functions requires somewhat more involved methods. In **Chapter 3** we will have a closer look at two such methods: exact diagonalization (ED), and continuous-time quantum Monte Carlo (CT-QMC). The former assumes a bath with discrete energy levels, whereas the latter can solve impurity problems with a continuous bath in a numerically exact fashion. Since it is a Monte Carlo method, CT-QMC results suffer from noise. In Chapter 3 of this thesis we derive new, symmetric improved estimators to mitigate this problem.

A model that is arguably even more fundamental than the Anderson impurity model is the Hubbard model for correlated electrons on a lattice (Hubbard, 1963). It is defined by a Hamiltonian

$$H_{\mathrm{HM}} = \sum_{ij\sigma} t_{ij\sigma}\hat{c}^\dagger_{i\sigma}\hat{c}_{j\sigma} + U\sum_i \hat{c}^\dagger_{i\uparrow}\hat{c}^\dagger_{i\downarrow}\hat{c}_{i\downarrow}\hat{c}_{i\uparrow} \tag{1.2}$$

that combines a tight-binding model with a local interaction similar as in the Anderson impurity model, but now on each lattice site. While the kinetic energy, parametrized by the hopping amplitude t_{ij} between sites i and j, is diagonal in momentum space, the interaction term proportional to U is local on each site. As a consequence the Hubbard model is capable of capturing effects such as a metal-to-insulator transition (Mott, 1968).

Chapter 4 introduces the dynamical mean-field theory (DMFT), which states that in the limit of infinite dimensions the Hubbard model becomes equivalent to the Anderson impurity model. For a physical two- or three-dimensional lattice, DMFT represents an approximation. Since the parameters of the Hubbard model can be inferred from *ab initio* calculations, and the effective Anderson impurity model can be solved numerically exactly, the DMFT provides a way to capture local correlation effects in lattice models for realistic crystals.

Die approbierte gedruckte Originalversion dieser Dissertation ist an der TU Wien Bibliothek verfügbar.
The approved original version of this doctoral thesis is available in print at TU Wien Bibliothek.
TU Bibliothek WIEN Your knowledge hub

However, the parameters of the effective impurity have to be obtained self-consistently by an iterative procedure. We therefore investigate the effect of symmetric improved estimators on the convergence, and make an attempt to reduce the number of required iterations by Anderson[1] acceleration (Anderson, 1965).

While the DMFT considers only correlations of electrons that are located on the same site, we go beyond this in **Chapter 5** by means of the dynamical vertex approximation (DΓA) (Toschi et al., 2007). There, two-particle correlations are still treated on a local level, but one obtains momentum-dependent one-particle correlation functions. In particular, we present a new, self-consistent approach to ladder-DΓA, and apply it to different systems: The one-orbital square lattice Hubbard model, a two-orbital model, and a realistic Wannier model for the material $SrVO_3$. Furthermore the Hubbard model is extensively studied on a kagome lattice, where we also compare to determinant quantum Monte Carlo (DQMC) (Blankenbecler et al., 1981).

Finally, the results of this thesis are recapitulated in **Chapter 6**.

Since the author has done work on different topics in the field, there is a separate chapter dedicated to each of the fields. Each of the chapters contains a brief review of established knowledge, and a more detailed description of what was contributed to the field by this thesis. Sections that describe the author's original research are marked by an asterisk (*). Some of the results have already been published in peer-reviewed journals. Therefore we provide a list of publications and preprints on p. 183. Four publications, on which the author of this thesis is a coauthor, and which are discussed only briefly, are reprinted thereafter.

[1]Note that the Anderson impurity model was introduced by the physicist Philip Warren Anderson, whereas the Anderson acceleration algorithm was named after the mathematician Donald Gordon Anderson.

Die approbierte gedruckte Originalversion dieser Dissertation ist an der TU Wien Bibliothek verfügbar.
The approved original version of this doctoral thesis is available in print at TU Wien Bibliothek.
TU Bibliothek WIEN Your knowledge hub

Die approbierte gedruckte Originalversion dieser Dissertation ist an der TU Wien Bibliothek verfügbar.
The approved original version of this doctoral thesis is available in print at TU Wien Bibliothek.
TU Bibliothek WIEN Your knowledge hub

Chapter 2

Green's functions and analytic continuation

2.1 Brief recapitulation of the Green's function formalism

2.1.1 Definition

The explicit calculation of the propagation of all electrons in a crystal is not only impossible, it is not even very much desirable. A popular alternative is the approach of many body Green's functions. There, one considers the propagation of an additional particle in a many-body system over a certain time span. The whole formalism relies on second quantization, where field operators $\hat{c}^{(\dagger)}(\boldsymbol{r}, t)$ annihilate (create) a particle at position $\boldsymbol{r}$ in space at time t.

We define the *retarded* Green's function for fermions as

$$G_R(\boldsymbol{r}', t'; \boldsymbol{r}, t) = -i\Theta(t - t')\langle\{\hat{c}(\boldsymbol{r}', t'), \hat{c}^\dagger(\boldsymbol{r}, t)\}\rangle. \tag{2.1}$$

Here, the step function $\Theta(t-t')$ is 0 for $t < t'$ and 1 for $t > t'$. The curly braces $\{A, B\} = AB+BA$ denote the anticommutator. For bosonic operators the commutator has to be used instead. Angular brackets $\langle\ldots\rangle$ denote the grand-canonical expectation value

$$\langle\mathcal{O}\rangle = \frac{1}{Z}\,\mathrm{Tr}\left[e^{-\frac{H-\mu N}{k_B T}}\mathcal{O}\right] \quad \text{with} \quad Z = \mathrm{Tr}\left[e^{-\frac{H-\mu N}{k_B T}}\right] \tag{2.2}$$

being the partition function. The Boltzmann constant k_B is set to unity throughout this thesis. H is the many-body Hamiltonian, N is the particle number operator, and μ the chemical potential. In the case of zero temperature ($T = 0$), the grand-canonical expectation value reduces to the ground-state expectation value.

When considering systems at finite temperature, it is convenient to perform a Wick rotation (Wick, 1954)

$$t \longrightarrow -i\tau \tag{2.3}$$

With this transformation we can go from real to imaginary time, and instead of the retarded Green's function we then obtain the *temperature* Green's function

$$G(\boldsymbol{r}', \tau'; \boldsymbol{r}, \tau) = -\langle\mathrm{T}\hat{c}(\boldsymbol{r}', \tau')\hat{c}^\dagger(\boldsymbol{r}, \tau)\rangle. \tag{2.4}$$

Die approbierte gedruckte Originalversion dieser Dissertation ist an der TU Wien Bibliothek verfügbar.
The approved original version of this doctoral thesis is available in print at TU Wien Bibliothek.
TU Bibliothek WIEN Your knowledge hub

In this definition we make use of the time-ordering operator $\mathbf{T}$ to ensure that the operators are ordered with increasing time arguments from right to left. It also includes a minus sign when exchanging two fermionic operators:

$$\mathbf{T}A(\tau)B(0) = \Theta(\tau)A(\tau)B(0) \pm \Theta(-\tau)B(0)A(\tau), \tag{2.5}$$

with a '+' for bosons and a '–' for fermions.

2.1.2 Spatial/momentum dependence

Since in this thesis spatial dependence is considered only in the context of periodic lattices, we can make two important simplifications: First, the creation operators can create particles only on a discrete set of points in space, and second, these points are the nodes of a periodic lattice with translational symmetry. Let us denote the coordinates of lattice point l as $\boldsymbol{r}_l$. We define the Fourier transformation of creation (annihilation) operators as

$$\hat{c}^{(\dagger)}(\boldsymbol{r}_l, \tau) = \frac{1}{\sqrt{N_k}} \sum_{\boldsymbol{k}}^{1.\,\mathrm{BZ}} e^{(-)i\boldsymbol{k}\cdot\boldsymbol{r}_l}\, \hat{c}^{(\dagger)}(\boldsymbol{k}, \tau) \tag{2.6}$$

$$\hat{c}^{(\dagger)}(\boldsymbol{k}, \tau) = \frac{1}{\sqrt{N_k}} \sum_{\boldsymbol{r}_l} e^{-(-)i\boldsymbol{k}\cdot\boldsymbol{r}_l}\, \hat{c}^{(\dagger)}(\boldsymbol{r}_l, \tau) \tag{2.7}$$

where N_k is the number of lattice sites, which is equal to the number of discrete values of the crystal momentum in the first Brillouin zone (1. BZ). Translation symmetry then allows us to write the Green's function with only one position or momentum argument,

$$G(\boldsymbol{r}_m, \tau'; \boldsymbol{r}_l, \tau) \equiv G(\boldsymbol{r}_m - \boldsymbol{r}_l; \tau', \tau) \tag{2.8}$$

$$G(\boldsymbol{k}', \tau'; \boldsymbol{k}, \tau) \equiv G(\boldsymbol{k}; \tau', \tau)\delta(\boldsymbol{k} - \boldsymbol{k}'), \tag{2.9}$$

and switching between real and momentum space is achieved by

$$G(\boldsymbol{r}_l; \tau', \tau) = \frac{1}{N_k} \sum_{\boldsymbol{k}}^{1.\,\mathrm{BZ}} e^{-i\boldsymbol{k}\cdot\boldsymbol{r}_l} G(\boldsymbol{k}; \tau', \tau) \tag{2.10}$$

$$G(\boldsymbol{k}; \tau', \tau) = \sum_{\boldsymbol{r}_l} e^{i\boldsymbol{k}\cdot\boldsymbol{r}_l} G(\boldsymbol{r}_l; \tau', \tau). \tag{2.11}$$

2.1.3 Time/frequency dependence

Let us now turn to the time or frequency dependence of the Green's function. In this thesis we consider only systems in equilibrium, such that the Hamiltonian does not explicitly depend on time. As a consequence, the time dependence of $G(\boldsymbol{k}; \tau, \tau')$ reduces to a dependence on the time difference of creation and annihilation operator. Thus we write

$$G(\boldsymbol{k}, \tau) \equiv G(\boldsymbol{k}; \tau, 0) \equiv G(\boldsymbol{k}; \tau + \tau', \tau'). \tag{2.12}$$

In Appendix A.1 we show that the imaginary time argument of the Green's function is restricted to the finite interval $[-\beta, \beta]$, on which it is (anti-)periodic with period β for bosons (fermions).

Die approbierte gedruckte Originalversion dieser Dissertation ist an der TU Wien Bibliothek verfügbar.
The approved original version of this doctoral thesis is available in print at TU Wien Bibliothek.
TU Bibliothek WIEN Your knowledge hub

The restriction to a finite time interval implies that Green's functions can be represented by Fourier series (with discrete frequencies), and the (anti-)periodicity additionally makes coefficients of odd (even) frequencies vanish. These so-called Matsubara frequencies (Matsubara, 1955) are

$$\omega_n^{\text{bos}} = \frac{2\pi}{\beta} n \tag{2.13}$$

$$\omega_n^{\text{ferm}} = \frac{\pi}{\beta}\big(2n+1\big), \tag{2.14}$$

with integer n. The Green's function in Matsubara frequencies is then

$$G(\boldsymbol{k}, \omega_n) = \int_0^\beta d\tau\, e^{i\omega_n \tau} G(\boldsymbol{k}, \tau), \tag{2.15}$$

where for bosonic/fermionic Green's function we have to use bosonic or fermionic Matsubara frequencies, respectively.

2.1.4 Analytic properties

In the following, we assume that the system is characterized by a Hamiltonian H with eigenstates $|m\rangle$ and corresponding eigenenergies ε_m. In favor of notational simplicity the term $-\mu N$ from Eq. (2.2) is absorbed in H, and momentum-dependence is not treated explicitly. Expressing the retarded Green's function $G_R(t) = -i\Theta(t)\langle\{\hat{c}(t), \hat{c}^\dagger(0)\}\rangle$ in the eigenbasis of H, we have

$$G_R(t) = \frac{-i\Theta(t)}{Z} \sum_{m,n} \left(e^{-\beta\varepsilon_m} + e^{-\beta\varepsilon_n}\right) e^{i(\varepsilon_m - \varepsilon_n)t} |\langle m|\hat{c}|n\rangle|^2. \tag{2.16}$$

We can go from time to frequency domain by a Fourier transformation

$$G_R(\omega) = \int_{-\infty}^{\infty} dt\, e^{i\omega t} G_R(t) = \frac{1}{Z} \sum_{mn} |\langle m|\hat{c}|n\rangle|^2 \frac{e^{-\beta\varepsilon_m} + e^{-\beta\varepsilon_n}}{\omega + i0^+ + \varepsilon_m - \varepsilon_n}. \tag{2.17}$$

In the same way, also the Matsubara Green's function Eq. (2.4) can be expressed:

$$G(i\omega_j) = \frac{1}{Z} \sum_{mn} |\langle m|\hat{c}|n\rangle|^2 \frac{e^{-\beta\varepsilon_m} + e^{-\beta\varepsilon_n}}{i\omega_j + \varepsilon_m - \varepsilon_n}. \tag{2.18}$$

Apparently, the Green's function at complex frequency z can be expressed as a convolution

$$G(z) = \int_{-\infty}^{\infty} d\omega' \frac{A(\omega')}{z - \omega'}, \tag{2.19}$$

where $A(\omega)$ is the *spectral density*

$$A(\omega) = \frac{1}{Z} \sum_{m,n} \left(e^{-\beta\varepsilon_m} + e^{-\beta\varepsilon_n}\right) |\langle m|\hat{c}|n\rangle|^2 \delta\big(\omega - (\varepsilon_n - \varepsilon_m)\big). \tag{2.20}$$

Die approbierte gedruckte Originalversion dieser Dissertation ist an der TU Wien Bibliothek verfügbar.
The approved original version of this doctoral thesis is available in print at TU Wien Bibliothek.
TU Bibliothek WIEN Your knowledge hub

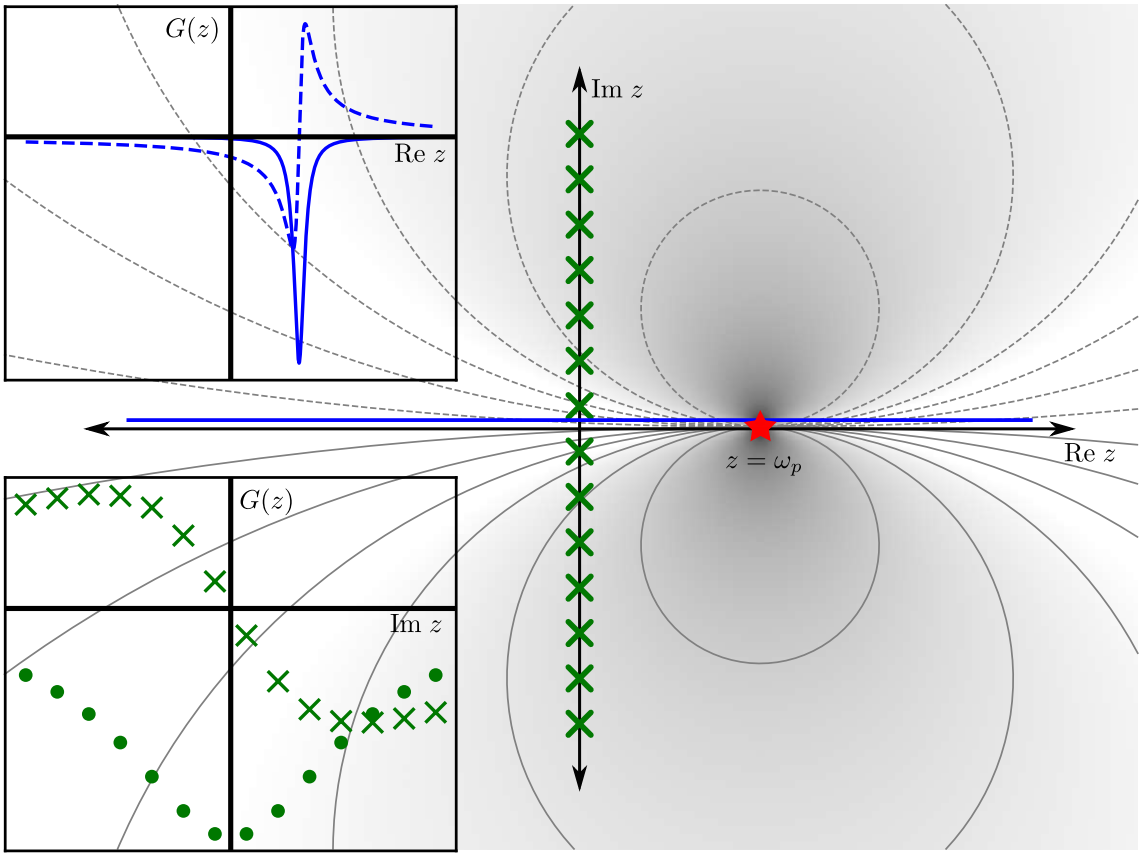

Figure 2.1: Simple one-pole Green's function $G(z) = 1/(z - \omega_p)$ on the complex plane. The background density/contours show only the imaginary part. The pole location ω_p is marked by a red asterisk. The inset in the upper left shows the retarded Green's function (evaluated along the blue line on the complex plane), where the full line is the imaginary part and the dashed line is the real part. Clearly, the imaginary part of the retarded Green's function has a peak at $\omega = \omega_p$. The inset in the lower left shows the Matsubara Green's function (evaluated at the green crosses on the complex plane). Its real and imaginary part are drawn by dots and crosses, respectively.

By evaluating Eq. (2.19) at Matsubara frequencies $z = i\omega_n$, we get the Matsubara Green's function, and at $z = \omega + i0^+$ we get the retarded Green's function, as depicted in Fig. 2.1. By applying the Sokhotski-Plemelj theorem (often called Weierstrass formula)

$$\lim_{\epsilon\to 0^+} \int_{-\infty}^{\infty} dx \, \frac{f(x)}{x + i\epsilon} = -i\pi f(0) + \mathcal{P} \int_{-\infty}^{\infty} dx \, \frac{f(x)}{x} \tag{2.21}$$

we obtain the important relation

$$A(\omega) = -\frac{1}{\pi}\mathrm{Im}G_R(\omega) = -\frac{1}{\pi}\mathrm{Im}G(\omega + i0^+). \tag{2.22}$$

2.2 Pade interpolation

In Section 2.1.4 we have seen that the Matsubara Green's function is connected to the spectral density through the integral relation Eq. (2.19). Since the spectral density contains valuable

Die approbierte gedruckte Originalversion dieser Dissertation ist an der TU Wien Bibliothek verfügbar.
The approved original version of this doctoral thesis is available in print at TU Wien Bibliothek.
TU Bibliothek WIEN Your knowledge hub

information, it is of interest to extract the spectral density from the Matsubara Green's function.

If the Green's function is given analytically, one may just substitute $i\omega_n$ by $\omega + i0^+$. Considering that in most calculations the Green's function is evaluated only numerically, a different approach is required.

A logical next step is to approximate the numerical values of the Green's function by an analytical function, which can be evaluated on the real axis through substitution as above. This is realized in the technique of Pade approximants (Press et al., 2007), where a given set of data points is interpolated by a rational function. An efficient algorithm, designed for Green's functions, was put forward already by Vidberg and Serene (1977). Although frequently called a fit, the Pade approximation is thus actually an interpolation of given data.

Vidberg and Serene (1977) show that using Pade approximants for analytic continuation works remarkably well. They however also discuss a major drawback of the method. Namely, it is by no means clear *a priori*, which Matsubara frequencies should be selected for constructing the interpolation. Instead they propose to compare several Pade approximants, where different sets of Matsubara frequencies are used.

Another problem in the construction of Pade approximants arises, when the data points on the imaginary axis are subject to stochastic uncertainty or noise. It is then impossible to still interpolate these points by a rational function without poles in the upper half-plane.

In Fig. 2.2 we illustrate this behavior by taking a simple test function with four poles. We evaluate it on a set of Matsubara frequencies and generate four test data sets with additional noise by adding random numbers from a normal distribution with four different standard deviations on different orders of magnitude. The Pade approximant constructed from the exact data perfectly reproduces the original function, its poles coincide with the true poles of the analytic function. Adding noise of magnitude 10^{-9} just slightly shifts some of the poles, leaving the resulting spectral function practically unchanged. Noise of magnitude 10^{-6} already has a much more drastic effect. Pairs of almost canceling poles and zeros appear on the upper half plane, which is necessary for interpolation of the noisy test data. Further increasing the standard deviation of the noise to 10^{-3}, a value that is by no means uncommon in actual numerical calculations, increases the number of pole-zero pairs and the spectral function is already somewhat deteriorated.

2.3 Probabilistic approach - Maximum Entropy

2.3.1 Formulation of the analytic continuation problem

To a large extent, the computational methods that were used in this thesis rely on Monte Carlo integration, such that the results always contain some uncertainty. Although we have shown above that the Pade approximation can yield good results even in the case of noisy data, it is difficult to assess their quality in real-world cases, where the exact solution is unknown. The interpolation treats data with random noise as if they were exact, and thus also the deviation of the spectral function from the true underlying spectral function has an element of arbitrariness.

For this reason, most methods for analytic continuation do not try to construct an exactly

Die approbierte gedruckte Originalversion dieser Dissertation ist an der TU Wien Bibliothek verfügbar.
The approved original version of this doctoral thesis is available in print at TU Wien Bibliothek.
TU Bibliothek WIEN Your knowledge hub

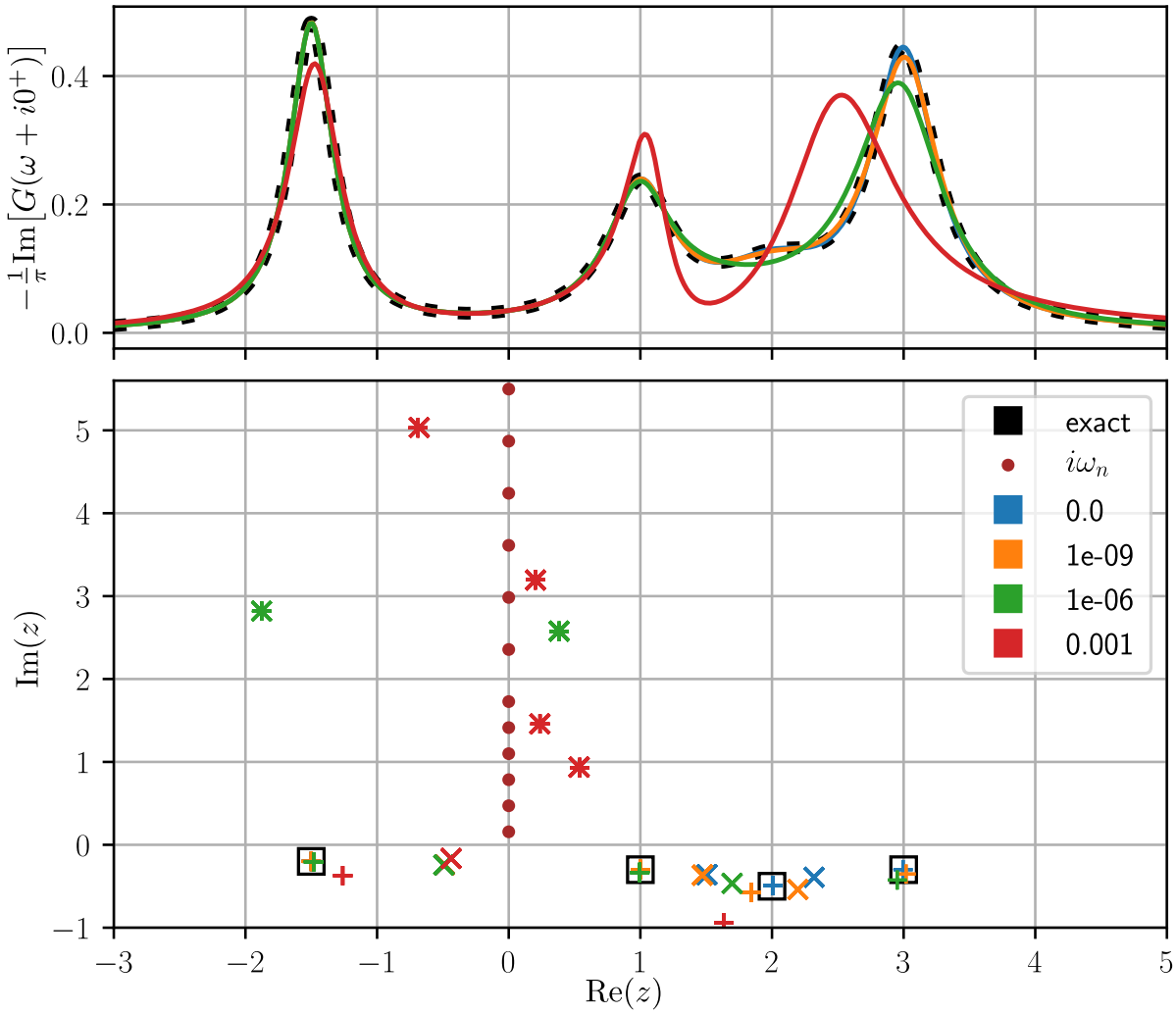

Figure 2.2: Pade approximation for a test function with four poles (black squares). The Matsubara frequencies used to construct the approximant are marked by dots. Reconstructed poles and zeros are marked by + and × symbols, respectively.

interpolating analytic function. Instead, one tries to answer the following question: Assume that N normal-distributed data G_n have been measured with corresponding uncertainty σ_n. Given a linear relation like Eq. (2.19) between the spectral function $A(\omega)$ and G_n,

$$G_n = \int_{-\infty}^{\infty} d\omega\, K(i\omega_n, \omega)\, A(\omega) \qquad \text{or} \qquad G = KA, \tag{2.23}$$

what is the most probable spectral function $A(\omega)$ that fits the data? One can immediately write down the probability for measuring G if the spectral function is $A(\omega)$:

$$\Pr[G|A] = \frac{(2\pi)^{-N/2}}{\prod_i \sigma_i} \exp\Big[-\sum_i \frac{(G_i - KA)^2}{2\sigma_i^2}\Big] \tag{2.24}$$

The maximum likelihood method [cf., e.g., Press et al. (2007)] is based on the assumption that this is numerically equivalent to the probability of A being the true spectral function, after G

Die approbierte gedruckte Originalversion dieser Dissertation ist an der TU Wien Bibliothek verfügbar.
The approved original version of this doctoral thesis is available in print at TU Wien Bibliothek.
TU Bibliothek WIEN Your knowledge hub

has been measured:

$$\Pr[A|G] = \Pr[G|A]. \tag{2.25}$$

Then, the most probable spectral function is the one that maximizes the exponent of Eq. (2.24), or in other words, minimizes the merit function χ^2

$$\chi^2[A] = \sum_{n=1}^{N} \frac{[G_n - \int d\omega\, K(i\nu_n, \omega)\, A(\omega)]^2}{\sigma_n^2}. \tag{2.26}$$

This is a general least squares problem (Press et al., 2007). Let us for further analysis discretize the integral,

$$\int d\omega\, K(i\nu_n, \omega)\, A(\omega) \approx \sum_k K(i\nu_n, \omega_k) A(\omega_k) \Delta\omega_k. \tag{2.27}$$

Only for the sake of demonstration, assume that the measurement uncertainty σ_n is constant for all n and the discretization of ω is uniform, $\Delta\omega_k = \Delta\omega$. In this case the least squares problem is reduced to the following set of linear equations:

$$0 = G_n - \sum_k K_{nk} A_k \Delta\omega. \tag{2.28}$$

Hence, the kernel determines the "hardness" of the problem and it is justified to have a closer look at its properties.

2.3.2 Properties of the kernel

The kernel that relates spectral functions to Green's functions in Matsubara frequencies is

$$K(i\nu_n, \omega) = \frac{1}{i\nu_n - \omega}. \tag{2.29}$$

Here, ω is a frequency on the real axis and $i\nu_n$ are (fermionic or bosonic) Matsubara frequencies. The properties of the kernel are best understood by first discretizing the real-frequency axis, such that the kernel becomes a matrix $K_{jk} = K(i\nu_j, \omega_k)$. It is however not a quadratic matrix, since the number of real frequencies has to be large enough to resolve all features of the spectral function, and the number of Matsubara frequencies has to be large enough to reach the asymptotic region. These criteria are mutually independent and thus it would not be justified to choose the kernel to be a quadratic matrix.

A singular-value decomposition can be readily performed also for general non-quadratic matrices:

$$K_{jk} = \sum_m U_{jm} \xi_m V_{km}, \tag{2.30}$$

where U and V are column-orthogonal matrices and ξ is the vector of singular values. In Fig. 2.3 the imaginary part of the matrix V^T is shown, together with the singular values. The columns of V can be understood as basis functions for the spectral function (Shinaoka et al., 2017b). The contribution of the m-th component of the spectral function in this basis to the Matsubara data is then weighted by the m-th singular value. Since only few singular values are of significant size, the problem of minimizing χ^2 in Eq. (2.26) is ill-conditioned and there is a large space of degenerate solutions.

Die approbierte gedruckte Originalversion dieser Dissertation ist an der TU Wien Bibliothek verfügbar.
The approved original version of this doctoral thesis is available in print at TU Wien Bibliothek.
TU Bibliothek WIEN Your knowledge hub

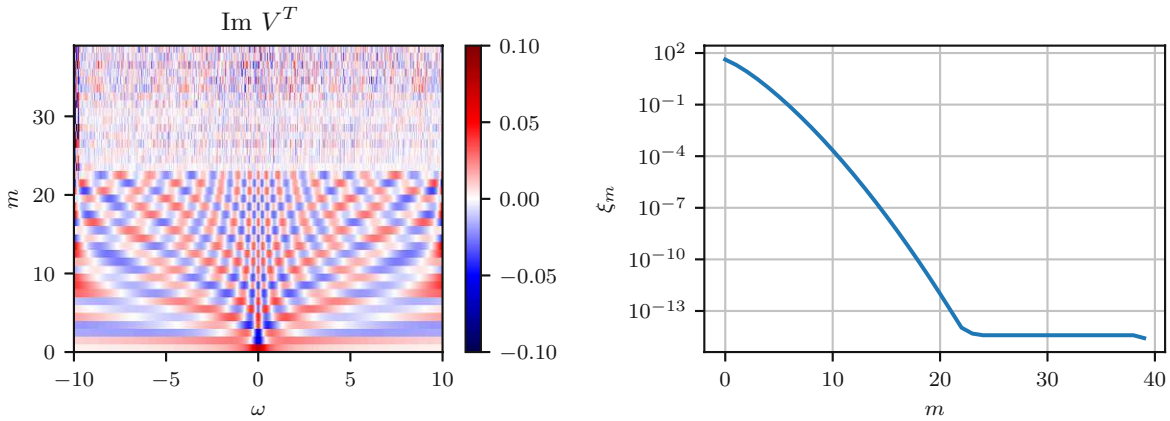

Figure 2.3: Singular-value decomposition of the kernel for the analytic continuation [Eq. (2.30)]. Left panel: matrix of right singular vectors V, right panel: log-plot of the singular values ξ.

2.3.3 Regularization term or prior probability

If there are many completely different solutions to the problem, this may mean that we do not have enough information to actually solve the problem. It may however also mean that we do not use all our knowledge about the problem in the right way. Our inference has to make use of all available information, and this can be done by means of Bayes' theorem

$$\Pr[A|G] = \frac{\Pr[A]\,\Pr[G|A]}{\Pr[G]}, \tag{2.31}$$

where we want to find the spectral function A (hypothesis) that maximizes the conditional or posterior probability $\Pr[A|G]$ of the hypothesis being true if data G have been measured. The likelihood function $\Pr[G|A]$ has already been defined in Eq. (2.24). Additionally, with $\Pr[A]$ and $\Pr[G]$ we now have the prior probabilities of the hypothesis and the data, respectively. Eq. (2.31) is much richer compared to Eq. (2.25) and there is hope that with Bayesian statistics we get better results than with the maximum likelihood method. However, we first have to model the prior probability of a spectral function, $\Pr[A]$. This modeling is not univocal (Press et al., 2007), but a highly successful and state of the art choice of the entropic prior is

$$\Pr[A] \propto e^{\alpha S[A]} \tag{2.32}$$

with the entropy

$$S[A] = \int d\omega \left[A(\omega) - D(\omega) - A(\omega) \log \frac{A(\omega)}{D(\omega)} \right] \tag{2.33}$$

relative to a default model $D(\omega)$, which leads to the maximum entropy method (MaxEnt). The concept of entropy was introduced into information theory by Shannon (1948), and Jaynes (1957) established the principle of maximum entropy as "a method of reasoning" in statistical mechanics. Very successfully the maximum entropy method was employed for deconvolution of optical data (Frieden, 1972; Gull and Daniell, 1978). After further developments and applications to image processing (Gull and Skilling, 1984), it was also applied to the analytical continuation problem (Silver et al., 1990b; a; Jarrell and Gubernatis, 1996).

Die approbierte gedruckte Originalversion dieser Dissertation ist an der TU Wien Bibliothek verfügbar.
The approved original version of this doctoral thesis is available in print at TU Wien Bibliothek.
TU Bibliothek WIEN Your knowledge hub

Combining Eq. (2.31) with Eq. (2.24), Eq. (2.32), and Eq. (2.33), we have to maximize the probability

$$\Pr[A|G] = \frac{1}{\Pr[G]} e^{-Q_\alpha[A]}, \tag{2.34}$$

where

$$Q_\alpha[A] = \frac{1}{2}\chi^2[A] - \alpha S[A] \tag{2.35}$$

with a yet unspecified scale parameter $\alpha > 0$. The prior probability of the data, $\Pr[G]$, also referred to as evidence, does not depend on the spectral function. In our considerations we can therefore absorb it into the normalization of $\Pr[A|G]$.

Instead of the least-squares problem of Eq. (2.26) we now face the minimization of the functional $Q_\alpha[A]$. The entropy, which was introduced as the prior probability of the spectral function, now serves as a regularization term to the ill-conditioned least-squares problem. This becomes apparent by looking at the Hessian matrix of Q with respect to A,

$$\frac{\partial^2 Q_\alpha}{\partial A_l \, \partial A_m} = \sum_n \frac{K_{nl}\Delta\omega_l \, K_{nm}\Delta\omega_m}{\sigma_n^2} + \alpha\delta_{lm}\frac{\Delta\omega_l}{A_l}, \tag{2.36}$$

which was computed by choosing a discretization of the real-frequency axis and deriving by the value of the spectral function at these discrete points. The first term of Eq. (2.36) contains a product $K^T K$, thus its conditioning is even worse than that of K: most of its eigenvalues are practically zero. However, the second term of Eq. (2.36) adds a positive diagonal matrix, scaled by α. This has the effect of increasing the eigenvalues, i. e. the curvature of Q at its minimum, and thus makes it easier to actually locate the minimum.

Let us note that, instead of the entropy, one may also choose a different regularization term. Otsuki et al. (2017) introduced the so-called sparse modeling technique, where solutions are prioritized if they are sparse in the singular space of the kernel. An implicit regularization effect can be achieved in stochastic sampling methods (Sandvik, 1998; Mishchenko et al., 2000; Nordström et al., 2016; Ghanem and Koch, 2020).

2.4* Technical aspects of the Maximum Entropy method

2.4.1 Choice of α

Having seen that the functional $Q_\alpha[A]$ can be minimized for $\alpha > 0$, we now have to determine how to actually choose a good value of α. The importance of this choice is illustrated in Fig. 2.4. We choose the asymmetric two-peak spectrum that is shown as a black curve in the right panel. By Eq. (2.29) it is transformed to Matsubara frequencies and noise with an amplitude of 10^{-4} is added. Assuming a flat default model, we calculate the spectral function $A(\omega)$ that minimizes Eq. (2.35) for a large range of different values of α. The influence of α is shown as a density plot in the top left panel of Fig. 2.4. At very high values of α, we recover the constant default model, no influence of the data can be noticed. As α is decreased, the spectral weight concentrates in the middle, then we observe the formation of two distinct peaks. At small values of α, the peaks split and in the end we get six very sharp peaks instead of two broad ones. Since apparently the result of the analytic continuation is to a large extent controlled

Die approbierte gedruckte Originalversion dieser Dissertation ist an der TU Wien Bibliothek verfügbar.
The approved original version of this doctoral thesis is available in print at TU Wien Bibliothek.
TU Bibliothek WIEN Your knowledge hub

by α, it is extremely important to choose it in a reasonable and automatizable way. Various approaches have been proposed in order to tackle this problem.

In so-called *historic* MaxEnt, α was chosen in a way that the χ^2-deviation (Eq. (2.26)) is approximately equal to the number of data points on the imaginary axis (Gull, 1989). It was however found to under-fit the data and Gull (1989) and Skilling (1989) argue that it is somewhat *ad hoc*.

The *classic* MaxEnt extends the Bayesian inference scheme to α and D (Skilling, 1989; Jarrell and Gubernatis, 1996):

$$\Pr[A, \alpha|G, D] \propto \Pr[A|G, D, \alpha]\Pr[\alpha] \propto \frac{e^{-Q_\alpha[A]}}{\alpha}, \tag{2.37}$$

where the scale invariant Jeffreys' prior $1/\alpha$ (Jeffreys, 1939) was used for the prior probability of α. Subsequently, the dependence on the spectral function in Eq. (2.37) is integrated out and one obtains an explicit form for $\Pr[\alpha|G, D]$. In the bottom left panel of Fig. 2.4 the logarithm of the posterior probability $\Pr[\alpha|G, D]$ is shown as an orange curve. Classic MaxEnt takes the spectral function at the most probable value of α to be the best solution to the problem. This value is usually obtained by setting $\partial\Pr[\alpha|G, D]/\partial\alpha = 0$, which can be analytically transformed to an equation $N_g = -2\alpha S$ after a few approximations. N_g is called the "number of good measurements", for its definition we refer to Jarrell and Gubernatis (1996). In the bottom left panel of Fig. 2.4 we plot $-N_g/2\alpha S$ as a blue line; its intersection with 1 is the classic MaxEnt solution, marked by a blue vertical line. The corresponding spectrum is shown in the right panel.

Closely related is *Bryan's method* (Bryan, 1990), where one takes the average over all values of α, weighted by the probability:

$$A(\omega) = \int d\alpha\, A(\alpha, \omega)\, \Pr[\alpha|G, D] \tag{2.38}$$

The results are usually very close to classic MaxEnt, since the probability of α is sharply peaked, see the blue and orange dashed lines in Fig. 2.4. As one can clearly see, the solutions of classic and Bryan's MaxEnt may lead to unphysical extra peaks — a drawback already noticed by Gull (1989).

However, there is yet another approach to the decision of the best α. It is based on the so-called L-curve criterion (Lawson and Hanson, 1974; 1995), but in the context of MaxEnt, it was to our knowledge first proposed and explained by Bergeron and Tremblay (2016) and in the following also applied by Kraberger et al. (2017). It is somewhat more heuristic than classic or Bryan's MaxEnt in that it relies only on the behavior of χ^2 (like historic MaxEnt). For apprehending this approach, we plot χ^2 as a green curve in the lower left panel of Fig. 2.4. In the limit of $\alpha \longrightarrow \infty$ it goes to a constant high value, and for $\alpha \longrightarrow 0$ another constant of lower value is approached. Following the reasoning of Bergeron and Tremblay (2016), there is a clear interpretation for this behavior. In the high-α limit, the (large) χ^2-deviation has negligible weight, such that the default model D minimizes $Q_\alpha[A]$. What we see is thus $\chi^2[A = D]$. On the other hand, in the low-α limit, the contribution of the entropy is reduced to enforcing positivity of the spectrum; and χ^2 slowly approaches its global minimum. The low-α region, where χ^2 is relatively flat, and the subsequent region with steep increase of χ^2, are coined *noise-fitting* and

Die approbierte gedruckte Originalversion dieser Dissertation ist an der TU Wien Bibliothek verfügbar.
The approved original version of this doctoral thesis is available in print at TU Wien Bibliothek.
TU Bibliothek WIEN Your knowledge hub

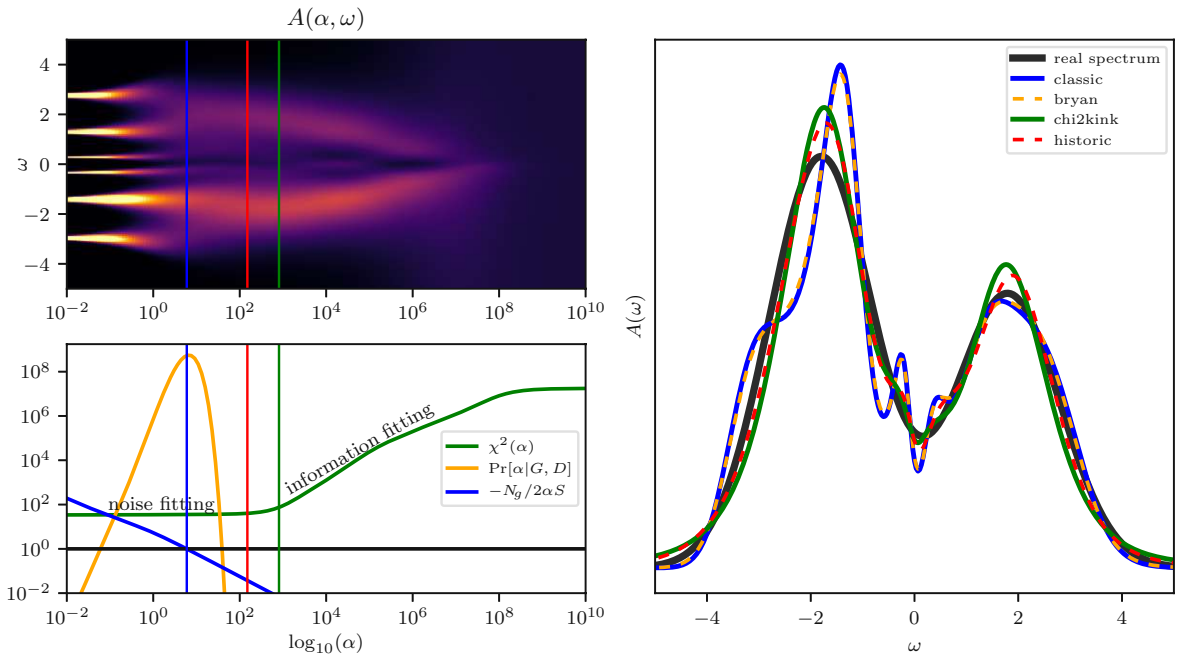

Figure 2.4: Methods for determining α. A model spectrum (black curve in the right panel) is transformed to Matsubara frequencies and noise is added. The MaxEnt functional Q is minimized for various values of α (upper left panel). The lower left panel illustrates the four different methods of determining the optimal value of α, where the red and blue vertical lines mark historic and classic MaxEnt, respectively. The value of α obtained by the "chi2kink" method is marked by a green vertical line. Note that Bryan's method can not be highlighted in such a way since it is a weighted average over a range of α. (The probability that serves as a weight is however drawn in orange.)

information-fitting regions (Bergeron and Tremblay, 2016). The optimal value of α is situated in the transition region between information fitting and noise fitting, where $\log\chi^2(\log\alpha)$ has a kink. We therefore call this method to determine α "chi2kink". This optimal α is indicated by a maximum in the curvature $\chi''(\alpha)$ (Bergeron and Tremblay, 2016; Kraberger et al., 2017). A more numerically stable and flexible approach is to fit a function

$$\phi(x; a, b, c, d) = a + \frac{b}{1 + e^{-d(x-c)}} \tag{2.39}$$

to several values of $\log_{10}\chi^2(\log_{10}\alpha)$. The curvature of ϕ in Eq. (2.39) is maximal at $x = c - \ln(2 + \sqrt{3})/d \approx c - 1.317/d$. Since this usually leads to strong underfitting, we suggest to use a more general $x = c - f/d$ or $\alpha = 10^{c-f/d}$, with preferred values of $f \in [2, 2.5]$. In Fig. 2.4 the value corresponding to $f = 2$ is marked by green vertical lines.

In summary, historic MaxEnt seems to underfit only with respect to classic MaxEnt, since the latter tends to grave overfitting. Bergeron and Tremblay (2016) note that the formula for the posterior probability of α is an approximation that works well only when a good default model is used.

In order to get good results with classic MaxEnt, it has therefore become common practice to increase the standard deviation σ_n by a manually chosen factor to shift the peak in the probability to a larger value of α. Since the rescaling factor is not known *a priori* (although a

Die approbierte gedruckte Originalversion dieser Dissertation ist an der TU Wien Bibliothek verfügbar.
The approved original version of this doctoral thesis is available in print at TU Wien Bibliothek.
TU Bibliothek WIEN Your knowledge hub

dependence on the actual noise amplitude is noticed), this procedure introduces an additional degree of arbitrariness.

Determining the optimal α as the point where noise-fitting starts and information fitting ends ("chi2kink") leads to considerably larger values of α, even with respect to historic MaxEnt. Despite the drawback of not being "Bayesian", it does not rely on approximations and the noise amplitude of the data has to be known only up to a constant prefactor. The only remaining source of arbitrariness is the parameter f mentioned above, which controls the actual value of α to be accepted. It is however restricted to a rather narrow range, whereas the error rescaling factor in classic MaxEnt can vary by several orders of magnitude.

At least in the present context of analytic continuation, we are therefore convinced that the best method of determining α is extracting it as the border between noise- and information-fitting.

2.4.2 Elimination of unphysical features: Preblur

Even though we are now able to find the "best" value of α, the spectrum corresponding to it may show some undesirable artifacts. In the right panel of Fig. 2.4 we can see that all solutions have an enlarged curvature around $\omega = 0$ and side peaks emerge with lowering α. An analogous tendency was observed already in the original application of MaxEnt in image processing, where it manifested itself in huge peaks in the intensity distribution. In order to address this problem, Skilling showed that the entropy does not have to be evaluated from the spectral function directly, but from a "hidden" function $h(\omega)$ that is related to the spectral function in a linear way (Skilling, 1991)

$$A = \Omega h. \tag{2.40}$$

In standard MaxEnt, Ω is just unity. Although initially requiring Ω to be an orthogonal matrix, Skilling (1991) subsequently assumed a Gaussian convolution $A = g_b * h$ with great success and named the technique "preblur". In the latter case, Ω is a matrix that contains a Gaussian function $g_b(\omega) = \exp[-\omega^2/2b^2]/\sqrt{2\pi}b$ in each row, i.e. $\Omega_{ij} = g_b(\omega_i - \omega'_j)$. In the context of analytic continuation, preblur was introduced by Kraberger et al. (2017), although already Sandvik (1998) uses a somewhat similar smoothing algorithm.

The functional of Eq. (2.35), which we have to minimize, thus becomes

$$Q_{\alpha b}[h] = \frac{1}{2}\chi^2[g_b * h] - \alpha S[h]. \tag{2.41}$$

There we now have, after α, a second hyperparameter b that controls the width of the Gaussian g.

Let us now have a closer look at the χ^2-term of Eq. (2.41). It sums up the difference of the

Die approbierte gedruckte Originalversion dieser Dissertation ist an der TU Wien Bibliothek verfügbar.
The approved original version of this doctoral thesis is available in print at TU Wien Bibliothek.
TU Bibliothek WIEN Your knowledge hub

fit "KA" to the data G. Explicitly the fit function is now

$$\begin{aligned} KA &\equiv \int_{-\infty}^{\infty} d\omega\, K(i\nu_n, \omega)\, A(\omega) \\ &= \int_{-\infty}^{\infty} d\omega\, K(i\nu_n, \omega) \int_{-\infty}^{\infty} d\omega'\, g_b(\omega - \omega')\, h(\omega') \\ &= \int_{-\infty}^{\infty} d\omega \Big[\int_{-\infty}^{\infty} d\omega'\, K(i\nu_n, \omega')\, g_b(\omega - \omega') \Big] h(\omega) \\ &\equiv \tilde{K} h. \end{aligned} \tag{2.42}$$

This means that the hidden spectral function is related to the Matsubara Green's function in a similar way as the spectral function, the only difference being a "blurred" kernel $\tilde{K}$. Therefore, preblur is realized by minimizing the functional Q with a slightly modified kernel, which then yields the hidden spectral function h. The spectral function A itself is subsequently obtained by convolution of h with the same Gaussian $g_b(\omega)$ as above.

Although the minimization of Q itself does not become more difficult by introducing preblur, we now face the problem that the blur width b is not known *a priori*, similar as the entropy-scaling parameter α. However, knowing that we can determine a good value for α by analyzing $\chi^2(\alpha)$, it is now worth to analyze the χ^2-deviation as a function of both α and b. This is done in the upper left panel of Fig. 2.5. Over a large range of b, χ^2 depends only on α. Only after a sharp border (at $b \approx 1$ in our example) the χ^2-deviation increases steeply with b, which can be seen best in the lower left panel of Fig. 2.5. In other words, increasing b up to a certain value does not change the quality of the fit (but potentially the result.) Only afterwards it is suddenly impossible to get a good fit. A heuristic explanation of this is that convolving the kernel with a Gaussian permits only peaks with a minimal width of $2b$ in the spectrum. Once this exceeds the "real" width of one of the peaks in the spectrum, a fit becomes impossible. This observation is corroborated by the fact that we find the maximal permissive b to be close to 1 in Fig. 2.5, and the actual spectrum (black curve) consists of two Gaussians with standard deviation 1.

The observations made in the upper left panel of Fig. 2.5 can be used to propose the following algorithm for the determination of the hyperparameters: Determine the optimal α for different values of b, starting from 0 and increasing. Accept the last value of b, where χ^2 at the optimal α is smaller than, e. g., 1.5 times χ^2 at the optimal α for $b = 0$. The optimal values of α are marked as a red dashed line in the upper left panel of Fig. 2.5, and the thus determined (α, b) is marked by a red asterisk. Since the optimal values of α hardly change in the reasonable range for b, we may simplify the algorithm: Determine the optimal α for $b = 0$, then increase b, keeping always the same α. If χ^2 exceeds, e. g., 1.5 times its value at $b = 0$, accept the last value of b before this as the best value. The corresponding (α, b) is marked in Fig. 2.5 by a green asterisk.

As we can see in the upper right panel, the corresponding red and green curves obtained by analytical continuation with these two (α, b) are practically indistinguishable. In the lower right panel, the differences of these reconstructed spectra are plotted and show that the deviation from the actual result is now satisfactorily small.

Die approbierte gedruckte Originalversion dieser Dissertation ist an der TU Wien Bibliothek verfügbar.
The approved original version of this doctoral thesis is available in print at TU Wien Bibliothek.
TU Bibliothek WIEN Your knowledge hub

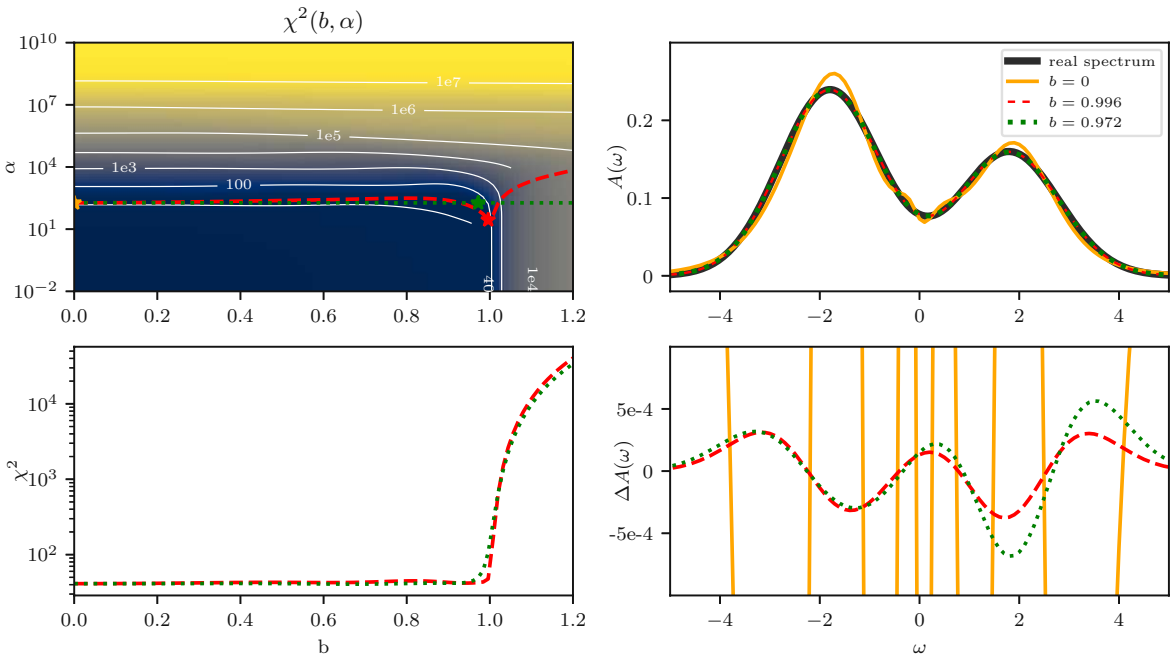

Figure 2.5: Analyzing the preblur-parameter b. Upper left panel: χ^2-deviation of the fit for hyperparameters (b, α). The red dashed line marks the optimal α at each b, the green dotted line shows the optimal α at $b = 0$ for comparison. Lower left panel: χ^2 along the red dashed and green dotted lines in the upper left panel. Upper right panel: The true spectral function (black), and its MaxEnt reconstructions at the points marked by orange, red and green asterisks in the upper left panel, drawn in the respective colors. The lower right panel shows the differences of these reconstructions to the true spectrum. The orange $\Delta A(\omega)$ (corresponding to $b = 0$) is as large as 10^{-2}.

2.4.3 MaxEnt for offdiagonal elements

This subsection is based on the supplementary material of Geffroy et al. (2019), where the respective section was written solely by the author of this thesis.

The considerations above were done for positive definite spectral function with a finite norm $\int d\omega A(\omega) > 0$. This property is fulfilled by diagonal elements of correlation functions. In some cases it is however necessary to do an analytical continuation of offdiagonal elements, which have zero norm $\int d\omega A(\omega) = 0$, as a direct consequence of the fermionic anticommutation relation. A vanishing norm is not consistent with a positive definite function, thus the spectral function cannot have a definite sign for offdiagonal elements. Clearly the definition of the entropy, Eq. (2.33), has to be adapted to this new circumstance (Kraberger et al., 2017). At this point, let us mention that the kernel $K(i\omega_n, \omega)$ is the same for diagonal and offdiagonal elements.

Let us, for offdiagonal components, write the spectrum as

$$A(\omega) = A^+(\omega) - A^-(\omega), \tag{2.43}$$

Die approbierte gedruckte Originalversion dieser Dissertation ist an der TU Wien Bibliothek verfügbar.
The approved original version of this doctoral thesis is available in print at TU Wien Bibliothek.
TU Bibliothek WIEN Your knowledge hub

where both A^+ and A^- are positive definite and have the same norm. Then we can write the entropy as[1]

$$S[A^+, A^-] = \int d\omega \Big[A^+(\omega) - D(\omega) - A^+(\omega) \log \frac{A^+(\omega)}{D(\omega)} + A^-(\omega) - D(\omega) - A^-(\omega) \log \frac{A^-(\omega)}{D(\omega)} \Big] \tag{2.44}$$

Instead of treating A^+, A^- and A as completely independent, we can use Eq. (2.43) to eliminate A^- and write

$$Q_\alpha[A, A^+] = \frac{1}{2}\chi^2[A] - \alpha S[A, A^+]. \tag{2.45}$$

Since we are searching for a minimum of Q with respect to both A and A^+, we can use

$$\frac{\partial Q_\alpha[A, A^+]}{\partial A^+} = -\alpha \frac{\partial S[A, A^+]}{\partial A^+} = 0 \tag{2.46}$$

to eliminate also A^+. Thus, A^+ and A^-, expressed by A, are

$$A^\pm[A] = \frac{\sqrt{A^2 + 4D^2} \pm A}{2}. \tag{2.47}$$

Inserting this in Eq. (2.44), we arrive at the so-called *positive-negative entropy*

$$S[A] = \int d\omega\, A(\omega) \log \frac{A^+[A](\omega)}{D(\omega)}. \tag{2.48}$$

As a reasonable choice for the default model, Kraberger et al. (2017) propose to include the diagonal elements of the spectrum in the following way:

$$D_{ll'} = \sqrt{A_{ll} A_{l'l'}} + \varepsilon. \tag{2.49}$$

In our implementation, it is not necessary to add a small number ε.

Also methods that continue matrix-valued Green's functions as a whole, and not component-wise, have been developed (Kraberger et al., 2017; Sim and Han, 2018).

2.5* Python package for analytic continuation: ana_cont

This section is based on the supplementary material of Geffroy et al. (2019), where the respective section was written solely by the author of this thesis.

In the previous sections we have presented two methods for analytic continuation, the Pade approximation and the Maximum Entropy method. Although they both are well-established and have been implemented many times [e.g. by Bergeron and Tremblay (2016), Levy et al.

[1] Usually, two default models D^+ and D^- are introduced, and assumed to be equal at a later point. For the sake of brevity, we omit this step.

Die approbierte gedruckte Originalversion dieser Dissertation ist an der TU Wien Bibliothek verfügbar.
The approved original version of this doctoral thesis is available in print at TU Wien Bibliothek.
TU Bibliothek WIEN Your knowledge hub

(2017), Kraberger et al. (2017)], I decided to write yet another code for analytic continuation. In contrast to other implementations, it is a Python package. The advantage of this approach is increased maintainability. There are too many ways of doing analytic continuation to encode all of them into a few command line arguments. The `ana_cont` package is available open source at `https://github.com/josefkaufmann/ana_cont`.

2.5.1 Package structure

The central class of `ana_cont` is `AnalyticContinuationProblem`, which holds problem-specific information: real-frequency grid, imaginary-frequency/time grid, data on imaginary axis, inverse temperature, and type of the kernel. It has a method `solve`, which takes several keyword arguments. The most important one is `method`. Currently, only two methods, `pade` and `maxent_svd` are implemented. Calling `solve` creates an instance of a solver object. In case of `method='maxent_svd'`, the class `MaxentSolverSVD` is instantiated. The class contains all necessary functions to solve the analytic continuation problem defined before.

The kernel for the continuation problem at hand is provided by the class `Kernel`. It handles real-frequency discretization of the kernel, preblur, and rotation to the eigenbasis of the covariance matrix if provided.

Furthermore there is a class `GreensFunction`, whose main purpose is to construct a full complex-valued Green's function out of a given spectrum, by applying the Kramers-Kronig relation Eq. (2.19).

We want to stress that this package does not contain an executable script that can do analytic continuations by just specifying some parameters. While this may sound rather discouraging, we believe that in fact this *reduces* the required amount of work both for the user and for the maintainer. On the user-side, a working script can be composed of as few as 10 lines of Python code; example scripts can be found in the github repository. There is full freedom in which way to provide the imaginary-axis data: They can be read from a favorite file format, or calculated on-the-fly. Computed real-axis data can be plotted or further processed without the detour of file-IO. Thus the present analytic continuation code can be easily embedded in complex postprocessing procedures. Also for the developers this principle is a large gain, since they do not have to take care of a sophisticated user interface and flow-control.
Since knowledge and experience of analytic continuation are absolutely necessary to use any analytic continuation program, we do not see a principal downside to the present approach.

2.5.2 Numerics

Analytic continuation is, compared to large QMC simulations or Bethe-Salpeter equation inversions, a numerically rather inexpensive task. Therefore the performance of the code does not have to be the main goal. The `ana_cont` package is written entirely in Python, partly trading performance for flexibility and readability, while still keeping the possibility of later optimization. Nevertheless several actions have been taken in order to make the code reasonably fast.

Die approbierte gedruckte Originalversion dieser Dissertation ist an der TU Wien Bibliothek verfügbar.
The approved original version of this doctoral thesis is available in print at TU Wien Bibliothek.
TU Bibliothek WIEN Your knowledge hub

Frequency-space discretization.

For a numerical treatment it is necessary to discretize the real-frequency axis: $\omega \longrightarrow \omega_i$. For an arbitrary function $F(\omega)$ we then define $F_i \equiv F(\omega_i)$. Integrals over frequency space are converted to sums by $\int d\omega F(\omega) \approx \sum_i F_i \Delta_i$, where Δ_i is the width of the frequency interval centered at ω_i.

Singular value decomposition.

One of the most important steps of MaxEnt is the minimization of the functional $Q_\alpha[A]$ in the space of spectral functions. If the real-frequency axis is discretized into, say, 1000 intervals, the space of solutions has 1000 dimensions. This is too large for a deterministic solver, and a Monte Carlo method is needed (Sandvik, 1998). However, Jarrell and Gubernatis (1996) perform a singular value decomposition of the kernel and thereby achieve a large reduction of dimensions, e. g. from 1000 to 20 in typical cases. The optimization problem can then be solved by deterministic methods like Newton root finding or the Levenberg-Marquart algorithm. The `MaxentSolverSVD` follows the strategy of singular value decomposition of the kernel, as defined in Eq. (2.30). The vector ξ of singular values is truncated such that only values larger than a certain threshold (10^{-10} in our case) are kept. In the singular space the spectrum is parametrized through

$$A_j = D_j \exp \sum_m V_{jm} u_m \tag{2.50}$$

as proposed by Jarrell and Gubernatis (1996).

Minimization problem.

The above definitions are inserted into Eq. (2.35), and after a few intermediate steps the stationarity condition $\partial Q_\alpha / \partial A_m = 0$ leads to

$$f_m(u) \equiv \alpha u_m + \xi_m \sum_k E_k U_{km} \left(\sum_l K_{kl} A_l(u) \Delta_l - G_k \right) = 0, \tag{2.51}$$

which has to be solved for u_m. Root finding algorithms work better, when the derivative of the root function is known analytically. Therefore, we take the derivative of f with respect to u:

$$\frac{\partial f_m}{\partial u_i} \equiv J_{mi} = \alpha \delta_{mi} + \xi_m \sum_k U_{km} E_k \sum_l K_{kl} \Delta_l A_l(u) V_{li} \tag{2.52}$$

The expressions Eq. (2.51) and Eq. (2.52) can be put in a form that is more efficient for numerical evaluation by making the following definitions:

$$w_l \equiv \exp\left(\sum_m V_{lm} u_m \right) \tag{2.53a}$$

$$W_{ml} \equiv \sum_{km} E_k U_{km} \xi_m U_{kn} \xi_n V_{ln} \Delta_l D_l \tag{2.53b}$$

$$W_{mil} \equiv W_{ml} V_{li} \tag{2.53c}$$

$$B_m \equiv \sum_k U_{km} \xi_m E_k G_k \tag{2.53d}$$

Die approbierte gedruckte Originalversion dieser Dissertation ist an der TU Wien Bibliothek verfügbar.
The approved original version of this doctoral thesis is available in print at TU Wien Bibliothek.
TU Bibliothek WIEN Your knowledge hub

Then we have

$$f_m = \alpha u_m + \sum_l W_{ml} w_l - B_m \tag{2.54a}$$

$$J_{mi} = \alpha \delta_{mi} + \sum_l W_{mil} w_l, \tag{2.54b}$$

where the quantities W_{ml}, W_{mil}, and B_m are precomputed in order to minimize the number of matrix multiplications during the optimization procedure. Please note that we do *not* use the Einstein summation convention. For the optimization, the Levenberg-Marquart implementation of `scipy.optimize.root` can be used by passing `optimizer='scipy_lm'` to the solver. However, we found simple Newton root finding to be much faster and numerically stable. This is activated by setting `optimizer='newton'`.

Offdiagonal elements.

While the above formulas are used for diagonal elements of correlation functions, with only very small changes we arrive at a different form that can be used for offdiagonal elements. The singular-space parametrization becomes (Kraberger et al., 2017)

$$A_j = D_j \left[\exp\left(\sum_m V_{jm} u_m \right) - \exp\left(- \sum_m V_{jm} u_m \right) \right] = D_j \left(w_j - 1/w_j \right) \tag{2.55}$$

and the minimization problem is set by

$$f_m = \alpha u_m + \sum_l W_{ml}(w_l - 1/w_l) - B_m \tag{2.56a}$$

$$J_{mi} = \alpha \delta_{mi} + \sum_l W_{mil}(w_l + 1/w_l). \tag{2.56b}$$

Determination of optimal α.

In Section 2.4.1 we have discussed various ways of determining a good value of the hyperparameter α. All of these methods are implemented in `ana_cont` and can be used by setting the solver keyword `alpha_determination` to one of 'historic', 'classic', 'bryan' or, as recommended, 'chi2kink'.

From the algorithmic point of view, all these methods have in common that the optimization is done for several values of α, where one starts at a very high value of, e.g., $\alpha = 10^{12}$. If `alpha_determination='chi2kink'`, this can be adapted by setting the keyword `alpha_start`. One should use a value that leads to a solution very close to the default model. Subsequently α is decreased by a constant factor `alpha_div` in each step, which has the advantage that the solution of the previous step can be used as a starting point. After reaching the smallest value of α (`alpha_end`) the function of Eq. (2.39) is fitted and the parameter f is specified by the keyword `fit_position`.

Especially careful about the choice of α one has to be when continuing offdiagonal elements of correlation functions. With a spectrum that is not positive definite, one has more degrees of freedom for noise fitting. Therefore in the double logarithmic plot of $\chi^2(\alpha)$ the noise fitting region is not any more a plateau, but rather another linear slope. The optimal alpha has to be chosen at the point, where the slope changes.

Die approbierte gedruckte Originalversion dieser Dissertation ist an der TU Wien Bibliothek verfügbar.
The approved original version of this doctoral thesis is available in print at TU Wien Bibliothek.
TU Bibliothek WIEN Your knowledge hub

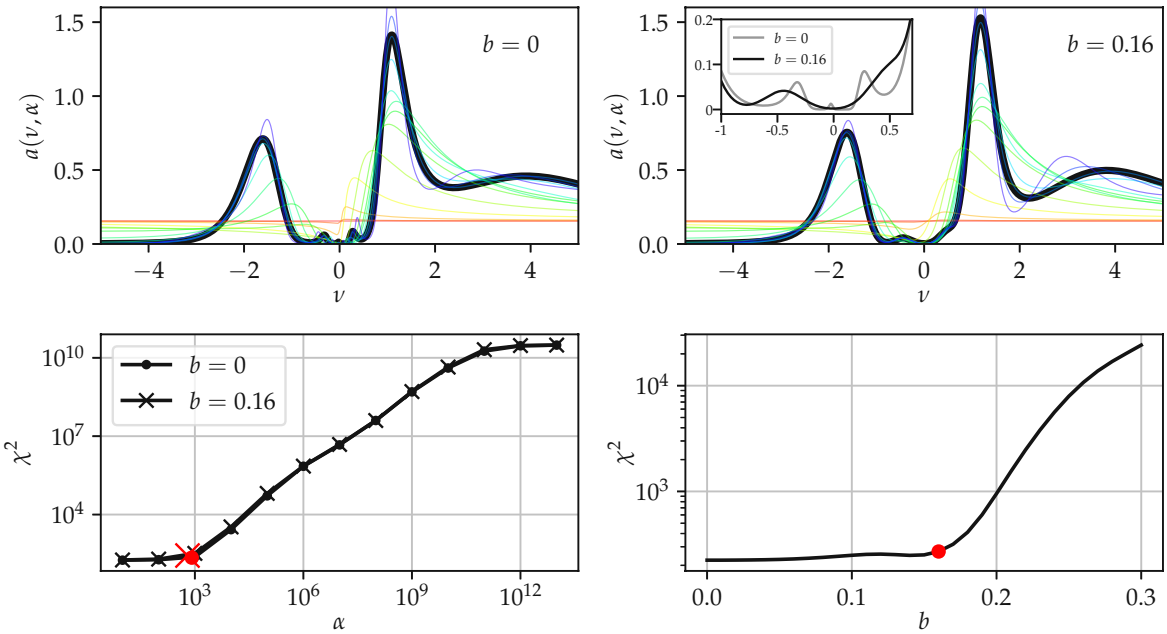

Figure 2.6: Analytic continuation of the DMFT self-energy of the V-t_{2g} orbitals of $SrVO_3$, which was obtained with symmetric improved estimators for extra precision(Kaufmann et al., 2019). *Upper row*: Spectrum of the imaginary part of the self-energy spectrum $a(\omega) = -\mathrm{Im}\Sigma(\omega)/\pi$ for $SrVO_3$ without [left] and with [right] preblur. The figures show optimization results for several different values of α. Red corresponds to $\alpha = 10^{13}$, and as the color changes into blue, the value is lowered by a factor of 10 in every step. The final result, at optimal α, is drawn in black. Clearly, for the highest values of α, we recover the constant default model. *Lower row*: Behavior of χ^2 as a function of α [left] and b [right] for the MaxEnt analytical continuation of $SrVO_3$. The values taken as optimal are highlighted in red. The figure is taken from the supplementary material of Si et al. (2020a), for which it was created by the author of this thesis.

Preblur

Maxent with preblur, as described in Section 2.4.2 is implemented in `ana_cont`. Preblur is activated by passing `preblur=True` to the solver, and specifying the parameter b by `blur_width=`b. Our recommended workflow is to always first do an analytic continuation with $b = 0$, and then increase it step-by-step. The final value b^* should be large enough to eliminate spurious features in the spectrum, but still small enough so that the limit $\lim_{\alpha\to 0} \log\chi^2(\alpha)$ is not significantly increased with respect to $b = 0$. For a real-world case ($SrVO_3$ self-energy) the procedure is illustrated in Fig. 2.6.

2.5.3 MaxEnt for susceptibilities

The analytic continuation of susceptibilities, i. e. bosonic Green's functions, from the imaginary to the real axis is a frequently required task. In `ana_cont` it can be achieved by initializing the `AnalyticContinuationProblem` with `kernel_mode='freq_bosonic'`. Like in the case of fermionic correlation functions, a relation that connects the values of the susceptibility on the real and imaginary axis is required. A susceptibility $\chi(\omega)$ is a response function, therefore causality implies that its imaginary part is anti-symmetric in frequencies, $\chi(\omega) = \chi^*(-\omega)$.

Die approbierte gedruckte Originalversion dieser Dissertation ist an der TU Wien Bibliothek verfügbar.
The approved original version of this doctoral thesis is available in print at TU Wien Bibliothek.
TU Bibliothek WIEN Your knowledge hub

Inserting this fact in the Kramers-Kronig relation

$$\mathrm{Re}\,[\chi(i\omega_n)] = \frac{1}{\pi}\int_{-\infty}^{\infty} d\omega\, \frac{\mathrm{Im}[\chi(\omega)]}{\omega - i\omega_n}$$

yields

$$\mathrm{Re}\,[\chi(i\omega_n)] = \frac{2}{\pi}\int_{0}^{\infty} d\omega\, \frac{\omega}{\omega^2 + \omega_n^2}\,\mathrm{Im}[\chi(\omega)]\,,$$

connecting the susceptibility at real frequencies with its values at the bosonic Matsubara frequencies ω_n.
Since the factor $\omega/(\omega^2 + \omega_n^2)$ is divergent for $\omega = \omega_n = 0$, it is common to introduce another function

$$S(\omega) \equiv \frac{2}{\pi}\frac{\mathrm{Im}\chi(\omega)}{\omega}, \tag{2.57}$$

such that we can now write

$$\mathrm{Re}[\chi(i\omega_n)] = \int_{0}^{\infty} d\omega\, K_b(\omega_n, \omega)\, S(\omega) \tag{2.58}$$

with a *kernel*

$$K_b(\omega_n, \omega) = \frac{\omega^2}{\omega_n^2 + \omega^2} \tag{2.59}$$

that is well-defined for all values of ω and ω_n. Correspondingly the result of the analytic continuation that is returned by the solver of `ana_cont` is $S(\omega)$.

2.5.4 MaxEnt for self-energies

Besides one-particle Green's functions and susceptibilities, it often is necessary to analytically continue self-energies from Matsubara to real frequencies. Self-energies essentially have the same analytic properties as one-particle Green's functions (Luttinger, 1961). The difference is that the high-frequency limit is a non-zero constant Σ_0 (the so-called Hartree term), and the imaginary part decays like $\Sigma_1/(i\omega_n)$ as opposed to $1/(i\omega_n)$ in case of the Green's function. Σ_0 and Σ_1 are called the zeroth and first moments of the self-energy and can be calculated from density matrices (Wang et al., 2011). The zeroth moment is frequently referred to as Hartree term. Note that ω_n are fermionic Matsubara frequencies here. In absence of particle-hole symmetry, the spectral representation is

$$\Sigma(i\omega_n) = \Sigma_0 + \Sigma_1 \int_{-\infty}^{\infty} d\omega\, \frac{a(\omega)}{i\omega_n - \omega}, \tag{2.60}$$

where we defined the spectrum a of the self-energy as

$$a(\omega) \equiv -\frac{1}{\pi}\mathrm{Im}\frac{\Sigma(\omega) - \Sigma_0}{\Sigma_1}. \tag{2.61}$$

Thus, we can write the analytic continuation problem for the self-energy in a form very similar to Eq. (2.58):

$$\frac{\Sigma(i\omega_n) - \Sigma_0}{\Sigma_1} = \int_{-\infty}^{\infty} d\omega\, K_f(\omega_n, \omega)\, a(\omega) \tag{2.62}$$

Die approbierte gedruckte Originalversion dieser Dissertation ist an der TU Wien Bibliothek verfügbar.
The approved original version of this doctoral thesis is available in print at TU Wien Bibliothek.
TU Bibliothek WIEN Your knowledge hub

with the fermionic kernel

$$K_f(\omega_n, \omega) = \frac{1}{i\omega_n - \omega}. \tag{2.63}$$

We do not see any necessity for normalizing the self-energy by division through its first moment, but merely keep this notation for consistency with the literature. The solver of ana_cont then returns $a(\omega)$. From this we can construct the imaginary part of the retarded self-energy by inverting Eq. (2.62):

$$\mathrm{Im}\Sigma_R(\omega) = -\pi\Sigma_1 a(\omega). \tag{2.64}$$

If one wants to use the retarded self-energy for the calculation of the retarded Green's function, it is necessary to also obtain the real part of the retarded self-energy, which is given by the Kramers-Kronig relation Eq. (2.19). This is implemented in the kkt method of the GreensFunction class.

Die approbierte gedruckte Originalversion dieser Dissertation ist an der TU Wien Bibliothek verfügbar.
The approved original version of this doctoral thesis is available in print at TU Wien Bibliothek.
TU Bibliothek WIEN Your knowledge hub

Die approbierte gedruckte Originalversion dieser Dissertation ist an der TU Wien Bibliothek verfügbar.
The approved original version of this doctoral thesis is available in print at TU Wien Bibliothek.
TU Bibliothek WIEN Your knowledge hub

Die approbierte gedruckte Originalversion dieser Dissertation ist an der TU Wien Bibliothek verfügbar.
The approved original version of this doctoral thesis is available in print at TU Wien Bibliothek.
TU Bibliothek WIEN Your knowledge hub

Chapter 3

Correlation functions for the Anderson impurity model

This chapter is largely based on Kaufmann et al. (2019), for which the author has written most of the manuscript. Citations from there are marked by a vertical bar.

After showing some general properties of Green's functions and especially the analytical continuation from imaginary to real frequencies, we now turn to their actual calculation. Since many-body Green's functions are expectation values like Eq. (2.2), it is necessary to start by specifying a Hamiltonian H. The Hamiltonian encodes all properties of a physical model and is the basis for simulations. In Chapter 1, one of the most fundamental models for the physics of strongly correlated electrons was introduced, the Anderson Impurity Model (AIM) Eq. (1.1) (Anderson, 1961).

For the more general multi-orbital case its Hamiltonian can be written as

$$H_{\mathrm{AIM}} = \frac{1}{2}\sum_{ijkl} U_{ijkl}\hat{d}_i^\dagger \hat{d}_j^\dagger \hat{d}_l \hat{d}_k + \sum_i \tilde{\varepsilon}_i\, \hat{d}_i^\dagger \hat{d}_i + \sum_{Ki} \varepsilon_{Ki}\hat{c}_{Ki}^\dagger \hat{c}_{Ki} + \sum_{Kij}\left[V_K^{ij}\hat{c}_{Ki}^\dagger \hat{d}_j + (V_K^{ji})^* \hat{d}_i^\dagger \hat{c}_{Kj}\right]. \tag{3.1}$$

Here, $\hat{d}_i$ ($\hat{d}_i^\dagger$) is the annihilation (creation) operator of an electron with spin-orbital flavor i on the impurity; $\hat{c}_{Ki}$ ($\hat{c}_{Ki}^\dagger$) is the annihilation (creation) operator of an electron with impurity flavor i in the non-interacting bath and K subsumes the remaining bath degrees of freedom (e. g. the momentum $\mathbf{k}$). The impurity is described by a local one-particle potential $\tilde{\varepsilon}_i$ (e.g. the crystal field), the interaction matrix U_{ijkl}, the bath dispersion ε_{Ki}, and the hybridization strength V_K^{ij}. Since the bath degrees of freedom appear in Eq. (3.1) at most quadratically, they can be formally integrated out yielding a one-body term in the impurity operators. This contains the hybridization function $\Delta_{ab}(\tau_1, \tau_2)$ encoding the entire influence of the bath. In the following we assume a diagonal hybridization $\Delta_{ab}(\tau_1, \tau_2) \equiv \Delta_a(\tau_1, \tau_2)\delta_{ab}$ resulting in a diagonal one-particle Green's function $G_{ab}^{\tau_1\tau_2} = G_a^{\tau_1\tau_2}\delta_{ab}$.

The hybridization function is most conveniently written in Matsubara frequencies as

$$\Delta_a^\nu = \sum_K \frac{V_K^{aa}(V_K^{aa})^*}{i\nu - \varepsilon_{Ka}}, \tag{3.2}$$

and thus the non-interacting Green's function of the impurity is

$$\mathcal{G}_a^\nu = \frac{1}{i\nu - \tilde{\varepsilon}_a - \Delta_a^\nu}\,. \tag{3.3}$$

In accordance with Eq. (2.4), we define the interacting one-particle Green's function for the multi-orbital AIM of Eq. (3.1) as

$$G_a(\tau_1, \tau_2) = -\left\langle T_\tau \hat{d}_a(\tau_1)\hat{d}_a^\dagger(\tau_2)\right\rangle, \tag{3.4}$$

where $d_a(\tau)$ $[d_a^\dagger(\tau)]$ are now the annihilation (creation) operators for electrons of flavor a at (imaginary) time τ. Furthermore, T_τ is the imaginary-time ordering operator, and $\langle\ldots\rangle = (\mathrm{Tr}e^{-\beta H}\ldots)/Z$ the thermal expectation value at temperature T ($\beta = 1/T$), Z is the partition function. The Green's function is related to the density as $n_a \equiv \langle \hat{d}_a^\dagger \hat{d}_a\rangle = 1 + G_a(0+, 0)$.

Analogously, we define the two-particle Green's function of the AIM as

$$G_{abcd}(\tau_1, \tau_2, \tau_3, \tau_4) = \left\langle T_\tau \hat{d}_a(\tau_1)\hat{d}_b^\dagger(\tau_2)\hat{d}_c(\tau_3)\hat{d}_d^\dagger(\tau_4)\right\rangle. \tag{3.5}$$

The Fourier transforms to fermionic Matsubara frequencies (Matsubara, 1955) $\nu = (2l + 1)\pi/\beta$ at integer numbers l are given by

$$G_a^\nu = \frac{1}{\beta}\int_0^\beta d\tau_1 d\tau_2\, e^{i\nu(\tau_1-\tau_2)} G_a(\tau_1, \tau_2) \tag{3.6}$$

and

$$G_{abcd}^{\nu_1\nu_2\nu_3\nu_4} = \frac{1}{\beta^2}\int_0^\beta d\tau_1 d\tau_2 d\tau_3 d\tau_4\, e^{i(\nu_1\tau_1-\nu_2\tau_2+\nu_3\tau_3-\nu_4\tau_4)} G_{abcd}(\tau_1, \tau_2, \tau_3, \tau_4) \tag{3.7}$$

for the one- and two-particle Green's function, respectively.

Since H_{AIM} does not explicitly depend on time, the Green's functions defined above are invariant with respect to translations in (imaginary) time. This is equivalent to energy conservation, which for the two-particle Green's function reads

$$\nu_1 + \nu_3 = \nu_2 + \nu_4, \tag{3.8}$$

i.e. the total energy of the incoming particles equals the total energy of the outgoing particles. The energy conservation Eq. (3.8) allows to reduce the number of frequency arguments of the two-particle Green's function from four to three. It is therefore more common to assume a

Die approbierte gedruckte Originalversion dieser Dissertation ist an der TU Wien Bibliothek verfügbar.
The approved original version of this doctoral thesis is available in print at TU Wien Bibliothek.
TU Bibliothek WIEN Your knowledge hub

mixed bosonic-fermionic frequency representation with two fermionic- and one bosonic frequency (a bosonic frequency being a sum or difference of two fermionic Matsubara frequencies). However, the choice of these frequencies is ambiguous and therefore the derivations in Section 3.2 are done in four fermionic frequencies. With the definitions above, one can easily adapt the results to ones favorite convention. (Sometimes we use generic bosonic frequencies ω which are however replaced by $\nu_1 \dots \nu_4$ in the final expression.)

The parquet equations in convention-agnostic notation are given in Appendix C.

3.1 Impurity solvers

Here we briefly discuss two approaches for solving impurity models, exact diagonalization and continuous-time quantum Monte Carlo.

3.1.1 Exact diagonalization

In order to compute correlation functions for the AIM, such as Eq. (3.4), one may evaluate the expectation value, as defined in Eq. (2.2), in a straightforward way. Although this is only efficient when the system is small, such a strategy is of great value for benchmarking more sophisticated methods (see Section 3.2).

The expectation value of Eq. (2.2) can be evaluated explicitly, if the Hamiltonian H and the operator $\mathcal{O}$ are expressed by fermionic creation and annihilation operators. For an AIM with two spin flavors, N_{imp} impurity orbitals, and N_{bath} bath sites, one needs $N = 2(N_{\text{bath}} + N_{\text{imp}})$ distinct fermionic operators. Thus, there are 2^N Fock states in the system such that creation/annihilation operators as well as the Hamiltonian may be written as $2^N \times 2^N$-matrices. For a one-orbital impurity that does not hybridize with a bath (known as "Hubbard atom" or "atomic limit"), there are only 4 Fock states and calculations can even be done analytically. If only a single bath site is included, the Fock space has 16 dimensions and calculations are numerically still not very demanding. In fact, such a system is still tractable analytically if symmetries are exploited.

Once the fermionic operators and the Hamiltonian are constructed, one can proceed as indicated in Section 2.1.4. This means that the Hamiltonian has to be diagonalized in order to obtain the eigen-energies ε_n. Then the Lehmann representation of any correlation function that is given in terms of the fermionic operators can be evaluated directly, such as the fermionic one-particle Green's function Eq. (2.18). It is important to emphasize here that for avoiding exponentials of operators the matrix elements, $\langle m|\hat{c}|n\rangle$ or $\langle m|\hat{d}|n\rangle$, have to be taken in the eigenbasis of the Hamiltonian, and not in the occupation number basis.

This procedure can also be carried out for bosonic Green's functions with bosonic operators B_1 and B_2,

$$P(i\omega_j) = \int_0^\beta d\tau\, e^{i\omega_j \tau} \left\langle \mathbf{T} B_1(\tau) B_2 \right\rangle, \tag{3.9}$$

which have the Lehmann representation

$$P(i\omega_j) = \frac{1}{Z} \sum_{mn} \left\langle m|B_1|n\right\rangle \left\langle n|B_2|m\right\rangle \frac{e^{-\beta\varepsilon_n} - e^{-\beta\varepsilon_m}}{i\omega_j + \varepsilon_m - \varepsilon_n}. \tag{3.10}$$

Die approbierte gedruckte Originalversion dieser Dissertation ist an der TU Wien Bibliothek verfügbar.
The approved original version of this doctoral thesis is available in print at TU Wien Bibliothek.
TU Bibliothek WIEN Your knowledge hub

This is indeed very similar to Eq. (2.18), except that we have matrix elements of bosonic operators B_1, B_2 and bosonic Matsubara frequencies. Since the bosonic operators are products of even numbers of fermionic creation or annihilation operators, the matrix elements can be evaluated. However, a problem arises when the value of the Matsubara frequency is zero, since the denominator vanishes for $n = m$. In theory this is not a problem, since L'Hôpital's rule gives

$$\lim_{\varepsilon_n \to \varepsilon_m} \frac{e^{-\beta\varepsilon_n} - e^{-\beta\varepsilon_m}}{\varepsilon_m - \varepsilon_n} = \beta e^{-\beta\varepsilon_m}. \tag{3.11}$$

In practice, it is usually more convenient to overcome this problem by shifting ε_n (but not ε_m) by a small constant to $\varepsilon_n + \delta\varepsilon$, both in the numerator and in the denominator.

This was done in the calculation of the two-particle Green's function (Toschi et al., 2007) and can be applied also to other Green's functions that depend both on fermionic and bosonic frequencies. Some Lehmann representations of more complicated Green's functions are given in Appendix B.

The main problem of ED is that only systems with finite-dimensional Fock space can be treated, i. e. discrete systems. In many cases however, one wants to study impurities in a *continuous* bath. It turns out that relatively simple systems can be approximated very well by fitting the hybridization function to a few bath states (Caffarel and Krauth, 1994), but such a straight-forward diagonalization of the full Hamiltonian in the occupation-number basis becomes prohibitively expensive already if there are more than $N \sim 7$ fermionic states per spin. Since it is often desirable to include more bath states, one resorts to the Lanczos algorithm (Lanczos, 1950). For zero-temperature calculations this was done by Caffarel and Krauth (1994), and subsequently it was adapted for usage at high (Jaklič and Prelovšek, 1994) and low finite temperatures (Capone et al., 2007). Exploiting symmetries and sparseness of the Hamiltonian has led to a further impressive increase of the number of tractable bath sites (Lu et al., 2014). For zero- and low-temperature calculations, the numerical renormalization group (NRG) Bulla et al., 2008 has been used with great success.

3.1.2 Continuous-time quantum Monte Carlo

An entirely different approach is taken in quantum Monte Carlo (QMC) methods. There, correlation functions are computed by stochastically sampling their Feynman-diagrammatic perturbation series. With the help of path-integral discretization in imaginary time and subsequent Hubbard-Stratonovich decoupling this was first done in the Hirsch-Fye QMC solver (Hirsch and Fye, 1986). However, for low temperatures the time discretization becomes a serious issue, and except for very simple interactions the Hubbard-Stratonovic transformation is problematic. In order to overcome these problems, so-called continuous-time quantum Monte Carlo (CT-QMC) methods were devised (Gull et al., 2011). They rely on an expansion of the partition function Z of the AIM in the interaction picture. This means that the Hamiltonian $H_{\mathrm{AIM}} = H_a + H_b$ is split into a part H_a that is treated exactly, and a part H_b that serves as a perturbation. We elaborate on the choice of H_a and H_b below. Since the expansion is not truncated

Die approbierte gedruckte Originalversion dieser Dissertation ist an der TU Wien Bibliothek verfügbar.
The approved original version of this doctoral thesis is available in print at TU Wien Bibliothek.
TU Bibliothek WIEN Your knowledge hub

at any finite order it is not an approximation but an exact relation:

$$\begin{aligned} Z &= \mathrm{Tr}\left[e^{-\beta H_{\mathrm{AIM}}}\right] = \mathrm{Tr}\left[e^{-\beta(H_a+H_b)}\right] \\ &= \mathrm{Tr}\,\mathrm{T}e^{-\beta H_a}\exp\left[-\int_0^\beta d\tau\, H_b(\tau)\right] \\ &= \sum_{n=0}^{\infty}\frac{(-1)^n}{n!}\int_0^\beta d\tau_1 \ldots \int_0^\beta d\tau_n\, \mathrm{Tr}\left[\mathrm{T}\, e^{-\beta H_a} H_b(\tau_1)\ldots H_b(\tau_n)\right] \end{aligned} \tag{3.12}$$

If one chooses

$$H_b = \frac{1}{2}\sum_{ijkl} U_{ijkl} d_i^\dagger d_j^\dagger d_l d_k \equiv H_{\mathrm{int}}, \tag{3.13}$$

one arrives at the interaction expansion (CT-INT), which historically was the first to be used for impurity models by Rubtsov and Lichtenstein (2004). Another possibility is

$$H_b = \sum_{Kij}\left[V_K^{ij}\hat{c}_{Ki}^\dagger d_j + (V_K^{ij})^* d_i^\dagger c_{Kj}\right] \equiv H_{\mathrm{hyb}}, \tag{3.14}$$

which corresponds to the hybridization expansion (CT-HYB) (Werner et al., 2006; Werner and Millis, 2006). Algorithms like CT-INT or CT-HYB then proceed by evaluating Eq. (3.12) stochastically, in a Monte Carlo algorithm.

Monte Carlo integration

Before delving into the CT-QMC algorithm, let us first briefly recapitulate the basic principle of Monte Carlo, following Gull et al. (2011). Suppose we want to compute an expectation value $\langle A\rangle_p$ of some observable $A(x)$. By x we denote a random variable (or configuration), which can be a vector of many components. It is distributed according to a multivariate probability density proportional to $p(x)$. Thus, we have

$$\langle A\rangle_p = \frac{1}{Z}\int_C dx\; p(x)A(x) \qquad \text{with} \qquad Z = \int_C dx\; p(x), \tag{3.15}$$

where C denotes the space of all configurations x.

A Monte Carlo estimator for $\langle A\rangle_p$ is constructed by randomly choosing configurations x_i from the distribution $p(x)/Z$, and taking the average of the values $A(x_i)$ evaluated at these points:

$$\langle A\rangle_{\mathrm{MC}} = \frac{1}{N_{\mathrm{MC}}}\sum_{i=1}^{N_{\mathrm{MC}}} A(x_i) \tag{3.16}$$

The statistical uncertainty of $\langle A\rangle_{\mathrm{MC}}$ then decreases with N_{MC} as

$$\Delta A = \sqrt{\frac{\mathrm{Var}\,A\,(2\tau_A+1)}{N_{\mathrm{MC}}}}, \tag{3.17}$$

where τ_A is the autocorrelation time. In case of perfectly random configurations x_i it is $\tau_A = 0$, but otherwise we have $\tau_A > 0$. It is of particular importance to keep this in mind when generating the configurations as a Markov chain (see below).

Die approbierte gedruckte Originalversion dieser Dissertation ist an der TU Wien Bibliothek verfügbar.
The approved original version of this doctoral thesis is available in print at TU Wien Bibliothek.
TU Bibliothek WIEN Your knowledge hub

There may be cases, where it is better to draw random configurations from a different distribution $\pi(x)/\int dx\ \pi(x)$, instead of $p(x)/Z$. In such a situation, Eq. (3.16) can be rewritten as

$$\langle A\rangle_p = \frac{\int dx\ \pi(x)A(x)\frac{p(x)}{\pi(x)}}{\int dx\ \pi(x)\frac{p(x)}{\pi(x)}} = \frac{\left\langle A\frac{p}{\pi}\right\rangle_\pi}{\left\langle \frac{p}{\pi}\right\rangle_\pi}. \tag{3.18}$$

Markov chain Monte Carlo

In order to make use of Eq. (3.16) or Eq. (3.18) it is necessary to actually generate random configurations from a distribution $p(x)$ or $\pi(x)$, which may be very complicated and a priori unknown. In principle it is possible to do this by uniform sampling, i.e. using a constant $\pi(x)$. However, such a procedure is highly inefficient. In practice one therefore usually resorts to constructing a Markov chain of configurations x_i, in which subsequent samples are modifications of the previous configuration. Such a chain is fully characterized by the transition matrix $w(x\longrightarrow y)$ that indicates the probability of going from a configuration x to a configuration y. The distribution of x_i drawn from such a chain exponentially converges to the desired $p(x)$ if two conditions are met. The first condition concerns *ergodicity*: Any configuration y has to be reachable from any other configuration x within a finite number of steps. As a second condition, one has to require *balance*: The probability of configuration y can, according to Bayes' theorem, be decomposed as

$$p(y) = \int_C dx\ p(x)w(x\longrightarrow y). \tag{3.19}$$

In order to fulfill the condition of balance, it is sufficient (but not necessary) to fulfill the stronger condition of *detailed balance*,

$$\frac{w(x\longrightarrow y)}{w(y\longrightarrow x)} = \frac{p(y)}{p(x)}. \tag{3.20}$$

In practice, a Markov chain with detailed balance is generated by the Metropolis-Hastings algorithm (Metropolis et al., 1953; Hastings, 1970). The Metropolis-Hastings algorithm proceeds in the following way. One splits the transition matrix $w(x\longrightarrow y)$ into a proposal and acceptance probability for the transition from x to y, $w(x\longrightarrow y) = w_{\text{prop}}(x\longrightarrow y)w_{\text{acc}}(x\longrightarrow y)$. In order to fulfill detailed balance, the acceptance probability is chosen as

$$w_{\text{acc}}(x\longrightarrow y) = \min\left[1, r(x\longrightarrow y)\right] \tag{3.21}$$

with an acceptance ratio

$$r(x\longrightarrow y) = \frac{p(y)w_{\text{prop}}(y\longrightarrow x)}{p(x)w_{\text{prop}}(x\longrightarrow y)}. \tag{3.22}$$

Let it be noted that the configuration weight $p(x)$ is in general not positive when dealing with fermionic systems. This so-called *sign problem* was shown to be nondeterministic polynomial (NP) hard (Troyer and Wiese, 2005) and intrinsic to fermionic systems. Exponential scaling in system size and inverse temperature thus may lead to prohibitively long computation time. A variety of strategies to mitigate this problem has been proposed (Berger et al.,

Die approbierte gedruckte Originalversion dieser Dissertation ist an der TU Wien Bibliothek verfügbar.
The approved original version of this doctoral thesis is available in print at TU Wien Bibliothek.
TU Bibliothek WIEN Your knowledge hub

2021), but in the case of impurity models it is much less severe than for lattice models. In some cases it can even be proven to be absent (Yoo et al., 2005). Therefore in CT-QMC for impurity models it is usually sufficient to adopt a simple reweighting procedure, where the absolute $|p(x)|$ is sampled and in the end the result is divided by the mean sign, according to Eq. (3.18). A mean sign close to zero means that contributions of configurations with the same magnitude but opposite sign cancel each other, which leads to error amplification. However, all CT-QMC calculations in this thesis had a mean sign of −1, i.e. no sign problem.

Sampling the hybridization expansion

Having established the theoretical basis for Monte Carlo sampling, we can now turn back to our actual task of computing expectation values for the Anderson impurity model, again following Gull et al. (2011). In order to sample the hybridization expansion of the partition function of the AIM, let us now insert Eq. (3.14) into Eq. (3.12). We directly obtain

$$Z = \sum_{n=0}^{\infty}(-1)^n \int_0^{\tau_2} d\tau_1 \dots \int_0^{\beta} d\tau_n \, \mathrm{Tr}\left[\mathbf{T} e^{-\beta(H_{\mathrm{bath}}+H_{\mathrm{loc}})} H_{\mathrm{hyb}}(\tau_n) \dots H_{\mathrm{hyb}}(\tau_1)\right], \tag{3.23}$$

where the $n!$ in the denominator is compensated by the integral boundaries, which enforce a certain time ordering. Since H_{hyb} consists of two parts, $H_{\mathrm{hyb}} = \tilde{H}_{\mathrm{hyb}} + \tilde{H}^{\dagger}_{\mathrm{hyb}}$, with one bath and one impurity operator each, the contributions from odd expansion orders vanish. Furthermore, only the terms with an equal number of operators $\tilde{H}_{\mathrm{hyb}}$ and $\tilde{H}^{\dagger}_{\mathrm{hyb}}$ yield a non-zero contribution to the trace. Thus we arrive at

$$\begin{aligned} Z = \sum_{n=0}^{\infty} \int_0^{\tau_2} d\tau_1 \dots \int_0^{\beta} d\tau_n \int_0^{\tau_2'} d\tau_1' \dots \int_0^{\beta} d\tau_n' \\ \mathrm{Tr}\left[\mathbf{T} e^{-\beta(H_{\mathrm{bath}}+H_{\mathrm{loc}})} \tilde{H}_{\mathrm{hyb}}(\tau_n)\, \tilde{H}^{\dagger}_{\mathrm{hyb}}(\tau_n') \dots \tilde{H}_{\mathrm{hyb}}(\tau_1)\, \tilde{H}^{\dagger}_{\mathrm{hyb}}(\tau_1')\right] \end{aligned} \tag{3.24}$$

Inserting the explicit expressions for $\tilde{H}_{\mathrm{hyb}}$ and $\tilde{H}^{\dagger}_{\mathrm{hyb}}$ allows for splitting the trace in two parts: A trace over non-interacting bath operators c and a trace over the impurity operators d:

$$\begin{aligned} Z = \sum_{n=0}^{\infty} \int_0^{\tau_2} d\tau_1 \dots \int_0^{\beta} d\tau_n \int_0^{\tau_2'} d\tau_1' \dots \int_0^{\beta} d\tau_n' \sum_{\substack{K_1 a_1 \\ K_1' a_1'}} \dots \sum_{\substack{K_n a_n \\ K_n' a_n'}} V^{a_1}_{K_1} (V^{a_1'}_{K_1'})^* \dots V^{a_n}_{K_n} (V^{a_n'}_{K_n'})^* \times \\ \times \mathrm{Tr}_c \left[\mathbf{T} e^{-\beta H_{\mathrm{bath}}} \hat{c}^{\dagger}_{a_n}(\tau_n) \hat{c}_{a_n'}(\tau_n') \dots \hat{c}^{\dagger}_{a_1}(\tau_1) \hat{c}_{a_1'}(\tau_1')\right] \times \\ \times \mathrm{Tr}_d \left[\mathbf{T} e^{-\beta H_{\mathrm{loc}}} \hat{d}_{a_n}(\tau_n) \hat{d}^{\dagger}_{a_n'}(\tau_n') \dots \hat{d}_{a_1}(\tau_1) \hat{d}^{\dagger}_{a_1'}(\tau_1')\right] \end{aligned} \tag{3.25}$$

The second line in Eq. (3.25) is proportional to a non-interacting expectation value, which can be decomposed into products of operator pairs, according to Wick's theorem. If we additionally define $Z_{\mathrm{bath}} = \mathrm{Tr}_c\left[\mathrm{T}\exp(-\beta H_{\mathrm{bath}})\right]$ and the hybridization function

$$\Delta_{ab}(\tau) = \sum_K \frac{(V^a_K)^* V^b_K}{e^{\beta\varepsilon_K} + 1} \times \begin{cases} e^{-\varepsilon_K \tau} & -\beta < \tau < 0, \\ -e^{-\varepsilon_K(\tau-\beta)} & 0 < \tau < \beta, \end{cases} \tag{3.26}$$

Die approbierte gedruckte Originalversion dieser Dissertation ist an der TU Wien Bibliothek verfügbar.
The approved original version of this doctoral thesis is available in print at TU Wien Bibliothek.
TU Bibliothek WIEN Your knowledge hub

then Eq. (3.25) can be greatly simplified:

$$Z = Z_{\text{bath}} \sum_{n=0}^{\infty} \int_0^{\tau_2} d\tau_1 \ldots \int_0^{\beta} d\tau_n \int_0^{\tau_2'} d\tau_1' \ldots \int_0^{\beta} d\tau_n' \times$$
$$\times \sum_{a_1, a_1'} \ldots \sum_{a_n, a_n'} \text{Tr}_d \left[\mathbf{T} e^{-\beta H_{\text{loc}}} \hat{d}_{a_n}(\tau_n) \hat{d}^{\dagger}_{a_n'}(\tau_n') \ldots \hat{d}_{a_1}(\tau_1) \hat{d}^{\dagger}_{a_1'}(\tau_1') \right] \det\Delta \tag{3.27}$$

This means that for any configuration $x = \{a_1, \tau_1; \ldots; a_n', \tau_n'\}$ the bath trace can be evaluated as the determinant of a matrix $\mathbf{\Delta}$, whose elements are $\mathbf{\Delta}_{ij} = \Delta_{a_i a_j'}(\tau_i - \tau_j')$, as given in Eq. (3.26).

The sums and integrals in Eq. (3.27) can be computed with Monte Carlo, if a Markov chain sampling procedure is established. The distribution $p(x)$ one wants to sample is proportional to the integrand of Eq. (3.27):

$$p(x) = \underbrace{\text{Tr}_d \left[\mathbf{T} e^{-\beta H_{\text{loc}}} \hat{d}_{a_n}(\tau_n) \hat{d}^{\dagger}_{a_n'}(\tau_n') \ldots \hat{d}_{a_1}(\tau_1) \hat{d}^{\dagger}_{a_1'}(\tau_1') \right]}_{w_{\text{loc}}} \underbrace{\det\Delta}_{w_{\text{bath}}} \tag{3.28}$$

In order to perform such a sampling, one has to do Monte Carlo *updates* (also called *moves*) which change the current configuration x to a new configuration y. A configuration is, as written above, the set of all quantum numbers and time arguments in the integrand of Eq. (3.27). Having chosen a certain update, it is necessary to compute the acceptance ratio $r(x \longrightarrow y)$ for the Metropolis-Hastings algorithm Eq. (3.21).

The most important updates concern the insertion and removal of operator pairs in the local trace. They are in principle sufficient for ergodicity, but other updates can help to reduce autocorrelation times (Wallerberger et al., 2019). For the insertion of an operator pair, we have

$$r(x \longrightarrow y) = \frac{|w_{\text{loc}}(y) w_{\text{bath}}(y)|}{|w_{\text{loc}}(x) w_{\text{loc}}(x)|} \frac{N\beta^2}{(n+1)^2}, \tag{3.29}$$

where the configuration y has one more pair of operators than the configuration x. Here, N denotes the number of spin-orbitals of the impurity, which is the range of values the quantum numbers a_i of the impurity operators can take. The acceptance ratio for the inverse move, i. e. pair removal, is just the inverse of the acceptance ratio for pair insertion, such as to satisfy detailed balance.

Z-sampling measurement of the Green's function

Based on the above described sampling procedure for the hybridization expansion we are now able to introduce a method for actually computing the expectation value of the one-particle Green's function. We recall that it is defined as

$$G_a(\tau - \tau') = -\frac{1}{Z} \text{Tr} \left[e^{-\beta H_{\text{AIM}}} \hat{d}_a(\tau) \hat{d}^{\dagger}_a(\tau') \right]. \tag{3.30}$$

A hybridization expansion of Eq. (3.30) leads to an expression that is very similar to Eq. (3.25). The only difference, except the prefactor $-1/Z$, is that the trace over the $\hat{d}$-operators [last line in Eq. (3.25)] contains two more operators $\hat{d}_a(\tau)\hat{d}^{\dagger}_a(\tau')$. Their quantum numbers and time arguments are excluded from the summation or integration. Such operators are usually referred

Die approbierte gedruckte Originalversion dieser Dissertation ist an der TU Wien Bibliothek verfügbar.
The approved original version of this doctoral thesis is available in print at TU Wien Bibliothek.
TU Bibliothek WIEN Your knowledge hub

to as "not hybridizing." Conversely, each $\hat{d}$-operator in the expansion of the partition function has a matching $\hat{c}$-operator and is thus called "hybridizing" or "connected to hybridization lines."

Hence, a Green's function configuration can be generated by "removing hybridization lines" from an operator pair in a partition function configuration. More formally, this means that one pair of $\hat{c}$-operators is removed from the trace, such that the dimension of the hybridization matrix $\mathbf{\Delta}$ is reduced by one. We denote the reduced hybridization matrix, where line i [corresponding to $\hat{c}^\dagger_{a_i}(\tau_i)$] and column j [corresponding to $\hat{c}_{a'_j}(\tau'_j)$] have been removed by $\mathbf{\Delta}^{\tau_i \tau'_j}_{a_i a'_j}$. The weight of a Green's function configuration, where hybridization lines at τ_i and τ'_j have been removed is thus given by the ratio of the determinants

$$\frac{p_{G_{ij}}}{Z} = \frac{\det \mathbf{\Delta}^{\tau_i \tau'_j}_{a_i a'_j}}{\det \mathbf{\Delta}} = M_{ji}. \tag{3.31}$$

An estimator for the one-particle Green's function is thus constructed by accumulating the contributions of all configurations that are generated by removal of hybridization lines from *one* operator pair (Gull et al., 2011). Formally this is written as

$$G_a(\tau) = \frac{1}{\beta} \left\langle \sum_{ij}^{n} M_{ji}\ \tilde{\delta}(\tau, \tau_i - \tau'_j)\ \delta_{t(i)\,a}\ \delta_{t(j)\,a} \right\rangle_{\mathrm{MC}}, \tag{3.32}$$

where

$$\tilde{\delta}(\tau, \tau') = \begin{cases} \delta(\tau - \tau'), & \tau' > 0 \\ -\delta(\tau - \tau' - \beta), & \tau' < 0 \end{cases} \tag{3.33}$$

generates an imaginary-time binning and $t(i)$ is the orbital index of the operator in row/column i in the hybridization matrix.

In order to avoid the reduction of precision introduced by the binning, one may instead do a Fourier transform to fermionic Matsubara frequencies $i\nu$:

$$G^\nu_a = \frac{1}{\beta} \left\langle \sum_{ij}^{n} M_{ji}\ e^{i\nu(\tau_i - \tau'_j)}\ \delta_{t(i)\,a}\ \delta_{t(j)\,a} \right\rangle_{\mathrm{MC}}. \tag{3.34}$$

Since a "measurement", i.e. the evaluation of the angular brackets in Eq. (3.32) and Eq. (3.34), is rather costly, one usually performs several updates of the configuration between two measurements. Ideally, measurements should be done on uncorrelated configurations. The procedure of Z-sampling with measurement of Green's functions is illustrated in the left panel of Fig. 3.1.

While this way of measuring the one-particle Green's function is considered state-of-the-art, it can nevertheless be problematic in the case of very low expansion order. Removal of hybridization lines is only possible, if there are operators in the trace. Thus the above described estimator fails in the case of (nearly) vanishing hybridization. As recently shown, also impurity models with discrete bath states can lead to problems in some cases, because the autocorrelation time τ_A may become extremely large (Hausoel et al., 2021).

Die approbierte gedruckte Originalversion dieser Dissertation ist an der TU Wien Bibliothek verfügbar.
The approved original version of this doctoral thesis is available in print at TU Wien Bibliothek.
TU Bibliothek WIEN Your knowledge hub

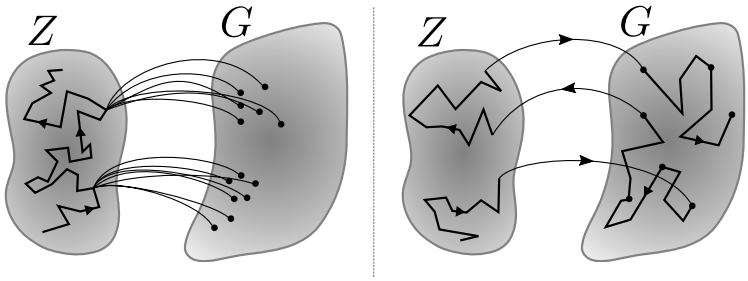

Figure 3.1: Illustration of the two sampling procedures to measure the Green's function. Arrows indicate the direction that the random walker moves, black circles give the points in G-space where the Green's function is measured. In Z-sampling (left) the sampling is done in Z-space, and for generating Green's function configurations the Z-configuration is changed (two hybridization lines are removed). In worm sampling (right) the random walk is done in both spaces.

Worm sampling

In cases where one wants to compute more complicated observables than the one-particle Green's function, the construction of a removal estimator may lead to serious complications. Especially if the observable contains products of operators at equal times, the necessary configurations cannot simply be generated from partition function configurations any more. One may therefore opt for a more general procedure based on the *insertion* of operators: the so-called *worm sampling*.

Warm sampling was first used in interaction expansion approaches (Prokof'ev et al., 1998; Burovski et al., 2006). Here, we describe the application of worm sampling in the hybridization expansion (Gull et al., 2011; Gunacker et al., 2015; Shinaoka et al., 2017a).

The concept is based on an enlargement of the configuration space that is sampled in the Monte Carlo simulation,

$$\mathcal{C} = \mathcal{C}_Z \cup \mathcal{C}_{\mathcal{O}}, \tag{3.35}$$

where $\mathcal{C}_Z$ is the space of partition function configurations that is also sampled in usual CT-HYB, as described above. $\mathcal{C}_{\mathcal{O}}$ is the configuration space of a hybridization expansion of the expectation value $\langle \mathcal{O}(\boldsymbol{\tau}) \rangle$. Here $\mathcal{O}$ is an arbitrary observable that can be written as a product of fermionic creation and annihilation operators $\hat{d}$, $\hat{d}^\dagger$. A potential dependence on several imaginary times is denoted by the vector $\boldsymbol{\tau}$.

This extended configuration space $\mathcal{C}$ now has a partition function

$$Z_{\mathcal{C}} = Z + \eta Z_{\mathcal{O}} \quad \text{with} \quad Z_{\mathcal{O}} = \int d^d\tau \, \mathrm{Tr}\left[e^{-\beta H_{\mathrm{AIM}}} \, \mathcal{O}(\boldsymbol{\tau}) \right], \tag{3.36}$$

in which an additional contribution $Z_{\mathcal{O}}$ comes from the operator $\mathcal{O}$, whose d imaginary-time arguments are integrated over. Since $Z_{\mathcal{O}}$ may differ from Z considerably, its contribution is scaled by a factor η. In practice, η is chosen such that the number of Monte Carlo steps performed in partition function space is similar to the number of steps in the worm space. The value of η strongly depends on system parameters, as shown for an exemplary case in the left panel of Fig. 3.2 for the case of the one- and two-particle Green's function.

In order to sample the enlarged configuration space $\mathcal{C}$, two more Monte Carlo updates are required: The worm insertion and worm removal. These are responsible for the random

Die approbierte gedruckte Originalversion dieser Dissertation ist an der TU Wien Bibliothek verfügbar.
The approved original version of this doctoral thesis is available in print at TU Wien Bibliothek.
TU Bibliothek WIEN Your knowledge hub

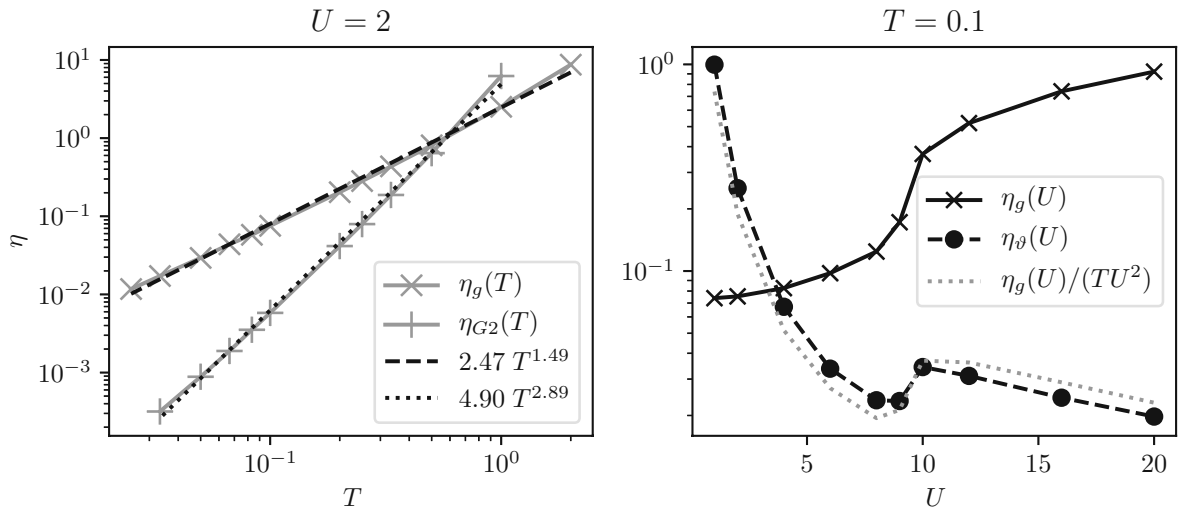

Figure 3.2: Ratio of sampling spaces Z/Z_g for the DMFT impurity of a half-filled square-lattice Hubbard model. Here, η is adjusted in such a way that a similar number of steps is done in Z and worm space. The left panel shows the temperature dependence (at $U = 2t$) of η for the one-particle Green's function and the two-particle Green's function Eq. (3.5). In this case the values of η are similar for all spin components of the two-particle Green's function. On the right side we show the dependence of η on the interaction U, comparing the one-particle Green's function and its symmetric improved estimator ϑ, as defined in Eq. (3.43).

walk to "jump" between the configuration spaces $\mathcal{C}_Z$ and $\mathcal{C}_\mathcal{O}$, as illustrated in the right panel of Fig. 3.1. In many cases it is furthermore necessary to perform worm replacement steps Gunacker et al., 2015. In these, a worm operator and a hybridizing operator exchange their time arguments.

The estimator for such a worm operator $\mathcal{O}$ then takes on a rather simple form,

$$\left\langle \mathcal{O}(\boldsymbol{\tau}) \right\rangle = \left\langle \mathrm{sgn} \times \delta(\boldsymbol{\tau} - \boldsymbol{\tau}') \right\rangle_{\mathrm{MC}}, \tag{3.37}$$

where $\boldsymbol{\tau}'$ are the time arguments of the worm in the randomly generated configurations and sgn is the configuration sign. Let us emphasize here again that the estimator Eq. (3.37) acquires such a simple generic form owing to the rather complicated Markov chain sampling, where all properties of the operator $\mathcal{O}$ enter.

Especially if there is more than one time argument, a time-binning estimator such as Eq. (3.37) is problematic and one replaces the δ-function by a phase factor that generates a Fourier transformation to Matsubara frequencies:

$$\left\langle \mathcal{O}(i\boldsymbol{\nu}) \right\rangle = \left\langle \mathrm{sgn} \times e^{i\boldsymbol{\nu}\cdot\boldsymbol{\tau}} \right\rangle_{\mathrm{MC}}. \tag{3.38}$$

In this rather abstract notation, the dot product between the vector of fermionic Matsubara frequencies and imaginary times is defined in a way that frequencies corresponding to creation and annihilation operators have opposite sign. If an even number of time arguments are equal to each other, the resulting sum or difference of fermionic Matsubara frequencies is a bosonic Matsubara frequency.

Since worm sampling is a very general method, there is a large choice for the operator $\mathcal{O}$ in the above equations. So far the implementation in w2dynamics (Wallerberger et al., 2019)

Die approbierte gedruckte Originalversion dieser Dissertation ist an der TU Wien Bibliothek verfügbar.
The approved original version of this doctoral thesis is available in print at TU Wien Bibliothek.
TU Bibliothek WIEN Your knowledge hub

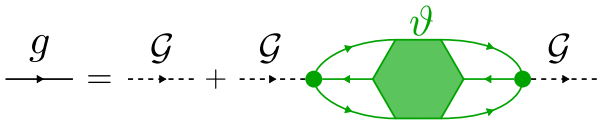

Figure 3.3: Feynman-diagrammatic visualization of the symmetric improved estimator Eq. (3.43) for the one-particle Green's function. The part of the diagram that is drawn in green, will be computed by CT-QMC in the following. Solid lines are full one-particle Green's functions G, dashed lines are non-interacting Green's functions $\mathcal{G}$, and dots are U-matrices. The three-particle Green's function is represented by the hexagon. Note that the Hartree-term $\propto \sum_j U_{[aj][aj]} n_j$ is excluded.

has been used to compute the one- and two-particle Green's function for the AIM (Gunacker et al., 2015), improved estimators (Gunacker et al., 2016), vertex asymptotics (Kaufmann et al., 2017), and symmetric improved estimators (Kaufmann et al., 2019).

3.2* Symmetric improved estimators

3.2.1 Derivation

One-particle estimator

It is well-known that the Heisenberg equation of motion for a one-particle Green's function is an equation that connects the one- and two-particle Green's functions. This has been exploited in the CT-HYB (Hafermann et al., 2012; Hafermann, 2014; Gunacker et al., 2016) and numerical renormalization group (NRG) (Bulla et al., 1998) algorithms. It leads to the so-called "improved estimator" equation

$$G_a^\nu = \mathcal{G}_a^\nu \left(1 + \xi_a^\nu\right), \tag{3.39}$$

where

$$\xi_{ab}^\nu = \xi_a^\nu \delta_{ab} = \frac{1}{\beta} \int_0^\beta d\tau_1 d\tau_2 \underbrace{\left\langle - T_\tau \hat{q}_a(\tau_1) \hat{d}_b^\dagger(\tau_2) \right\rangle}_{\equiv \xi_a(\tau_1,\tau_2)} e^{i\nu(\tau_1-\tau_2)} \tag{3.40}$$

is a two-particle Green's function [often referred to as "$G\Sigma$"] and $\hat{q}$ contracts three operators at equal time, i.e.,

$$\hat{q}_a = \sum_{jkl} U_{[aj]kl} \hat{d}_j^\dagger \hat{d}_l \hat{d}_k \,, \tag{3.41}$$

$$\hat{q}_a^\dagger = \sum_{mno} U_{mn[ao]} \hat{d}_m^\dagger \hat{d}_n^\dagger \hat{d}_o. \tag{3.42}$$

The explicit derivation of this equation of motion can be found in Appendix D.1 and is based on the derivative with respect to the first time argument of G_a.

In this paper, we now express $\xi_a(\tau_1, \tau_2)$ by using the equation of motion again. This time, we apply it to the second time argument of $\xi_a(\tau_1, \tau_2)$, insert it into Eq. (3.39), and finally arrive

Die approbierte gedruckte Originalversion dieser Dissertation ist an der TU Wien Bibliothek verfügbar.
The approved original version of this doctoral thesis is available in print at TU Wien Bibliothek.
TU Bibliothek WIEN Your knowledge hub

at (for the detailed calculation see Appendix D.1)

$$G_a^\nu = \mathcal{G}_a^\nu \left(1 + \mathcal{G}_a^\nu \left(2 \sum_j U_{[aj][aj]} n_j + \vartheta_a^\nu \right) \right), \tag{3.43}$$

which is also shown by Feynman diagrams in Fig. 3.3. Here, we make use of the anti-symmetric U-matrix Eq. (D.8) in Appendix D.1

$$\frac{1}{2} \left(U_{ijkl} - U_{jikl} \right) =: U_{[ij]kl} \tag{3.44}$$

$$\frac{1}{2} \left(U_{ijkl} - U_{ijlk} \right) =: U_{ij[kl]}. \tag{3.45}$$

and the following three-particle Green's function with only two distinct time arguments is employed

$$\vartheta_{ab}^\nu = \vartheta_a^\nu \delta_{ab} = -\frac{1}{\beta} \int_0^\beta d\tau_1 d\tau_2 \left\langle T_\tau \hat{q}_a(\tau_1) \hat{q}_b^\dagger(\tau_2) \right\rangle e^{i\nu(\tau_1 - \tau_2)}. \tag{3.46}$$

Error propagation. The declared goal of improved estimators is to reduce high-frequency noise in the quantity of interest. Among one-particle quantities, noise is most prominent in the self-energy. Using Eq. (3.43) and the Dyson equation, we get

$$\Sigma_a^\nu = \frac{2 \sum_j U_{[aj][aj]} n_j + \vartheta_a^\nu}{1 + \mathcal{G}_a^\nu (2 \sum_j U_{[aj][aj]} n_j + \vartheta_a^\nu)}. \tag{3.47}$$

The variance of the self-energy can hence approximately be computed by error propagation as (neglecting the error in the density n_i):

$$\mathrm{var}[\Sigma] = \left| \frac{\partial \Sigma}{\partial \vartheta} \right|^2 \mathrm{var}[\vartheta]. \tag{3.48}$$

Since the derivative goes to 1 in the limit of high frequencies, we conclude that the high-frequency noise amplitude is indeed identical to the noise amplitude of the estimator ϑ_a^ν, which should be independent of ν for large ν. This result for the symmetric improved estimator can be compared to the behavior of the conventional improved estimator for which a discussion of the error propagation can be found elsewhere (Wallerberger, 2016). The main result is that the error of the conventional improved estimator grows linearly with ν.

Note that Eq. (3.43) can be further simplified by using the Hartree self-energy $\Sigma_H = 2 \sum_j U_{[aj][aj]} n_j$. Then we have

$$G_a^\nu = \mathcal{G}_a^\nu \left[1 + \mathcal{G}_a^\nu \left(\Sigma_H + \vartheta_a^\nu \right) \right] \tag{3.49}$$

for the Green's function and

$$\Sigma_a^\nu = \frac{\Sigma_H + \vartheta_a^\nu}{1 + \mathcal{G}_a^\nu (\Sigma_H + \vartheta_a^\nu)}. \tag{3.50}$$

Furthermore we want to note that ϑ_a^ν can be analytically continued in the same way as the one-particle Green's function, e.g. by MaxEnt. In cases, where the non-interacting impurity

Die approbierte gedruckte Originalversion dieser Dissertation ist an der TU Wien Bibliothek verfügbar.
The approved original version of this doctoral thesis is available in print at TU Wien Bibliothek.
TU Bibliothek WIEN Your knowledge hub

Name	Formula
ξ^{ν}_{ab}	$-\frac{1}{\beta}\int_0^\beta d\tau_1\, d\tau_2\, \left\langle T_\tau \hat{q}_a(\tau_1)\hat{d}^\dagger_b(\tau_2)\right\rangle\, e^{i\nu(\tau_1-\tau_2)}$
ϑ^{ν}_{ab}	$-\frac{1}{\beta}\int_0^\beta d\tau_1\, d\tau_2\, \left\langle T_\tau \hat{q}_a(\tau_1)\hat{q}^\dagger_b(\tau_2)\right\rangle\, e^{i\nu(\tau_1-\tau_2)}$
ϕ^{ω}_{abcd}	$\frac{1}{\beta}\int d\tau_1\, d\tau_2\, \left\langle T_\tau (Un)_{ab}(\tau_1)(Un)_{cd}(\tau_2)\right\rangle\, e^{i\omega(\tau_1-\tau_2)}$
ψ^{ω}_{abcd}	$\frac{1}{\beta}\int d\tau_1\, d\tau_2\, \left\langle T_\tau (U\hat{d}\hat{d})_{ac}(\tau_1)(U\hat{d}^\dagger\hat{d}^\dagger)_{bd}(\tau_2)\right\rangle\, e^{i\omega(\tau_1-\tau_2)}$
$f^{\nu\omega}_{abcd}$	$\frac{1}{\beta}\int d\tau_1\, d\tau_2\, d\tau_3\, \left\langle T_\tau \hat{q}_a(\tau_1)\hat{q}^\dagger_b(\tau_2)(Un)_{cd}(\tau_3)\right\rangle\, e^{i\nu(\tau_1-\tau_2)+i\omega(\tau_2-\tau_3)}$
$g^{\nu\nu'}_{abcd}$	$\frac{1}{\beta}\int d\tau_1\, d\tau_2\, d\tau_3\, \left\langle T_\tau \hat{q}_a(\tau_1)\hat{q}_c(\tau_2)(U\hat{d}^\dagger\hat{d}^\dagger)_{bd}(\tau_3)\right\rangle\, e^{i\nu(\tau_1-\tau_3)+i\nu'(\tau_2-\tau_3)}$
$h^{\nu_1\nu_2\nu_3\nu_4}_{abcd}$	$\frac{1}{\beta}\int d\tau_1\, d\tau_2\, d\tau_3\, d\tau_4\, \left\langle T_\tau \hat{q}_a(\tau_1)\hat{q}^\dagger_b(\tau_2)\hat{q}_c(\tau_3)\hat{q}^\dagger_d(\tau_4)\right\rangle\, e^{i(\nu_1\tau_1-\nu_2\tau_2+\nu_3\tau_3-\nu_4\tau_4)}$

Table 3.1: Terms of the symmetric improved estimators. We use the abbreviations $(Un)_{ab} = \sum_{jk} U_{[aj][bk]}\hat{d}^\dagger_j\hat{d}_k$, $(U\hat{d}^\dagger\hat{d}^\dagger)_{ab} = \sum_{jk} U_{jk[ab]}\hat{d}^\dagger_j\hat{d}^\dagger_k$ and $(U\hat{d}\hat{d})_{ab} = \sum_{jk} U_{[ab]jk}\hat{d}_k\hat{d}_j$. Frequencies $\nu_{(i)}$ and ω are fermionic and bosonic Matsubara frequencies, respectively.

Green's function $\mathcal{G}^{\nu}_a$ is known analytically, this allows for obtaining the spectral function with higher precision, because all information about the non-interacting system enters exactly. In principle the same can be achieved by analytically continuing the self-energy and using the usual Dyson equation, but the data of the self-energy are obtained by the non-linear relation Eq. (3.43) and thus, in general, not normal distributed.

If the non-interacting Green's function is known only on the Matsubara axis, it is however better to analytically continue the self-energy, and not ϑ^{ν}_a. Otherwise one would have to combine the analytically continued $\mathcal{G}$ with the analytically continued ϑ, which leads to spectral functions that are not positive definite, if done in a straightforward way.

Two-particle estimator

For the symmetric improved estimator of the two-particle Green's function, we obtain (again see the Appendix D.2 for the derivation):

$$G^{\nu_1\nu_2\nu_3\nu_4}_{abcd} = \mathcal{G}^{\nu_1}_a\left(-R^{\nu_1\nu_2\nu_3\nu_4}_{1,abcd} + \mathcal{G}^{\nu_2}_b\left(R^{\nu_1\nu_2\nu_3\nu_4}_{2,abcd} + \mathcal{G}^{\nu_3}_c\left(-R^{\nu_1\nu_2\nu_3\nu_4}_{3,abcd} + \mathcal{G}^{\nu_4}_d\left(R^{\nu_1\nu_2\nu_3\nu_4}_{4,abcd} + \frac{1}{\beta}h^{\nu_1\nu_2\nu_3\nu_4}_{abcd}\right)\right)\right)\right) \tag{3.51}$$

Die approbierte gedruckte Originalversion dieser Dissertation ist an der TU Wien Bibliothek verfügbar.
The approved original version of this doctoral thesis is available in print at TU Wien Bibliothek.
TU Bibliothek WIEN Your knowledge hub

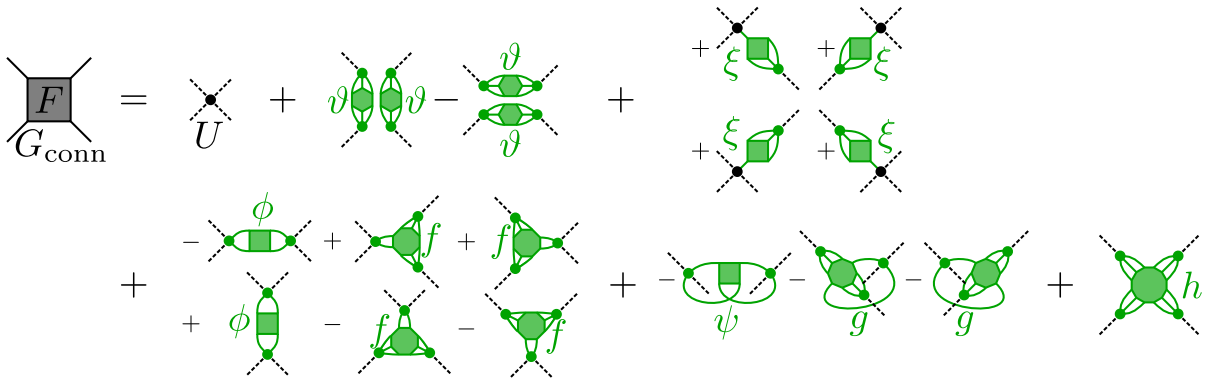

Figure 3.4: Heuristic drawing of the Feynman-diagrammatic decomposition of the connected part of the two-particle Green's function, as obtained by symmetric improved estimators. The estimators that are later computed by CT-QMC are drawn in green. Solid lines represent interacting one-particle Green's functions G, dashed lines are non-interacting Green's functions $\mathcal{G}$, and dots are U-matrices. The terms involving ϑ are to be understood as products. Note that Hartree-like terms and products thereof are not shown, in order to make the picture more concise.

where

$$R_1^{\nu_1\nu_2\nu_3\nu_4} = -\delta_{12}G_d^{\nu_4} + \delta_{14}G_b^{\nu_2}, \tag{3.52}$$

$$R_2^{\nu_1\nu_2\nu_3\nu_4} = -\delta_{12}\mathcal{G}_c^{\nu_3}2\sum_j U_{[aj][aj]}n_j - \delta_{14}\xi_d^{\nu_4} - \frac{2}{\beta}\mathcal{G}_c^{\nu_3}\mathcal{G}_d^{\nu_4}\left[-U_{[ac][bd]} + \sum_i\left(U_{[ai][bd]}\xi_{ci}^{\nu_3} + U_{[ac][bi]}\xi_{di}^{\nu_4}\right) - 2\phi_{abcd}^{\nu_4-\nu_3} + f_{cdab}^{\nu_3(\nu_3-\nu_4)}\right], \tag{3.53}$$

$$R_3^{\nu_1\nu_2\nu_3\nu_4} = \delta_{12}\vartheta_a^{\nu_1} + \frac{1}{\beta}\mathcal{G}_d^{\nu_4}\left[2\sum_i\left(U_{[ic][bd]}\xi_{ai}^{\nu_1} + U_{[ac][id]}\xi_{bi}^{\nu_2}\right)\right. \tag{3.54}$$

$$\left. - \psi_{abcd}^{\nu_1+\nu_3} + 4\phi_{adcb}^{\nu_1-\nu_4} + 2f_{adcb}^{\nu_1(\nu_1-\nu_4)} - g_{dcba}^{\nu_4\nu_2}\right], \tag{3.55}$$

$$R_4^{\nu_1\nu_2\nu_3\nu_4} = \frac{1}{\beta}\left[2f_{cbad}^{\nu_3(\nu_4-\nu_1)} + g_{abcd}^{\nu_1\nu_3} - 2f_{abcd}^{\nu_1(\nu_1-\nu_2)}\right]. \tag{3.56}$$

All estimators occurring on the right-hand side of Eqs. (3.52)-(3.56) are defined in Table 3.1. In order to obtain a more symmetric form, we further made use of the relations $\delta_{\nu_1\nu_2} \equiv \delta_{\nu_1\nu_2}\delta_{\nu_3\nu_4}$ and $\delta_{\nu_1\nu_4} \equiv \delta_{\nu_2\nu_3}\delta_{\nu_3\nu_4}$, which are valid due to energy conservation. Additionally we employed $\delta_{12} \equiv \delta_{ab}\delta_{cd}\delta_{\nu_1\nu_2}\delta_{\nu_3\nu_4}$ and $\delta_{14} \equiv \delta_{ad}\delta_{bc}\delta_{\nu_1\nu_4}\delta_{\nu_2\nu_3}$ to make the expressions shorter.
Inserting the R_i terms from Eqs. (3.52)-(3.56) into Eq. (3.51) and regrouping the terms leads to the following expression for the symmetric improved two-particle Green's function:

Die approbierte gedruckte Originalversion dieser Dissertation ist an der TU Wien Bibliothek verfügbar.
The approved original version of this doctoral thesis is available in print at TU Wien Bibliothek.
TU Bibliothek WIEN Your knowledge hub

$$
\begin{aligned}
G^{\nu_1\nu_2\nu_3\nu_4}_{abcd} &= \left(\delta_{12}-\delta_{14}\right)G^{\nu_1}_{a}G^{\nu_3}_{c} - \frac{1}{\beta}\mathcal{G}^{\nu_1}_{a}\mathcal{G}^{\nu_2}_{b}\mathcal{G}^{\nu_3}_{c}\mathcal{G}^{\nu_4}_{d}\mathfrak{F}^{\nu_1\nu_2\nu_3\nu_4}_{abcd} \quad \text{with} \\
\mathfrak{F}^{\nu_1\nu_2\nu_3\nu_4}_{abcd} &= \beta\left(\delta_{12}-\delta_{14}\right)\left(2\sum_i U_{[ai][ai]}n_i + \vartheta^{\nu_1}_{a}\right)\left(2\sum_j U_{[cj][cj]}n_j + \vartheta^{\nu_3}_{c}\right) \\
&\quad + 2U_{[ac][bd]} + 2\sum_i\left(U_{[ic][bd]}\xi^{\nu_1}_{ai} + U_{[ac][id]}\xi^{\nu_2}_{bi} + U_{[ai][bd]}\xi^{\nu_3}_{ci} + U_{[ac][bi]}\xi^{\nu_4}_{di}\right) \\
&\quad \underbrace{-4\phi^{\nu_1-\nu_2}_{abcd} + 2f^{\nu_1(\nu_1-\nu_2)}_{abcd} + 2f^{\nu_3(\nu_2-\nu_1)}_{cdab}}_{(i)} \underbrace{+4\phi^{\nu_1-\nu_4}_{adcb} - 2f^{\nu_1(\nu_1-\nu_4)}_{adcb} - 2f^{\nu_3(\nu_4-\nu_1)}_{cbad}}_{(ii)} \\
&\quad \underbrace{-\psi^{\nu_1+\nu_3}_{abcd} - g^{\nu_1\nu_3}_{abcd} - g^{\nu_4\nu_2}_{dcba}}_{(iii)} + h^{\nu_1\nu_2\nu_3\nu_4}_{abcd} \,. \qquad (3.57)
\end{aligned}
$$

(A pictorial representation of this formula is found in Fig. 3.4.) The quantities entering here are the antisymmetrized Coulomb interaction U, the one-particle density n_i and the correlators ϑ and ξ which already appeared for the one-particle Green's function in Section 3.2.1. In order to shorten the expression, we singled out the disconnected part $(\delta_{12}-\delta_{14})G^{\nu_1}_{a}G^{\nu_3}_{c}$ of the two-particle Green's function by applying Eq. (3.43). However, there remains another term proportional to $(\delta_{12}-\delta_{14})$ in $\mathfrak{F}$. This is rooted in the expansion via equations of motion, which always leads to expressions involving non-interacting Green's functions $\mathcal{G}$. The 10 terms in the last line of Eq. (3.57) are genuinely related to the two-particle Green's function. Further, the frequency structure of the terms (i)-(iii) resembles the contributions from the particle-hole, transversal particle-hole and particle-particle channel (Rohringer et al., 2018). The last term $h^{\nu_1\nu_2\nu_3\nu_4}_{abcd}$ must hence include fully irreducible contributions.

Two-particle vertex. As for two-particle quantities, one is often interested in vertex functions instead of the Green's function itself, e.g. when calculating susceptibilities (Georges et al., 1996; Kuneš, 2011) or for diagrammatic extensions of DMFT (Toschi et al., 2007; Rubtsov et al., 2008; Rohringer et al., 2018). The full vertex F is related to the two-particle Green's function by

$$
G^{\nu_1\nu_2\nu_3\nu_4}_{abcd} = (\delta_{12}-\delta_{14})G^{\nu_1}_{a}G^{\nu_3}_{c} - \frac{1}{\beta}G^{\nu_1}_{a}G^{\nu_2}_{b}G^{\nu_3}_{c}G^{\nu_4}_{d}F^{\nu_1\nu_2\nu_3\nu_4}_{abcd}. \qquad (3.58)
$$

This bears a certain similarity to Eq. (3.57), and it becomes apparent, that the full vertex is given by

$$
F^{\nu_1\nu_2\nu_3\nu_4}_{abcd} = \frac{\mathcal{G}^{\nu_1}_{a}\mathcal{G}^{\nu_2}_{b}\mathcal{G}^{\nu_3}_{c}\mathcal{G}^{\nu_4}_{d}}{G^{\nu_1}_{a}G^{\nu_2}_{b}G^{\nu_3}_{c}G^{\nu_4}_{d}}\mathfrak{F}^{\nu_1\nu_2\nu_3\nu_4}_{abcd} \,. \qquad (3.59)
$$

Error propagation. Assuming that quantities measured in CT-QMC have approximately the same noise amplitude over the whole frequency range, we can conclude that this holds for $\mathfrak{F}$ as well. We furthermore conclude from Eq. (3.59) that the noise amplitude is rescaled by $\mathcal{G}^{\nu}/G^{\nu}$ in every frequency variable. Since this ratio goes to 1 in the limit of high frequency, we may finally conclude that the noise amplitude of the vertex F in the high-frequency region is

Die approbierte gedruckte Originalversion dieser Dissertation ist an der TU Wien Bibliothek verfügbar.
The approved original version of this doctoral thesis is available in print at TU Wien Bibliothek.
TU Bibliothek WIEN Your knowledge hub

identical to the noise amplitude of $\mathfrak{F}$ and thus directly proportional to the error of the Monte Carlo simulation. We hence expect (and will confirm this later) a constant noise level for large Matsubara frequencies.

In contrast, for conventional CT-QMC calculations in the hybridization expansion a strong increase of noise in F with increasing Matsubara frequencies is observed. This yields a too noisy vertex at high frequencies so that approaches to circumvent the calculation of F at large frequencies have been developed, as e.g. replacing the vertex by its high frequency asymptotics (Kaufmann et al., 2017). This high noise level of conventional CT-HYB calculations can be understood from Eq. (3.58). If we assume a constant noise level of the two-particle Green's function on the left hand side, extracting F by dividing through four Green's functions increases the error four times by a factor $\sim \nu_i$ for large ν_i.

Three-leg vertex

Let us further define the particle-hole three-leg Green's function as

$$G^{\nu_1\nu_2}_{abcd} = \frac{1}{\beta}\int_0^\beta d\tau_1 d\tau_2 d\tau_3\, e^{i\nu_1(\tau_1-\tau_3)-i\nu_2(\tau_2-\tau_3)}\left\langle T_\tau d_a(\tau_1) d^\dagger_b(\tau_2)[d_c\, d^\dagger_d](\tau_3)\right\rangle, \tag{3.60}$$

where ν_1 and ν_2 are fermionic Matsubara frequencies. Differentiation with respect to τ_1 and τ_2 leads to the symmetric improved version

$$\begin{aligned} G^{\nu_1\nu_2}_{abcd} = &-\beta\delta_{12}(1-n_c)G^{\nu_1}_a - \delta_{14}G^{\nu_1}_a G^{\nu_2}_b \\ &- \mathcal{G}^{\nu_1}_a \mathcal{G}^{\nu_2}_b \left[\beta\delta_{12} n_c(2(Un)_a + \vartheta^{\nu_1}_a) - \delta_{14}\xi^{\nu_1}_a \xi^{\nu_2}_b - 2\hat{\phi}^{\nu_1-\nu_2}_{abcd} + \hat{f}^{\nu_1(\nu_1-\nu_2)}_{abcd}\right], \end{aligned} \tag{3.61}$$

with the auxiliary definitions

$$\hat{\phi}^{\omega}_{abcd} = \frac{1}{\beta}\int d\tau_1 d\tau_2\, e^{i\omega(\tau_1-\tau_2)}\left\langle T_\tau \sum_{jk} U_{[aj][bk]}[d^\dagger_j d_k](\tau_1)[d^\dagger_d d_c](\tau_2)\right\rangle \tag{3.62}$$

and

$$\hat{f}^{\nu\omega}_{abcd} = \frac{1}{\beta}\int d\tau_1 d\tau_2 d\tau_3\, e^{i\nu(\tau_1-\tau_2)+i\omega(\tau_2-\tau_3)}\left\langle T_\tau q_a(\tau_1) q^\dagger_b(\tau_2)[d^\dagger_d d_c](\tau_3)\right\rangle. \tag{3.63}$$

Since the R_2 term of the symmetric improved estimator of the two-particle Green's function essentially contains a threeleg Green's function, the derivation of the threeleg symmetric improved estimator is completely analogous to the one shown in the last subsection of Appendix D.2.

For diagrammatic extensions of DMFT, the associated three-leg vertex functions are often particularly interesting, see e.g. Katanin et al. (2009), Rubtsov et al. (2012), Ayral and Parcollet (2015), Galler et al. (2017), and Loon et al. (2018b). These are related to the three-leg Green's function by subtraction of disconnected parts and division by two one-particle Green's functions. Representative for the variety of definitions, we show the so-called Kernel-2 function in the particle-hole channel (for a definition see Li et al. (2016), Wentzell et al. (2020), and

Die approbierte gedruckte Originalversion dieser Dissertation ist an der TU Wien Bibliothek verfügbar.
The approved original version of this doctoral thesis is available in print at TU Wien Bibliothek.
TU Bibliothek WIEN Your knowledge hub

Kaufmann et al. (2017)), which can be obtained through the following symmetric improved estimator

$$K^{(2),ph,\nu_1\nu_2}_{abcd} = \left[4\beta\delta_{12}(Un)_a(Un)_c - 4\phi^{\nu_1-\nu_2}_{abcd}\right]\left(\frac{\mathcal{G}^{\nu_1}_a\mathcal{G}^{\nu_2}_b}{G^{\nu_1}_a G^{\nu_2}_b} - 1\right) + 2\frac{\mathcal{G}^{\nu_1}_a\mathcal{G}^{\nu_2}_b}{G^{\nu_1}_a G^{\nu_2}_b}\left[\beta\delta_{12}\vartheta^{\nu_1}_a(Un)_c - \xi^{\nu_1}_a\xi^{\nu_2}_b U_{[cb][da]} + f^{\nu_1(\nu_1-\nu_2)}_{abcd}\right]. \tag{3.64}$$

3.2.2 Implementation

As discussed before, the expressions for e.g. the one- or two-particle Green's functions derived using the EOM (Eq. (3.43) and Eq. (3.57)) can be employed in a CT-HYB simulation to obtain results with asymptotically smaller error for high frequencies. In the simulation, we need to get the QMC estimates for the values of each individual term contributing to the symmetric improved estimators (cf. Tab. 3.1), i.e. of correlation functions consisting of up to 12 operators with up to 4 different imaginary time or 3 different Matsubara frequency arguments with several components corresponding to possible combinations of the discrete quantum numbers of the operators.

The method of choice for computing such complicated correlation functions in CT-HYB is worm sampling, which was described in Section 3.1.2. It allows us to compute each component $k_{a_1\ldots a_n}$ of each correlation function k (see Table 3.1) in a separate sampling run. The balancing parameter $\eta_{k_{a_1\ldots a_n}}$ that was introduced in Eq. (3.36) guarantees that a similar amount of steps is done both in partition function and worm space. Here it is important that also $\eta_{k_{a_1\ldots a_n}}$ is determined separately for each component of each correlation function, such that all components are measured with comparable precision.

A comparison of the weight factor η_ϑ of the symmetric improved estimator ϑ for a one-orbital impurity, with the weight factor η_g for the one-particle Green's function is shown in the right panel of Fig. 3.2. Note that in this case there is only one inequivalent component of the correlation function that has to be measured. Therefore the additional component index is omitted.

The value of η gives a feeling about the "volume" of the worm space. Since η enters the acceptance ratio for worm insertions as a multiplicative factor, a larger value of η corresponds to a "smaller" worm space. In contrast to the space of the one-particle Green's function, which is continuously "shrinking" as the interaction is increased, the worm space of ϑ is growing. This can however be related to its additional prefactor U^2.

The sampling of correlation functions that contain operators $\hat{q}$ or $\hat{q}^\dagger$ can be made more effective by devising spectial replacement moves (cf. Section 3.1.2).

In Ref. Gunacker et al., 2015, these moves transfer the "worm status" from a worm operator to a hybridization operator, i.e. they change which operators are connected with hybridization events (and accordingly only change the bath weight). Since, contrary to Ref. Gunacker et al., 2015, our estimators contain several operators at equal times, the procedure needs to be slightly modified as compared to a simple replacement: After we select one impurity operator

Die approbierte gedruckte Originalversion dieser Dissertation ist an der TU Wien Bibliothek verfügbar.
The approved original version of this doctoral thesis is available in print at TU Wien Bibliothek.
TU Bibliothek WIEN Your knowledge hub

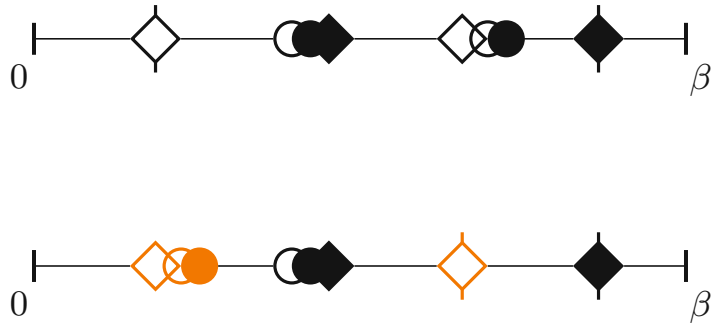

Figure 3.5: Symbolic representation of a "replacement" move applied to a worm operator that is at equal time with two other operators. Operators are represented as symbols (flavors) on the imaginary time axis before (top) and after (bottom) the move, with filled symbols representing creators and little vertical tags at the symbols' top and bottom signifying operators connected to hybridization events. Changes due to the move are marked in orange.

connected to a hybridization event at τ_h and one worm operator at τ_w for a replacement, we not only "exchange" them (changing only the bath part of the weight), but also move any other worm operators at τ_w to τ_h to reconstruct the same equal-time object at another position (cf. Fig. 3.5). This may cause a lower acceptance rate compared to simpler replacements, but especially if the other worm operators are density-like (which may e.g. be the case when performed on a $\hat{q}$), these moves are reasonably effective.

3.2.3 Validation

The best way to validate CT-QMC results is benchmarking against exact diagonalization (ED). To this end CT-QMC results were calculated in w2dynamics (Wallerberger et al., 2019) and, at the same time, all estimators were calculated exactly by evaluating their Lehmann representation for a small Hamiltonian, i.e. an impurity model with one orbital and a discrete bath. The ED results were also used to confirm the validity of Eq. (3.57).
Specifically, we choose a bath with one energy level $\varepsilon_{\text{bath}} = 0.5$ and hybridization amplitude $V = 0.3$. The chemical potential is set to $\mu = -0.1$, the inverse temperature is chosen to be $\beta = 10$ and the local interaction $U = 2$. At these parameters, every spin-orbital is on average occupied by 0.307 electrons.

Self-energy

The quantities G^ν, ξ^ν and ϑ^ν were evaluated by performing 1.44×10^9 QMC measurements on their respective estimators. Subsequently the one-particle Green's function and the self-energy were calculated from Eq. (3.39) and Eq. (3.43). Fig. 3.6 shows a comparison of the improved and the symmetric improved self-energy as well as the one obtained directly from the CT-HYB Green's function as calculated by worm sampling without improved estimators. We note that both "improved" ways to calculate the self-energy suffer from lower precision in the low-frequency regime. However, except for the first few Matsubara frequencies, where

Die approbierte gedruckte Originalversion dieser Dissertation ist an der TU Wien Bibliothek verfügbar.
The approved original version of this doctoral thesis is available in print at TU Wien Bibliothek.
TU Bibliothek WIEN Your knowledge hub

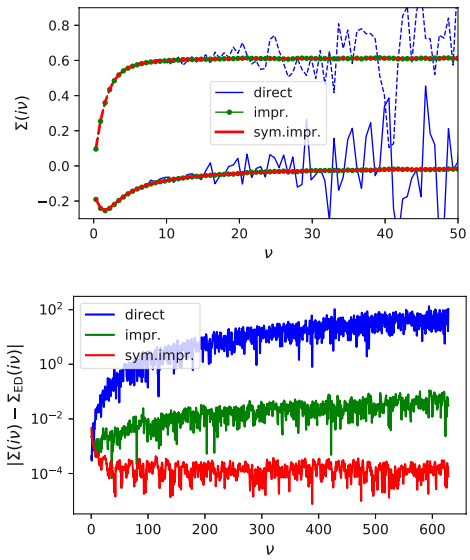

Figure 3.6: Upper panel: Comparison of the self-energy (for the AIM specified in Sec. 3.2.3), as calculated from the directly measured one-particle Green's function (*direct*) vs. the result obtained with improved (*impr.*) and symmetrically improved (*sym. impr.*) estimators. Lower panel: logplot of the absolute difference to exact diagonalization data.

precise quantities can be obtained by conventional Z-sampling of the Green's function, the symmetric improved one-particle estimator yields considerably better results. As anticipated in Section 3.2.1, we also observe a better scaling of the error at high Matsubara frequencies.

Vertex functions

Vertex functions are related to the two-particle Green's function. In order to assemble the symmetric improved form by Eq. (3.57), one needs to sample all seven occurring estimators. The full vertex $F^{\nu\nu'\omega} \equiv F^{\nu(\nu-\omega)(\nu'-\omega)\nu'}$ can be obtained from the connected part of the two-particle Green's function by "amputation" of its legs, i. e. division by a product of four Green's functions, cf. Eq. (3.58). In the high-frequency case this leads to massive noise amplification, if the two-particle Green's function is directly computed in QMC. However, as discussed in Sec. 3.2.1, this is healed by symmetric improved estimators. In Fig. 3.7 we show slices through $F^{\nu\nu'\omega}_{\uparrow\uparrow\downarrow\downarrow}$ at two fixed bosonic frequencies ω. In analogy to the one-particle estimator, we get precise results over the whole frequency range, and in particular, there is no increase of noise at high Matsubara frequencies.

Three-leg vertex

Eq. (3.64) allows us to compute the kernel-2 function $K^{(2),ph,\nu(\nu-\omega)}$ from QMC-estimators that were also used for the full two-particle vertex. In order to judge the improvement introduced by Eq. (3.64), we compute $K^{(2),ph,\nu(\nu-\omega)}_{\uparrow\uparrow\downarrow\downarrow}$ not only in this new way, but also in the way of Kaufmann et al. (2017) from the three-leg Green's function Eq. (3.60) measured in QMC. In Fig. 3.8

Die approbierte gedruckte Originalversion dieser Dissertation ist an der TU Wien Bibliothek verfügbar.
The approved original version of this doctoral thesis is available in print at TU Wien Bibliothek.
TU Bibliothek WIEN Your knowledge hub

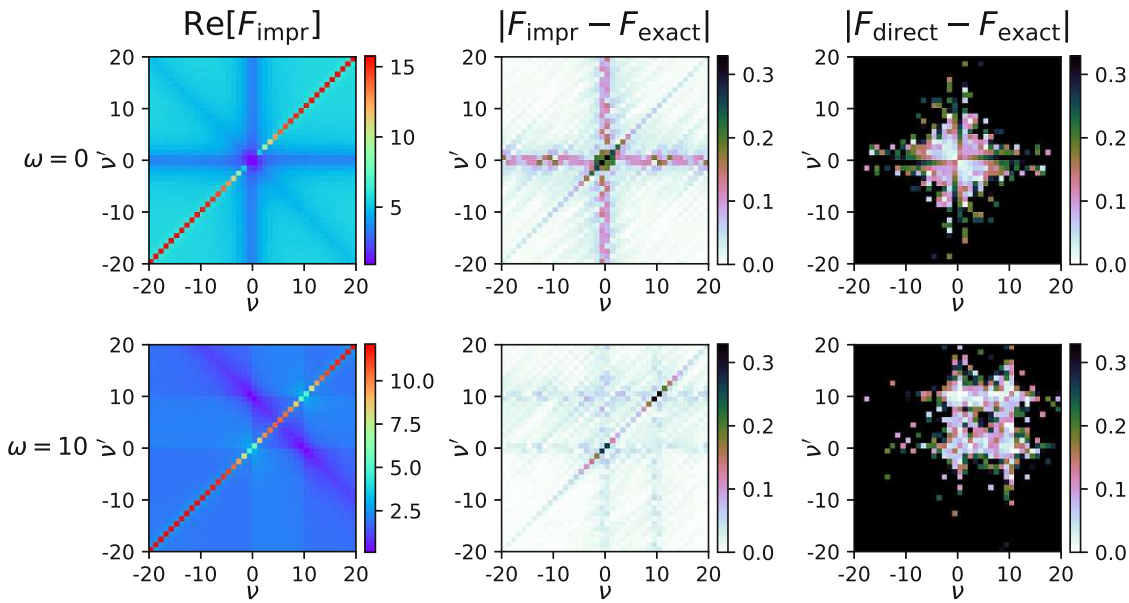

Figure 3.7: Reducible vertex $F^{\nu\nu'\omega}_{\uparrow\uparrow\downarrow\downarrow}$. Upper row: bosonic frequency ν_1–$\nu_2 = \omega = 0$; lower row: ν_1–$\nu_2 = \omega = 10 \times 2\pi/\beta$. First column: F as calculated with symmetric improved estimators; second column: difference of the symmetric improved to the exact result, third column: difference of the conventional calculation (directly measured two-particle Green's function) to the exact result.

we compare the result obtained by symmetric improved estimators to the exact result and to the result of the conventional calculation. Notably also here the increase of noise at high Matsubara frequencies is absent.

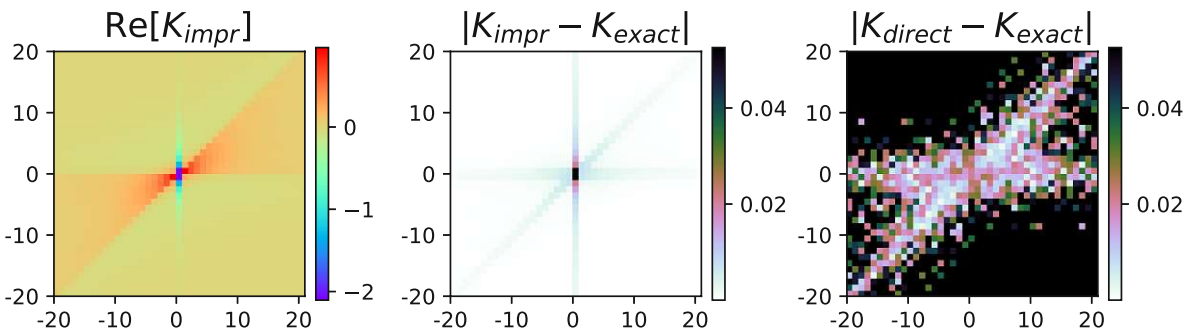

Figure 3.8: Three-leg kernel function $K^{(2),ph,\nu(\nu-\omega)}_{\uparrow\uparrow\downarrow\downarrow}$, calculated by Eq. (3.64) (left), its difference to the exact result (middle), and the difference of the conventional, direct calculation to the exact result (right).

Die approbierte gedruckte Originalversion dieser Dissertation ist an der TU Wien Bibliothek verfügbar.
The approved original version of this doctoral thesis is available in print at TU Wien Bibliothek.
TU Bibliothek WIEN Your knowledge hub

Die approbierte gedruckte Originalversion dieser Dissertation ist an der TU Wien Bibliothek verfügbar.
The approved original version of this doctoral thesis is available in print at TU Wien Bibliothek.
TU Bibliothek WIEN Your knowledge hub

Die approbierte gedruckte Originalversion dieser Dissertation ist an der TU Wien Bibliothek verfügbar.
The approved original version of this doctoral thesis is available in print at TU Wien Bibliothek.
TU Bibliothek WIEN Your knowledge hub

Chapter 4

Local correlations in the Hubbard model

In the previous chapter, we have shown how to compute correlation functions for the AIM. Anderson (1961) devised it for the description of correlated magnetic impurities dissolved in non-magnetic metals, such as Fe/Ni/Co in Al. But in a large number of materials, correlated centers form a regular lattice, which is better described by the Hubbard model Eq. (1.2) and multi-orbital extensions thereof. In order to understand complex phenomena in solids, it is therefore often not enough to model them by an impurity model; instead, it is important to take spatial degrees of freedom of the lattice into account.

As an introduction to this chapter, we will first use the tight-binding model to study non-interacting electrons on a lattice in Section 4.1. Then, by adding a local interaction, the multi-orbital Hubbard model is obtained in Section 4.2. In Section 4.3 we introduce the dynamical mean-field theory (DMFT) as a way to solve the Hubbard model in infinite dimensions. Since DMFT is usually implemented as an iterative procedure, we look at Anderson mixing as a means of convergence acceleration in Section 4.4. Subsequently, we study scattering rates in Section 4.5 and compare them to Boltzmann theory in Section 4.6. The following Section 4.7 and Section 4.8 summarize two papers in which DMFT was applied to excitonic magnets and nickelate superconductors, respectively.

4.1 Tight-binding model

Let us for a moment ignore the electron-electron interaction and consider non-interacting electrons in a periodic potential. The so-called tight-binding model was treated already by Bloch (1929) and later refined by Slater and Koster (1954). Based on the assumption of overlapping localized orbitals it allows for an approximate description of the bandstructure of many materials with a partly filled d-shell.

The main ingredients to this model are the lattice structure and the overlap/transfer integrals $t_{ab}^{(IJ)}(\boldsymbol{R}, \boldsymbol{R}')$. The latter can be interpreted as the probability amplitude for electron hopping from a spin-orbital labeled a and centered on atom (I) of the unit cell located at $\boldsymbol{R}$ to spin-orbital b on atom (J) at $\boldsymbol{R}'$.

For obtaining $t_{ab}^{(IJ)}(\boldsymbol{R}, \boldsymbol{R}')$, there are two approaches: *(i)* one may compute the overlap integral explicitly, e.g., from atomic wave functions or Wannier functions to study certain compounds, or *(ii)* one may construct simple toy models for studying general trends. In this thesis

we mostly use the latter strategy.

Using second quantization, the Hamiltonian for the tight-binding model can be written as

$$H_{\mathrm{TB}} = \sum_{\boldsymbol{R}\boldsymbol{R}'} \sum_{IJ} \sum_{ab} t_{ab}^{(IJ)}(\boldsymbol{R}, \boldsymbol{R}')\, \hat{c}_a^{\dagger(I)}(\boldsymbol{R})\, \hat{c}_b^{(J)}(\boldsymbol{R}'). \tag{4.1}$$

Now we may express the fermionic operators by their momentum-space representation Eq. (2.6) and rewrite the Hamiltonian as

$$H_{\mathrm{TB}} = \sum_{\boldsymbol{k}} \sum_{IJ} \sum_{ab} h_{ab}^{(IJ)}(\boldsymbol{k})\, \hat{c}_a^{\dagger(I)}(\boldsymbol{k})\, \hat{c}_b^{(J)}(\boldsymbol{k}) \tag{4.2}$$

with a dispersion matrix $h_{ab}^{(IJ)}(\boldsymbol{k})$ that is the spatial Fourier transform of the hopping amplitude $t_{ab}^{(IJ)}(\boldsymbol{R}, \boldsymbol{R}')$:

$$h_{ab}^{(IJ)}(\boldsymbol{k}) = \sum_{\boldsymbol{R}} e^{-i\boldsymbol{k}\boldsymbol{R}}\, t_{ab}^{(IJ)}(\boldsymbol{R}, \boldsymbol{0}). \tag{4.3}$$

If $h_{ab}^{(IJ)}(\boldsymbol{k})$ is regarded as a matrix with respect to an orbital-site compound index, then its $\boldsymbol{k}$-dependent eigenvalues form the so-called tight-binding bands $\varepsilon_\alpha(\boldsymbol{k})$:

$$h_{ab}^{(IJ)}(\boldsymbol{k}) = \sum_{\alpha=1}^{N_{\mathrm{bands}}} \left[U(\boldsymbol{k})\right]_{a\alpha}^{(I)} \varepsilon_\alpha(\boldsymbol{k}) \left[U^*(\boldsymbol{k})\right]_{b\alpha}^{(J)}. \tag{4.4}$$

In this notation, U is a unitary square matrix. Its rows are addressed by a compound index of spin-orbital (a) and site index (I), and its columns correspond to the combined band index α.

Since the Hamiltonian Eq. (4.2) is only quadratic in fermionic operators, the retarded Green's function of the tight-binding model can be calculated in a straight-forward way

$$G_{\mathrm{R},ab}^{(IJ)}(\boldsymbol{k}, \omega) = \left[\left[(\omega + i0^+ + \mu)\mathbf{1} - h(\boldsymbol{k})\right]^{-1}\right]_{ab}^{(IJ)}, \tag{4.5}$$

where the inversion is with respect to the spin-orbital-site compound index. Since $h(\boldsymbol{k})$ is diagonal in the band basis, this holds also for the Green's function. We can thus write it with only one band index and without matrix inversion as

$$G_{\mathrm{R},\alpha}(\boldsymbol{k}, \omega) = \frac{1}{\omega + i0^+ + \mu - \varepsilon_\alpha(\boldsymbol{k})}. \tag{4.6}$$

According to Eq. (2.21) and Eq. (2.22), the associated spectral density is a Dirac delta

$$A_\alpha(\boldsymbol{k}, \omega) = \delta(\omega + \mu - \varepsilon_\alpha(\boldsymbol{k})). \tag{4.7}$$

Since there is no interaction, the local spectral density $A(\omega)$ is in this case equivalent to the density of states $A_0(\omega)$:

$$A(\omega) = \sum_\alpha \frac{1}{N_k} \sum_{\boldsymbol{k}} A_\alpha(\boldsymbol{k}, \omega) = \sum_\alpha \frac{1}{N_k} \sum_{\boldsymbol{k}} \delta(\omega + \mu - \varepsilon_\alpha(\boldsymbol{k})) \equiv A_0(\omega). \tag{4.8}$$

Die approbierte gedruckte Originalversion dieser Dissertation ist an der TU Wien Bibliothek verfügbar.
The approved original version of this doctoral thesis is available in print at TU Wien Bibliothek.
TU Bibliothek WIEN Your knowledge hub

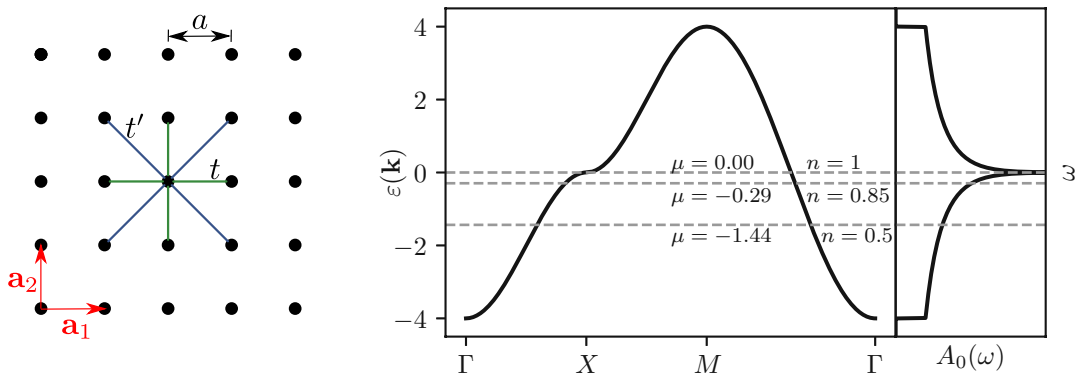

Figure 4.1: Tight-binding model of the square lattice. Left: real-space picture with nearest- (t) and next-nearest (t') neighbor hopping. Right: dispersion relation for $t = 1$ and $t' = 0$ along a high-symmetry path $\Gamma = (0,0)$, $X = (\pi/a, 0)$, $M = (\pi/a, \pi/a)$, Γ through the Brillouin zone. Also the density of states $A_0(\omega)$ is shown. The dashed horizontal lines show the chemical potential μ that is necessary to get a certain electron number $n = n_\uparrow + n_\downarrow$ at zero temperature. $n = 1$ is frequently referred to as "half filling."

4.1.1 Square lattice

The perhaps simplest example of a tight-binding model, depicted in Fig. 4.1, is the two-dimensional square lattice with basis vectors $\boldsymbol{a}_1 = \begin{pmatrix} a \\ 0 \end{pmatrix}$, $\boldsymbol{a}_2 = \begin{pmatrix} 0 \\ a \end{pmatrix}$, the first Brillouin zone is a square with the reciprocal basis vectors $\boldsymbol{b}_1 = \frac{2\pi}{a}\begin{pmatrix} 1 \\ 0 \end{pmatrix}$, $\boldsymbol{b}_2 = \frac{2\pi}{a}\begin{pmatrix} 0 \\ 1 \end{pmatrix}$. The unit cell contains only one atom[1], and if we assume that on each atom there is only one orbital, then the hopping matrix $t(\boldsymbol{R}, \boldsymbol{R}')$ can be written without orbital or site indices as

$$\begin{aligned} t(\boldsymbol{R}, \boldsymbol{R}') = &- t(\delta_{\boldsymbol{R}',\boldsymbol{R}+\boldsymbol{a}_1} + \delta_{\boldsymbol{R}',\boldsymbol{R}-\boldsymbol{a}_1} + \delta_{\boldsymbol{R}',\boldsymbol{R}+\boldsymbol{a}_2} + \delta_{\boldsymbol{R}',\boldsymbol{R}-\boldsymbol{a}_2}) \\ &+ t'(\delta_{\boldsymbol{R}',\boldsymbol{R}+\boldsymbol{a}_1+\boldsymbol{a}_2} + \delta_{\boldsymbol{R}',\boldsymbol{R}-\boldsymbol{a}_1+\boldsymbol{a}_2} + \delta_{\boldsymbol{R}',\boldsymbol{R}+\boldsymbol{a}_1-\boldsymbol{a}_2} + \delta_{\boldsymbol{R}',\boldsymbol{R}-\boldsymbol{a}_1-\boldsymbol{a}_2}) \end{aligned} \tag{4.9}$$

where the negative sign in front of the t term in the first line is chosen by convention. After Fourier transform by Eq. (4.3), at a point $\boldsymbol{k} = k_x\boldsymbol{b}_1 + k_y\boldsymbol{b}_2$ in reciprocal (momentum) space this becomes

$$h(\boldsymbol{k}) = \epsilon(\boldsymbol{k}) = -2t[\cos(2\pi k_x) + \cos(2\pi k_y)] + 4t'\cos(2\pi k_x)\cos(2\pi k_y). \tag{4.10}$$

The density of states $A_0(\omega)$ can in this case be calculated analytically, see e.g. Katanin et al. (2012). For the simplified case of $t' = 0$ it is

$$A_0(\omega) = \frac{1}{2\pi t} K\left(\sqrt{1 - \left(\frac{\omega}{4t}\right)^2}\right), \tag{4.11}$$

where K is the complete elliptic integral of the first kind.[2]

[1] In principle it is possible to use different tilings with larger supercells containing, e.g., two or four atoms. Then the Brillouin zone is smaller, but there are as many bands as atoms in the supercell.

[2] The literature knows various conventions of the elliptic integral K. For example, the implementation in scipy.special.ellipk relates to the convention used in Eq. (4.11) as $K_{\text{scipy}}(x) = K(\sqrt{x})$.

Die approbierte gedruckte Originalversion dieser Dissertation ist an der TU Wien Bibliothek verfügbar.
The approved original version of this doctoral thesis is available in print at TU Wien Bibliothek.
TU Bibliothek WIEN Your knowledge hub

4.2 Hubbard model

Augmenting the tight-binding model with one orbital per site by a local interaction like in the Anderson model Eq. (3.1) for single-orbital impurities leads to the prototypical Hubbard model (HM) Eq. (1.2). This can be generalized to a multi-orbital lattice model by adding a general local interaction to each site of a tight-binding model Eq. (4.1). For such cases, the Hamiltonian can be written as

$$H_{\mathrm{HM}} = \sum_{\boldsymbol{k}} \sum_{IJ} \sum_{ab} h_{ab}^{(IJ)}(\boldsymbol{k})\, \hat{c}_a^{\dagger(I)}(\boldsymbol{k})\, \hat{c}_b^{(J)}(\boldsymbol{k}) + \frac{1}{2} \sum_{\boldsymbol{R}} \sum_{I} \sum_{abcd} U_{abcd}^{(I)}\, \hat{c}_a^{\dagger(I)}(\boldsymbol{R})\, \hat{c}_b^{\dagger(I)}(\boldsymbol{R})\, \hat{c}_d^{(I)}(\boldsymbol{R})\, \hat{c}_c^{(I)}(\boldsymbol{R}), \tag{4.12}$$

where the local interaction on site I is parametrized by the matrix $U_{abcd}^{(I)}$. Since we have only local interaction on a periodic lattice, there is no dependence of the U-matrix on the unit cell position $\boldsymbol{R}$.

The Green's function of the Hubbard model is given by the Dyson equation (DE)

$$G_{ab}^{(IJ)}(\boldsymbol{k}, i\omega_n) = \left[\left[(i\omega_n + \mu)\mathbf{1} - h(\boldsymbol{k}) - \Sigma(\boldsymbol{k}, i\omega_n) \right]^{-1} \right]_{ab}^{(IJ)}, \tag{4.13}$$

where the inversion is done with respect to a combined orbital-site index. All effects of correlation are incorporated in the self-energy $\Sigma_{ab}^{(IJ)}(\boldsymbol{k}, i\omega_n)$. The chemical potential μ sets the desired particle number and $\mathbf{1}$ is the unit matrix in site-orbital space. However, unfortunately it is not possible to compute $\Sigma_{ab}^{(IJ)}(\boldsymbol{k}, i\omega_n)$ in general. In Section 4.3.1 we will therefore consider a special limiting case, namely the limit of infinite dimensions, in which a mapping to the AIM and thus a solution can be found.

4.3 From Hubbard model to Anderson model: dynamical mean-field theory

4.3.1 Limit of infinite dimensions

Increasing the dimensionality of the lattice is equivalent to increasing its coordination number. It can be shown that in the limit of infinite coordination number (or infinite dimensions) all nonlocal Feynman diagrams for the self-energy vanish (Metzner and Vollhardt, 1989), if the hopping amplitudes between sites at $\boldsymbol{r}_i$ and $\boldsymbol{r}_j$ are scaled properly as

$$t(\boldsymbol{r}_i, \boldsymbol{r}_j) \longrightarrow \frac{t(\boldsymbol{r}_i, \boldsymbol{r}_j)}{\sqrt{\mathcal{Z}_{\|\boldsymbol{r}_i - \boldsymbol{r}_j\|}}}. \tag{4.14}$$

Here, $\mathcal{Z}_{\|\boldsymbol{r}_i - \boldsymbol{r}_j\|}$ is the number of equivalent neighbors at a certain distance, see Held (2007). The self-energy thus becomes a purely local quantity, $\Sigma(\boldsymbol{k}, i\omega_n) \equiv \Sigma(i\omega_n)$. It depends only on the local Green's function and the local interaction. It could thus in principle be computed by summing up all such local self-energy diagrams. However, the locality of the self-energy also

Die approbierte gedruckte Originalversion dieser Dissertation ist an der TU Wien Bibliothek verfügbar.
The approved original version of this doctoral thesis is available in print at TU Wien Bibliothek.
TU Bibliothek WIEN Your knowledge hub

motivates that one can actually find an *auxiliary* AIM (Georges and Kotliar, 1992) whose interacting Green's function $G(i\omega_n)$ is equal to the local ($\boldsymbol{k}$-integrated) interacting Green's function of the HM

$$G(i\omega_n) = \frac{1}{N_k} \sum_{\boldsymbol{k}} G(\boldsymbol{k}, i\omega_n), \tag{4.15}$$

where orbital indices have been suppressed. Here, for the computation of $G(i\omega_n)$ one can use an impurity solver such as CT-QMC, which was described in Chapter 3. Eq. (4.15) can now be rewritten by using the Dyson equation Eq. (4.13) both for the impurity Green's function $G(i\omega_n)$ and lattice Green's function $G(\boldsymbol{k}, i\omega_n)$:

$$G(i\omega_n) = \left[[\mathcal{G}(i\omega_n)]^{-1} - \Sigma(i\omega_n)\right]^{-1}, \tag{4.16}$$

$$G(\boldsymbol{k}, i\omega_n) = \left[(i\omega_n + \mu)\mathbf{1} - h(\boldsymbol{k}) - \Sigma(i\omega_n)\right]^{-1}, \tag{4.17}$$

where $\mathcal{G}(i\omega_n)$ is the non-interacting impurity Green's function, defining the auxiliary AIM, as in Chapter 3. One more relation is rooted in the fact that the impurity problem, specified by $\mathcal{G}(i\omega_n)$, can be solved for either the impurity Green's function $G(i\omega_n)$ or the self-energy $\Sigma(i\omega_n)$. In general, all quantities in Eq. (4.16) and Eq. (4.17) are matrices in orbital indices, and the inversions have to be done in orbital space as well.

Together with the condition Eq. (4.15), the above relations have the character of a mean-field theory, where both the "mean-field" $\mathcal{G}$ and the self-energy Σ are determined such as to fulfill Eq. (4.15). Since the mean-field $\mathcal{G}(i\omega_n)$ is time- or frequency-dependent, it is called dynamical, giving rise to the name *dynamical mean-field theory* (DMFT) (Georges et al., 1996). Let us note that the locality of the self-energy is the basis for the equivalence of the Hubbard model and the Anderson impurity model. In infinite dimensions the self-energy cannot have momentum dependence and thus the exact self-energy of the Hubbard model can be obtained from an auxiliary impurity model.

When considering finite-dimensional systems, the mapping is still an excellent approximation if the momentum-dependence of the lattice self-energy is weak. Therefore the merger of density functional theory (DFT) and DMFT has become a successful method for the *ab initio* calculation of materials with strong electronic correlations (Held, 2007; Kotliar et al., 2006; Aichhorn et al., 2016).

4.3.2 Self-consistent algorithm

The only way how one can solve the problem posed in Section 4.3.1 is a fixed-point iteration which, in the end, converges to the correct self-energy. This comprises the following steps:

1. Lattice problem: In this step, the local Green's function of the lattice is calculated by integrating the momentum-dependent Green's function over the whole Brillouin zone (BZ):

$$G(i\omega_n) = \frac{1}{V_{\mathrm{BZ}}} \int d^d k \left[(i\omega_n + \mu)\mathbf{1} - h(\boldsymbol{k}) - \Sigma(i\omega_n)\right]^{-1}. \tag{4.18}$$

   In the first iteration, one has to guess a starting self-energy. Even the simplest possible choice, $\Sigma = 0$, is usually sufficient. Importantly the locality of the self-energy implies

Die approbierte gedruckte Originalversion dieser Dissertation ist an der TU Wien Bibliothek verfügbar.
The approved original version of this doctoral thesis is available in print at TU Wien Bibliothek.
TU Bibliothek WIEN Your knowledge hub

not only momentum independence, but also $\Sigma^{(IJ)}(i\omega_n) = 0$ if $I \neq J$. At this point also the chemical potential has to be chosen in a way that the particle number has the desired value

$$n = \mathrm{Tr}\,\rho_{\mathrm{loc}} = \sum_{Ia} \frac{1}{\beta} \sum_j e^{-i\omega_j 0^-} G^{(II)}_{aa}(i\omega_j). \tag{4.19}$$

Through Eq. (4.18), $G(i\omega_j)$ depends on μ and Eq. (4.19) can be solved for μ by simple one-dimensional numerical root finding. In some special cases, where the chemical potential is known *a priori*, the root finding for Eq. (4.19) can be omitted. Alternatively, it is possible to do calculations where instead of the density, the chemical potential is fixed.

2 Construct impurity problem(s): The multi-orbital Hubbard model Eq. (4.12) represents a periodic lattice. However, the unit cell that is repeated periodically can contain more than one atom with correlated orbitals. In this case there will be a separate impurity problem for each such atom. Therefore, for the construction of impurity problem I, it is necessary to first enter the subspace of orbitals corresponding to atom I of the unit cell. Formally this is achieved by projection operators P_I, such that we have $G^{(I)}(i\omega_n) = P_I G^{(IJ)}(i\omega_n) P_I^\dagger$ (Aichhorn et al., 2016). The self-energy $\Sigma^{(I)}$ that corresponds to impurity I is extracted in the same way. In all cases considered here, the projection P_I amounts to simply picking out one element of the full matrix in site indices. Then, the non-interacting Green's function of the I-th impurity is

$$\mathcal{G}^{(I)}(i\omega_n) = \left[[G^{(I)}(i\omega_n)]^{-1} - \Sigma^{(I)}(i\omega_n) \right]^{-1} \tag{4.20}$$

The inversions are done only with respect to the orbitals of atom I.

3 Solve impurity problem(s): For each of the impurity problems, specified by $\mathcal{G}^{(I)}$, an impurity Green's function $G^{(I)}$ is computed, e.g. by CT-QMC or ED. The impurity self-energy then follows from Dyson's equation as $\Sigma^{(I)} = [\mathcal{G}^{(I)}]^{-1} - [G^{(I)}]^{-1}$. Once all impurity problems are solved, the local self-energy for the whole unit cell is obtained as $\Sigma = \sum_I P_I^\dagger \Sigma^{(I)} P_I$. This new self-energy is then inserted into Eq. (4.18), starting the next iteration.

We can summarize this procedure as follows. The parameters of the Hubbard Hamiltonian Eq. (4.12), namely the tight-binding dispersion $h(\boldsymbol{k})$ and the interaction U-matrix, remain unchanged throughout the whole calculation and are thus also the parameters of the self-consistent DMFT cycle. Since we consider a grand canonical ensemble, also either the particle number n or the chemical potential μ can be regarded as an additional parameter.

The input at step **1** of each iteration is a local self-energy Σ, which we will refer to as *trial* self-energy. Together with the model parameters it determines all other quantities in steps **1** and **2**. The main output of step **3** is again a local self-energy, which we will refer to as *result* self-energy. If the difference between result and trial self-energy is below a certain tolerance, or several subsequent iterations yield sufficiently similar results, the calculation is converged. Equivalently to the self-energy, also the hybridization function or the Green's function can be used to assess convergence, but we will adhere to the self-energy.

Die approbierte gedruckte Originalversion dieser Dissertation ist an der TU Wien Bibliothek verfügbar.
The approved original version of this doctoral thesis is available in print at TU Wien Bibliothek.
TU Bibliothek WIEN Your knowledge hub

Convergence and mixing

Thus the DMFT self-consistency cycle can be regarded as the search for the fixed point of a very complicated functional $\mathfrak{D}$, which summarizes the steps **1–3** described above:

$$\Sigma = \mathfrak{D}_{h,U,n}[\Sigma] \tag{4.21}$$

Although there are cases, where, e.g., $\mathfrak{D}$ has two different fixed points within the coexistence region of the metal insulator transition(Georges and Krauth, 1993; Rozenberg et al., 1994; Georges et al., 1996), we shall here mainly focus on cases where there is a unique solution.

The arguably simplest way to find the fixed-point in Eq. (4.21) is starting at some guess Σ_0. Then $\Sigma_1 = \mathfrak{D}[\Sigma_0]$ is the results of the first iteration and the procedure continues by always taking the result of the previous iteration as an input for the next iteration,

$$\Sigma_n = \mathfrak{D}[\Sigma_{n-1}]. \tag{4.22}$$

If the functional $\mathfrak{D}$ is not a contraction, this simple procedure may fail to find the fixed point. In such a case a slightly modified procedure can nevertheless lead to success, the so-called *linear mixing*

$$\Sigma_n = (1-\alpha)\Sigma_{n-1} + \alpha\mathfrak{D}[\Sigma_{n-1}] = \Sigma_{n-1} + \alpha(\mathfrak{D}[\Sigma_{n-1}] - \Sigma_{n-1}) \tag{4.23}$$

with a relaxation parameter α. For $0 < \alpha < 1$ we get under-relaxation which slows down convergence in some cases, but also dampens oscillations. If the self-consistency iterations diverge without mixing, convergence may still be facilitated by the use of under-relaxation. Choosing $\alpha = 1$ reproduces Eq. (4.22). In principle it is also possible to choose $\alpha > 1$ for over-relaxation, which can have predictive behavior and thus reduce the number of iterations until convergence. However, it also amplifies errors and will lead to divergence in many cases.

The convergence behavior of a simple DMFT calculation without mixing [Eq. (4.22)] is illustrated in Fig. 4.2. We consider the square-lattice Hubbard model with $t = 1$ and a filling of $n = 0.85$ at interaction $U = 4$ and inverse temperature $\beta = 5$. Concretely, we show the chemical potential μ and the imaginary part of the self-energy at three Matsubara frequencies as a function of the iteration number. The calculation is done twice in order to show the effect of using different strategies for solving the impurity model. In one case we use the Z-sampling estimator Eq. (3.34), the other is done with symmetric improved estimators Eq. (3.43). For comparability the number of QMC measurements was adapted such that both calculations use the same computational time. The plots on the left-hand side of Fig. 4.2 show that in both cases convergence seems to be reached quickly. Looking at the zoom-in at the right-hand side, we however notice that calculations with symmetric improved estimator have a more stable convergence behavior, which can be attributed to the drastically reduced high-frequency noise. It is worth noting that higher Matsubara frequencies of the self-energy converge faster than lower ones. This is not surprising, since the asymptotic behavior is, in principle, known analytically. The chemical potential converges slightly slower, since it depends on all frequencies of the self-energy. In a simple case like the metallic regime of the square-lattice Hubbard model, we may thus regard the chemical potential as an overall convergence indicator. (Note however that in an insulating system the chemical potential is not a well-defined quantity.)

Die approbierte gedruckte Originalversion dieser Dissertation ist an der TU Wien Bibliothek verfügbar.
The approved original version of this doctoral thesis is available in print at TU Wien Bibliothek.
TU Bibliothek WIEN Your knowledge hub

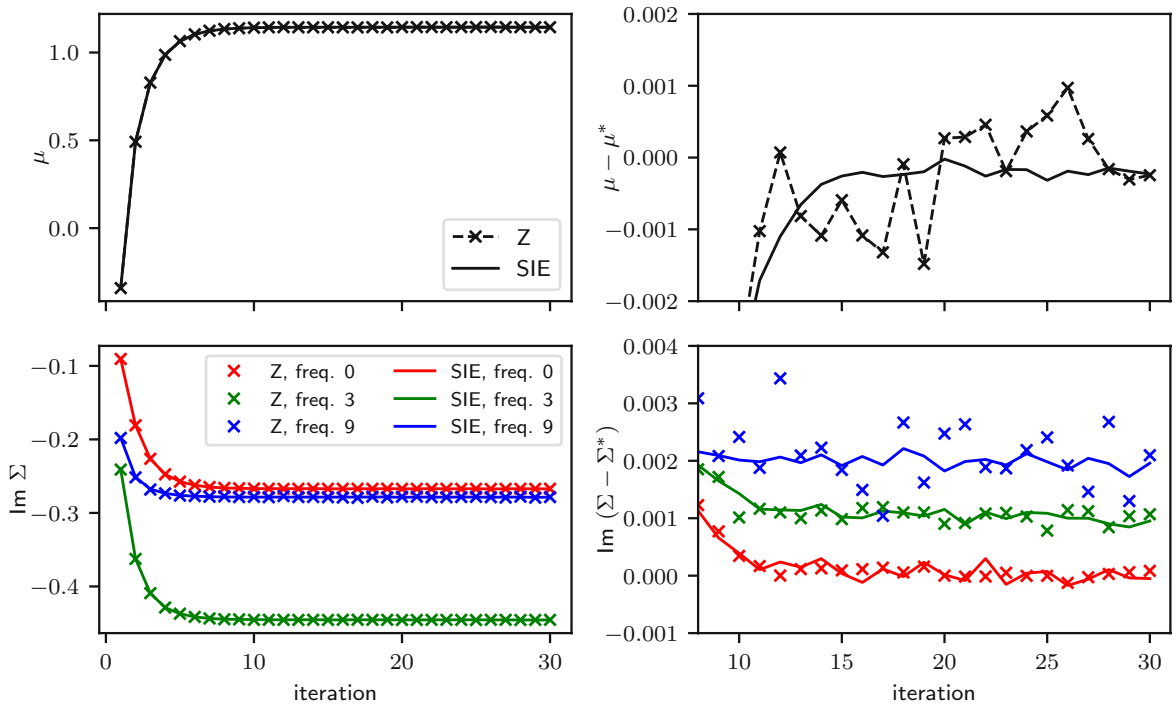

Figure 4.2: DMFT convergence, using Z-sampling (×-markers) versus symmetric improved estimators (SIE, solid lines) for solving the impurity problem. Top left: chemical potential μ in dependence of iteration number, bottom left: imaginary part of the self-energy at three different Matsubara frequencies in dependence of iteration number. Top right: Difference $|\mu - \mu^*|$ of chemical potential to average value μ^* of the last 10 iterations. Bottom right: Difference of the self-energy to the average of the last 10 iterations. The lines for the corresponding to the different Matsubara frequencies are shifted by 0.001 and 0.002 for better visibility.

Let us now turn to the effect of linear mixing, studying the same model as above. Before each iteration the self-energy is now updated according to Eq. (4.23) with $\alpha = 0.8$. The convergence behavior is shown in Fig. 4.3, where we also compare to the case of $\alpha = 1$ that was examined in Fig. 4.2. The comparison shows that the number of iterations required for convergence is increased from approximately 15 to approximately 20, owing to the under-relaxation. It is however also visible that the convergence of the self-energy is considerably smoothened.

4.4* Convergence acceleration

This section was partly done together with a project student, Andreas Stefl, whom I supervised.

If one wants to accelerate convergence of a self-consistent procedure, it seems reasonable to use information from multiple previous iterations. One of the first methods to do so is the Anderson acceleration/mixing, developed by Donald G. Anderson (1965). It uses so-called direct inversion in iterative subspace (DIIS) and is also known under the name or Pulay mixing (Pulay, 1980; Pulay, 1982; Walker and Ni, 2011). Furthermore, Anderson mixing was shown to be identical to the modified second Broyden method (Eyert, 1996).

Die approbierte gedruckte Originalversion dieser Dissertation ist an der TU Wien Bibliothek verfügbar.
The approved original version of this doctoral thesis is available in print at TU Wien Bibliothek.
TU Bibliothek WIEN Your knowledge hub

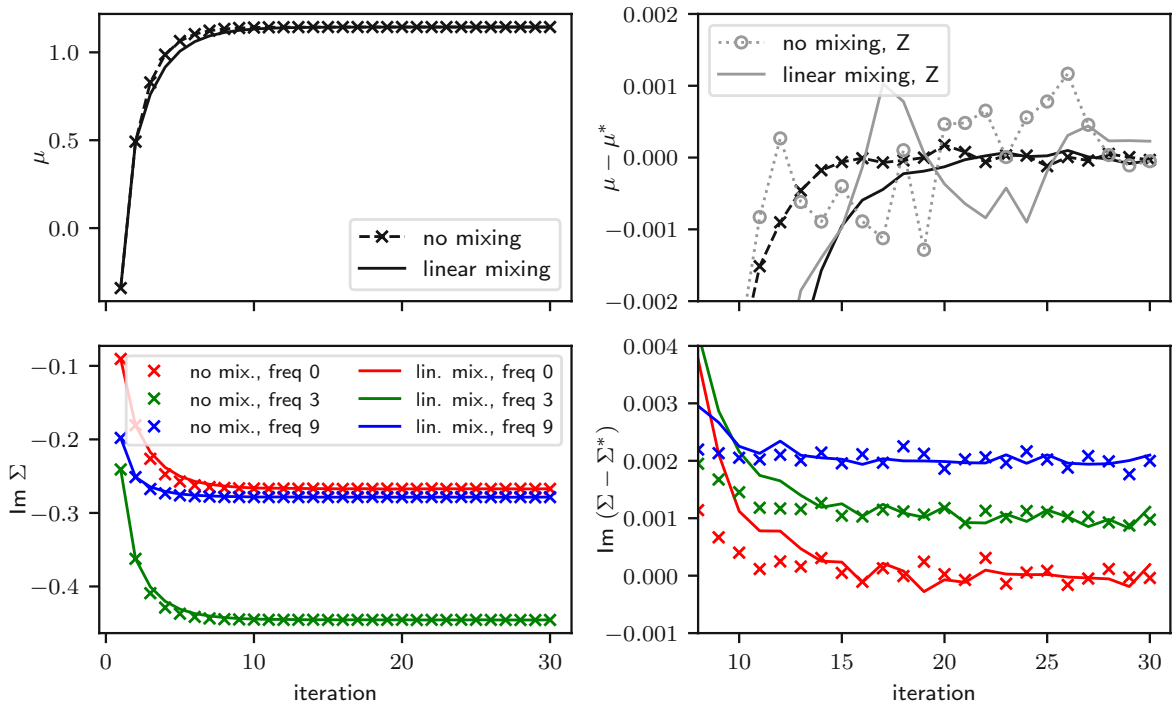

Figure 4.3: Comparison of DMFT with (solid lines) and without (×-markers) linear mixing. Top left: chemical potential μ in dependence of iteration number, bottom left: imaginary part of the self-energy at three different Matsubara frequencies in dependence of iteration number. Top right: Difference $|\mu - \mu^*|$ of chemical potential to average value μ^* of the last 10 iterations. Additionally, in gray also the behavior with Z-sampling estimators is shown. Bottom right: Difference of the self-energy to the average of the last 10 iterations. The lines for the corresponding to the different Matsubara frequencies are shifted by 0.001 and 0.002 for better visibility.

Anderson mixing methods are used with great success in electronic structure calculations (Johnson, 1988; Kresse and Furthmüller, 1996). Although such a procedure has been shown to be useful also in DMFT (Žitko, 2009; Strand et al., 2011), this was not done in connection with a stochastic impurity solver. Furthermore, the target quantity was the hybridization function, and not the self-energy as in our formulation. Since our newly developed symmetric improved estimators (see Section 3.2) allow for a much more precise computation of the self-energy than conventional CT-HYB impurity solvers, we implemented Anderson mixing in w2dynamics and tested it for DMFT calculations.

In the context of Anderson mixing we clearly have to distinguish between the *trial* and *result* self-energies mentioned before. In these terms, DMFT is the search for a trial self-energy that remains unchanged when applying the DMFT functional $\mathfrak{D}$ to it. Anderson mixing attempts to construct (or "predict") a better trial self-energy by using multiple previous trials and results.

Since the algorithm is a very general concept, we will keep its description in a more general notation, consistent with recent literature (Sherrill, 2000; Walker and Ni, 2011; Pratapa and Suryanarayana, 2015; Banerjee et al., 2016). In this notation, the trial in the k'th iteration is x_k. In the case of DMFT, x_k contains all frequency, spin, and orbital components of the self-energy, as well as its moments.

Die approbierte gedruckte Originalversion dieser Dissertation ist an der TU Wien Bibliothek verfügbar.
The approved original version of this doctoral thesis is available in print at TU Wien Bibliothek.
TU Bibliothek WIEN Your knowledge hub

The method assumes that a good approximation $\bar{x}_k$ of the fixed point x^* can be written as a linear combination of previous trials

$$\bar{x}_k = \sum_{j=0}^{m} c_j x_{k-j}, \tag{4.24}$$

where m is the number of previous iterations to take into account. The sum can be rewritten in terms of the true fixed point x^* and a vector of deviations $e_k = x_k - x^*$.

$$\bar{x}_k = \sum_{j=0}^{m} c_j (x^* + e_{k-j}) = x^* \sum_{j=0}^{m} c_j + \sum_{j=0}^{m} c_j e_{k-j} \tag{4.25}$$

In the case of a converged calculation the deviations e_k are zero and $\bar{x}_k = x^*$. Hence we have to require a normalization of the coefficients c_j, i.e. $\sum_{j=0}^{m} c_j = 1$.

The true value x^* is unknown, and instead of the deviations e_k we use the residuals $f_k = \mathfrak{D}[x_k] - x_k$. Accordingly, we replace the second term on the right-hand side of Eq. (4.25) by

$$\bar{f}_k = \sum_{j=0}^{m} c_j f_{k-j}. \tag{4.26}$$

The central task is now to determine the coefficients c_j such that $\bar{f}_k$ is minimal in the least squares sense. Since there is the normalization constraint for the m coefficients c_j, we can instead use a reduced set of $m-1$ coefficients γ_j, where the norm is already contained if we write

$$\bar{f}_k = f_k - \sum_{j=1}^{m} \gamma_j^{(k)} \Delta f_{k-m+1} = f_k - F_k \Gamma_k. \tag{4.27}$$

For the last equality, we used $\Delta f_k = f_k - f_{k-1}$, $F_k = \left[\Delta f_{k-m+1}\right]_{j=1\ldots m}$ and $\Gamma_k = \left[\gamma_j^{(k)}\right]_{j=1\ldots m}$.

Due to this rewriting, the minimization of $|\bar{f}_k|^2$ is now a standard least squares problem that can be solved for Γ_k by

$$\Gamma_k = \left(F_k^\dagger F_k\right)^{-1} F_k^\dagger f_k = F_k^+ f_k\,, \tag{4.28}$$

where F_k^+ denotes the Moore-Penrose inverse of F_k.

After writing $\bar{x}_k$ in the same way as Eq. (4.27) with $X_k = \left[x_{k-m+j} - x_{k-m+j-1}\right]_{j=1\ldots m}$ instead of F_k, we construct a new trial

$$x_{k+1} = \bar{x}_k + \alpha \bar{f}_k = x_k + \alpha f_k - (X_k + \alpha F_k) F_k^+ f_k. \tag{4.29}$$

Here the parameter α decides whether we use only trials ($\alpha = 0$) or only results ($\alpha = 1$) for the new prediction x_{k+1}. We use $\alpha = 0.5$ for a balanced procedure, following Eyert (1996).

In Fig. 4.4 we compare DMFT calculations without mixing and with Anderson mixing for the same square-lattice Hubbard model as in Fig. 4.2 and Fig. 4.3 of the previous subsection ($n = 0.85$, $U = 4$, $T = 0.2$). The mixing parameter was chosen as $\alpha = 0.5$ and the history size is $m = 10$. Again, we study the behavior of the chemical potential and self-energy over a range of 30 iterations. Clearly, Anderson mixing is not a viable option if one uses the Z-sampling estimator for solving the impurity problem. As one can see in the top left panel of Fig. 4.4,

Die approbierte gedruckte Originalversion dieser Dissertation ist an der TU Wien Bibliothek verfügbar.
The approved original version of this doctoral thesis is available in print at TU Wien Bibliothek.
TU Bibliothek WIEN Your knowledge hub

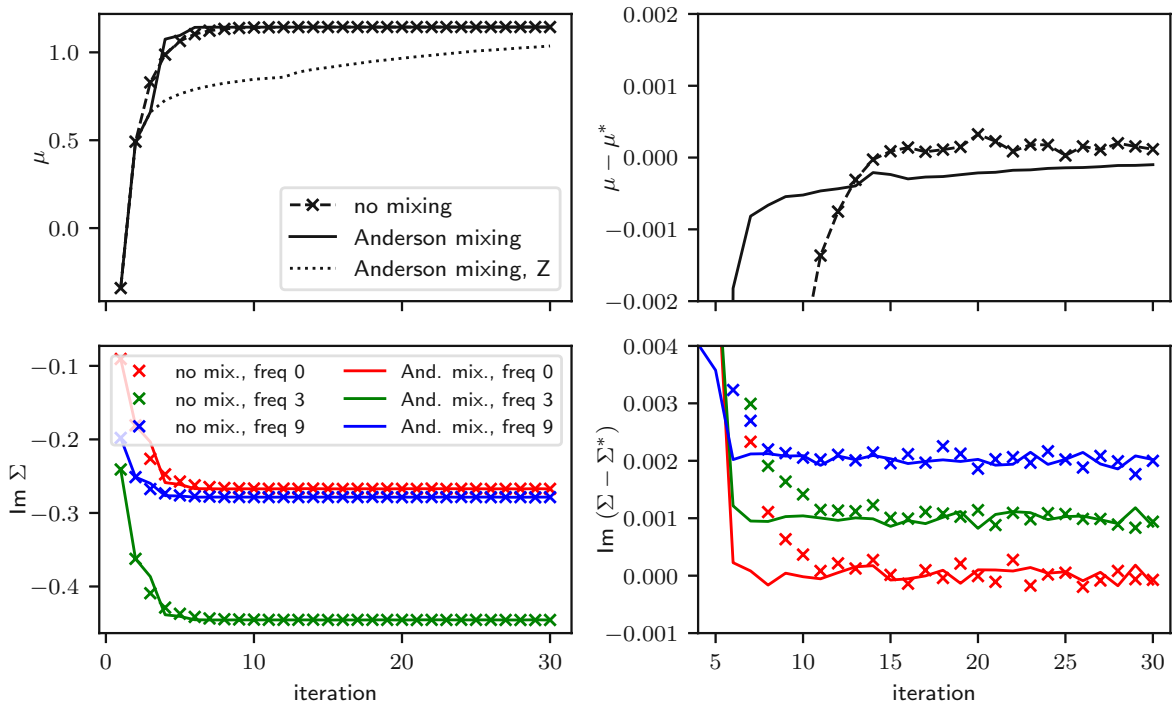

Figure 4.4: Impact of Anderson mixing on DMFT convergence. ×-symbols mark a reference calculation with symmetric improved estimators, but without mixing. Solid lines correspond to a calculation done with Anderson mixing. Top left: chemical potential μ in dependence of iteration number, for comparison the dotted line shows the behavior of Anderson mixing when the impurity problem is solved by the Z-sampling estimator. Bottom left: imaginary part of the self-energy at three different Matsubara frequencies in dependence of iteration number. Top right: Difference $|\mu - \mu^*|$ of chemical potential to average value μ^* of the last 10 iterations. Bottom right: Difference of the self-energy to the average of the last 10 iterations. The lines corresponding to the different Matsubara frequencies are shifted by 0.001 and 0.002 for better visibility.

the chemical potential μ is still far from convergence after 30 iterations. For this reason, we consider only symmetric improved estimators in the other subplots. The most visible impact of Anderson mixing can be seen already in the plots on the left-hand side of Fig. 4.4. The evolution of quantities with iteration number is less "smooth" than without mixing or with linear mixing, but it rather makes an abrupt jump after the first three iterations, i.e. as soon as the history size allows for making a prediction. As a result the self-energy does not considerably change already after six iterations. The chemical potential potential seems to converge to a slightly lower value than without mixing, but the difference is smaller than 0.02% of the Hartree self-energy. A stagnation of convergence due to noise was also noticed by Toth et al. (2017).

Let us shortly also discuss the choice of the mixing history m. In Fig. 4.5 we illustrate the DMFT convergence for the one-orbital square lattice model studied before with different values of the mixing history m. Both the chemical potential μ and the self-energy Σ show that a history size of $m = 2$, the minimal value for which Anderson mixing differs from linear mixing, still does not increase the speed of convergence. However, already $m = 3$ leads to considerable improvement. In fact, from the present results it is not possible to make a reliable statement, whether a value of $m > 3$ leads to faster convergence than $m = 3$.

Die approbierte gedruckte Originalversion dieser Dissertation ist an der TU Wien Bibliothek verfügbar.
The approved original version of this doctoral thesis is available in print at TU Wien Bibliothek.
TU Bibliothek WIEN Your knowledge hub

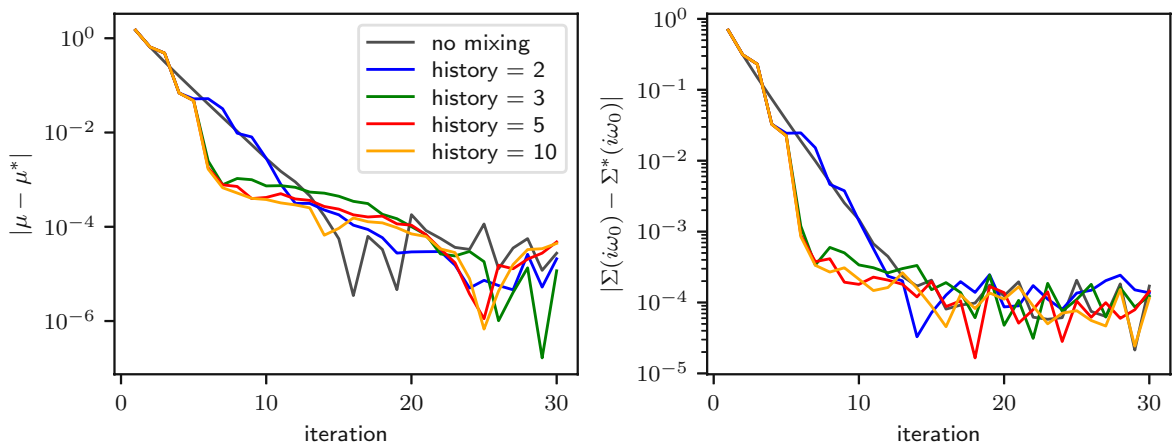

Figure 4.5: Influence of the mixing history. The plot on the left-hand side shows the evolution of the chemical potential in comparison to its converged value μ^*. On the right-hand side the absolute difference of the first Matsubara frequency to its converged value is shown.

Equation (4.27) motivates an investigation of the singular values of the matrix F. For a history size $m = 10$, F has 9 columns and correspondingly also 9 singular values. In the left panel of Fig. 4.6 the singular values of F are plotted for the first 13 iterations in which Anderson mixing was used. The inset, showing the evolution of the chemical potential, confirms that the calculation is already converged at this point. The singular values of all subsequent iterations are not shown, because they hardly change any more. Overall, the behavior of the singular values undergoes a drastic change after the calculation is converged: All singular values are in the same order of magnitude, which can be attributed to a matrix F containing only noise. In the right panel of Fig. 4.6 we show that this behavior is reproduced in a completely different system, namely a three orbital Wannier model for $SrVO_3$.

4.5* Quasi-particle scattering rates in DMFT

This section is based on the manuscript Wais et al. (2020b), which was written in part by the author of this thesis. A vertical bar marks citations from there. Slight adaptations were made for better consistency with this thesis.

4.5.1 Scattering rates in the Green's function formalism

For the following considerations we assume that both the tight-binding dispersion matrix $h(\boldsymbol{k})$ and the retarded self-energy $\Sigma_R(i\omega_n)$ are diagonal in orbital indices. The diagonal elements of $h(\boldsymbol{k})$ are then equal to the tight-binding bands that we denote by $\epsilon(\boldsymbol{k})$.

In order to start with a heuristic approach to the scattering rates,

Die approbierte gedruckte Originalversion dieser Dissertation ist an der TU Wien Bibliothek verfügbar.
The approved original version of this doctoral thesis is available in print at TU Wien Bibliothek.
TU Bibliothek WIEN Your knowledge hub

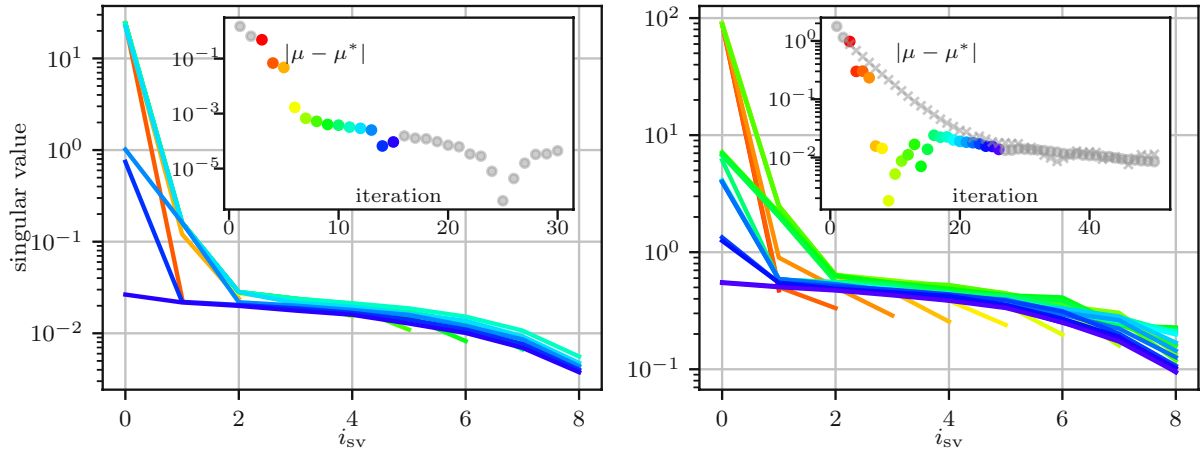

Figure 4.6: Singular values of the matrix F in Eq. (4.27). Left: DMFT calculation for a square-lattice Hubbard model. The color red represents the first iteration in which Anderson mixing was used. The color of the dots in the plot of the chemical potential (inset) is the same as the color of the plot of the singular values. Gray dots correspond to iterations, for which no singular values are shown. The inset shows the absolute difference of the chemical potential to the mean value of the last 10 iterations, μ^*. Right: Same as left, but for a t_{2g} Wannier model of $SrVO_3$. Additionally the behavior of the chemical potential with linear mixing is shown by gray crosses.

we recapitulate the physical meaning of the time-dependent retarded Green's function Eq. (2.1). For the special case of zero temperature the system is in the ground state $|\mathrm{GS}\rangle$ and if the momentum $\boldsymbol{k}$ is not occupied in the ground state, Eq. (2.1) is reduced to

$$G_R(\boldsymbol{k}, t) = -i\langle \mathrm{GS}|\hat{c}_{\boldsymbol{k}}(t)\hat{c}^\dagger_{\boldsymbol{k}}(0)|\mathrm{GS}\rangle \,. \tag{4.30}$$

That is, at time $t = 0$ a particle is added to the system which is thus in the state $|\phi\rangle = \hat{c}^\dagger_{\boldsymbol{k}}(0)|\mathrm{GS}\rangle$. Projecting this state onto its propagated version at time $t > 0$, i.e. $\langle\phi(t)| = e^{iE_{\mathrm{GS}}t}\langle \mathrm{GS}|c_{\boldsymbol{k}}(t)$, yields the probability amplitude (E_{GS} is the ground state energy) that this state still exists after a time t has elapsed (Nolting, 2015). This motivates the interpretation of $|G_R(\boldsymbol{k}, t)|^2$ as the probability that a state created by addition of a particle at $t = 0$ still exists at later time $t > 0$.

We can then define the lifetime τ as the time, after which $|G_R(\boldsymbol{k}, t)|^2$ has decayed by a factor of $1/e$. In order to actually compute the lifetime, we switch to frequency domain, where the retarded Green's function is algebraically related to the retarded self-energy Σ_R by the Dyson equation

$$G_R(\boldsymbol{k}, \omega) = \Big[\omega + \mu - \epsilon(\boldsymbol{k}) - \Sigma_R(\omega)\Big]^{-1} . \tag{4.31}$$

We can linearize the self-energy around the real part of the pole $\tilde{\epsilon}(\boldsymbol{k}) = Z[\epsilon(\boldsymbol{k}) + \mathrm{Re}\Sigma_R(0) - \mu]$, and parametrize it through the quasiparticle weight Z, i.e., $\mathrm{Re}\Sigma_R(\omega) \approx \mathrm{Re}\Sigma_R(0) + [1 - Z^{-1}]\omega$. Then the approximate form of the Green's function Eq. (4.31) is

$$G_R(\boldsymbol{k}, \omega) \approx Z\Big[\omega - \tilde{\epsilon}(\boldsymbol{k}) - Z\mathrm{Im}\Sigma_R(\omega)\Big]^{-1}, \tag{4.32}$$

which has a quasiparticle pole at $\omega = \tilde{\epsilon}(\boldsymbol{k}) = Z[\epsilon(\boldsymbol{k}) + \mathrm{Re}\Sigma_R(0) - \mu]$ with a Lorentzian broadening

Die approbierte gedruckte Originalversion dieser Dissertation ist an der TU Wien Bibliothek verfügbar.
The approved original version of this doctoral thesis is available in print at TU Wien Bibliothek.
TU Bibliothek WIEN Your knowledge hub

of full-width–half-maximum of $-2Z\mathrm{Im}\Sigma_R(\tilde{\epsilon}(\boldsymbol{k}))$.

We can derive the lifetime if we again consider the retarded Green's function in time domain, which is given by Fourier transformation of Eq. (4.32),

$$G(\boldsymbol{k}, t) = \frac{1}{2\pi}\int_{-\infty}^{\infty} d\omega \frac{Ze^{-i\omega t}}{\omega - \tilde{\epsilon}(\boldsymbol{k}) - Z\mathrm{Im}\Sigma_R(\omega)}. \tag{4.33}$$

Note that a linearization of the self-energy around $\omega = 0$ might not be justified any longer if the pole is at large frequencies and that there may be more than one pole at a given $\boldsymbol{k}$. For example for the Mott insulator we have two poles for each $\boldsymbol{k}$. However this merely means that we have $\mathrm{Re}\Sigma_R(\tilde{\epsilon})$ instead of $\mathrm{Re}\Sigma_R(0)$ and that we have a sum of poles in Eq. (4.33) instead of a single one, respectively. With these modifications, we can use the same procedure as discussed in the following for a single pole.

The integral (4.33) can be solved by closing the contour on the lower complex half-plane of frequencies (since $t > 0$ the integrand is exponentially suppressed here). Then, Eq. (4.33) can be computed by the residue theorem. The pole is at $[\mathrm{Re}\omega_p, \mathrm{Im}\omega_p] = [\tilde{\epsilon}(\boldsymbol{k}), Z\mathrm{Im}\Sigma(\omega_p \approx \tilde{\epsilon}(\boldsymbol{k}))]$. Here, in principle the exact pole location ω_p would have to be obtained self-consistently, but if $\mathrm{Im}\Sigma$ is small we can (approximately) calculate it using only the real part the pole. The residue theorem then yields for the integral in Eq. (4.33)

$$2\pi i \lim_{\omega\to\omega_p} (\omega - \omega_p)\frac{Ze^{-i\omega t}}{\omega - \tilde{\epsilon}(\boldsymbol{k}) - Z\mathrm{Im}\Sigma_R(\tilde{\epsilon})} \propto e^{-it\tilde{\epsilon}} e^{tZ\mathrm{Im}\Sigma_R(\tilde{\epsilon})}; \tag{4.34}$$

or for the probability to find a particle that is added at time 0 to the quasiparticle state $\boldsymbol{k}$ with energy $\tilde{\epsilon}(\boldsymbol{k})$ still in this state at a later time t:

$$|G_R(\boldsymbol{k}, t)|^2 \propto e^{2Z\mathrm{Im}\Sigma_R(\tilde{\epsilon}(\boldsymbol{k}))t} \equiv e^{-t/\tau(\tilde{\epsilon}(\boldsymbol{k}))}. \tag{4.35}$$

Equation (4.35) motivates the definition of the scattering rate or inverse lifetime as

$$\frac{1}{\tau[\omega = \tilde{\epsilon}(\boldsymbol{k})]} = -2Z\mathrm{Im}\Sigma_R(\omega = \tilde{\epsilon}(\boldsymbol{k})). \tag{4.36}$$

4.5.2 Analytical example

It is instructive to consider an example, where everything can be computed exactly, such that we can test the above approximations. We consider a self-energy of the form

$$\Sigma(\omega) = A\left(\frac{1}{\omega - E + i\alpha} + \frac{1}{\omega + E + i\alpha}\right). \tag{4.37}$$

For parameters $A = 0.1$, $E = 4$, $\alpha = 1.5$ it is very similar in size and shape to our results for the single-orbital weak coupling results for $\beta \approx 2$, as shown in Fig. 4.7.

If we insert this self-energy together with $\mu = 0$ into the Green's function Eq. (4.31), the locations of the poles are determined by a cubic equation in ω. It is possible to solve this equation analytically for arbitrary parameters. Notably, the pole locations will depend on

Die approbierte gedruckte Originalversion dieser Dissertation ist an der TU Wien Bibliothek verfügbar.
The approved original version of this doctoral thesis is available in print at TU Wien Bibliothek.
TU Bibliothek WIEN Your knowledge hub

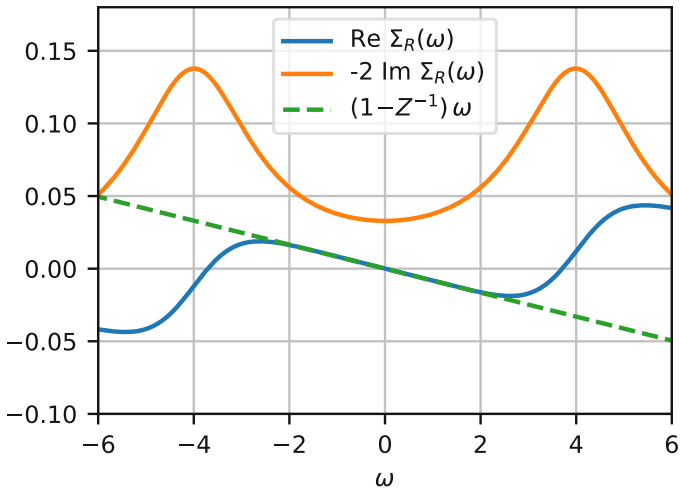

Figure 4.7: Model self-energy of Eq. (4.37) for $A = 0.1$.

$\epsilon(\mathbf{k})$. The locations of the poles in dependence of ϵ are shown in the left panel of Fig. 4.8, and for a larger value of $A = 0.8$ in the right panel of Fig. 4.8. Pole 2 is the one we usually associate with the quasiparticle.

Now it is possible to compute the time-dependent Green's function exactly by evaluating the Fourier integral in Eq. (4.33). The results for a few different values of ϵ are shown as solid lines in Fig. 4.9. Given the exact $G(t)$ as a reference, we show the contribution of the residue of the pole (pole 2) that is closest to the real axis, Eq. (4.34) as dashed lines. Finally we also show the exponential decay where the scattering rate was approximated by the imaginary part of the self-energy. Clearly, for small values of ϵ this is an excellent approximation. Closer to the band edge it does not match so well any more, especially in the case of the large self-energy (large A; right panel). This mismatch may already be anticipated when looking at the right panel of Fig. 4.8.

4.6* Comparison of scattering rates in DMFT and Boltzmann transport theory

This section is based on the manuscript by Wais et al. (2020b), which was partly written by the author of this thesis.

In this section we compare scattering rates calculated by DMFT with those calculated by the Boltzmann scattering equation. For an explanation of the latter, we refer to the literature (Wais et al., 2020a; b; Wais, 2020).

Die approbierte gedruckte Originalversion dieser Dissertation ist an der TU Wien Bibliothek verfügbar.
The approved original version of this doctoral thesis is available in print at TU Wien Bibliothek.
TU Bibliothek WIEN Your knowledge hub

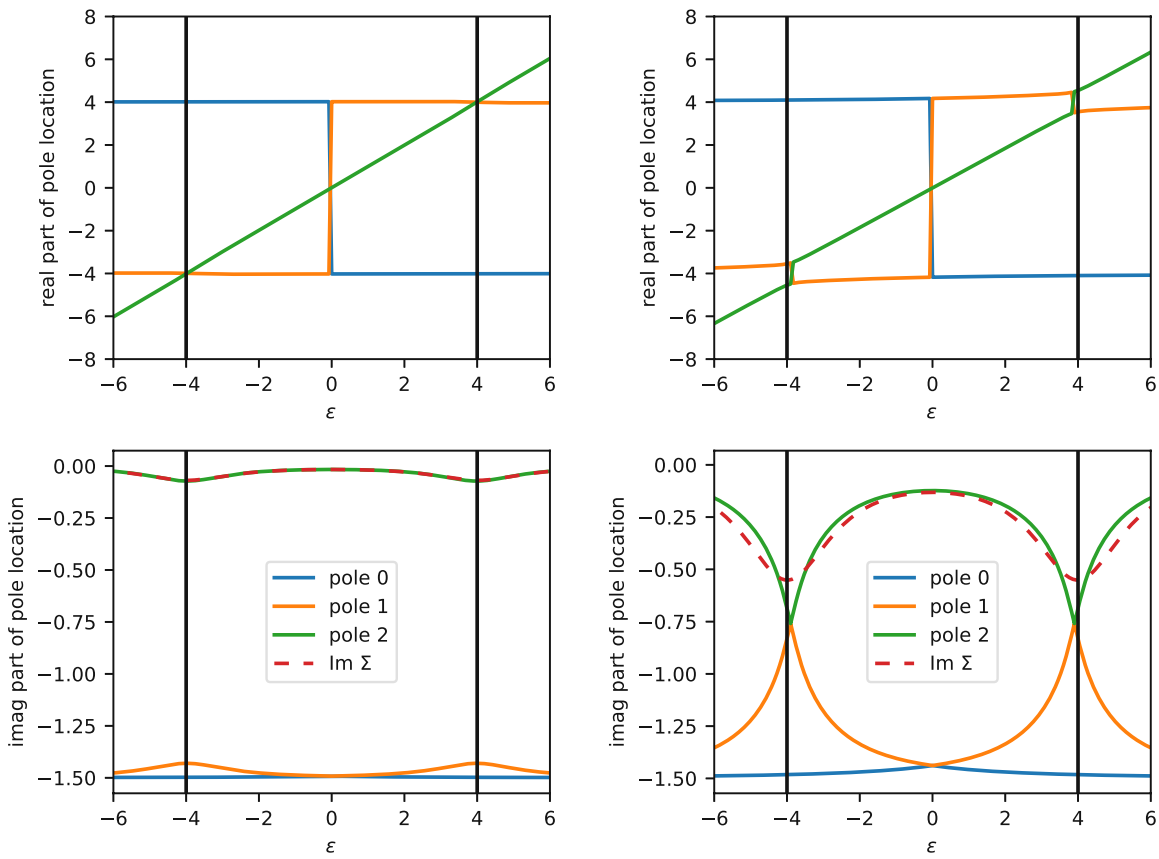

Figure 4.8: Left: Pole locations with model self-energy. Clearly the imaginary part of the location of the pole with the smallest imaginary part (pole 2) agrees well with the imaginary part of the self-energy $\Im\Sigma(\omega = \tilde{\epsilon})$. The imaginary parts of the other two poles are much larger. $Z \approx 0.99$ for this case. Right: Pole locations with model self-energy, where A is increased by a factor of 8. Also here the imaginary part of the location of the pole with the smallest imaginary part is similar to the imaginary part of the self-energy, but not in quantitative agreement. At the band edge, a second pole is of similar size and will thus have considerable influence on the scattering rate. $Z \approx 0.94$ for this case.

4.6.1 One-band Hubbard model at weak coupling

As a first comparison, we discuss the case of the prototypical one-band Hubbard model in two dimensions at half-filling. Depending on the strength of the local interaction U and the temperature $T = 1/\beta$, such a system is predicted by DMFT to be either metallic or Mott-insulating.

For the weak coupling case we may employ the Boltzmann scattering equation (BSE) with the dispersion relation of the non-interacting Hamiltonian Eq. (4.10) with $t' = 0$, and the corresponding DOS Eq. (4.11). As hopping parameter and unit of energy we choose $t \equiv 1$ in the following.

Die approbierte gedruckte Originalversion dieser Dissertation ist an der TU Wien Bibliothek verfügbar.
The approved original version of this doctoral thesis is available in print at TU Wien Bibliothek.
TU Bibliothek WIEN Your knowledge hub

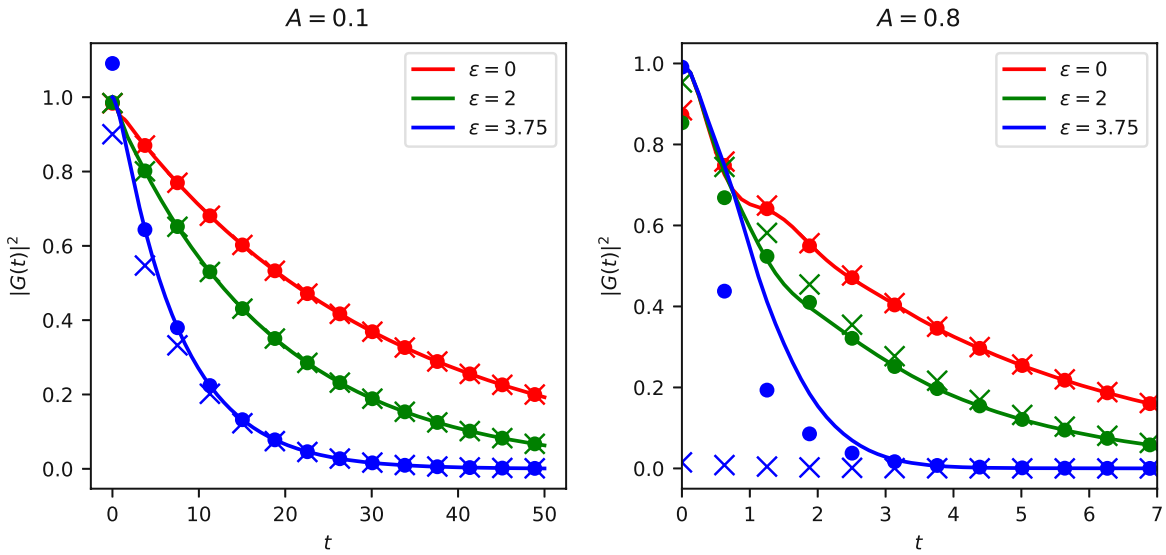

Figure 4.9: Absolute square of the time-dependent Green's function for the model self-energy with $A = 0.1$ (left) and $A = 0.8$ (right). Solid lines are time-dependent Green's functions that are computed by Eq. (4.33). Dots show the contribution of the residue at the pole with smallest $|\mathrm{Im}\hat{\omega}|$. Crosses show the approximation given by Eq. (4.35).

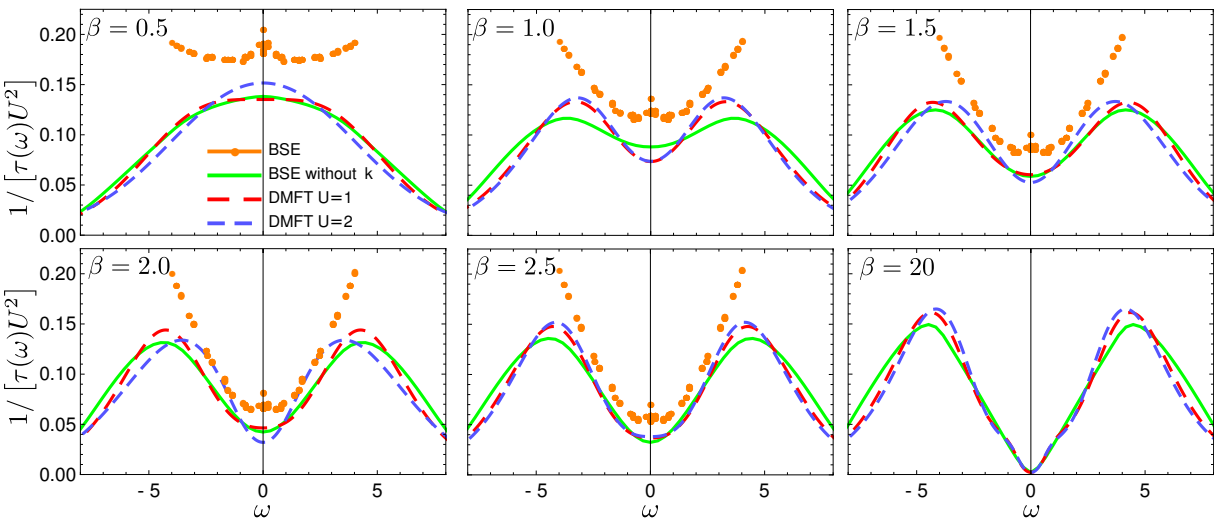

Figure 4.10: Scattering rates $1/\tau$ normalized by the interaction squared (U^2) for the two-dimensional Hubbard model at half-filling calculated by DMFT and BSE with and without $\mathbf{k}$ conservation. The case $\beta = 20$ could not be calculated with full Boltzmann due to computational limitations. The scattering rates shown are the same for both spins in the paramagnetic phase.

Die approbierte gedruckte Originalversion dieser Dissertation ist an der TU Wien Bibliothek verfügbar.
The approved original version of this doctoral thesis is available in print at TU Wien Bibliothek.
TU Bibliothek WIEN Your knowledge hub

The scattering amplitude for this system can be calculated in perturbation theory as

$$w(\mathbf{k}_0 \dots \mathbf{k}_3) = \frac{2\pi}{{V_{BZ}}^2} U^2 \delta_{\sigma_0 \bar{\sigma}_1} \delta_{\sigma_2 \bar{\sigma}_3} \tag{4.38}$$

with the short-hand notation $\bar{\sigma}_i \equiv -\sigma_i$ for the BSE scattering rate Eq. (13) in Wais et al. (2020b), and

$$\tilde{w}(\epsilon_0 \dots \epsilon_3) = 2\pi U^2 \delta_{\sigma_0 \bar{\sigma}_1} \delta_{\sigma_2 \bar{\sigma}_3} \tag{4.39}$$

for the case of BSE without $\mathbf{k}$ in Eq. (14) in Wais et al. (2020b), cf. Wais et al. (2018).

In Fig. 4.10 we show the calculated scattering rates for different temperatures comparing DMFT and the BSE with and without momentum conservation. The quasi-particle renormalization is $Z \approx 1$ for these values of the interaction. In order to compare the structure of the scattering rates for different interaction strengths, we divide the scattering rate by U^2. The Boltzmann scattering rates then become completely independent of U. In contrast, the DMFT scattering rates depend on U in a non-trivial fashion (Fig. 4.10 shows $U = 1$ and $U = 2$) since it is a non-perturbative approach. Nonetheless in the limit $U \longrightarrow 0$, the DMFT normalized scattering rates must be U-independent.

Comparing the DMFT scattering rates for both interaction strengths, one notices that the thus normalized scattering rates lie almost on top of each other for the inverse temperatures $\beta = 1.0$, $\beta = 2.5$ and $\beta = 20$, while they slightly deviate for $\beta = 0.5$, $\beta = 1.5$, $\beta = 2.0$. Since there is a rather large uncertainty from the maximum entropy analytical continuation and the deviation is not systematic, we can conclude that the differences in the normalized DMFT scattering rates at $U = 1$ and $U = 2$ are within the error bars.

The scattering rates calculated by the BSE without $\mathbf{k}$ are in very good agreement with the DMFT data for all inverse temperatures except for $\beta = 1.0$. Again, this deviation may well originate from the uncertainties of the analytic continuation. In any case, the good agreement of the scattering rates from BSE without k and DMFT along with the $\sim U^2$ scaling of the DMFT results, clearly show that even at $U = 2t$ we are still in the perturbative regime. As we show in Appendix C of Wais et al. (2020b), to second order in U the scattering rates as calculated in DMFT and BSE without $\mathbf{k}$ are indeed identical.

Note however that the spectral density in Fig. 4.11 is already significantly smeared, especially at the band edges and the Van-Hove singularity, because of the stronger interaction. This smearing is a direct consequence of the scattering rate in Fig. 4.10; and through the DMFT self-consistency it will in turn affect the scattering rates, but only in higher order in U (when self-consistently calculating the spectral function as indicated in Appendix C of Wais et al. (2020b)). Possibly this explains why the BSE without $\mathbf{k}$ in Fig. 4.10 has a lower scattering rate at the band edge $\omega = \pm 4$ and a larger one for larger $|\omega|$, albeit we cannot exclude this to be an artifact of the analytical continuation.

Both DMFT and BSE without $\mathbf{k}$ show a two-peak structure in the scattering rates with the peak positions roughly at the band-edges. The width of these peaks increases with temperature. At the highest temperature ($\beta = 0.5$) there is only one peak visible which actually consists of the two peaks that are strongly overlapping. In Appendix B of Wais et al. (2020b), we show that the position of the two peaks can be approximately calculated from the first moment of the particle- and hole-density. The width and height of the peaks can be calculated

Die approbierte gedruckte Originalversion dieser Dissertation ist an der TU Wien Bibliothek verfügbar.
The approved original version of this doctoral thesis is available in print at TU Wien Bibliothek.
TU Bibliothek WIEN Your knowledge hub

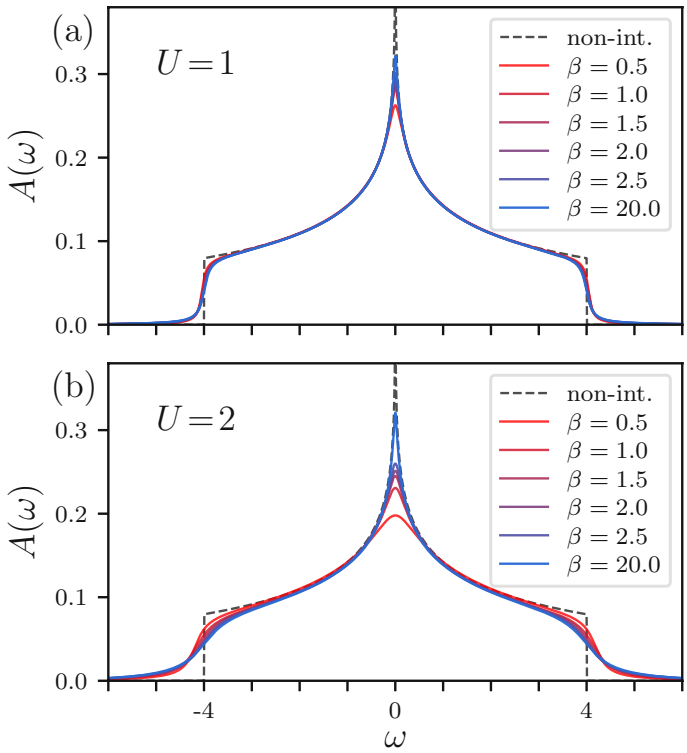

Figure 4.11: DMFT spectral densities for (a) $U = 1$ and (b) $U = 2$ for different temperatures

when the zeroth and second moment of the particle-density is taken into account in addition to the first moment.

After establishing a good agreement between DMFT and BSE without **k** at weak coupling, we next turn to the full BSE with momentum conservation. The thus calculated BSE scattering rates (dots in Fig. 4.10) deviate from the rates obtained with the other methods. First of all, as already mentioned, we highlight that several values, corresponding to different momenta, are present for each energy. Fig. 4.10 shows a particularly strong spread at the Fermi level ($\omega = 0$). Furthermore, in contrast to BSE without **k** and DMFT, there are no scattering rates outside the non-interacting bandwidth ($|\omega| > 4$) any longer, as there is no momentum that has such an energy. In DMFT due to the aforementioned smearing of the band-edges there are such states, and in BSE without **k** we can at least calculate the scattering rate a state at such an energy would have.

Another difference is that the BSE scattering rates are generally higher than DMFT or BSE without **k**, especially at the band edge ($|\omega| \lesssim 4$ and at higher temperatures also around the Fermi level ($\omega = 0$). As DMFT and BSE without **k** agree with each other, we can safely conclude that this difference originate from neglecting the momentum conservation of the scattering vertex. One can also smoothly interpolate between the results for the BSE with and without **k**, by replacing the momentum conserving δ-function by a Gaussian and increasing its width (not shown here). The reason for these discrepancies is that the momentum averaged scattering amplitude does not take into account that there is e.g. a particularly strong scattering among

Die approbierte gedruckte Originalversion dieser Dissertation ist an der TU Wien Bibliothek verfügbar.
The approved original version of this doctoral thesis is available in print at TU Wien Bibliothek.
TU Bibliothek WIEN Your knowledge hub

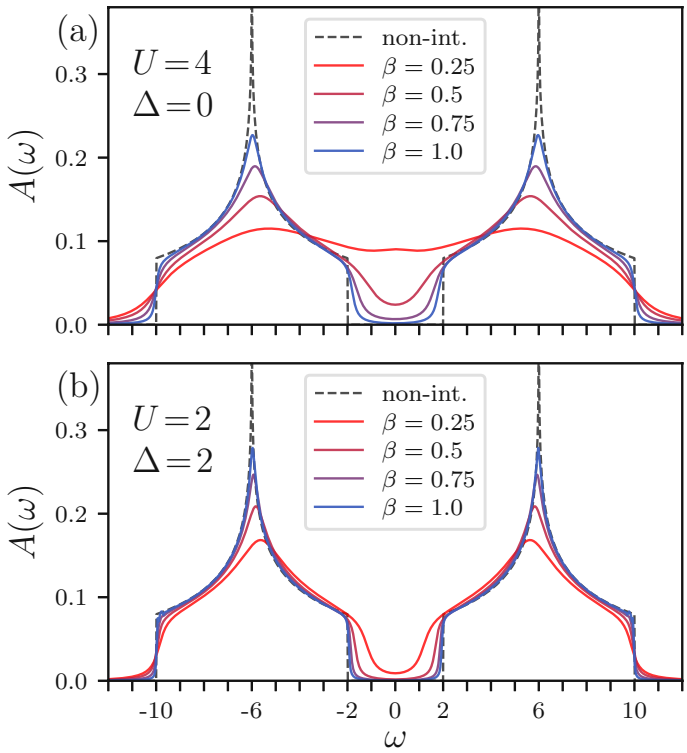

Figure 4.12: Spectral-densities for different temperatures for the case (a) $U = 4$, $\Delta = 0$ and (b) $U = 2$, $\Delta = 2$. For both cases, the effective band gap is $\Delta_{\text{eff.}} \approx 4$.

momenta at the Hove singularities $(\pm\pi, 0)$ and $(0, \pm\pi)$. At low temperatures this scattering even leads to the formation of a pseudogap (Vilk and Tremblay, 1997; Norman et al., 1998; Timusk and Statt, 1999; Keimer et al., 2015a; Lee et al., 2006; Sordi et al., 2012; Gunnarsson et al., 2015; Wu et al., 2018) which requires a beyond DMFT description (Sadovskii et al., 2005; Zhang and Imada, 2007; Katanin et al., 2009; Gull et al., 2013; Schäfer et al., 2015; Rohringer et al., 2018). A precursor thereof is visible here as the strong-momentum dependence of the scattering rate on the Fermi surface.

4.6.2 Two-orbital band insulator

In this section, we address the case of a band insulator in the weak to intermediate coupling regime. We consider a two-dimensional Hubbard-type model with two orbitals (A and B) at half-filling, i.e., $n = 2$ electrons per site in the two orbitals. This corresponds to $\mu = 0$ for our dispersion relation below. For simplicity, we assume that electrons may only hop to neighboring orbitals of the same type and that the hopping amplitude has the same absolute size but opposite sign for both orbitals ($t_A = -1$, $t_B = 1 = t$). Further, we add a local one-particle energy $\mp(\Delta/2 + 4t)$ for orbital A and B, respectively. This results in a band gap of size Δ in the non-interacting DOS, with the top of the valence(A)-band and the bottom of the conduction(B)-band both at the Γ point. The interaction U is local and the same within and

Die approbierte gedruckte Originalversion dieser Dissertation ist an der TU Wien Bibliothek verfügbar.
The approved original version of this doctoral thesis is available in print at TU Wien Bibliothek.
TU Bibliothek WIEN Your knowledge hub

between both orbitals such that the interaction term of the Hubbard model Eq. (4.12) acquires the simple form $\frac{U}{2}\sum_i\sum_{(l\sigma)\neq(m\sigma')} n_{il\sigma} n_{im\sigma'}$.

We now discuss two different systems, one with $U = 4$ and one-particle gap $\Delta = 0$ and one with $U = 2$ and $\Delta = 2$. Due to the constant Hartree term in the self-energy, the effective gap in the interacting system is essentially the same $\Delta_{\text{eff.}} \approx U + \Delta = 4$ for both setups. This is because at sufficiently low temperatures, orbital A is almost completely filled with two electrons per site and orbital B is empty. Hence an electron in orbital B perceives a Hartree energy $2U$ (interacts with both A electrons); an electron in orbital A instead has a Hartree energy $1U$ (as it only interacts with the electron of opposite spin in orbital A). The difference enlarges the band gap to $\Delta_{\text{eff.}} = U + \Delta$.

The spectral densities for both cases are displayed in Fig. 4.12 and follow the above reasoning. At higher temperatures, we however induce holes in the valence and electrons in the conduction band. The difference in occupation is reduced, the band gap hence smaller. For the highest temperature ($\beta = 0.25$), the gap disappears completely for the case $U = 4$, $\Delta = 0$. The non-interacting DOS in Fig. 4.12 is constructed with the above enhanced effective band gap $\Delta_{\text{eff.}}$ instead of Δ.

As this describes the DMFT spectrum at low temperatures reasonably well, we employ for the BSE the corresponding effective bandstructure

$$\epsilon_A(\mathbf{k}) = -\epsilon(\mathbf{k}) - \left(\frac{\Delta_{\text{eff.}}}{2} + 4t\right), \tag{4.40}$$

$$\epsilon_B(\mathbf{k}) = \epsilon(\mathbf{k}) + \left(\frac{\Delta_{\text{eff.}}}{2} + 4t\right), \tag{4.41}$$

where $\epsilon(\mathbf{k})$ is defined by Eq. (4.10) (with $t' = 0$). The corresponding DOS of the non-interacting system corrected by the Hartree shift is used for the BSE without $\mathbf{k}$ and given by

$$A_0^A(\omega) = A_0\left(\omega + \left(\frac{\Delta_{\text{eff.}}}{2} + 4t\right)\right), \tag{4.42}$$

$$A_0^B(\omega) = A_0^A(-\omega) \tag{4.43}$$

with $A_0(\omega)$ defined in Eq. (4.11). Due to particle-hole symmetry and the simple form of the interaction, the BSE calculation can be simplified as outlined in Appendix D of Wais et al. (2020b).

Figure 4.13 shows the scattering rate of the two-band system. The BSE with momentum conservation shows a seemingly parabolic increase starting with a sizable value at the lower band edge ($\omega = 2$). Superimposed on this trend is an enhanced scattering rate in the middle of the band at $\omega = 6$ with a strong momentum spread of the scattering rate. This is akin to the behavior at the Fermi level for the weakly correlated one-band Hubbard model in Fig. 4.10 and can again be attributed to the van Hove singularity.

Similar as for the one-band case, the scattering rates in BSE without $\mathbf{k}$ are slightly smaller than in the BSE with $\mathbf{k}$ conservation and already decay toward the upper band edge ($\omega = 10$). They closely resemble the DMFT values for the $U = 2$ case; only the peak of the scatterings

Die approbierte gedruckte Originalversion dieser Dissertation ist an der TU Wien Bibliothek verfügbar.
The approved original version of this doctoral thesis is available in print at TU Wien Bibliothek.
TU Bibliothek WIEN Your knowledge hub

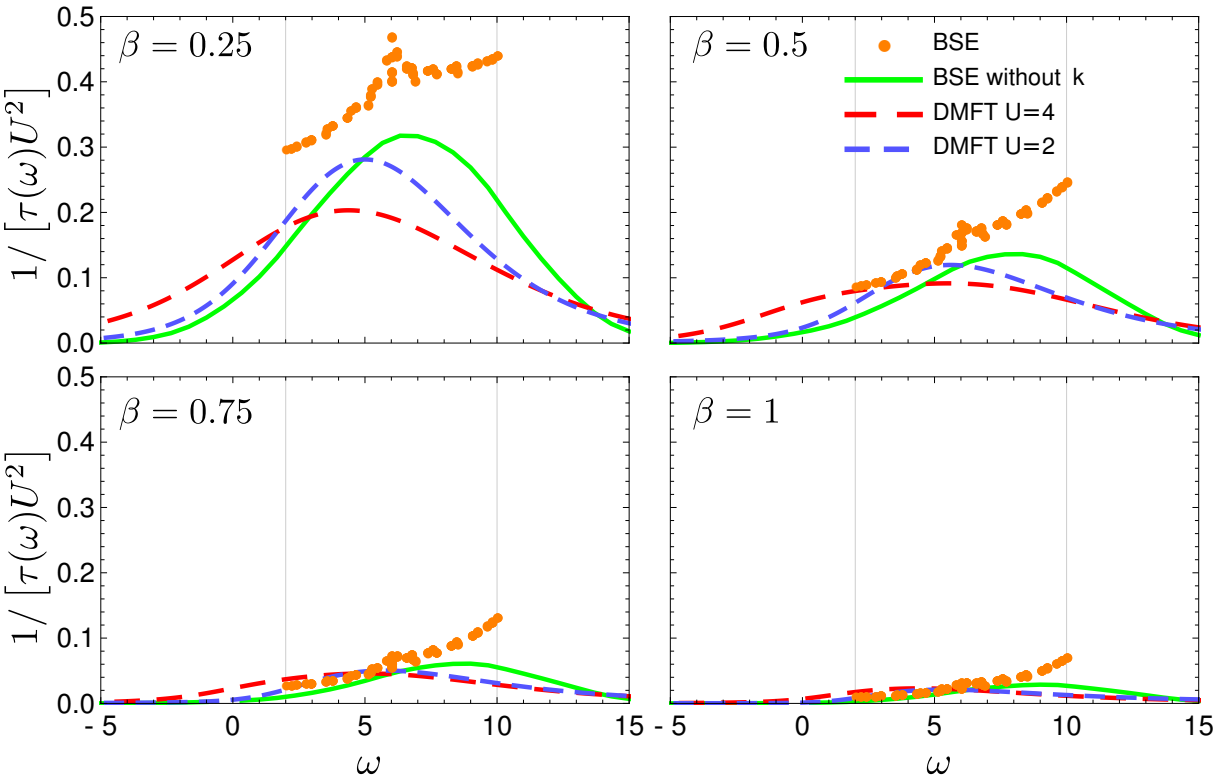

Figure 4.13: Scattering rates normalized by the squared interaction for an electron in the upper band of a two-orbital band insulator as calculated with DMFT, BSE with and without **k**. Two different sets of parameters are used: $U = 4$, $\Delta = 0$ and $U = 2$, $\Delta = 2$. The gray, vertical lines indicate the band edges of the non-interacting system.

is shifted to slightly higher energies than in DMFT. There are larger differences to the DMFT data at the intermediate coupling $U = 4$, which have systematically higher scattering rates at low energies. This is because stronger smearing of the spectral density at $U = 4$ leads to a smaller effective gap and some in-gap spectral weight, see Fig. 4.13. This, in turn, leads to more thermal excitations and therefore more scatterings. These effects can be included in BSE without **k** if we use the interacting spectral density $A^n(\omega)$ instead of the non-interacting one $A_0^n(\omega)$, which leads to a good agreement with the DMFT results, see Appendix E of Wais et al. (2020b).

Eye catching is the strong suppression of the scattering rate upon decreasing temperature. The reason for this is the dramatic reduction of the number of thermally excited carriers which are needed to act as scattering partners. Note that with a density-density Coulomb interaction, the electron in the conduction(B)-band either needs (i) another B-electron to scatter with [the final state being again two B-electrons], or (ii) a hole in the valence(A)-band into which an A-electron can scatter [final and initial state being one A- and one B-electron]. Both B-electron and A-hole scattering partners however require thermally excited carriers that are absent at low temperatures.

For the Mott insulator discussed in the next section, the scattering rates are much higher because of impact ionization processes. Here, an electron in the upper Hubbard band excites

Die approbierte gedruckte Originalversion dieser Dissertation ist an der TU Wien Bibliothek verfügbar.
The approved original version of this doctoral thesis is available in print at TU Wien Bibliothek.
TU Bibliothek WIEN Your knowledge hub

an additional electron-hole pair across the gap. In the band insulator impact ionization corresponds to a process $c^\dagger_{iB\sigma} c_{iA\sigma} c^\dagger_{iB\bar{\sigma}} c_{iB\bar{\sigma}}$ which is not possible in lowest order perturbation theory in the interaction, nor are Auger processes $c^\dagger_{iB\sigma} c_{iA\sigma} c^\dagger_{iA\bar{\sigma}} c_{iA\bar{\sigma}}$. In the one-band Mott insulator, the two Hubbard bands have the same orbital index and such processes hence dominate the scattering rate if ω is sufficiently large to allow impact ionization (Werner et al., 2014; Sorantin et al., 2018; Wais et al., 2018; Maislinger and Evertz, 2020; Kauch et al., 2020b).

Even if we generalize the Coulomb interaction to the widely employed Kanamori form (Kanamori, 1963) with spin-flip and pair-hopping terms, we still need a thermally excited second electron or hole for scattering. Only, the full Slater interaction (Slater, 1960; Griffith, 1971) also contains interaction terms that directly mediate impact ionization. These interaction terms are however small, which is the reason why they are often disregarded in the first place. A more viable route to enhance the scattering rate through impact or Auger processes in a band insulator is if the bands strongly hybridize so that the conduction and valence bands are admixtures of the A and B orbitals.

It is interesting to note that the scattering rate preserves its two-band like structure even in the case $U = 4$, $\beta = 0.25$ when the spectral density does not show a gap any longer. The reason for this is again that the density-density interaction does not allow for impact excitation and Auger emission, which are very gap-size sensitive. Instead the scattering processes induced by the density-density interaction are agnostic about the gap-size per-se. The additional B electron still needs another B (or A) electron to scatter with, and two empty final B states (or an empty A and an empty B state). The scattering process does not need to overcome the size of the gap, in contrast to impact ionization.

4.6.3 Strong coupling: Mott-insulator

Finally, we compare the approaches introduced above in the strong coupling regime of the single-orbital Hubbard model. Since the BSE is a perturbative treatment in the interaction, this is certainly the most problematic case for the BSE. For sufficiently large interaction, the non-interacting DOS splits into two, the upper and lower Hubbard band, see Fig. 4.14 (top). We have a Mott insulator, one of the cornerstones of strongly correlated electron systems (Gebhard, 1997).

If we use the BSE with the non-interacting DOS, this dramatic reshuffling of the DOS is not incorporated. The scattering rate is still the very same with a two peak structure as for weak coupling—just with the prefactor rescaled by U^2, see black-dotted line in Fig. 4.14. This kind of description assumes that we have a metal with states at low energies. It is not an appropriate description of a Mott insulator.

This problem can be mitigated if we consider better suited quasiparticles instead of the non-interacting ones. This is in general not trivial, and not always can proper quasiparticles with a long life time and weak interaction be identified. They might not even exist. Taking the electronic DMFT excitations of the Hubbard bands as our quasiparticles in the BSE without $\mathbf{k}$, we have to replace the non-interacting DOS $A_0(\omega)$ by the interacting spectral density $A(\omega)$ of Fig. 4.14 (top) in Eq. (14) of Wais et al. (2020b). Even if we have no well defined quasiparticles such a quantum Boltzmann description is possible (Wais et al., 2018) if we have a separation of

Die approbierte gedruckte Originalversion dieser Dissertation ist an der TU Wien Bibliothek verfügbar.
The approved original version of this doctoral thesis is available in print at TU Wien Bibliothek.
TU Bibliothek WIEN Your knowledge hub

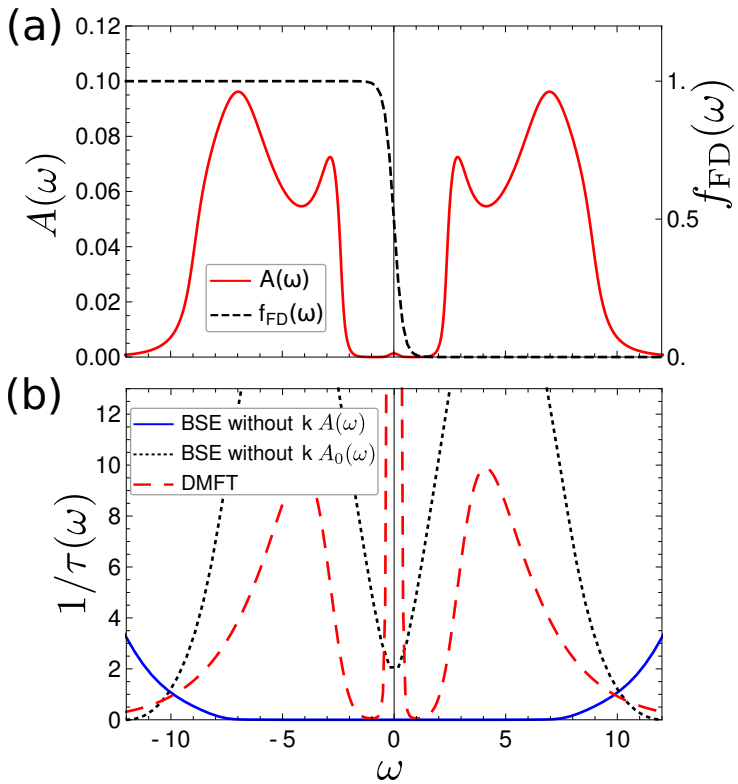

Figure 4.14: (a) Spectral density as obtained by DMFT and Fermi-Dirac distribution for the case $U = 12$ and $\beta = 5$. (b) Scattering rates as obtained from DMFT, and BSE without **k** using either the non-interacting density of states (BSE without k $A_0(\omega)$) or the interacting DMFT spectral density shown (BSE without k $A(\omega)$).

time scales, and the average-time (distribution function) dynamics is slower than the relative-time dynamics. As was shown by Wais et al. (2018) the thus modified BSE without **k** provides a good description of the DMFT impact ionization processes and redistribution of spectral weight in non-equilibrium. The calculation of scattering in this work is however still possible within equilibrium DMFT theory, whereas the non-equilibrium processes of Wais et al. (2018) required the non-equilibrium DMFT (Freericks et al., 2006; Aoki et al., 2014).

Here, we instead study in Fig. 4.14 (bottom, blue line) the one-particle scattering rates in the BSE without **k** and interacting $A(\omega)$: The Mott insulator is described as two split quasiparticle bands with the gap ~ 4 being much larger than temperature $T = 1/5$. Hence, if we add an extra electron in the upper Hubbard quasiparticle band it has no partners to scatter in BSE, the scattering rate is zero similar to the suppression of the scattering rate in the band insulator. However, if the added electron has an excess energy [$\omega - \omega_{LBE}$ relative to the lower band edge of the upper Hubbard band $\omega_{LBE} \gtrsim 2$ in Fig. 4.14] which is larger than the Mott gap [$\Delta_{\text{Mott}} \gtrsim 4$], i.e., $\omega \gtrsim 6$, impact ionization processes with an electron-hole excitation across the gap become possible. The phase space of such scattering processes increase quadratically with $\omega - \omega_{LBE} - \Delta_{\text{Mott}}$ for a box shaped DOS. This explains the BSE without **k** scattering rate in Fig. 4.14, which as already mentioned well describes impact ionization processes, including the change of the double occupation and redistribution of spectral weight with time in non-equilibrium (Wais et al., 2018).

Die approbierte gedruckte Originalversion dieser Dissertation ist an der TU Wien Bibliothek verfügbar.
The approved original version of this doctoral thesis is available in print at TU Wien Bibliothek.
TU Bibliothek WIEN Your knowledge hub

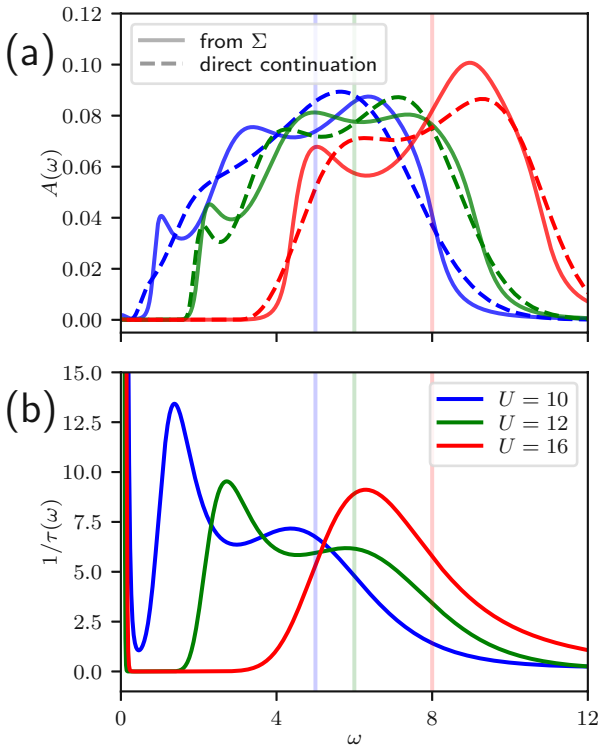

Figure 4.15: (a) Spectral density as obtained by DMFT for $\beta = 10$ and different interaction strengths $U = 10$, 12, 16. The solid line $A(\omega)$'s are calculated from the analytically continued $\Sigma(\omega)$; the dashed lines are directly analytically continued from the Matsubara Green's function. (b) DMFT scattering rates for the same parameters as in (a).

Let us now turn to the DMFT scattering rate as extracted from the self-energy and shown in Fig. 4.14 (bottom, red-dashed line). As we do not have a linear quasiparticle renormalization in the self-energy, we plot $1/\tau(\omega) = 2\mathrm{Im}\Sigma(\omega)$. The by far dominating feature (cut-off by the finite y-axis scale) is at $\omega = 0$ where $\Sigma(\omega) = (U^2/4)\ 1/(\omega + i\alpha)$ in the large U limit of the Mott insulator with a Lorentzian broadening $\alpha \sim \pi T$. This pole is responsible for the splitting of the DOS into two Mott bands and yields the δ-like peak in $\mathrm{Im}\Sigma$ at $\omega = 0$. As a matter of course we cannot expect this feature to be described in the BSE without $\mathbf{k}$. It is also not necessary as $\omega = 0$ is in the middle of the Mott gap where there are essentially no states—essentially since at low temperature the aforementioned finite broadening leads to a very small spectral weight. This filling of the Mott gap with temperature (Mo et al., 2004) is a feature distinct from a band insulator. These in-gap states have an extremely short life time.

Let us now turn to the more relevant DMFT scattering rate within the Hubbard bands. These are orders of magnitude larger in DMFT than those from the BSE without $\mathbf{k}$ and with interacting $A(\omega)$. Also their shape is completely different: There is no suppression at the lower edge of the upper Hubbard bands which, as argued above, was the case if the scattering is due to impact ionization requiring a threshold energy; neither are the DMFT scattering rates flat or follow the shape of the upper Hubbard band. Instead the scattering rates are strongest around $\omega \sim 4$ close to the lower band edge, and are dramatically reduced for larger ω. Similar as the

Die approbierte gedruckte Originalversion dieser Dissertation ist an der TU Wien Bibliothek verfügbar.
The approved original version of this doctoral thesis is available in print at TU Wien Bibliothek.
TU Bibliothek WIEN Your knowledge hub

pole at $\omega = 0$, the maximum at $\omega \sim 4$ leads to a suppression of the spectral weight. Fig. 4.14 (top) where we have calculated $A(\omega)$ from the analytically continued $\Sigma(\omega)$ even shows a two peak structure in the upper Hubbard band. Such a two peak structure was previously observed on the metallic side of the Mott transition, immediately before the quasiparticle peak vanishes (Karski et al., 2008; Ganahl et al., 2015; Lee et al., 2017). On the Mott insulating side, Granath and Schött (2014) and Nishimoto et al. (2004) show an extra peak or a shoulder feature on the inner side of the Hubbard bands, similar to our findings. In Fig. 4.15 we also compare the $A(\omega)$ that is directly continued from the Green's function on the imaginary axis, which shows a shoulder rather than a double peak. While we hence cannot resolve within the maximum entropy uncertainty, whether we actually have a shoulder or double peak structure, it is clear that there is a feature in the upper Hubbard band. Mathematically, this is necessitated by the strong scattering rate in this region. A simple physical picture or understanding of these side structures in the Hubbard bands is still missing. Note, that also in strong coupling perturbation theory to second order such a shoulder and hence asymmetry of the self-energy within the upper Hubbard band is observed (Kalinowski and Gebhard, 2002), whereas the Hubbard-III approximation (Hubbard, 1964) and the Falicov-Kimball model (Dongen and Leinung, 1997; Freericks and Zlatić, 2003) do not show such a shoulder. In agreement, Fig. 4.15 shows this feature for different values of U. Since the scattering in BSE without $\mathbf{k}$ and with non-interacting $A_0(\omega)$ is merely rescaled by U^2, it is clear from Fig. 4.15 that the agreement of the position of the maximal scattering rate between BSE and DMFT in Fig. 4.14 (bottom, black-dotted vs. red-dashed line) was by chance.

We can conclude that the one-electron scattering rate in a Mott insulator is very different from an impact ionization picture. It is associated with the formation ($\omega \sim 0$) of the Hubbard bands and even side structures therein ($\omega \sim 4$ in Fig. 4.14). The Hubbard bands are created by the interaction of the same electrons we also use as a test charge for calculating the scattering rate. If there is a local extra hole or electron, locally the Hubbard bands deform. Most noticeable this is in the filling of the Mott gap, which does not only occur with increasing temperature (Mo et al., 2004) but also if we drive the system out of equilibrium (Werner et al., 2014; Sorantin et al., 2018; Wais et al., 2018). If we have an extra electron in a disordered spin background of the DMFT Mott insulator, it can hop or cannot hop to a neighboring site depending on the spin orientation of this neighbor. This leads to a large scattering rate without changing the number of double occupations. These processes are included in the DMFT but not in the BSE, they do not contribute to impact ionization (do not change the number of double occupations) or major energy redistributions.

Die approbierte gedruckte Originalversion dieser Dissertation ist an der TU Wien Bibliothek verfügbar.
The approved original version of this doctoral thesis is available in print at TU Wien Bibliothek.
TU Bibliothek WIEN Your knowledge hub

4.7* Collective modes in excitonic magnets: Dynamical mean-field study

This is a short summary of the paper Geffroy et al., 2019, which is included in the Appendix on p. 185.

In DMFT it is possible to calculate dynamical response functions by solving the Bethe Salpeter equation with momentum-dependent one-particle propagators from DMFT and the irreducible two-particle vertex of the auxiliary impurity (Georges et al., 1996). In this work, we studied dynamical susceptibilities in the following two-band Hubbard model

$$H = \sum_{ij,\sigma}(\hat{a}^\dagger_{i\sigma}, \hat{b}^\dagger_{i\sigma}) \begin{pmatrix} t_{aa} & t_{ab} \\ t_{ab} & t_{bb} \end{pmatrix} \begin{pmatrix} \hat{a}_{j\sigma} \\ \hat{b}_{j\sigma} \end{pmatrix} + \frac{\Delta}{2}\sum_{i,\sigma}(n^a_{i\sigma} - n^b_{i\sigma}) + U\sum_{i\alpha} n^\alpha_{i\uparrow} n^\alpha_{i\downarrow} + \sum_{i,\sigma\sigma'}(U' - J\delta_{\sigma\sigma'}) n^a_{i\sigma} n^b_{i\sigma'}, \quad (4.44)$$

both in the normal and in the excitonic condensate phase. Here, the operators $\hat{a}^\dagger(\hat{b}^\dagger)$ create electrons in orbital $a(b)$ and the parameter Δ is the crystal field splitting between the bands. This model has a rich phase diagram (Kuneš and Augustinský, 2014; Kuneš, 2015; Hoshino and Werner, 2016), but we focus on the polar excitonic condensate phase. For certain values of t_{aa}, t_{ab}, t_{bb}, U, U' and J, the excitonic condensate phase can be reached from the normal phase either via a conventional thermal phase transition by cooling, or via a quantum phase transition by reducing the crystal field splitting.

In particular, we look at the behavior of correlation functions

$$\chi^{OO}_{\eta\eta}(\boldsymbol{k}, i\nu_n) = \sum_R \int_0^\beta d\tau e^{i(\nu_n\tau + \boldsymbol{k}\cdot\boldsymbol{R})} \langle O^\eta_{\boldsymbol{i}+\boldsymbol{R}}(\tau) O_{\boldsymbol{i}}(0)\rangle - \langle O^\eta\rangle^2 \quad (4.45)$$

close to this phase transition. The operators O are excitonic fields and the z-component of the spin moment. If $t_{ab} = 0$, the system exhibits a $U(1)$ symmetry for spin rotation around the z axis, and a $U(1)$ gauge symmetry due to the conservation of $\sum_{i,\sigma}(n^a_{i\sigma} - n^b_{i\sigma})$. The latter symmetry is not present if $t_{ab} \neq 0$.

Our calculations show the appearance of two gapless linear Goldstone modes (Goldstone et al., 1962; Watanabe and Murayama, 2012) when the $U(1)$ symmetries are broken at the phase transitions. In case there is only one $U(1)$ symmetry in the $t_{ab} \neq 0$ case, only one Goldstone mode is observed, but additionally there is a gapped Higgs mode (Pekker and Varma, 2015). The spin-spin correlation function χ^{SS}_{zz} is very small in the normal phase, almost vanishing at low temperatures, since the spin-excitations across the one-particle gap are frozen. However, in the excitonically ordered phase it obtains a strongly dispersive spin-wave structure that is shown to follow some of the excitonic modes. It is suggested that this connection between excitonic dispersion and spin susceptibility can serve as an experimental signature for the emergence of excitonic order, which is otherwise still a challenge to detect.

Die approbierte gedruckte Originalversion dieser Dissertation ist an der TU Wien Bibliothek verfügbar.
The approved original version of this doctoral thesis is available in print at TU Wien Bibliothek.
TU Bibliothek WIEN Your knowledge hub

4.8* Topotactic Hydrogen in Nickelate Superconductors and Akin Infinite-Layer Oxides ABO_2

This is a short summary of the paper Si et al. (2020b), which is included in the Appendix on p. 191.

The recent discovery of superconductivity in Sr-doped $NdNiO_2$ films grown on $SrTiO_3$ (Li et al., 2019a) has opened the research field of nickelate superconductors. In cuprates (Bednorz and Müller, 1986), which are very similar to the nickelates, it is possible to find superconductivity in many isoelectronic compositions. However, in nickelates this is much more challenging. In this work we provide answers to the question why some nickelates are superconducting, while others are not.

A look at the synthesis of an infinite-layer rare-earth nickelate $ANiO_2$, which is obtained from the topotactic reduction of $ANiO_3$ with the help of CaH_2, points to a different possible product of this reaction: the oxide-hydride $ANiO_2H$. Indeed the latter has a completely different electronic structure.

To this end we first calculate the hydrogen binding energy

$$E_B = E[ABO_2] + \frac{1}{2}E[H_2] - E[ABO_2H], \tag{4.46}$$

which has a positive value if the synthesis of the oxide-hydride compound is energetically favorable. From this consideration it becomes apparent that E_B strongly depends on the kind of transition metal B due to the filling of the d-band. The case B=Ni is exactly at the point, where E_B undergoes a sign change: For B=Ti…Co, hydrogen intercalation is common, whereas for B=Cu (i.e. cuprates), it does not occur. Nickelates are thus at the borderline.

By means of density functional theory (DFT) it is possible to calculate and compare the electronic band structures of $LaNiO_2$ and $LaNiO_2H$. The infinite-layer compound LaNiO2 is mainly characterized by a dispersive Ni-$d_{x^2-y^2}$-band, which almost does not hybridize with other bands. Additionally, a La-5d band crosses the Fermi level around the A-point. The oxide-hydride compound $LaNiO_2H$ has a completely different band structure. Not only the Ni-$d_{x^2-y^2}$ band, but also the Ni-d_{z^2} band is now partially filled. On the other hand, there are no La-states in the low-energy region. Thus the band structure is completely different from cuprates here.

Finally DFT+DMFT calculations show that the Ni-$d_{x^2-y^2}$ band in $LaNiO_2$ is strongly renormalized by a factor of $Z \sim 1/7$. In $LaNiO_2H$ the situation is again strikingly different, since due to the absence of self-doping through the La band the Ni bands are half-filled, which renders the system a Mott insulator.

We thus conclude that for the synthesis of nickelate superconductors it is of high importance to control the environment such as to prevent hydrogen intercalation.

Die approbierte gedruckte Originalversion dieser Dissertation ist an der TU Wien Bibliothek verfügbar.
The approved original version of this doctoral thesis is available in print at TU Wien Bibliothek.
TU Bibliothek WIEN Your knowledge hub

Chapter 5

Nonlocal correlations in the Hubbard model

In the previous chapter we have seen that local correlations in the Hubbard model can be described exactly by DMFT. To which extent nonlocal correlations play a role, very much depends on the system considered. While vanishing in infinite dimensions, as discussed in Chapter 4, and often considered small in three-dimensional systems, they can completely change the behavior in two dimensions.

The mean-field treatment of spatial correlations in DMFT leads to incorrect critical exponents of susceptibilities and correlation lengths in the vicinity of phase transitions in three-dimensional systems. Furthermore it predicts, e.g., a finite-temperature phase transition to the antiferromagnetically ordered state in two-dimensional systems, such as the square lattice Hubbard model, which is however forbidden by the Mermin-Wagner theorem (Mermin and Wagner, 1966).

For these reasons the development of beyond-DMFT methods to include spatial fluctuations is a very active topic in the field of strong electronic correlations. Let us therefore first give a short overview over currently used methods, cf. Schäfer et al. (2020) and Rohringer et al. (2018).

There are several methods that work in the regime of *weak coupling* strength, such as the functional renormalization group (fRG) Metzner et al., 2012 and the parquet approximation (PA) De Dominicis and Martin, 1964b. Diagrammatic Monte Carlo (DiagMC) (Prokof'ev and Svistunov, 1998; Rossi, 2017) yields numerically exact results up to statistical errors in case of convergence with respect to the expansion order in the interaction. A weak-to-intermediate coupling method is the two-particle self-consistent approach by Vilk and Tremblay (1997), which can be applied to systems with many orbitals.

Another important category of methods considers *finite clusters*. By considering clusters of growing size, an extrapolation to infinite cluster size, and thus exact results, becomes possible. In determinant quantum Monte Carlo (DQMC) (Blankenbecler et al., 1981) the imaginary time interval is split into finite intervals in order to perform a Trotter decomposition. Then, by means of a Hubbard-Stratonovic transformation, an auxiliary field is introduced and sampled by a Monte Carlo algorithm. The errors that are introduced by time discretization and finite clusters have to be treated by extrapolation. A cluster extension of DMFT is the dynamical cluster approximation (DCA) (Hettler et al., 1998), where the Brillouin zone is split into

Die approbierte gedruckte Originalversion dieser Dissertation ist an der TU Wien Bibliothek verfügbar.
The approved original version of this doctoral thesis is available in print at TU Wien Bibliothek.
TU Bibliothek WIEN Your knowledge hub

a number of patches. Within such a patch the self-energy is momentum independent, but it varies from patch to patch. Complementary to the DCA, there is the cellular DMFT (CDMFT) (Georges et al., 1996), where instead of the single-site impurity an interacting cluster is considered to be coupled to the non-interacting bath. Both DCA and CDMFT can be systematically improved by increasing the number of patches or the cluster size, respectively. For a review see Maier et al. (2005).

The group of *vertex based diagrammatic extensions* of DMFT, recently reviewed by Rohringer et al. (2018), contains the dynamical vertex approximation (DΓA) (Toschi et al., 2007), which is the main topic of this chapter. Importantly, into this category also fall the dual fermion (DF) by Rubtsov et al. (2008) and dual boson (DB) approach (Rubtsov et al., 2012). Inspired by DMFT, where the one-particle vertex (i.e. the self-energy) is local, they assume locality on the level of the two-particle vertex. These approaches can be systematically improved by raising the locality to the n-particle level, becoming exact for $n \longrightarrow \infty$ (Rohringer et al., 2018). The impact of three-particle corrections on DF calculations has been estimated by Ribic et al. (2017). Further diagrammatic extensions of DMFT include the triply irreducible local expansion (TRILEX) (Ayral and Parcollet, 2015), the quadruply irreducible local expansion (QUADRILEX) (Ayral and Parcollet, 2016), and the more recent D-TRILEX by Stepanov et al. (2019), which is based on a consistent partial bosonization of the Hubbard model.

5.1 Dynamical vertex approximation

This section is based on Kaufmann et al. (2021). Quotations from there are marked by a vertical bar. Parts that have been written only by the author of this thesis have no bar.

Let us now turn to the dynamical vertex approximation, which is a central topic of this thesis. Since its invention by Toschi et al. (2007) and Katanin et al. (2009), several variants have been developed. Among these there is the AbinitioDΓA (Galler et al., 2017; 2018; 2019),

> which extends the concept of the dynamical vertex approximation (DΓA) (Toschi et al., 2007; Katanin et al., 2009) to realistic materials calculations. It inherits from DMFT the non-perturbative treatment of strong local correlations, but on top of this also includes nonlocal correlations. To this end, a two-particle ladder is built with the local DMFT irreducible vertex and the nonlocal Green's function as building blocks. These ladder diagrams then yield a nonlocal contribution to the self-energy.
>
> Hitherto such AbinitioDΓA calculations have been restricted to so-called "one-shot" calculations without an update of the DMFT vertex and nonlocal Green's function. Obviously, such a one-shot calculation is only expected to be reasonable as long as the nonlocal corrections to DMFT remain small. It also does not suppress the DMFT critical temperatures nor modifies the DMFT critical exponents. In the case of DΓA calculations for one-band models, so-far a Moriyaesque λ-correction (Katanin et al., 2009; Rohringer and Toschi, 2016) was devised as a cure. It imposes a sum rule on the spin (or alternatively spin and charge) susceptibility, reduces the critical temperature and yields reasonable critical exponents (Rohringer et al., 2011;

Die approbierte gedruckte Originalversion dieser Dissertation ist an der TU Wien Bibliothek verfügbar.
The approved original version of this doctoral thesis is available in print at TU Wien Bibliothek.
TU Bibliothek WIEN Your knowledge hub

Schäfer et al., 2017; 2019). Superconductivity in cuprates (Kitatani et al., 2019) and nickelates (Kitatani et al., 2020) is described surprisingly accurately, even correctly predicted in the latter case. The extension to the multi-orbital case however makes this Moriyaesque λ-correction difficult. One would need to introduce and determine various λ parameters for all orbital combinations and spin channels. This would result in a multi-dimensional optimization problem that is likely to have several local optima of comparable quality; details of how the λ-correction is modeled (which is nonunique) might be decisive.

Another route has been taken in the closely related dual fermion approach (Rubtsov et al., 2008) with ladder diagrams (Hafermann et al., 2009). Here, the Green's function is updated with the calculated nonlocal self-energy in a so-called "inner self-consistency". Hitherto applied to one-band model Hamiltonians such as the Hubbard (Hirschmeier et al., 2015) and Falicov-Kimball model (Antipov et al., 2014) yields very reasonable critical temperatures and exponents. Also a self-consistent update of the dual fermion vertex has been discussed (Ribic et al., 2018; Loon et al., 2018a; Tanaka, 2019).

In case of the DΓA such an update of the Green's function has also been made, however only for the much more involved parquet DΓA (Valli et al., 2015b; Li et al., 2016; 2019b; Kauch et al., 2019; Eckhardt et al., 2020) [For the analogous parquet dual fermion approach, see Astleithner et al. (2020), Astretsov et al. (2020), and Krien et al. (2020).] Here, besides the self-consistent update of the Green's function and self-energy, all three scattering (ladder) channels are mutually fed back into all other channels through the parquet equation (De Dominicis and Martin, 1964a; b; Bickers, 2004; Vasil'ev, 1998). The drawback is the extreme numerical effort needed to solve the parquet equations, which limits the method to one-band models so far (Valli et al., 2015b; Li et al., 2016; Kauch et al., 2019; Kauch et al., 2020a).

In this paper we present a self-consistent ladder DΓA (sc-DΓA) for multi-orbital models. We update the Green's function lines, as it is also done in parquet and dual fermion approaches but neither in the original AbinitioDΓA method nor in previous ladder DΓA calculations. This allows for a self-energy feedback into the ladder diagrams contained in the Bethe-Salpeter equation, and leads to substantial damping of the fluctuations in the respective scattering channel. Since this approach only requires a repeated evaluation of the AbinitioDΓA equations, its application to multi-orbital models is straightforward. Our results demonstrate that sc-DΓA works well for single- and multi-orbital systems and also when doping away from integer filling.

Being a diagrammatic extension of DMFT, the DΓA relies on the local irreducible vertices. These can be taken, e.g., from the auxiliary impurity problem of a DMFT calculation. In this case, the two-particle Green's function Eq. (3.5) is computed for the given AIM by an impurity solver, see Chapter 3. From the two-particle Green's function, one can directly obtain the generalized susceptibility

$$\chi_{abcd}^{\nu_1\nu_2\nu_3\nu_4} = \beta\left(G_{abcd}^{\nu_1\nu_2\nu_3\nu_4} - G_a^{\nu_1}G_c^{\nu_3}\delta_{12}\right) \tag{5.1}$$

$$\equiv \chi_{0,abcd}^{\nu_1\nu_2\nu_3\nu_4} + \chi_{\mathrm{conn},abcd}^{\nu_1\nu_2\nu_3\nu_4}, \tag{5.2}$$

with the bare bubble susceptibility

$$\chi_{0,abcd}^{\nu_1\nu_2\nu_3\nu_4} = -\beta G_a^{\nu_1}G_c^{\nu_3}\delta_{14}. \tag{5.3}$$

Die approbierte gedruckte Originalversion dieser Dissertation ist an der TU Wien Bibliothek verfügbar.
The approved original version of this doctoral thesis is available in print at TU Wien Bibliothek.
TU Bibliothek WIEN Your knowledge hub

Furthermore, the two-particle Green's function contains the reducible two-particle vertex $F_{abcd}^{\nu_1\nu_2\nu_3\nu_4}$, defined in Eq. (3.58).

If we choose the bosonic frequency as $\omega_{\text{ph}} = \nu_1 - \nu_2$, the Bethe-Salpeter equation (BSE) in the particle-hole channel can be solved separately at each bosonic frequency. In the particle-particle channel, we have to choose $\omega_{\text{pp}} = \nu_1 + \nu_3$ instead. Furthermore, the Bethe-Salpeter equations can be diagonalized in spin space by the following linear combinations:

$$F_{\text{d},nlhm} = F_{n\uparrow l\uparrow h\uparrow m\uparrow} + F_{n\uparrow l\uparrow h\downarrow m\downarrow}\,, \tag{5.4}$$

$$F_{\text{m},nlhm} = F_{n\uparrow l\uparrow h\uparrow m\uparrow} - F_{n\uparrow l\uparrow h\downarrow m\downarrow}\,, \tag{5.5}$$

$$F_{\text{s},nlhm} = F_{n\uparrow l\uparrow h\uparrow m\uparrow} + F_{n\uparrow l\uparrow h\downarrow m\downarrow}\,, \tag{5.6}$$

$$F_{\text{t},nlhm} = F_{n\uparrow l\uparrow h\uparrow m\uparrow} - F_{n\uparrow l\uparrow h\downarrow m\downarrow}\,. \tag{5.7}$$

The Bethe-Salpeter equations for the impurity in the particle-hole (ph) channel are thus

$$F_{r,lmm'l'}^{\nu\nu'\omega} = \Gamma_{r,lmm'l'}^{\nu\nu'\omega} + \sum_{\substack{nn'hh'\\ \nu''}} \Gamma_{r,lmhn}^{\nu\nu''\omega}\chi_{0,nhh'n'}^{\nu''\nu''\omega}F_{r,n'h'm'l'}^{\nu''\nu'\omega} \tag{5.8}$$

where $r = d, m$ denotes the afore-defined channel and $\omega \equiv \omega_{ph}$ is the bosonic frequency. For better readability we will adopt the shorthand notation

$$F_r^{\omega} = \Gamma_r^{\omega} + \Gamma_r^{\omega}\chi_0^{\omega}F_r^{\omega}, \tag{5.9}$$

where all quantities are matrices in an orbital-frequency compound index.

The DΓA is a diagrammatic extension of DMFT that assumes locality of the irreducible vertex, which is taken as input from an auxiliary impurity problem (usually from a converged DMFT solution to the original problem).

Since its original formulation by Toschi et al. (2007), the DΓA was developed in three main directions (often called different DΓA *flavors*):

(i) the original parquet formulation (p-DΓA), where the locality is assumed on the level of the fully irreducible vertex Λ – this flavor treats the smallest set of diagrams as local, and correspondingly it is computationally most demanding (Li et al., 2019b; Eckhardt et al., 2020);

(ii) ladder-DΓA (in combination with DFT input also called AbinitioDΓA (Galler et al., 2017; 2018; 2019)), where it is the irreducible vertex in the particle-hole channel (Γ_{ph}) that is assumed local;

(iii) λ-corrected DΓA (usually also called ladder-DΓA), where as in (ii) the irreducible vertex Γ_{ph} is taken as local. However, after the solution of the Bethe-Salpeter equations, a sum rule is imposed on the susceptibility by introducing the so-called Moriyaesque λ-correction (Katanin et al., 2009; Rohringer and Toschi, 2016; Schäfer et al., 2016b) to the susceptibility and self-energy.

Die approbierte gedruckte Originalversion dieser Dissertation ist an der TU Wien Bibliothek verfügbar.
The approved original version of this doctoral thesis is available in print at TU Wien Bibliothek.
TU Bibliothek WIEN Your knowledge hub

Below we first briefly review these three existing flavors, as this allows placing the new flavor (sc-DΓA; introduced in the next section) into its proper methodological context.

5.1.1 Parquet-DΓA

The parquet-scheme is a method to self-consistently calculate 1-particle and 2-particle quantities (De Dominicis and Martin, 1964a; b; Bickers, 2004; Vasil'ev, 1998) (it is closely related to the multiloop generalization (Kugler and Delft, 2018; Hille et al., 2020) of the functional renormalization group (fRG) method (Metzner et al., 2012)). Given a one-particle Green's function G and the fully 2-particle irreducible (That is, cutting any two Green's function lines does not separate the Feynman diagram into two pieces) 2-particle vertex Λ, one can iterate the parquet equation

$$F_r = \Lambda_r + \sum_{r'} c_{r'} \underbrace{\Gamma_{r'} \chi_0 F_{r'}}_{\Phi_{r'}} \tag{5.10}$$

and the lattice BSE

$$F_r^q = \Gamma_r^q + \Gamma_r^q \chi_0^q F_r^q \tag{5.11}$$

to obtain the (in general nonlocal) vertices F_r and Γ_r. Here the index $r = d, m, s, t$ is as defined earlier the channel index, c_r denotes a real prefactor, and Eq. (5.11) is diagonal in the bosonic variable (4-index q). In our short notation F_r^q and Γ_r^q are matrices in two fermionic multi-indices as before. The parquet equation Eq. (5.10) is not diagonal in the bosonic 4-index and its evaluation requires evaluation of the per definition reducible vertices Φ_r at different frequency and momentum combinations (for explicit formulation see e.g. Li et al. (2019b)).

The Green's function entering the above Eqs. (5.10)–(5.11) via χ_0 can also be updated, since the full vertex F is related to self-energy through the Schwinger-Dyson equation (SDE, see e.g. Li et al. (2019b)).

The SDE together with the Dyson equation and Eqs. (5.10)–(5.11) constitute a closed set with only one input quantity: Λ. For an exact Λ, the parquet scheme produces the exact one- and two-particle quantities. In practice, for example $\Lambda = U$ is taken, which is the lowest order in perturbation expansion widely known as the parquet approximation (De Dominicis and Martin, 1964b; Bickers, 2004). In the parquet DΓA method Λ is assumed local and taken from a converged DMFT calculation. In principle it is not necessary to take Λ from the DMFT impurity. One could also improve the auxiliary Anderson impurity model, such that it produced the same local Green's function as the one resulting from p-DΓA. This would add another level of self-consistency, which however turned out to be unnecessary for the parameters presented in this paper.

Truncated unity approximation. The parquet scheme is numerically extremely costly (Li et al., 2019b). We thus employ an additional approximation. Specifically, we transform the fermionic momentum dependence of the 2-particle reducible vertices Φ_r into a real space basis, leaving only the bosonic momentum $\mathbf{q}$:

$$\tilde{\Phi}_r^{\ell\ell' q} = \frac{1}{N} \sum_{k,k'} (f^{k\ell})^* \Phi_r^{kk' q} f^{k'\ell'} \tag{5.12}$$

Die approbierte gedruckte Originalversion dieser Dissertation ist an der TU Wien Bibliothek verfügbar.
The approved original version of this doctoral thesis is available in print at TU Wien Bibliothek.
TU Bibliothek WIEN Your knowledge hub

where $f^{k\ell}$ are basis functions (typically known as form factors) of a suitable transformation-matrix which we choose to obey certain symmetries. Exploiting the relative locality (Husemann and Salmhofer, 2009; Eckhardt et al., 2020) of the reducible vertices Φ in their two fermionic momenta we limit the number of basis functions $f^{k\ell}$ used for the transformation (hence the name *truncated unity*). This amounts to setting the more nonlocal parts (in the fermionic arguments) of the 2-particle reducible vertices to zero.

$$\tilde{\Phi}_r^{\ell\ell' q} = 0 \text{ for } \ell, \ell' > l_{\max}. \tag{5.13}$$

The calculations to transform the entire parquet-scheme including convergence studies in the number of basis functions can be found in Eckhardt et al. (2018) and Eckhardt et al. (2020). The truncated unity implementation (TUPS) (Eckhardt et al., 2020) with 1 or 9 form factors was used to generate the comparison data in Sec. 5.4.

5.1.2 Ladder-DΓA

Even with the truncated unity approximation the parquet-DΓA is numerically very costly. It also suffers from the presence of divergencies (Schäfer et al., 2013; 2016a; Gunnarsson et al., 2017; Vučićević et al., 2018; Chalupa et al., 2018) in the fully irreducible vertex Λ that is directly taken as input. Therefore it is often preferable to use ladder-DΓA, where the locality level is raised to the irreducible vertex in the particle-hole channel $\Gamma_{d/m,\text{imp}}$. The choice of channel is here determined by the dominant type of nonlocal fluctuations. By choosing the particle-hole channel we take nonlocal magnetic and density fluctuations into account, while treating particle-particle fluctuations only at the local level. The transversal particle-hole fluctuations will later be included on the same level by using the crossing symmetry, which relates it to the particle-hole channel.

Then, DΓA becomes significantly simpler and essentially consists of two steps: First one has to compute the Bethe-Salpeter equations

$$F_r^q = \left[1 - \Gamma_{r,\text{imp}}^{\omega} \chi_0^q\right]^{-1} \Gamma_{r,\text{imp}}^{\omega} \tag{5.14}$$

in the particle-hole channels $r = \text{d}, \text{m}$. Since the irreducible impurity vertices $\Gamma_{r,\text{imp}}$ can also exhibit divergences, it is better to reformulate the above equation. This is done by expressing Γ by Eq. (5.9) and rearranging the terms, as shown by Galler et al. (2017). Then one arrives at

$$F_r^q = F_r^{\omega} \left[1 - \chi_0^{\text{nl},q} F_r^{\omega}\right]^{-1} \tag{5.15}$$

containing only the full reducible vertex F, and the nonlocal part of the bubble $\chi_0^{\text{nl},q} = \chi_0^q - \chi_0^{\omega}$.

The momentum-dependent reducible vertices F_r^q from the longitudinal and transversal particle-hole channels are then combined. We do not need to calculate the latter explicitly, because it can be obtained from the former through the crossing-symmetry (Rohringer et al., 2018). The combined vertex $\mathcal{F}$ is then

$$\mathcal{F}_{\text{d},nlhm}^{kk'q} = F_{d,nlhm}^{\nu\nu'\omega} + F_{d,nlhm}^{\text{nl},\nu\nu' q} - \frac{1}{2} F_{d,hlnm}^{\text{nl},(\nu'-\omega)\nu'(k'-k)} - \frac{3}{2} F_{m,hlnm}^{\text{nl},(\nu'-\omega)\nu'(k'-k)} \tag{5.16}$$

Die approbierte gedruckte Originalversion dieser Dissertation ist an der TU Wien Bibliothek verfügbar.
The approved original version of this doctoral thesis is available in print at TU Wien Bibliothek.
TU Bibliothek WIEN Your knowledge hub

(see also Eq. (54) in Galler et al. (2017)). Vertices labeled "nl" are nonlocal, i. e. $F^{\mathrm{nl},\nu\nu' q}_{r,nlhm} = F^{\nu\nu' q}_{r,nlhm} - F^{\nu\nu'\omega}_{r,nlhm}$. Inserting this into the Schwinger-Dyson equation of motion (Galler et al., 2017)

$$\Sigma^{\mathrm{con},k}_{mm'} = -\frac{1}{\beta} \sum_{\substack{nlh \\ n'l'h'}} \sum_{k'q} U_{mlhn} \chi^{k'k'q}_{0,nll'n'} \mathcal{F}^{kk'q}_{\mathrm{d},n'l'h'm'} G^{k-q}_{hh'} \tag{5.17}$$

yields the connected part of the momentum-dependent self-energy. In practice this equation is evaluated separately for the summands of $\mathcal{F}$ in Eq. (5.16) (Galler et al., 2019), such that one can identify the nonlocal corrections to the DMFT self-energy.

Eqs. (5.15)–(5.17) can be evaluated efficiently even for multi-orbital models with $h(\boldsymbol{k})$ from DFT as input. This is known as the AbinitioDΓA (Galler et al., 2017; 2018; 2019). Hitherto they are evaluated only once, and this flavor is therefore referred to as one-shot DΓA (1-DΓA) in the following.

5.1.3 λ-corrected DΓA

The self-energy obtained in the one-shot ladder-DΓA calculation does not always exhibit the correct asymptotic behavior, especially if the susceptibility is large. In addition, the susceptibilities related to Eq. (5.15) diverge at the DMFT Néel temperature, violating the Mermin-Wagner theorem (Mermin and Wagner, 1966) for 2-dimensional models. This problem was partially solved by so-called λ-corrections (Katanin et al., 2009; Rohringer and Toschi, 2016), where one enforces the sum rule for the spin (or spin and charge) susceptibility(-ies) by adapting a parameter λ (hence the name).

While very successful for one-band models (Schäfer et al., 2016b; Schäfer et al., 2017; 2019; Kitatani et al., 2019; 2020; Schäfer et al., 2020), this solution is not straightforwardly extensible to multi-orbital systems. The reasons are twofold. Firstly, λ would be a matrix with as many independent entries as there are different spin-orbital combinations, resulting in a multi-dimensional optimization problem. Secondly, the solution to this problem is quite likely nonunique and there are at the moment no criteria how the physical matrix λ should be chosen. While we do not exclude that a reasonable scheme can be devised for the multi-orbital case in the future (see e.g. Miyahara et al. (2013) and Arya et al. (2015) for the application of sum rules in the multi-orbital two-particle self-consistent approach (Tremblay, 2011)), we focus here on an alternative scheme, that does not rely on enforcing sum rules.

5.2* Self-consistent ladder DΓA (sc-DΓA)

This section is based on Kaufmann et al. (2021). Quotations from there are marked by a vertical bar. Parts that have been written only by the author of this thesis have no bar.

While the λ-correction is impractical or perhaps not even possible for multi-orbital systems, a one-shot ladder-DΓA calculation as hitherto employed for realistic materials calculations also

Die approbierte gedruckte Originalversion dieser Dissertation ist an der TU Wien Bibliothek verfügbar.
The approved original version of this doctoral thesis is available in print at TU Wien Bibliothek.
TU Bibliothek WIEN Your knowledge hub

has severe limits. Where the nonlocal corrections become strong, its application is not justified. When the DMFT susceptibility diverges at a phase transition, the nonlocal corrections of a one-shot DΓA calculation are not meaningful any more.

There are two main physical reasons why this is wrong: Firstly, the ladder diagrams of say the particle-hole channel lack insertions from the particle-particle channel, which dampen the particle-hole fluctuations. These diagrams are taken into account only on the level of the impurity. In order to correctly incorporate the nonlocal contributions to such insertions, we need to evaluate the full parquet scheme that is at the moment numerically too costly for multi-orbital calculations.

Secondly and arguably even more important, the self-energy that enters the propagators in the BSE is still the local DMFT self-energy in a one-shot DΓA. This DMFT self-energy fulfills the local SDE with local F^{ω}, where the nonlocal contributions do not enter. By using the updated nonlocal self-energy in the BSE, we can introduce feedback from two-particle nonlocal correlations to the one-particle quantities. For example, spin fluctuations lead to a reduced life-time which, when included in the ladder Green's function or self-energy, reduces the spin fluctuations in turn. This mechanism hence suppresses the magnetic transition temperature below the DMFT mean-field value.

The approach we propose here consists in finding a momentum-dependent self-energy for a lattice, defined by the tight-binding Hamiltonian $h(\boldsymbol{k})$, that is consistent with the local irreducible vertex $\Gamma_{ph,\mathrm{imp}}$. This can be achieved by using an iterative scheme illustrated in the lower left panel of Fig. 5.1 in order to underline its formal similarity to DMFT: The first step is again the construction of propagators by the Dyson equation (DE), Eq. (4.13), with a chemical potential that constrains the electron number. But in contrast to DMFT the self-energy is now momentum-dependent. In the second step we sum up all self-energy diagrams that are generated from the local vertex Γ. More explicitly, this step consists of the subsequent evaluation of the BSE [Eq. (5.15)] and SDE [Eq. (5.17)]. Just as in DMFT, also here the second step is numerically much more expensive than the first (DE) step.

The self-energy resulting from the first iteration of ladder-DΓA is taken to be the input (or "trial") for the second iteration. Starting from the third iteration, linear combinations of trial and result self-energies from several previous iterations are used as new trials. The linear combination is constructed by the Anderson acceleration algorithm (Anderson, 1965; Walker and Ni, 2011); see also Section 4.4. If the result is equal to the trial, the iteration is stopped. The workflow of such a calculation is illustrated in Fig. 5.1.

To our knowledge there is no proof of uniqueness or existence of such a fixed point. However, we find the procedure to be convergent over a large range of parameters (cf. Fig. 5.2 which is discussed in Sec. 5.4).

In case of convergence, the asymptotic behavior of the self-energy is largely repaired with respect to one-shot DΓA calculations. Furthermore, the magnetic susceptibility in two-dimensional models stays finite at all temperatures in agreement with the Mermin-Wagner theorem.

5.2.1 Implementation

The sc-DΓA is applicable to multi-orbital calculations using the AbinitioDΓA code (Galler et al., 2019), with the slight modification of allowing for momentum-dependent self-energies in

Die approbierte gedruckte Originalversion dieser Dissertation ist an der TU Wien Bibliothek verfügbar.
The approved original version of this doctoral thesis is available in print at TU Wien Bibliothek.
TU Bibliothek WIEN Your knowledge hub

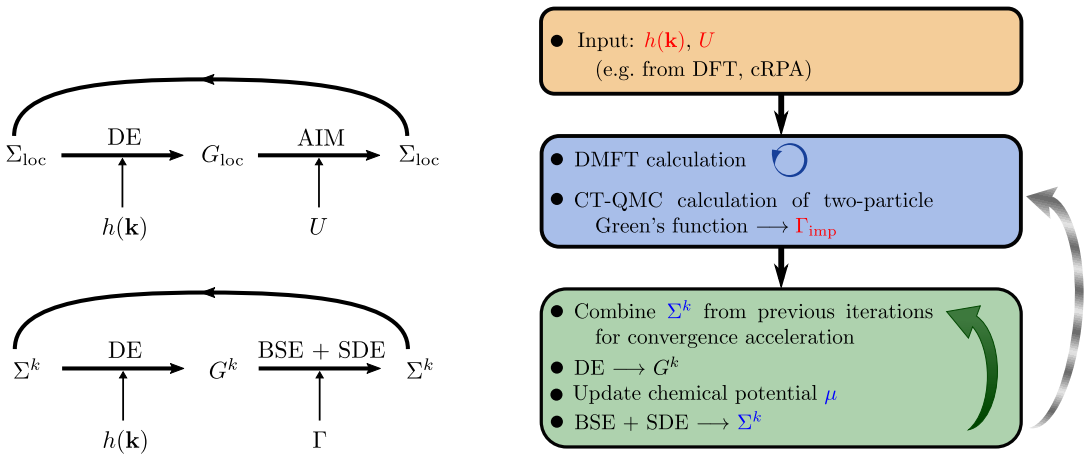

Figure 5.1: Left: Schematic explanation of DMFT and DΓA loops. Right: Step-by-step illustration of a self-consistent ladder DΓA calculation. The first box (orange color) shows preliminary calculations to set up the model. The second box (blue color) concerns the DMFT calculations, and the third one (green color) shows the sc-DΓA-cycle. Quantities written in red are kept constant throughout the whole calculation; those in blue are self-consistently determined in sc-DΓA.

the input. Since the author of this thesis is also a coauthor of the respective paper about the AbinitioDΓA code by Galler et al. (2019), it is included after the Appendix on p. 199.

A step-by-step description of the workflow is given in Fig. 5.1; below we provide some technical details of how this is done in operation with the AbinitioDΓA, as implemented by the author of this thesis.

The first step (orange box in Fig. 5.1) is the creation of a model. It can be based on *ab initio* calculations and consists of a tight-binding Hamiltonian as well as a parametrization of the interaction in form of a U-matrix.

The second step is to determine a local (impurity) vertex Γ_{imp}. Here, this is obtained from the local impurity problem at DMFT self-consistency as indicated in the blue box in Fig. 5.1; then usually the DMFT self-energy is also taken as a starting point for the following DΓA calculations. It is however not strictly required to start from a converged DMFT calculation. One might as well start from GW or calculate Γ_{imp} from the DΓA Green's function in an additional self-consistency step, as indicated by the dashed gray arrow in Fig. 5.1 but not done in this thesis.

Finally, the actual sc-DΓA cycle is illustrated in the green box of Fig. 5.1. It essentially amounts to the execution of the AbinitioDΓA code (Galler et al., 2019), but in the repeated evaluation of Eqs. (5.15)–(5.17), we have to generate updated input quantities after every iteration, until convergence is reached.

Input structure

Solving the aforementioned equations self-consistently means that the AbinitioDΓA code is executed several times in a loop in order to do a fixed-point iteration. Before each iteration, we create an updated trial input, until the point where the output does not differ from the input any more. Therefore, in order to describe the details of the updates, we have to recapitulate

Die approbierte gedruckte Originalversion dieser Dissertation ist an der TU Wien Bibliothek verfügbar.
The approved original version of this doctoral thesis is available in print at TU Wien Bibliothek.
TU Bibliothek WIEN Your knowledge hub

the input structure of AbinitioDΓA first.

Apart from the system-defining parameters (tight-binding Hamiltonian and U-matrix) the following quantities are required as input:

1. lattice self-energy Σ^k (can also be momentum-independent)
2. impurity self-energy Σ^ν_{imp} (can be identical to the lattice self-energy, as in 1-DΓA)
3. impurity Green's function G^ν
4. impurity two-particle Green's function $G^{\nu\nu'\omega}$

The update proceeds in the two steps described in the following.

Update of the self-energy and one-particle Green's function

This step defines the update. We take trial and result self-energies from several preceding iterations and compose a new trial self-energy $\Sigma^{k\,(j)}_{\text{trial}}$ for the j-th iteration. This prediction is usually made by the Anderson acceleration algorithm (Anderson, 1965; Walker and Ni, 2011) (also known as Pulay-mixing (Pulay, 1980) or direct inversion in iterative subspace, DIIS (Császár and Pulay, 1984)). This trial self-energy is then used to compute a new local propagator $G^{\nu\,(j)}_{\text{loc}}$ by

$$G^{\nu\,(j)}_{\text{loc}} = \frac{1}{V_{\text{BZ}}} \int \mathrm{d}^d k \left[(i\nu + \mu^{(j)})\mathbf{1} - h(\boldsymbol{k}) - \Sigma^{k\,(j)}_{\text{trial}} \right]^{-1}, \tag{5.18}$$

where the chemical potential $\mu^{(j)}$ is adapted such that the expectation value of the particle number stays at the desired value. The change of the chemical potential usually stays in the range of a few percent. Once the new local Green's function is determined, we project (downfold) it to the correlated impurity subspaces. Thus, each impurity I obtains its new Green's function $G^{\nu\,(j)}_I$.

Update of impurity quantities

This step is inherent to our specific implementation of AbinitioDΓA, and not part of the algorithm *per se*. But since AbinitioDΓA reads the one- and two-particle Green's function instead of the irreducible vertex, we need to "wrap" the irreducible vertex (unchanged throughout all iterations) in the new impurity propagator by means of the Bethe-Salpeter equation. In order to avoid direct computation of the irreducible vertex, we compute the updated generalized susceptibility for iteration (j) in channel r by

$$\chi_r^{(j)} = \chi_r^{\text{DMFT}} \left[\chi_r^{\text{DMFT}} + \chi_0^{(j)} - \chi_0^{(j)} \left(\chi_0^{\text{DMFT}} \right)^{-1} \chi_r^{\text{DMFT}} \right]^{-1} \chi_0^{(j)}. \tag{5.19}$$

Note that all susceptibilities in this equations are compound-index matrices in the orbital space of the impurity and fermionic frequencies. The new impurity one-particle Green's function enters into this equation only through $\chi_0^{(j)}$ of Eq. (5.3), where updated impurity Green's functions $G^{(j)}$ are used. The two-particle Green's function is obtained by dividing through β and adding a disconnected part, according to Eq. (5.1).

Die approbierte gedruckte Originalversion dieser Dissertation ist an der TU Wien Bibliothek verfügbar.
The approved original version of this doctoral thesis is available in print at TU Wien Bibliothek.
TU Bibliothek WIEN Your knowledge hub

Furthermore, it is necessary to compute an updated ("fake") impurity self-energy by the equation of motion. The reason for this can be seen in Eq. (75) of Galler et al. (2017). There, the DMFT self-energy appears as a separate term. However, in its essence it is not the DMFT self-energy, but rather the result of the Schwinger-Dyson equation of motion for the impurity. In Galler et al. (2017), this term is subtracted and substituted by the actual DMFT self-energy, in order to mitigate effects of finite frequency boxes. Therefore, we compute the impurity self-energy from the equation of motion,

$$\Sigma^{\nu(j)}_{\mathrm{con},m,I} = \frac{1}{\beta} \sum_{\nu'\omega} \sum_{lhn} U_{I,mlhn} G^{\nu'\nu\omega(j)}_{\mathrm{con},I,nlhm} / G^{\nu(j)}_{I,m} \tag{5.20}$$

using both the new (j) and the DMFT one- and two-particle Green's function. The index I labels the I-th impurity of the unit cell. Importantly, the frequency boxes have to be identical. Then the difference of these two self-energies is added to the DMFT self-energy and taken as the new (fake) impurity self-energy. In this way the effects of finite-box summation are canceled. We emphasize that the "fake" impurity self-energy is merely an auxiliary quantity and never used to extract any physical properties of the result. Only the lattice self-energy is subject to physical interpretation in our computations.

5.2.2 Computational effort

At this point, it is appropriate to comment on the computational effort of the present self-consistent ladder DΓA. The cost of a DMFT calculation and the two-particle Green's function depends mainly on the desired accuracy, if one is using a Monte Carlo method as an impurity solver. The scaling of the CT-QMC with temperature and number of orbitals has been discussed in the literature (Gull et al., 2011). The measurement of the two-particle Green's function in worm sampling of w2dynamics scales as $\sim (\#\omega)^3 M_{\mathrm{comp}}$, where M_{comp} is the number of non-vanishing spin-orbital components. In the case of Kanamori interaction this goes as $M_{\mathrm{comp}} \sim M^2$, where M is the number of impurity orbitals To be precise, for Kanamori interaction we find $M_{\mathrm{comp}}(M) = 6x_M$ where $x_M = 3M^2 - 2M$ are *octagonal numbers*. For a general dense U-matrix, the number of components is $M_{\mathrm{comp}} = (2M)^4$. The number of frequencies $\#\omega$ has to be scaled linearly with β as lower temperatures are approached. Note that at this point we do not distinguish between the number of fermionic and bosonic frequencies, since at least their scaling with temperature is the same.

Having calculated the two-particle Green's function, the remaining time of the computation is direct proportional to the number of iterations (N_{iter}) needed for convergence. N_{iter} ranges from a few (~10) at high-temperatures to many (~200) iterations at low temperatures. However, in problems with weak spin fluctuations, N_{iter} is hardly dependent on temperature. In our experience, convergence is accelerated if the DMFT self-energy Σ used as a starting point has little noise. Therefore we use symmetric improved estimators (Kaufmann et al., 2019) to compute it in CT-QMC. Noise in the vertex, on the other hand, does not have a large influence on the self-energy in DΓA, as shown recently by Kappl et al. (2020).

We shortly summarize this work in Section 5.3 and include it in the Appendix on p. 219.

Die approbierte gedruckte Originalversion dieser Dissertation ist an der TU Wien Bibliothek verfügbar.
The approved original version of this doctoral thesis is available in print at TU Wien Bibliothek.
TU Bibliothek WIEN Your knowledge hub

Case	$[\text{Time}]_{\Gamma_{\text{imp}}}$	$[\text{Time}]_{\text{sc-D}\Gamma\text{A}}$
Sq. latt., $U = 2$, $1/T = 4$	2400 h	65 h
Sq. latt., $U = 2$, $1/T = 20$	43000 h	11000 h
2-band, $1/T = 10$	13000 h	3000 h
2-band, $1/T = 20$	40000 h	70000 h

Table 5.1: Computational effort [time measured in core hours (h) on an Intel Skylake Platinum 8174 processors with 3.1 GHz] for the calculation of the local two-particle vertex Γ_{imp} (blue box in Fig. 5.1) and the sc-DΓA (green box in Fig. 5.1) for a few cases treated in this paper. "Sq. latt." (square lattice) refers to Section 5.4, "2-band" refers to the two-band model treated in Section 5.5.

The computational effort of one DΓA iteration has been discussed in Galler et al. (2019). Let us give a brief overview for the sake of completeness. In this part, most time has to be spent with the BSE, where it is necessary to $(\#\omega\#\boldsymbol{q})$ times invert a matrix of dimension $(M^2\#\omega)$. Overall this gives a scaling of $\sim \#\boldsymbol{q}(\#\omega)^{3.5}M^5$ (Galler et al., 2019).

In order to give a rough feeling or rule of thumb for the computational cost, we remark that at high temperatures the DMFT and CT-QMC calculations take considerably more time than the DΓA self-consistency cycle. For the most complicated cases, where many iterations are needed for convergence, one may expect to spend about twice as much time for ladder DΓA than for the CT-QMC. We illustrate this by providing the actual CPU hours that were spent on some of the calculations in Table 5.1.

5.2.3 Relation to p-DΓA

The self-consistency imposed on the self-energy that is obtained by iterative application of BSE (5.15), crossing symmetry (5.16) and SDE (5.17) is reminiscent of the parquet scheme. The main difference is the lack of the full parquet equation (5.10), which would include also nonlocal particle-particle insertions in the full vertex F. In the full p-DΓA the level of local approximation is also different, since Λ contains fewer diagrams than Γ. In the truncated unity approximation however, Γ is also effectively local if we do calculations with only one form factor (1FF p-DΓA). It can be explicitly seen e.g. in Eq. (21) in Eckhardt et al. (2020). The difference between the irreducible vertices Γ in the two approaches is that in sc-DΓA it is taken from DMFT and never updated during the self-consistency cycle, whereas in 1FF p-DΓA it is updated through the parquet equation in every iteration. This update allows for mixing of scattering channels in 1FF p-DΓA, notwithstanding the fact that the nonlocal contributions from other channels into Γ are averaged over momenta.

Die approbierte gedruckte Originalversion dieser Dissertation ist an der TU Wien Bibliothek verfügbar.
The approved original version of this doctoral thesis is available in print at TU Wien Bibliothek.
TU Bibliothek WIEN Your knowledge hub

5.3* Statistical error estimates in dynamical mean-field theory and extensions thereof

This is a short summary of a paper by Kappl et al. (2020), which is included in the Appendix on p. 219.

The statistical estimation of errors is usually done in calculations that solve a problem in a stochastic way, such as CT-QMC. How such statistical errors affect calculations that use results of CT-QMC merely as an input for complicated nonlinear functions, has been investigated much less. In fact, this is not a simple task, since straightforward evaluation of statistical estimators can lead to biased results. In this work, we therefore used the jackknife resampling method (Miller, 1964; 1974) to provide unbiased results and consistent error and correlation estimates for (one-shot) AbinitioDΓA calculations: DMFT susceptibilities, and DΓA self-energies. The input random variable is here the two-particle Green's function and we denote it by x. An AbinitioDΓA calculation is symbolically denoted by $f(x)$, yielding a result y.

As a first step, n samples (or "bins") x_i of the two-particle Green's function are computed in CT-QMC with different random seeds and a certain number of Monte Carlo measurements. Then we apply a resampling procedure to generate the "leave-one-out" samples x_i'

$$x_i \longrightarrow x_i' = \frac{1}{n-1}\sum_{j\neq i} x_j = \frac{n\bar{x} - x_i}{n-1}, \tag{5.21}$$

where $\bar{x} = \sum_{i=1}^{n} x_i/n$ is the sample mean. After applying AbinitioDΓA to each of these samples and also the mean, we transform the results by

$$y_i' = nf(\bar{x}) - (n-1)f(x_i'). \tag{5.22}$$

The sample mean of this set $\{y_i'\}$ is now the bias-corrected jackknife estimator for y. This means that its bias goes to zero as $O(n^{-2})$, whereas there would have been an $O(n^{-1})$ term if the simpler estimator $\hat{y} = f(\bar{x})$ had been used. It is also possible to obtain consistent estimators for the variance, standard error of the mean (SEM), correlation, etc. simply by applying the corresponding sample estimators to the $\{y_i'\}$.

Before studying the SEM of susceptibilities and the DΓA self-energy, we assert that there are no correlations between different frequencies of the two-particle Green's function. Since we use symmetric improved estimators for the calculation of the DMFT self-energy, it is safe to assume that its contribution to the SEM of the DΓA self-energy is negligible. In the following we find that it can be estimated reliably also with few bins of the two-particle Green's function and its dependence on the total number of Monte Carlo measurements n_t is $1/\sqrt{n_t}$ – as expected. Different frequencies of the DΓA self-energy turn out to be moderately correlated, as opposed to the susceptibility, and the quality of the correlation matrix strongly depends on the number of bins n. Nevertheless, we show that these correlations do not considerably worsen the MaxEnt analytic continuation.

Die approbierte gedruckte Originalversion dieser Dissertation ist an der TU Wien Bibliothek verfügbar.
The approved original version of this doctoral thesis is available in print at TU Wien Bibliothek.
TU Bibliothek WIEN Your knowledge hub

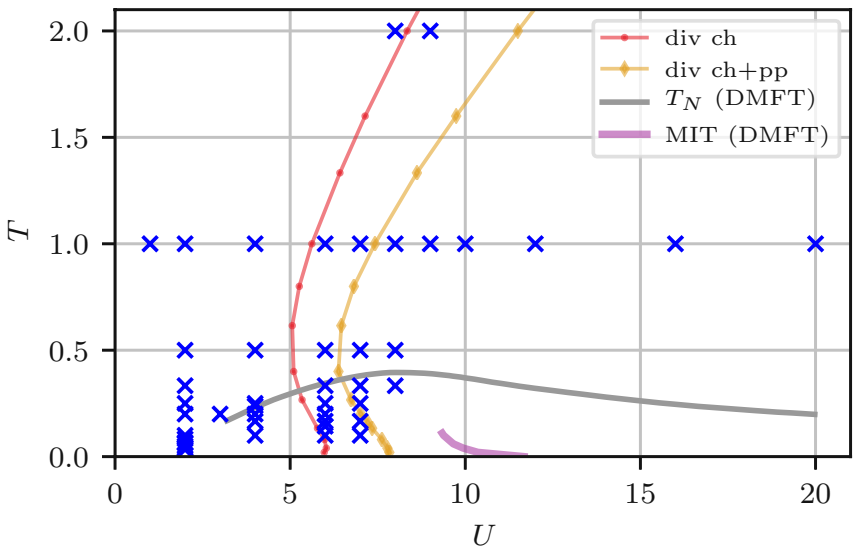

Figure 5.2: Phase diagram of the square-lattice Hubbard model at half-filling. Blue crosses denotes points at which the sc-DΓA could be converged. The DMFT-Néel temperature is shown in gray (from Kuneš (2011)). The magenta line indicates the DMFT metal-insulator transition. We also show the first two vertex divergence lines (from Schäfer et al. (2013)).

5.4* Square lattice Hubbard model

This section is based on Kaufmann et al. (2021). Quotations from there are marked by a vertical bar.

We begin the application of the sc-DΓA method by considering a relatively simple system, which already has been studied well in some parameter regimes: the one-orbital Hubbard model on a square lattice with nearest-neighbor hopping. The dispersion $h(\boldsymbol{k})$ in Eq. (4.12) is then simply

$$h(\boldsymbol{k}) = -2\big(\cos(k_x) + \cos(k_y)\big), \tag{5.23}$$

where the nearest-neighbor hopping amplitude is set to $t \equiv 1$ to define our unit of energy for this section (with $\hbar \equiv 1$ setting the frequency unit). Furthermore, the lattice constant $a \equiv 1$ sets the unit of length and $k_B \equiv 1$ the unit of temperature; and the orbital indices l, m, l', m' are restricted to a single orbital at each site.

In Fig. 5.2 we show the DMFT phase diagram of the Hubbard model on a square lattice at half-filling ($n = 1$ electron per site). With blue crosses we denote points in the phase diagram for which we were able to obtain a converged sc-DΓA solution. Please note, that the sc-DΓA method can be used both below the DMFT Néel temperature (indicated by the gray curve in Fig. 5.2) as well as between the divergence lines (red and orange curves in Fig. 5.2). It is only on or directly next to divergence lines that we were not able to obtain convergence.

The phase diagram in Fig. 5.2 serves as a proof of principle and it is not our intention to

Die approbierte gedruckte Originalversion dieser Dissertation ist an der TU Wien Bibliothek verfügbar.
The approved original version of this doctoral thesis is available in print at TU Wien Bibliothek.
TU Bibliothek WIEN Your knowledge hub

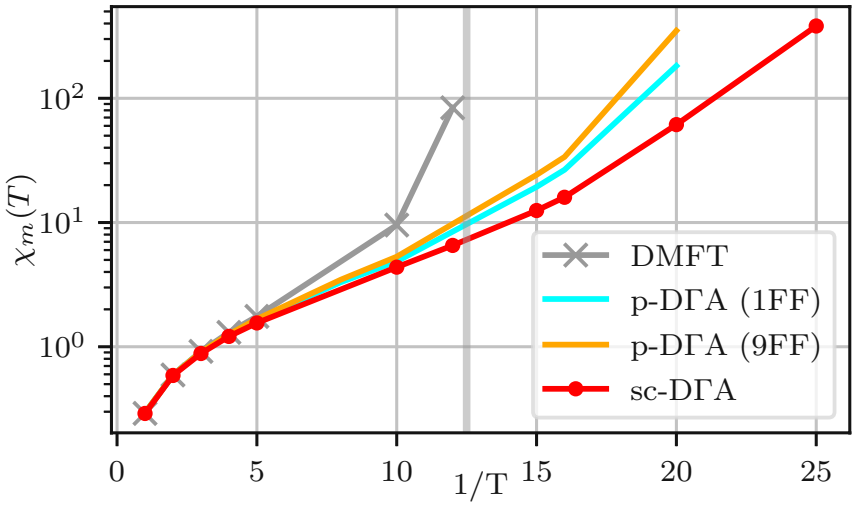

Figure 5.3: Static magnetic susceptibility of the square-lattice Hubbard model with $U = 2$ and $n = 1$ at momentum $\boldsymbol{q} = (\pi, \pi)$ as a function of inverse temperature. Different colors and symbols denote different methods. The gray vertical line marks the DMFT Néel temperature.

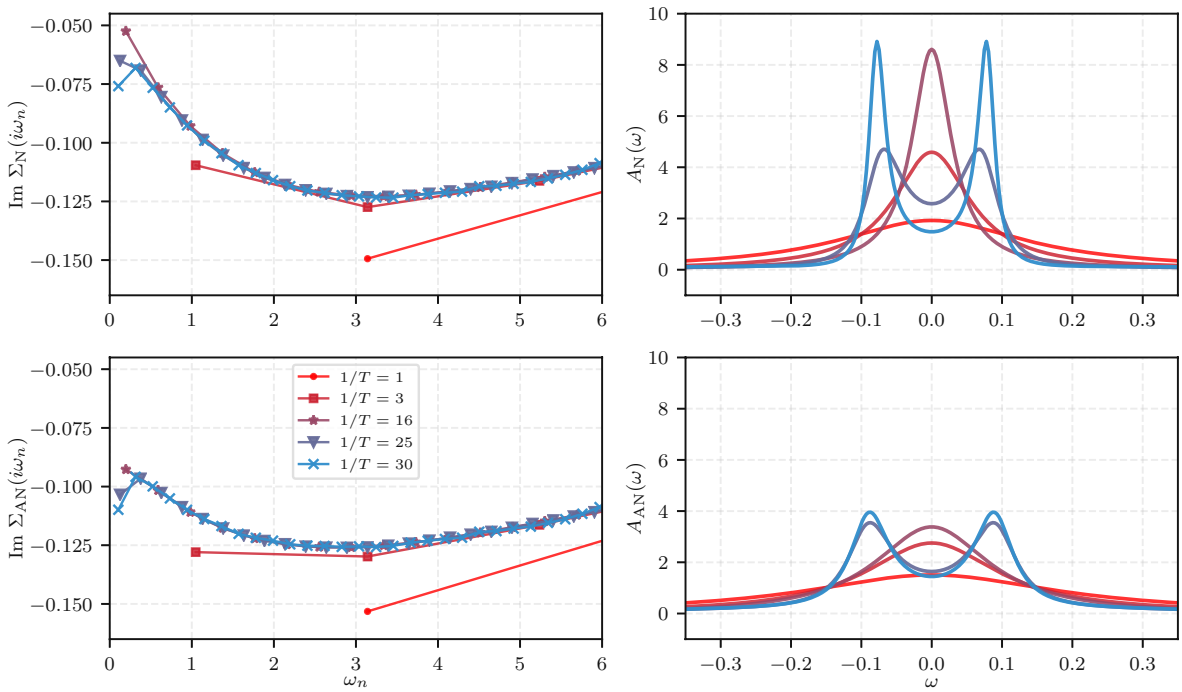

Figure 5.4: The imaginary part of sc-DΓA self-energy (left) and the corresponding spectral function (right) at $U = 2$ and half-filling for two momenta on the Fermi surface: nodal point, $\boldsymbol{k}_{\mathrm{N}} = (\pi/2, \pi/2)$ and antinodal point, $\boldsymbol{k}_{\mathrm{AN}} = (\pi, 0)$. Different colors and symbols denote different temperatures. The spectral functions were obtained by analytic continuation with the maximum entropy method (Geffroy et al., 2019; Kaufmann, 2020).

Die approbierte gedruckte Originalversion dieser Dissertation ist an der TU Wien Bibliothek verfügbar.
The approved original version of this doctoral thesis is available in print at TU Wien Bibliothek.
TU Bibliothek WIEN Your knowledge hub

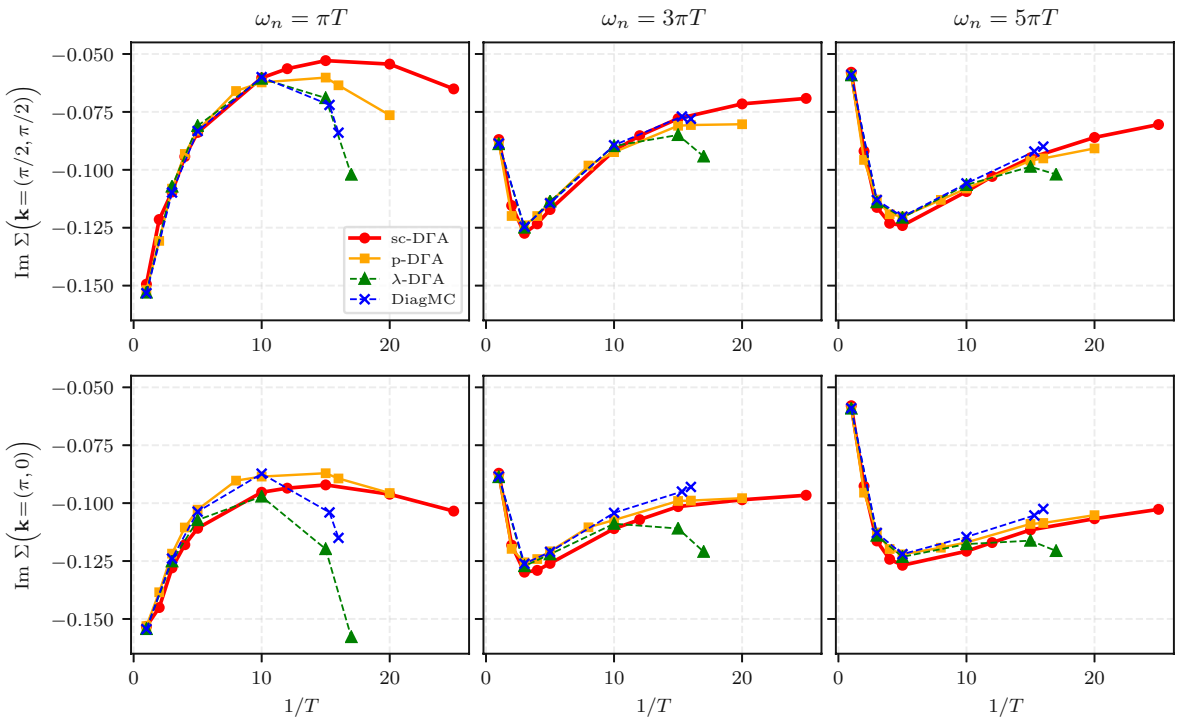

Figure 5.5: Inverse temperature dependence of the imaginary part of self-energy at $U = 2$ and half-filling for the first three Matsubara frequencies $\omega_n = \{\pi T, 3\pi T, 5\pi T\}$ for two momenta on the Fermi surface: $\boldsymbol{k}_{\mathrm{N}} = (\pi/2, \pi/2)$ and $\boldsymbol{k}_{\mathrm{AN}} = (\pi, 0)$. Different colors and symbols denote different methods. The λ-DΓA and DiagMC data in this figure were kindly provided by the authors of Schäfer et al. (2020).

discuss the sc-DΓA results in the different parameter regimes in the current paper. Instead, we show selected results for weak ($U = 2$) and intermediate ($U = 4$) coupling, where comparison to other methods is possible, as well as for strong coupling ($U = 8$) and out of half-filling ($n = 0.85$) to show the applicability of the method in this interesting (e.g. with regard to superconductivity) regime.

5.4.1 Weak coupling

In order to benchmark the method against known results, we first study a half-filled weak coupling case, with the interaction $U = 2$ (in our units the bandwidth is $W = 8$). This case was intensively studied by various methods in Schäfer et al. (2020); and in the spirit of Schäfer et al. (2020) we focus on spin fluctuations and the formation of the pseudogap at low temperature.

In Fig. 5.3 the static magnetic susceptibility at $\boldsymbol{q} = (\pi, \pi)$ is shown. For $U = 2$ DMFT predicts a phase transition at $T_N \approx 0.08$. The sc-DΓA leads to a seemingly non-diverging antiferromagnetic (AFM) susceptibility; the updated self-energy in the BSE dampens the magnetic fluctuations and removes the divergence. In the temperature range accessible, the sc-DΓA susceptibility shows first a $1/(T - T_N)$ behavior, as in DMFT which has a finite Néel temperature T_N, and then deviates to a linear behavior on the log-scale of Fig. 5.3, corresponding to $\chi_m(T) \sim \exp(\alpha/T)$ with some constant α. Such an exponential scaling with a divergence

Die approbierte gedruckte Originalversion dieser Dissertation ist an der TU Wien Bibliothek verfügbar.
The approved original version of this doctoral thesis is available in print at TU Wien Bibliothek.
TU Bibliothek WIEN Your knowledge hub

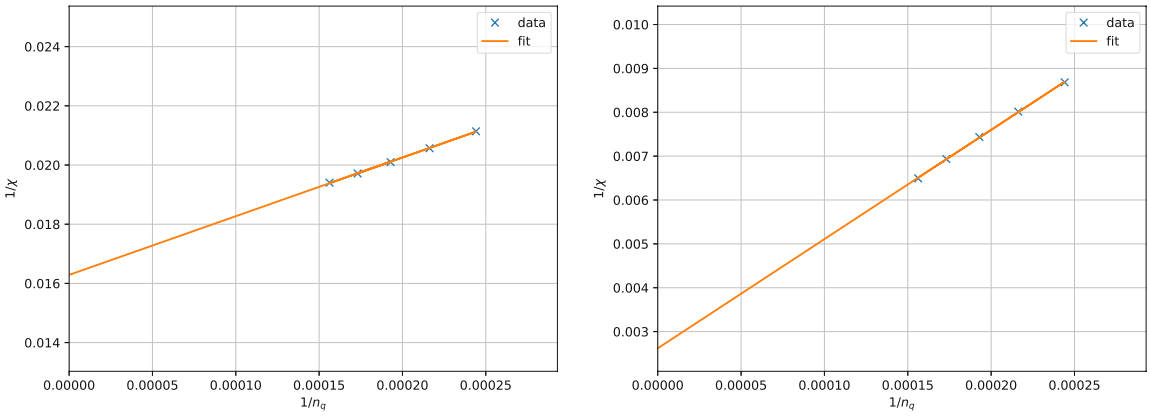

Figure 5.6: Extrapolation of antiferromagnetic susceptibility of the square-lattice Hubbard model with $U = 2$ at $T = 0.05$ (left) and $T = 0.04$ (right). The largest $\boldsymbol{q}$-grid is 80×80.

only at $T = 0$ is to be expected for a two-dimensional system, fulfilling the Mermin-Wagner theorem (Mermin and Wagner, 1966) (cf. also Fig. 13 in Schäfer et al. (2020)).

The sc-DΓA AFM susceptibility is somewhat smaller than the one from λ-corrected DΓA presented in Schäfer et al. (2020) (not shown here) as well as slightly smaller than the parquet-DΓA results (shown in Fig. 5.3 for 1 and 9 form factors). The overall behavior is however well reproduced.

In order to correctly resolve the growing correlation length when lowering the temperature, the size of the momentum grid has to be increased. For the lowest two temperatures shown in Fig. 5.3 we performed extrapolation to infinite grid size.

This is possible due to the observation that the inverse of the antiferromagnetic susceptibility depends linearly on the inverse of the number of $\boldsymbol{q}$-points. In particular, the extrapolation was necessary for sc-DΓA on the square-lattice Hubbard model with $U = 2$ at $T = 0.05$ and $T = 0.04$. There the DΓA calculation was done with 48×48, 64×64, 68×68, 72×72, 76×76, 80×80 $\boldsymbol{k}$- and $\boldsymbol{q}$-points. In Fig. 5.6 it is visible that the extrapolation with above mentioned linear relation is indeed possible. Although a deviation from this behavior is to be expected as $n_{\boldsymbol{q}} \longrightarrow \infty$, it can only lead to a small change in the logarithmic plot in Fig. 5.3 and thus our conclusions remain unchanged.

On the other hand, for $\boldsymbol{k}$- and $\boldsymbol{q}$-grids of 48×48 or larger, we find that the self-energy is practically independent on the number of $\boldsymbol{k}$- and $\boldsymbol{q}$-points, such that no extrapolation is necessary there.

With lowering the temperature the growing spin-fluctuations lead to enhanced scattering and suppression of the one-particle spectral weight at the Fermi energy and to opening of a pseudogap (Vilk and Tremblay, 1997; Rubtsov et al., 2009; Katanin et al., 2009; Rost et al., 2012; Schäfer et al., 2015; Schäfer et al., 2020). Due to the van Hove singularity (González et al., 2000; Halboth and Metzner, 2000; Honerkamp and Salmhofer, 2001; Wu et al., 2020) at the antinodal point $\boldsymbol{k}_{\mathrm{AN}} = (\pi, 0)$, the suppression happens earlier (upon lowering T) at this point than at the nodal point $\boldsymbol{k}_{\mathrm{N}} = (\pi/2, \pi/2)$. In Fig. 5.4 we show the spectral functions (right) as well as the corresponding self-energies on the imaginary (Matsubara) frequency axis (left) for

Die approbierte gedruckte Originalversion dieser Dissertation ist an der TU Wien Bibliothek verfügbar.
The approved original version of this doctoral thesis is available in print at TU Wien Bibliothek.
TU Bibliothek WIEN Your knowledge hub

the two momenta $\boldsymbol{k}_{\mathrm{N}}$ and $\boldsymbol{k}_{\mathrm{AN}}$ and for different temperatures.

The pseudogap behavior of the spectral function is also visible in the imaginary part of self-energy on the Matsubara frequency axis. Upon lowering the temperature we first see metallic behavior at both nodal and antinodal points: $|\mathrm{Im}\Sigma_N|$ at the first Matsubara frequency is smaller than at the second . At lower temperatures, the slope of $\mathrm{Im}\Sigma_N$ at the first two Matsubara frequencies changes sign; first only at the antinodal point (pseudogap) and finally at both nodal and antinodal points. This is usually taken as a criterion for the opening of a pseudogap.

Note however that for $1/T = 25$ there is already a pseudogap for $\boldsymbol{k}_{\mathrm{N}}$ in Fig. 5.4 (top right) while the slope of $\mathrm{Im}\Sigma_N$ is still negative in Fig. 5.4 (top left). However, a kink is visible. This kink of the analytic Σ_N function is apparently already enough for the analytic continuation to yield a large negative $\mathrm{Im}\Sigma_N$ at low real frequencies, which is needed for seeing a pseudogap.

In Fig. 5.5 we show the behavior of the imaginary part of the self-energy at the first three Matsubara frequencies for the nodal and antinodal points as a function of inverse temperature. Here we compare the sc-DΓA to parquet-DΓA and λ-corrected ladder-DΓA(Schäfer et al., 2020), and the diagrammatic Quantum Monte Carlo (DiagMC) (Šimkovic and Kozik, 2019; Schäfer et al., 2020). For the first Matsubara frequency all the methods lie almost on top of each other down to approx. $1/T = 10$ (at the nodal point differences already become noticeable at $1/T = 10$). For lower temperatures the methods still qualitatively agree, but $|\mathrm{Im}\Sigma(\omega_n = \pi T)|$ grows faster in the λ-DΓA and quantitatively agrees better with the DiagMC benchmark. In the sc-DΓA, as well as in the p-DΓA, this growth happens at lower temperatures. This is in correspondence to the behavior of AFM susceptibility, which also grows slower in these methods upon lowering the temperature compared to λ-DΓA and DiagMC, while correctly reproducing the overall behavior.

If we however look at the two larger frequencies (middle and right panel of Fig. 5.5), the situation is opposite. Here both the p-DΓA as well as sc-DΓA follow the DiagMC benchmark closely up to $1/T = 15$ and do not show any enhancement in $|\mathrm{Im}\Sigma|$ with lowering T, while in the λ-DΓA the 2nd and 3rd Matsubara frequency follow the behavior of the first one. This is probably a consequence of the λ-correction that is applied *a posteriori* to the self-energy. While it works very well for the AFM susceptibility and it gives the correct behavior for the low energy part in the self-energy, that is closely influenced (enhanced) by the strong spin fluctuations, it overestimates this influence for larger energies.

All in all, the comparison with the DiagMC benchmark shows the ability of sc-DΓA to describe the behavior of self-energy in all different temperature regimes: incoherent behavior at high temperatures, metalicity in the intermediate temperature regime and the opening of spin-fluctuation induced pseudogap. Quantitatively the agreement with DiagMC is excellent down to approx. $1/T = 10$, with small quantitative differences visible for the lowest temperatures. The most pronounced difference is that the opening of the pseudogap is shifted to lower temperature than in DiagMC.

Die approbierte gedruckte Originalversion dieser Dissertation ist an der TU Wien Bibliothek verfügbar.
The approved original version of this doctoral thesis is available in print at TU Wien Bibliothek.
TU Bibliothek WIEN Your knowledge hub

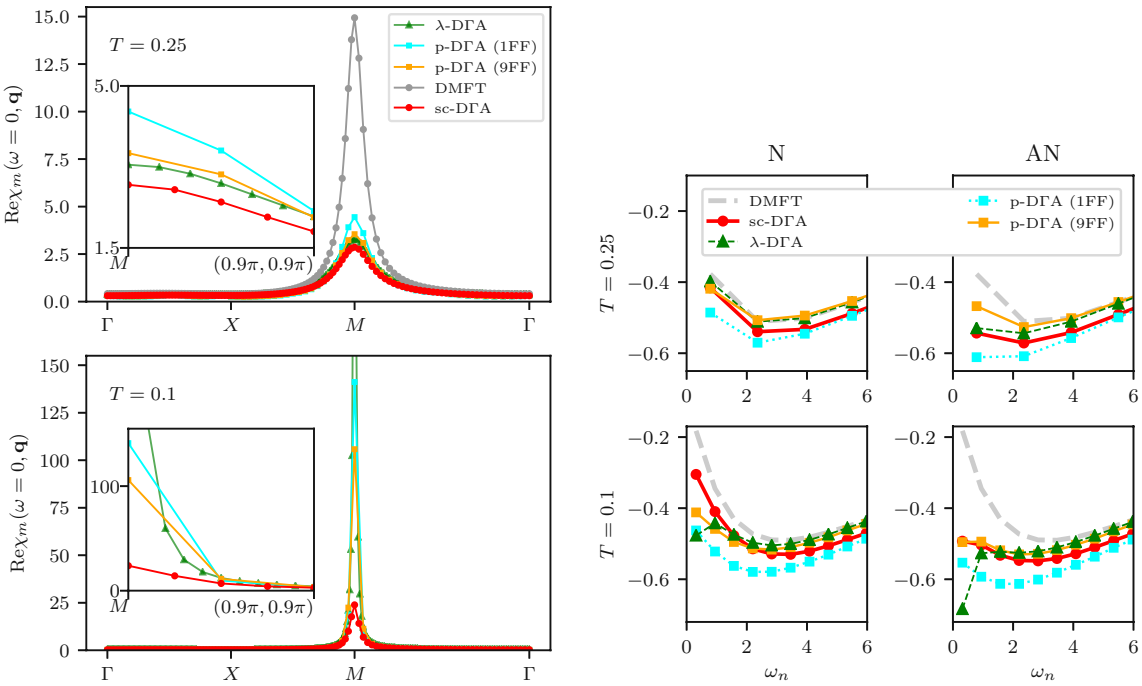

Figure 5.7: Left: Static magnetic susceptibility for $U = 4$ on a path through the Brillouin zone for $T = 0.25$ and $T = 0.1$. The value of λ-DΓA susceptibility at the M point is $\chi_m(\omega = 0, \boldsymbol{q} = (\pi, \pi)) = 415$ (beyond the y-range of the plot). A smaller momentum window is shown in the insets. Right: Imaginary part of self-energy for the nodal (N) and antinodal (AN) points as a function of Matsubara frequencies for $U = 4$, $n = 1$ and two temperatures: $T = 0.25$ and $T = 0.1$. Different methods are distinguished by different symbols and colors. The 1FF and 9FF p-DΓA data are reproduced from Eckhardt et al. (2020).

5.4.2 Intermediate coupling

Next, we increase the interaction to $U = 4$ but stay at half-filling. Since we already enter a regime, where the numerically exact methods are limited to high temperatures, we do not show comparisons to benchmarks. We focus here on the comparison to parquet-DΓA and the λ-corrected DΓA.

In the left panel of Fig. 5.7 we show the static magnetic susceptibility as a function of momentum $\boldsymbol{q}$ for two temperatures. We choose $T = 0.25$ for also comparing with the DMFT result that diverges for slightly lower temperature. Already for $T = 0.25$ we see a large difference to the DMFT result. As for the different DΓA methods, the results fall almost on top of each other with the exception of 1FF p-DΓA, where the susceptibility is somewhat larger close to the M-point. For the lower temperature of $T = 0.1$ the situation is quite different. Although all methods agree for momenta far from $\boldsymbol{q} = (\pi, \pi)$, close to it the results differ significantly, as it was the case for $U = 2$. The sc-DΓA susceptibility is again the smallest, followed by the p-DΓA results.

In the right panel of Fig. 5.7 we show the imaginary part of self-energy as a function of Matsubara frequency for the same two temperatures as in the left panel. For $T = 0.25$ the DΓA

Die approbierte gedruckte Originalversion dieser Dissertation ist an der TU Wien Bibliothek verfügbar.
The approved original version of this doctoral thesis is available in print at TU Wien Bibliothek.
TU Bibliothek WIEN Your knowledge hub

methods agree well, although not any more quantitatively as it was in the weak-coupling case for this temperature. Here the 1FF p-DΓA result is noticeably different: at $U = 4$ the 1FF approximation is not sufficient any longer at this temperature [cf. Eckhardt et al. (2020)]. For $T = 0.1$ at the antinodal point we already start to see the pseudogap behavior of self-energy in the sc-DΓA and p-DΓA methods, whereas in λ-DΓA the pseudogap sets in at a higher temperature of $T \approx 0.17$ (Schäfer et al., 2016b). Except for the first Matsubara frequency, the three DΓA methods are in excellent, almost quantitative agreement. As in the $U = 2$ case, the difference in the first Matsubara frequency is likely to be caused by much smaller AFM susceptibility in sc-DΓA as compared to λ-DΓA.

An open question remains why the sc-DΓA produces sizably smaller AFM susceptibility than the λ-DΓA upon going to low temperatures. For the case of $U = 2$ it is also significantly smaller than the DiagMC result (Schäfer et al., 2020). An intuitive partial understanding can be gained by looking at the p-DΓA results for one and nine form factors (1FF and 9FF). As already mentioned in Section 5.2.3 and explained by Eckhardt et al. (2020), for the 1FF approximation to p-DΓA the irreducible vertex Γ is also local. But contrary to sc-DΓA, it is updated after each update of the self-energy. Therefore when the damping effect of self-energy at low temperature becomes big, it can be counterbalanced by a larger Γ which results in a larger susceptibility (cf. Fig. 5.3 and Fig. 5.7, left). In sc-DΓA this vertex stays the same throughout the calculation; the two-particle feedback onto the self-energy is reduced [a]. There is also no feedback from the particle-particle channel that is present in p-DΓA.

In the truncated unity p-DΓA we can make Γ systematically less local by using more form factors. It has also a strong effect on the susceptibility, as the 9FF p-DΓA results show. In the case of $U = 2$ the susceptibility is larger for 9FF, it is however smaller than the 1FF result for $U = 4$ (cf. left panel of Fig. 5.7). Similar (opposite) tendencies of the AFM susceptibility were seen for the two values of U in Eckhardt et al. (2020). Although the convergence study in Eckhardt et al. (2020) shows that at $T = 0.25$ the 9FF p-DΓA result is converged with respect to the number of form factors, it is quite likely not the case for much lower temperatures.

In the λ-corrected DΓA the vertex is also local and not updated. The imposed sum rule however imitates the mutual feedback of the one- and two-particle quantities.

[a] In this case the Ward identity relating the irreducible vertex and self-energy $\Gamma = \frac{\delta\Sigma}{\delta G}$ is violated. This is also the case in the parquet approach, but certainly to a much smaller extent.

5.4.3 Strong coupling

Another interesting parameter regime that we can use the sc-DΓA method for is the doped strong-coupling case, which is relevant for superconductivity, as shown e.g. in Gull et al. (2013), Chen et al. (2013), Otsuki et al. (2014), Jia et al. (2014), LeBlanc et al. (2019), and Kitatani et al. (2019), 2020. Going to sufficiently low temperatures, such as in case of λ-DΓA (Kitatani et al., 2019; 2020), is a highly non-trivial task that requires computations with high numerical efficiency, since the momentum and frequency grids have to be sufficient to capture the growing correlation length.

In the following we show results for the Hubbard model on a square lattice with $U = 8$ and 15% hole doping ($n = 0.85$) in the temperature range $T \in [0.05, 0.5]$. With lowering the temperature the magnetic fluctuations, still antiferromagnetic at $T = 0.5$, become incommen-

Die approbierte gedruckte Originalversion dieser Dissertation ist an der TU Wien Bibliothek verfügbar.
The approved original version of this doctoral thesis is available in print at TU Wien Bibliothek.
TU Bibliothek WIEN Your knowledge hub

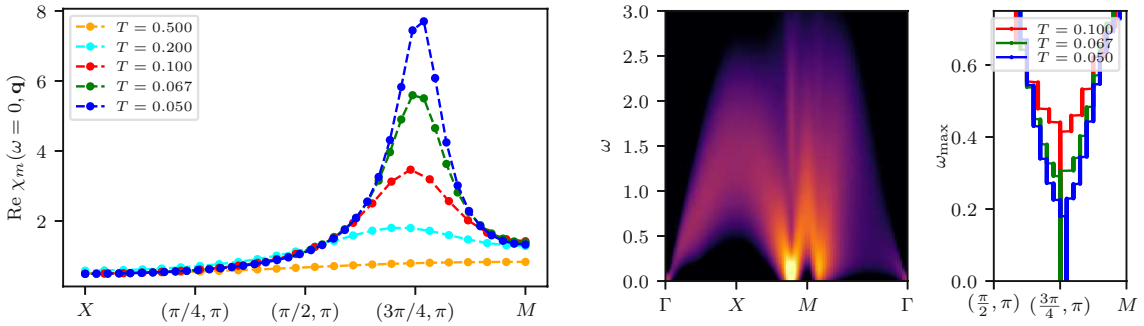

Figure 5.8: Left: Static magnetic susceptibility in sc-DΓA along the $X - M$ path in the Brillouin zone ($q_y = \pi$) for different temperatures T, $U = 8t$ and $n = 0.85$. Center: logarithmic plot of the dynamic magnetic structure factor $\mathrm{Im}\chi_m(\boldsymbol{q}, \omega)/(1 - e^{-\omega/T})$ at $U = 8$, $n = 0.85$ and $T = 0.05$, obtained by analytic continuation. The analytic continuation was done with the maximum entropy method (Geffroy et al., 2019; Kaufmann, 2020). Right panel: Y-shaped spin-excitation dispersion obtained from the dynamic magnetic susceptibility at $\boldsymbol{q} = (q_x, \pi)$ for different temperatures T.

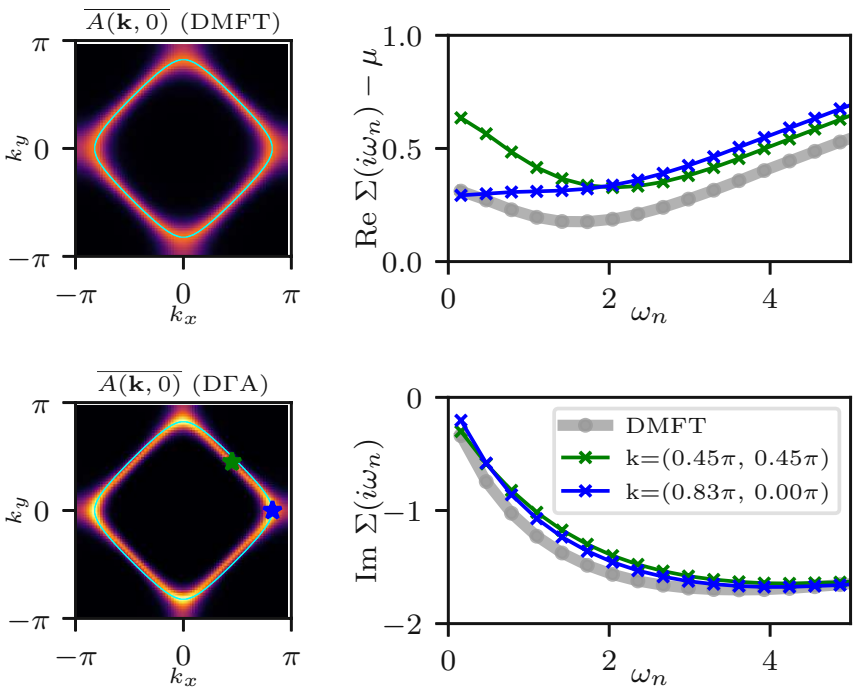

Figure 5.9: Fermi surface (FS) and the corresponding real and imaginary part of self-energy as a function of Matsubara frequency as obtained in DMFT and sc-DΓA. For sc-DΓA we show two different momenta on the FS, as indicated with green and blue stars on the FS plot. The FS was obtained by plotting $\overline{A_{\boldsymbol{k}}(0)} \approx G(\boldsymbol{k}, \tau = 1/(2T))$ (which avoids the analytical continuation and averages the spectral fucntion over an interval $\sim T$ around the FS). The non-interacting tight-binding FS is plotted with a thin cyan line in both FS plots. The parameters are $T = 0.05$, $U = 8$, $n = 0.85$.

Die approbierte gedruckte Originalversion dieser Dissertation ist an der TU Wien Bibliothek verfügbar.
The approved original version of this doctoral thesis is available in print at TU Wien Bibliothek.
TU Bibliothek WIEN Your knowledge hub

surate. This is indicated by the shift of the maximum of the static magnetic susceptibility from $\boldsymbol{q} = (\pi, \pi)$ to $\boldsymbol{q} = (3\pi/4, \pi)$ in the left panel of Fig. 5.8. If we look at the dynamic susceptibility $\chi_m(\omega, \boldsymbol{q})$ at finite frequencies ω, we can identify a splitting of the peak maximum. In the center panel of Fig. 5.8 we show the dynamic magnetic structure factor $\mathrm{Im}\chi_m(\boldsymbol{q}, \omega)/(1-e^{-\omega/T})$, obtained by analytic continuation with the maximum entropy method (Geffroy et al., 2019; Kaufmann, 2020) for $T = 0.05$ and also the position ω_{max} of the maximum (or maxima) as a function of $\boldsymbol{q}$ for different temperatures. The plots form characteristic Y-shaped spin-excitation dispersions, also seen experimentally (Chan et al., 2016) and discussed in LeBlanc et al. (2019). We observe that the frequency ω_{max}, at which the splitting occurs, moves to lower values as the temperature is lowered. It could be interpreted as sharpening of the dispersion relation upon lowering the temperature.

In the right panels of Fig. 5.9 the corresponding self-energy for the lowest temperature in the left panel of Fig. 5.8, $T = 0.05$, is shown. The imaginary part becomes slightly smaller at the lowest Matsubara frequencies in DΓA. In stark contrast to the particle-hole symmetric systems studied above, the momentum dependence is rather small and visible mainly in the real part. This results in a slight deformation of the Fermi surface, which we can see in the left panels of Fig. 5.9. While purely local correlations cannot change the shape of the Fermi surface with respect to the tight-binding model, nonlocal correlations of DΓA in this case make the Fermi surface slightly more "quadratic", since in the nodal direction the real part of the self-energy at low frequencies is larger than DMFT. Furthermore, we observe that spectral weight is redistributed and more concentrated at the corners.

Our results demonstrate that sc-DΓA works very well also in the doped case. This has been a weak spot for 1-DΓA since in contrast to the symmetric half-filled model, nonlocal correlations change the filling. If the Coulomb interaction is rather large and we are close to half-filling, this effect is rather weak. Indeed previous 1-DΓA calculations have hence focused on this parameter regime. However, in other cases the filling of the DMFT serving as an input to the one-shot calculation can and will be quite different from the filling of the 1-DΓA. This renders a self-consistent treatment with an adjustment of the chemical potential obvious, so that the filling remains as that for which the vertex Γ was calculated.

5.5* Multi-orbital calculations

This section is largely based on Kaufmann et al. (2021). Quotations from there are marked by a vertical bar.

5.5.1 Two-orbital model

In order to demonstrate that self-consistent DΓA also works for more than one orbital, we consider next a simple two-orbital model on a square lattice. Here, electrons can hop only to neighboring atoms with hopping amplitudes $t_1 = 1$ and $t_2 = 0.25$ for the two orbitals. This gives rise to a wide and a narrow cosine band with band-width 8 and 2, respectively. Along

Die approbierte gedruckte Originalversion dieser Dissertation ist an der TU Wien Bibliothek verfügbar.
The approved original version of this doctoral thesis is available in print at TU Wien Bibliothek.
TU Bibliothek WIEN Your knowledge hub

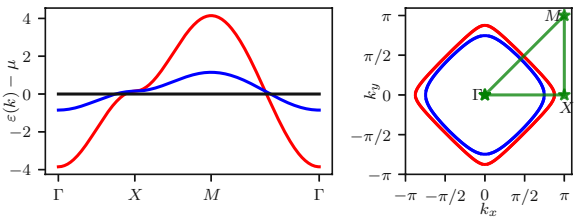

Figure 5.10: Two-band model: band structure (left) and Fermi surfaces at $T = 0.1$ (right). The filling is $n = 1.7$, such that the chemical potential is slightly temperature-dependent.

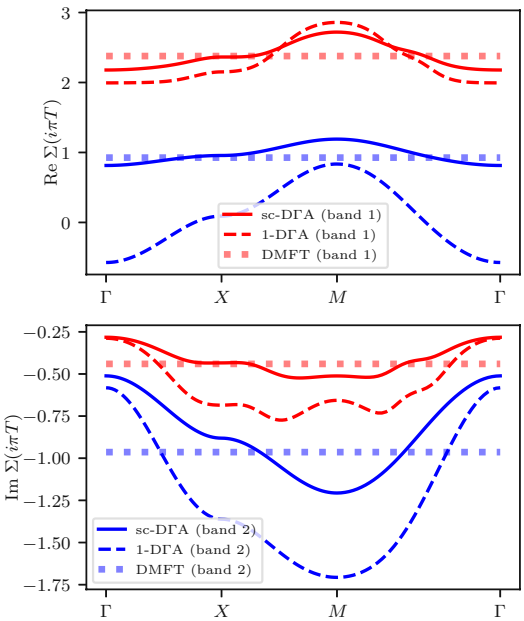

Figure 5.11: Real (top) and imaginary part (bottom) of the self energy at the lowest Matsubara frequency for the two band Hubbard model at $T = 0.1$ along a high-symmetry path through the Brillouin zone.

a high-symmetry path, the bandstructure is shown in Fig. 5.10 (left) and the Fermi surface of the non-interacting tight-binding model in Fig. 5.10 (right). This tight-binding model is supplemented by a Coulomb repulsion parametrized in the Kanamori form with intra-orbital interaction $U = 4$, Hund's coupling $J = 1$, and inter-orbital interaction $V = U - 2J$. The spin flip and pair hopping processes are of the same magnitude J. Considering the different band widths, the wide band will be weakly correlated, since U is only one half of the band width. The narrow band, however, is strongly correlated since U is twice as large as its band width.

In the context of an orbital-selective Mott transition (Anisimov et al., 2002; Liebsch, 2003; 2004; Koga et al., 2005; Biermann et al., 2005; Arita and Held, 2005; Knecht et al., 2005; Sakai et al., 2006; Ferrero et al., 2005; Costi and Liebsch, 2007; Koga et al., 2004; Greger et al., 2013; Valli et al., 2015a; Tocchio et al., 2016; Philipp et al., 2017; Hu et al., 2017), such simple half-filled two-band models with different bandwidths and intra-orbital hopping have been studied very intensively in DMFT. Early calculations however did not include the spin flip and pair

Die approbierte gedruckte Originalversion dieser Dissertation ist an der TU Wien Bibliothek verfügbar.
The approved original version of this doctoral thesis is available in print at TU Wien Bibliothek.
TU Bibliothek WIEN Your knowledge hub

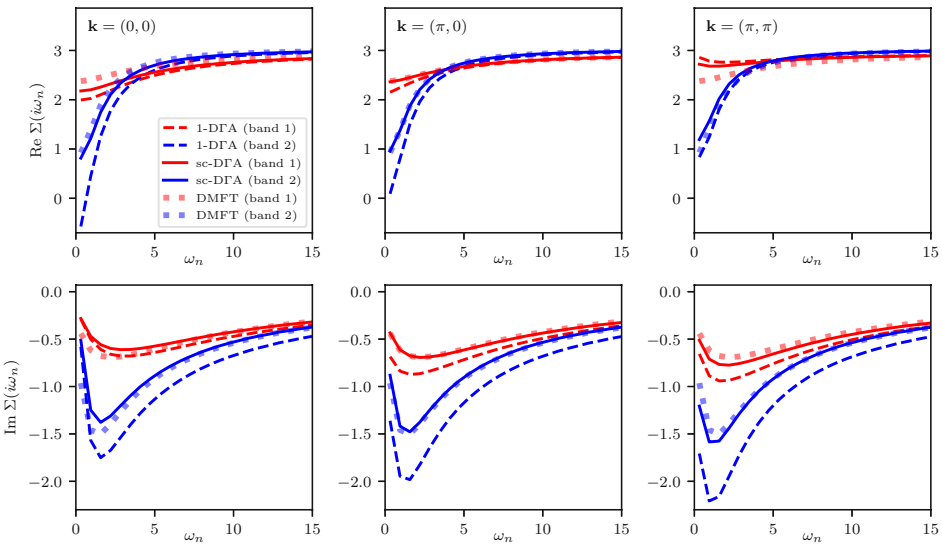

Figure 5.12: Real (top) and imaginary (bottom) part of the self-energy vs. Matsubara frequency at $T = 0.1$ for the Γ, X and M-point, comparing DMFT, 1-DΓA and sc-DΓAfor a two-band Hubbard model. The different colors refer to the two bands, as plotted in Fig. 5.10; the different line types to the different methods.

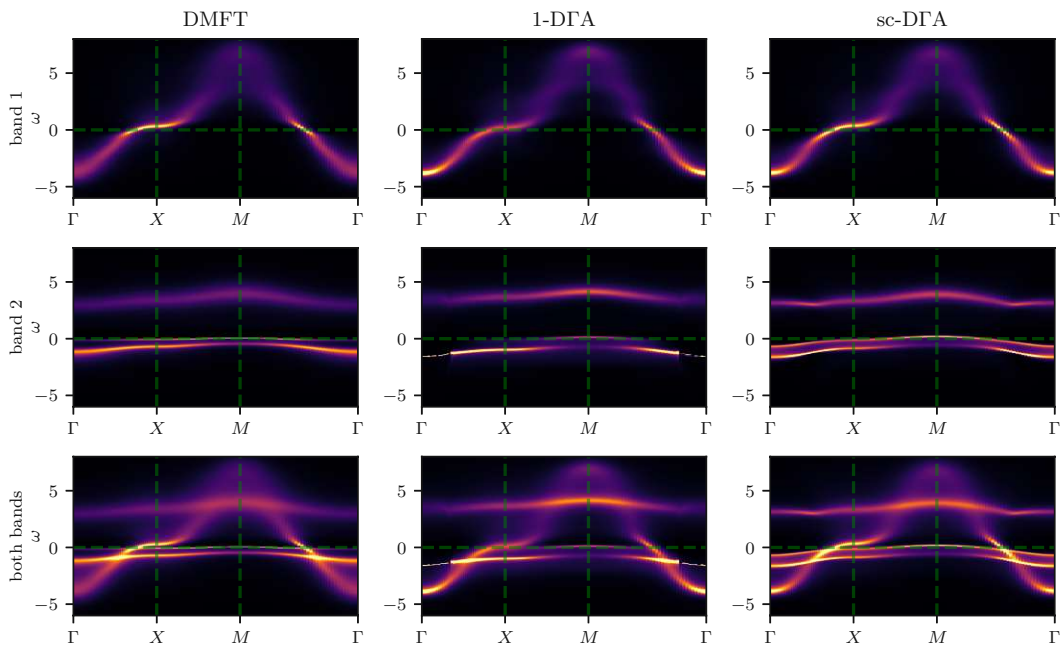

Figure 5.13: Momentum-resolved spectral function of the two-orbital Hubbard model at $T = 0.1$ along a high-symmetry path through the Brillouin zone. The first column shows only the component corresponding to the wide band, the second column only the component corresponding to the narrow band. In the third row the full spectral function is shown.

Die approbierte gedruckte Originalversion dieser Dissertation ist an der TU Wien Bibliothek verfügbar.
The approved original version of this doctoral thesis is available in print at TU Wien Bibliothek.
TU Bibliothek WIEN Your knowledge hub

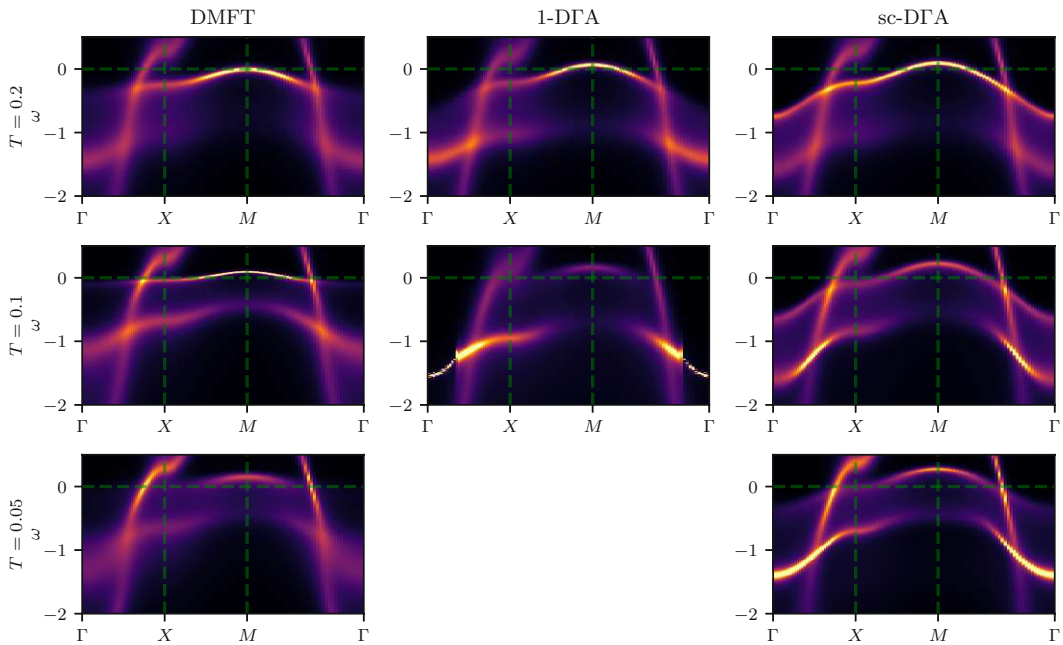

Figure 5.14: Low-frequency zoom of momentum-resolved spectral function for the two-orbital Hubbard model at temperatures $T = 0.2, 0.1, 0.05$ on a path through the Brillouin zone. In the 1-DΓA-spectrum at $T = 0.1$ it is clearly visible that the analytic continuation does not work well in the vicinity of the Γ-point. This is a typical issue for 1-DΓA calculations where nonlocal self-energy corrections become large.

hopping processes, but only the density-density interactions for technical reasons. In this situation, the tendency toward an orbital selective Mott transition is largely exaggerated: a spin $S_z = \pm 1$ formed by the Hund's exchange cannot undergo a joint SU(4) Kondo effect, while the spin-1 of the SU(2)-symmetric interaction can. As we are primarily interested in testing the sc-DΓA method, we consider here the case where the model is doped away from half-filling or $n = 2$ electrons per site. Specifically, we consider the doping $n = 1.7$. This gives rise also to a non-zero real part of the self-energy and (slightly) different fillings of the two orbitals; and hence tests various aspects at the same time.

In Fig. 5.12 we show the self-energy at selective $\boldsymbol{k}$-points. For the given parameters, the 1-DΓA corrections to the self-energy are extremely strong, even exceeding the value of the DMFT self-energy. The reason for this is that we are quite close to an (incommensurate) antiferromagnetic phase transition in DMFT. Immediately before the phase transition, the 1-DΓA corrections become even larger and turn the system insulating.

Similar as for the one-band model, the self-consistency suppresses the antiferromagnetic fluctuations; the actual phase transition occurs only at zero temperature because we are in two dimensions. Hence the sc-DΓA corrections are much weaker at the fixed temperature close to the DMFT phase transition. They will, as a matter of course, become stronger at lower temperatures which are not reachable by 1-DΓA exactly because of the DMFT phase transition. Indeed, Fig. 5.12 suggests that sc-DΓA is not too distinct from the DMFT result. That is, the self-consistency dampens away much of the one-shot corrections.

However, there is actually a quite important difference: Depending on the $\boldsymbol{k}$-point the sc-

Die approbierte gedruckte Originalversion dieser Dissertation ist an der TU Wien Bibliothek verfügbar.
The approved original version of this doctoral thesis is available in print at TU Wien Bibliothek.
TU Bibliothek WIEN Your knowledge hub

DΓA imaginary part of the self-energy at low Matsubara frequencies is above or below the DMFT self-energy in Fig. 5.12. This becomes even more obvious in Fig. 5.11, where we plot the self-energy at the lowest Matsubara frequency and see that the low frequency self-energy strongly depends on the momentum. A strong momentum differentiation of the imaginary part of the self-energy (i. e. the scattering rate) has also been reported for a $SrVO_3$ monolayer by Pickem et al. (2020).

In contrast to the imaginary part, the real part of the self-energy only shows a weak momentum dependence around the DMFT value in Fig. 5.11. This is different for 1-DΓA where the strong corrections are also reflected in a sizable momentum-dependence of the real part of the self-energy; the strongly correlated band (band 2; blue) also displays a sizable overall shift compared to the DMFT result in 1-DΓA.

But let us turn back to the momentum dependence of the self-energy in sc-DΓA. It has a larger influence on the spectral function (Fig. 5.13) than what one might expect from the Matsubara-frequency dependence in Fig. 5.12. In Fig. 5.13 we see, for all three methods, that the weakly correlated band 1 is still close to the tight-binding starting point in Fig. 5.10, whereas the strongly correlated band 2 is split into an upper Hubbard band (around $\omega \sim 4$), a lower Hubbard band (around $\omega = -0.5$), and a central quasiparticle peak around the Fermi level ($\omega = 0$). The last is better visible in the zoom-in provided by Fig. 5.14. The aforementioned momentum differentiation of the self-energy results in a considerably wider central quasiparticle band in sc-DΓA than in DMFT or 1-DΓA. In 1-DΓA the strong fluctuations around the phase transition also smear out the central band when reducing temperature from $T = 0.2$ to $T = 0.1$; $T = 0.05$ is below the DMFT ordering temperature and a one-shot calculation is hence no-longer possible (the reduction of the Néel temperature and susceptibility requires the self-consistency or a Moriya λ-correction (Katanin et al., 2009)).

In Fig. 5.15, we further show the spectral weight at the Fermi level in DMFT and sc-DΓA, summed over both orbitals. Clearly a Fermi surface close to the tight binding ones is visible. This stems mostly from the wide, less correlated band. The narrow, strongly correlated band is slightly shifted downwards to lower energy and considerably broadened, cf. Fig. 5.14. Since the band is so flat, this tiny shift results in a sizeable deformation of the spectral weight distribution on the Fermi level: Considering also that $\overline{A(\boldsymbol{k}, 0)}$ averages over a frequency range $\sim T$, we get diffuse arcs around the M-point, i.e., (π, π), which is visible in Fig. 5.15. However, due to the strong renormalization that is already present in DMFT, the narrow band gives only a small contribution to the spectral weight on the Fermi level.

5.5.2 Strontium vanadate

As a second, archetypical multi-orbital application we study bulk strontium vanadate $SrVO_3$ at room temperature ($T = 26.3$meV). This material has served as a testbed for the development of realistic materials calculations with strong correlations, and is hence most intensively studied (Sekiyama et al., 2004; Pavarini et al., 2004; Nekrasov et al., 2006; Maiti et al., 2006; Leonov et al., 2014; Karolak et al., 2011; Lee et al., 2012; Casula et al., 2012; Tomczak et al., 2012; Taranto et al., 2013; Miyake et al., 2013; Sakuma et al., 2013; Tomczak et al., 2014; Wadati et al., 2014; Ribic et al., 2014; Zhong et al., 2015; Boehnke et al., 2016; Nakamura et al., 2016;

Die approbierte gedruckte Originalversion dieser Dissertation ist an der TU Wien Bibliothek verfügbar.
The approved original version of this doctoral thesis is available in print at TU Wien Bibliothek.
TU Bibliothek WIEN Your knowledge hub

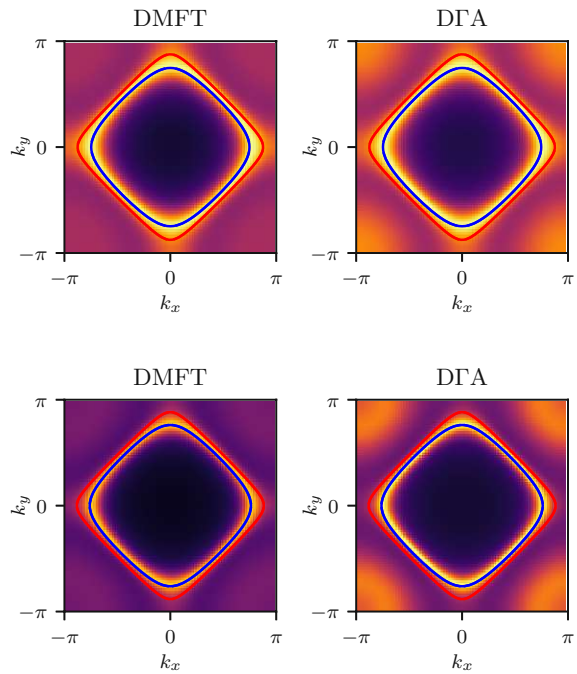

Figure 5.15: Spectral weight at the Fermi level $\overline{A(\boldsymbol{k},0)} \approx G(\boldsymbol{k},\tau = 1/2T)$ of the two-band Hubbard model for $T = 0.1$ (top) and $T = 0.05$ (bottom), comparing DMFT (left) and sc-DΓA (right) and the tight-binding model without interaction (red and blue lines).

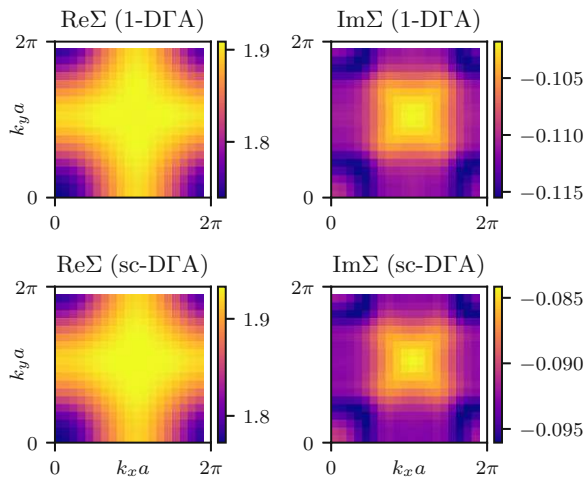

Figure 5.16: Momentum dependence of the self-energy of strontium vanadate at the lowest positive Matsubara frequency and $k_z = 0$. Upper row: one-shot abinitioDΓA, lower row: self-consistent DΓA. The DMFT value is (1.861-0.104i)eV.

Die approbierte gedruckte Originalversion dieser Dissertation ist an der TU Wien Bibliothek verfügbar.
The approved original version of this doctoral thesis is available in print at TU Wien Bibliothek.
TU Bibliothek WIEN Your knowledge hub

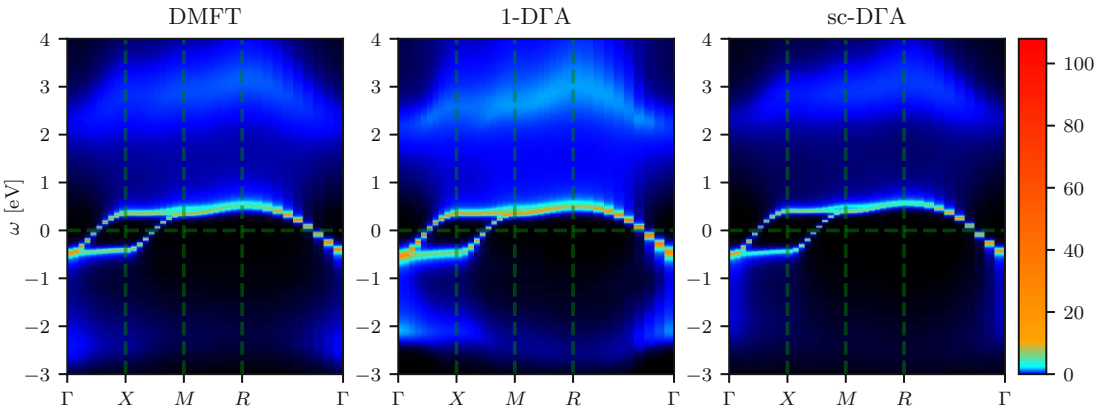

Figure 5.17: Momentum-dependent spectral function of $SrVO_3$, comparing DMFT, one-shot DΓA, and self-consistent DΓA.

Backes et al., 2016; Bhandary et al., 2016; J. M. Tomczak et al., 2017; Kaufmann et al., 2017; Bauernfeind et al., 2017; Sim and Han, 2019). Also the first realistic materials calculations using diagrammatic extensions of DMFT, i.e., *ab initio* DΓA, have been performed for this perovskite (Galler et al., 2017). $SrVO_3$ is a strongly correlated metal with a quasiparticle renormalization of about two (Sekiyama et al., 2004). Electronic correlations also lead to a kink in the self-energy and energy-momentum dispersion relation (Nekrasov et al., 2006; Byczuk et al., 2007; Aizaki et al., 2012; Held et al., 2013). Theoretical calculations and experiments do not indicate any long-range order.

For this realistic *ab initio* calculation, we start with a Wien2K calculation (Blaha et al., 2001; Schwarz et al., 2002) using the PBE exchange correlation potential in the generalized gradient approximation (GGA) (Perdew et al., 1996), and a lattice constant of $a = 3.8$Å. The calculated bandstructure is projected onto maximally localized t_{2g} Wannier orbitals (Pizzi et al., 2020; Marzari et al., 2012; Mostofi et al., 2008) using wien2wannier (Kuneš et al., 2010) This three-band Wannier Hamiltonian, available open source [a], is supplemented by a Kanamori Coulomb interaction including the same terms as for the two-band model and parameterized by $U' = 3.5$eV, $J = 0.75$eV and corresponding $U = U' + 2J = 5$eV. The interactions U' and J have been calculated by the constrained local density approximation (cLDA) in (Sekiyama et al., 2004); J was later slightly corrected as outlined in Section 4.1.3 of Held (2007) to account for the precise way J enters the Hamiltonian Eq. (4.12) and the cLDA. The difference to earlier AbinitioDΓA (Galler et al., 2017; 2018; 2019) calculations, which have been one-shot non-self-consistent calculations, is that we now perform a self-consistent calculation.

As already mentioned, a Moriya-λ correction is extremely difficult for such realistic multi-orbital calculations. There is not only a magnetic and charge λ for every orbital but additionally also various orbital combinations. Hence, we hold that a self-consistent calculation shall be preferable compared to a high-dimensional fit of the various λ parameters. Also conceptionally it is a clearer approach.

In Fig. 5.16 we compare the self-energy of the one-shot and self-consistent DΓA calculation. In contrast to the two-band Hubbard model study above, the differences are here only minor. The reason for this is that in case of the two-band Hubbard model we were close to the DMFT

Die approbierte gedruckte Originalversion dieser Dissertation ist an der TU Wien Bibliothek verfügbar.
The approved original version of this doctoral thesis is available in print at TU Wien Bibliothek.
TU Bibliothek WIEN Your knowledge hub

phase transition, whereas $SrVO_3$ is rather far away from any phase transition. Hence, the 1-DΓA corrections are much smaller to start with. In such a situation, the self-consistency is not necessary. This justifies *a posteriori* the use of non-self-consistent DΓA in Galler et al. (2017), 2018, 2019.

Nevertheless, Fig. 5.17 indicates some minor differences between the DMFT, 1-DΓA and sc-DΓA spectral functions. There are minor differences between 1-DΓA and sc-DΓA regarding the weight of the lower Hubbard band and the broadening of the quasiparticle peak. This behavior is perfectly in-line with the effect of 1-DΓA in other systems studied above. Furthermore there is a shift of the position of the lower Hubbard band toward lower binding energies visible at the Γ point. Experimentally, the maximum of the lower Hubbard band is slightly above -2 eV (Sekiyama et al., 2004).

[a] See https://github.com/AbinitioDGA/ADGA/blob/master/srvo3-testdata/srvo3_k20.hk

5.6* Kagome lattice Hubbard model

This section is based on Kaufmann et al. (2020). Quotations from there are marked by a vertical bar. Parts that have been written only by the author of this thesis have no bar.

Electronic correlations are at the origin of a large variety of exotic phases in transition metal oxides and intermetallic compounds (Dagotto, 2005; Pesin and Balents, 2010; Basov et al., 2011). Yet, an adequate description of correlated materials remains a long-standing conundrum in condensed matter physics (Imada and Miyake, 2010). Pioneering works of Kanamori (1963), Hubbard (1963), and Gutzwiller (1963) enlightened the key role of onsite Coulomb repulsion as the leading source of electronic correlations. The ensuing model, known as the Hubbard model, became a paradigm of correlated materials: it is widely used to rationalize the experimentally observed phenomena such as metal-to-insulator transitions (MIT) (Imada et al., 1998), the formation of local moments (Anderson, 1961) and high-temperature superconductivity (Pickett, 1989).

The flip side of such a rich physics and complexity is that a solution of the Hubbard model becomes intractable for physically relevant regimes. Two prominent exceptions are the one-dimensional (Lieb and Wu, 1968) and the infinitely-dimensional Hubbard models. The latter can be solved within the dynamical mean-field theory (DMFT) (Georges and Kotliar, 1992; Georges et al., 1996), a self-consistent mapping of a lattice Hubbard model onto a single-site Anderson impurity model. This mapping is justified by the rapid suppression of nonlocal correlations concomitant with an increase of the spatial dimensionality or the nearest neighbor coordination number (Metzner and Vollhardt, 1989; Müller-Hartmann, 1989). While in infinite dimensions the DMFT offers an exact solution of the Hubbard model (Jarrell, 1992), it remains a well-justified approximation for realistic three-dimensional models.

The restriction to local correlations may break down in two-dimensional models rele-

Die approbierte gedruckte Originalversion dieser Dissertation ist an der TU Wien Bibliothek verfügbar.
The approved original version of this doctoral thesis is available in print at TU Wien Bibliothek.
TU Bibliothek WIEN Your knowledge hub

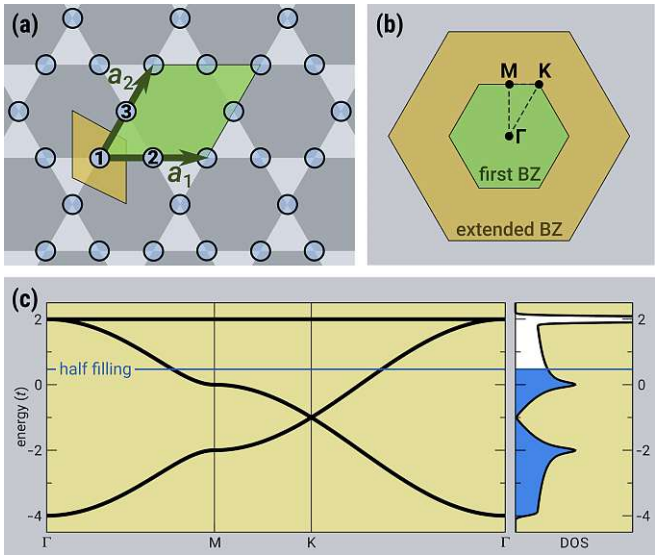

Figure 5.18: (a) Unit cell (shaded green) of the kagome lattice described by the basis vectors a_1 and a_2 comprises three sites labeled 1, 2, and 3. The Wigner-Seitz cell is shaded ochre. (b) High-symmetry points of the reciprocal space, the first and the extended Brillouin zones (BZ). (c) The band structure (left) and the density of states (DOS, right) of the tight-binding kagome model with a positive t. The blue line marks the chemical potential $\mu_{\text{tb}} \approx 0.47$, for which the non-interacting system is half-filled.

vant for various experimental situations, e.g. in high-temperature superconductors (Keimer et al., 2015b), ultrathin van der Waals superlattices (Cao et al., 2018), and oxide heterostructures (Mannhart and Schlom, 2010; Hwang et al., 2012). Coordination numbers in such systems are typically small, and hence the outcome of an onsite scattering event strongly depends on the configuration of the neighboring sites. A striking example showing the importance of nonlocal correlations is the square-lattice Hubbard model at half-filling, which describes the physics of parent compounds of cuprate high-temperature superconductors. Here, DMFT finds a first-order Mott transition from a metal to a paramagnetic insulator at low temperatures. Nonlocal correlations drastically change the physics: while short-range antiferromagnetic correlations significantly reduce the critical interaction U, long-range antiferromagnetic correlations shift the MIT to much smaller interactions, even to $U = 0$ for a square lattice Hubbard model with perfect nesting (Schäfer et al., 2015; Schäfer et al., 2020). Long-range antiferromagnetic correlations open a gap. This conclusion is corroborated by quantum Monte Carlo simulations on large finite lattices (White et al., 1989; Hirsch and Tang, 1989; Schäfer et al., 2015; Varney et al., 2009). For two-dimensional lattices without perfect nesting these results suggest a MIT at still considerably lower values of U. As we will see below, for a magnetically frustrated model with only short-range antiferromagnetic correlations, such as the kagome lattice Hubbard model (KHM), DMFT only slightly overestimates the critical U of the MIT.

The situation becomes qualitatively different in the presence of frustration. As sizable ground-state degeneracy is typical for a frustrated model, magnetic instabilities may spread over different momenta, suppressing the overall tendency towards magnetic ordering. Ramifications for the MIT are surmised, but model-specific information is scarce. The most studied

Die approbierte gedruckte Originalversion dieser Dissertation ist an der TU Wien Bibliothek verfügbar.
The approved original version of this doctoral thesis is available in print at TU Wien Bibliothek.
TU Bibliothek WIEN Your knowledge hub

case, the Hubbard model on the triangular lattice, shows a conventional MIT even if nonlocal correlations are taken into account. However, the triangular lattice has the sizable coordination number of six bonds per site, which is the same as in the 3D cubic lattice. As a result, quantum fluctuations in the triangular lattice are largely suppressed (Antipov et al., 2011; Li et al., 2014).

The kagome lattice (Fig. 5.18, a) is a much more apt playground to study the interplay of nonlocal correlations and frustration. This simple tessellation of regular hexagons and triangles exhibits a remarkably involved magnetism: the ground state of the $S = \frac{1}{2}$ Heisenberg model on a kagome lattice remains under debate for several decades, with the handful of candidate states comprising a Dirac spin liquid (Ran et al., 2007; Hermele et al., 2008; Ma and Marston, 2008; Iqbal et al., 2013; He et al., 2017; Liao et al., 2017; Chen et al., 2018), a Z_2 spin liquid (Yan et al., 2011; Depenbrock et al., 2012; Jiang et al., 2012; Nishimoto et al., 2013; Kolley et al., 2015; Mei et al., 2017; Läuchli et al., 2019), a chiral spin liquid (Messio et al., 2012; Capponi et al., 2013; Gong et al., 2014; Bauer et al., 2014; He et al., 2014; Wietek et al., 2015; Gong et al., 2015; Hu et al., 2015; Messio et al., 2017), and a valence bond solid (Marston and Zeng, 1991; Syromyatnikov and Maleyev, 2002; Nikolic and Senthil, 2003; Singh and Huse, 2007; Budnik and Auerbach, 2004; Evenbly and Vidal, 2010; Schwandt et al., 2010; Poilblanc et al., 2010; Poilblanc and Misguich, 2011). The vibrant research is boosted by experimental studies of herbertsmithite γ-$Cu_3Zn(OH)_6Cl_2$ (Helton et al., 2007; Han et al., 2012; Khuntia et al., 2020). This correlated insulator material does not show any sign of magnetic ordering down to lowest temperatures (Mendels et al., 2007), despite the sizable antiferromagnetic exchange of ~200 K (Janson, 2012; Jeschke et al., 2013). As typical for cuprates, the (screened) onsite Coulomb repulsion U largely exceeds the intersite hopping amplitude t, placing herbertsmithite into the strongly correlated limit of the Hubbard model ($U \gg t$). Interactions between localized $S = \frac{1}{2}$ spins in this limit are well-described by the Heisenberg model.

Much less is known about less correlated regimes of the half-filled kagome Hubbard model. Dynamical spin correlations were studied using cluster DMFT on a $N = 3$ site clusters (Ohashi et al., 2006; Ohashi et al., 2007) where the first-order metal to insulator transition (MIT) occurs at $U_c = 8.4t$ (Ohashi et al., 2006). As was noticed by Higa and Asano (2016), a major drawback of odd-numbered clusters is their incompatibility with valence bond states. Instead, variational cluster calculations on $N = 6$ and $N = 12$ clusters demonstrate that the formation of intersite singlets (valence bonds) underlies the MIT, and propels it to a smaller U value. A very recent study suggests that the KHM harbors a topologically nontrivial state, a higher-order topological Mott insulator, characterized by corner modes whose spin excitation spectrum is gapless (Kudo et al., 2019).

For a long time, the KHM attracted little attention: although their potential modifications of herbertsmithite hold promise for unconventional phases (Mazin et al., 2014), pristine herbertsmithite and related quantum magnets (Janson et al., 2008; Fåk et al., 2012; Iqbal et al., 2015) are correlated insulators deep in the Heisenberg limit, The situation changed drastically after the discovery of metallic kagome materials Mn_3Sn (Nakatsuji et al., 2015; Nayak et al., 2016; Kuroda et al., 2017; Kimata et al., 2019; Li et al., 2019d; Wuttke et al., 2019), Fe_3Sn_2 (Fenner et al., 2009; Kida et al., 2011; Hou et al., 2017; Ye et al., 2018; Yin et al., 2018; Lin et al., 2018; Li et al., 2019c; Li et al., 2019e; Tanaka et al., 2020), $Co_3Sn_2S_2$ (Liu et al., 2018; Wang et al., 2018; Yin et al., 2019; Liu et al., 2019; Shen et al., 2019; Lachman et al., 2020; Howard et al.,

Die approbierte gedruckte Originalversion dieser Dissertation ist an der TU Wien Bibliothek verfügbar.
The approved original version of this doctoral thesis is available in print at TU Wien Bibliothek.
TU Bibliothek WIEN Your knowledge hub

2019; Xing et al., 2020; Yin et al., 2020; Liu et al., 2021), $Gd_3Ru_4Al_{12}$ (Nakamura et al., 2018; Matsumura et al., 2019), and very recently, FeSn (Inoue et al., 2019; Kang et al., 2019; Lin et al., 2020; Sales et al., 2019). Interestingly, the first three materials exhibit a sizable anomalous Hall effect, associated with a nonvanishing Berry curvature of the occupied bands (Nayak et al., 2016; Ye et al., 2018; Liu et al., 2018). While the magnetic moments are associated with the electrons localized in $3d$ or $4f$ shells, neither of the five materials is insulating. Hence, a key to their electronic and magnetic properties should be sought in less correlated regimes of the KHM, which remain hitherto largely unexplored.

In this paper, we fill this gap by performing an extensive numerical investigation of the KHM using three different many-body techniques: the determinant quantum Monte Carlo (DQMC) (Blankenbecler et al., 1981), the dynamical mean-field theory (DMFT) (Georges and Kotliar, 1992; Georges et al., 1996), and the dynamical vertex approximation (DΓA) (Toschi et al., 2007; Rohringer et al., 2018). DQMC is a numerically exact technique for fermionic lattice models. With the caveat that finite lattices beget finite size effects, it provides a sound benchmark for quantum impurity methods. Since frustration of the KHM gives rise to a severe sign problem, we restrict our DQMC calculations to relatively high temperatures. We use these results as a benchmark for DΓA, a diagrammatic extension of DMFT. In contrast to cluster extensions of DMFT (Maier et al., 2005), this method accounts for nonlocal correlations on all length scales — from short-range to long-range. And unlike many QMC-based techniques, diagrammatic extensions of DMFT are immune to the sign problem (Rohringer et al., 2018), allowing us to explore more correlated regimes of the KHM. In this study, we apply the recently implemented self-consistent DΓA scheme (Kaufmann et al., 2021), which eliminates the need to restore the sum rules by means of so-called λ-corrections (Katanin et al., 2009; Rohringer and Toschi, 2016).

Our main finding is the gradual correlation-induced change in the regime of magnetic correlations: While maxima at the K-point of the extended Brillouin zone are indicative of dominant $\sqrt{3}\times\sqrt{3}$ correlations, the enhancement of interaction strength gives rise to the sign change of third-neighbor correlations. Interestingly, this crossover occurs in the metallic phase, while spin correlations in the moderately correlated regime are similar to those of the Heisenberg model. This finding gives us a key to distinguish between weakly and strongly correlated regimes in the growing family of kagome materials. Furthermore, we compute the dynamical structure factors $S(\boldsymbol{q}, \omega)$ for the different regimes of the kagome Hubbard model. Since these quantities are accessible in inelastic neutron scattering experiments, the relative strength of electronic correlations in real materials can be estimated by a direct comparison to our calculated $S(\boldsymbol{q}, \omega)$.

Our study is equally important for method development in the field of electronic correlations: it applies a diagrammatic beyond-DMFT method, DΓA, to a strongly frustrated two-dimensional model. Extensive comparisons with the numerically exact lattice-based method (DQMC) reveal an overall good agreement, indicating that a self-consistent DΓA calculation captures the leading effects of nonlocal fluctuations, even if tendencies towards magnetic ordering are strongly suppressed.

This section is organized as follows. In Section 5.6.1 we introduce the Hubbard model on a kagome lattice, and briefly explain the methods we use to obtain our results. The main results are presented in Section 5.6.2, where we first present the phase diagram and then discuss the magnetic structure factors. In Section 5.6.3 our results are compared to previous theoretical

Die approbierte gedruckte Originalversion dieser Dissertation ist an der TU Wien Bibliothek verfügbar.
The approved original version of this doctoral thesis is available in print at TU Wien Bibliothek.
TU Bibliothek WIEN Your knowledge hub

results from the literature and put in the context of present-day experimental research.

5.6.1 Numerical methods

KHM Hamiltonian

The Hamiltonian for the Hubbard model on a kagome lattice can be derived from the generalized Hubbard Hamiltonian Eq. (4.12) by setting three atoms in the unit cell and only one local orbital on each atom. We thus have

$$H = \sum_{\boldsymbol{k}} \sum_{j,l=1}^{3} \sum_{\sigma=\uparrow,\downarrow} h_{jl}(\boldsymbol{k}) \hat{c}^{\dagger}_{j\sigma}(\boldsymbol{k}) \hat{c}_{l\sigma}(\boldsymbol{k}) + \sum_{\boldsymbol{R}} \sum_{j=1}^{3} U n_{\boldsymbol{R}j\uparrow} n_{\boldsymbol{R}j\downarrow}, \tag{5.24}$$

where $\boldsymbol{k}$ is the 2D crystal momentum in the first Brillouin zone (Fig. 5.18), and indices j and l refer to the sites within the unit cell, thus running from 1 to 3. The three sites comprising the unit cell (as shown in Fig. 5.18, a) form an equilateral triangle whose side length is a half of the lattice constant. The tight-binding Hamiltonian $h_{jl}(\boldsymbol{k})$ incorporates the lattice geometry and hopping amplitudes. In the second term, we have a sum over all unit cells, where site $j = 1$ is located at the Bravais lattice position $\boldsymbol{R}$. The interaction, parametrized by a scalar U, is of density-density type.

As hopping is allowed only between neighbor sites, the non-interacting part of the Hamiltonian reads:

$$h_{jl}(\boldsymbol{k}) = -t \begin{pmatrix} 0 & 1 + e^{ik_1} & 1 + e^{ik_2} \\ 1 + e^{-ik_1} & 0 & 1 + e^{-i(k_1-k_2)} \\ 1 + e^{-ik_2} & 1 + e^{i(k_1-k_2)} & 0 \end{pmatrix}, \tag{5.25}$$

where k_1 and k_2 are the projections of $\boldsymbol{k}$ onto the reciprocal basis vectors $\boldsymbol{b}_1$ and $\boldsymbol{b}_2$. We set the hopping amplitude to unity $t \equiv 1$, which defines our unit of energy used throughout this section. By further setting $\hbar \equiv 1$ and $k_B \equiv 1$ we also fix the units of frequency and temperature.

By applying a unitary transformation $\mathcal{U}(\boldsymbol{K})$ as in Eq. (4.4), the Hamiltonian matrix Eq. (5.25) can be diagonalized

$$h(\boldsymbol{k}) = \mathcal{U}(\boldsymbol{k})\, \varepsilon(\boldsymbol{k}) \mathbf{1}\, \mathcal{U}^{\dagger}(\boldsymbol{k}), \tag{5.26}$$

where h and $\mathcal{U}$ are $\boldsymbol{k}$-dependent matrices of dimension three, $\mathbf{1}$ is a 3×3 identity matrix, and ε is a $\boldsymbol{k}$-dependent three-dimensional vector, defining the tight-binding bands. The latter are shown in Fig. 5.18, c. Remarkably, one band is completely flat, corresponding to a δ-peak in the density of states (DOS). The two dispersive bands are identical to those in a honeycomb lattice, featuring two Van Hove singularities and a Dirac crossing. The eigenstates of the flat band correspond to states that are localized on hexagonal plaquettes and combinations thereof (Bergman et al., 2008).

The evaluation of the eigenenergies of the full Hubbard Hamiltonian Eq. (5.24) is not possible, as the tight-binding term and the interaction term do not commute. We are therefore restricted to a handful of numerical methods that allow us to calculate correlation functions within a certain approximation. In this work, we use three many-body methods to compute properties of the Hubbard model on a kagome lattice: the dynamical mean-field theory (DMFT), exhaustively described in Chapter 4, the dynamical vertex approximation (DΓA) that was described in Section 5.2, and the determinant quantum Monte Carlo (DQMC). For the latter, we now give a brief outline:

Die approbierte gedruckte Originalversion dieser Dissertation ist an der TU Wien Bibliothek verfügbar.
The approved original version of this doctoral thesis is available in print at TU Wien Bibliothek.
TU Bibliothek WIEN Your knowledge hub

Determinant quantum Monte Carlo (DQMC)

Mapping onto an auxiliary impurity problem lies at the core of both DMFT and DΓA approaches. It is therefore crucial to cross-check the DMFT/DΓA results with an independent numerically exact method working explicitly with a *lattice* problem. To this end, we employ determinant quantum Monte Carlo (DQMC) simulations (Blankenbecler et al., 1981). This technique explicitly computes nonlocal correlation functions, such as the lattice Green's function. Therefore, the main approximation lies in the restriction to a finite cluster. As a consequence, quantities such as the susceptibility or equal time structure factor, which sample correlations to large distance, have corrections which scale as $1/L$, where L is the linear lattice size. However, local (e.g. near neighbor) correlation functions are usually converged to a few percent on lattices of linear extent $L \sim 10$. In the present case computations were done for clusters of 5×5 unit cells (i. e. 75 sites). DQMC calculations also have 'Trotter' errors proportional to the square of the discretization interval of the inverse temperature $\beta = 1/T$. In our work Trotter errors are of the same order as, or smaller than, the statistical errors from the Monte Carlo sampling. Finally, as noted earlier, DQMC calculations are limited by the sign problem (Loh et al., 1990; Iglovikov et al., 2015). A rough rule of thumb is that DQMC can be done down to temperatures $T \sim W/30$, where W is the bandwidth, for interaction strengths $U \sim W$.

5.6.2 Results

We divide our results in two parts. In Sec. 5.6.2, we focus on the phase diagram of the KHM in the metallic regime and discuss how the spectral function evolves as a function of the interaction strength and temperature. While it is a common way to describe the physics of a model, we surmise that from the experimental viewpoint such a discussion is largely disconnected from the physics of kagome materials: there is no recipe to extract the information on the interaction strength U for a given material. To alleviate this problem, we present our results for the equal-time $S(\boldsymbol{q})$ as well as dynamical $S(\boldsymbol{q}, \omega)$ structure factors for different U values in Sec. 5.6.2. As these quantities are experimentally accessible, a direct comparison between theory and experiment can yield an estimate for U.

Phase diagram of the kagome Hubbard model

The Hubbard model is famous for exhibiting a transition between a metallic state and an insulating state upon variation of the interaction strength. This generic trend holds for the kagome lattice: In the KHM, the local spectral functions [1] (Fig. 5.19) show a reduction of the spectral weight around the Fermi level (at $\omega = 0$) upon increasing U, and the system eventually turns insulating once the interaction exceeds a certain critical value U_c. In the high-temperature regime ($T = 0.33$), some spectral weight remains in the gap, but the spectral function develops a distinct dip at the Fermi level, with $U_c \approx 7$ in DQMC and $U_c \approx 9$ in DMFT.

The transition also manifests itself in the DMFT quasiparticle renormalization factor Z

[1] All analytic continuations are done using the maximum entropy method as implemented in ana-cont (Kaufmann, 2020).

Die approbierte gedruckte Originalversion dieser Dissertation ist an der TU Wien Bibliothek verfügbar.
The approved original version of this doctoral thesis is available in print at TU Wien Bibliothek.
TU Bibliothek WIEN Your knowledge hub

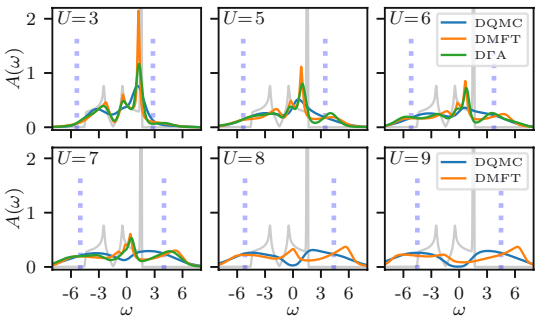

Figure 5.19: Local spectral functions for interaction strength ranging from $U = 3$ to 9 at $T = 0.33$ in units of the hopping $t \equiv 1$ as obtained by DMFT, DQMC, and DΓA. The gray line is the density of states of the underlying tight-binding model, the opaque dotted blue bars show the approximate position of the Hubbard bands calculated by Eq. (5.28).

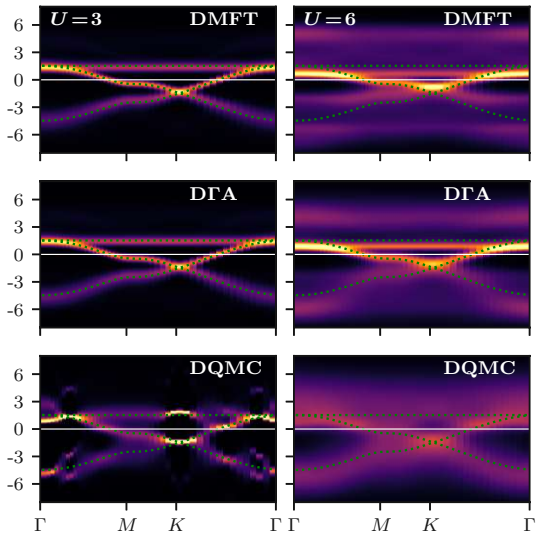

Figure 5.20: Spectral functions of DMFT, DΓA and DQMC on a high-symmetry path through the Brillouin zone. The dotted green lines are the tight-binding bands. At weak interaction (left column) there is no sizable renormalization, whereas strong interactions considerably change the spectrum (right column).

defined as

$$Z = \left[1 - \mathrm{Re}\frac{d\Sigma(\omega)}{d\omega}\Big|_{\omega=0}\right]^{-1}, \tag{5.27}$$

which decreases from unity in the non-interacting case to zero at the transition to the insulating state. In Fig. 5.21, we illustrate this behavior for two different temperatures $T = 0.33$ and $T = 0.1$. For the latter, Z vanishes around $U_c \approx 9.45$. At the higher temperature $T = 0.33$, the critical U is reduced, but its precise estimation is impeded due to thermal broadening. In the same plot, we plot a rough estimate for Z from DQMC, which are estimated as the fraction of the spectral weight located in the quasiparticle region. The latter is determined from the DMFT spectral function for the same U value. For DΓA we calculate a momentum-dependent Z which is presented in Fig. 5.22 below.

Another characteristic correlation-induced phenomenon is the formation of the Hubbard bands — two incoherent spectral features separated by $\sim U$. As these bands are strongly asymmetric, we estimate their position by

$$\omega_{\text{upper/lower}} = Z_{\text{DMFT}} \times \omega_{\text{max/min}} \pm \frac{U}{2} \tag{5.28}$$

where $\omega_{\text{max/min}}$ are the upper/lower band edge of the tight binding Hamiltonian, i.e. $2 - \mu_{\text{tb}}$ and $-4 - \mu_{\text{tb}}$. This heuristic formula interpolates between the non-interacting regime and the strongly correlated insulting regime where the Hubbard bands are at $\pm\frac{U}{2}$. It accounts for the fact that the separation of the Hubbard bands is more than $\pm U$ at small U, and describes the position of the Hubbard bands in Fig. 5.19 very well.

Die approbierte gedruckte Originalversion dieser Dissertation ist an der TU Wien Bibliothek verfügbar.
The approved original version of this doctoral thesis is available in print at TU Wien Bibliothek.
TU Bibliothek WIEN Your knowledge hub

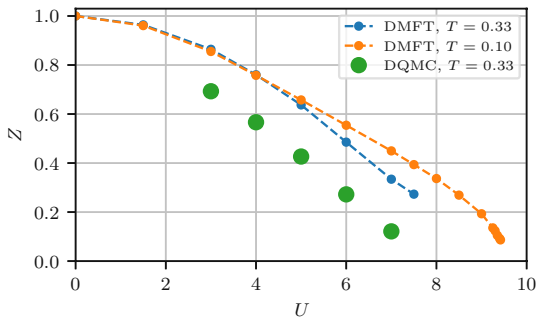

Figure 5.21: Quasiparticle renormalization factor Z [Eq. 5.27] based on DMFT and DQMC data as a function of the interaction strength U for the temperatures specified in the legend box.

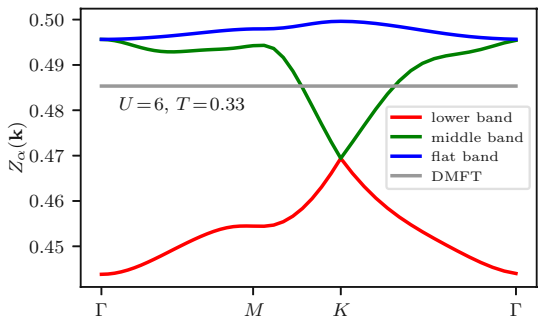

Figure 5.22: Momentum- and band-resolved quasiparticle renormalization $Z_\alpha(\boldsymbol{k})$ at $U = 6$ and $T = 0.33$ obtained by projection of the DΓA self-energy onto the tight-binding eigenbasis.

Next, we discuss the momentum-resolved spectral functions in the top panels of Fig. 5.20. In DMFT, they show a textbook behavior, with a renormalized tight-binding band structure and distinct Hubbard bands. Nonlocal correlations alter this picture: the bottom edge of the quasiparticle band merges with the lower Hubbard band at larger interactions, as can be clearly seen in DΓA (Fig. 5.20, middle panels), and it is even more prominent in DQMC (Fig. 5.20, bottom panels). More pronounced in DΓA spectrum is a waterfall-like structure between the Γ-point and M/K in the lowest-lying band below the Fermi energy. Such waterfalls have been observed experimentally in angular resolved photoemission spectra (ARPES) of cuprate superconductors (Graf et al., 2007).

We can extract more insights by comparing the DMFT and DΓA self-energies. In DMFT, the self-energy is diagonal with respect to the three basis-lattice sites j; all three diagonal elements are even identical and there is no off-site contribution within DMFT. In DΓA, the diagonal elements are almost identical to the DMFT self-energy and show only a weak dependence on the momentum. The main difference is the presence of sizable off-diagonal elements that are strongly momentum-dependent.

Analysis of matrix-valued quantities computed on the Matsubara axis is not straightforward. In the case of the KHM, however, we find an interesting property of the DΓA self-energy. For each momentum and frequency, the complex eigenvalues of the 3×3 matrix can be obtained by projecting it onto the eigenbasis of the tight-binding dispersion matrix $h(\boldsymbol{k})$ at the same $\boldsymbol{k}$-point. It is of course possible to obtain the eigenvalues directly, but then they are returned in an unsorted way for each momentum and frequency. Contrary to that, projecting onto eigenvectors of the dispersion matrix $h(\boldsymbol{k})$ allows for an identification of eigenvalues with the tight-binding bands. We show an example for this advantage in Fig. 5.23. On the left-hand side we see that by projection we get three distinct self-energies with "usual" frequency dependence, denoted by opaque colored lines. However, the directly computed eigenvalues, marked by symbols, behave in a discontinuous way. This would make an analytic continuation impossible without performing some kind of sorting first. (Straightforward sorting is not possible since the numbers are complex.) On the right-hand side of Fig. 5.23 we see that also in momentum space the projection procedure leads to smooth "bands", whereas direct computation of eigenvalues would result in jumps between those bands. For DMFT this relation between

Die approbierte gedruckte Originalversion dieser Dissertation ist an der TU Wien Bibliothek verfügbar.
The approved original version of this doctoral thesis is available in print at TU Wien Bibliothek.
TU Bibliothek WIEN Your knowledge hub

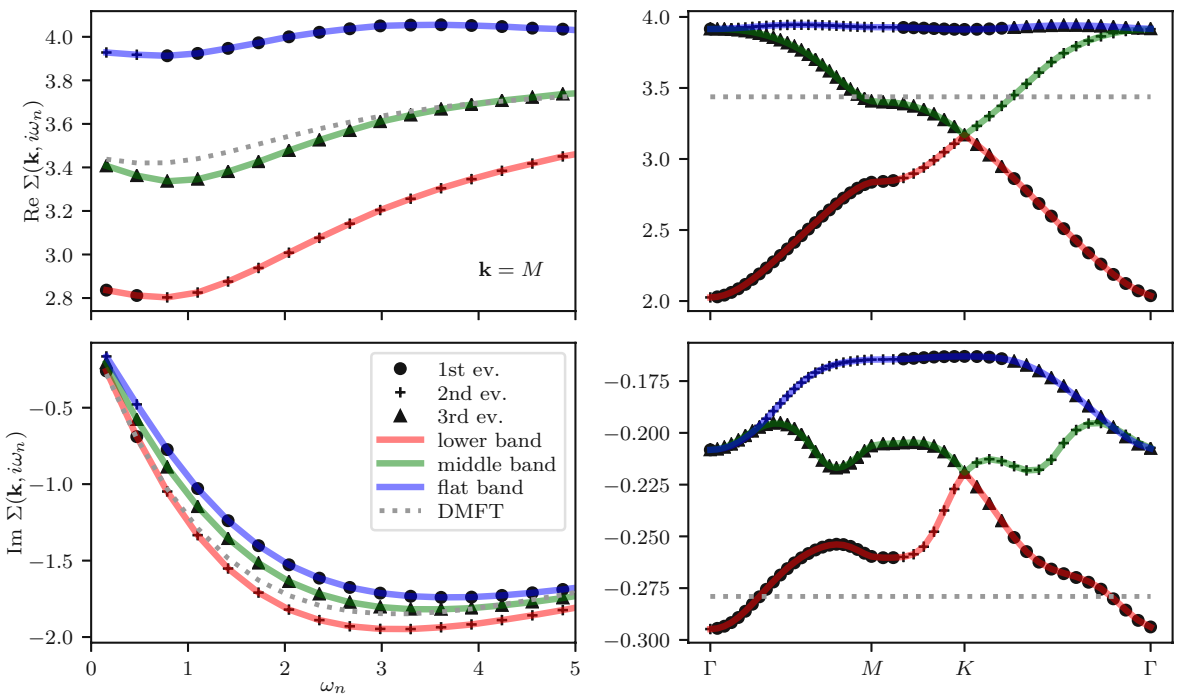

Figure 5.23: Eigenvalues of the DΓA self-energy for $U = 7.5$ and $T = 1/20$, comparing direct computation (symbols) and projections onto the eigenbasis of the tight-binding Hamiltonian (lines). The left column shows the frequency dependence at the M-point, the right column shows the lowest Matsubara frequency along a path through the Brillouin zone. The upper and lower row show the real and imaginary part, respectively.

eigenvalues and projections is fulfilled trivially, as Σ is $\boldsymbol{k}$-independent and proportional to the 3×3 unit matrix for the three sites of the unit cell. In DQMC we do not have direct access to the self-energy, but from the fact that the lattice Green's function approximately fulfills the property, we can conclude that this holds for the self-energy as well.

This implies that the tight-binding bands are mapped onto interacting quasiparticle bands with associated Hubbard bands, but they are not mixed by nonlocal correlations, because the interaction is local. The momentum dependence entails that the self-energy in the band basis is, albeit diagonal, no longer proportional to the unit matrix as in the DMFT. This leads to a momentum- and band-dependent, but still well-defined, quasiparticle renormalization factor $Z_\alpha(\boldsymbol{k})$, where α is the band index. We show this quantity for $U = 6$ and $T = 1/3$ in Fig. 5.22. Since smaller Z implies stronger renormalization, it explains why the lowest-lying quasiparticle band merges with the lower Hubbard band at Γ, the center of the Brillouin zone.

Let us compare these results with the well-studied Hubbard model on a square lattice. There, antiferromagnetic fluctuations dominate the phase diagram at all temperatures, leading to an insulating antiferromagnetic state even at smallest values of the interaction U (Schäfer et al., 2015) in the limit of zero temperature. Looking at the magnetic susceptibility of the kagome lattice, we have to keep in mind that it is defined as

$$\chi_m^{jl}(\boldsymbol{q}, i\omega_n) = \sum_{\boldsymbol{R}} e^{i\boldsymbol{q}\cdot\boldsymbol{R}} \int_0^\beta d\tau \, e^{i\omega_n\tau} \left\langle S_z^j(\boldsymbol{R}, \tau) S_z^l(\boldsymbol{0}, 0) \right\rangle, \tag{5.29}$$

Die approbierte gedruckte Originalversion dieser Dissertation ist an der TU Wien Bibliothek verfügbar.
The approved original version of this doctoral thesis is available in print at TU Wien Bibliothek.
TU Bibliothek WIEN Your knowledge hub

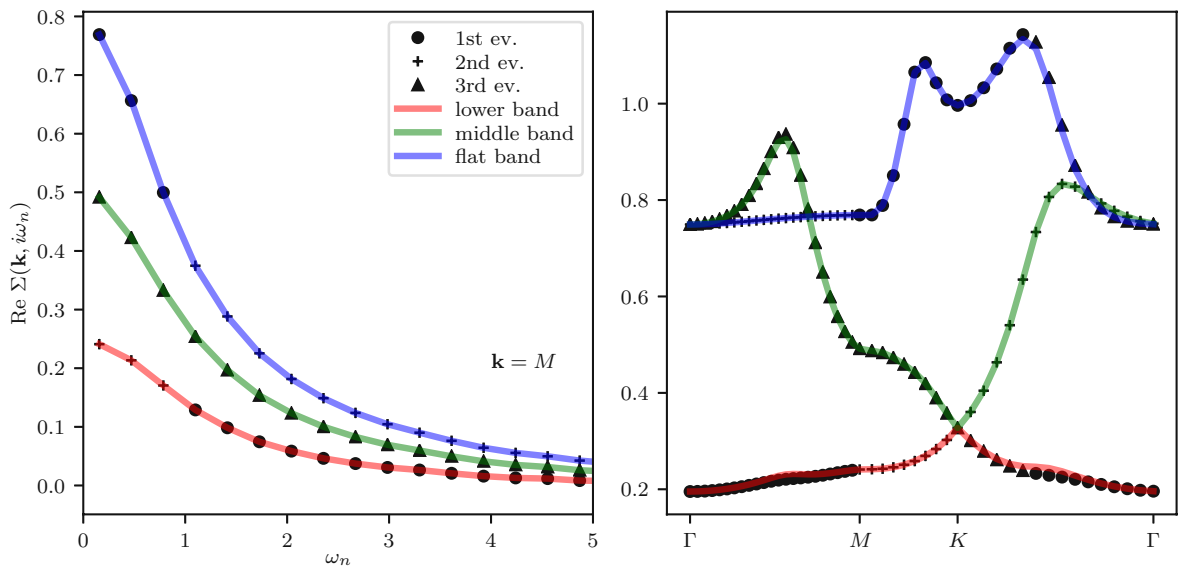

Figure 5.24: Eigenvalues of the susceptibility at $U = 7.5$ and $T = 1/20$ as obtained by direct computation (symbols) and projection onto tight-binding eigenstates (lines). The left panel shows the frequency dependence for the M-point, on the right-hand side the momentum dependence along a path through the Brillouin zone is depicted.

i.e. it is a 3×3 matrix for each momentum and frequency. For numerical and technical reasons our DΓA calculations are restricted to $\langle S_z^j S_z^l \rangle$ correlation functions, which yield the standard magnetic susceptibility. Note that in the absence of magnetic field, diagonal correlations are equal to one-third of full correlations: $\langle S_z^j S_z^l \rangle = \frac{1}{3}\langle \mathbf{S}^j \cdot \mathbf{S}^l \rangle$. Without symmetry breaking, and as we will see below there are no signs of any long range order, spin-off diagonal correlation functions such as $\langle S_z^j S_x^l \rangle$ or $\langle S_z^j S_+^l \rangle$ vanish [2].

For a quantitative analysis, we resort to the eigenvalues of χ_m^{jl}. Similar as in the case of the self-energy, we find that the eigenvalues are reproduced well by projecting the 3×3 susceptibility matrix at a given momentum and frequency onto the eigenbasis of $h(\boldsymbol{k})$ at the same $\boldsymbol{k}$. Although the susceptibility is a real quantity and thus a sorting of eigenvalues would be possible, we nevertheless consider the projections to be superior, since they allow for identification of eigenvalues with tight-binding bands. Also a sorting of eigenvalues would lead to non-analytic frequency dependence on the Matsubara axis in many cases[3]. In the left panel of Fig. 5.24, we show that the projections indeed restore continuity on the Matsubara axis, and even achieve a "disentanglement" in momentum space. This can be clearly seen in the right panel of Fig. 5.24: At the Γ-point the eigenvalues corresponding to the middle and the flat band are degenerate, but when moving towards the M-point the eigenvalue corresponding to the middle band becomes dominant. Only shortly before the M-point it experiences a sharp drop

[2]Due to the topology of the lattice with three sites in the unit cell and a triangular Bravais lattice, one might expect e.g. 120° orientations of the spins on neighboring sites. However, the −120° orientation is symmetrically equivalent, so that a prevalence toward such spin-orientation translates to a negative (albeit incomplete) $\left\langle S_z^j S_z^l \right\rangle$ correlation.

[3]One may think of one susceptibility component being strongly peaked but quickly going to zero, and another component being rather flat and decaying slowly. There would be an intersection that leads to a discontinuity.

Die approbierte gedruckte Originalversion dieser Dissertation ist an der TU Wien Bibliothek verfügbar.
The approved original version of this doctoral thesis is available in print at TU Wien Bibliothek.
TU Bibliothek WIEN Your knowledge hub

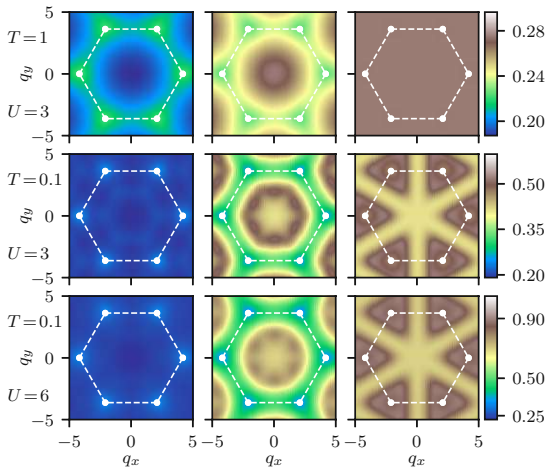

Figure 5.25: Eigenvalues of the static magnetic susceptibility in the first BZ for $U = 3$ at $T = 1$ (upper row) and $T = 0.1$ (middle row), and $U = 6$, $T = 0.1$ (lower row). There are three eigenvalues corresponding to the three bands in Fig. 5.18 (c): the left column shows the projection of χ on the lowest-energy eigenstate [energies below the Dirac point in Fig. 5.18 (c)]; the middle column that of the part of the bandstructure above the Dirac point and below the flat band; finally the right column corresponds to the flat-band states.

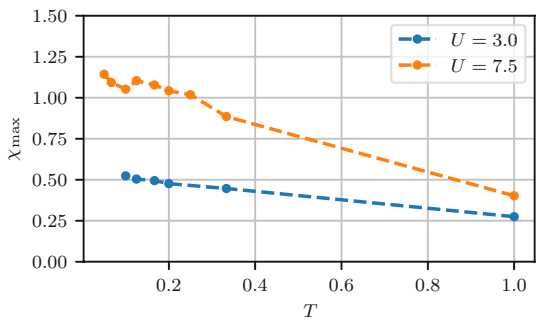

Figure 5.26: Temperature dependence of the maximal magnetic susceptibility $\chi_{\max}$ with respect to the momenta and the three eigenvectors (three panels in Fig. 5.25) at $\omega = 0$ for the weakly ($U = 3$) and moderately ($U = 7.5$) correlated regimes.

and at the Brillouin zone border the eigenvalue corresponding to the flat band is dominant. Let us stress that in this case a simple sorting of the eigenvalues would lead to a non-smooth momentum dependence of the susceptibility components. In Fig. 5.25 we show the (projected) eigenvalues of the zeroth Matsubara frequency on the $\boldsymbol{q}$-plane for $U = 3$ at high and low temperature.

Notably, the projection of the susceptibility on flat-band eigenstates is also flat at high temperature, but develops an inconspicuous structure at lower temperatures. Most importantly, Fig. 5.26 reveals that the maximal value of the susceptibility does not increase significantly as the temperature is lowered. Therefore, in sharp contrast to the square lattice, there is no visible tendency towards magnetic ordering. Instead, the flat structure of the magnetic susceptibility indicates short-ranged spin fluctuations.

Structure factors

Structure factors are on the one hand inherently connected with magnetic susceptibilities, and on the other hand can be addressed experimentally e.g. by neutron spectroscopy. Following work on the Heisenberg kagome model (Punk et al., 2014; Sherman and Singh, 2018), we calculate the equal-time structure factor $S_0(\boldsymbol{q})$ given by

$$S_0(\boldsymbol{q}) = \sum_{j,l} e^{i\boldsymbol{q}\cdot(\boldsymbol{r}_j - \boldsymbol{r}_l)} \sum_{\omega_n} \chi_{jl}(\boldsymbol{q}, i\omega_n) \tag{5.30}$$

Die approbierte gedruckte Originalversion dieser Dissertation ist an der TU Wien Bibliothek verfügbar.
The approved original version of this doctoral thesis is available in print at TU Wien Bibliothek.
TU Bibliothek WIEN Your knowledge hub

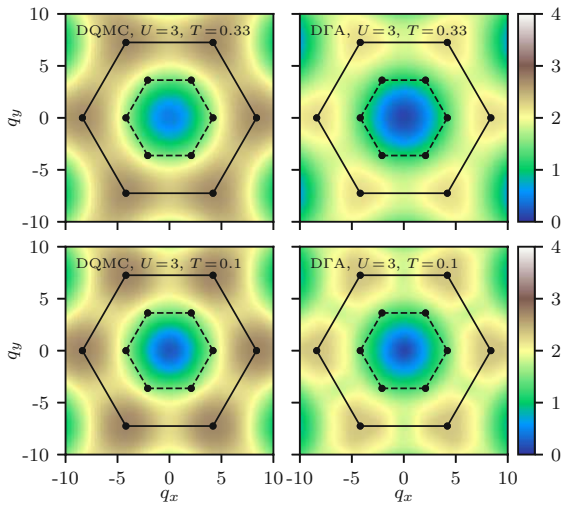

Figure 5.27: Equal-time structure factors $S_0(\boldsymbol{q})$ [Eq. (5.30)] in the weakly correlated regime ($U = 3$) as a function of temperature (top: $T = 0.33$, bottom: $T = 0.1$). Left: DQMC, right: DΓA. The dashed (solid) hexagons denote the boundary of the (extended) Brillouin zones.

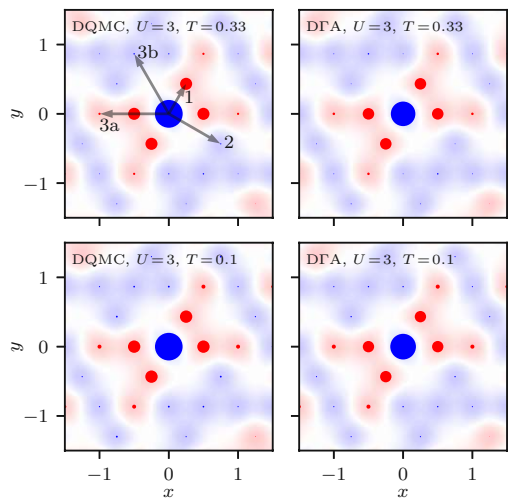

Figure 5.28: Equal-time susceptibility $\chi(\boldsymbol{R} \equiv (x, y))$ in real space for the weakly correlated regime ($U = 3$). Units along the x and y axes are unit cell constants. The area of a circle reflects the absolute value of the respective term, blue color denotes positive (ferromagnetic) correlations, red color denotes negative (antiferromagnetic) correlations. Since the magnitude of the long-range correlations is very small, we add a background shading to indicate the sign. Note that weak long-range correlations are antiferromagnetic for $\boldsymbol{R}_{3a}$ and ferromagnetic for $\boldsymbol{R}_2$ and $\boldsymbol{R}_{3b}$ (see Table 5.2 for the notation of intersite vectors).

and the dynamical structure factor $S(\boldsymbol{q}, \omega)$ given by

$$S(\boldsymbol{q}, \omega) = \frac{-\mathrm{Im} \sum_{j,l} e^{i\boldsymbol{q}\cdot(\boldsymbol{r}_j - \boldsymbol{r}_l)} \chi_{jl}(\boldsymbol{q}, \omega + i0^+)/\pi}{1 - e^{-\beta\omega}}. \tag{5.31}$$

In Eqs. (5.30) and (5.31), $\boldsymbol{r}_j$ denotes the position of the j-th atom in the unit cell. Since the shortest distance between two sites ($\frac{1}{2}$) is twice smaller than the unit cell constant (1), the structure factor is periodic in the extended Brillouin zone (Fig. 5.18, b). The analytic continuation of Matsubara frequencies or imaginary time to real frequencies is performed using ana_cont (Geffroy et al., 2019; Kaufmann, 2020) employing the maximum entropy method (Jarrell and Gubernatis, 1996). As a technical remark, we note that in DΓA we can analytically continue the projected eigenvalues of the susceptibility matrix individually, and then go back to the sublattice space, where the summation in Eq. (5.31) is carried out. In the following we present our results for the extended BZ of Fig. 5.18 (b). Upfolding the three eigenvectors of the first BZ (e.g. for the magnetic susceptibility in Fig. 5.25) yields a single eigenvector for the larger (extended) BZ.

Fig. 5.27 shows a smooth distribution of the equal-time structure factor over the extended Brillouin zone, and a weak temperature dependence. In all plots, $S_0(\boldsymbol{q})$ grows as we move from the center towards the boundary of the extended Brillouin zone, and forms round maxima at its corners [the K-points in Fig. 5.18 (b)]. To get a deeper insight into magnetic correlations, we return to real space and plot the equal-time susceptibility χ as a function of real-space vector

Die approbierte gedruckte Originalversion dieser Dissertation ist an der TU Wien Bibliothek verfügbar.
The approved original version of this doctoral thesis is available in print at TU Wien Bibliothek.
TU Bibliothek WIEN Your knowledge hub

notation	$\lvert\boldsymbol{R}\rvert$	multiplicity	$\boldsymbol{R} \equiv \left(R_x, R_y\right)$
$\boldsymbol{R}_1$	$\frac{1}{2}$	4	$\pm\left(\frac{1}{2};0\right), \pm\left(\frac{1}{4};\frac{\sqrt{3}}{4}\right)$
$\boldsymbol{R}_2$	$\frac{\sqrt{3}}{2}$	4	$\pm\left(0;\frac{\sqrt{3}}{2}\right), \pm\left(-\frac{3}{4};\frac{\sqrt{3}}{4}\right)$
$\boldsymbol{R}_{3a}$	1	4	$\pm(1;0), \pm\left(\frac{1}{2};\frac{\sqrt{3}}{2}\right)$
$\boldsymbol{R}_{3b}$	1	2	$\pm\left(-\frac{1}{2};\frac{\sqrt{3}}{2}\right)$

Table 5.2: Four shortest vectors $\boldsymbol{R}$ in the kagome lattice, connecting nearest neighbors ($\boldsymbol{R}_1$), second-neighbors ($\boldsymbol{R}_2$), and third-neighbors ($\boldsymbol{R}_{3a}$) and ($\boldsymbol{R}_{3b}$). Vector components and distances are given in units of the lattice constant. (For a visualization of these vectors, see Fig. 5.28.)

$\boldsymbol{R}$ connecting two sites. As expected for a strongly frustrated model, the resulting pattern in Fig. 5.28 is dominated by two contributions: the on-site contribution, which is trivially positive and yields a momentum-independent shift, and sizable negative, i. e. antiferromagnetic, correlations between the nearest neighbors ($\boldsymbol{R} = \boldsymbol{R}_1$). As we show in Appendix 5.6.2, the latter are largely responsible for the maxima at the K-points.

More intriguing is the pattern formed by weak longer-range correlations. In particular, by doubling the four $\boldsymbol{R}_1$, we obtain the $\boldsymbol{R}_{3a}$ vectors (Table 5.2) that point to four (out of six) third-neighbors on the kagome lattice. A key observation is that the respective correlations are also antiferromagnetic (red circles in Fig. 5.28). In contrast, the second-neighbor correlations ($\boldsymbol{R}_2$) and the remaining two third-neighbor correlations ($\boldsymbol{R}_{3b}$) are ferromagnetic (blue circles in Fig. 5.28). In momentum space, shown in Fig. 5.27 this has the following effect: strong negative correlations at $\boldsymbol{R}_1$ create the peaks at the K-points and positive correlations at $\boldsymbol{R}_2$ further increase them. The negative correlations at $\boldsymbol{R}_{3a}$ overcompensate the positive ones at $\boldsymbol{R}_{3b}$ and thus reduce the structure factor at the M-points. Altogether this leads to well-separated peaks at the K-points.

So far, we discussed the structure factor in the weakly correlated regime (U=3). If we now increase the interaction U, we observe an apparent change, both in momentum (Fig. 5.29) and real (Fig. 5.30) space. While $S_0(\boldsymbol{q})$ is still peaked at the K-points, the intensity grows over the entire boundary of the extended Brillouin zone. Again the behavior is understood better by looking at the lattice. Still, antiferromagnetic nearest-neighbor correlations generate the dominating peaks at the K-points, supported by $\boldsymbol{R}_2$-correlations. However, in the shell of third neighbors now the positive correlations prevail and increase the structure factor at the M-points, i. e. *between* the K-points. This means that the peaks become slightly less separated. More quantitatively, the ratio between the structure factor at the M-point and K-point at $U = 3$ is 0.87 (0.85) in DQMC (DΓA), and it increases to 0.90 (0.87) at $U = 6$.

Interestingly, our patterns are in excellent agreement with the equal-time structure factor computed using numerical linked cluster expansion for the Heisenberg kagome model (Sherman and Singh, 2018). We will discuss the ramifications in Sec. 5.6.3.

Since our calculations provide direct access to dynamical quantities, it is instructive to inspect the energy dependence of the structure factors. In Fig. 5.31 we plot the dynamical structure factor $S(\boldsymbol{q}, \omega)$ on a path through the extended Brillouin zone (Fig. 5.18) at weak interaction $U = 3$ for two different temperatures. In line with the equal-time structure factor, the dominant weight is located around the K-point. Additionally, there is a splitting into a

Die approbierte gedruckte Originalversion dieser Dissertation ist an der TU Wien Bibliothek verfügbar.
The approved original version of this doctoral thesis is available in print at TU Wien Bibliothek.
TU Bibliothek WIEN Your knowledge hub

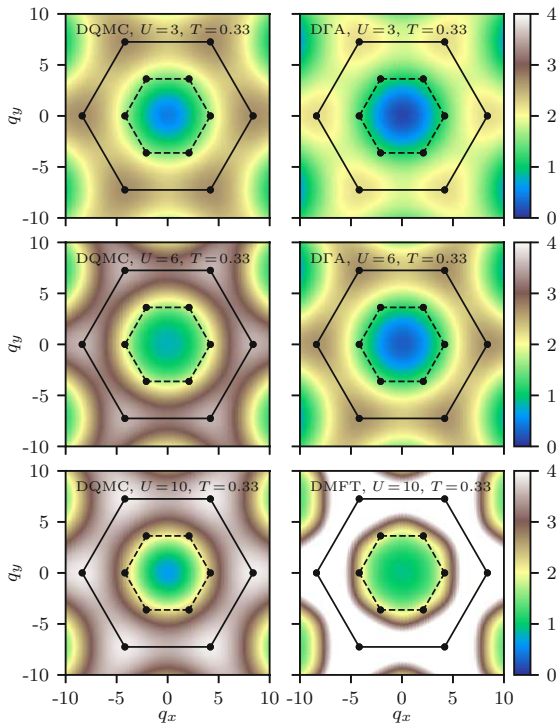

Figure 5.29: Equal-time structure factors $S_0(\boldsymbol{q})$ [Eq. (5.30)] as a function of U (top to bottom) for DQMC (left), DΓA(top right, middle right), and DMFT (bottom right) at $T = 0.33$. We used the DMFT susceptibility for $U = 10$ to calculate the structure factor, as the respective DΓA calculation did not converge.

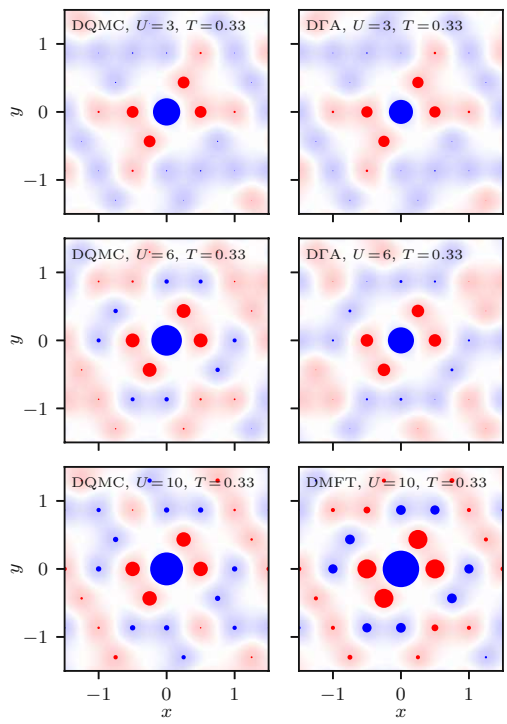

Figure 5.30: Equal-time susceptibility $\chi(\boldsymbol{R} \equiv (x, y))$ as a function of U (top: $U = 6$, bottom: $U = 10$) as calculated by DQMC (left), DΓA(top right) and DMFT (bottom right) at $T = 0.33$. The area of a circle reflects the absolute value of the respective term, blue color denotes positive (ferromagnetic) correlations, red color denotes negative (antiferromagnetic) correlations. Note that weak long-range correlations are ferromagnetic for $\boldsymbol{R}_2$, $\boldsymbol{R}_{3a}$ and antiferromagnetic for $\boldsymbol{R}_{3a}$ (see Table 5.2 for the notation of intersite vectors).

low- and a high-energy mode at the M-point (cf. Fig. 5.18, b), although at high energies it is concealed by thermal broadening in DΓA.

Finally, we present the evolution of the dynamical structure factor as a function of correlation strength in Fig. 5.32. The main effect is squeezing the frequency spread of the intensity to lower energies accompanied by a gradual dissipation of spectral features. Note that it was not possible to converge a self-consistent DΓA calculation for the $U = 10$ case, and in DMFT the spectral weight is pushed to zero energy.

Fingerprint of real-space correlations

For a better understanding of how spin-spin correlations between certain points in the lattice affect the susceptibility or structure factor in momentum space, it is helpful to study the connection analytically. The basis for this is Eq. (5.29), where we set $\langle S_z^j(\boldsymbol{R}, \tau) S_z^l(\boldsymbol{0}, 0)\rangle = 1$ for a certain vector $\boldsymbol{R}$ and all vectors that are related by symmetry transformations. Fig. 5.33 shows,

Die approbierte gedruckte Originalversion dieser Dissertation ist an der TU Wien Bibliothek verfügbar.
The approved original version of this doctoral thesis is available in print at TU Wien Bibliothek.
TU Bibliothek WIEN Your knowledge hub

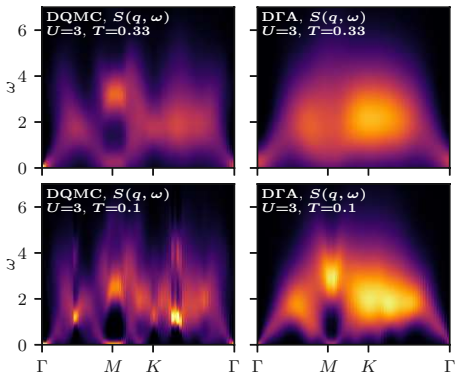

Figure 5.31: Dynamical structure factor $S(\boldsymbol{q}, \omega)$ in the weakly correlated regime (U = 3) at T = 0.33 (top) and T = 0.1 (bottom) calculated using DQMC (left) and DΓA (right) on a path through the extended Brillouin zone (Fig. 5.18).

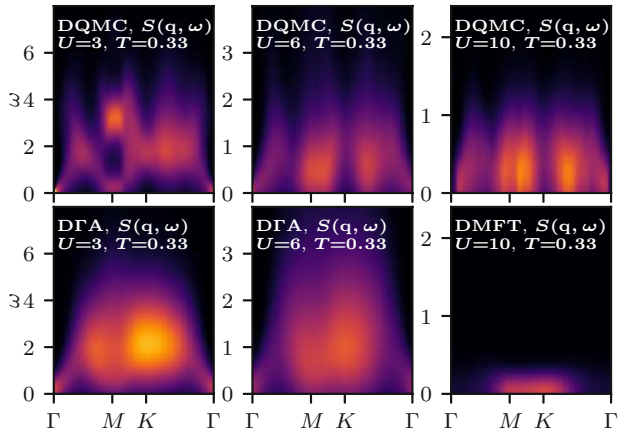

Figure 5.32: Dynamical structure factor as a function of interaction strength (left to right) as calculated by DQMC (top) and DΓA(bottom, except for DMFT in the right bottom plot) on a path through the extended Brillouin zone (Fig. 5.18) at T = 0.33. Note that the upper limit of the ω-axis (y-axis) is reduced as $1/U$ upon increasing U to resolve the feature-rich range; for large U such a rescaling must hold as the coupling of the Heisenberg model is $J = 4t^2/U$.

row by row, how correlations to a certain neighbor $\boldsymbol{R}$ and its symmetrically related counterparts reflect in $\boldsymbol{k}$-space. The first three rows are the projections to tight-binding eigenstates, and the fourth row is the structure factor.

Unsurprisingly, on-site correlations yield just a constant contribution. $\boldsymbol{R}_1$- and $\boldsymbol{R}_2$-correlations lead to peaks at the K-point in the extended Brillouin zone, whereas $\boldsymbol{R}_3$-correlations enhance the M-point (last two rows in Fig. 5.33).

It is important to note that, for this analysis, we always consider positive correlations (of unit magnitude) between neighboring sites at the indicated distance, negative ones just change the sign. For the nearest-neighbor correlations ($\boldsymbol{R}_1$) this means, e.g., that we get negative peaks at the K-points, whereas the actual correlations at $\boldsymbol{R}_1$ are negative yielding positiv peaks around the K-points. Furthermore let us note that the number of neighbors at $\boldsymbol{R}_{3a}$ is twice as large as the number of neighbors at $\boldsymbol{R}_{3b}$. Therefore also their influence on the structure factor is twice as large.

5.6.3 Discussion

Diagrammatic extensions alleviate the main drawback of DMFT — its restriction to local correlations. An alternative route to include nonlocal correlations are cluster extensions of DMFT. In the conceptually simple cellular DMFT (CMDFT) approach, such clusters are constructed in real space and typically comprise a small number of sites. Correlations in CDMFT are still purely local, but the locality spans now the entire cluster. As a result, nonlocal correlations at the length scale of the cluster are included, while longer-range fluctuations are still absent. In addition to this sharp cutoff between the short-range (included) and long-range (omitted) cor-

Die approbierte gedruckte Originalversion dieser Dissertation ist an der TU Wien Bibliothek verfügbar.
The approved original version of this doctoral thesis is available in print at TU Wien Bibliothek.
TU Bibliothek WIEN Your knowledge hub

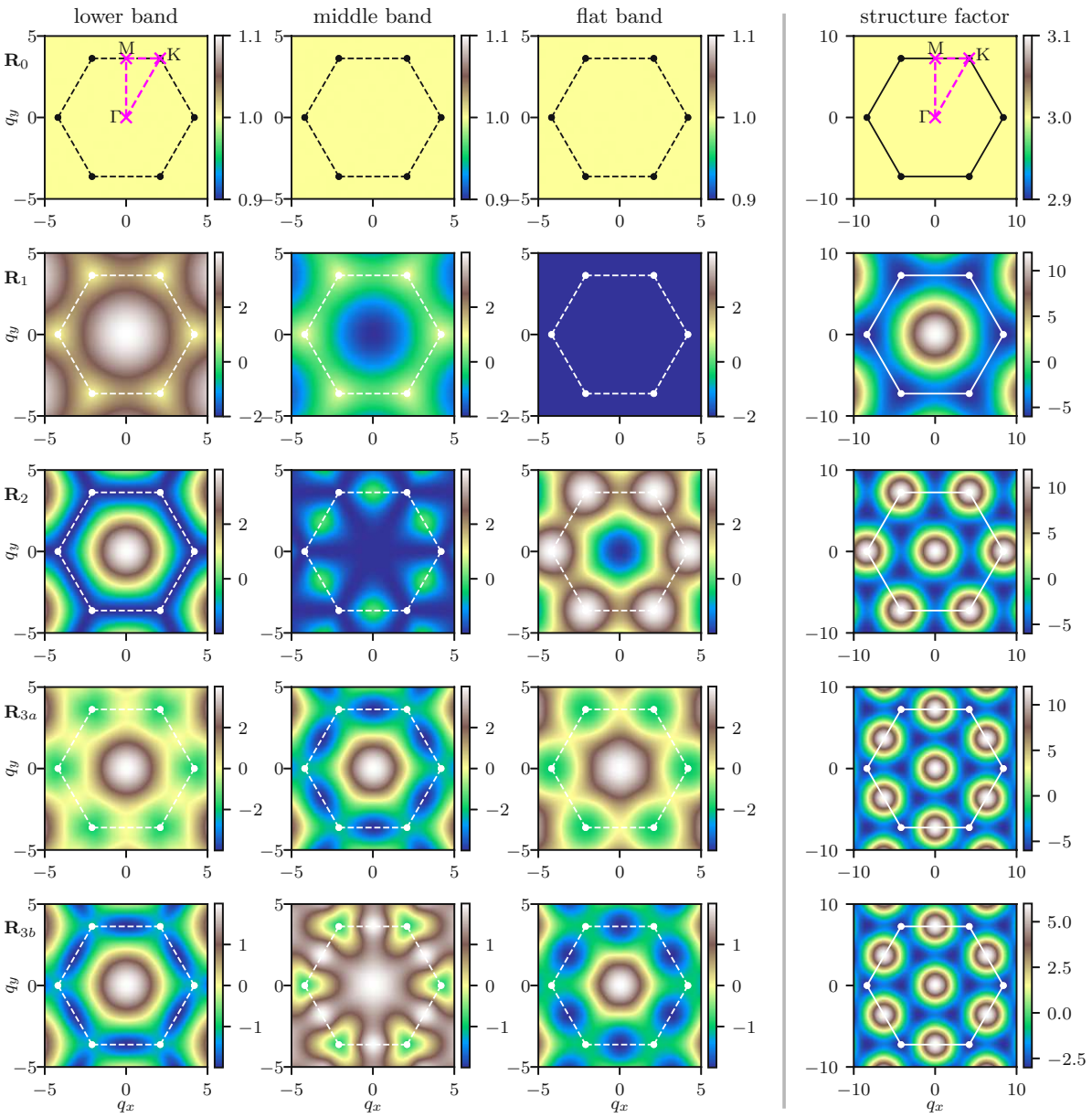

Figure 5.33: How certain real-space correlations influence the magnetic susceptibility and structure factor. In the first three columns we show the projection of the magnetic susceptibility on the lower-band, middle-band and flat-band eigenstates of the tight-binding Hamiltonian, respectively. The right-most column shows the corresponding structure factor $S(\boldsymbol{q})$ on the extended Brillouin zone. The rows correspond to various correlations in real space: Thus in the first row we show momentum-space correlations arising from on-site correlations. The second row corresponds to nearest-neighbor correlations ($\boldsymbol{R}_1$). The third, fourth and fifth row correspond to $\boldsymbol{R}_2$, $\boldsymbol{R}_{3a}$ and $\boldsymbol{R}_{3b}$ correlations.

Die approbierte gedruckte Originalversion dieser Dissertation ist an der TU Wien Bibliothek verfügbar.
The approved original version of this doctoral thesis is available in print at TU Wien Bibliothek.
TU Bibliothek WIEN Your knowledge hub

relations, CDMFT introduces a spurious disparity between the sites falling within the cluster and all other sites. We can illustrate this by considering the kagome lattice, where each site has four equivalent nearest neighbors. In the simplest possible cluster, a triangle, this equivalence is violated: only two of the four neighboring sites belong to the cluster. Keeping these intrinsic limitations of CDMFT in mind, we compare the results of three different CDMFT studies (Ohashi et al., 2006; Udagawa and Motome, 2010; Kita et al., 2013) with our DΓA and DQMC results.

In three-site CDMFT employing a Hirsch-Fye impurity solver, Ohashi *et al.* reported a first-order transition at the critical $U_c = 8.22$ (Ohashi et al., 2006). While we were not aiming at a precise estimate for the critical interaction strength, the three-site CDMFT values is somewhat lower than our DMFT value and higher than our DQMC estimate with 75 sites (and no DMFT bath).

In the strongly correlated regime ($U = 6.6$), the largest eigenvalue of the magnetic susceptibility plotted as a function of $\boldsymbol{q}$, is nearly flat in CDMFT, with shallow minima along the six Γ-M lines. Precisely this behavior is observed in the DΓA susceptibility (Fig. 5.25). Interestingly, Ohashi *et al.* report a drastic change of magnetic correlations in the insulating phase: they argue that a starlike structure in the structure factor indicates the onset of 1D antiferromagnetic correlations (Ohashi et al., 2006). We believe that this is an artifact of CDMFT. This is corroborated by the fact that the spin correlations that we obtain in DΓA and DQMC for the moderately correlated regime of the Hubbard model are similar to those of the Heisenberg model (Sherman and Singh, 2018).

The more recent CMDFT study by Udagawa and Motome (2010) employs a continuous-time auxiliary-field QMC impurity solver and uses, in addition to triangles, also more extended nine-site clusters. While the density matrix defined from microscopic states of a cluster is not accessible in the diagrammatic extensions, our temperature-dependent susceptibility (Fig. 5.26) agrees with the CDMFT results plotted in Fig. 4(d) of Udagawa and Motome (2010), except for the lowest temperatures, where we do not find the downturn of $\chi(T)$ characteristic for antiferromagnetic correlations or the formation of localized dimers. While not much is known for the KHM, we note that in the kagome Heisenberg model, dimer tunneling processes around the loops comprising eight sites play a pivotal role (Ralko et al., 2018). The absence of such loops in the nine-site clusters used in Udagawa and Motome (2010) may give rise to the formation of static antiferromagnetic dimers, and hence a suppressed susceptibility.

Finally, Kita et al. (2013) focus on the behavior of the KHM in a magnetic field. Nevertheless, it is instructive to discuss their CDMFT spectral function in zero field, computed for $U = 4$ and $U = 8$ (Fig. 1 in Kita et al. (2013)). The former agrees well with our DΓA results for $U = 3$, except for the substantial broadening in the CDMFT data at low frequencies, which might be an artifact of our analytic continuation. The $U = 8$ case is more interesting. Here, in contrast to single-site DMFT and in agreement with DΓA, no distinct lower Hubbard band is formed; instead, a dispersive feature stemming from the lowest-lying branch of the kagome band structure shows up at low frequencies. Close to the Fermi level, two narrow, nearly dispersionless bands form in CDMFT (Kita et al., 2013). We do not observe such structures in our $U = 6$ calculations, neither in DΓA, nor in DQMC: the intensity maxima lie above the Fermi level. At higher frequencies corresponding to the upper Hubbard band, CDMFT shows a broad spectral maximum in the vicinity of the Γ-point which rapidly decreases for finite momenta.

Die approbierte gedruckte Originalversion dieser Dissertation ist an der TU Wien Bibliothek verfügbar.
The approved original version of this doctoral thesis is available in print at TU Wien Bibliothek.
TU Bibliothek WIEN Your knowledge hub

A similar, albeit less pronounced distribution of the spectral weight is visible in DΓA results (Fig. 5.20): the intensity at the Γ-point is maximal.

Structure factors are a direct source of information on the dominant magnetic correlations and instabilities. A prominent example is the antiferromagnetic instability of the square-lattice Hubbard model, signaled by the diverging structure factor at $\boldsymbol{q} = (\pi, \pi)$, the propagation vector of the Néel state. In contrast, the structure factors of the KHM in the metallic regime lack any apparent instabilities, and instead show an intricate evolution on the frequency/momentum grid. Thus, to get insights into the magnetic correlations, we compare the behavior of $S(\boldsymbol{q})$ and $S(\boldsymbol{q}, \omega)$ with the literature data for the Heisenberg model.

The kagome Heisenberg model features several low-lying states with marginally different energies. While the debate on the ground state is still not settled, structure factors recently came into the forefront as a possible fingerprint to distinguish these states experimentally. A popular strategy is to pick a certain candidate state and calculate its structure factor using various mean-field techniques (Messio et al., 2010; Iqbal et al., 2013; Dodds et al., 2013; Punk et al., 2014; Halimeh and Punk, 2016; Messio et al., 2017; Halimeh and Singh, 2019). However, in the context of our study, a more appropriate starting point is the direct simulation of the Heisenberg model on a finite lattice, followed by the evaluation of structure factors from the spin correlations. Regardless of the method used, the resulting $S(\boldsymbol{q})$ of the Heisenberg model smoothly evolves from the minimum at Γ to the maximum at the boundary of the extended Brillouin zone. Further details depend on the computational method: While exact diagonalization on 36-site finite lattices yields feeble, yet discernible peaks at M (Läuchli and Lhuillier, 2009; Seman et al., 2015), these features are practically wiped out in density-matrix renormalization group (DMRG) simulations (Kolley et al., 2015; Zhu et al., 2019) that are less prone to finite-size effects. The featureless structure factor indicates that tendencies to ordering are strongly suppressed, even on a short range. Since they arise from competing correlations, this balance can be destroyed by small deviations from the Heisenberg model, such as anisotropies and/or longer-range exchanges. A common ramification is the appearance of maxima at K or M points of the extended Brillouin zone, indicative of so-called (Messio et al., 2011) $\sqrt{3}\times\sqrt{3}$ or $\mathbf{q} = 0$ antiferromagnetic correlations, respectively.

We are now in the position to compare the equal-time structure factors of the KHM in Figs. 5.27 and 5.29 with that of the Heisenberg model. First, the smooth $\boldsymbol{q}$-evolution and the minimum at Γ are common for both models. For all studied U and T values, the maximal intensity is at K, indicating the predominance of $\sqrt{3}\times\sqrt{3}$ correlations. This is seemingly at odds with the Heisenberg model, where weak maxima, if any, are found at M (Läuchli and Lhuillier, 2009; Seman et al., 2015). However, a key difference lies in the methods: we do calculations at finite temperature. Looking at the finite-temperature structure factors for the Heisenberg model (Sherman and Singh, 2018), we see a strikingly similar picture: a smooth evolution with maxima at K. This brings us to one of the main conclusions: at moderate temperatures, the magnetic correlations of the KHM are similar to those of the Heisenberg model.

While our equal-time structure factors are quantitatively similar in the weakly and strongly correlated regime (cf. Fig. 5.27 and Fig. 5.29), real-space plots of respective susceptibilities reveal a subtle change in third-neighbor correlations (cf. Fig. 5.28 and Fig. 5.30). At weak coupling ($U = 3$), Fig. 5.30 shows along the direction of the two Bravais lattice vectors a negative($\boldsymbol{R}_1$)-negative($\boldsymbol{R}_{3a}$)-positive spin correlation function, hinting at tendencies toward a

Die approbierte gedruckte Originalversion dieser Dissertation ist an der TU Wien Bibliothek verfügbar.
The approved original version of this doctoral thesis is available in print at TU Wien Bibliothek.
TU Bibliothek WIEN Your knowledge hub

120° spin-orientation. At strong coupling ($U = 6$ and $U = 10$) the third nearest-neighbor ($\boldsymbol{R}_{3a}$) changes sign. In the half-filled one-band Hubbard model with a strong negative (antiferromagnetic) preference between nearest neighbors, this is arguably the most dramatic change one might expect, devoid an actual ordering that is prevented by the frustrated lattice. Note that the third nearest neighbors and second nearest neighbors are both at a distance of two hopping elements, they only differ by their distance in real space because of the geometry.

We attribute this difference to the correlation-induced onset of $\mathbf{q} = 0$ magnetic correlations that compete with dominating $\sqrt{3} \times \sqrt{3}$ correlations. At the same time, susceptibilities in the moderately correlated regime (Fig. 5.30) are qualitatively similar to those in the Heisenberg model (Sherman and Singh, 2018). Therefore, we conclude that $\boldsymbol{q} = 0$ correlations develop already in the moderately correlated regime, i.e. in the metallic phase. This nontrivial result provides a key to distinguish between the weakly and moderately correlated regimes in real materials: The former features predominantly $\sqrt{3} \times \sqrt{3}$ correlations, while in the latter additional $\mathbf{q} = 0$ correlations become manifest.

Next, we discuss the features of the dynamical structure factor $S(\boldsymbol{q}, \omega)$. While details of the plots are prone to uncertainties of the analytic continuation, we comment on one salient feature: the difference between the frequency dependencies at K and M. The highest spectral density is associated with K (consistent with the maxima in the equal-time structure factor), but is it shifted to higher frequencies as compared to M. Interestingly, the same structure is found in the structure factor of a Z_2 spin liquid with a moderate spinon-vison interaction (Punk et al., 2014). Our work should motivate further studies to clarify whether metallic kagome magnets can serve as a playground for topological vison excitations, which have been suggested in (Punk et al., 2014).

Finally, we put our results in the context of ongoing experimental activities on metallic kagome magnets. While we computed the quantities that can be measured by inelastic neutron scattering, several aspects impede a direct comparision. First, all so far discovered metallic kagome materials are multi-orbital systems. A simplified effective one-orbital description is generally possible, but the mapping scheme depends on the specifics of a particular material and has to be adjusted accordingly. Second, a kagome-like arrangement of magnetic atoms in the crystal structure does not guarantee the applicability of the KHM: coupling beyond nearest neighbors as well as interplane couplings can play a significant role. This is the case for Mn_3Sn, where neutron scattering experiments reveal the relevance of multiple magnetic exchanges (Kang et al., 2019). Bilayer kagome systems Fe_3Sn_2 (Tanaka et al., 2020) and $Co_3Sn_2S_2$ (Liu et al., 2021) that entail a sizable interlayer coupling fall in the same category. Also the band filling, whose estimation in a real material is per se challenging, can deviate from the case in point: KHM at strict half-filling. All in all, we believe that presently the most promising case is FeSn, whose band structure (Fig. 4 in Kang et al. (2019)) bears apparent similarities to the half-filled tight-binding kagome model. We are looking forward to future inelastic neutron scattering experiments (announced in Sales et al. (2019)) that can be compared with our structure factors and dynamical susceptibilities.

Die approbierte gedruckte Originalversion dieser Dissertation ist an der TU Wien Bibliothek verfügbar.
The approved original version of this doctoral thesis is available in print at TU Wien Bibliothek.
TU Bibliothek WIEN Your knowledge hub

Die approbierte gedruckte Originalversion dieser Dissertation ist an der TU Wien Bibliothek verfügbar.
The approved original version of this doctoral thesis is available in print at TU Wien Bibliothek.
TU Bibliothek WIEN Your knowledge hub

Chapter 6

Conclusion

This work consists of several projects concerned with strongly correlated electrons. In the beginning we give a short introduction to the Green's function formalism and describe the development of a library for analytic continuation to the real-frequency domain. Progress in this field is made by carefully investigating the parameters and through this improving the quality of the analytic continuation as well as optimizing the workflow. Since computations in this work are done in the domain of imaginary time or Matsubara frequencies, the analytical continuation is a necessary task in all subsequent projects.

In the following we present the Anderson impurity model, for which it is possible to compute Green's functions numerically exactly. In particular we describe the hybridization expansion of the continuous-time quantum Monte Carlo. By means of worm sampling it is possible to compute not only the one-particle Green's function, but also much more complicated objects. Therefore worm sampling becomes a necessary tool for implementing the newly derived symmetric improved estimators, which allows us to precisely compute the self-energy and vertex functions.

In the following we turn to lattice models, but first within the framework of the dynamical mean-field theory. There one makes the approximation of a purely local self-energy, which becomes exact in infinite dimensions. Since the self-energy is purely local, it can be assigned to an auxiliary Anderson impurity model, whose parameters are determined self-consistently. Previously developed impurity solvers can thus be employed in dynamical mean-field theory calculations. After showing that using symmetric improved estimators in the impurity solver leads to more precise convergence of the DMFT loop, an attempt is made to reduce the number of required iterations by means of the Anderson acceleration algorithm. From our results it is evident that the use of such a convergence acceleration can lead to a large reduction of computational time, but in order to make it a more generally applicable option it is still necessary to deal with noise in a more controlled way. We then use the dynamical mean-field theory for the computation of scattering rates in the two dimensional square-lattice Hubbard model and a band insulator. These are compared to results of the Boltzmann scattering equation.

Subsequently we move away from the restriction to local correlations. After reviewing methods for the computation of nonlocal correlations, we focus on the dynamical vertex approximation. We develop a self-consistent extension to the AbinitioDΓA method (sc-DΓA), and apply it to the square-lattice Hubbard model at weak coupling, where benchmarking against other methods is possible. Although sc-DΓA systematically leads to smaller values of

Die approbierte gedruckte Originalversion dieser Dissertation ist an der TU Wien Bibliothek verfügbar.
The approved original version of this doctoral thesis is available in print at TU Wien Bibliothek.
TU Bibliothek WIEN Your knowledge hub

the antiferromagnetic susceptibility, the qualitative scaling with temperature agrees with the benchmark methods. Also the formation of a pseudogap in the one-particle spectral function is observed. In the intermediate and strong coupling regimes of the square-lattice Hubbard model, sc-DΓA is still applicable, as opposed to exact benchmark methods. We then move on to show that our method can also be used for systems with more than one orbital. Namely, we compute momentum-dependent spectral functions of a two-orbital square lattice Hubbard model with hole doping, and of a three-orbital Wannier model for strontium vanadate.

Finally, we perform an extensive study of the Hubbard model on a kagome lattice. By means of DMFT, sc-DΓA and determinant quantum Monte Carlo we compute and compare one-particle spectral functions and the spin structure factor. Due to the strong geometric frustration of the kagome lattice, spin fluctuations are suppressed even at low temperatures. Making the transition from momentum to real space allows us to identify a qualitative change in the pattern of spin-spin correlations.

Die approbierte gedruckte Originalversion dieser Dissertation ist an der TU Wien Bibliothek verfügbar.
The approved original version of this doctoral thesis is available in print at TU Wien Bibliothek.
TU Bibliothek WIEN Your knowledge hub

Appendices

Die approbierte gedruckte Originalversion dieser Dissertation ist an der TU Wien Bibliothek verfügbar.
The approved original version of this doctoral thesis is available in print at TU Wien Bibliothek.
TU Bibliothek WIEN Your knowledge hub

Die approbierte gedruckte Originalversion dieser Dissertation ist an der TU Wien Bibliothek verfügbar.
The approved original version of this doctoral thesis is available in print at TU Wien Bibliothek.

Appendix A

Properties of Green's functions

A.1 Imaginary-time dependence

A.1.1 Time interval

For the sake of notational simplicity, let us neglect the spatial and orbital dependence of operators. Then the Green's function reads

$$G(\tau) = \langle \mathrm{T} c(\tau) c^\dagger \rangle = \frac{1}{Z} \mathrm{Tr}\left[\mathrm{T} e^{-\beta H} e^{\tau H} c e^{-\tau H} c^\dagger \right]. \tag{A.1}$$

As a first step, let us assume that $\tau > 0$ and evaluate the time ordering operator:

$$G(\tau > 0) = \frac{1}{Z} \mathrm{Tr}\left[e^{-\beta H} e^{\tau H} c e^{-\tau H} c^\dagger \right]. \tag{A.2}$$

Now we use the spectral representation of the Hamiltonian H,

$$H|m\rangle = \varepsilon_m |m\rangle, \qquad \sum_m |m\rangle\langle m| = 1 \tag{A.3}$$

where the eigen-energies ε_m in general only have a lower bound, i. e. $\varepsilon_m = E_0 + E_m$ for some ground state energy E_0 and $E_m > 0$. Inserting the eigenbasis of the Hamiltonian into Eq. (A.2) leads to

$$G(\tau > 0) = -\frac{1}{Z} e^{-\beta E_0} \sum_{mn} e^{(\tau-\beta)E_m - \tau E_n} |\langle m|c|n\rangle|^2. \tag{A.4}$$

Since the energies E_m can become arbitrarily large, we must require their coefficients to be negative. Otherwise the exponential can diverge. We thus conclude:

$$\tau < \beta \quad \text{for } \tau > 0. \tag{A.5}$$

Looking at $\tau < 0$, the time ordering operator evaluates to

$$G(\tau < 0) = \frac{1}{Z} \mathrm{Tr}\left[e^{-\beta H} c^\dagger e^{\tau H} c e^{-\tau H} \right]. \tag{A.6}$$

and in the Hamiltonian eigenbasis we get

$$G(\tau < 0) = (-)\frac{1}{Z} e^{-\beta E_0} \sum_{mn} e^{-(\tau+\beta)E_m + \tau E_n} |\langle n|c|m\rangle|^2, \tag{A.7}$$

Die approbierte gedruckte Originalversion dieser Dissertation ist an der TU Wien Bibliothek verfügbar.
The approved original version of this doctoral thesis is available in print at TU Wien Bibliothek.
TU Bibliothek WIEN Your knowledge hub

where the minus sign has to be left out for fermionic operators c. Similar considerations as above lead to the restriction

$$\tau > -\beta \quad \text{for } \tau < 0. \tag{A.8}$$

In summary, we see that the imaginary time is restricted to the finite interval

$$-\beta < \tau < \beta \tag{A.9}$$

A.1.2 Periodicity in imaginary time

Assuming $\tau > 0$, let us consider $G(\tau - \beta)$:

$$G(\tau - \beta) = -\langle \mathbf{T} c(\tau - \beta) c^\dagger(0) \rangle = \pm \langle c^\dagger(0) c(\tau - \beta) \rangle \tag{A.10}$$

The upper sign corresponds to fermions, the lower to bosons. We can write the expectation value explicitly now:

$$G(\tau - \beta) = \pm \frac{1}{Z} \mathrm{Tr}\left[e^{-\beta H} c^\dagger \color{blue}{e^{(\tau-\beta)H} c e^{-(\tau-\beta)H}} \right] \tag{A.11}$$

Exploiting the cyclic property of the trace, we can move the expression written in blue to the front and appropriately rearrange the exponentials:

$$G(\tau - \beta) = \pm \frac{1}{Z} \mathrm{Tr}\left[e^{-\beta H} e^{\tau H} c e^{-\tau H} c^\dagger \right] \tag{A.12}$$

We recognize the definition of the Green's function and conclude

$$G(\tau - \beta) = \mp G(\tau) \tag{A.13}$$

Thus, bosonic Green's functions are periodic, and fermionic Green's functions are anti-periodic.

Die approbierte gedruckte Originalversion dieser Dissertation ist an der TU Wien Bibliothek verfügbar.
The approved original version of this doctoral thesis is available in print at TU Wien Bibliothek.
TU Bibliothek WIEN Your knowledge hub

Die approbierte gedruckte Originalversion dieser Dissertation ist an der TU Wien Bibliothek verfügbar.
The approved original version of this doctoral thesis is available in print at TU Wien Bibliothek.
TU Bibliothek WIEN Your knowledge hub

Appendix B

Lehmann representations

B.1 Lehmann representations for two-frequency objects

This section was published in Kaufmann et al. (2019), but entirely written by the author of this thesis.

For objects depending on a single fermionic/bosonic frequency, the standard Lehmann representations for fermionic/bosonic Green's functions can be used. For objects depending on two fermionic and one bosonic Green's function, we use the form published in Toschi et al., 2007. Additionally, we need it for

$$f^{\nu\omega} = \int_0^\beta d\tau_1 d\tau_2 d\tau_3 e^{i[\nu(\tau_1-\tau_2)+\omega(\tau_2-\tau_3)]} \times \langle \mathbf{T}_\tau F_1(\tau_1)F_2(\tau_2)B(\tau_3)\rangle \tag{B.1}$$

Here, F_i (B) are fermionic (bosonic) operators, and ν (ω) are fermionic (bosonic) frequencies. Inserting the eigenbasis of the Hamiltonian and evaluating the integrals analytically, we obtain

$$\begin{aligned} f^{\nu\omega} = &\frac{1}{Z}\sum_{mnl} F_1^{mn}F_2^{nl}B^{lm}\frac{1}{-i\nu+i\omega+E_n-E_l}\times\left[\frac{e^{-\beta E_l}-e^{-\beta E_m}}{i\omega+E_m-E_l}+\frac{e^{-\beta E_n}+e^{-\beta E_m}}{i\nu+E_m-E_n}\right] \\ &+\frac{1}{Z}\sum_{mnl} F_2^{mn}F_1^{nl}B^{lm}\frac{1}{i\nu+E_n-E_l}\times\left[\frac{e^{-\beta E_l}-e^{-\beta E_m}}{i\omega+E_m-E_l}+\frac{e^{-\beta E_n}+e^{-\beta E_m}}{-i\nu+i\omega+E_m-E_n}\right] \end{aligned} \tag{B.2}$$

Furthermore, we need

$$g^{\nu\omega} = \int_0^\beta d\tau_1 d\tau_2 d\tau_3 e^{i[\nu_1(\tau_1-\tau_3)+\nu_2(\tau_2-\tau_3)]} \times \langle \mathbf{T}_\tau F_1(\tau_1)F_2(\tau_2)B(\tau_3)\rangle. \tag{B.3}$$

with two fermionic frequencies ν_1, ν_2. The result is

$$g^{\nu\omega} = \frac{1}{Z}\sum_{mkl} F_1^{mn} F_2^{nl} B^{lm} \frac{1}{i\nu_2 + E_n - E_l} \times \left[\frac{e^{-\beta E_l} - e^{-\beta E_m}}{i\nu_1 + i\nu_2 + E_m - E_l} + \frac{e^{-\beta E_n} + e^{-\beta E_m}}{i\nu_1 + E_m - E_n}\right]$$
$$+\frac{1}{Z}\sum_{mnl} F_2^{mn} F_1^{nl} B^{lm} \frac{1}{i\nu_1 + E_n - E_l} \times \left[\frac{e^{-\beta E_l} - e^{-\beta E_m}}{i\nu_1 + i\nu_2 + E_m - E_l} + \frac{e^{-\beta E_n} + e^{-\beta E_m}}{i\nu_2 + E_m - E_n}\right] \tag{B.4}$$

B.2 Raman diagram

Raman scattering in a system in equilibrium can be described by diagrams of the form

$$R_{i_1\ldots i_6}(\tau_1, \tau_2) = \left\langle \mathrm{T}_\tau [d_{i_1}^\dagger d_{i_2}](\tau_1)[d_{i_3}^\dagger d_{i_4}](\tau_2)[d_{i_5}^\dagger d_{i_6}]\right\rangle. \tag{B.5}$$

The Fourier transform to Matsubara frequencies is given by

$$R_{i_1\ldots i_6}^{\omega_1\omega_2} = \int_0^\beta d\tau_1 \int_0^\beta d\tau_2 e^{i(\omega_1\tau_1+\omega_2\tau_2)} R_{i_1\ldots i_6}(\tau_1, \tau_2) \tag{B.6}$$

with bosonic Matsubara frequencies ω_1, ω_2. In the following we will write Eq. (B.5) as

$$R_{i_1\ldots i_6}(\tau_1, \tau_2) = \left\langle \mathrm{T}_\tau B_1(\tau_1) B_2(\tau_2) B_3\right\rangle, \tag{B.7}$$

where B_i are in principle arbitrary bosonic operators. For the present derivation it is not necessary to further specify them.

Here we would like to compute such diagrams for the Anderson impurity model with a discrete bath by exact diagonalization of the Hamiltonian.

B.3 Eigenbasis representation

The first step towards our goal is the explicit insertion of the definitions of the expectation value, the time-ordering operator and the imaginary-time evolution. We get

$$R_{i_1\ldots i_6}(\tau_1, \tau_2) = \frac{1}{Z}\Big[\Theta(\tau_1 - \tau_2)\mathrm{Tr}\left(e^{(\tau_1-\beta)H} B_1 e^{(\tau_2-\tau_1)H} B_2 e^{-\tau_2 H} B_3\right)$$
$$+\Theta(\tau_2 - \tau_1)\mathrm{Tr}\left(e^{(\tau_2-\beta)H} B_2 e^{(\tau_1-\tau_2)H} B_1 e^{-\tau_1 H} B_3\right)\Big]. \tag{B.8}$$

Now we assume that the Hamiltonian has a finite number of eigenvalues and can be written as

$$H = \sum_m \varepsilon_m |m\rangle\langle m| \tag{B.9}$$

The traces in Eq. (B.8) are now a sum over the Hamiltonian eigenstates, and inserting unity matrices in the Hamiltonian eigenbasis transforms the time evolution operators to simple multiplications:

$$R_{i_1\ldots i_6}(\tau_1, \tau_2) = \frac{1}{Z}\sum_{mnl} e^{-\beta\varepsilon_m}\Big[\Theta(\tau_1 - \tau_2) e^{(\varepsilon_m-\varepsilon_n)\tau_1+(\varepsilon_n-\varepsilon_l)\tau_2} B_1^{mn} B_2^{nl} B_3^{lm}$$
$$+\Theta(\tau_2 - \tau_1) e^{(\varepsilon_n-\varepsilon_l)\tau_1+(\varepsilon_m-\varepsilon_n)\tau_2} B_1^{nl} B_2^{mn} B_3^{lm}\Big]. \tag{B.10}$$

Die approbierte gedruckte Originalversion dieser Dissertation ist an der TU Wien Bibliothek verfügbar.
The approved original version of this doctoral thesis is available in print at TU Wien Bibliothek.
TU Bibliothek WIEN Your knowledge hub

It is now straightforward to insert this expression into the Fourier transform Eq. (B.6), where the effect of the step functions is just a change of integral bounds.

$$\begin{aligned} R^{\omega_1\omega_2}_{i_1\ldots i_6} =& \frac{1}{Z}\sum_{mnl} e^{-\beta\varepsilon_m} B_1^{mn} B_2^{nl} B_3^{lm} \int_0^\beta d\tau_1 \int_0^{\tau_1} d\tau_2 e^{(i\omega_1+\varepsilon_m-\varepsilon_n)\tau_1+(i\omega_2+\varepsilon_n-\varepsilon_l)\tau_2} \\ &+\frac{1}{Z}\sum_{mnl} e^{-\beta\varepsilon_m} B_2^{mn} B_1^{nl} B_3^{lm} \int_0^\beta d\tau_2 \int_0^{\tau_2} d\tau_1 e^{(i\omega_1+\varepsilon_n-\varepsilon_l)\tau_1+(i\omega_2+\varepsilon_m-\varepsilon_n)\tau_2} \end{aligned} \tag{B.11}$$

In the second integral now let us rename τ_1 and τ_2. We obtain

$$\begin{aligned} R^{\omega_1\omega_2}_{i_1\ldots i_6} =& \frac{1}{Z}\sum_{mnl} e^{-\beta\varepsilon_m} B_1^{mn} B_2^{nl} B_3^{lm} \underbrace{\int_0^\beta d\tau_1 \int_0^{\tau_1} d\tau_2 e^{(i\omega_1+\varepsilon_m-\varepsilon_n)\tau_1+(i\omega_2+\varepsilon_n-\varepsilon_l)\tau_2}}_{r^{\omega_1\omega_2}_{mnl}} \\ &+\frac{1}{Z}\sum_{mnl} e^{-\beta\varepsilon_m} B_2^{mn} B_1^{nl} B_3^{lm} \underbrace{\int_0^\beta d\tau_1 \int_0^{\tau_1} d\tau_2 e^{(i\omega_2+\varepsilon_m-\varepsilon_n)\tau_1+(i\omega_1+\varepsilon_n-\varepsilon_l)\tau_2}}_{r^{\omega_2\omega_1}_{mnl}} . \end{aligned} \tag{B.12}$$

It becomes apparent that we only have to calculate one of the integrals, since the second one is then given by exchanging the frequency variables.

B.4 Calculation of the integral

The calculation of the integral is in principle straight-forward. However, it is unfortunately necessary to consider several special cases. This has the reason that (i) all involved frequencies are bosonic and can hence have the value 0, and (ii) the eigenvalues ε_i of the Hamiltonian can be degenerate.

B.4.1 $\omega_1 \neq 0$ and $\omega_2 \neq 0$

Let us first consider the case that none of the frequencies are zero. The straightforward calculation yields

$$r^{\omega_1\omega_2}_{mnl} = \frac{1}{i\omega_2+\varepsilon_n-\varepsilon_l}\left[\frac{e^{-\beta\varepsilon_l}-e^{-\beta\varepsilon_m}}{i\omega_1+i\omega_2+\varepsilon_m-\varepsilon_l}+\frac{e^{-\beta\varepsilon_m}-e^{\beta\varepsilon_n}}{i\omega_1+\varepsilon_m-\varepsilon_n}\right] \tag{B.13}$$

From Eq. (B.13) we see that there are several cases where one can get a problem. Whereas for other observables, like the two-particle Green's function, these can be avoided by a shift of eigenvalues, this is not possible. Instead, we re-calculate the integrals in $r^{\omega_1\omega_2}$ from scratch for the following seven cases:

1. $\omega_1 = 0$, $\omega_2 \neq 0$, $\varepsilon_m = \varepsilon_n = \varepsilon$

$$r = \frac{1}{i\omega_2+\varepsilon-\varepsilon_l}\left(\frac{e^{-\beta\varepsilon_l}-e^{-\beta\varepsilon}}{i\omega_2+\varepsilon-\varepsilon_l}-\beta e^{-\beta\varepsilon}\right) \tag{B.14}$$

Die approbierte gedruckte Originalversion dieser Dissertation ist an der TU Wien Bibliothek verfügbar.
The approved original version of this doctoral thesis is available in print at TU Wien Bibliothek.
TU Bibliothek WIEN Your knowledge hub

2. $\omega_2 = 0$, $\omega_1 \neq 0$, $\varepsilon_n = \varepsilon_l = \varepsilon$

$$r = \frac{1}{i\omega_1 + \varepsilon_m - \varepsilon}\left(\frac{e^{-\beta\varepsilon_m} - e^{-\beta\varepsilon}}{i\omega_1 + \varepsilon_m - \varepsilon} + \beta e^{-\beta\varepsilon}\right) \tag{B.15}$$

3. $\omega_1 = \omega_2 = 0$, $\varepsilon_m = \varepsilon_n = \varepsilon \neq \varepsilon_l$

$$r = \frac{1}{\varepsilon - \varepsilon_l}\left(\frac{e^{-\beta\varepsilon_l} - e^{-\beta\varepsilon}}{\varepsilon - \varepsilon_l} - \beta e^{-\beta\varepsilon}\right) \tag{B.16}$$

4. $\omega_1 = \omega_2 = 0$, $\varepsilon_m \neq \varepsilon_n = \varepsilon = \varepsilon_l$

$$r = \frac{1}{\varepsilon - \varepsilon_m}\left(\frac{e^{-\beta\varepsilon_m} - e^{-\beta\varepsilon}}{\varepsilon - \varepsilon_m} - \beta e^{-\beta\varepsilon}\right) \tag{B.17}$$

5. $\omega_1 = \omega_2 = 0$, $\varepsilon_n \neq \varepsilon_m = \varepsilon = \varepsilon_l$

$$r = \frac{1}{\varepsilon - \varepsilon_n}\left(\frac{e^{-\beta\varepsilon_n} - e^{-\beta\varepsilon}}{\varepsilon - \varepsilon_n} - \beta e^{-\beta\varepsilon}\right) \tag{B.18}$$

6. $\omega_1 = \omega_2 = 0$, $\varepsilon_n = \varepsilon_m = \varepsilon_l = \varepsilon$

$$r = \frac{1}{2}\beta^2 e^{-\beta\varepsilon} \tag{B.19}$$

7. $\omega_1 = -\omega_2 = \omega$, $\varepsilon_m = \varepsilon_l = \varepsilon$

$$r = \frac{1}{i\omega + \varepsilon_n - \varepsilon}\left(\frac{e^{-\beta\varepsilon} - e^{-\beta\varepsilon_n}}{i\omega + \varepsilon - \varepsilon_n} + \beta e^{-\beta\varepsilon}\right) \tag{B.20}$$

We can now compute $r_{mnl}^{\omega_1\omega_2}$ and thus the full Raman diagram:

$$R_{i_1\ldots i_6}^{\omega_1\omega_2} = \frac{1}{Z}\sum_{mnl} e^{-\beta\varepsilon_m}\left[B_1^{mn}B_2^{nl}B_3^{lm}r_{mnl}^{\omega_1\omega_2} + B_2^{mn}B_1^{nl}B_3^{lm}r_{mnl}^{\omega_2\omega_1}\right]. \tag{B.21}$$

Die approbierte gedruckte Originalversion dieser Dissertation ist an der TU Wien Bibliothek verfügbar.
The approved original version of this doctoral thesis is available in print at TU Wien Bibliothek.
TU Bibliothek WIEN Your knowledge hub

Die approbierte gedruckte Originalversion dieser Dissertation ist an der TU Wien Bibliothek verfügbar.
The approved original version of this doctoral thesis is available in print at TU Wien Bibliothek.
TU Bibliothek WIEN Your knowledge hub

Appendix C

Parquet equations in convention-agnostic frequency notation

As we have mentioned in Chapter 3, the energy conservation relation Eq. (3.8) makes it possible to write two-particle vertices as functions of three frequencies, instead of four. One of those frequencies is bosonic, but the particular choice of this bosonic frequency is ambiguous. The resultant variety of conventions often leads to confusion. In this Appendix we therefore show how to make the transition from a frequency convention with a particular choice of bosonic frequency to a convention with four fermionic frequencies in Appendix C.2. Subsequently, we go from four-frequency notation to a different three-frequency convention in Appendix C.3.

Throughout this Appendix, we will denote fermionic Matsubara frequencies by ν, and bosonic Matsubara frequencies by ω.

C.1 Green's functions in AbinitioDΓA

Combining Eq. (3.4)and Eq. (3.6), the one-particle Green's function for the AIM is

$$G_a^\nu = \frac{1}{\beta}\int_0^\beta d\tau_1 d\tau_2 e^{i\nu(\tau_1-\tau_2)}\langle T_\tau d_a(\tau_1) d_a^\dagger(\tau_2)\rangle \tag{C.1}$$

The two-particle Green's function from Eq. (3.5) and Eq. (3.7) is

$$G_{abcd}^{\nu_1\nu_2\nu_3\nu_4} = \frac{1}{\beta^2}\int_0^\beta d\tau_1 d\tau_2 d\tau_3 d\tau_4 e^{i(\nu_1\tau_1-\nu_2\tau_2+\nu_3\tau_3-\nu_4\tau_4)}\langle T_\tau d_a(\tau_1) d_b^\dagger(\tau_2) d_c(\tau_3) d_d^\dagger(\tau_4)\rangle \tag{C.2}$$

In practice, we can use relation (3.8) to save storage space by using just three frequency indices instead of four. The choice how to do this reduction is of course ambiguous. This has led to the wide-spread fear of frequency-conventions. In AbinitioDΓA, we make the following choice:

ν_1	ν	ν
ν_2	$\nu - \omega_{ph}$	$\omega_{pp} - \nu'$
ν_3	$\nu' - \omega_{ph}$	$\omega_{pp} - \nu$
ν_4	ν'	ν'

Here we explicitly write different symbols for the bosonic frequencies in particle-particle (*pp*) and particle-hole (*ph*) channel, because they are just really different quantities. It has always led to a lot of confusion that the same symbol was used.

C.2 Irreducible vertex

The irreducible vertex in the density channel, Λ_d, in the frequency convention of Rohringer et al. (2018) is given by

$$\Lambda_d^{\nu\nu'\omega_{ph}} = \Gamma_d^{\nu\nu'\omega_{ph}} + \frac{1}{2}\Phi_d^{\nu(\nu+\omega_{ph})(\nu'-\nu)} + \frac{3}{2}\Phi_m^{\nu(\nu+\omega_{ph})(\nu'-\nu)} - \frac{1}{2}\Phi_s^{\nu\nu'(\nu+\nu'+\omega_{ph})} - \frac{3}{2}\Phi_t^{\nu\nu'(\nu+\nu'+\omega_{ph})}. \tag{C.3}$$

In the above equation, Γ_r and Φ_r are the irreducible and reducible vertex in channel r, respectively. There are four channels: the density (charge) channel $r = d$, the magnetic (spin) channel $r = m$, the singlet channel $r = s$, and the triplet channel $r = t$.

As a first step, we insert the frequency convention:

ν_1	ν	ν
ν_2	$\nu + \omega_{ph}$	$\omega_{pp} - \nu'$
ν_3	$\nu' + \omega_{ph}$	$\omega_{pp} - \nu$
ν_4	ν'	ν'

So we have

$$\Lambda_d^{\nu_1\nu_4(\nu_2-\nu_1)} = \Gamma_d^{\nu_1\nu_4(\nu_2-\nu_1)} + \frac{1}{2}\Phi_d^{\nu_1\nu_2(\nu_4-\nu_1)} + \frac{3}{2}\Phi_m^{\nu_1\nu_2(\nu_4-\nu_1)} - \frac{1}{2}\Phi_s^{\nu_1\nu_4(\nu_1+\nu_3)} - \frac{3}{2}\Phi_t^{\nu_1\nu_4(\nu_1+\nu_3)} \tag{C.4}$$

As a next step we want to rewrite the symbols with 4 frequency indices. For a particle-hole type object the transition is the following:

$$A_{ph}^{\nu\nu'\omega_{ph}} \equiv A_{ph}^{\nu(\nu+\omega_{ph})(\nu'+\omega_{ph})\nu'} = A_{ph}^{\nu_1\nu_2\nu_3\nu_4} \tag{C.5}$$

We have to apply it to the density and magnetic channel objects. And for a particle-particle type object it is

$$A_{pp}^{\nu\nu'\omega_{pp}} \equiv A_{pp}^{\nu(\omega_{pp}-\nu')(\omega_{pp}-\nu)\nu'} = A_{pp}^{\nu_1\nu_2\nu_3\nu_4} \tag{C.6}$$

We have to apply it to the singlet and triplet channel objects. Thus we get

$$\Lambda_d^{\nu_1\nu_2\nu_3\nu_4} = \Gamma_d^{\nu_1\nu_2\nu_3\nu_4} + \frac{1}{2}\Phi_d^{\nu_1\nu_4\nu_3\nu_2} + \frac{3}{2}\Phi_m^{\nu_1\nu_4\nu_3\nu_2} - \frac{1}{2}\Phi_s^{\nu_1\nu_2\nu_3\nu_4} - \frac{3}{2}\Phi_t^{\nu_1\nu_2\nu_3\nu_4} \tag{C.7}$$

Now we have the equation in convention-free notation and we can choose any frequency convention we want.

The equation for Λ_m is very similar:

$$\Lambda_m^{\nu_1\nu_2\nu_3\nu_4} = \Gamma_m^{\nu_1\nu_2\nu_3\nu_4} + \frac{1}{2}\Phi_d^{\nu_1\nu_4\nu_3\nu_2} - \frac{1}{2}\Phi_m^{\nu_1\nu_4\nu_3\nu_2} + \frac{1}{2}\Phi_s^{\nu_1\nu_2\nu_3\nu_4} - \frac{1}{2}\Phi_t^{\nu_1\nu_2\nu_3\nu_4} \tag{C.8}$$

Die approbierte gedruckte Originalversion dieser Dissertation ist an der TU Wien Bibliothek verfügbar.
The approved original version of this doctoral thesis is available in print at TU Wien Bibliothek.
TU Bibliothek WIEN Your knowledge hub

For Λ_s we repeat the procedure, since it is given in particle-particle notation.

$$\Lambda_s^{\nu\nu'\omega_{pp}} = \Gamma_s^{\nu\nu'\omega_{pp}} - \frac{1}{2}\Phi_d^{\nu\nu'(\omega_{pp}-\nu-\nu')} + \frac{3}{2}\Phi_m^{\nu\nu'(\omega_{pp}-\nu-\nu')} - \frac{1}{2}\Phi_d^{\nu(\omega_{pp}-\nu')(\nu'-\nu)} + \frac{3}{2}\Phi_m^{\nu(\omega_{pp}-\nu')(\nu'-\nu)} \tag{C.9}$$

We again just insert the definition of the frequency convention as a first step:

$$\Lambda_s^{\nu_1\nu_4(\nu_1+\nu_3)} = \Gamma_s^{\nu_1\nu_4(\nu_1+\nu_3)} - \frac{1}{2}\Phi_d^{\nu_1\nu_4(\nu_2-\nu_1)} + \frac{3}{2}\Phi_m^{\nu_1\nu_4(\nu_2-\nu_1)} - \frac{1}{2}\Phi_d^{\nu_1\nu_2(\nu_4-\nu_1)} + \frac{3}{2}\Phi_m^{\nu_1\nu_2(\nu_4-\nu_1)} \tag{C.10}$$

Finally we again make the transition from three-frequency notation to convention-free four-frequency notation, considering that d and m objects are of particle-hole type, and s and t objects of particle-particle type.

$$\Lambda_s^{\nu_1\nu_2\nu_3\nu_4} = \Gamma_s^{\nu_1\nu_2\nu_3\nu_4} - \frac{1}{2}\Phi_d^{\nu_1\nu_2\nu_3\nu_4} + \frac{3}{2}\Phi_m^{\nu_1\nu_2\nu_3\nu_4} - \frac{1}{2}\Phi_d^{\nu_1\nu_4\nu_3\nu_2} + \frac{3}{2}\Phi_m^{\nu_1\nu_4\nu_3\nu_2} \tag{C.11}$$

The same form we get now also for Λ_t:

$$\Lambda_t^{\nu_1\nu_2\nu_3\nu_4} = \Gamma_t^{\nu_1\nu_2\nu_3\nu_4} - \frac{1}{2}\Phi_d^{\nu_1\nu_2\nu_3\nu_4} - \frac{1}{2}\Phi_m^{\nu_1\nu_2\nu_3\nu_4} + \frac{1}{2}\Phi_d^{\nu_1\nu_4\nu_3\nu_2} + \frac{1}{2}\Phi_m^{\nu_1\nu_4\nu_3\nu_2} \tag{C.12}$$

There are also equations to express the particle-particle channel by the particle-hole channel:

$$\Lambda_s^{\nu\nu'\omega_{pp}} = \frac{1}{2}\Lambda_d^{\nu\nu'(\omega_{pp}-\nu-\nu')} - \frac{3}{2}\Lambda_m^{\nu\nu'(\omega_{pp}-\nu-\nu')} \tag{C.13}$$

We insert the definitions of the frequencies

$$\Lambda_s^{\nu_1\nu_4(\nu_1+\nu_3)} = \frac{1}{2}\Lambda_d^{\nu_1\nu_4(\nu_2-\nu_1)} - \frac{3}{2}\Lambda_m^{\nu_1\nu_4(\nu_2-\nu_1)} \tag{C.14}$$

and make the transition to convention-free four-frequency notation:

$$\Lambda_s^{\nu_1\nu_2\nu_3\nu_4} = \frac{1}{2}\Lambda_d^{\nu_1\nu_2\nu_3\nu_4} - \frac{3}{2}\Lambda_m^{\nu_1\nu_2\nu_3\nu_4} \tag{C.15}$$

Similarly we get in the triplet channel

$$\Lambda_t^{\nu_1\nu_2\nu_3\nu_4} = \frac{1}{2}\Lambda_d^{\nu_1\nu_2\nu_3\nu_4} + \frac{1}{2}\Lambda_m^{\nu_1\nu_2\nu_3\nu_4} \tag{C.16}$$

C.3 Transition to AbinitioDΓA convention

The transition from four frequencies to the three frequency convention used in AbinitioDΓA is the following for the ph-objects (in the ph-notation)

$$A_{ph}^{\nu_1\nu_2\nu_3\nu_4} \equiv A_{ph}^{\nu_1\nu_4(\nu_1-\nu_2)} \tag{C.17}$$

and for the pp-objects (written in the pp-notation)

$$A_{pp}^{\nu_1\nu_2\nu_3\nu_4} \equiv A_{pp}^{\nu_1\nu_4(\nu_1+\nu_3)}. \tag{C.18}$$

Die approbierte gedruckte Originalversion dieser Dissertation ist an der TU Wien Bibliothek verfügbar.
The approved original version of this doctoral thesis is available in print at TU Wien Bibliothek.
TU Bibliothek WIEN Your knowledge hub

First we go back from four to three frequencies:

$$\Lambda_d^{\nu_1\nu_4(\nu_1-\nu_2)} = \Gamma_d^{\nu_1\nu_4(\nu_1-\nu_2)} + \frac{1}{2}\Phi_d^{\nu_1\nu_2(\nu_1-\nu_4)} + \frac{3}{2}\Phi_m^{\nu_1\nu_2(\nu_1-\nu_4)} - \frac{1}{2}\Phi_s^{\nu_1\nu_4(\nu_1+\nu_3)} - \frac{3}{2}\Phi_t^{\nu_1\nu_4(\nu_1+\nu_3)}. \tag{C.19}$$

Recalling the AbinitioDΓA convention for ν,ν', ω_{ph} we write the fully irredulcible vertex as:

$$\Lambda_d^{\nu\nu'\omega_{ph}} = \Gamma_d^{\nu\nu'\omega_{ph}} + \frac{1}{2}\Phi_d^{\nu(\nu-\omega_{ph})(\nu-\nu')} + \frac{3}{2}\Phi_m^{\nu(\nu-\omega_{ph})(\nu-\nu')} - \frac{1}{2}\Phi_s^{\nu\nu'\omega_{pp}} - \frac{3}{2}\Phi_t^{\nu\nu'\omega_{pp}}. \tag{C.20}$$

And finally as:

$$\Lambda_d^{\nu\nu'\omega_{ph}} = \Gamma_d^{\nu\nu'\omega_{ph}} + \frac{1}{2}\Phi_d^{\nu(\nu-\omega_{ph})(\nu-\nu')} + \frac{3}{2}\Phi_m^{\nu(\nu-\omega_{ph})(\nu-\nu')} - \frac{1}{2}\Phi_s^{\nu\nu'(\nu+\nu'-\omega_{ph})} - \frac{3}{2}\Phi_t^{\nu\nu'(\nu+\nu'-\omega_{ph})}. \tag{C.21}$$

The magnetic channel is analogous:

$$\Lambda_m^{\nu\nu'\omega_{ph}} = \Gamma_m^{\nu\nu'\omega_{ph}} + \frac{1}{2}\Phi_d^{\nu(\nu-\omega_{ph})(\nu-\nu')} - \frac{1}{2}\Phi_m^{\nu(\nu-\omega_{ph})(\nu-\nu')} + \frac{1}{2}\Phi_s^{\nu\nu'(\nu+\nu'-\omega_{ph})} - \frac{1}{2}\Phi_t^{\nu\nu'(\nu+\nu'-\omega_{ph})} \tag{C.22}$$

$$\Lambda_s^{\nu_1\nu_4(\nu_1+\nu_3)} = \Gamma_s^{\nu_1\nu_4(\nu_1+\nu_3)} - \frac{1}{2}\Phi_d^{\nu_1\nu_4(\nu_1-\nu_2)} + \frac{3}{2}\Phi_m^{\nu_1\nu_4(\nu_1-\nu_2)} - \frac{1}{2}\Phi_d^{\nu_1\nu_2(\nu_1-\nu_4)} + \frac{3}{2}\Phi_m^{\nu_1\nu_2(\nu_1-\nu_4)} \tag{C.23}$$

$$\Lambda_s^{\nu\nu'\omega_{pp}} = \Gamma_s^{\nu\nu'\omega_{pp}} - \frac{1}{2}\Phi_d^{\nu\nu'\omega_{ph}} + \frac{3}{2}\Phi_m^{\nu\nu'\omega_{ph}} - \frac{1}{2}\Phi_d^{\nu(\nu-\omega_{ph})(\nu-\nu')} + \frac{3}{2}\Phi_m^{\nu(\nu-\omega_{ph})(\nu-\nu')} \tag{C.24}$$

$$\Lambda_s^{\nu\nu'\omega_{pp}} = \Gamma_s^{\nu\nu'\omega_{pp}} - \frac{1}{2}\Phi_d^{\nu\nu'(\nu+\nu'-\omega_{pp})} + \frac{3}{2}\Phi_m^{\nu\nu'(\nu+\nu'-\omega_{pp})} - \frac{1}{2}\Phi_d^{\nu(\omega_{pp}-\nu')(\nu-\nu')} + \frac{3}{2}\Phi_m^{\nu(\omega_{pp}-\nu')(\nu-\nu')} \tag{C.25}$$

$$\Lambda_t^{\nu\nu'\omega_{pp}} = \Gamma_t^{\nu\nu'\omega_{pp}} - \frac{1}{2}\Phi_d^{\nu\nu'(\nu+\nu'-\omega_{pp})} - \frac{1}{2}\Phi_m^{\nu\nu'(\nu+\nu'-\omega_{pp})} + \frac{1}{2}\Phi_d^{\nu(\omega_{pp}-\nu')(\nu-\nu')} + \frac{1}{2}\Phi_m^{\nu(\omega_{pp}-\nu')(\nu-\nu')} \tag{C.26}$$

C.4 From four frequencies back to RMP convention

The recipe to go back from four to three frequencies in the convention of Rohringer et al. (2018) is

$$A_{ph}^{\nu_1\nu_2\nu_3\nu_4} \equiv A_{ph}^{\nu_1\nu_4(\nu_2-\nu_1)} \tag{C.27}$$

in the particle-hole channels and

$$A_{pp}^{\nu_1\nu_2\nu_3\nu_4} \equiv A_{pp}^{\nu_1\nu_4(\nu_1+\nu_3)}. \tag{C.28}$$

for the pp-objects, written in the pp-notation.

Die approbierte gedruckte Originalversion dieser Dissertation ist an der TU Wien Bibliothek verfügbar.
The approved original version of this doctoral thesis is available in print at TU Wien Bibliothek.
TU Bibliothek WIEN Your knowledge hub

Appendix D

Detailed derivation of symmetric improved estimators

This appendix is largely based on Kaufmann et al. (2019), for which the author has written most of the manuscript. Citations from there are marked by a vertical bar.

D.1 One-particle Symmetric Improved Estimator

The first-order equations (i.e. improved estimators) were already derived by Hafermann et al. (2012). We nevertheless give a detailed derivation to introduce notation and concepts necessary to derive higher-order estimators (i.e. symmetric improved estimators) in the following. This further sets the stage for the two-particle symmetric improved estimators.

The time derivative of the one-particle Green's function follows as:

$$\partial_{\tau_1} G_a(\tau_1, \tau_2) = -\partial_{\tau_1} \left\langle T_\tau \hat{d}_a(\tau_1) \hat{d}_a^\dagger(\tau_2) \right\rangle \tag{D.1}$$

$$= -\partial_{\tau_1} \left(\Theta(\tau_1 - \tau_2) \left\langle \hat{d}_a(\tau_1) \hat{d}_a^\dagger(\tau_2) \right\rangle - \Theta(\tau_2 - \tau_1) \left\langle \hat{d}_a^\dagger(\tau_2) \hat{d}_a(\tau_1) \right\rangle \right) \tag{D.2}$$

$$= -\delta(\tau_1 - \tau_2) \left\langle \underbrace{\{\hat{d}_a, \hat{d}_a^\dagger\}}_{=1}(\tau_1) \right\rangle - \left\langle T_\tau (\partial_{\tau_1} \hat{d}_a(\tau_1)) \hat{d}_a^\dagger(\tau_2) \right\rangle \tag{D.3}$$

$$= -\delta(\tau_1 - \tau_2) - \left\langle T_\tau [H_{\mathrm{AIM}}, \hat{d}_a](\tau_1) \hat{d}_a^\dagger(\tau_2) \right\rangle. \tag{D.4}$$

The commutator between the local Hamiltonian and the impurity-annihilation operator on

Die approbierte gedruckte Originalversion dieser Dissertation ist an der TU Wien Bibliothek verfügbar.
The approved original version of this doctoral thesis is available in print at TU Wien Bibliothek.
TU Bibliothek WIEN Your knowledge hub

the right hand side can be calculated as:

$$[H_{\mathrm{AIM}}, \hat{d}_a] = \frac{1}{2}\sum_{ijkl} U_{ijkl}(\hat{d}_i^\dagger \hat{d}_j^\dagger \hat{d}_l \hat{d}_k \hat{d}_a - \hat{d}_a \hat{d}_i^\dagger \hat{d}_j^\dagger \hat{d}_l \hat{d}_k) + \sum_i \tilde{\varepsilon}_i(\hat{d}_i^\dagger \hat{d}_i \hat{d}_a - \hat{d}_a \hat{d}_i^\dagger \hat{d}_i)$$
$$+ \sum_{Ki}(V_K^{ii})^*(\hat{d}_i^\dagger \hat{c}_{Ki}\hat{d}_a - \hat{d}_a \hat{d}_i^\dagger \hat{c}_{Ki}) \tag{D.5}$$
$$= \frac{1}{2}\sum_{ijkl} U_{ijkl}(\hat{d}_i^\dagger \delta_{aj} \hat{d}_l \hat{d}_k - \delta_{ai}\hat{d}_j^\dagger \hat{d}_l \hat{d}_k) - \sum_i \tilde{\varepsilon}_i \delta_{ai}\hat{d}_i - \sum_{Ki}(V_K^{ii})^* \delta_{ai}\hat{c}_{Ki} \tag{D.6}$$
$$= -\sum_{jkl} U_{[aj]kl}\hat{d}_j^\dagger \hat{d}_l \hat{d}_k - \tilde{\varepsilon}_a \hat{d}_a - \sum_K (V_K^{aa})^* \hat{c}_{Ka}, \tag{D.7}$$

with hybridization V_K^{aa} and the anti-symmetrizations of the interaction matrix:

$$\frac{1}{2}\left(U_{ijkl} - U_{jikl}\right) =: U_{[ij]kl} \tag{D.8}$$
$$\frac{1}{2}\left(U_{ijkl} - U_{ijlk}\right) =: U_{ij[kl]}. \tag{D.9}$$

It is convenient to introduce new operators for the contractions of the interaction matrix with three local operators:

$$\hat{q}_a = \sum_{jkl} U_{[aj]kl}\hat{d}_j^\dagger \hat{d}_l \hat{d}_k \tag{D.10}$$
$$\hat{q}_a^\dagger = \sum_{mno} U_{mn[ao]}\hat{d}_m^\dagger \hat{d}_n^\dagger \hat{d}_o. \tag{D.11}$$

With these equal-time three-particle operators, the one-particle Green's function follows as:

$$\partial_{\tau_1} G_a(\tau_1, \tau_2) = -\delta(\tau_1 - \tau_2) + \left\langle T_\tau \hat{q}_a(\tau_1)\hat{d}_a^\dagger(\tau_2)\right\rangle + \left\langle T_\tau \tilde{\varepsilon}_a \hat{d}_a(\tau_1)\hat{d}_a^\dagger(\tau_2)\right\rangle$$
$$+ \left\langle T_\tau \sum_K (V_K^{aa})^* \hat{c}_{Ka}(\tau_1)\hat{d}_a^\dagger(\tau_2)\right\rangle, \tag{D.12}$$

which is the equation of motion for the impurity Green's function of the AIM. The mixed impurity-bath Green's function can be further calculated by applying the above procedure onto the bath operator once again:

$$\partial_{\tau_1}\left\langle T_\tau \hat{c}_{Ka}(\tau_1)\hat{d}_a^\dagger(\tau_2)\right\rangle = \delta(\tau_1 - \tau_2)\left\langle \underbrace{\{\hat{c}_{Ka}, \hat{d}_a^\dagger\}}_{=0}(\tau_1)\right\rangle + \left\langle T_\tau[H_{\mathrm{AIM}}, \hat{c}_{Ka}](\tau_1)\hat{d}_a^\dagger(\tau_2)\right\rangle \tag{D.13}$$

Here, the commutator between the local Hamiltonian and the bath-annihilation operator can be calculated as:

$$[H_{\mathrm{AIM}}, \hat{c}_{Ka}] = \sum_{K'i} \varepsilon_{K'i}(\hat{c}_{K'i}^\dagger \hat{c}_{K'i}\hat{c}_{Ka} - \hat{c}_{Ka}\hat{c}_{K'i}^\dagger \hat{c}_{K'i}) + \sum_{K'i} V_{K'}^{ii}(\hat{c}_{K'i}^\dagger \hat{d}_i \hat{c}_{Ka} - \hat{c}_{Ka}\hat{c}_{K'i}^\dagger \hat{d}_i) \tag{D.14}$$
$$= -\sum_{K'i} \varepsilon_{K'i}\delta_{KK'}\delta_{ai}\hat{c}_{K'i} - \sum_{K'i} V_{K'}^{ii}\delta_{KK'}\delta_{ai}\hat{d}_i. \tag{D.15}$$

Die approbierte gedruckte Originalversion dieser Dissertation ist an der TU Wien Bibliothek verfügbar.
The approved original version of this doctoral thesis is available in print at TU Wien Bibliothek.
TU Bibliothek WIEN Your knowledge hub

Thus we can relate the time-derivative of the mixed impurity-bath Green's function to the impurity Green's function:

$$(\partial_{\tau_1} + \varepsilon_{Ka})\left\langle T_\tau \hat{c}_{Ka}(\tau_1)\hat{d}_a^\dagger(\tau_2)\right\rangle = -V_K^{aa}\left\langle T_\tau \hat{d}_a(\tau_1)\hat{d}_a^\dagger(\tau_2)\right\rangle. \tag{D.16}$$

In order to insert this into Eq. (D.12), we have to Fourier-transform the above expression with respect to τ_1:

$$\int_0^\beta \mathrm{d}\tau_1 e^{i\nu_1\tau_1}\partial_{\tau_1}\left\langle T_\tau \hat{c}_{Ka}(\tau_1)\hat{d}_a^\dagger(\tau_2)\right\rangle = -\int_0^\beta \mathrm{d}\tau_1 e^{i\nu_1\tau_1}\left[\varepsilon_{Ka}\left\langle T_\tau \hat{c}_{Ka}(\tau_1)\hat{d}_a^\dagger(\tau_2)\right\rangle + V_K^{aa}\left\langle T_\tau \hat{d}_a(\tau_1)\hat{d}_a^\dagger(\tau_2)\right\rangle\right]$$

Now the expression on the left-hand side of Eq. (D.17) can be simplified by integration by parts and we have

$$\int_0^\beta \mathrm{d}\tau_1 e^{i\nu_1\tau_1}\left\langle T_\tau \hat{c}_{Ka}(\tau_1)\hat{d}_a^\dagger(\tau_2)\right\rangle = \frac{V_K^{aa}}{i\nu_1 - \varepsilon_{Ka}}\int_0^\beta \mathrm{d}\tau_1 e^{i\nu_1\tau_1}\left\langle T_\tau \hat{d}_a(\tau_1)\hat{d}_a^\dagger(\tau_2)\right\rangle \tag{D.17}$$

Applying the same Fourier transform and integration by parts also to Eq. (D.12) allows us to insert the above result and we get

$$\begin{aligned} i\nu_1\int_0^\beta \mathrm{d}\tau_1 e^{i\nu_1\tau_1}\left\langle T_\tau \hat{d}_a(\tau_1)\hat{d}_a^\dagger(\tau_2)\right\rangle = &-\int_0^\beta \mathrm{d}\tau_1 e^{i\nu_1\tau_1}\delta(\tau_1-\tau_2) \\ &+\int_0^\beta \mathrm{d}\tau_1 e^{i\nu_1\tau_1}\left\langle T_\tau \hat{q}_a(\tau_1)\hat{d}_a^\dagger(\tau_2)\right\rangle \\ &+\tilde{\varepsilon}\int_0^\beta \mathrm{d}\tau_1 e^{i\nu_1\tau_1}\left\langle T_\tau \hat{d}_a(\tau_1)\hat{d}_a^\dagger(\tau_2)\right\rangle \\ &+\underbrace{\sum_K \frac{V_K^{aa}(V_K^{aa})^*}{i\nu_1 - \varepsilon_{Ka}}}_{\Delta_a^{\nu_1}}\int_0^\beta \mathrm{d}\tau_1 e^{i\nu_1\tau_1}\left\langle T_\tau \hat{d}_a(\tau_1)\hat{d}_a^\dagger(\tau_2)\right\rangle \end{aligned} \tag{D.18}$$

Now the terms can be regrouped to express the Green's function:

$$\begin{aligned} &\underbrace{(i\nu_1 - \tilde{\varepsilon}_a - \Delta_a^{\nu_1})}_{[\mathcal{G}_a^{\nu_1}]^{-1}}\int_0^\beta \mathrm{d}\tau_1 e^{i\nu_1\tau_1}\left\langle T_\tau \hat{d}_a(\tau_1)\hat{d}_a^\dagger(\tau_2)\right\rangle \\ &\qquad = -\int_0^\beta \mathrm{d}\tau_1 e^{i\nu_1\tau_1}\left[\delta(\tau_1-\tau_2) - \left\langle T_\tau \hat{q}_a(\tau_1)\hat{d}_a^\dagger(\tau_2)\right\rangle\right] \end{aligned} \tag{D.19}$$

This expression can be Fourier-transformed with respect to τ_2 by applying $\int_0^\beta \mathrm{d}\tau_2 \exp(-i\nu_2\tau_2)$ to both sides of the equation. Considering the definitions of the Green's function and the function ξ, one arrives at Eq. (3.39).

Die approbierte gedruckte Originalversion dieser Dissertation ist an der TU Wien Bibliothek verfügbar.
The approved original version of this doctoral thesis is available in print at TU Wien Bibliothek.
TU Bibliothek WIEN Your knowledge hub

In order to obtain the symmetric improved estimator, the equal-time two-particle Green's function is differentiated with respect to the impurity creation operator at time τ_2, such that:

$$\partial_{\tau_2}\left\langle T_\tau \hat{q}(\tau_1)\hat{d}_a^\dagger(\tau_2)\right\rangle = -\delta(\tau_1-\tau_2)\left\langle\{\hat{q}_a,\hat{d}_a^\dagger\}(\tau_1)\right\rangle + \left\langle T_\tau \hat{q}_a(\tau_1)[H_{\mathrm{AIM}},\hat{d}_a^\dagger](\tau_2)\right\rangle. \tag{D.20}$$

The anti-commutator $\{\hat{q}_a,\hat{d}_a^\dagger\}$ for diagonal hybridization functions follows as:

$$\{\hat{q}_a,\hat{d}_a^\dagger\} = \left\langle \sum_{jkl} U_{[aj]kl}(\hat{d}_j^\dagger\hat{d}_l\delta_{ak} - \hat{d}_j^\dagger\delta_{al}\hat{d}_k)(\tau_1)\right\rangle \tag{D.21}$$

$$= 2\sum_j U_{[aj][aj]}n_j \tag{D.22}$$

The commutator between the local Hamiltonian and the creation operator is calculated in analogy to Eq.(D.5) and follows as:

$$[H_{\mathrm{AIM}},\hat{d}_a^\dagger] = \hat{q}_a^\dagger + \tilde{\varepsilon}_a\hat{d}_a^\dagger + \sum_K V_K^{aa}\hat{c}_{Ka}^\dagger. \tag{D.23}$$

Thus:

$$\begin{aligned}\partial_{\tau_2}\left\langle T_\tau \hat{q}_a(\tau_1)\hat{d}_a^\dagger(\tau_2)\right\rangle = &-2\delta(\tau_1-\tau_2)\sum_j U_{[aj][aj]}n_j + \left\langle T_\tau \hat{q}_a(\tau_1)\hat{q}_a^\dagger(\tau_2)\right\rangle \\ &+ \left\langle T_\tau \hat{q}_a(\tau_1)\tilde{\varepsilon}_a\hat{d}_a^\dagger(\tau_2)\right\rangle + \left\langle T_\tau \hat{q}_a(\tau_1)\sum_K V_K^{aa}\hat{c}_{Ka}^\dagger(\tau_2)\right\rangle.\end{aligned}$$

The mixed bath-impurity expectation value is calculated in analogy to Eqs.(D.14)-(D.16) and follows as:

$$\partial_{\tau_2}\left\langle T_\tau \hat{q}_a(\tau_1)\hat{c}_{Ka}^\dagger(\tau_2)\right\rangle = \left\langle T_\tau \hat{q}_a(\tau_1)[H_{\mathrm{AIM}},\hat{c}_{Ka}^\dagger](\tau_2)\right\rangle \tag{D.24}$$

$$(\partial_{\tau_2}-\varepsilon_{Ka})\left\langle T_\tau \hat{q}_a(\tau_1)\hat{c}_{Ka}^\dagger(\tau_2)\right\rangle = (V_K^{aa})^*\left\langle T_\tau \hat{q}_a(\tau_1)\hat{d}_a^\dagger(\tau_2)\right\rangle. \tag{D.25}$$

This allows one to express the mixed bath-impurity expectation value as an impurity expectation value. Again the equation can be made algebraic by Fourier transforming it, but this time with respect to τ_2:

$$\int_0^\beta \mathrm{d}\tau_2 e^{-i\nu_2\tau_2}\left\langle T_\tau \hat{q}_a(\tau_1)\hat{c}^\dagger Ka(\tau_2)\right\rangle = \frac{(V_K^{aa})^*}{i\nu_2-\varepsilon_{Ka}}\int_0^\beta \mathrm{d}\tau_2 e^{-i\nu_2\tau_2}\left\langle T_\tau \hat{q}_a(\tau_1)\hat{d}_a^\dagger(\tau_2)\right\rangle \tag{D.26}$$

Die approbierte gedruckte Originalversion dieser Dissertation ist an der TU Wien Bibliothek verfügbar.
The approved original version of this doctoral thesis is available in print at TU Wien Bibliothek.
TU Bibliothek WIEN Your knowledge hub

Re-inserting into the (Fourier-transformed) Eq.(D.24) gives:

$$
\begin{aligned}
i\nu_2 \int_0^\beta \mathrm{d}\tau_2 e^{-i\nu_2\tau_2} \left\langle T_\tau \hat{q}_a(\tau_1)\hat{d}_a^\dagger(\tau_2)\right\rangle = &- \int_0^\beta \mathrm{d}\tau_2 e^{-i\nu_2\tau_2}\delta(\tau_1-\tau_2)\sum_j U_{[aj][aj]} n_j \\
&+ \int_0^\beta \mathrm{d}\tau_2 e^{-i\nu_2\tau_2} \left\langle T_\tau \hat{q}_a(\tau_1)\hat{q}_a^\dagger(\tau_2)\right\rangle \\
&+ \tilde{\varepsilon}_a \int_0^\beta \mathrm{d}\tau_2 e^{-i\nu_2\tau_2} \left\langle T_\tau \hat{q}_a(\tau_1)\hat{d}_a^\dagger(\tau_2)\right\rangle \\
&+ \underbrace{\sum_K \frac{V_K^{aa}(V_K^{aa})^*}{i\nu_2 - \varepsilon_{Ka}}}_{\Delta_a^{\nu_2}} \int_0^\beta \mathrm{d}\tau_2 e^{-i\nu_2\tau_2} \left\langle T_\tau \hat{q}_a(\tau_1)\hat{d}_a^\dagger(\tau_2)\right\rangle
\end{aligned}
$$

Rearranging gives:

$$
\begin{aligned}
&\underbrace{(i\nu_2 - \tilde{\varepsilon}_a - \Delta_a^{\nu_2})}_{[\mathcal{G}_a^{\nu_2}]^{-1}} \int_0^\beta \mathrm{d}\tau_2 e^{-i\nu_2\tau_2} \left\langle T_\tau \hat{q}_a(\tau_1)\hat{d}_a^\dagger(\tau_2)\right\rangle \\
&\qquad = -\int_0^\beta \mathrm{d}\tau_2 e^{-i\nu_2\tau_2} \left[2\sum_j U_{[aj][aj]} n_j \delta(\tau_1-\tau_2) - \left\langle T_\tau \hat{q}_a(\tau_1)\hat{q}_a^\dagger(\tau_2)\right\rangle\right]
\end{aligned} \tag{D.27}
$$

Together with the definitions of Table 3.1 we obtain the one-particle symmetric improved estimator Eq. (3.43):

$$
G_a^\nu = \mathcal{G}_a^\nu + [\mathcal{G}_a^\nu]^2 \left(2\sum_j U_{[aj][aj]} n_j + \vartheta_a^\nu\right). \tag{D.28}
$$

D.2 Two-particle Symmetric Improved Estimator

In the following we derive the two-particle symmetric improved estimators. Again the conventional improved estimators were already derived by Hafermann et al. (2012). The procedure in deriving the higher order (up to fourth-order) equations is in principle equivalent to the one-particle symmetric improved estimators. Nevertheless, the equations are more involved due to the necessity of considering multiple hierarchies of equations of motions. Repeating derivations (such as the explicit calculation of mixed impurity-bath expectation values) are omitted.

Die approbierte gedruckte Originalversion dieser Dissertation ist an der TU Wien Bibliothek verfügbar.
The approved original version of this doctoral thesis is available in print at TU Wien Bibliothek.
TU Bibliothek WIEN Your knowledge hub

First Order

Applying the time derivative onto the first annihilation operator of the two-particle Green's function gives:

$$\partial_{\tau_1} G^{\tau_1,\tau_2,\tau_3,\tau_4}_{abcd} = R_1 + \left\langle T_\tau \underbrace{[H_{\mathrm{AIM}}, \hat{d}_a]}_{-\hat{q}_a - \tilde{\varepsilon}_a \hat{d}_a - \sum_K (V_K^{aa})^* \hat{c}_{Ka}}(\tau_1)\hat{d}_b^\dagger(\tau_2)\hat{d}_c(\tau_3)\hat{d}_d^\dagger(\tau_4)\right\rangle \tag{D.29}$$

$$(\partial_{\tau_1} + \tilde{\varepsilon}_a)\, G^{\tau_1,\tau_2,\tau_3,\tau_4}_{abcd} = R_1 - \underbrace{\left\langle T_\tau \hat{q}_a(\tau_1)\hat{d}_b^\dagger(\tau_2)\hat{d}_c(\tau_3)\hat{d}_d^\dagger(\tau_4)\right\rangle}_{=:S_1} - \underbrace{\left\langle T_\tau \sum_K (V_K^{aa})^* \hat{c}_{Ka}(\tau_1)\hat{d}_b^\dagger(\tau_2)\hat{d}_c(\tau_3)\hat{d}_d^\dagger(\tau_4)\right\rangle}_{\to \Delta_a^{\nu_1}\, G^{\nu_1,\tau_2,\tau_3,\tau_4}_{abcd}} \tag{D.30}$$

Again, Fourier transformation with respect to the first time argument converts the differential equation to an algebraic one, and we have

$$G^{\nu_1,\tau_2,\tau_3,\tau_4}_{abcd} = \mathcal{G}^{\nu_1}_a \left(-R^{\nu_1,\tau_2,\tau_3,\tau_4}_{1,abcd} + S^{\nu_1,\tau_2,\tau_3,\tau_4}_{1,abcd}\right). \tag{D.31}$$

R_1 describes the equal-time contribution due to the derivation of the time-ordering operator:

$$R^{\tau_1,\tau_2,\tau_3,\tau_4}_{1,abcd} = \delta(\tau_1 - \tau_2)\left\langle T_\tau\{\hat{d}_a, \hat{d}_b^\dagger\}(\tau_1)\hat{d}_c(\tau_3)\hat{d}_d^\dagger(\tau_4)\right\rangle + \delta(\tau_1 - \tau_4)\left\langle T_\tau\{\hat{d}_a, \hat{d}_d^\dagger\}(\tau_1)\hat{d}_b^\dagger(\tau_2)\hat{d}_c(\tau_3)\right\rangle \tag{D.32}$$

$$= \delta(\tau_2 - \tau_2)\delta_{ab} \underbrace{\left\langle T_\tau \hat{d}_c(\tau_3)\hat{d}_d^\dagger(\tau_4)\right\rangle}_{-G^{\tau_3\tau_4}_{cd}} - \delta(\tau_1 - \tau_4)\delta_{ad} \underbrace{\left\langle T_\tau \hat{d}_c(\tau_3)\hat{d}_b^\dagger(\tau_2)\right\rangle}_{-G^{\tau_3\tau_2}_{cb}} \tag{D.33}$$

At this stage one can already observe that it is possible to apply further (imaginary) time derivatives, or equivalently, hierarchies of equations of motion onto the R_1 term. The corresponding time-derivatives of the one-particle Green's function are given by the one-particle symmetric improved estimators and where already calculated explicitly in Appendix D.1.

Die approbierte gedruckte Originalversion dieser Dissertation ist an der TU Wien Bibliothek verfügbar.
The approved original version of this doctoral thesis is available in print at TU Wien Bibliothek.
TU Bibliothek WIEN Your knowledge hub

Second Order

Applying the time derivative onto the first creation operator of S_1 gives:

$$\partial_{\tau_2} S_1 = R_2 + \left\langle T_\tau \hat{q}_a(\tau_1) \underbrace{[H_{\mathrm{AIM}}, \hat{d}_b^\dagger]}_{\hat{q}_b^\dagger + \tilde{\varepsilon}_b \hat{d}_b^\dagger + \sum_K V_K^{bb} \hat{c}_{Kb}^\dagger}(\tau_2) \hat{d}_c(\tau_3) \hat{d}_d^\dagger(\tau_4) \right\rangle \tag{D.34}$$

$$(\partial_{\tau_2} - \tilde{\varepsilon}_b) S_1 = R_2 + \underbrace{\left\langle T_\tau \hat{q}_a(\tau_1) \hat{q}_b^\dagger(\tau_2) \hat{d}_c(\tau_3) \hat{d}_d^\dagger(\tau_4) \right\rangle}_{=: S_2} + \underbrace{\left\langle T_\tau \hat{q}_a(\tau_1) \sum_K V_K^{bb} \hat{c}_{Kb}^\dagger(\tau_2) \hat{d}_c(\tau_3) \hat{d}_d^\dagger(\tau_4) \right\rangle}_{\to \Delta_b^{\nu_2} S_1^{\tau_1, \nu_2, \tau_3, \tau_4}} \tag{D.35}$$

$$S_1^{\tau_1, \nu_2, \tau_3, \tau_4} = \mathcal{G}_b^{\nu_2} \left(R_2^{\tau_1, \nu_2, \tau_3, \tau_4} + S_2^{\tau_1, \nu_2, \tau_3, \tau_4} \right) \tag{D.36}$$

Fourier-transforming this also with respect to τ_1 and plugging it into Eq. (D.31) yields:

$$G_{abcd}^{\nu_1, \nu_2, \tau_3, \tau_4} = \mathcal{G}_a^{\nu_1} \left(-R_{1,abcd}^{\nu_1, \nu_2, \tau_3, \tau_4} + \mathcal{G}_b^{\nu_2} \times \left(R_{2,abcd}^{\nu_1, \nu_2, \tau_3, \tau_4} + S_{2,abcd}^{\nu_1, \nu_2, \tau_3, \tau_4} \right) \right) \tag{D.37}$$

R_2 describes the equal-time contribution due to the derivation of the time-ordering operator of S_1:

$$R_{2,abcd}^{\tau_1, \tau_2, \tau_3, \tau_4} = -\delta(\tau_1 - \tau_2) \left\langle T_\tau \underbrace{\{\hat{q}_a, \hat{d}_b^\dagger\}}_{2 \sum_{ef} U_{[ae][bf]} \hat{d}_e^\dagger \hat{d}_f}(\tau_1) \hat{d}_c(\tau_3) \hat{d}_d^\dagger(\tau_4) \right\rangle + \delta(\tau_2 - \tau_3) \left\langle T_\tau \hat{q}_a(\tau_1) \{\hat{d}_b^\dagger, \hat{d}_c\}(\tau_2) \hat{d}_d^\dagger(\tau_4) \right\rangle \tag{D.38}$$

$$= -2\delta(\tau_1 - \tau_2) \left\langle T_\tau \sum_{ef} U_{[ae][bf]} \hat{d}_e^\dagger \hat{d}_f(\tau_1) \hat{d}_c(\tau_3) \hat{d}_d^\dagger(\tau_4) \right\rangle + \delta(\tau_2 - \tau_3) \delta_{bc} \left\langle T_\tau \hat{q}_a(\tau_1) \hat{d}_d^\dagger(\tau_4) \right\rangle \tag{D.39}$$

Time derivatives of R_2 with respect to τ_3 and τ_4 are shown below.

Third Order

Applying the time derivative onto the remaining annihilation operator of S_2 gives:

$$\partial_{\tau_3} S_2 = R_3 + \left\langle T_\tau \hat{q}_a(\tau_1) \hat{q}_b^\dagger(\tau_2) \underbrace{[H_{\mathrm{AIM}}, \hat{d}_c]}_{-\hat{q}_c - \tilde{\varepsilon}_c \hat{d}_c - \sum_K (V_K^{cc})^* \hat{c}_{Kc}}(\tau_3) \hat{d}_d^\dagger(\tau_4) \right\rangle \tag{D.40}$$

$$(\partial_{\tau_3} + \tilde{\varepsilon}_c) S_2 = R_3 - \underbrace{\left\langle T_\tau \hat{q}_a(\tau_1) \hat{q}_b^\dagger(\tau_2) \hat{q}_c(\tau_3) \hat{d}_d^\dagger(\tau_4) \right\rangle}_{=: S_3} - \underbrace{\left\langle T_\tau \hat{q}_a(\tau_1) \hat{q}_b^\dagger(\tau_2) \sum_K (V_K^{cc})^* \hat{c}_{Kc}(\tau_3) \hat{d}_d^\dagger(\tau_4) \right\rangle}_{\to \Delta_c^{\nu_3} S_2} \tag{D.41}$$

$$S_{2,abcd}^{\tau_1, \tau_2, \nu_3, \tau_4} = \mathcal{G}_c^{\nu_3} \left(-R_{3,abcd}^{\tau_1, \tau_2, \nu_3, \tau_4} + S_{3,abcd}^{\tau_1, \tau_2, \nu_3, \tau_4} \right) \tag{D.42}$$

Die approbierte gedruckte Originalversion dieser Dissertation ist an der TU Wien Bibliothek verfügbar.
The approved original version of this doctoral thesis is available in print at TU Wien Bibliothek.
TU Bibliothek WIEN Your knowledge hub

Fourier-transforming this expression for S_2 now also with respect to τ_1 and τ_2, and plugging it into Eq. (D.37) yields:

$$G^{\nu_1,\nu_2,\nu_3,\tau_4}_{abcd} = \mathcal{G}^{\nu_1}_a\Big(- R^{\nu_1,\nu_2,\nu_3,\tau_4}_{1,abcd} + \mathcal{G}^{\nu_2}_b \times \Big(R^{\nu_1,\nu_2,\nu_3,\tau_4}_{2,abcd} + \mathcal{G}^{\nu_3}_c\Big(- R^{\nu_1,\nu_2,\nu_3,\tau_4}_{3,abcd} + S^{\nu_1,\nu_2,\nu_3,\tau_4}_{3,abcd}\Big)\Big)\Big) \tag{D.43}$$

R_3 describes the equal-time contribution due to the derivation of the time-ordering operator of S_2:

$$\begin{aligned}
R^{\tau_1,\tau_2,\tau_3,\tau_4}_{3,abcd} &= \delta(\tau_1-\tau_3)\Big\langle T_\tau \underbrace{\{\hat{q}_a, \hat{d}_c\}}_{\sum_{fg} U_{[ac]fg}\hat{d}_g\hat{d}_f}(\tau_1)\hat{q}^\dagger_b(\tau_2)\hat{d}^\dagger_d(\tau_4)\Big\rangle \\
&\quad - \delta(\tau_2-\tau_3)\Big\langle T_\tau \hat{q}_a(\tau_1)\underbrace{\{\hat{q}^\dagger_b, \hat{d}_c\}}_{2\sum_{ij} U_{[ci][bj]}\hat{d}^\dagger_i\hat{d}_j}(\tau_2)\hat{d}^\dagger_d(\tau_4)\Big\rangle \\
&\quad + \delta(\tau_3-\tau_4)\Big\langle T_\tau \hat{q}_a(\tau_1)\hat{q}^\dagger_b(\tau_2)\{\hat{d}_c, \hat{d}^\dagger_d\}(\tau_3)\Big\rangle \qquad \text{(D.44)} \\
&= \delta(\tau_1-\tau_3)\Big\langle T_\tau \sum_{fg} U_{[ac]fg}\hat{d}_g\hat{d}_f(\tau_1)\hat{q}^\dagger_b(\tau_2)\hat{d}^\dagger_d(\tau_4)\Big\rangle \\
&\quad - 2\delta(\tau_2-\tau_3)\Big\langle T_\tau \hat{q}_a(\tau_1)\sum_{ij} U_{[ci][bj]}\hat{d}^\dagger_i\hat{d}_j(\tau_2)\hat{d}^\dagger_d(\tau_4)\Big\rangle \\
&\quad + \delta(\tau_3-\tau_4)\delta_{cd}\Big\langle T_\tau \hat{q}_a(\tau_1)\hat{q}^\dagger_b(\tau_2)\Big\rangle \qquad \text{(D.45)}
\end{aligned}$$

Time derivatives of R_3 with respect to τ_4 are shown below.

Fourth Order

Applying the time derivative onto the remaining creation operator of S_3 gives:

$$\partial_{\tau_4} S_3 = R_4 + \Big\langle T_\tau \hat{q}_a(\tau_1)\hat{q}^\dagger_b(\tau_2)\hat{q}_c(\tau_3)\underbrace{[H_{\mathrm{AIM}}, \hat{d}^\dagger_d]}_{\hat{q}^\dagger_d + \tilde{\varepsilon}_d\hat{d}^\dagger_d + \sum_K V^{dd}_K \hat{c}^\dagger_{Kd}}(\tau_4)\Big\rangle \tag{D.46}$$

$$(\partial_{\tau_4} - \tilde{\varepsilon}_d)S_3 = R_4 + \underbrace{\Big\langle T_\tau \hat{q}_a(\tau_1)\hat{q}^\dagger_b(\tau_2)\hat{q}_c(\tau_3)\hat{q}^\dagger_d(\tau_4)\Big\rangle}_{=:S_4} + \underbrace{\Big\langle T_\tau \hat{q}_a(\tau_1)\hat{q}^\dagger_b(\tau_2)\hat{q}_c(\tau_3)\sum_K V^{dd}_K \hat{c}^\dagger_{Kd}(\tau_4)\Big\rangle}_{\to \Delta^{\nu_4}_d S_3} \tag{D.47}$$

$$S^{\tau_1,\tau_2,\tau_3,\nu_4}_{3,abcd} = \mathcal{G}^{\nu_4}_d\left(R^{\tau_1,\tau_2,\tau_3,\nu_4}_{4,abcd} + S^{\tau_1,\tau_2,\tau_3,\nu_4}_{4,abcd}\right) \tag{D.48}$$

Fourier-transforming S_3 with respect to the remaining time arguments and inserting it into Eq. (D.43) yields:

$$G^{\nu_1\nu_2\nu_3\nu_4}_{abcd} = \mathcal{G}^{\nu_1}_a\Big[-R^{\nu_1\nu_2\nu_3\nu_4}_{1,abcd} + \mathcal{G}^{\nu_2}_b\Big[R^{\nu_1\nu_2\nu_3\nu_4}_{2,abcd} + \mathcal{G}^{\nu_3}_c\Big(-R^{\nu_1\nu_2\nu_3\nu_4}_{3,abcd} + \mathcal{G}^{\nu_4}_d\Big(R^{\nu_1\nu_2\nu_3\nu_4}_{4,abcd} + S^{\nu_1\nu_2\nu_3\nu_4}_{4,abcd}\Big)\Big)\Big]\Big], \tag{D.49}$$

Die approbierte gedruckte Originalversion dieser Dissertation ist an der TU Wien Bibliothek verfügbar.
The approved original version of this doctoral thesis is available in print at TU Wien Bibliothek.
TU Bibliothek WIEN Your knowledge hub

where $S^{\nu_1,\nu_2,\nu_3,\nu_4}_{4,abcd} = h^{\nu_1,\nu_2,\nu_3,\nu_4}_{abcd}/\beta$, as defined in Table 3.1. R_4 describes the equal-time contribution due to the derivation of the time-ordering operator of S_3:

$$\begin{aligned}
R^{\tau_1,\tau_2,\tau_3,\tau_4}_{4,abcd} &= -\,\delta(\tau_1-\tau_4)\Big\langle T_\tau \underbrace{\{\hat{q}_a, \hat{d}^\dagger_d\}}_{2\sum_{ef} U_{[ae][df]}\hat{d}^\dagger_e \hat{d}_f}(\tau_1)\hat{q}^\dagger_b(\tau_2)\hat{q}_c(\tau_3)\Big\rangle \\
&\quad +\delta(\tau_2-\tau_4)\Big\langle T_\tau \hat{q}_a(\tau_1)\underbrace{\{\hat{q}^\dagger_b, \hat{d}^\dagger_d\}}_{\sum_{hi} U_{hi[bd]}\hat{d}^\dagger_h \hat{d}^\dagger_i}(\tau_2)\hat{q}_c(\tau_3)\Big\rangle \\
&\quad -\delta(\tau_3-\tau_4)\Big\langle T_\tau \hat{q}_a(\tau_1)\hat{q}^\dagger_b(\tau_2)\underbrace{\{\hat{q}_c, \hat{d}^\dagger_d\}}_{2\sum_{kl} U_{[ck][dl]}\hat{d}^\dagger_k \hat{d}_l}(\tau_3)\Big\rangle
\end{aligned} \tag{D.50}$$

$$\begin{aligned}
&= -2\delta(\tau_1-\tau_4)\Big\langle T_\tau \sum_{ef} U_{[ae][df]}\hat{d}^\dagger_e \hat{d}_f(\tau_1)\hat{q}^\dagger_b(\tau_2)\hat{q}_c(\tau_3)\Big\rangle \\
&\quad +\delta(\tau_2-\tau_4)\Big\langle T_\tau \hat{q}_a(\tau_1)\sum_{hi} U_{hi[bd]}\hat{d}^\dagger_h \hat{d}^\dagger_i(\tau_2)\hat{q}_c(\tau_3)\Big\rangle \\
&\quad -2\delta(\tau_3-\tau_4)\Big\langle T_\tau \hat{q}_a(\tau_1)\hat{q}^\dagger_b(\tau_2)\sum_{kl} U_{[ck][dl]}\hat{d}^\dagger_k \hat{d}_l(\tau_3)\Big\rangle
\end{aligned} \tag{D.51}$$

Unlike the previous terms R_1, R_2, R_3, the above R_4 cannot be derived any further.

Third and fourth order of R_2 and R_3

Looking at equation Eq. (D.49) one notices that in fact only R_4 and S_4 are multiplied by a product of four non-interacting Green's functions. R_1 consists of one-particle Green's functions, which can be expressed by their symmetric improved estimators. However, R_2 and R_3 are multiplied only by products of 2 and 3 non-interacting Green's functions, respectively. This means that we need to express them by their equations of motion recursively.
First, let us take a closer look at the first term of R_2, Eq. (D.39). It is very similar to the three-leg Green's function of Eq. (3.60), the only difference being in the operator ordering and the additional U-matrix. The following steps may therefore also serve as a derivation of the threeleg improved estimator.
Taking the time-derivative with respect to τ_3 generically yields

$$\partial_{\tau_3}\Big\langle T_\tau \sum_{ef} U_{[ae][bf]}\hat{d}^\dagger_e \hat{d}_f(\tau_1)\hat{d}_c(\tau_3)\hat{d}^\dagger_d(\tau_4)\Big\rangle = R_{21} + \Big\langle T_\tau \sum_{ef} U_{[ae][bf]}\hat{d}^\dagger_e \hat{d}_f(\tau_1)\partial_{\tau_3}\hat{d}_c(\tau_3)\hat{d}^\dagger_d(\tau_4)\Big\rangle \tag{D.52}$$

Die approbierte gedruckte Originalversion dieser Dissertation ist an der TU Wien Bibliothek verfügbar.
The approved original version of this doctoral thesis is available in print at TU Wien Bibliothek.
TU Bibliothek WIEN Your knowledge hub

Analogously as before, we express the time derivative by the Heisenberg equation of motion and Fourier-transform the equation with respect to τ_3 to make it algebraic. We thus obtain

$$\int_0^\beta \mathrm{d}\tau_3 e^{i\nu_3\tau_3}\Big\langle \sum_{ef} U_{[ae][bf]}\hat{d}_e^\dagger \hat{d}_f(\tau_1)\hat{d}_c(\tau_3)\hat{d}_d^\dagger(\tau_4)\Big\rangle$$
$$= \mathcal{G}_c^{\nu_3}\int_0^\beta \mathrm{d}\tau_3 e^{i\nu_3\tau_3}\Big[-R_{21}^{\tau_1,\tau_3,\tau_4} + \Big\langle \sum_{ef} U_{[ae][bf]}\hat{d}_e^\dagger \hat{d}_f(\tau_1)\hat{q}_c(\tau_3)\hat{d}_d^\dagger(\tau_4)\Big\rangle\Big] \quad \text{(D.53)}$$

The rest-term R_{21} that originates from the derivative of the time-ordering operator, is

$$R_{21}^{\tau_1,\tau_3,\tau_4} = \delta(\tau_1-\tau_3)\Big\langle T_\tau\Big[\sum_{ef} U_{[ae][bf]}\hat{d}_e^\dagger \hat{d}_f, \hat{d}_c\Big](\tau_3)\hat{d}_d^\dagger(\tau_4)\Big\rangle$$
$$+\delta(\tau_3-\tau_4)\Big\langle T_\tau \sum_{ef} U_{[ae][bf]}\hat{d}_e^\dagger \hat{d}_f\{\hat{d}_c, \hat{d}_d^\dagger\}(\tau_3)\Big\rangle. \quad \text{(D.54)}$$

We want to emphasize that due to the bosonic operator $\hat{d}^\dagger\hat{d}$, a commutator occurs in the first line. After evaluation of the commutator and anti-commutator, we get

$$R_{21}^{\tau_1,\tau_3,\tau_4} = \delta(\tau_1-\tau_3)U_{[ac][bd]}\Big\langle T_\tau \hat{d}_d(\tau_1)\hat{d}_d^\dagger(\tau_4)\Big\rangle + \delta(\tau_3-\tau_4)\delta_{cd}\sum_{ef} U_{[ae][bf]}n_{ef} \quad \text{(D.55)}$$

In order to obtain the final form, we also have to apply the equation of motion with respect to τ_4. In R_{21} this concerns only the first term. This is, however, just a one-particle Green's function and we can insert the improved-estimator formula Eq. (3.39) and we thus get

$$R_{21}^{\tau_1,\tau_3,\nu_4} = \delta(\tau_1-\tau_3)\sum_f U_{[ac][bf]}\mathcal{G}_d^{\nu_4}\Big[-e^{-i\nu_4\tau_1}\delta_{fd}$$
$$+\int_0^\beta \mathrm{d}\tau_4 e^{-i\nu_4\tau_4}\Big\langle T_\tau \hat{d}_f(\tau_1)\hat{q}_d^\dagger(\tau_4)\Big\rangle\Big] + e^{-i\nu_4\tau_3}\delta_{cd}\sum_{ef} U_{[ae][bf]}n_{ef} \quad \text{(D.56)}$$

Whereas the rest-term R_{21} contains only the one-particle improved estimator and the occupation number, we can differentiate the last term in equation Eq. (D.53) by its last time argument τ_4. The same procedure as above yields now

$$\int_0^\beta \mathrm{d}\tau_4 e^{-i\nu_4\tau_4}\Big\langle \sum_{ef} U_{[ae][bf]}\hat{d}_e^\dagger \hat{d}_f(\tau_1)\hat{q}_c(\tau_3)\hat{d}_d^\dagger(\tau_4)\Big\rangle$$
$$= \mathcal{G}_d^{\nu_4}\int_0^\beta \mathrm{d}\tau_4 e^{-i\nu_4\tau_4}\Big[R_{23}^{\tau_1,\tau_3,\tau_4} + \Big\langle \sum_{ef} U_{[ae][bf]}\hat{d}_e^\dagger \hat{d}_f(\tau_1)\hat{q}_c(\tau_3)\hat{q}^\dagger(\tau_4)\Big\rangle\Big] \quad \text{(D.57)}$$

Die approbierte gedruckte Originalversion dieser Dissertation ist an der TU Wien Bibliothek verfügbar.
The approved original version of this doctoral thesis is available in print at TU Wien Bibliothek.
TU Bibliothek WIEN Your knowledge hub

The rest-term R_{22} again requires some precaution, since it contains both a commutator and an anti-commutator:

$$\begin{aligned} R_{22}^{\tau_1,\tau_3,\tau_4} &= \delta(\tau_1-\tau_4)\Big\langle T_\tau\Big[\sum_{ef} U_{[ae][bf]}\hat{d}_e^\dagger\hat{d}_f, \hat{d}_d^\dagger\Big](\tau_1)\hat{q}_c(\tau_3)\Big\rangle \\ &\quad - \delta(\tau_3-\tau_4)\Big\langle T_\tau \sum_{ef} U_{[ae][bf]}\hat{d}_e^\dagger\hat{d}_f(\tau_1)\{\hat{q}_c, \hat{d}_d^\dagger\}(\tau_3)\Big\rangle \end{aligned} \tag{D.58}$$

After evaluation of the commutator and the anti-commutator, we obtain

$$\begin{aligned} R_{22}^{\tau_1,\tau_3,\tau_4} &= \delta(\tau_1-\tau_4)\Big\langle T_\tau \sum_{e} U_{[ae][bd]}\hat{d}_e^\dagger(\tau_1)\hat{q}_c(\tau_3)\Big\rangle \\ &\quad - 2\delta(\tau_3-\tau_4)\Big\langle \sum_{ef} U_{[ae][bf]}\hat{d}_e^\dagger\hat{d}_f(\tau_1)\sum_{gh} U_{[ag][bh]}\hat{d}_g^\dagger\hat{d}_h(\tau_3)\Big\rangle. \end{aligned} \tag{D.59}$$

We are now able to write down the full expression for R_2 by combining Eq. (D.39) with Eq. (D.56) and Eq. (D.59). Since in the end we need it in Matsubara frequencies, it is of advantage to perform a Fourier transform with respect to all time arguments already here. Furthermore this allows us to make the equation more compact by using the definitions of Table 3.1 and the relation $\langle T_\tau \hat{q}_j(\tau)\hat{d}_k^\dagger\rangle = \langle T_\tau \hat{d}_k(\tau)\hat{q}_j^\dagger\rangle$, such that we finally arrive at Eq. (3.53).

For R_3 we only have to apply the equation of motion with respect to τ_4 to the first two terms of Eq. (D.45). Again we perform a Fourier transform with respect to all time arguments and compactify the expression by the definitions of Table 3.1. Thus, we obtain Eq. (3.54).

Die approbierte gedruckte Originalversion dieser Dissertation ist an der TU Wien Bibliothek verfügbar.
The approved original version of this doctoral thesis is available in print at TU Wien Bibliothek.
TU Bibliothek WIEN Your knowledge hub

Die approbierte gedruckte Originalversion dieser Dissertation ist an der TU Wien Bibliothek verfügbar.
The approved original version of this doctoral thesis is available in print at TU Wien Bibliothek.
TU Bibliothek WIEN Your knowledge hub

Bibliography

Abrikosov, A. A., I. Dzyaloshinskii, and L. P. Gorkov (1975). "Methods of quantum field theory in statistical physics". New York, NY: Dover.

Aichhorn, Markus, Leonid Pourovskii, Priyanka Seth, Veronica Vildosola, Manuel Zingl, Oleg E. Peil, Xiaoyu Deng, Jernej Mravlje, Gernot J. Kraberger, Cyril Martins, Michel Ferrero, and Olivier Parcollet (2016). "TRIQS/DFTTools: A TRIQS application for ab initio calculations of correlated materials". *Computer Physics Communications* 204, pp. 200–208. ISSN: 0010-4655.

Aizaki, S., T. Yoshida, K. Yoshimatsu, M. Takizawa, M. Minohara, S. Ideta, A. Fujimori, K. Gupta, P. Mahadevan, K. Horiba, H. Kumigashira, and M. Oshima (2012). "Self-Energy on the Low- to High-Energy Electronic Structure of Correlated Metal $SrVO_3$". *Phys. Rev. Lett.* 109 (5), p. 056401.

Anderson, Donald G. (1965). "Iterative Procedures for Nonlinear Integral Equations". *J. ACM* 12.4, pp. 547–560. ISSN: 0004-5411.

Anderson, P. W. (1961). "Localized Magnetic States in Metals". *Phys. Rev.* 124 (1), pp. 41–53.

Anderson, P. W. (1972). "More Is Different". *Science* 177.4047, pp. 393–396. ISSN: 0036-8075.

Anisimov, V.I., I.A. Nekrasov, D.E. Kondakov, T.M. Rice, and M. Sigrist (2002). "Orbital-selective Mott-insulator transition in $Ca_{2-x}Sr_xRuO_4$". *Eur. Phys. J. B* 25, pp. 97–103.

Antipov, A. E., A. N. Rubtsov, M. I. Katsnelson, and A. I. Lichtenstein (2011). "Electron energy spectrum of the spin-liquid state in a frustrated Hubbard model". *Phys. Rev. B* 83 (11), p. 115126.

Antipov, Andrey E., Emanuel Gull, and Stefan Kirchner (2014). "Critical Exponents of Strongly Correlated Fermion Systems from Diagrammatic Multiscale Methods". *Phys. Rev. Lett.* 112 (22), p. 226401.

Aoki, Hideo, Naoto Tsuji, Martin Eckstein, Marcus Kollar, Takashi Oka, and Philipp Werner (2014). "Nonequilibrium dynamical mean-field theory and its applications". *Rev. Mod. Phys.* 86, p. 779.

Arita, R. and K. Held (2005). "Orbital-selective Mott-Hubbard transition in the two-band Hubbard model". *Phys. Rev. B* 72 (20), p. 201102.

Arya, S., P. V. Sriluckshmy, S. R. Hassan, and A.-M. S. Tremblay (2015). "Antiferromagnetism in the Hubbard model on the honeycomb lattice: A two-particle self-consistent study". *Phys. Rev. B* 92 (4), p. 045111.

Astleithner, K., A. Kauch, T. Ribic, and K. Held (2020). "Parquet dual fermion approach for the Falicov-Kimball model". *Phys. Rev. B* 101 (16), p. 165101.

Astretsov, Grigory V., Georg Rohringer, and Alexey N. Rubtsov (2020). "Dual parquet scheme for the two-dimensional Hubbard model: Modeling low-energy physics of high-T_c cuprates with high momentum resolution". *Phys. Rev. B* 101 (7), p. 075109.

Die approbierte gedruckte Originalversion dieser Dissertation ist an der TU Wien Bibliothek verfügbar.
The approved original version of this doctoral thesis is available in print at TU Wien Bibliothek.
TU Bibliothek WIEN Your knowledge hub

Ayral, Thomas and Olivier Parcollet (2015). "Mott physics and spin fluctuations: A unified framework". *Phys. Rev. B* 92 (11), p. 115109.

Ayral, Thomas and Olivier Parcollet (2016). "Mott physics and collective modes: An atomic approximation of the four-particle irreducible functional". *Phys. Rev. B* 94 (7), p. 075159.

Backes, S., T. C. Rödel, F. Fortuna, E. Frantzeskakis, P. Le Fèvre, F. Bertran, M. Kobayashi, R. Yukawa, T. Mitsuhashi, M. Kitamura, K. Horiba, H. Kumigashira, R. Saint-Martin, A. Fouchet, B. Berini, Y. Dumont, A. J. Kim, F. Lechermann, H. O. Jeschke, M. J. Rozenberg, R. Valenti, and A. F. Santander-Syro (2016). "Hubbard band versus oxygen vacancy states in the correlated electron metal $SrVO_3$". *Phys. Rev. B* 94 (24), p. 241110.

Banerjee, Amartya S., Phanish Suryanarayana, and John E. Pask (2016). "Periodic Pulay method for robust and efficient convergence acceleration of self-consistent field iterations". *Chemical Physics Letters* 647, pp. 31–35. ISSN: 0009-2614.

Basov, D. N., Richard D. Averitt, Dirk van der Marel, Martin Dressel, and Kristjan Haule (2011). "Electrodynamics of correlated electron materials". *Rev. Mod. Phys.* 83 (2), pp. 471–541.

Bauer, B., L. Cincio, B. P. Keller, M. Dolfi, G. Vidal, S. Trebst, and A.W.W. Ludwig (2014). "Chiral spin liquid and emergent anyons in a Kagome lattice Mott insulator". *Nat. Commun.* 5, p. 5137.

Bauernfeind, Daniel, Manuel Zingl, Robert Triebl, Markus Aichhorn, and Hans Gerd Evertz (2017). "Fork Tensor-Product States: Efficient Multiorbital Real-Time DMFT Solver". *Phys. Rev. X* 7 (3), p. 031013.

Bednorz, J. G. and K. A. Müller (1986). "Possible highTc superconductivity in the Ba-La-Cu-O system". *Zeitschrift für Physik B Condensed Matter* 64.2, pp. 189–193. ISSN: 1431-584X.

Berger, C.E., L. Rammelmüller, A.C. Loheac, F. Ehmann, J. Braun, and J.E. Drut (2021). "Complex Langevin and other approaches to the sign problem in quantum many-body physics". *Physics Reports* 892. Complex Langevin and other approaches to the sign problem in quantum many-body physics, pp. 1–54. ISSN: 0370-1573.

Bergeron, Dominic and A.-M. S. Tremblay (2016). "Algorithms for optimized maximum entropy and diagnostic tools for analytic continuation". *Phys. Rev. E* 94 (2), p. 023303.

Bergman, Doron L., Congjun Wu, and Leon Balents (2008). "Band touching from real-space topology in frustrated hopping models". *Phys. Rev. B* 78 (12), p. 125104.

Bhandary, Sumanta, Elias Assmann, Markus Aichhorn, and Karsten Held (2016). "Charge self-consistency in density functional theory combined with dynamical mean field theory: *k*-space reoccupation and orbital order". *Phys. Rev. B* 94 (15), p. 155131.

Bickers, N. E. (2004). "Self-Consistent Many-Body Theory for Condensed Matter Systems". *Theoretical Methods for Strongly Correlated Electrons. CRM Series in Mathematical Physics.* Ed. by D. Sénéchal, A.-M. Tremblay, and C. Bourbonnais. Springer.

Biermann, S., L. de'Medici, and A. Georges (2005). "Non-Fermi-Liquid Behavior and Double-Exchange Physics in Orbital-Selective Mott Systems". *Phys. Rev. Lett.* 95 (20), p. 206401.

Die approbierte gedruckte Originalversion dieser Dissertation ist an der TU Wien Bibliothek verfügbar.
The approved original version of this doctoral thesis is available in print at TU Wien Bibliothek.
TU Bibliothek WIEN Your knowledge hub

Blaha, Peter et al. (2001). "wien2k: An augmented plane wave + local orbitals program for calculating crystal properties", Technische Universität Wien, Vienna.

Blankenbecler, R., D. J. Scalapino, and R. L. Sugar (1981). "Monte Carlo calculations of coupled boson-fermion systems. I". *Phys. Rev. D* 24 (8), pp. 2278–2286.

Bloch, Felix (1929). "Über die Quantenmechanik der Elektronen in Kristallgittern". *Zeitschrift für Physik* 52.7, pp. 555–600. ISSN: 0044-3328.

Boehnke, L., F. Nilsson, F. Aryasetiawan, and P. Werner (2016). "When strong correlations become weak: Consistent merging of GW and DMFT". *Phys. Rev. B* 94 (20), p. 201106.

Bryan, R. K. (1990). "Maximum entropy analysis of oversampled data problems". *European Biophysics Journal* 18.3, pp. 165–174. ISSN: 1432-1017.

Budnik, Ran and Assa Auerbach (2004). "Low-Energy Singlets in the Heisenberg Antiferromagnet on the Kagome Lattice". *Phys. Rev. Lett.* 93, p. 187205.

Bulla, Ralf, Theo A. Costi, and Thomas Pruschke (2008). "Numerical renormalization group method for quantum impurity systems". *Rev. Mod. Phys.* 80 (2), pp. 395–450.

Bulla, Ralf, Alex C. Hewson, and Thomas Pruschke (1998). "Numerical renormalization group calculations for the self-energy of the impurity Anderson model". *Journal of Physics: Condensed Matter* 10.37, pp. 8365–8380.

Burovski, Evgeni, Nikolay Prokof'ev, Boris Svistunov, and Matthias Troyer (2006). "The Fermi–Hubbard model at unitarity". *New Journal of Physics* 8.8, pp. 153–153.

Byczuk, K., M. Kollar, K. Held, Y.-F. Yang, I. A. Nekrasov, Th. Pruschke, and D. Vollhardt (2007). "Kinks in the dispersion of strongly correlated electrons". *Nature Physics*, p. 168.

Caffarel, Michel and Werner Krauth (1994). "Exact diagonalization approach to correlated fermions in infinite dimensions: Mott transition and superconductivity". *Phys. Rev. Lett.* 72 (10), pp. 1545–1548.

Cao, Yuan, Valla Fatemi, Ahmet Demir, Shiang Fang, Spencer L. Tomarken, Jason Y. Luo, Javier D. Sanchez-Yamagishi, Kenji Watanabe, Takashi Taniguchi, Efthimios Kaxiras, Ray C. Ashoori, and Pablo Jarillo-Herrero (2018). "Correlated insulator behaviour at half-filling in magic-angle graphene superlattices". *Nature (London)* 556, p. 80.

Capone, Massimo, Luca de'Medici, and Antoine Georges (2007). "Solving the dynamical mean-field theory at very low temperatures using the Lanczos exact diagonalization". *Phys. Rev. B* 76 (24), p. 245116.

Capponi, Sylvain, V. Ravi Chandra, Assa Auerbach, and Marvin Weinstein (2013). "$p6$ chiral resonating valence bonds in the kagome antiferromagnet". *Phys. Rev. B* 87, p. 161118.

Casula, Michele, Alexey Rubtsov, and Silke Biermann (2012). "Dynamical screening effects in correlated materials: Plasmon satellites and spectral weight transfers from a Green's function ansatz to extended dynamical mean field theory". *Phys. Rev. B* 85 (3), p. 035115.

Die approbierte gedruckte Originalversion dieser Dissertation ist an der TU Wien Bibliothek verfügbar.
The approved original version of this doctoral thesis is available in print at TU Wien Bibliothek.
TU Bibliothek WIEN Your knowledge hub

Chalupa, P., P. Gunacker, T. Schäfer, K. Held, and A. Toschi (2018). "Divergences of the irreducible vertex functions in correlated metallic systems: Insights from the Anderson impurity model". *Phys. Rev. B* 97 (24), p. 245136.

Chan, M. K., C. J. Dorow, L. Mangin-Thro, Y. Tang, Y. Ge, M. J. Veit, G. Yu, X. Zhao, A. D. Christianson, J. T. Park, Y. Sidis, P. Steffens, D. L. Abernathy, P. Bourges, and M. Greven (2016). "Commensurate antiferromagnetic excitations as a signature of the pseudogap in the tetragonal high-Tc cuprate HgBa2CuO4+δ". *Nature Communications* 7.1, p. 10819. ISSN: 2041-1723.

Chen, K.-S., Z. Y. Meng, S.-X. Yang, T. Pruschke, J. Moreno, and M. Jarrell (2013). "Evolution of the superconductivity dome in the two-dimensional Hubbard model". *Phys. Rev. B* 88 (24), p. 245110.

Chen, Xi, Shi-Ju Ran, Tao Liu, Cheng Peng, Yi-Zhen Huang, and Gang Su (2018). "Thermodynamics of spin-1/2 Kagomé Heisenberg antiferromagnet: algebraic paramagnetic liquid and finite-temperature phase diagram". *Sci. Bull.* 63, pp. 1545–1550.

Costi, T. A. and A. Liebsch (2007). "Quantum Phase Transition in the Two-Band Hubbard Model". *Phys. Rev. Lett.* 99 (23), p. 236404.

Császár, Pál and Péter Pulay (1984). "Geometry optimization by direct inversion in the iterative subspace". *Journal of Molecular Structure* 114, pp. 31–34. ISSN: 0022-2860.

Dagotto, Elbio (2005). "Complexity in Strongly Correlated Electronic Systems". *Science* 309, pp. 257–262.

De Dominicis, Cyrano and Paul C. Martin (1964a). "Stationary Entropy Principle and Renormalization in Normal and Superfluid Systems. I. Algebraic Formulation". *Journal of Mathematical Physics* 5.1, pp. 14–30.

De Dominicis, Cyrano and Paul C. Martin (1964b). "Stationary Entropy Principle and Renormalization in Normal and Superfluid Systems. II. Diagrammatic Formulation". *Journal of Mathematical Physics* 5.1, pp. 31–59.

Depenbrock, Stefan, Ian P. McCulloch, and Ulrich Schollwöck (2012). "Nature of the Spin-Liquid Ground State of the $S = 1/2$ Heisenberg Model on the Kagome Lattice". *Phys. Rev. Lett.* 109, p. 067201.

Dodds, Tyler, Subhro Bhattacharjee, and Yong Baek Kim (2013). "Quantum spin liquids in the absence of spin-rotation symmetry: Application to herbertsmithite". *Phys. Rev. B* 88, p. 224413.

Dongen, P. G. J. van and C. Leinung (1997). "Mott-Hubbard transition in a magnetic field". *Annalen der Physik* 509.1, pp. 45–67.

Eckhardt, C. J., G. A. H. Schober, J. Ehrlich, and C. Honerkamp (2018). "Truncated-unity parquet equations: Application to the repulsive Hubbard model". *Phys. Rev. B* 98 (7), p. 075143.

Eckhardt, Christian J., Carsten Honerkamp, Karsten Held, and Anna Kauch (2020). "Truncated unity parquet solver". *Phys. Rev. B* 101 (15), p. 155104.

Die approbierte gedruckte Originalversion dieser Dissertation ist an der TU Wien Bibliothek verfügbar.
The approved original version of this doctoral thesis is available in print at TU Wien Bibliothek.
TU Bibliothek WIEN Your knowledge hub

Evenbly, G. and G. Vidal (2010). "Frustrated Antiferromagnets with Entanglement Renormalization: ground State of the Spin-1/2 Heisenberg Model on a Kagome Lattice". *Phys. Rev. Lett.* 104, p. 187203.

Eyert, V. (1996). "A Comparative Study on Methods for Convergence Acceleration of Iterative Vector Sequences". *Journal of Computational Physics* 124.2, pp. 271–285. ISSN: 0021-9991.

Fåk, B., E. Kermarrec, L. Messio, B. Bernu, C. Lhuillier, F. Bert, P. Mendels, B. Koteswararao, F. Bouquet, J. Ollivier, A. D. Hillier, A. Amato, R. H. Colman, and A. S. Wills (2012). "Kapellasite: A Kagome Quantum Spin Liquid with Competing Interactions". *Phys. Rev. Lett.* 109, p. 037208.

Fenner, L. A., A. A. Dee, and A. S. Wills (2009). "Non-collinearity and spin frustration in the itinerant kagome ferromagnet Fe_3Sn_2". *J. Phys.: Condens. Matter* 21, p. 452202.

Ferrero, Michel, Federico Becca, Michele Fabrizio, and Massimo Capone (2005). "Dynamical behavior across the Mott transition of two bands with different bandwidths". *Phys. Rev. B* 72 (20), p. 205126.

Freericks, J. K., V. M. Turkowski, and V. Zlatić (2006). "Nonequilibrium Dynamical Mean-Field Theory". *Phys. Rev. Lett.* 97 (26), p. 266408.

Freericks, J. K. and V. Zlatić (2003). "Exact dynamical mean-field theory of the Falicov-Kimball model". *Rev. Mod. Phys.* 75 (4), pp. 1333–1382.

Frieden, B. Roy (1972). "Restoring with Maximum Likelihood and Maximum Entropy*". *J. Opt. Soc. Am.* 62.4, pp. 511–518.

Friedrich, W., P. Knipping, and M. Laue (1912). "Interferenz-Erscheinungen bei Röntgenstrahlen." *Verl. der Königlich Bayer. Akad. der Wiss.*

Galler, Anna, Josef Kaufmann, Patrik Gunacker, Matthias Pickem, Patrik Thunström, Jan M. Tomczak, and Karsten Held (2018). "Towards ab initio Calculations with the Dynamical Vertex Approximation". *Journal of the Physical Society of Japan* 87.4, p. 041004.

Galler, Anna, Patrik Thunström, Patrik Gunacker, Jan M. Tomczak, and Karsten Held (2017). "Ab initio dynamical vertex approximation". *Phys. Rev. B* 95 (11), p. 115107.

Galler, Anna, Patrik Thunström, Josef Kaufmann, Matthias Pickem, Jan M. Tomczak, and Karsten Held (2019). "The AbinitioDΓA Project v1.0: Non-local correlations beyond and susceptibilities within dynamical mean-field theory". *Computer Physics Communications* 245, p. 106847. ISSN: 0010-4655.

Ganahl, Martin, Markus Aichhorn, Hans Gerd Evertz, Patrik Thunström, Karsten Held, and Frank Verstraete (2015). "Efficient DMFT impurity solver using real-time dynamics with matrix product states". *Phys. Rev. B* 92 (15), p. 155132.

Gebhard, F. (1997). "The Mott Metal-insulator transition". Springer-Verlag (Berlin).

Geffroy, D., J. Kaufmann, A. Hariki, P. Gunacker, A. Hausoel, and J. Kuneš (2019). "Collective Modes in Excitonic Magnets: Dynamical Mean-Field Study". *Phys. Rev. Lett.* 122 (12), p. 127601.

Die approbierte gedruckte Originalversion dieser Dissertation ist an der TU Wien Bibliothek verfügbar.
The approved original version of this doctoral thesis is available in print at TU Wien Bibliothek.
TU Bibliothek WIEN Your knowledge hub

Georges, Antoine and Gabriel Kotliar (1992). "Hubbard model in infinite dimensions". *Phys. Rev. B* 45 (12), pp. 6479–6483.

Georges, Antoine, Gabriel Kotliar, Werner Krauth, and Marcelo J. Rozenberg (1996). "Dynamical mean-field theory of strongly correlated fermion systems and the limit of infinite dimensions". *Rev. Mod. Phys.* 68.1, p. 13.

Georges, Antoine and Werner Krauth (1993). "Physical properties of the half-filled Hubbard model in infinite dimensions". *Phys. Rev. B* 48 (10), pp. 7167–7182.

Ghanem, Khaldoon and Erik Koch (2020). "Average spectrum method for analytic continuation: Efficient blocked-mode sampling and dependence on the discretization grid". *Phys. Rev. B* 101 (8), p. 085111.

Goldstone, Jeffrey, Abdus Salam, and Steven Weinberg (1962). "Broken Symmetries". *Phys. Rev.* 127 (3), pp. 965–970.

Gong, Shou-Shu, Wei Zhu, Leon Balents, and D. N. Sheng (2015). "Global phase diagram of competing ordered and quantum spin-liquid phases on the kagome lattice". *Phys. Rev. B* 91, p. 075112.

Gong, Shou-Shu, Wei Zhu, and D. N. Sheng (2014). "Emergent Chiral Spin Liquid: Fractional Quantum Hall Effect in a Kagome Heisenberg Model". *Sci. Rep.* 4, p. 6713.

González, J., F. Guinea, and M. A. H. Vozmediano (2000). "Kinematics of Electrons near a Van Hove Singularity". *Phys. Rev. Lett.* 84 (21), pp. 4930–4933.

Graf, J., G.-H. Gweon, K. McElroy, S. Y. Zhou, C. Jozwiak, E. Rotenberg, A. Bill, T. Sasagawa, H. Eisaki, S. Uchida, H. Takagi, D.-H. Lee, and A. Lanzara (2007). "Universal High Energy Anomaly in the Angle-Resolved Photoemission Spectra of High Temperature Superconductors: Possible Evidence of Spinon and Holon Branches". *Phys. Rev. Lett.* 98 (6), p. 067004.

Granath, Mats and Johan Schött (2014). "Signatures of coherent electronic quasiparticles in the paramagnetic Mott insulator". *Phys. Rev. B* 90 (23), p. 235129.

Greger, Markus, Marcus Kollar, and Dieter Vollhardt (2013). "Emergence of a Common Energy Scale Close to the Orbital-Selective Mott Transition". *Phys. Rev. Lett.* 110 (4), p. 046403.

Griffith, J. S. (1971). "The Theory of Transition-MetalIons". Cambridge University Press, Cambridge.

Gull, Emanuel, Andrew J. Millis, Alexander I. Lichtenstein, Alexey N. Rubtsov, Matthias Troyer, and Philipp Werner (2011). "Continuous-time Monte Carlo methods for quantum impurity models". *Rev. Mod. Phys.* 83 (2), pp. 349–404.

Gull, Emanuel, Olivier Parcollet, and Andrew J. Millis (2013). "Superconductivity and the Pseudogap in the Two-Dimensional Hubbard Model". *Phys. Rev. Lett.* 110 (21), p. 216405.

Gull, S. F. and G. J. Daniell (1978). "Image reconstruction from incomplete and noisy data". *Nature* 272.5655, pp. 686–690. ISSN: 1476-4687.

Die approbierte gedruckte Originalversion dieser Dissertation ist an der TU Wien Bibliothek verfügbar.
The approved original version of this doctoral thesis is available in print at TU Wien Bibliothek.
TU Bibliothek WIEN Your knowledge hub

Gull, S.F. and J. Skilling (1984). "Maximum entropy method in image processing". English. *IEE Proceedings F (Communications, Radar and Signal Processing)* 131 (6), 646–659(13). ISSN: 0143-7070.

Gull, Stephen F. (1989). "Developments in Maximum Entropy Data Analysis". *Maximum Entropy and Bayesian Methods*. Ed. by John Skilling. Kluwer Academic Publishers, pp. 53–71.

Gunacker, P., M. Wallerberger, E. Gull, A. Hausoel, G. Sangiovanni, and K. Held (2015). "Continuous-time quantum Monte Carlo using worm sampling". *Phys. Rev. B* 92 (15), p. 155102.

Gunacker, P., M. Wallerberger, T. Ribic, A. Hausoel, G. Sangiovanni, and K. Held (2016). "Worm-improved estimators in continuous-time quantum Monte Carlo". *Phys. Rev. B* 94 (12), p. 125153.

Gunnarsson, O., G. Rohringer, T. Schäfer, G. Sangiovanni, and A. Toschi (2017). "Breakdown of Traditional Many-Body Theories for Correlated Electrons". *Phys. Rev. Lett.* 119 (5), p. 056402.

Gunnarsson, O., T. Schäfer, J. P. F. LeBlanc, E. Gull, J. Merino, G. Sangiovanni, G. Rohringer, and A. Toschi (2015). "Fluctuation Diagnostics of the Electron Self-Energy: Origin of the Pseudogap Physics". *Phys. Rev. Lett.* 114 (23), p. 236402.

Gutzwiller, Martin C. (1963). "Effect of Correlation on the Ferromagnetism of Transition Metals". *Phys. Rev. Lett.* 10, pp. 159–162.

Hafermann, H., G. Li, A. N. Rubtsov, M. I. Katsnelson, A. I. Lichtenstein, and H. Monien (2009). "Efficient Perturbation Theory for Quantum Lattice Models". *Phys. Rev. Lett.* 102 (20), p. 206401.

Hafermann, H., K. R. Patton, and P. Werner (2012). "Improved estimators for the self-energy and vertex function in hybridization-expansion continuous-time quantum Monte Carlo simulations". *Phys. Rev. B* 85 (20), p. 205106.

Hafermann, Hartmut (2014). "Self-energy and vertex functions from hybridization-expansion continuous-time quantum Monte Carlo for impurity models with retarded interaction". *Phys. Rev. B* 89 (23), p. 235128.

Halboth, Christoph J. and Walter Metzner (2000). "*d*-Wave Superconductivity and Pomeranchuk Instability in the Two-Dimensional Hubbard Model". *Phys. Rev. Lett.* 85 (24), pp. 5162–5165.

Halimeh, Jad C. and Matthias Punk (2016). "Spin structure factors of chiral quantum spin liquids on the kagome lattice". *Phys. Rev. B* 94, p. 104413.

Halimeh, Jad C. and Rajiv R. P. Singh (2019). "Rapid filling of the spin gap with temperature in the Schwinger-boson mean-field theory of the antiferromagnetic Heisenberg kagome model". *Phys. Rev. B* 99, p. 155151.

Die approbierte gedruckte Originalversion dieser Dissertation ist an der TU Wien Bibliothek verfügbar.
The approved original version of this doctoral thesis is available in print at TU Wien Bibliothek.
TU Bibliothek WIEN Your knowledge hub

Han, Tian-Heng, Joel S. Helton, Shaoyan Chu, Daniel G. Nocera, Jose A. Rodriguez-Rivera, Collin Broholm, and Young S. Lee (2012). "Fractionalized excitations in the spin-liquid state of a kagome-lattice antiferromagnet". *Nature* 492, pp. 406–410.

Hastings, W. K. (1970). "Monte Carlo Sampling Methods Using Markov Chains and Their Applications". *Biometrika* 57.1, pp. 97–109. ISSN: 00063444.

Hausoel, Andreas, Markus Wallerberger, Josef Kaufmann, and Giorgio Sangiovanni (2021). "Inconsistency of standard Green's function estimator in diagrammatic quantum Monte Carlo for finite systems", (in preparation).

He, Yin-Chen, D. N. Sheng, and Yan Chen (2014). "Chiral Spin Liquid in a Frustrated Anisotropic Kagome Heisenberg Model". *Phys. Rev. Lett.* 112, p. 137202.

He, Yin-Chen, Michael P. Zaletel, Masaki Oshikawa, and Frank Pollmann (2017). "Signatures of Dirac cones in a DMRG study of the Kagome Heisenberg model". *Phys. Rev. X* 7, p. 031020.

Held, K., R. Peters, and A. Toschi (2013). "Poor Man's Understanding of Kinks Originating from Strong Electronic Correlations". *Phys. Rev. Lett.* 110 (24), p. 246402.

Held, Karsten (2007). "Electronic structure calculations using dynamical mean field theory". *Advances in Physics* 56.6, pp. 829–926.

Helton, J. S., K. Matan, M. P. Shores, E. A. Nytko, B. M. Bartlett, Y. Yoshida, Y. Takano, A. Suslov, Y. Qiu, J.-H. Chung, D. G. Nocera, and Y. S. Lee (2007). "Spin Dynamics of the Spin-1/2 Kagome Lattice Antiferromagnet $ZnCu_3(OH)_6Cl_2$". *Phys. Rev. Lett.* 98, p. 107204.

Hermele, Michael, Ying Ran, Patrick A. Lee, and Xiao-Gang Wen (2008). "Properties of an algebraic spin liquid on the kagome lattice". *Phys. Rev. B* 77, p. 224413.

Hettler, M. H., A. N. Tahvildar-Zadeh, M. Jarrell, T. Pruschke, and H. R. Krishnamurthy (1998). "Nonlocal dynamical correlations of strongly interacting electron systems". *Phys. Rev. B* 58 (12), R7475–R7479.

Higa, Ryota and Kenichi Asano (2016). "Bond formation effects on the metal-insulator transition in the half-filled kagome Hubbard model". *Phys. Rev. B* 93, p. 245123.

Hille, Cornelia, Fabian B. Kugler, Christian J. Eckhardt, Yuan-Yao He, Anna Kauch, Carsten Honerkamp, Alessandro Toschi, and Sabine Andergassen (2020). "Quantitative functional renormalization group description of the two-dimensional Hubbard model". *Phys. Rev. Research* 2 (3), p. 033372.

Hirsch, J. E. and R. M. Fye (1986). "Monte Carlo Method for Magnetic Impurities in Metals". *Phys. Rev. Lett.* 56 (23), pp. 2521–2524.

Hirsch, J. E. and S. Tang (1989). "Antiferromagnetism in the Two-Dimensional Hubbard Model". *Phys. Rev. Lett.* 62 (5), pp. 591–594.

Hirschmeier, Daniel, Hartmut Hafermann, Emanuel Gull, Alexander I. Lichtenstein, and Andrey E. Antipov (2015). "Mechanisms of finite-temperature magnetism in the three-dimensional Hubbard model". *Phys. Rev. B* 92 (14), p. 144409.

Die approbierte gedruckte Originalversion dieser Dissertation ist an der TU Wien Bibliothek verfügbar.
The approved original version of this doctoral thesis is available in print at TU Wien Bibliothek.
TU Bibliothek WIEN Your knowledge hub

Hohenberg, P. and W. Kohn (1964). "Inhomogeneous Electron Gas". *Phys. Rev.* 136 (3B), B864–B871.

Honerkamp, Carsten and Manfred Salmhofer (2001). "Magnetic and Superconducting Instabilities of the Hubbard Model at the Van Hove Filling". *Phys. Rev. Lett.* 87 (18), p. 187004.

Hoshino, Shintaro and Philipp Werner (2016). "Electronic orders in multiorbital Hubbard models with lifted orbital degeneracy". *Phys. Rev. B* 93 (15), p. 155161.

Hou, Zhipeng, Weijun Ren, Bei Ding, Guizhou Xu, Yue Wang, Bing Yang, Qiang Zhang, Ying Zhang, Enke Liu, Feng Xu, Wenhong Wang, Guangheng Wu, Xixiang Zhang, Baogen Shen, and Zhidong Zhang (2017). "Observation of Various and Spontaneous Magnetic Skyrmionic Bubbles at Room Temperature in a Frustrated Kagome Magnet with Uniaxial Magnetic Anisotropy". *Adv. Mater.* 29, p. 1701144.

Howard, Sean, Lin Jiao, Zhenyu Wang, Praveen Vir, Chandra Shekhar, Claudia Felser, Taylor Hughes, and Vidya Madhavan (2019). "Observation of linearly dispersive edge modes in a magnetic Weyl semimetal $Co_3Sn_2S_2$", arXiv:1910.11205

Hu, Wen-Jun, Wei Zhu, Yi Zhang, Shoushu Gong, Federico Becca, and D. N. Sheng (2015). "Variational Monte Carlo study of a chiral spin liquid in the extended Heisenberg model on the kagome lattice". *Phys. Rev. B* 91, p. 041124.

Hu, Wenjian, Richard T. Scalettar, Edwin W. Huang, and Brian Moritz (2017). "Effects of an additional conduction band on the singlet-antiferromagnet competition in the periodic Anderson model". *Phys. Rev. B* 95 (23), p. 235122.

Hubbard, J. (1963). "Electron Correlations in Narrow Energy Bands". *Proc. Royal Soc. London. Series A, Mat. Phys. Sci.* 276, pp. 238–257.

Hubbard, J. (1964). "Electron Correlations in Narrow Energy Bands. III. An Improved Solution". *Proc R. Soc. London* 281.1386, pp. 401–419.

Husemann, C. and M. Salmhofer (2009). "Efficient parametrization of the vertex function, Ω scheme, and the t, t' Hubbard model at van Hove filling". *Phys. Rev. B* 79 (19), p. 195125.

Hwang, H. Y., Y. Iwasa, M. Kawasaki, B. Keimer, N. Nagaosa, and Y. Tokura (2012). "Emergent phenomena at oxide interfaces". *Nature Mater.* 11, pp. 103–113.

Iglovikov, V. I., E. Khatami, and R. T. Scalettar (2015). "Geometry dependence of the sign problem in quantum Monte Carlo simulations". *Phys. Rev. B* 92 (4), p. 045110.

Imada, Masatoshi, Atsushi Fujimori, and Yoshinori Tokura (1998). "Metal-insulator transitions". *Rev. Mod. Phys.* 70, pp. 1039–1263.

Imada, Masatoshi and Takashi Miyake (2010). "Electronic Structure Calculation by First Principles for Strongly Correlated Electron Systems". *J. Phys. Soc. Jpn.* 79, p. 112001.

Inoue, Hisashi, Minyong Han, Linda Ye, Takehito Suzuki, and Joseph G. Checkelsky (2019). "Molecular beam epitaxy growth of antiferromagnetic Kagome metal FeSn". *Appl. Phys. Lett* 115, p. 072403.

Die approbierte gedruckte Originalversion dieser Dissertation ist an der TU Wien Bibliothek verfügbar.
The approved original version of this doctoral thesis is available in print at TU Wien Bibliothek.
TU Bibliothek WIEN Your knowledge hub

Iqbal, Yasir, Federico Becca, Sandro Sorella, and Didier Poilblanc (2013). "Gapless spin-liquid phase in the kagome spin-$\frac{1}{2}$ Heisenberg antiferromagnet". *Phys. Rev. B* 87, p. 060405.

Iqbal, Yasir, Harald O. Jeschke, Johannes Reuther, Roser Valenti, I. I. Mazin, Martin Greiter, and Ronny Thomale (2015). "Paramagnetism in the kagome compounds (Zn,Mg,Cd)$Cu_3(OH_6)Cl_2$". *Phys. Rev. B* 92, p. 220404.

J. M. Tomczak, J.M., P. Liu, A. Toschi, G. Kresse, and K. Held (2017). "Merging GW with DMFT and non-local correlations beyond". *Eur. Phys. J.: Special Topics* 226, p. 2565.

Jaklič, J. and P. Prelovšek (1994). "Lanczos method for the calculation of finite-temperature quantities in correlated systems". *Phys. Rev. B* 49 (7), pp. 5065–5068.

Janson, O., J. Richter, and H. Rosner (2008). "Modified Kagome Physics in the Natural Spin-1/2 Kagome Lattice Systems: kapellasite $Cu_3Zn(OH)_6Cl_2$ and haydeeite $Cu_3Mg(OH)_6Cl_2$". *Phys. Rev. Lett.* 101, p. 106403.

Janson, Oleg (2012). "DFT-based microscopic magnetic modeling for low-dimensional spin systems". PhD thesis. Technische Universität Dresden.

Jarrell, M. (1992). "Hubbard model in infinite dimensions: A quantum Monte Carlo study". *Phys. Rev. Lett.* 69, pp. 168–171.

Jarrell, Mark and J.E. Gubernatis (1996). "Bayesian inference and the analytic continuation of imaginary-time quantum Monte Carlo data". *Physics Reports* 269.3, pp. 133–195. ISSN: 0370-1573.

Jaynes, E. T. (1957). "Information Theory and Statistical Mechanics". *Phys. Rev.* 106 (4), pp. 620–630.

Jeffreys, Harold (1939). "Theory of Probability". Oxford: Clarendon Press.

Jeschke, Harald O., Francesc Salvat-Pujol, and Roser Valenti (2013). "First-principles determination of Heisenberg Hamiltonian parameters for the spin-$\frac{1}{2}$ kagome antiferromagnet $ZnCu_3(OH)_6Cl_2$". *Phys. Rev. B* 88, p. 075106.

Jia, C. J., E. A. Nowadnick, K. Wohlfeld, Y. F. Kung, C.-C. Chen, S. Johnston, T. Tohyama, B. Moritz, and T. P. Devereaux (2014). "Persistent spin excitations in doped antiferromagnets revealed by resonant inelastic light scattering". *Nature Communications* 5.1, p. 3314. ISSN: 2041-1723.

Jiang, Hong-Chen, Zhenghan Wang, and Leon Balents (2012). "Identifying topological order by entanglement entropy". *Nat. Phys.* 8, pp. 902–905.

Johnson, D. D. (1988). "Modified Broyden's method for accelerating convergence in self-consistent calculations". *Phys. Rev. B* 38 (18), pp. 12807–12813.

Kalinowski, Eva and Florian Gebhard (2002). "Mott-Hubbard insulator in infinite dimensions". *J. Low Temperature Phys.* 126, p. 979.

Kanamori, Junjiro (1963). "Electron correlation and ferromagnetism of transition metals". *Progress of Theoretical Physics* 30.3, pp. 275–289.

Die approbierte gedruckte Originalversion dieser Dissertation ist an der TU Wien Bibliothek verfügbar.
The approved original version of this doctoral thesis is available in print at TU Wien Bibliothek.
TU Bibliothek WIEN Your knowledge hub

Kang, Mingu, Linda Ye, Shiang Fang, Jhih-Shih You, Abe Levitan, Minyong Han, Jorge I. Facio, Chris Jozwiak, Aaron Bostwick, Eli Rotenberg, Mun K. Chan, Ross D. McDonald, David Graf, Konstantine Kaznatcheev, Elio Vescovo, David C. Bell, Efthimios Kaxiras, Jeroen van den Brink, Manuel Richter, Madhav Prasad Ghimire, Joseph G. Checkelsky, and Riccardo Comin (2019). "Dirac fermions and flat bands in the ideal kagome metal FeSn". *Nat. Mater.* 19, pp. 163–169.

Kappl, Patrick, Markus Wallerberger, Josef Kaufmann, Matthias Pickem, and Karsten Held (2020). "Statistical error estimates in dynamical mean-field theory and extensions thereof". *Phys. Rev. B* 102 (8), p. 085124.

Karolak, M, T O Wehling, F Lechermann, and A I Lichtenstein (2011). "General DFT++ method implemented with projector augmented waves: electronic structure of $SrVO_3$ and the Mott transition in $Ca_{2-x}Sr_xRuO_4$". *Journal of Physics: Condensed Matter* 23.8, p. 085601.

Karski, Michał, Carsten Raas, and Götz S. Uhrig (2008). "Single-particle dynamics in the vicinity of the Mott-Hubbard metal-to-insulator transition". *Phys. Rev. B* 77 (7), p. 075116.

Katanin, A. A., V. Yu. Irkhin, and P. A. Igoshev (2012). "Model'nye podhody k magnetizmu dvumernyh zonnyh sistem". Moscow: Fizmatlit.

Katanin, A. A., A. Toschi, and K. Held (2009). "Comparing pertinent effects of antiferromagnetic fluctuations in the two- and three-dimensional Hubbard model". *Phys. Rev. B* 80 (7), p. 075104.

Kauch, A., P. Pudleiner, K. Astleithner, P. Thunström, T. Ribic, and K. Held (2020a). "Generic Optical Excitations of Correlated Systems: π-tons". *Phys. Rev. Lett.* 124 (4), p. 047401.

Kauch, Anna, Felix Hörbinger, Gang Li, and Karsten Held (2019). "Interplay between magnetic and superconducting fluctuations in the doped 2d Hubbard model". *preprint*, arXiv:1901.09743.

Kauch, Anna, Paul Worm, Paul Prauhart, Michael Innerberger, Clemens Watzenböck, and Karsten Held (2020b). "Enhancement of impact ionization in Hubbard clusters by disorder and next-nearest-neighbor hopping". *preprint*, arXiv:2007.16035.

Kaufmann, J., P. Gunacker, A. Kowalski, G. Sangiovanni, and K. Held (2019). "Symmetric improved estimators for continuous-time quantum Monte Carlo". *Phys. Rev. B* 100 (7), p. 075119.

Kaufmann, Josef (2020). "ana_cont: Package for analytic continuation of many-body Green's functions", `https://github.com/josefkaufmann/ana_cont`.

Kaufmann, Josef, Christian Eckhardt, Matthias Pickem, Motoharu Kitatani, Anna Kauch, and Karsten Held (2021). "Self-consistent ladder dynamical vertex approximation". *Phys. Rev. B* 103 (3), p. 035120.

Kaufmann, Josef, Patrik Gunacker, and Karsten Held (2017). "Continuous-time quantum Monte Carlo calculation of multiorbital vertex asymptotics". *Phys. Rev. B* 96 (3), p. 035114.

Die approbierte gedruckte Originalversion dieser Dissertation ist an der TU Wien Bibliothek verfügbar.
The approved original version of this doctoral thesis is available in print at TU Wien Bibliothek.
TU Bibliothek WIEN Your knowledge hub

Kaufmann, Josef, Klaus Steiner, Richard T. Scalettar, Karsten Held, and Oleg Janson (2020). "How correlations change the magnetic structure factor of the kagome Hubbard model". *preprint*, arXiv:2011.01085.

Keimer, B., S. A. Kivelson, M. R. Norman, S. Uchida, and J. Zaanen (2015a). "From quantum matter to high-temperature superconductivity in copper oxides". *Nature* 518.7538, pp. 179–186. ISSN: 1476-4687.

Keimer, B., S. A. Kivelson, M. R. Norman, S. Uchida, and J. Zaanen (2015b). "From quantum matter to high-temperature superconductivity in copper oxides". *Nature (London)* 518, p. 179.

Khuntia, P., M. Velazquez, Q. Barthélemy, F. Bert, E. Kermarrec, A. Legros, B. Bernu, L. Messio, A. Zorko, and P. Mendels (2020). "Gapless ground state in the archetypal quantum kagome antiferromagnet $ZnCu_3(OH)_6Cl_2$". *Nat. Phys.* 16, pp. 469–474.

Kida, T., L. A. Fenner, A. A. Dee, I. Terasaki, M. Hagiwara, and A. S. Wills (2011). "The giant anomalous Hall effect in theferromagnet Fe_3Sn_2 — a frustrated kagome metal". *J. Phys.: Condens. Matter* 23, p. 112205.

Kimata, Motoi, Hua Chen, Kouta Kondou, Satoshi Sugimoto, Prasanta K. Muduli, Muhammad Ikhlas, Yasutomo Omori, Takahiro Tomita, Allan. H. MacDonald, Satoru Nakatsuji, and Yoshichika Otani (2019). "Magnetic and magnetic inverse spin Hall effects in a non-collinear antiferromagnet". *Nature* 565, pp. 627–630.

Kita, Tomoko, Takuma Ohashi, and Norio Kawakami (2013). "Field-induced Mott transition in kagome lattice Hubbard model". *Phys. Rev. B* 87, p. 155119.

Kitatani, Motoharu, Thomas Schäfer, Hideo Aoki, and Karsten Held (2019). "Why the critical temperature of high-T_c cuprate superconductors is so low: The importance of the dynamical vertex structure". *Phys. Rev. B* 99 (4), p. 041115.

Kitatani, Motoharu, Liang Si, Oleg Janson, Ryotaro Arita, Zhicheng Zhong, and Karsten Held (2020). "Nickelate superconductors – a renaissance of the one-band Hubbard model". *npj Quantum Materials* 5 (1), p. 59.

Knecht, C., N. Blümer, and P. G. J. van Dongen (2005). "Orbital-selective Mott transitions in the anisotropic two-band Hubbard model at finite temperatures". *Phys. Rev. B* 72 (8), p. 081103.

Koga, Akihisa, Norio Kawakami, T. M. Rice, and Manfred Sigrist (2004). "Orbital-Selective Mott Transitions in the Degenerate Hubbard Model". *Phys. Rev. Lett.* 92 (21), p. 216402.

Koga, Akihisa, Norio Kawakami, T. M. Rice, and Manfred Sigrist (2005). "Spin, charge, and orbital fluctuations in a multiorbital Mott insulator". *Phys. Rev. B* 72 (4), p. 045128.

Kohn, W. and L. J. Sham (1965). "Self-Consistent Equations Including Exchange and Correlation Effects". *Phys. Rev.* 140 (4A), A1133–A1138.

Kolley, F., S. Depenbrock, I. P. McCulloch, U. Schollwöck, and V. Alba (2015). "Phase diagram of the $J_1 - J_2$ Heisenberg model on the kagome lattice". *Phys. Rev. B* 91, p. 104418.

Die approbierte gedruckte Originalversion dieser Dissertation ist an der TU Wien Bibliothek verfügbar.
The approved original version of this doctoral thesis is available in print at TU Wien Bibliothek.
TU Bibliothek WIEN Your knowledge hub

Kotliar, G., S. Y. Savrasov, K. Haule, V. S. Oudovenko, O. Parcollet, and C. A. Marianetti (2006). "Electronic structure calculations with dynamical mean-field theory". *Rev. Mod. Phys.* 78 (3), pp. 865–951.

Kraberger, Gernot J., Robert Triebl, Manuel Zingl, and Markus Aichhorn (2017). "Maximum entropy formalism for the analytic continuation of matrix-valued Green's functions". *Phys. Rev. B* 96 (15), p. 155128.

Kresse, G. and J. Furthmüller (1996). "Efficiency of ab-initio total energy calculations for metals and semiconductors using a plane-wave basis set". *Computational Materials Science* 6.1, pp. 15–50. ISSN: 0927-0256.

Krien, Friedrich, Angelo Valli, Patrick Chalupa, Massimo Capone, Alexander I. Lichtenstein, and Alessandro Toschi (2020). "Boson-exchange parquet solver for dual fermions". *Phys. Rev. B* 102 (19), p. 195131.

Kudo, Koji, Tsuneya Yoshida, and Yasuhiro Hatsugai (2019). "Higher-order Topological Mott Insulators". *Phys. Rev. Lett.* 123, p. 196402.

Kugler, Fabian B and Jan von Delft (2018). "Derivation of exact flow equations from the self-consistent parquet relations". *New Journal of Physics* 20.12, p. 123029.

Kuneš, J., R. Arita, P. Wissgott, A. Toschi, H. Ikeda, and K. Held (2010). "Wien2wannier: From linearized augmented plane waves to maximally localized Wannier functions". *Computer Physics Communications* 181.11, pp. 1888–1895. ISSN: 0010-4655.

Kuneš, Jan (2011). "Efficient treatment of two-particle vertices in dynamical mean-field theory". *Phys. Rev. B* 83 (8), p. 085102.

Kuneš, Jan (2015). "Excitonic condensation in systems of strongly correlated electrons". *Journal of Physics: Condensed Matter* 27.33, p. 333201.

Kuneš, Jan and Pavel Augustinský (2014). "Excitonic instability at the spin-state transition in the two-band Hubbard model". *Phys. Rev. B* 89 (11), p. 115134.

Kuroda, K., T. Tomita, M.-T. Suzuki, C. Bareille, A. A. Nugroho, P. Goswami, M. Ochi, M. Ikhlas, M. Nakayama, S. Akebi, R. Noguchi, R. Ishii, N. Inami, K. Ono, H. Kumigashira, A. Varykhalov, T. Muro, T. Koretsune, R. Arita, S. Shin, Takeshi Kondo, and S. Nakatsuji (2017). "Evidence for magnetic Weyl fermions in a correlated metal". *Nat. Mater.* 16, p. 1090.

Lachman, Ella, Ryan A. Murphy, Nikola Maksimovic, Robert Kealhofer, Shannon Haley, Ross D. McDonald, Jeffrey R. Long, and James G. Analytis (2020). "Exchange biased anomalous Hall effect driven by frustration in a magnetic kagome lattice". *Nat. Commun.* 11, p. 560.

Lanczos, C. (1950). "An iteration method for the solution of the eigenvalue problem of linear differential and integral operators". *Journal of research of the National Bureau of Standards* 45, pp. 255–282.

Läuchli, Andreas M. and Claire Lhuillier (2009). "Dynamical Correlations of the Kagome $S = 1/2$ Heisenberg Quantum Antiferromagnet". *preprint*, arXiv:0901.1065.

Die approbierte gedruckte Originalversion dieser Dissertation ist an der TU Wien Bibliothek verfügbar.
The approved original version of this doctoral thesis is available in print at TU Wien Bibliothek.
TU Bibliothek WIEN Your knowledge hub

Läuchli, Andreas M., Julien Sudan, and Roderich Moessner (2019). "$S = \frac{1}{2}$ kagome Heisenberg antiferromagnet revisited". *Phys. Rev. B* 100, p. 155142.

Lawson, Charles L. and Richard J. Hanson (1974). "Solving Least Squares Problems". Englewood Cliffs: Prentice-Hall.

Lawson, Charles L. and Richard J. Hanson (1995). "Solving Least Squares Problems". Society for Industrial and Applied Mathematics.

LeBlanc, J. P. F., Shaozhi Li, Xi Chen, Ryan Levy, A. E. Antipov, Andrew J. Millis, and Emanuel Gull (2019). "Magnetic susceptibility and simulated neutron signal in the two-dimensional Hubbard model". *Phys. Rev. B* 100 (7), p. 075123.

Lee, Hunpyo, Kateryna Foyevtsova, Johannes Ferber, Markus Aichhorn, Harald O. Jeschke, and Roser Valenti (2012). "Dynamical cluster approximation within an augmented plane wave framework: Spectral properties of $SrVO_3$". *Phys. Rev. B* 85 (16), p. 165103.

Lee, Patrick A., Naoto Nagaosa, and Xiao-Gang Wen (2006). "Doping a Mott insulator: Physics of high-temperature superconductivity". *Rev. Mod. Phys.* 78 (1), pp. 17–85.

Lee, Seung-Sup B., Jan von Delft, and Andreas Weichselbaum (2017). "Doublon-Holon Origin of the Subpeaks at the Hubbard Band Edges". *Phys. Rev. Lett.* 119 (23), p. 236402.

Leonov, I., V. I. Anisimov, and D. Vollhardt (2014). "First-Principles Calculation of Atomic Forces and Structural Distortions in Strongly Correlated Materials". *Phys. Rev. Lett.* 112 (14), p. 146401.

Levy, Ryan, J.P.F. LeBlanc, and Emanuel Gull (2017). "Implementation of the maximum entropy method for analytic continuation". *Computer Physics Communications* 215, pp. 149–155. ISSN: 0010-4655.

Li, Danfeng, Kyuho Lee, Bai Yang Wang, Motoki Osada, Samuel Crossley, Hye Ryoung Lee, Yi Cui, Yasuyuki Hikita, and Harold Y. Hwang (2019a). "Superconductivity in an infinite-layer nickelate". *Nature* 572.7771, pp. 624–627. ISSN: 1476-4687.

Li, Gang, Andrey E. Antipov, Alexey N. Rubtsov, Stefan Kirchner, and Werner Hanke (2014). "Competing phases of the Hubbard model on a triangular lattice: Insights from the entropy". *Phys. Rev. B* 89 (16), p. 161118.

Li, Gang, Anna Kauch, Petra Pudleiner, and Karsten Held (2019b). "The victory project v1.0: An efficient parquet equations solver". *Computer Physics Communications* 241, pp. 146–154. ISSN: 0010-4655.

Li, Gang, Nils Wentzell, Petra Pudleiner, Patrik Thunström, and Karsten Held (2016). "Efficient implementation of the parquet equations: Role of the reducible vertex function and its kernel approximation". *Phys. Rev. B* 93 (16), p. 165103.

Li, Hang, Bei Ding, Jie Chen, Zefang Li, Zhipeng Hou, Enke Liu, Hongwei Zhang, Xuekui Xi, Guangheng Wu, and Wenhong Wang (2019c). "Large topological Hall effect in a geometrically frustrated kagome magnet Fe_3Sn_2". *Appl. Phys. Lett.* 114, p. 192408.

Die approbierte gedruckte Originalversion dieser Dissertation ist an der TU Wien Bibliothek verfügbar.
The approved original version of this doctoral thesis is available in print at TU Wien Bibliothek.
TU Bibliothek WIEN Your knowledge hub

Li, Xiaokang, Clément Collignon, Liangcai Xu, Huakun Zuo, Antonella Cavanna, Ulf Gennser Dominique Mailly, Benoît Fauqué, Leon Balents, Zengwei Zhu, and Kamran Behnia (2019d). "Chiral domain walls of Mn_3Sn and their memory". *Nat. Commun.* 10, p. 3021.

Li, Yangmu, Qi Wang, Lisa DeBeer-Schmitt, Zurab Guguchia, Ryan D. Desautels, Jia-Xin Yin, Qianheng Du, Weijun Ren, Xinguo Zhao, Zhidong Zhang, Igor A. Zaliznyak, Cedomir Petrovic, Weiguo Yin, M. Zahid Hasan, Hechang Lei, and John M. Tranquada (2019e). "Magnetic-Field Control of Topological Electronic Response near Room Temperature in Correlated Kagome Magnets". *Phys. Rev. Lett.* 123, p. 196604.

Liao, H. J., Z. Y. Xie, J. Chen, Z. Y. Liu, H. D. Xie, R. Z. Huang, B. Normand, and T. Xiang (2017). "Gapless Spin-Liquid Ground State in the $S = 1/2$ Kagome Antiferromagnet". *Phys. Rev. Lett.* 118, p. 137202.

Lieb, Elliott H. and F. Y. Wu (1968). "Absence of Mott Transition in an Exact Solution of the Short-Range, One-Band Model in One Dimension". *Phys. Rev. Lett.* 20, pp. 1445–1448.

Liebsch, A (2003). "Absence of orbital-dependent Mott transition in $Ca_{2-x}Sr_xRuO_4$". *Europhysics Letters (EPL)* 63.1, pp. 97–103.

Liebsch, A. (2004). "Single Mott transition in the multiorbital Hubbard model". *Phys. Rev. B* 70 (16), p. 165103.

Lin, Zhiyong, Jin-Ho Choi, Qiang Zhang, Wei Qin, Seho Yi, Pengdong Wang, Lin Li, Yifan Wang, Hui Zhang, Zhe Sun, Laiming Wei, Shengbai Zhang, Tengfei Guo, Qingyou Lu, Jun-Hyung Cho, Changgan Zeng, and Zhenyu Zhang (2018). "Flatbands and Emergent Ferromagnetic Ordering in Fe_3Sn_2 Kagome Lattices". *Phys. Rev. Lett.* 121, p. 096401.

Lin, Zhiyong, Chongze Wang, Pengdong Wang, Seho Yi, Lin Li, Qiang Zhang, Yifan Wang, Zhongyi Wang, Hao Huang, Yan Sun, Yaobo Huang, Dawei Shen, Donglai Feng, Zhe Sun, Jun-Hyung Cho, Changgan Zeng, and Zhenyu Zhang (2020). "Dirac fermions in antiferromagnetic FeSn kagome lattices with combined space inversion and time-reversal symmetry". *Phys. Rev. B* 102 (15), p. 155103.

Liu, Chang, JianLei Shen, JiaCheng Gao, ChangJiang Yi, Di Liu, Tao Xie, Lin Yang, Sergey Danilkin, GuoChu Deng, WenHong Wang, ShiLiang Li, YouGuo Shi, HongMing Weng, EnKe Liu, and HuiQian Luo (2021). "Spin excitations and spin wave gap in the ferromagnetic Weyl semimetal $Co_3Sn_2S_2$". *China Phys. Mech. Astron.* 64, p. 217062.

Liu, D. F., A. J. Liang, E. K. Liu, Q. N. Xu, Y. W. Li, C. Chen, D. Pei, W. J. Shi, S. K. Mo, P. Dudin, T. Kim, C. Cacho, G. Li, Y. Sun, L. X. Yang, Z. K. Liu, S. S. P. Parkin, C. Felser, and Y. L. Chen (2019). "Magnetic Weyl semimetal phase in a Kagomé crystal". *Science* 365, pp. 1282–1285.

Liu, Enke, Yan Sun, Nitesh Kumar, Lukas Muechler, Aili Sun, Lin Jiao, Shuo-Ying Yang, Defa Liu, Aiji Liang, Qiunan Xu, Johannes Kroder, Vicky Süß, Horst Borrmann, Chandra Shekhar, Zhaosheng Wang, Chuanying Xi, Wenhong Wang, Walter Schnelle, Steffen Wirth, Yulin Chen, Sebastian T. B. Goennenwein, and Claudia Felser (2018). "Giant anomalous Hall effect in a ferromagnetic kagome-lattice semimetal". *Nat. Phys.* 14, pp. 1125–1131.

Die approbierte gedruckte Originalversion dieser Dissertation ist an der TU Wien Bibliothek verfügbar.
The approved original version of this doctoral thesis is available in print at TU Wien Bibliothek.
TU Bibliothek WIEN Your knowledge hub

Loh, E. Y., J. E. Gubernatis, R. T. Scalettar, S. R. White, D. J. Scalapino, and R. L. Sugar (1990). "Sign problem in the numerical simulation of many-electron systems". *Phys. Rev. B* 41 (13), pp. 9301–9307.

Loon, Erik G. C. P. van, Mikhail I. Katsnelson, and Hartmut Hafermann (2018a). "Second-order dual fermion approach to the Mott transition in the two-dimensional Hubbard model". *Phys. Rev. B* 98 (15), p. 155117.

Loon, Erik G. C. P. van, Friedrich Krien, Hartmut Hafermann, Alexander I. Lichtenstein, and Mikhail I. Katsnelson (2018b). "Fermion-boson vertex within dynamical mean-field theory". *Phys. Rev. B* 98 (20), p. 205148.

Lu, Y., M. Höppner, O. Gunnarsson, and M. W. Haverkort (2014). "Efficient real-frequency solver for dynamical mean-field theory". *Phys. Rev. B* 90 (8), p. 085102.

Luttinger, J. M. (1961). "Analytic Properties of Single-Particle Propagators for Many-Fermion Systems". *Phys. Rev.* 121 (4), pp. 942–949.

Ma, Ookie and J. B. Marston (2008). "Weak Ferromagnetic Exchange and Anomalous Specific Heat in $ZnCu_3OH_6Cl_2$". *Phys. Rev. Lett.* 101, p. 027204.

Maier, Thomas, Mark Jarrell, Thomas Pruschke, and Matthias H. Hettler (2005). "Quantum cluster theories". *Rev. Mod. Phys.* 77 (3), pp. 1027–1080.

Maislinger, F. and H. G. Evertz (2020). "Impact ionization and multiple photon absorptions in the two-dimensional photoexcited Hubbard model". *preprint*, arXiv:2007.16201.

Maiti, Kalobaran, U. Manju, Sugata Ray, Priya Mahadevan, I. H. Inoue, C. Carbone, and D. D. Sarma (2006). "Understanding the bulk electronic structure of $Ca_{1-x}Sr_xVO_3$". *Phys. Rev. B* 73 (5), p. 052508.

Mannhart, J. and D. G. Schlom (2010). "Oxide Interfaces — An Opportunity for Electronics". *Science* 327, pp. 1607–1611.

Marston, J. B. and C. Zeng (1991). "Spin-Peierls and spin-liquid phases of Kagome quantum antiferromagnets". *J. Appl. Phys.* 69, pp. 5962–5964.

Marzari, Nicola, Arash A. Mostofi, Jonathan R. Yates, Ivo Souza, and David Vanderbilt (2012). "Maximally localized Wannier functions: Theory and applications". *Rev. Mod. Phys.* 84 (4), pp. 1419–1475.

Matsubara, Takeo (1955). "A New Approach to Quantum-Statistical Mechanics". *Progress of Theoretical Physics* 14.4, pp. 351–378. ISSN: 0033-068X.

Matsumura, Takeshi, Yusaku Ozono, Shintaro Nakamura, Noriyuki Kabeya, and Akira Ochiai (2019). "Helical Ordering of Spin Trimers in a Distorted Kagome Lattice of $Gd_3Ru_4Al_{12}$ Studied by Resonant X-ray Diffraction". *J. Phys. Soc. Jpn.* 88, p. 023704.

Mazin, I. I., Harald O. Jeschke, Frank Lechermann, Hunpyo Lee, Mario Fink, Ronny Thomale, and Roser Valenti (2014). "Theoretical prediction of a strongly correlated Dirac metal". *Nat. Commun.* 5, p. 4261.

Die approbierte gedruckte Originalversion dieser Dissertation ist an der TU Wien Bibliothek verfügbar.
The approved original version of this doctoral thesis is available in print at TU Wien Bibliothek.
TU Bibliothek WIEN Your knowledge hub

Mei, Jia-Wei, Ji-Yao Chen, Huan He, and Xiao-Gang Wen (2017). "Gapped spin liquid with $\mathbb{Z}_2$ topological order for the kagome Heisenberg model". *Phys. Rev. B* 95, p. 235107.

Mendels, P., F. Bert, M. A. de Vries, A. Olariu, A. Harrison, F. Duc, J. C. Trombe, J. S. Lord, A. Amato, and C. Baines (2007). "Quantum Magnetism in the Paratacamite Family: towards an Ideal Kagome Lattice". *Phys. Rev. Lett.* 98, p. 077204.

Mermin, N. D. and H. Wagner (1966). "Absence of Ferromagnetism or Antiferromagnetism in One- or Two-Dimensional Isotropic Heisenberg Models". *Phys. Rev. Lett.* 17 (26), pp. 1307–1307.

Messio, L., O. Cépas, and C. Lhuillier (2010). "Schwinger-boson approach to the kagome antiferromagnet with Dzyaloshinskii–Moriya interactions: phase diagram and dynamical structure factors". *Phys. Rev. B* 81, p. 064428.

Messio, Laura, Bernard Bernu, and Claire Lhuillier (2012). "Kagome Antiferromagnet: A Chiral Topological Spin Liquid?" *Phys. Rev. Lett.* 108, p. 207204.

Messio, Laura, Samuel Bieri, Claire Lhuillier, and Bernard Bernu (2017). "Chiral Spin Liquid on a Kagome Antiferromagnet Induced by the Dzyaloshinskii-Moriya Interaction". *Phys. Rev. Lett.* 118, p. 267201.

Messio, Laura, Claire Lhuillier, and Grégoire Misguich (2011). "Lattice symmetries and regular magnetic orders in classical frustrated antiferromagnets". *Phys. Rev. B* 83.18, p. 184401.

Metropolis, Nicholas, Arianna W. Rosenbluth, Marshall N. Rosenbluth, Augusta H. Teller, and Edward Teller (1953). "Equation of State Calculations by Fast Computing Machines". *The Journal of Chemical Physics* 21.6, pp. 1087–1092.

Metzner, Walter, Manfred Salmhofer, Carsten Honerkamp, Volker Meden, and Kurt Schönhammer (2012). "Functional renormalization group approach to correlated fermion systems". *Rev. Mod. Phys.* 84 (1), pp. 299–352.

Metzner, Walter and Dieter Vollhardt (1989). "Correlated Lattice Fermions in $d = \infty$ Dimensions". *Phys. Rev. Lett.* 62 (3), pp. 324–327.

Miller, Rupert G. (1964). "A Trustworthy Jackknife". *Ann. Math. Statist.* 35.4, pp. 1594–1605.

Miller, Rupert G. (1974). "The Jackknife–A Review". *Biometrika* 61.1, pp. 1–15. ISSN: 00063444.

Mishchenko, A. S., N. V. Prokof'ev, A. Sakamoto, and B. V. Svistunov (2000). "Diagrammatic quantum Monte Carlo study of the Fröhlich polaron". *Phys. Rev. B* 62 (10), pp. 6317–6336.

Miyahara, Hideyuki, Ryotaro Arita, and Hiroaki Ikeda (2013). "Development of a two-particle self-consistent method for multiorbital systems and its application to unconventional superconductors". *Phys. Rev. B* 87 (4), p. 045113.

Miyake, T., C. Martins, R. Sakuma, and F. Aryasetiawan (2013). "Effects of momentum-dependent self-energy in the electronic structure of correlated materials". *Phys. Rev. B* 87 (11), p. 115110.

Die approbierte gedruckte Originalversion dieser Dissertation ist an der TU Wien Bibliothek verfügbar.
The approved original version of this doctoral thesis is available in print at TU Wien Bibliothek.
TU Bibliothek WIEN Your knowledge hub

Mo, S.-K., H.-D. Kim, J. W. Allen, G.-H. Gweon, J. D. Denlinger, J.-H. Park, A. Sekiyama, A. Yamasaki, S. Suga, P. Metcalf, and K. Held (2004). "Filling of the Mott-Hubbard Gap in the High Temperature Photoemission Spectrum of $(V_{0.972}Cr_{0.028})_2O_3$". *Phys. Rev. Lett.* 93 (7), p. 076404.

Mostofi, Arash A, Jonathan R Yates, Young-Su Lee, Ivo Souza, David Vanderbilt, and Nicola Marzari (2008). "wannier90: A tool for obtaining maximally-localised Wannier functions". *Computer physics communications* 178.9, pp. 685–699.

Mott, N. F. (1968). "Metal-Insulator Transition". *Rev. Mod. Phys.* 40 (4), pp. 677–683.

Müller-Hartmann, E. (1989). "Correlated fermions on a lattice in high dimensions". *Z. Phys. B* 74, pp. 507–512.

Nakamura, Kazuma, Yoshiro Nohara, Yoshihide Yosimoto, and Yusuke Nomura (2016). "Ab initio *GW* plus cumulant calculation for isolated band systems: Application to organic conductor $(TMTSF)_2PF_6$ and transition-metal oxide $SrVO_3$". *Phys. Rev. B* 93 (8), p. 085124.

Nakamura, S., N. Kabeya, M. Kobayashi, K. Araki, K. Katoh, and A. Ochiai (2018). "Spin trimer formation in the metallic compound $Gd_3Ru_4Al_{12}$ with a distorted kagome lattice structure". *Phys. Rev. B* 98, p. 054410.

Nakatsuji, Satoru, Naoki Kiyohara, and Tomoya Higo (2015). "Large anomalous Hall effect in a non-collinear antiferromagnet at room temperature". *Nature (London)* 527, p. 212.

Nayak, Ajaya K., Julia Erika Fischer, Yan Sun, Binghai Yan, Julie Karel, Alexander C. Komarek, Chandra Shekhar, Nitesh Kumar, Walter Schnelle, Jürgen Kübler, Claudia Felser, and Stuart S. P. Parkin (2016). "Large anomalous Hall effect driven by a nonvanishing Berry curvature in the noncolinear antiferromagnet Mn_3Ge". *Sci. Adv.* 2, e1501870.

Nekrasov, I. A., K. Held, G. Keller, D. E. Kondakov, Th. Pruschke, M. Kollar, O. K. Andersen, V. I. Anisimov, and D. Vollhardt (2006). "Momentum-resolved spectral functions of $SrVO_3$ calculated by LDA + DMFT". *Phys. Rev. B* 73 (15), p. 155112.

Nikolic, P. and T. Senthil (2003). "Physics of low-energy singlet states of the Kagome lattice quantum Heisenberg antiferromagnet". *Phys. Rev. B* 68, p. 214415.

Nishimoto, Satoshi, Florian Gebhard, and Eric Jeckelmann (2004). "Dynamical density-matrix renormalization group for the Mott–Hubbard insulator in high dimensions". *Journal of Physics: Condensed Matter* 16.39, pp. 7063–7081.

Nishimoto, Satoshi, Naokazu Shibata, and Chisa Hotta (2013). "Controlling frustrated liquids and solids with an applied field in a kagome Heisenberg antiferromagnet". *Nat. Commun.* 4, p. 2287.

Nolting, W. (2015). "Grundkurs Theoretische Physik 7: Viel-Teilchen-Theorie". Springer Spektrum.

Nordström, Johan, Johan Schött, Inka L.M. Locht, and Igor Di Marco (2016). "A GPU code for analytic continuation through a sampling method". *SoftwareX* 5, pp. 178–182. ISSN: 2352-7110.

Die approbierte gedruckte Originalversion dieser Dissertation ist an der TU Wien Bibliothek verfügbar.
The approved original version of this doctoral thesis is available in print at TU Wien Bibliothek.
TU Bibliothek WIEN Your knowledge hub

Norman, M. R., H. Ding, M. Randeria, J. C. Campuzano, T. Yokoya, T. Takeuchi, T. Takahashi, T. Mochiku, K. Kadowaki, P. Guptasarma, and D. G. Hinks (1998). "Destruction of the Fermi surface in underdoped high-Tc superconductors". *Nature* 392.6672, pp. 157–160. ISSN: 1476-4687.

Ohashi, T., S. Suga, N. Kawakami, and H. Tsunetsugu (2007). "Magnetic correlations around the Mott transition in the Kagomé lattice Hubbard model". *J. Phys.: Condens. Matter* 19, p. 145251.

Ohashi, Takuma, Norio Kawakami, and Hirokazu Tsunetsugu (2006). "Mott Transition in Kagomé Lattice Hubbard Model". *Phys. Rev. Lett.* 97, p. 066401.

Otsuki, Junya, Hartmut Hafermann, and Alexander I. Lichtenstein (2014). "Superconductivity, antiferromagnetism, and phase separation in the two-dimensional Hubbard model: A dual-fermion approach". *Phys. Rev. B* 90 (23), p. 235132.

Otsuki, Junya, Masayuki Ohzeki, Hiroshi Shinaoka, and Kazuyoshi Yoshimi (2017). "Sparse modeling approach to analytical continuation of imaginary-time quantum Monte Carlo data". *Phys. Rev. E* 95 (6), p. 061302.

Pavarini, E., S. Biermann, A. Poteryaev, A. I. Lichtenstein, A. Georges, and O. K. Andersen (2004). "Mott Transition and Suppression of Orbital Fluctuations in Orthorhombic $3d^1$ Perovskites". *Phys. Rev. Lett.* 92 (17), p. 176403.

Pekker, David and C.M. Varma (2015). "Amplitude/Higgs Modes in Condensed Matter Physics". *Annual Review of Condensed Matter Physics* 6.1, pp. 269–297.

Perdew, John P., Kieron Burke, and Matthias Ernzerhof (1996). "Generalized Gradient Approximation Made Simple". *Phys. Rev. Lett.* 77 (18), pp. 3865–3868.

Pesin, Dmytro and Leon Balents (2010). "Mott physics and band topology in materials with strong spin-orbit interaction". *Nature Phys.* 6, pp. 376–381.

Philipp, M.-T., M. Wallerberger, P. Gunacker, and K. Held (2017). "Mott-Hubbard transition in the mass-imbalanced Hubbard model". *Eur. Phys. J. B* 0, p. 114.

Pickem, Matthias, Josef Kaufmann, Jan M Tomczak, and Karsten Held (2020). "Particle-hole asymmetric lifetimes promoted by spin and orbital fluctuations in ultrahin SrVO3 films". *preprint*, arXiv:2008.12227.

Pickett, Warren E. (1989). "Electronic structure of the high-temperature oxide superconductors". *Rev. Mod. Phys.* 61, pp. 433–512.

Pizzi, Giovanni et al. (2020). "Wannier90 as a community code: new features and applications". *Journal of Physics: Condensed Matter* 32.16, p. 165902.

Poilblanc, Didier, Matthieu Mambrini, and David Schwandt (2010). "Effective quantum dimer model for the kagome Heisenberg antiferromagnet: nearby quantum critical point and hidden degeneracy". *Phys. Rev. B* 81, p. 180402.

Poilblanc, Didier and Grégoire Misguich (2011). "Competing valence bond crystals in the kagome quantum dimer model". *Phys. Rev. B* 84, p. 214401.

Die approbierte gedruckte Originalversion dieser Dissertation ist an der TU Wien Bibliothek verfügbar.
The approved original version of this doctoral thesis is available in print at TU Wien Bibliothek.
TU Bibliothek WIEN Your knowledge hub

Pratapa, Phanisri P. and Phanish Suryanarayana (2015). "Restarted Pulay mixing for efficient and robust acceleration of fixed-point iterations". *Chemical Physics Letters* 635, pp. 69–74. ISSN: 0009-2614.

Press, William H., Saul A. Teukolsky, William T. Vetterling, and Brian P. Flannery (2007). "Numerical Recipes 3rd Edition: The Art of Scientific Computing". 3rd ed. USA: Cambridge University Press. ISBN: 0521880688.

Prokof'ev, N. V., B. V. Svistunov, and I. S. Tupitsyn (1998). "Exact, complete, and universal continuous-time worldline Monte Carlo approach to the statistics of discrete quantum systems". *Journal of Experimental and Theoretical Physics* 87.2, pp. 310–321. ISSN: 1090-6509.

Prokof'ev, Nikolai V. and Boris V. Svistunov (1998). "Polaron Problem by Diagrammatic Quantum Monte Carlo". *Phys. Rev. Lett.* 81 (12), pp. 2514–2517.

Pulay, P. (1982). "Improved SCF convergence acceleration". *Journal of Computational Chemistry* 3.4, pp. 556–560.

Pulay, Péter (1980). "Convergence acceleration of iterative sequences. the case of scf iteration". *Chemical Physics Letters* 73.2, pp. 393–398. ISSN: 0009-2614.

Punk, Matthias, Debanjan Chowdhury, and Subir Sachdev (2014). "Topological excitations and the dynamic structure factor of spin liquids on the kagome lattice". *Nature Physics* 10 (4), pp. 289–293.

Ralko, Arnaud, Frédéric Mila, and Ioannis Rousochatzakis (2018). "Microscopic theory of the nearest-neighbor valence bond sector of the spin-$\frac{1}{2}$ kagome antiferromagnet". *Phys. Rev. B* 97, p. 104401.

Ran, Ying, Michael Hermele, Patrick A. Lee, and Xiao-Gang Wen (2007). "Projected-Wave-Function Study of the spin-1/2 Heisenberg Model on the Kagome Lattice". *Phys. Rev. Lett.* 98, p. 117205.

Ribic, T., E. Assmann, A. Tóth, and K. Held (2014). "Cubic interaction parameters for t_{2g} Wannier orbitals". *Phys. Rev. B* 90 (16), p. 165105.

Ribic, T., P. Gunacker, and K. Held (2018). "Impact of self-consistency in dual fermion calculations". *Phys. Rev. B* 98 (12), p. 125106.

Ribic, T., P. Gunacker, S. Iskakov, M. Wallerberger, G. Rohringer, A. N. Rubtsov, E. Gull, and K. Held (2017). "Role of three-particle vertex within dual fermion calculations". *Phys. Rev. B* 96 (23), p. 235127.

Rohringer, G., H. Hafermann, A. Toschi, A. A. Katanin, A. E. Antipov, M. I. Katsnelson, A. I. Lichtenstein, A. N. Rubtsov, and K. Held (2018). "Diagrammatic routes to nonlocal correlations beyond dynamical mean field theory". *Rev. Mod. Phys.* 90 (2), p. 025003.

Rohringer, G. and A. Toschi (2016). "Impact of nonlocal correlations over different energy scales: A dynamical vertex approximation study". *Phys. Rev. B* 94 (12), p. 125144.

Rohringer, G., A. Toschi, A. Katanin, and K. Held (2011). "Critical Properties of the Half-Filled Hubbard Model in Three Dimensions". *Phys. Rev. Lett.* 107 (25), p. 256402.

Die approbierte gedruckte Originalversion dieser Dissertation ist an der TU Wien Bibliothek verfügbar.
The approved original version of this doctoral thesis is available in print at TU Wien Bibliothek.
TU Bibliothek WIEN Your knowledge hub

Rossi, Riccardo (2017). "Determinant Diagrammatic Monte Carlo Algorithm in the Thermodynamic Limit". *Phys. Rev. Lett.* 119 (4), p. 045701.

Rost, D., E. V. Gorelik, F. Assaad, and N. Blümer (2012). "Momentum-dependent pseudogaps in the half-filled two-dimensional Hubbard model". *Phys. Rev. B* 86 (15), p. 155109.

Rozenberg, M. J., G. Kotliar, and X. Y. Zhang (1994). "Mott-Hubbard transition in infinite dimensions. II". *Phys. Rev. B* 49 (15), pp. 10181–10193.

Rubtsov, A. N., M. I. Katsnelson, and A. I. Lichtenstein (2008). "Dual fermion approach to nonlocal correlations in the Hubbard model". *Phys. Rev. B* 77 (3), p. 033101.

Rubtsov, A. N., M. I. Katsnelson, A. I. Lichtenstein, and A. Georges (2009). "Dual fermion approach to the two-dimensional Hubbard model: Antiferromagnetic fluctuations and Fermi arcs". *Phys. Rev. B* 79.4, p. 045133.

Rubtsov, A. N. and A. I. Lichtenstein (2004). "Continuous-time quantum Monte Carlo method for fermions: Beyond auxiliary field framework". *Journal of Experimental and Theoretical Physics Letters* 80.1, pp. 61–65. ISSN: 1090-6487.

Rubtsov, A.N., M.I. Katsnelson, and A.I. Lichtenstein (2012). "Dual boson approach to collective excitations in correlated fermionic systems". *Annals of Physics* 327.5, pp. 1320–1335. ISSN: 0003-4916.

Sadovskii, M. V., I. A. Nekrasov, E. Z. Kuchinskii, Th. Pruschke, and V. I. Anisimov (2005). "Pseudogaps in strongly correlated metals: A generalized dynamical mean-field theory approach". *Phys. Rev. B* 72, p. 155105.

Sakai, Shiro, Ryotaro Arita, Karsten Held, and Hideo Aoki (2006). "Quantum Monte Carlo study for multiorbital systems with preserved spin and orbital rotational symmetries". *Phys. Rev. B* 74 (15), p. 155102.

Sakuma, R., Ph. Werner, and F. Aryasetiawan (2013). "Electronic structure of $SrVO_3$ within GW+DMFT". *Phys. Rev. B* 88 (23), p. 235110.

Sales, Brian C., Jiaqiang Yan, William R. Meier, Andrew D. Christianson, Satoshi Okamoto, and Michael A. McGuire (2019). "Electronic, magnetic, and thermodynamic properties of the kagome layer compound FeSn". *Phys. Rev. Materials* 3, p. 114203.

Sandvik, Anders W. (1998). "Stochastic method for analytic continuation of quantum Monte Carlo data". *Phys. Rev. B* 57 (17), pp. 10287–10290.

Schäfer, T., S. Ciuchi, M. Wallerberger, P. Thunström, O. Gunnarsson, G. Sangiovanni, G. Rohringer, and A. Toschi (2016a). "Nonperturbative landscape of the Mott-Hubbard transition: Multiple divergence lines around the critical endpoint". *Phys. Rev. B* 94 (23), p. 235108.

Schäfer, T., F. Geles, D. Rost, G. Rohringer, E. Arrigoni, K. Held, N. Blümer, M. Aichhorn, and A. Toschi (2015). "Fate of the false Mott-Hubbard transition in two dimensions". *Phys. Rev. B* 91, p. 125109.

Die approbierte gedruckte Originalversion dieser Dissertation ist an der TU Wien Bibliothek verfügbar.
The approved original version of this doctoral thesis is available in print at TU Wien Bibliothek.
TU Bibliothek WIEN Your knowledge hub

Schäfer, T., A. A. Katanin, K. Held, and A. Toschi (2017). "Interplay of Correlations and Kohn Anomalies in Three Dimensions: Quantum Criticality with a Twist". *Phys. Rev. Lett.* 119 (4), p. 046402.

Schäfer, T., A. A. Katanin, M. Kitatani, A. Toschi, and K. Held (2019). "Quantum Criticality in the Two-Dimensional Periodic Anderson Model". *Phys. Rev. Lett.* 122 (22), p. 227201.

Schäfer, T., G. Rohringer, O. Gunnarsson, S. Ciuchi, G. Sangiovanni, and A. Toschi (2013). "Divergent Precursors of the Mott-Hubbard Transition at the Two-Particle Level". *Phys. Rev. Lett.* 110 (24), p. 246405.

Schäfer, Thomas, Alessandro Toschi, and Karsten Held (2016b). "Dynamical vertex approximation for the two-dimensional Hubbard model". *Journal of Magnetism and Magnetic Materials* 400. Proceedings of the 20th International Conference on Magnetism (Barcelona) 5-10 July 2015, pp. 107–111. ISSN: 0304-8853.

Schäfer, Thomas, Nils Wentzell, Fedor Šimkovic IV, Yuan-Yao He, Cornelia Hille, Marcel Klett, Christian J. Eckhardt, Behnam Arzhang, Viktor Harkov, François-Marie Le Régent, Alfred Kirsch, Yan Wang, Aaram J. Kim, Evgeny Kozik, Evgeny A. Stepanov, Anna Kauch, Sabine Andergassen, Philipp Hansmann, Daniel Rohe, Yuri M. Vilk, James P. F. LeBlanc, Shiwei Zhang, A. -M. S. Tremblay, Michel Ferrero, Olivier Parcollet, and Antoine Georges (2020). "Tracking the Footprints of Spin Fluctuations: A Multi-Method, Multi-Messenger Study of the Two-Dimensional Hubbard Model". *preprint*, arXiv:2006.10769.

Schwandt, David, Matthieu Mambrini, and Didier Poilblanc (2010). "Generalized hard-core dimer model approach to low-energy Heisenberg frustrated antiferromagnets: general properties and application to the kagome antiferromagnet". *Phys. Rev. B* 81, p. 214413.

Schwarz, K., P. Blaha, and G.K.H. Madsen (2002). "Electronic structure calculations of solids using the WIEN2k package for material sciences". *Comp. Phys. Commun.* 147, pp. 71–76.

Sekiyama, A., H. Fujiwara, S. Imada, S. Suga, H. Eisaki, S. I. Uchida, K. Takegahara, H. Harima, Y. Saitoh, I. A. Nekrasov, G. Keller, D. E. Kondakov, A. V. Kozhevnikov, Th. Pruschke, K. Held, D. Vollhardt, and V. I. Anisimov (2004). "Mutual Experimental and Theoretical Validation of Bulk Photoemission Spectra of $Sr_{1-x}Ca_xVO_3$". *Phys. Rev. Lett.* 93.15, p. 156402.

Seman, Tsezar F., Cheng-Chien Chen, Rajiv R. P. Singh, and Michel van Veenendaal (2015). "The many faces of quantum kagome materials: Interplay of further-neighbour exchange and Dzyaloshinskii-Moriya interaction". *preprint*, arXiv:1508.01523.

Shannon, C. E. (1948). "A mathematical theory of communication". *The Bell System Technical Journal* 27.3, pp. 379–423.

Shen, Jianlei, Qingqi Zeng, Shen Zhang, Wei Tong, Langsheng Ling, Chuanying Xi, Zhaosheng Wang, Enke Liu, Wenhong Wang, Guangheng Wu, and Baogen Shen (2019). "On the anisotropies of magnetization and electronic transport of magnetic Weyl semimetal $Co_3Sn_2S_2$". *Appl. Phys. Lett.* 115, p. 212403.

Sherman, Nicholas E. and Rajiv R. P. Singh (2018). "Structure factors of the kagome-lattice Heisenberg antiferromagnets at finite temperatures". *Phys. Rev. B* 97 (1), p. 014423.

Die approbierte gedruckte Originalversion dieser Dissertation ist an der TU Wien Bibliothek verfügbar.
The approved original version of this doctoral thesis is available in print at TU Wien Bibliothek.
TU Bibliothek WIEN Your knowledge hub

Sherrill, David (2000). "The Mathematics of DIIS". http://vergil.chemistry.gatech.edu/notes/diis/node2.html, Accessed: 2021-01-06.

Shinaoka, Hiroshi, Emanuel Gull, and Philipp Werner (2017a). "Continuous-time hybridization expansion quantum impurity solver for multi-orbital systems with complex hybridizations". *Computer Physics Communications* 215, pp. 128–136. ISSN: 0010-4655.

Shinaoka, Hiroshi, Junya Otsuki, Masayuki Ohzeki, and Kazuyoshi Yoshimi (2017b). "Compressing Green's function using intermediate representation between imaginary-time and real-frequency domains". *Phys. Rev. B* 96 (3), p. 035147.

Si, Liang, Josef Kaufmann, Jan M. Tomczak, Zhicheng Zhong, and Karsten Held (2020a). "Pitfalls and solutions for perovskite transparent conductors". *preprint*, arXiv:2009.14000.

Si, Liang, Wen Xiao, Josef Kaufmann, Jan M. Tomczak, Yi Lu, Zhicheng Zhong, and Karsten Held (2020b). "Topotactic Hydrogen in Nickelate Superconductors and Akin Infinite-Layer Oxides ABO_2". *Phys. Rev. Lett.* 124 (16), p. 166402.

Silver, R. N., J. E. Gubernatis, D. S. Sivia, and M. Jarrell (1990a). "Spectral densities of the symmetric Anderson model". *Phys. Rev. Lett.* 65 (4), pp. 496–499.

Silver, R. N., D. S. Sivia, and J. E. Gubernatis (1990b). "Maximum-entropy method for analytic continuation of quantum Monte Carlo data". *Phys. Rev. B* 41 (4), pp. 2380–2389.

Sim, Jae-Hoon and Myung Joon Han (2018). "Maximum quantum entropy method". *Phys. Rev. B* 98 (20), p. 205102.

Sim, Jae-Hoon and Myung Joon Han (2019). "Density functional theory plus dynamical mean-field theory with natural atomic orbital projectors". *Phys. Rev. B* 100 (11), p. 115151.

Šimkovic, Fedor and Evgeny Kozik (2019). "Determinant Monte Carlo for irreducible Feynman diagrams in the strongly correlated regime". *Phys. Rev. B* 100 (12), p. 121102.

Singh, Rajiv R. P. and David A. Huse (2007). "Ground state of the spin-1/2 kagome-lattice Heisenberg antiferromagnet". *Phys. Rev. B* 76, p. 180407.

Skilling, John (1989). "Classic maximum entropy". *Maximum Entropy and Bayesian Methods.* Ed. by John Skilling. Kluwer Academic Publishers, pp. 45–52.

Skilling, John (1991). "Classic maximum entropy". *Maximum Entropy in Action.* Ed. by Brian Buck and Vincent A. Macaulay. Oxford: Clarendon Press, pp. 19–40.

Slater, J. C. (1960). "Quantum Theory of Atomic Structure". McGraw-Hill, New York.

Slater, J. C. and G. F. Koster (1954). "Simplified LCAO Method for the Periodic Potential Problem". *Phys. Rev.* 94 (6), pp. 1498–1524.

Smith, Cyril Stanley (1965a). "Materials and the Development of Civilization and Science". *Science* 148.3672, pp. 908–917. ISSN: 00368075, 10959203.

Smith, Cyril Stanley (1965b). "The prehistory of solid-state physics". *Physics Today* 18 (12), pp. 18–30.

Die approbierte gedruckte Originalversion dieser Dissertation ist an der TU Wien Bibliothek verfügbar.
The approved original version of this doctoral thesis is available in print at TU Wien Bibliothek.
TU Bibliothek WIEN Your knowledge hub

Sorantin, Max E., Antonius Dorda, Karsten Held, and Enrico Arrigoni (2018). "Impact ionization processes in the steady state of a driven Mott-insulating layer coupled to metallic leads". *Phys. Rev. B* 97 (11), p. 115113.

Sordi, G., P. Sémon, K. Haule, and A.-M. S. Tremblay (2012). "Strong Coupling Superconductivity, Pseudogap, and Mott Transition". *Phys. Rev. Lett.* 108 (21), p. 216401.

Stepanov, E. A., V. Harkov, and A. I. Lichtenstein (2019). "Consistent partial bosonization of the extended Hubbard model". *Phys. Rev. B* 100 (20), p. 205115.

Strand, Hugo U. R., Andro Sabashvili, Mats Granath, Bo Hellsing, and Stellan Östlund (2011). "Dynamical mean field theory phase-space extension and critical properties of the finite temperature Mott transition". *Phys. Rev. B* 83 (20), p. 205136.

Syromyatnikov, A. V. and S. V. Maleyev (2002). "Hidden long-range order in kagomé Heisenberg antiferromagnets". *Phys. Rev. B* 66, p. 132408.

Tanaka, Arata (2019). "Metal-insulator transition in the two-dimensional Hubbard model: Dual fermion approach with Lanczos exact diagonalization". *Phys. Rev. B* 99 (20), p. 205133.

Tanaka, Hiroaki, Yuita Fujisawa, Kenta Kuroda, Ryo Noguchi, Shunsuke Sakuragi, Cédric Bareille, Barnaby Smith, Cephise Cacho, Sung Won Jung, Takayuki Muro, Yoshinori Okada, and Takeshi Kondo (2020). "Three-dimensional electronic structure in ferromagnetic Fe_3Sn_2 with breathing kagome bilayers". *Phys. Rev. B* 101 (16), p. 161114.

Taranto, C., M. Kaltak, N. Parragh, G. Sangiovanni, G. Kresse, A. Toschi, and K. Held (2013). "Comparing quasiparticle GW+DMFT and LDA+DMFT for the test bed material $SrVO_3$". *Phys. Rev. B* 88 (16), p. 165119.

Timusk, Tom and Bryan Statt (1999). "The pseudogap in high-temperature superconductors: an experimental survey". *Reports on Progress in Physics* 62.1, pp. 61–122.

Tocchio, Luca F, Federico Arrigoni, Sandro Sorella, and Federico Becca (2016). "Assessing the orbital selective Mott transition with variational wave functions". *J. Phys.: Condensed Matter* 28.10, p. 105602.

Tolstoy, Lev Nikolayevich (1869). "War and Peace".

Tomczak, Jan M., M. Casula, T. Miyake, and S. Biermann (2014). "Asymmetry in band widening and quasiparticle lifetimes in $SrVO_3$: Competition between screened exchange and local correlations from combined GW and dynamical mean-field theory GW + DMFT". *Phys. Rev. B* 90 (16), p. 165138.

Tomczak, Jan M., Michele Casula, Takashi Miyake, Ferdi Aryasetiawan, and Silke Biermann (2012). "Combined GW and dynamical mean-field theory: Dynamical screening effects in transition metal oxides". *EPL (Europhysics Letters)* 100.6, p. 67001.

Toschi, A., A. A. Katanin, and K. Held (2007). "Dynamical vertex approximation: A step beyond dynamical mean-field theory". *Phys. Rev. B* 75.4, 045118, p. 045118.

Die approbierte gedruckte Originalversion dieser Dissertation ist an der TU Wien Bibliothek verfügbar.
The approved original version of this doctoral thesis is available in print at TU Wien Bibliothek.
TU Bibliothek WIEN Your knowledge hub

Toth, Alex, J Austin Ellis, Tom Evans, Steven Hamilton, CT Kelley, Roger Pawlowski, and Stuart Slattery (2017). "Local improvement results for Anderson acceleration with inaccurate function evaluations". *SIAM Journal on Scientific Computing* 39.5, S47–S65.

Tremblay, A. M. S. (2011). "Two-particle-Self-Consistent Approach for the Hubbard model". *Strongly Correlated Systems: Theoretical Methods.* Ed. by F. Mancini and A. Avella. Berlin, Heidelberg: Springer. Chap. 13, pp. 409–455.

Troyer, Matthias and Uwe-Jens Wiese (2005). "Computational Complexity and Fundamental Limitations to Fermionic Quantum Monte Carlo Simulations". *Phys. Rev. Lett.* 94 (17), p. 170201.

Udagawa, Masafumi and Yukitoshi Motome (2010). "Chirality-Driven Mass Enhancement in the Kagome Hubbard Model". *Phys. Rev. Lett.* 104, p. 106409.

Valli, A., H. Das, G. Sangiovanni, T. Saha-Dasgupta, and K. Held (2015a). "Tunable site- and orbital-selective Mott transition and quantum confinement effects in $La_{0.5}Ca_{0.5}MnO_3$ nanoclusters". *Phys. Rev. B* 92 (11), p. 115143.

Valli, A., T. Schäfer, P. Thunström, G. Rohringer, S. Andergassen, G. Sangiovanni, K. Held, and A. Toschi (2015b). "Dynamical vertex approximation in its parquet implementation: Application to Hubbard nanorings". *Phys. Rev. B* 91 (11), p. 115115.

Varney, C. N., C.-R. Lee, Z. J. Bai, S. Chiesa, M. Jarrell, and R. T. Scalettar (2009). "Quantum Monte Carlo study of the two-dimensional fermion Hubbard model". *Phys. Rev. B* 80, p. 075116.

Vasil'ev, A. N. (1998). "Functional Methods in Quantum Field Theory and Statistical Physics". 1st ed. Vol. 1. 1. Taylor and Francis Group. ISBN: 9789056990350.

Vidberg, H. J. and J. W. Serene (1977). "Solving the Eliashberg equations by means ofN-point Padé approximants". *Journal of Low Temperature Physics.*

Vilk, YM and A-MS Tremblay (1997). "Non-perturbative many-body approach to the Hubbard model and single-particle pseudogap". *Journal de Physique I* 7.11, pp. 1309–1368.

Vučićević, J., N. Wentzell, M. Ferrero, and O. Parcollet (2018). "Practical consequences of the Luttinger-Ward functional multivaluedness for cluster DMFT methods". *Phys. Rev. B* 97 (12), p. 125141.

Wadati, H., J. Mravlje, K. Yoshimatsu, H. Kumigashira, M. Oshima, T. Sugiyama, E. Ikenaga, A. Fujimori, A. Georges, A. Radetinac, K. S. Takahashi, M. Kawasaki, and Y. Tokura (2014). "Photoemission and DMFT study of electronic correlations in $SrMoO_3$: Effects of Hund's rule coupling and possible plasmonic sideband". *Phys. Rev. B* 90 (20), p. 205131.

Wais, M. (2020). "Computational non-equilibrium dynamics in solids: solver for the far-from-equilibrium Boltzmann-equation". PhD thesis. TU Wien.

Wais, M., M. Eckstein, R. Fischer, P. Werner, M. Battiato, and K. Held (2018). "Quantum Boltzmann equation for strongly correlated systems: Comparison to dynamical mean field theory". *Phys. Rev. B* 98 (13), p. 134312.

Die approbierte gedruckte Originalversion dieser Dissertation ist an der TU Wien Bibliothek verfügbar.
The approved original version of this doctoral thesis is available in print at TU Wien Bibliothek.
TU Bibliothek WIEN Your knowledge hub

Wais, M., K. Held, and M. Battiato (2020a). "Numerical solver for the time-dependent far-from-equilibrium Boltzmann equation". *preprint*, arXiv:2004.02683.

Wais, M., J. Kaufmann, M. Battiato, and K. Held (2020b). "Comparing scattering rates from Boltzmann and dynamical mean-field theory". *preprint*, arXiv:2012.11257.

Walker, Homer F. and Peng Ni (2011). "Anderson Acceleration for Fixed-Point Iterations". *SIAM Journal on Numerical Analysis* 49.4, pp. 1715–1735.

Wallerberger, Markus (2016). "w2dynamics: continuous time quantum Monte Carlo calculations of one- and two-particle propagators". PhD thesis. Vienna University of Technology.

Wallerberger, Markus, Andreas Hausoel, Patrik Gunacker, Alexander Kowalski, Nicolaus Parragh, Florian Goth, Karsten Held, and Giorgio Sangiovanni (2019). "w2dynamics: Local one- and two-particle quantities from dynamical mean field theory". *Computer Physics Communications* 235, pp. 388–399. ISSN: 0010-4655.

Wang, Qi, Yuanfeng Xu, Rui Lou, Zhonghao Liu, Man Li, Yaobo Huang, Hongming Weng, Shancai Wang, and Hechang Lei (2018). "Large intrinsic anomalous Hall effect in half-metallic ferromagnet $Co_3Sn_2S_2$ with magnetic Weyl fermions". *Nat. Commun.* 9, p. 3681.

Wang, Xin, Hung The Dang, and Andrew J. Millis (2011). "High-frequency asymptotic behavior of self-energies in quantum impurity models". *Phys. Rev. B* 84 (7), p. 073104.

Watanabe, Haruki and Hitoshi Murayama (2012). "Unified Description of Nambu-Goldstone Bosons without Lorentz Invariance". *Phys. Rev. Lett.* 108 (25), p. 251602.

Wentzell, Nils, Gang Li, Agnese Tagliavini, Ciro Taranto, Georg Rohringer, Karsten Held, Alessandro Toschi, and Sabine Andergassen (2020). "High-frequency asymptotics of the vertex function: Diagrammatic parametrization and algorithmic implementation". *Phys. Rev. B* 102 (8), p. 085106.

Werner, Philipp, Armin Comanac, Luca de'Medici, Matthias Troyer, and Andrew J. Millis (2006). "Continuous-Time Solver for Quantum Impurity Models". *Phys. Rev. Lett.* 97 (7), p. 076405.

Werner, Philipp, Karsten Held, and Martin Eckstein (2014). "Role of impact ionization in the thermalization of photoexcited Mott insulators". *Phys. Rev. B* 90 (23), p. 235102.

Werner, Philipp and Andrew J. Millis (2006). "Hybridization expansion impurity solver: General formulation and application to Kondo lattice and two-orbital models". *Phys. Rev. B* 74 (15), p. 155107.

White, S. R., D. J. Scalapino, R. L. Sugar, E. Y. Loh, J. E. Gubernatis, and R. T. Scalettar (1989). "Numerical study of the two-dimensional Hubbard model". *Phys. Rev. B* 40 (1), pp. 506–516.

Wick, G. C. (1954). "Properties of Bethe-Salpeter Wave Functions". *Phys. Rev.* 96 (4), pp. 1124–1134.

Wietek, Alexander, Antoine Sterdyniak, and Andreas M. Läuchli (2015). "Nature of chiral spin liquids on the kagome lattice". *Phys. Rev. B* 92, p. 125122.

Die approbierte gedruckte Originalversion dieser Dissertation ist an der TU Wien Bibliothek verfügbar.
The approved original version of this doctoral thesis is available in print at TU Wien Bibliothek.
TU Bibliothek WIEN Your knowledge hub

Wu, Wei, Mathias S. Scheurer, Shubhayu Chatterjee, Subir Sachdev, Antoine Georges, and Michel Ferrero (2018). "Pseudogap and Fermi-Surface Topology in the Two-Dimensional Hubbard Model". *Phys. Rev. X* 8 (2), p. 021048.

Wu, Wei, Mathias S. Scheurer, Michel Ferrero, and Antoine Georges (2020). "Effect of Van Hove singularities in the onset of pseudogap states in Mott insulators". *Phys. Rev. Research* 2 (3), p. 033067.

Wuttke, Christoph, Federico Caglieris, Steffen Sykora, Francesco Scaravaggi, Anja U. B. Wolter, Kaustuv Manna, Vicky Süss, Chandra Shekhar, Claudia Felser, Bernd Büchner, and Christian Hess (2019). "Berry curvature unravelled by the anomalous Nernst effect in Mn_3Ge". *Phys. Rev. B* 100, p. 085111.

Xing, Yuqing, Jianlei Shen, Hui Chen, Li Huang, Yuxiang Gao, Qi Zheng, Yu-Yang Zhang, Geng Li, Bin Hu, Guojian Qian, Lu Cao, Xianli Zhang, Peng Fan, Ruisong Ma, Qi Wang, Qiangwei Yin, Hechang Lei, Wei Ji, Shixuan Du, Haitao Yang, Wenhong Wang, Chengmin Shen, Xiao Lin, Enke Liu, Baogen Shen, Ziqiang Wang, and Hong-Jun Gao (2020). "Localized spin-orbit polaron in magnetic Weyl semimetal Co3Sn2S2". *Nature Communications* 11.1, p. 5613. ISSN: 2041-1723.

Yan, Simeng, David A. Huse, and Steven R. White (2011). "Spin Liquid Ground State of the S=1/2 Kagome Heisenberg Antiferromagnet". *Science* 332, pp. 1173–1176.

Ye, Linda, Mingu Kang, Junwei Liu, Felix von Cube, Christina R. Wicker, Takehito Suzuki, Chris Jozwiak, Aaron Bostwick, Eli Rotenberg, David, Bell, Liang Fu, Riccardo Comin, and Joseph G. Checkelsky (2018). "Massive Dirac fermions in a ferromagnetic kagome metal". *Nature* 555, pp. 638–642.

Yin, Jia-Xin, Nana Shumiya, Yuxiao Jiang, Huibin Zhou, Gennevieve Macam, Hano Omar Mohammad Sura, Songtian S. Zhang, Zi-Jia Cheng, Zurab Guguchia, Yangmu Li, Qi Wang, Maksim Litskevich, Ilya Belopolski, Xian P. Yang, Tyler A. Cochran, Guoqing Chang, Qi Zhang, Zhi-Quan Huang, Feng-Chuan Chuang, Hsin Lin, Hechang Lei, Brian M. Andersen, Ziqiang Wang, Shuang Jia, and M. Zahid Hasan (2020). "Spin-orbit quantum impurity in a topological magnet". *Nat. Commun.* 11.1, p. 4415. ISSN: 2041-1723.

Yin, Jia-Xin, Songtian S. Zhang, Guoqing Chang, Qi Wang, Stepan S. Tsirkin, Zurab Guguchia, Biao Lian, Huibin Zhou, Kun Jiang, Ilya Belopolski, Nana Shumiya, Daniel Multer, Maksim Litskevich, Tyler A. Cochran, Hsin Lin, Ziqiang Wang, Titus Neupert, Shuang Jia, Hechang Lei, and M. Zahid Hasan (2019). "Negative flat band magnetism in a spin-orbit-coupled correlated kagome magnet". *Nat. Phys.* 15, p. 443.

Yin, Jia-Xin, Songtian S. Zhang, Hang Li, Kun Jiang, Guoqing Chang, Bingjing Zhang, Biao Lian, Cheng Xiang, Ilya Belopolski, Hao Zheng, Tyler A. Cochran, Su-Yang Xu, Guang Bian, Kai Liu, Tay-Rong Chang, Hsin Lin, Zhong-Yi Lu, Ziqiang Wang, Shuang Jia, Wenhong Wang, and M. Zahid Hasan (2018). "Giant and anisotropic many-body spin-orbit tunability in a strongly correlated kagome magnet". *Nature* 562, pp. 91–95.

Die approbierte gedruckte Originalversion dieser Dissertation ist an der TU Wien Bibliothek verfügbar.
The approved original version of this doctoral thesis is available in print at TU Wien Bibliothek.
TU Bibliothek WIEN Your knowledge hub

Yoo, Jaebeom, Shailesh Chandrasekharan, Ribhu K Kaul, Denis Ullmo, and Harold U Baranger (2005). "On the sign problem in the Hirsch–Fye algorithm for impurity problems". *Journal of Physics A: Mathematical and General* 38.48, pp. 10307–10310.

Zhang, Y. Z. and Masatoshi Imada (2007). "Pseudogap and Mott transition studied by cellular dynamical mean-field theory". *Phys. Rev. B* 76 (4), p. 045108.

Zhong, Zhicheng, Markus Wallerberger, Jan M. Tomczak, Ciro Taranto, Nicolaus Parragh, Alessandro Toschi, Giorgio Sangiovanni, and Karsten Held (2015). "Electronics with Correlated Oxides: $SrVO_3/SrTiO_3$ as a Mott Transistor". *Phys. Rev. Lett.* 114 (24), p. 246401.

Zhu, W., Shou-shu Gong, and D. N. Sheng (2019). "Identifying spinon excitations from dynamic structure factor of spin-1/2 Heisenberg antiferromagnet on the Kagome lattice". *Proc. Natl. Acad. Sci.* 116, pp. 5437–5441.

Žitko, Rok (2009). "Convergence acceleration and stabilization of dynamical mean-field theory calculations". *Phys. Rev. B* 80 (12), p. 125125.

Die approbierte gedruckte Originalversion dieser Dissertation ist an der TU Wien Bibliothek verfügbar.
The approved original version of this doctoral thesis is available in print at TU Wien Bibliothek.
TU Bibliothek WIEN Your knowledge hub

Acknowledgments

First and foremost I want to thank my supervisor Karsten Held, who gave me the opportunity to work in his truly remarkable group for more than five years. During this time he was always available for discussions and supported me in realizing what I actually considered impossible. Besides this he also gave me the freedom to follow my own ideas and side projects.

I also want to thank my co-supervisor Oleg Janson. Our countless discussions have given me more physical intuition as well as a whole different perspective on what we are doing. Oleg also made it possible that I could spend half a year in Dresden. In this very enjoyable time I had the opportunity to work in a new environment and also travel quite a lot.

When I had a question, or something was unclear to me, Anna Kauch was always happy to help. Patiently she answered so many questions about diagrammatics and self-consistency cycles. Without her confident guidance I probably would have gotten lost in technicalities.

In the first half of my PhD, I still had the opportunity to profit from the presence of Patrik Gunacker, the supervisor of my Master thesis. He was a great instructor and teacher to me. Not only did he give me insight to the w2dynamics code, he also gave me the incentive to write my own code for analytic continuation.

Furthermore I want to thank Jan Kuneš for many inspiring discussions, where I just wanted to ask a little question and came out of his office hours later. Through his mediation, I also had the chance of working with Dominique Geffroy – a very intensive and fruitful collaboration that considerably advanced also my programming skills.

Supervising students – Klaus Steiner for his master thesis and Andreas Stefl for a project work – has also been a valuable experience. I thank them for the close collaboration, from which I learned a lot about programming. In this spirit I also want to express my gratitude to Matthias Pickem for the productive coworking in the development of the AbinitioDΓA project.

Already since my Master thesis I have had the opportunity to be a part of the w2dynamics developers team. Thus I had the chance of working with Markus Wallerberger, Giorgio Sangiovanni, Andreas Hausoel and Alexander Kowalski. I also want to thank them for the hospitality when I visited them in Würzburg.

Let me further thank Alexander Lichtenstein and his group for numerous discussions and for sharing an often complementary view on things. Visiting their group in Hamburg was a great experience and I am grateful for the hospitality.

Trying to find sense in my sometimes confused thoughts can certainly be a complicated task. For careful proof-reading of this thesis I want to thank Anna Kauch, Clemens Watzenböck, Lukas Rammelmüller, whom I also thank for typesetting assistance.

Going to the office is a very nice thing if you share it with great colleagues and friends. Corona-related home office made me realize this fact even more. I had such an enjoyable time with all of you with all those lively and emotional discussions about physics, politics, weekends. And of course, lunch at 11:00 at Cafe Schrödinger! My deep gratitude goes to all members of AG Held, Kuneš and Toschi for the pleasant atmosphere, and to the members of IFW for making my stay in Dresden even more enjoyable.

The last years have been dominated by hard work – the fact that I have not lost faith and mind is largely due to my dear friends. I thank you so much for always being there for me! Last but not least I want to express my deepest gratitude to my parents, sisters and girlfriend. Without you I would not be where I am.

Die approbierte gedruckte Originalversion dieser Dissertation ist an der TU Wien Bibliothek verfügbar.
The approved original version of this doctoral thesis is available in print at TU Wien Bibliothek.
TU Bibliothek WIEN Your knowledge hub

Die approbierte gedruckte Originalversion dieser Dissertation ist an der TU Wien Bibliothek verfügbar.
The approved original version of this doctoral thesis is available in print at TU Wien Bibliothek.

Curriculum vitae

Personal Information

Name:	Josef Kaufmann
Date of Birth:	3 October 1990
Place of Birth:	St. Johann in Tirol

Education

2017-present:	Ph.D. in Physics, Vienna University of Technology
2014-2017:	M.Sc. in Technical Physics (with distinction), Vienna University of Technology
2010-2014:	B.Sc. in Technical Physics (with distinction), Vienna University of Technology
2009:	Matura (with distinction), BG/BORG St. Johann in Tirol

Academic Employment and Teaching

05/2017-present:	Project Assistant, Vienna University of Technology
05/2019-10/2019:	Project Assistant, Leibniz Institute for Solid State and Materials Research Dresden
03/2014-06/2016:	Tutor for Elektrodynamik 1, Quantentheorie 1, Numerische Methoden und Simulation
02/2014-07/2014:	Laboratory Assistant, Medical University Vienna

Co-Supervision of Students

2018	Electronic Correlations in the Hubbard Model on the Kagome Lattice, Klaus Steiner, Master's thesis (TU Wien, UC Davis)
2020	DIIS mixing of self energy in DMFT, Andreas Stefl, Project thesis.

Die approbierte gedruckte Originalversion dieser Dissertation ist an der TU Wien Bibliothek verfügbar.
The approved original version of this doctoral thesis is available in print at TU Wien Bibliothek.
TU Bibliothek WIEN Your knowledge hub

Conferences and Research Visits

10/2019: University of Hamburg (Germany). Research stay with Prof. Alexander Lichtenstein and Dr. Evgeny Stepanov. *Talk:* Symmetric Improved Estimators for Contiuous-time Quantum Monte Carlo.

09/2019: 5th Summer School of Condensed Matter "Energy," Szczecin (Poland). *Poster:* Density Functional Theory + Dynamical Mean-Field Theory with FPLO + w2dynamics.

09/2019: International conference AMM-2019 "Ab-initio modeling of advanced materials," Yekaterinburg (Russian Federation). *Contributed talk:* DΓA calculations for the Hubbard model on the Kagome lattice.

06/2019: University of Würzburg (Germany). Research stay with Prof. Giorgio Sangiovanni.

04/2019: German Physical Society Spring Meetings 2019, Regensburg (Germany). *Contributed talk:* Self-consistent ladder-DΓA.

02/2019: Leibniz Institute for Solid State and Materials Research Dresden (Germany). Research stay with Dr. Oleg Janson.

01/2019: University of Würzburg (Germany). Research stay with Prof. Giorgio Sangiovanni.

09/2018: Autumn school on correlated electrons 2018, Jülich (Germany). *Poster:* Electronic Correlations in the Hubbard Model on Square and Kagome Lattice.

07/2018: Summer school "Bandstructure meets quantum field theory," Vienna. Instructor at AbinitioDΓA tutorial.

11/2017: FPLO workshop, MPI Dresden (Germany). *Poster:* DMFT and DΓA for the Hubbard Model on a Kagome Lattice.

06/2017: Summer school "Teaching the Theory in Density Functional Theory," Lausanne (Switzerland). *Poster:* DMFT, DΓA and Vertex Asymptotics.

03/2017: Austrian High Performance Computing Meeting, Grundlsee (Austria). *Contributed talk:* High-Frequency Asymptotics of Multi-Orbital Vertex Functions In continuous-Time Quantum Monte Carlo.

12/2016: Institute for Metal Physics, Yekaterinburg (Russian Federation). Research stay with Prof. Andrey Katanin

Die approbierte gedruckte Originalversion dieser Dissertation ist an der TU Wien Bibliothek verfügbar.
The approved original version of this doctoral thesis is available in print at TU Wien Bibliothek.
TU Bibliothek WIEN Your knowledge hub

Publication List

Below we provide a list of published papers and preprints. Those publications marked by ★ form the basis for the present thesis. By ▶ we mark papers that could – for a lack of space – be discussed only briefly and are reprinted in the following. Papers marked by • are not part of this thesis.

Peer-reviewed journal publications:

- J. Kaufmann, P. Gunacker, and K. Held; Continuous-time quantum Monte Carlo calculation of multi-orbital vertex asymptotics. Phys. Rev. B. **96**, 035114 (2017)
- A. Galler, J. Kaufmann, P. Gunacker, M. Pickem, P. Thunström, J.M. Tomczak, and K. Held; Towards ab initio Calculations with the Dynamical Vertex Approximation. Journal of the Physical Society of Japan **87**(4), 041004 (2018)

▶ D. Geffroy, J. Kaufmann, A. Hariki, P. Gunacker, A. Hausoel, and J. Kuneš; Collective Modes in Excitonic Magnets: Dynamical Mean-Field Study. Phys. Rev. Lett. **122**, 127601 (2019)

★ J. Kaufmann, P. Gunacker, A. Kowalski, G. Sangiovanni, and K. Held; Symmetric improved estimators for continuous-time quantum Monte Carlo. Phys. Rev. B **100**, 075119 (2019)

▶ A. Galler, P. Thunström, J. Kaufmann, M. Pickem, J.M. Tomczak, and K. Held; The AbinitioDΓA Project v1.0: Non-local correlations beyond and susceptibilities within dynamical mean-field theory. Computer Physics Communications **245**, 106847 (2019)

▶ L. Si, W. Xiao, J. Kaufmann, J.M. Tomczak, Y. Lu, Z. Zhong, and K. Held; Topotactic Hydrogen in Nickelate Superconductors and Akin Infinite-Layer Oxides ABO_2. Phys. Rev. Lett. **124**, 166402 (2020)

▶ P. Kappl, M. Wallerberger, J. Kaufmann, M. Pickem, and K. Held; Statistical error estimates in dynamical mean-field theory and extensions thereof. Phys. Rev. B **102**, 085124 (2020)

★ J. Kaufmann, C. Eckhardt, M. Pickem, M. Kitatani, A. Kauch, and K. Held; Self-consistent ladder dynamical vertex approximation. Phys. Rev. B **103**, 035120 (2021)

Preprints:

- M. Pickem, J. Kaufmann, J.M. Tomczak, K. Held; Particle-hole asymmetric lifetimes promoted by spin and orbital fluctuations in ultrahin $SrVO_3$ films. arXiv:2008.12227 (2020)
- L. Si, J. Kaufmann, J.M. Tomczak, Z. Zhong, K. Held; Pitfalls and solutions for perovskite transparent conductors. arXiv:2009.14000 (2020)

★ J. Kaufmann, K. Steiner, R.T. Scalettar, K. Held, O. Janson; How correlations change the magnetic structure factor of the kagome Hubbard model. arXiv:2011.01085 (2020)

★ M. Wais, J. Kaufmann, M. Battiato, K. Held; Comparing scattering rates from Boltzmann and dynamical mean-field theory. arXiv:2012.11257 (2020)

Die approbierte gedruckte Originalversion dieser Dissertation ist an der TU Wien Bibliothek verfügbar.
The approved original version of this doctoral thesis is available in print at TU Wien Bibliothek.
TU Bibliothek WIEN Your knowledge hub

Die approbierte gedruckte Originalversion dieser Dissertation ist an der TU Wien Bibliothek verfügbar.
The approved original version of this doctoral thesis is available in print at TU Wien Bibliothek.

Collective Modes in Excitonic Magnets: Dynamical Mean-Field Study

D. Geffroy,[1,2] J. Kaufmann,[2] A. Hariki,[2] P. Gunacker,[2] A. Hausoel,[3] and J. Kuneš[2,4]
[1]*Department of Condensed Matter Physics, Faculty of Science, Masaryk University, Kotlářská 2, 611 37 Brno, Czechia*
[2]*Institute for Solid State Physics, TU Wien, 1040 Vienna, Austria*
[3]*Institute for Theoretical Physics and Astrophysics, University of Würzburg, Am Hubland 97074 Würzburg, Germany*
[4]*Institute of Physics, Czech Academy of Sciences, Na Slovance 2, 182 21 Praha 8, Czechia*

(Received 24 August 2018; revised manuscript received 23 January 2019; published 28 March 2019)

We present a dynamical mean-field study of dynamical susceptibilities in the two-band Hubbard model. Varying the model parameters we analyze the two-particle excitations in the normal as well as in the ordered phase, an excitonic condensate. The two-particle dynamical mean-field theory spectra in the ordered phase reveal the gapless Goldstone modes arising from spontaneous breaking of continuous symmetries. We also observe the gapped Higgs mode, characterized by vanishing of the gap at the phase boundary. Qualitative changes observed in the spin susceptibility can be used as an experimental probe to identify the excitonic condensation.

DOI: 10.1103/PhysRevLett.122.127601

Die approbierte gedruckte Originalversion dieser Dissertation ist an der TU Wien Bibliothek verfügbar.
The approved original version of this doctoral thesis is available in print at TU Wien Bibliothek.
TU Bibliothek WIEN Your knowledge hub

Long-rang order (LRO) and the concomitant spontaneous symmetry breaking are a prominent demonstration of collective behavior in solids. For common LROs, e.g., magnetic order, the order parameter can be observed directly with present technology. However, some exotic LROs, dubbed hidden orders, have been recognized through their thermodynamic properties so far [1–3]. In this case, dynamical response functions are invaluable for understanding the nature of the LRO. The excitonic insulator [4,5] is an example of LRO that after decades of defying detection has been identified through its dynamical fingerprint [6]. Recently, realization of the excitonic magnet [7], an analog of the excitonic insulator arising by condensation of spinful excitons, was proposed in $Pr_{0.5}Ca_{0.5}CoO_3$ [2,8,9] with conclusive evidence still missing. The excitonic interpretation of magnetism of Ca_2RuO_4 is a subject of current debate [10,11]. Excitonic condensation finds its formal analogy in the LRO in Heisenberg-dimer systems, experimentally studied in $TlCuCl_3$ [12].

In this Letter we use dynamical mean-field theory (DMFT) to study the dynamical response of an excitonic magnet realized in the two-band Hubbard model. We show that the symmetry lowering gives rise to a coupling between the exciton condensate fluctuations and spin, which leaves a unique signature in the dynamical spin structure factor and thus can be observed by experiments such as inelastic neutron or x-ray scattering.

Breaking of continuous symmetry in systems with short range interactions results in the appearance of gapless Goldstone modes (GMs) [13] as well as gapped Higgs excitations [14], which have been the subject of recent interest [10,12,14,15]. The description of interacting electron systems typically relies on perturbative approaches in the weak-coupling limit [9,16] or low-energy effective models in the strong-coupling limit [7,17]. The DMFT [18,19] uses a different approximation assuming a Luttinger-Ward functional with the local propagators only, which makes DMFT tractable for realistic multiorbital models [20,21]. DMFT has been widely used to study one-particle ($1P$) dynamics, while two-particle ($2P$) susceptibilities are rarely studied for multiorbital models [22–27] and their behavior in ordered phases is unexplored.

The Hamiltonian of studied model reads

$$H = \sum_{ij,\sigma} \begin{pmatrix} a^\dagger_{i\sigma} & b^\dagger_{i\sigma} \end{pmatrix} \begin{pmatrix} t_{aa} & t_{ab} \\ t_{ab} & t_{bb} \end{pmatrix} \begin{pmatrix} a_{j\sigma} \\ b_{j\sigma} \end{pmatrix} + \frac{\Delta}{2} \sum_{i,\sigma} (n^a_{i\sigma} - n^b_{i\sigma}) + U \sum_{i,\alpha} n^\alpha_{i\uparrow} n^\alpha_{i\downarrow} + \sum_{i,\sigma\sigma'} (U' - J\delta_{\sigma\sigma'}) n^a_{i\sigma} n^b_{i\sigma'}, \quad (1)$$

where $a^\dagger_{i\sigma}$ and $b^\dagger_{i\sigma}$ are fermionic operators that create electrons with the respective orbital flavors and spin σ at site i of a square lattice. The first term describes the nearest neighbor hopping. The rest, expressed in terms of local densities $n^c_{i,\sigma} \equiv c^\dagger_{i\sigma} c_{i\sigma}$, captures the crystal field Δ, the Hubbard interaction U, and Hund's exchange J in the Ising approximation. Parameters $U = 4$, $J = 1$, $U' = U - 2J$, [28] $t_{aa} = 0.4118$, $t_{bb} = -0.1882$, $t_{ab} = 0, 0.02, 0.06$ with magnitudes (in eV) typical for $3d$ transition metal oxides were used in previous studies [25,29,30].

We follow the standard DMFT procedure of self-consistently mapping the lattice model onto an auxiliary Anderson impurity model (AIM) [31,32], which is solved with the ALPS implementation [33–35] [36] of the matrix version of the strong-coupling continuous-time quantum Monte Carlo algorithm [38]. The susceptibilities [19,22,39,40] are obtained by solving the Bethe-Salpeter equation in the particle-hole channel with the DMFT $1P$

 © 2019 American Physical Society

propagators and $2P$-irreducible vertices of AIM using the orthogonal polynomial representation [41].

The susceptibilities $\chi^{OO}_{\eta\eta}(\mathbf{k},\omega)$ are obtained by analytic continuation [42,43] of their Matsubara representations,

$$\chi^{OO}_{\eta\eta}(\mathbf{k},i\nu_n)=\sum_{\mathbf{R}}\int_0^\beta d\tau e^{i(\nu_n\tau+\mathbf{k}\cdot\mathbf{R})}\langle O^\eta_{\mathbf{i}+\mathbf{R}}(\tau)O^\eta_{\mathbf{i}}(0)\rangle-\langle O^\eta\rangle^2,$$

with the observables O of interest being excitonic fields $R^\eta_i(I^\eta_i)=\sqrt{\pm 1}\sum_{\alpha\beta}\sigma^\eta_{\alpha\beta}(a^\dagger_{i\alpha}b_{i\beta}\pm b^\dagger_{i\alpha}a_{i\beta})$, respectively, with $\eta=x$, y and the z component of spin moment $S^z_i=\sum_{\alpha\beta}\sigma^z_{\alpha\beta}(a^\dagger_{i\alpha}a_{i\beta}+b^\dagger_{i\alpha}b_{i\beta})$.

Model (1) at half-filling has a rich phase diagram exhibiting a metal-insulator transition [50] as well as various types of LRO including antiferromagnetism, spin-state order, or superconductivity [25,26,51,52]. For the present parameters it undergoes a temperature- or crystal-field-controlled transition to polar excitonic condensate (PEC) [53], as shown in Fig. 1(b). PEC is characterized by a finite excitonic field. Throughout the Letter we choose the orientation $\langle I^y\rangle=\phi$, while R^y, I^x, and R^x remain fluctuating. This phase is an instance of the spin nematic state, which breaks spin-rotation symmetry without the appearance of spin polarization.

The behavior of the collective modes depends on the continuous symmetry broken by the LRO [13]. Here, it is the $U(1)$ spin (z-axis) rotation. If $t_{ab}=0$, an additional $U(1)$ gauge symmetry due to conservation of $\sum_{i,\sigma}(n^a_{i,\sigma}-n^b_{i,\sigma})$ makes the total broken symmetry $U(1)\times U(1)$. We refer to the general $t_{ab}\neq 0$ case as the $U(1)$ model and the $t_{ab}=0$ case as the $U^2(1)$ model.

Δ-driven transition.—While the system exhibits a sizable $1P$ gap throughout the studied Δ range, horizontal line in Fig. 1(b), low-energy $2P$ excitations show up in the excitonic susceptibilities, Fig. 2. In the normal phase ($\Delta>\Delta_c$), these can be viewed as spinful Frenkel excitons. The spin symmetry ensures the equivalence of x and y directions, while the gauge symmetry leads to equivalence of the excitonic fields R and I in the $U^2(1)$ model.

Reducing Δ closes the excitation gap and the system undergoes transition to the PEC phase. For the excitonic field, which freezes in an arbitrary direction both in the xy plane and the RI plane in the $U^2(1)$ case, we choose the orientation discussed above. Linear gapless GMs [43] corresponding to the spin rotation and phase fluctuation (RI rotation) are observed in χ^{II}_{xx} and χ^{RR}_{yy}, respectively. The intensities of both GMs diverge as $1/|\mathbf{k}|$ [43]. The corresponding sound velocities are shown in Fig. 3(a).

Finite cross-hopping t_{ab} leads to a generic $U(1)$ model. The equivalence between the R and I fields is lost; see Fig. 4. The excitonic field freezes in the I direction [53,54], while the xy orientation remains arbitrary. For the small t_{ab} studied here, the changes to the excitonic spectra [43] are concentrated in the low-energy region shown in Fig. 4. The spin-rotation GM, visible in χ^{II}_{xx}, remains gapless and linear. The phase mode acquires a Higgs gap that vanishes at the transition, Fig. 3(b), a behavior observed in bilayer Heisenberg system $TlCuCl_3$ [12].

Interestingly the character of this mode changes as we proceed deeper into the ordered phase, Fig. 4. Close to the phase boundary, its spectral weight is dominated by χ^{II}_{yy}, i.e., amplitude fluctuation of the condensed I^y field. Deeper

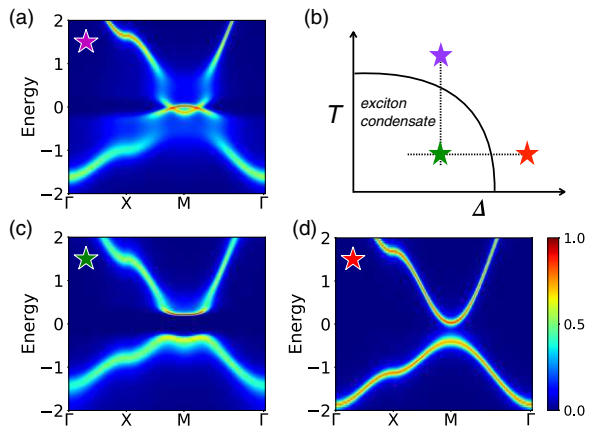

FIG. 1. The sketch of crystal field vs temperature ($\Delta-T$) phase diagram (b) with marked cuts, along which the susceptibilities are calculated. The $1P$ spectral function at selected (Δ,T) points marked with stars: violet (3.55, 1/11), green (3.55, 1/40), and blue (3.8, 1/40).

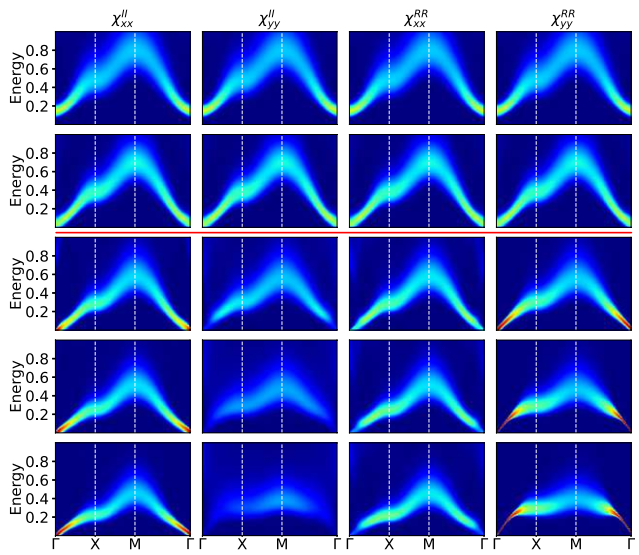

FIG. 2. Evolution of the excitonic modes of dynamical susceptibility in the $U^2(1)$ model ($t_{ab}=0$) across Δ-driven transition ($T=1/40$). The columns correspond to $-\mathrm{Im}\chi^{OO}_{\gamma\gamma}(\mathbf{k},\omega)$ with $O^\gamma=I^x$, I^y, R^x, R^y (left to right) along the high-symmetry lines in the two-dimensional Brillouin zone. The rows from top to bottom correspond to $\Delta=3.9$, 3.8, 3.65, 3.55, 3.45 with $\Delta_c\approx 3.75$. [The red line separates the normal state from the PEC phase.]

Die approbierte gedruckte Originalversion dieser Dissertation ist an der TU Wien Bibliothek verfügbar.
The approved original version of this doctoral thesis is available in print at TU Wien Bibliothek.
TU Bibliothek WIEN Your knowledge hub

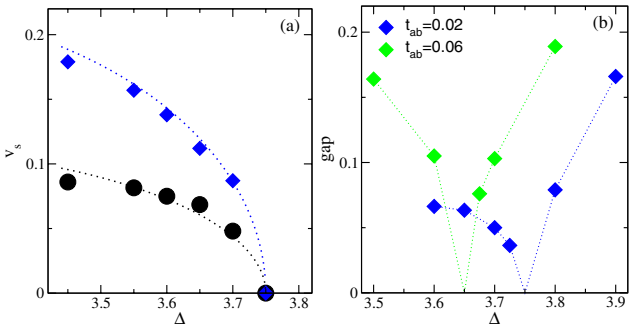

FIG. 3. (a) The sound velocity v_s of the GMs, the phase mode (χ^{RR}_{yy}, blue symbols), and the spin rotation mode (χ^{II}_{xx}, black symbols) in the $U^2(1)$ model as a function of the crystal field Δ. The dotted lines show the corresponding strong-coupling results. (b) The Higgs gap in the $U(1)$ model with $t_{ab} = 0.02$ and 0.06 as a function of Δ. The line is a guide for eyes.

in the ordered phase the spectral weight is mostly in χ^{RR}_{yy}, corresponding to phase fluctuation (RI rotation) as in the $U^2(1)$ model. We offer an interpretation in terms of the relative strength of the symmetry breaking term (t_{ab}) in the Hamiltonian and the spontaneously generated Weiss field. The Weiss field, the off-diagonal $F^{\uparrow\downarrow}_{ab}(\omega)$ part of the hybridization function in the present method, is in general a fluctuating (frequency dependent) object, which prohibits a direct comparison to t_{ab}. Nevertheless, we can compare their dynamical effects. A Weiss field dominating over the Hamiltonian term (t_{ab}) results in a gapped GM found deep in the ordered phase. A common example of such a situation is a gap in spin-wave spectra of magnets due to magnetocrystalline anisotropy. Dominance of the Hamiltonian term (t_{ab}) close to the phase boundary, where the Weiss field is small, results in amplitude fluctuations. This is a generic situation in cases without an approximate symmetry. This interpretation is supported by the observation that the extent of the amplitude-fluctuation regime shrinks when t_{ab} is reduced [43]. Moreover, the strong-coupling calculations [see Supplemental Material (SM) [43]], which make an explicit comparison possible, lead to the same conclusions.

Next, we discuss the impact of exciton condensation on the spin susceptibility χ^{SS}_{zz}, shown in Fig. 5. In the normal phase, $\chi^{SS}_{zz}(\mathbf{k},\omega)$ exhibits no distinct dispersion and essentially vanishes throughout the Brillouin zone, Fig. 5(b), as expected in a band insulator. In the PEC phase, it develops a sharp spin-wavelike dispersion although there are no ordered moments present. We point out a similarity of $\chi^{SS}_{zz}(\mathbf{k},\omega)$ to $\chi^{RR}_{xx}(\mathbf{k},\omega)$ that we discuss later. A distinct feature of $\chi^{SS}_{zz}(\mathbf{k},\omega)$ is the suppression of the spectral weight close to the Γ point. This suppression can be overcome by doping, which results in the appearance of ferromagnetic exciton condensate [29].

Strong-coupling limit.—To understand the numerical results, it is instructive to analyze the strong-coupling limit of (1), which can be expressed in terms of two-flavor hard-core bosons [53,55,56],

$$\mathcal{H} = \mu\sum_i n_i - \sum_{ij,\nu}\left[\mathcal{T} d^\dagger_{i\nu} d_{j\nu} - \frac{\mathcal{W}}{2}(d^\dagger_{i\nu} d^\dagger_{j\nu} + d_{i\nu} d_{j\nu})\right] + \frac{\mathcal{V}}{2}\sum_{ij} n_i n_j + \frac{\mathcal{J}}{2}\sum_{ij} S^z_i S^z_j. \tag{2}$$

Bosonic operators $d^\dagger_{i\nu}$ ($\nu = x,\ y$), which create high-spin (HS) states out of the low-spin (LS) state, are related to the excitonic fields by $R^\nu_i(I^\nu_i) \to \sqrt{\pm 1}(d^\dagger_{i\nu} \pm d_{i\nu})$. The number operators $n_i = \sum_\nu d^\dagger_{i\nu} d_{i\nu}$ measure the HS concentration and $S^z_i = -i(d^\dagger_{ix} d_{iy} - d^\dagger_{iy} d_{ix})$ is the z component of the spin operator. The relations of the coupling constants μ, $\mathcal{T}$, $\mathcal{W}$, $\mathcal{V}$, and $\mathcal{J}$ to the parameters of (1) can be found in SM [43] and Ref. [25]. Since $\mathcal{W} \sim t^2_{ab}$, the gauge symmetry of the $U^2(1)$ model reflects conservation of d charge for $\mathcal{W} = 0$.

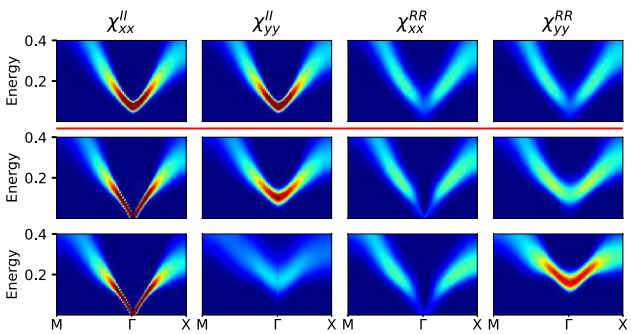

FIG. 4. The same susceptibilities as in Fig. 2 ($T = 1/40$) in the vicinity of the Γ point for the $U(1)$ model with cross-hopping $t_{ab} = 0.06$. The rows from top to bottom correspond to $\Delta = 3.675$, 3.60, 3.5, with $\Delta_c \approx 3.65$ [the red line separates the normal state from the PEC phase].

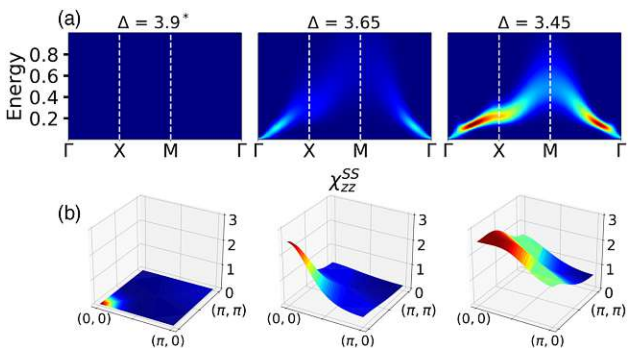

FIG. 5. (a) Evolution of dynamical spin susceptibility $-\mathrm{Im}\chi^{SS}_{zz}(\mathbf{k},\omega)$ across the Δ-driven transition in the $U^2(1)$ model of Fig. 2 (the asterisk marks the normal phase). (b) The corresponding static susceptibilities $\mathrm{Re}\chi^{SS}_{zz}(\mathbf{k},0)$ throughout the Brillouin zone.

Die approbierte gedruckte Originalversion dieser Dissertation ist an der TU Wien Bibliothek verfügbar.
The approved original version of this doctoral thesis is available in print at TU Wien Bibliothek.
TU Bibliothek WIEN Your knowledge hub

TABLE I. The parameters of Eq. (3). The variational parameter $0 \le \alpha^2 \le 1$, corresponding to the LS density, assumes 1 in the normal phase and $[\mu + z(\mathcal{T} + \mathcal{W}) + z\mathcal{V}]/[2z(\mathcal{T} + \mathcal{W}) + z\mathcal{V}]$ in the condensate.

μ_x	$\alpha^2\mu + z\alpha^2(1-\alpha^2)(2\mathcal{T} + 2\mathcal{W} + \mathcal{V})$
$\mathcal{T}_x$	$\alpha^2\mathcal{T} - (1-\alpha^2)\mathcal{J}$
$\mathcal{W}_x$	$\alpha^2\mathcal{W} + (1-\alpha^2)\mathcal{J}$
μ_y	$z(\mathcal{T} + \mathcal{W})$; μ if $\alpha^2 = 1$
$\mathcal{T}_y$	$\mathcal{T} - \alpha^2(1-\alpha^2)(2\mathcal{T} + 2\mathcal{W} + \mathcal{V})$
$\mathcal{W}_y$	$\mathcal{W} - \alpha^2(1-\alpha^2)(2\mathcal{T} - 2\mathcal{W} + \mathcal{V})$

Generalized spin-wave treatment [56,57] of the excitations over the variational ground state $|G\rangle = \prod_i(\alpha + i\sqrt{1-\alpha^2}d_{iy}^\dagger)|0\rangle$, see SM [43] for details, leads to a free boson model

$$\tilde{\mathcal{H}}_\nu = \mu_\nu \sum_i \tilde{n}_{i\nu} - \sum_{ij}\left(\mathcal{T}_\nu \tilde{d}_{i\nu}^\dagger \tilde{d}_{j\nu} - \frac{\mathcal{W}_\nu}{2}(\tilde{d}_{i\nu}^\dagger \tilde{d}_{j\nu}^\dagger + \text{H.c.})\right). \tag{3}$$

Note that the parameters of this effective model in the ordered phase, given in Table I, depend on the flavor $\nu = x,\ y$. The elementary excitations of (3) have the dispersion $\epsilon_\nu(\mathbf{k}) = \sqrt{[\mu_\nu - 2\mathcal{T}_\nu\delta(\mathbf{k})]^2 - [2\mathcal{W}_\nu\delta(\mathbf{k})]^2}$ with $\delta(\mathbf{k}) = \cos k_x + \cos k_y$. In the $U^2(1)$ case with $\mathcal{W} = 0$ both x and y modes are gapless with sound velocities $v_\nu \equiv \nabla_{\mathbf{k}}\epsilon_\nu(\mathbf{k} = 0) = \sqrt{8|\mathcal{W}_\nu|(\mathcal{T}_\nu + |\mathcal{W}_\nu|)}$ vanishing at the transition. Finite $\mathcal{W}$ in the $U(1)$ case leads to the opening of a gap for y excitations. The ratio of the spectral weights of $I-$ and $R-$ propagators corresponding to χ_{yy}^{II} and χ_{yy}^{RR} at Γ point is given by [43]

$$\frac{\text{Im}\chi_{yy}^{II}(0, \nu_{\text{gap}})}{\text{Im}\chi_{yy}^{RR}(0, \nu_{\text{gap}})} \approx \frac{4\mathcal{W}}{(2\mathcal{T} + \mathcal{V})\phi^2},$$

which supports the interpretation that a dominant Hamiltonian term ($\mathcal{W}$) favors the amplitude fluctuations, while a dominant Weiss field ($\sim\mathcal{T}\phi$) favors the gapped Goldstone fluctuations.

Finally, we address the behavior of the spin susceptibility χ_{zz}^{SS} in Fig. 5 We observe that replacing the operator d_{iy} in the strong-coupling expression for S_i^z by its finite PEC value yields $S_i^z \sim (d_{ix}^\dagger + d_{ix})\phi/2$. In the ordered phase, the spin susceptibility χ_{zz}^{SS} therefore follows χ_{xx}^{RR}, while they are decoupled in the normal phase.

Thermally driven transition.—Since the transition observed in $Pr_{0.5}Ca_{0.5}CoO_3$ [2] is driven by temperature we investigate the behavior of the $U^2(1)$ model along the vertical trajectory in Fig. 1(b). We observe that the $1P$ gap in the normal state is closed, Fig. 1(d). The excitonic susceptibilities possess a peak at finite frequency, whose tail extends to zero frequency, Fig. 6. Cooling is accompanied by a downward shift of the damped dispersive features; i.e., the phase transition can be viewed as a mode softening, an observation also made experimentally on $TlCuCl_3$ [12].

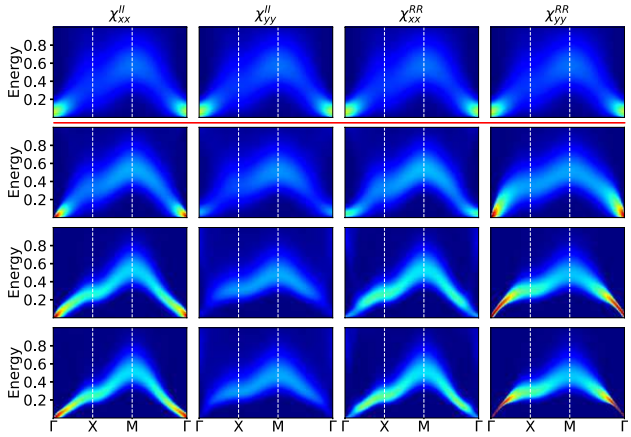

FIG. 6. The same susceptibilities of $U^2(1)$ model as in Fig. 2 calculated across the thermally driven transition for $\Delta = 3.55$. The rows from top to bottom correspond to temperatures $T = 1/11,\ 1/16,\ 1/30,\ 1/40$ with $T_c \approx 1/13$.

The normal state spin susceptibility χ_{zz}^{SS} in Fig. 7 does not vanish as in Fig. 5. The presence of thermally excited HS states gives rise to $\mathbf{k}$-featureless susceptibility with spectral weight concentrated at low energies. Nevertheless, $\chi_{zz}^{SS}(\mathbf{k}, \omega)$ changes qualitatively at the transition in this case as well. The dispersion becomes sharper and its bandwidth increases significantly. As a result, upon cooling below T_c, the low-energy region is depleted of spectral weight throughout the Brillouin zone, except in the vicinity of the Γ point. Recently, this behavior was reported in inelastic neutron scattering in the putative excitonic material $(Pr_{1-y}Y_y)_{1-x}Ca_xCoO_3$ [58].

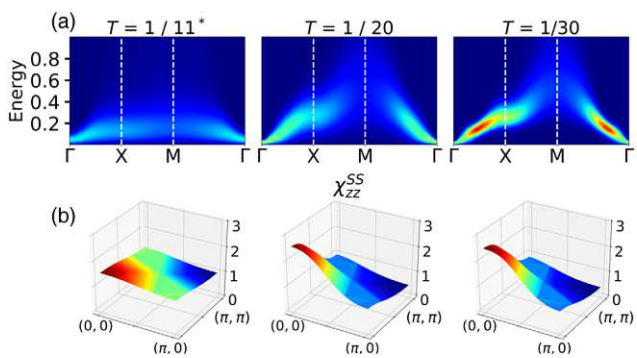

FIG. 7. (a) Evolution of dynamical spin susceptibility $-\text{Im}\chi_{zz}^{SS}(\mathbf{k}, \omega)$ across the thermally driven phase transition as in Fig. 6 for temperatures $T = 1/11,\ 1/20,\ 1/30$ (the asterisk marks the normal phase). (b) The corresponding static susceptibilities $\text{Re}\chi_{zz}^{SS}(\mathbf{k}, 0)$ throughout the Brillouin zone.

Die approbierte gedruckte Originalversion dieser Dissertation ist an der TU Wien Bibliothek verfügbar.
The approved original version of this doctoral thesis is available in print at TU Wien Bibliothek.
TU Bibliothek WIEN Your knowledge hub

In conclusion, we used DMFT to study the $2P$ response across exciton condensation transition in the two-orbital Hubbard model. We observed the formation of GMs as predicted by symmetry considerations [13]. Explicit breaking of continuous symmetry led to the appearance of a gapped mode [14], characterized by vanishing of the gap at the phase transitions similar to observations in $TlCuCl_3$ [12]. We have observed that the character of this mode changes from Higgs-like amplitude fluctuations close to the phase boundary, to Goldstone-like phase fluctuations deep in the ordered phase. We suggest that this behavior is common to systems with weakly broken symmetry and we provide its interpretation in terms of the relative strengths of the spontaneously generated Weiss field and the explicit symmetry-breaking term in the Hamiltonian.

Experimental observation of excitonic modes is in principle possible [59,60] using resonant inelastic x-ray scattering; however, practical limitations in energy resolution and $\mathbf{k}$-space accessibility [59] exist at the moment. We have shown that the measurement of dynamical spin susceptibility provides an alternative that can be used to identify spinful excitonic condensates with current experimental technology.

We thank J. Chaloupka, G. Sangiovanni, G. Khaliullin, and B. Hartl for discussions, H. Shinaoka for help with the ALPS code, K. Steiner and O. Janson for testing the maximum entropy code, and K. Held and A. Kauch for critical reading of the manuscript. This work was supported by the ERC Grants No. 646807 under EU Horizon 2020 (J. K., A. Har. and D. G.) and No. 306447 under EU Seventh Framework Program (Grant No. FP7/20072013)/ERC (J. K.), by the Czech Ministry of Education, Youth and Sports, project "IT4Innovations National Supercomputing Center—LM2015070" (D. G.), by FWF through Grant No. SFB ViCoM F41 (J. K.), by DFG through Grant No. SFB1170 "Tocotronics" (A. Hau.), and by the Austrian Federal Ministry of Science, Research and Economy through the Vienna Scientific Cluster (VSC) Research Center (P. G.). We gratefully acknowledge the Gauss Centre for Supercomputing e.V. for providing computing time on the GCS Supercomputer SuperMUC at Leibniz Supercomputing Centre, the program "Projects of large research, development, and innovations infrastructures" (Grant No. CESNET LM2015042) for the access to computing and storage facilities of the Czech National Grid Infrastructure MetaCentrum, and the Vienna Scientific Cluster (VSC) for access to its computing facilities.

[1] H.-H. Kung, R. E. Baumbach, E. D. Bauer, V. K. Thorsmølle, W.-L. Zhang, K. Haule, J. A. Mydosh, and G. Blumberg, Science **347**, 1339 (2015).
[2] S. Tsubouchi, T. Kyômen, M. Itoh, P. Ganguly, M. Oguni, Y. Shimojo, Y. Morii, and Y. Ishii, Phys. Rev. B **66**, 052418 (2002).
[3] Y. F. Lu, H. Kono, T. I. Larkin, A. W. Rost, T. Takayama, A. V. Boris, B. Keimer, and H. Takagi, Nat. Commun. **8**, 14408 (2017).
[4] N. F. Mott, Philos. Mag. **6**, 287 (1961).
[5] B. I. Halperin and T. M. Rice, *Solid State Physics* (Academic Press, New York, 1968), p. 115.
[6] A. Kogar, M. S. Rak, S. Vig, A. A. Husain, F. Flicker, Y. I. Joe, L. Venema, G. J. MacDougall, T. C. Chiang, E. Fradkin, J. van Wezel, and P. Abbamonte, Science **358**, 1314 (2017).
[7] G. Khaliullin, Phys. Rev. Lett. **111**, 197201 (2013).
[8] J. Kuneš and P. Augustinský, Phys. Rev. B **90**, 235112 (2014).
[9] T. Yamaguchi, K. Sugimoto, and Y. Ohta, J. Phys. Soc. Jpn. **86**, 043701 (2017).
[10] A. Jain, M. Krautloher, J. Porras, G. H. Ryu, D. P. Chen, D. L. Abernathy, J. T. Park, A. Ivanov, J. Chaloupka, G. Khaliullin, B. Keimer, and B. J. Kim, Nat. Phys. **13**, 633 (2017).
[11] G. Zhang and E. Pavarini, Phys. Rev. B **95**, 075145 (2017).
[12] P. Merchant, B. Normand, K. W. Krämer, M. Boehm, D. F. McMorrow, and C. Rüegg, Nat. Phys. **10**, 373 (2014).
[13] H. Watanabe and H. Murayama, Phys. Rev. Lett. **108**, 251602 (2012).
[14] D. Pekker and C. Varma, Annu. Rev. Condens. Matter Phys. **6**, 269 (2015).
[15] D. Sherman, U. S. Pracht, B. Gorshunov, S. Poran, J. Jesudasan, M. Chand, P. Raychaudhuri, M. Swanson, N. Trivedi, A. Auerbach, M. Scheffler, A. Frydman, and M. Dressel, Nat. Phys. **11**, 188 (2015).
[16] E. Bascones, A. A. Burkov, and A. H. MacDonald, Phys. Rev. Lett. **89**, 086401 (2002).
[17] T. Tatsuno, E. Mizoguchi, J. Nasu, M. Naka, and S. Ishihara, J. Phys. Soc. Jpn. **85**, 083706 (2016).
[18] W. Metzner and D. Vollhardt, Phys. Rev. Lett. **62**, 324 (1989).
[19] A. Georges, G. Kotliar, W. Krauth, and M. Rozenberg, Rev. Mod. Phys. **68**, 13 (1996).
[20] G. Kotliar, S. Y. Savrasov, K. Haule, V. S. Oudovenko, O. Parcollet, and C. A. Marianetti, Rev. Mod. Phys. **78**, 865 (2006).
[21] K. Held, Adv. Phys. **56**, 829 (2007).
[22] J. Kuneš, Phys. Rev. B **83**, 085102 (2011).
[23] H. Park, K. Haule, and G. Kotliar, Phys. Rev. Lett. **107**, 137007 (2011).
[24] L. Boehnke and F. Lechermann, Phys. Status Solidi (a) **211**, 1267 (2013).
[25] J. Kuneš and P. Augustinský, Phys. Rev. B **89**, 115134 (2014).
[26] S. Hoshino and P. Werner, Phys. Rev. B **93**, 155161 (2016).
[27] L. DelRe and M. Capone, Phys. Rev. A **98**, 063628 (2018).
[28] The results are little sensitive to variation of U' and J as long as the ratio Δ/J is fixed.
[29] J. Kuneš, Phys. Rev. B **90**, 235140 (2014).
[30] J. Kuneš and D. Geffroy, Phys. Rev. Lett. **116**, 256403 (2016).
[31] A. Georges and G. Kotliar, Phys. Rev. B **45**, 6479 (1992).
[32] M. Jarrell, Phys. Rev. Lett. **69**, 168 (1992).

Die approbierte gedruckte Originalversion dieser Dissertation ist an der TU Wien Bibliothek verfügbar.
The approved original version of this doctoral thesis is available in print at TU Wien Bibliothek.
TU Bibliothek WIEN Your knowledge hub

[33] B. Bauer *et al.*, J. Stat. Mech. (2011) P05001.
[34] H. Shinaoka, E. Gull, and P. Werner, Comput. Phys. Commun. **215**, 128 (2017).
[35] A. Gaenko, A. E. Antipov, G. Carcassi, T. Chen, X. Chen, Q. Dong, L. Gamper, J. Gukelberger, R. Igarashi, S. Iskakov, M. Könz, J. P. LeBlanc, R. Levy, P. N. Ma, J. E. Paki, H. Shinaoka, S. Todo, M. Troyer, and E. Gull, Comput. Phys. Commun. **213**, 235 (2017).
[36] Numerically identical results for the normal state susceptibilities were obtained with w2dymanics [37].
[37] M. Wallerberger, A. Hausoel, P. Gunacker, A. Kowalski, N. Parragh, F. Goth, K. Held, and G. Sangiovanni, Comput. Phys. Commun. **235**, 388 (2019).
[38] P. Werner, A. Comanac, L. de' Medici, M. Troyer, and A. J. Millis, Phys. Rev. Lett. **97**, 076405 (2006).
[39] E. G. C. P. van Loon, H. Hafermann, A. I. Lichtenstein, and M. I. Katsnelson, Phys. Rev. B **92**, 085106 (2015).
[40] F. Krien, E. G. C. P. van Loon, H. Hafermann, J. Otsuki, M. I. Katsnelson, and A. I. Lichtenstein, Phys. Rev. B **96**, 075155 (2017).
[41] L. Boehnke, H. Hafermann, M. Ferrero, F. Lechermann, and O. Parcollet, Phys. Rev. B **84**, 075145 (2011).
[42] J. E. Gubernatis, M. Jarrell, R. N. Silver, and D. S. Sivia, Phys. Rev. B **44**, 6011 (1991).
[43] See Supplemental Material at http://link.aps.org/supplemental/10.1103/PhysRevLett.122.127601 for the derivation of strong-coupling formulas, the description of maximum entropy algorithm and the summary of all numerical results, which includes Refs. [44–49].
[44] J. M. Luttinger, Phys. Rev. **121**, 942 (1961).
[45] J. Otsuki, M. Ohzeki, H. Shinaoka, and K. Yoshimi, Phys. Rev. E **95**, 061302 (2017).
[46] M. Jarrell and J. Gubernatis, Phys. Rep. **269**, 133 (1996).
[47] R. K. Bryan, Eur. Biophys. J. **18**, 165 (1990).
[48] G. J. Kraberger, R. Triebl, M. Zingl, and M. Aichhorn, Phys. Rev. B **96**, 155128 (2017).
[49] A. W. Sandvik, Phys. Rev. B **57**, 10287 (1998).
[50] P. Werner and A. J. Millis, Phys. Rev. Lett. **99**, 126405 (2007).
[51] T. Kaneko and Y. Ohta, Phys. Rev. B **90**, 245144 (2014).
[52] T. Kaneko, B. Zenker, H. Fehske, and Y. Ohta, Phys. Rev. B **92**, 115106 (2015).
[53] J. Kuneš, J. Phys. Condens. Matter **27**, 333201 (2015).
[54] D. Geffroy, A. Hariki, and J. Kuneš, Phys. Rev. B **97**, 155114 (2018).
[55] L. Balents, Phys. Rev. B **62**, 2346 (2000).
[56] J. Nasu, T. Watanabe, M. Naka, and S. Ishihara, Phys. Rev. B **93**, 205136 (2016).
[57] T. Sommer, M. Vojta, and K. Becker, Eur. Phys. J. B **23**, 329 (2001).
[58] T. Moyoshi, K. Kamazawa, M. Matsuda, and M. Sato, Phys. Rev. B **98**, 205105 (2018).
[59] R.-P. Wang, A. Hariki, A. Sotnikov, F. Frati, J. Okamoto, H.-Y. Huang, A. Singh, D.-J. Huang, K. Tomiyasu, C.-H. Du, J. Kuneš, and F. M. F. de Groot, Phys. Rev. B **98**, 035149 (2018).
[60] J. Kim, M. Daghofer, A. H. Said, T. Gog, J. van den Brink, G. Khaliullin, and B. J. Kim, Nat. Commun. **5**, 4453 (2014).

Die approbierte gedruckte Originalversion dieser Dissertation ist an der TU Wien Bibliothek verfügbar.
The approved original version of this doctoral thesis is available in print at TU Wien Bibliothek.
TU Bibliothek WIEN Your knowledge hub

Topotactic Hydrogen in Nickelate Superconductors and Akin Infinite-Layer Oxides ABO_2

Liang Si,[1,2] Wen Xiao,[1] Josef Kaufmann,[2] Jan M. Tomczak,[2] Yi Lu,[3] Zhicheng Zhong,[1,4,*] and Karsten Held[2,†]

[1]*Key Laboratory of Magnetic Materials and Devices and Zhejiang Province Key Laboratory of Magnetic Materials and Application Technology, Ningbo Institute of Materials Technology and Engineering (NIMTE), Chinese Academy of Sciences, Ningbo 315201, China*

[2]*Institute for Solid State Physics, Vienna University of Technology, 1040 Vienna, Austria*

[3]*Institute for Theoretical Physics, Heidelberg University, Philosophenweg 19, 69120 Heidelberg, Germany*

[4]*China Center of Materials Science and Optoelectronics Engineering, University of Chinese Academy of Sciences, Beijing 100049, China*

(Received 15 November 2019; accepted 1 April 2020; published 22 April 2020)

Superconducting nickelates appear to be difficult to synthesize. Since the chemical reduction of ABO_3 [rare earth (A), transition metal (B)] with CaH_2 may result in both ABO_2 and ABO_2H, we calculate the topotactic H binding energy by density functional theory (DFT). We find intercalating H to be energetically favorable for $LaNiO_2$ but not for Sr-doped $NdNiO_2$. This has dramatic consequences for the electronic structure as determined by DFT + dynamical mean field theory: that of $3d^9$ $LaNiO_2$ is similar to (doped) cuprates, $3d^8$ $LaNiO_2H$ is a two-orbital Mott insulator. Topotactic H might hence explain why some nickelates are superconducting and others are not.

DOI: 10.1103/PhysRevLett.124.166402

Most recently superconductivity was found in $Nd_{0.8}Sr_{0.2}NiO_2$ films grown on $SrTiO_3$ [1], a seminal work that opens the door wide to a new age of superconductivity: the nickelate age. These novel (Sr-doped) $NdNiO_2$ superconductors are not only isostructural to the well-known cuprate superconductor $CaCuO_2$ [2–5], but also both Ni and Cu are formally $3d^9$ in the respective parent compound.

Strikingly different to the cuprates [6] and iron pnictides [7], reproducing these outstanding results in isoelectronic compositions appears to be quite challenging. In a more bulklike crystal, no superconductivity was reported for $Nd_{0.8}Sr_{0.2}NiO_2$ [8], nor when directly pulsed laser depositing $Nd_{0.8}Sr_{0.2}NiO_x$ [9]. Also the parent compound $NdNiO_2$ is not superconducting [1], but shows a resistivity upturn toward low temperatures. Another nickelate, $LaNiO_2$, is also isostructural and isovalent, but is a (bad) metal [10] with neither superconductivity, nor antiferromagnetism [11].

An obvious difference between $Nd_{0.8}Sr_{0.2}NiO_2$ and $Nd(La)NiO_2$ is doping. However, in contrast to the cuprates, there is already a self-doping of the Ni bands in $Nd(La)NiO_2$ because one Nd(La) band crosses the Fermi energy [12–15], hardly hybridizing with the Ni $3d_{x^2-y^2}$ bands. Why are some of these nickelates, all of which have a similar paramagnetic (spin-unpolarized) density functional theory (DFT) electronic structure [12–14,16–28], superconducting but others are not?

Let us take a step back and recapitulate the synthesis of $ANiO_2$ nickelates with the unusual low oxidation state Ni^+. It is synthesized by first growing $ANiO_3$ on a $SrTiO_3$ substrate and then reducing it to $ANiO_2$ with the help of the reagent CaH_2, see Fig. 1. However, there is another possible end product: $ANiO_2H$. Indeed, for another perovskite, $SrVO_3$, it was shown in a detailed experimental analysis [29] that the CaH_2 reduction reaction leads to $SrVO_2H$; also $NdNiO_xH_y$ has been detected [30].

In this Letter, we show, based on DFT calculations [31–33], that the nickelates are just at the borderline of the two reaction paths of Fig. 1: While for $A = \mathrm{Nd}$ and, in particular, for $A = \mathrm{La}$, the oxide-hydrides $NdNiO_2H$ and $LaNiO_2H$ are energetically favorable, with Sr doping, the

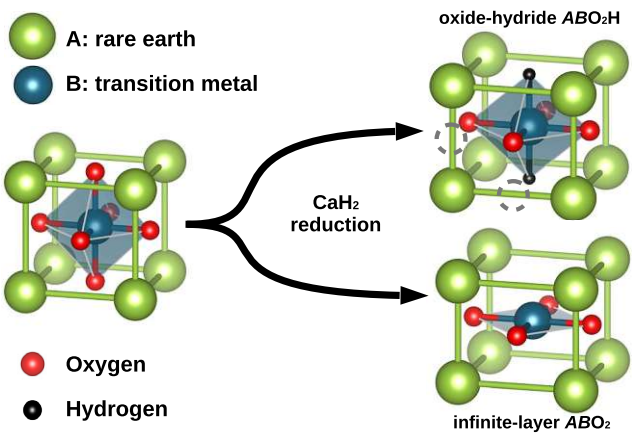

FIG. 1. Two possible products in the topotactic reduction of ABO_3 by means of CaH_2: oxide-hydride ABO_2H and infinite-layer ABO_2. The dashed circles indicate other possible H positions for ABO_2H, which are, however, energetically less favorable.

 © 2020 American Physical Society

Die approbierte gedruckte Originalversion dieser Dissertation ist an der TU Wien Bibliothek verfügbar.
The approved original version of this doctoral thesis is available in print at TU Wien Bibliothek.
TU Bibliothek WIEN Your knowledge hub

infinite-layer $Nd_{0.8}Sr_{0.2}NiO_2$ becomes more stable. As a matter of course, the reaction kinetics also influences the end products, and without carefully optimizing the reaction conditions, some mixed phase of $ANiO_2$ and $ANiO_2H$ may emerge. We further demonstrate that the H intercalation has dramatic consequences for the electronic structure as calculated by DFT and DFT + dynamical mean field theory (DMFT) [34–37]: While $ANiO_2$ is metallic with a very strong quasiparticle renormalization of the Ni $d_{x^2-y^2}$ band and Nd(La)-5d pocket, quite similar to doped cuprates, $ANiO_2H$ is a Mott insulator with two Ni bands, $d_{x^2-y^2}$ and d_{z^2}, and no Nd(La)-5d pocket.

Methods.—Structural details and H-topotactic binding energies are computed by DFT structural relaxations (yielding lattice constants $a = b = 3.889$, $c = 3.337$ Å for $LaNiO_2$, and $a = b = 3.914$, $c = 3.383$ Å for $LaNiO_2H$) and total energy calculations. Both WIEN2K [38,39] and Vienna *ab initio* simulation package (VASP) [40] codes within Perdew-Burke-Ernzerhof (PBE) [41] and PBE-sol [42] versions of the generalized gradient approximation (GGA) are employed on a $13 \times 13 \times 15$ momentum grid. The energy cutoff was 500 eV in VASP; $R_{MT}K_{max} = 7.0$ with a muffin-tin radius $R_{MT} = 2.50$, 1.96, 1.69, and 1.10 a.u. for La, Ni, O, and H, respectively, was employed in WIEN2K.

For the DMFT calculations, the WIEN2K band structure around the Fermi level is projected onto Wannier functions [43,44] using WIEN2WANNIER [45,46] and supplemented by a local density-density interaction, taking the fully localized limit [47] as double counting. Since for infinite-layer $LaNiO_2$, La-d bands cross the Fermi level E_F, here a full set of La-5d + Ni-3d bands is adopted. For $LaNiO_2H$, a projection onto the Ni-3d bands is possible only because now the La-5d bands are well separated from the Ni-3d bands (cf. Supplemental Material [48] for La-d bands included in DMFT). The interaction parameters are computed by constrained random phase approximation [49]: average interorbital interaction $U' = 3.10$ eV (2.00) and Hund's exchange $J = 0.65$ eV (0.25) for Ni (La). The intraorbital Hubbard interaction follows as $U = U' + 2J$. These interaction parameters are close to those of previous studies [50,51] for 3d oxides. The resulting Hamiltonian is then solved at room temperature (300 K) in DMFT using continuous-time quantum Monte Carlo simulations in the hybridization expansions [52] implemented in W2DYNAMIC [53,54]; the maximum entropy method [55,56] is employed for an analytic continuation of the spectra.

Energetics of topotactic hydrogen.—In addition to the two cornerstone end products, infinite-layer ABO_2 (e.g., $CaCuO_2$, $SrCuO_2$) and oxide-hydride ABO_2H (e.g., $SrVO_2H$) of Fig. 1, and also intermediate products such as $(Ba, Sr, Ca)TiO_{3-x}H_x$ [57,58] and $NdNiO_xH_y$ [30] have been experimentally confirmed when reducing ABO_3 with CaH_2 upon heating [59,60]. To investigate whether it is energetically favorable to intercalate hydrogen in the topotactic reaction or not, we compute the hydrogen binding energy

$$E_B = E[ABO_2] + \mu[\mathrm{H}] - E[ABO_2\mathrm{H}]. \tag{1}$$

Here, $E[ABO_2]$ and $E[ABO_2H]$ are the total energy of ABO_2 and ABO_2H; and $\mu[\mathrm{H}] = E[\mathrm{H}_2]/2$ is the chemical potential of H. Note that H_2 is a typical byproduct for the reduction with CaH_2 and also emerges when CaH_2 is in contact with H_2O. Hence, it can be expected to be present in the reaction. E_B is also the difference in binding energy for the two reaction paths of Fig. 1; i.e., it is energetically favorable by E_B to synthesize ABO_2H instead of ABO_2 and $H_2/2$. Of course, the reaction kinetics may change the outcome and the large entropy of $1/2$ H_2 might change the balance thermodynamically in favor of ABO_2 [63]. However, at the very least, the energetics gives us a first hint whether to expect ABO_2H or ABO_2.

As for the three H positions of Fig. 1, we always find that the vacancy left by the removed oxygen is the energetically favored H position. For a full H-topotactic intercalation, i.e., ABO_2H with all vacant oxygen positions occupied by H, this is plotted explicitly in Fig. 1. We first consider this complete intercalation, fully relax the ABO_2 and ABO_2H structures, and then calculate the respective total spin-unpolarized DFT energy and from this E_B through Eq. (1). Our conclusions remain unchanged when using spin-polarized DFT + U instead, see Supplemental Material [48].

For $SrBO_2$ and $LaBO_2$, E_B is positive from Ti to Co in Fig. 2(a), indicating the energetical preference for the oxide-hydride $SrBO_2H$ for $B = \mathrm{Ti}, \ldots, \mathrm{Co}$. This is consistent with finding $SrVO_2H$ and $SrTiO_xH_y$ after CaH_2 reduction [29,65–67]. Similarly, oxide-hydrides have been reported experimentally when reducing $(Sr, La)CoO_3$ [68,69] and $(Ba, Ca, Sr)TiO_3$ [58,70,71].

Surprisingly, for $LaNiO_2$, a positive E_B of 0.162 eV is predicted, too. This indicates incorporating H topotactically in infinite-layer $LaNiO_2$ is at least energetically favorable. For $SrNiO_2$, on the other hand, it is energetically unfavorable to intercalate H. That is, the nickelates $ANiO_2$ are just at the borderline $E_B = 0$ in Fig. 2(a); the cation A is decisive. The cuprates, on the other hand, are clearly on the $E_B < 0$ side; i.e., hydrogen will not be intercalated, consistent with the well-studied chemistry of the cuprates.

Besides the La- and Sr-based infinite-layer ABO_2, we also calculate E_B for a few additional materials: $CaCuO_2$ [2] has $E_B < 0$ as the other cuprate superconductors, and undoped $NdNiO_2$ [72] has $E_B = 0.133$ eV, which turns negative to $E_B = -0.113$ eV if 25% of Nd atoms are replaced by Sr. Hence, our results indicate that infinite-layer, superconducting Sr-doped $NdNiO_2$ is energetically stable against the topotactic inclusion of H, whereas other nickelates are not.

Die approbierte gedruckte Originalversion dieser Dissertation ist an der TU Wien Bibliothek verfügbar.
The approved original version of this doctoral thesis is available in print at TU Wien Bibliothek.
TU Bibliothek WIEN Your knowledge hub

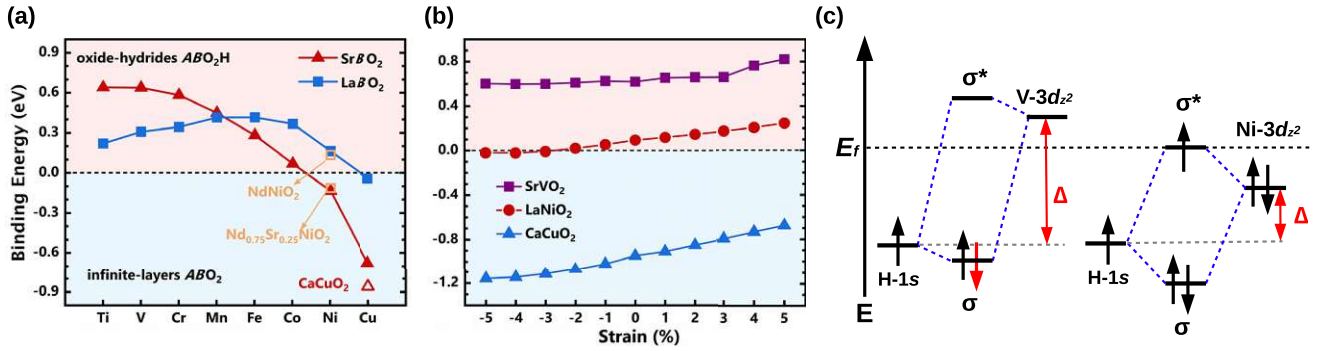

FIG. 2. (a) Binding energy E_B for topotactic H in infinite-layer ABO_2 [Sr or La (A), Ti to Cu (B)]. Further, E_B for $CaCuO_2$, $NdNiO_2$, and $Nd_{0.75}Sr_{0.25}NiO_2$ is plotted. (b) E_B for $SrVO_2$, $LaNiO_2$, and $CaCuO_2$ as a function of strain at a low H density of 12.5%. (c) Explanation of the evolution of the H-topotactic binding energy from AVO_2 to $ANiO_2$ based on the formation of bonding (σ) and antibonding (σ^*) states between H-1 s and transition metal $3d_{z^2}$. The up and down arrows indicate the electron spins; the red arrow for AVO_2 means the electron is from other (V-t_{2g}) orbitals.

The complete (full) topotactic inclusion of H, where all vacancies induced by removing oxygen are filled by H, is an ideal limiting case. Under varying experimental conditions, such as chemical reagent, substrate, temperature, and strain, the H-topotactic inclusion may be incomplete, and ABO_2H_y ($y < 1$) energetically favored. Hence, we also compute E_B at a rather low H-topotactic density: $ABO_2H_{0.125}$ (achieved by including a single H into $2 \times 2 \times 2$ ABO_2 supercells). Additionally, we model strain effects by changing the in-plane lattice constants (a, b) and relaxing the lattice in the z direction and the internal atomic positions.

Figure 2(b) shows the corresponding E_B for $SrVO_2H_{0.125}$, $LaNiO_2H_{0.125}$, and $CaCuO_2H_{0.125}$. Unstrained (0%), the binding energy E_B per hydrogen (0.620 eV for $SrVO_2H_{0.125}$, 0.094 eV for $LaNiO_2H_{0.125}$, and -0.945 eV for $CaCuO_2H_{0.125}$) is very similar to complete hydrogen intercalation ($E_B = 0.637$ eV for $SrVO_2H$, 0.162 eV for $LaNiO_2H$, and -0.859 eV for $CaCuO_2H$) in Fig. 2(a). This indicates that the topotactic intercalation with H does not depend too much on the amount of H. Figure 2(b) further shows that E_B is substantially reduced by compressive (negative) strain. This is because the compressive strain enlarges the z axis, which in turn leads to weaker H-B-H bonding. This suggests compression to be an effective way to eliminate residual H in $ANiO_2$. It might also explain why $NdNiO_2$ was found next to the interface of (compressive) $SrTiO_3$, whereas $NdNiO_xH_y$ was found further away from the interface [30].

Let us now ask why E_B varies remarkably for different ABO_2. In addition to the gradually changing lattice constants, the dominating factor is the d-band filling. By computing the band characteristics (Fig. 3), we find H^- which, similar to $O^{2-}_{0.5}$, absorbs one Ni electron. For early transition metals with positive E_B, as, e.g., $SrVO_2H$, the H-1 s forms bonding (σ) and antibonding (σ^*) states due to the orbital overlap with V-d_{z^2} as sketched on the left side of Fig. 2(c). The bonding σ orbital is fully occupied with one electron originating for the H-1 s and the second from the V-t_{2g} orbitals. This explains the stabilization and energy gain of $SrVO_2H$.

For late transition metals, e.g., $LaNiO_2H$, the $3d_{z^2}$ is fully filled, see right side of Fig. 2(c). Hence, when intercalating H, the antibonding σ^* orbital also needs to be occupied with one electron and then crosses E_F. This and the smaller bonding-antibonding splitting reduces the energy gain for the topotactic intercalation of H. This puts the nickelates at the borderline, whereas for the next transition metal, Cu, it is no longer energetically favorable to form $ACuO_2H$.

Spin-unpolarized DFT electronic structure.—Let us now address the question, how much does the electronic structure change if topotactic hydrogen is present? In the infinite-layer $LaNiO_2$, the Ni $d_{x^2-y^2}$ orbital shows a single-band dispersion without hybridization with other bands, similar to the Cu-$d_{x^2-y^2}$ dispersion in cuprates. However, in contrast to the cuprates, there is an itinerant La band that crosses E_F around the A point, see Fig. 3(a) and [13–16]. It is composed of La-5d, but also La-4f and with some Ni-t_{2g} intermixing. There is no discernible hybridization gap when this La band crosses the Ni-$d_{x^2-y^2}$ band in Fig. 3(a) because of the (symmetry-dictated) very weak hybridization between both [15].

For $LaNiO_2H$, the topotactic H alters the DFT band structure completely, see Fig. 3(b). First, the La band crossing at E_F around the A point is gone. This is because the La-d_{xy} hopping in the (110) direction changes sign when connected though the H-1 s orbital: from -0.098 eV for $LaNiO_2$ to 0.224 eV for $LaNiO_2H$. This turns the minimum (La-5d pocket) around the A point in Fig. 3(a) into a maximum in Fig. 3(b). Second, the Ni-d_{z^2} band is now partially occupied for $LaNiO_2H$ instead of being fully occupied in infinite-layer $LaNiO_2$. Three factors contribute

Die approbierte gedruckte Originalversion dieser Dissertation ist an der TU Wien Bibliothek verfügbar.
The approved original version of this doctoral thesis is available in print at TU Wien Bibliothek.
TU Bibliothek WIEN Your knowledge hub

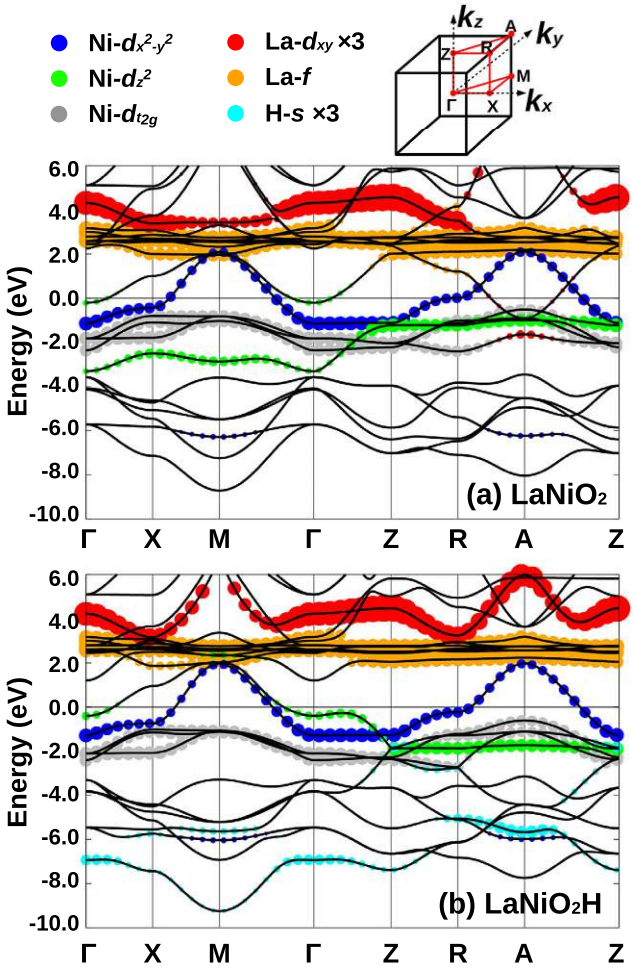

FIG. 3. DFT band structure and orbital characters for (a) $LaNiO_2$ and (b) $LaNiO_2H$ along a high symmetry path through the Brillouin zone (top).

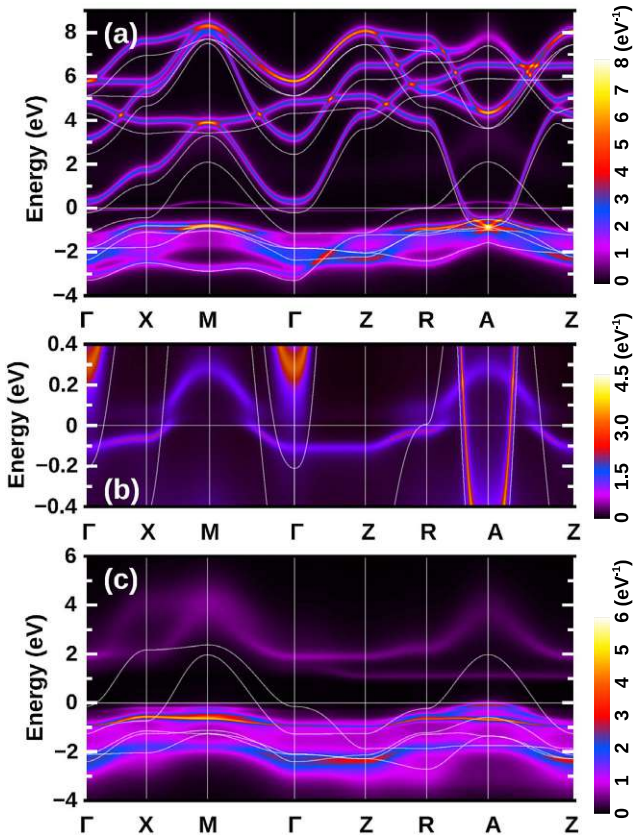

FIG. 4. DMFT spectral functions $A(k,\omega)$ of (a) $LaNiO_2$ and (c) $LaNiO_2H$; solid lines, DFT Wannier bands. (b) Enlargement of (a) around $E_F = 0$.

to this: (1) The local Ni-d_{z^2} potential is shifted up by ~1.5 eV because the d_{z^2} orbitals point toward the negatively charged H^-. (2) The intraorbital, nearest-neighbor hopping of the d_{z^2} electrons along k_z [Γ–Z in Figs. 3(a) and 3(b)] changes sign from −0.308 eV for $LaNiO_2$ to 0.781 eV for $LaNiO_2H$. (3) Last, but not least, H^- reduces the valence of Ni from Ni^{9+} to Ni^{8+}, effectively reducing E_F. Altogether, we end up in a situation that is much less akin to the cuprates: a $3d^8$ electronic configuration with two Ni orbitals, $3d_{x^2-y^2}$ and d_{z^2}, but no La-5d band around E_F.

DFT + DMFT *electronic structure.*—In transition metal oxides, we have strong effects of electronic correlations that are not properly described by the spin-unpolarized DFT band structure. One can describe the opening of a Mott-like gap by spin-polarized DFT + U (see Supplemental Material [48] and [73,74]) or by random spin orientations (or symmetry-lowering distortions) in a large supercell [75–80]. We will instead employ DFT + DMFT calculations in the paramagnetic phase at room temperature (300 K) in the following. For $LaNiO_2$ [Fig. 4(a)], electronic correlations lead to a dramatic quasiparticle renormalization Z or mass enhancement $m^*/m = 1/Z \sim 7$ of the almost half filled Ni $3d_{x^2-y^2}$ band, see enlargement in Fig. 4(b); the other Ni-3d bands are almost completely filled and below E_F. In DMFT, the La-5d band still crosses E_F around the A point, see Fig. 4(a), but the Γ pocket is lifted above E_F if we take the La-d interaction into account (cf. Supplemental Material [48]). Actually, its band dispersion hardly changes since the La-5d bands are only lightly occupied. One noteworthy effect of electronic correlations is, however, to reduce the number of holes (vs half filling) in the $3d_{x^2-y^2}$ orbital, from 0.08 per Ni site for the DFT-derived Wannier Hamiltonian to 0.03 in DMFT. Without additional doping, such a light hole doping is likely not enough to induce superconductivity.

Being so close to the Mott transition (a half filled Ni $3d_{x^2-y^2}$ band would be Mott insulating), minor modifications of the computational procedure, such as including the La-d, or changes of the experimental setup will slightly change the doping of the Ni $3d_{x^2-y^2}$ band. Even a slight change in doping will have a big effect on the quasiparticle renormalization (see Supplemental Material [48]). We think

Die approbierte gedruckte Originalversion dieser Dissertation ist an der TU Wien Bibliothek verfügbar.
The approved original version of this doctoral thesis is available in print at TU Wien Bibliothek.
TU Bibliothek Your knowledge hub WIEN

this explains the quite substantial variation of Z in different DFT + DMFT calculations [88–91].

For the oxide-hydride $LaNiO_2H$, on the other hand, the La-5d pockets around the A point are eliminated not only in DFT [Fig. 3(b)] but also in DFT + DMFT [Fig. 4(c)]. Without doping through the La-5d pocket and the additional H^-, Ni is in an undoped $3d^8$ configuration with holes in both the d_{z^2} and $d_{x^2-y^2}$ orbitals. This integer filling of the Ni d orbitals drives $LaNiO_2H$ into a Mott insulating phase with a gap of ~0.3 eV in Fig. 4(c); a similar electronic structure for $LaNiO_2H$ can also be described by DFT + U, see Supplemental Material [48]. It is consistent with the experimental observations that $LaNiO_{2.5}$, having formally the same Ni valence, was found to be insulating [93,94]. While here we find that already the paramagnetic phase is insulating, C- or G-type antiferromagnetic ordering [95] can be expected. Similarly, $SrVO_2H$ is antiferromagnetic with a high T_N [65], whereas $SrVO_3$ is a paramagnetic metal.

Conclusion and outlook.—In another class of correlated superconductors, the iron pnictides [7,96], it is well known that hydrogen plays an important role [104], and also when using CaH_2 as a reduction reagent [105]. Here, by performing DFT and DFT + U calculations, we find that the topotactic intercalation of hydrogen in infinite-layer ABO_2 is energetically favorable for early transition metals B.

This intercalation has dramatic consequences for the electronic structures. $LaNiO_2H$ is a $3d^8$ Mott insulator with two relevant orbitals around E_F, $3d_{z^2}$ and $3d_{x^2-y^2}$, but no La-5d pockets: A situation that is distinctively different from the cuprate superconductors. Indeed, this two-orbital situation bears some similarities to $LaNiO_3/LaAlO_3$ heterostructures prior to engineering their band structure to a cupratelike one [106–111]. On the other hand, $LaNiO_2$ with a $3d^9$ configuration and the holes only in the $d_{x^2-y^2}$ orbital closely resembles the band structure of the doped cuprates. This $d_{x^2-y^2}$ orbital is lightly doped already for the parent compound because of a La-5d pocket around the A point.

The strikingly different susceptibility toward topotactic intercalation of hydrogen and the dramatic consequences for the electronic structure may explain why some nickelates have been found to be superconducting and others not. In addition to $La(Nd)NiO_2H$, an incomplete reduction to $La(Nd)NiO_{2.5}$ [112] will also lead to a similar Ni $3d^8$ electronic configuration, and there may be mixed phases thereof in an actual experiment. While hydrogen is difficult to detect, careful studies already confirmed its presence when reducing $SrVO_3$ [29], SmFeAsO [105], and $NdNiO_3$ [30,113,114] with the reagent CaH_2.

Our findings call for a careful reanalysis of the hydrogen content in nickelates. Further, we suggest that for synthesizing $ANiO_2$ without H and an electronic structure prone to superconductivity, compressive strain and Sr doping are an advantage, as are long reaction times for reducing the H_2 pressure and, according to [30], low temperatures. Quite a number of capping layers might be needed to stabilize the system against further hydrogen intercalation, and doping with a divalent cation such as Sr appears to be necessary to arrive in the superconductive doping regime.

We thank O. Janson, P. Hansmann, and A. Prokofiev for helpful comments and discussions. L. S., W. X., and Z. Z. gratefully acknowledge financial support from the National Key R&D Program of China (2017YFA0303602), Key Research Program of Frontier Sciences of CAS (Grant No. ZDBS-LY-SLH008), and the National Nature Science Foundation of China (11774360, 11904373). L. S., J. K., J. M. T., and K. H. were supported by the Austrian Science Fund (FWF) through Projects No. P 30997 and No. P 32044. Y. L. acknowledges support by Deutsche Forschungsgemeinschaft (DFG) under Germany's Excellence Strategy EXC2181/1-390900948 (the Heidelberg STRUCTURES Excellence Cluster). Calculations have been done on the Vienna Scientific Clusters (VSC) and the Supercomputing Center at NIMTE CAS.

Note added.—Further information on the synthesis used in Ref. [1] became recently available in Ref. [115].

*Corresponding author.
zhong@nimte.ac.cn
†Corresponding author.
held@ifp.tuwien.ac.at

[1] D. Li, K. Lee, B. Y. Wang, M. Osada, S. Crossley, H. R. Lee, Y. Cui, Y. Hikita, and H. Y. Hwang, Nature (London) **572**, 624 (2019).
[2] T. Siegrist, S. Zahurak, D. Murphy, and R. Roth, Nature (London) **334**, 231 (1988).
[3] G. Balestrino, P. G. Medaglia, P. Orgiani, A. Tebano, C. Aruta, S. Lavanga, and A. A. Varlamov, Phys. Rev. Lett. **89**, 156402 (2002).
[4] P. Orgiani, C. Aruta, G. Balestrino, D. Born, L. Maritato, P. G. Medaglia, D. Stornaiuolo, F. Tafuri, and A. Tebano, Phys. Rev. Lett. **98**, 036401 (2007).
[5] D. Di Castro, C. Cantoni, F. Ridolfi, C. Aruta, A. Tebano, N. Yang, and G. Balestrino, Phys. Rev. Lett. **115**, 147001 (2015).
[6] J. G. Bednorz and K. A. Müller, Z. Phys. B **64**, 189 (1986).
[7] Y. Kamihara, H. Hiramatsu, M. Hirano, R. Kawamura, H. Yanagi, T. Kamiya, and H. Hosono, J. Am. Chem. Soc. **128**, 10012 (2006).
[8] Q. Li, C. He, J. Si, X. Zhu, Y. Zhang, and H.-H. Wen, Commun. Mater. **1**, 16 (2020).
[9] X. Zhou, Z. Feng, P. Qin, H. Yan, S. Hu, H. Guo, X. Wang, H. Wu, X. Zhang, H. Chen, X. Qiu, and Z. Liu, Rare Metals (2020), https://doi.org/10.1007/s12598-020-01389-2.
[10] D. Kaneko, K. Yamagishi, A. Tsukada, T. Manabe, and M. Naito, Physica (Amsterdam) **469C**, 936 (2009).

Die approbierte gedruckte Originalversion dieser Dissertation ist an der TU Wien Bibliothek verfügbar.
The approved original version of this doctoral thesis is available in print at TU Wien Bibliothek.
TU Bibliothek WIEN Your knowledge hub

[11] M. A. Hayward, M. A. Green, M. J. Rosseinsky, and J. Sloan, J. Am. Chem. Soc. **121**, 8843 (1999).
[12] G.-M. Zhang, Y.-F. Yang, and F.-C. Zhang, Phys. Rev. B **101**, 020501(R) (2020).
[13] Y. Nomura, M. Hirayama, T. Tadano, Y. Yoshimoto, K. Nakamura, and R. Arita, Phys. Rev. B **100**, 205138 (2019).
[14] M. Hirayama, T. Tadano, Y. Nomura, and R. Arita, Phys. Rev. B **101**, 075107 (2020).
[15] P. Jiang, L. Si, Z. Liao, and Z. Zhong, Phys. Rev. B **100**, 201106(R) (2019).
[16] K.-W. Lee and W. E. Pickett, Phys. Rev. B **70**, 165109 (2004).
[17] A. S. Botana and M. R. Norman, Phys. Rev. X **10**, 011024 (2020).
[18] H. Sakakibara, H. Usui, K. Suzuki, T. Kotani, H. Aoki, and K. Kuroki, arXiv:1909.00060.
[19] L.-H. Hu and C. Wu, Phys. Rev. Research **1**, 032046(R) (2019).
[20] X. Wu, D. Di Sante, T. Schwemmer, W. Hanke, H. Y. Hwang, S. Raghu, and R. Thomale, Phys. Rev. B **101**, 060504(R) (2020).
[21] J. Gao, Z. Wang, C. Fang, and H. Weng, arXiv:1909.04657.
[22] M. Jiang, M. Berciu, and G. A. Sawatzky, arXiv:1909.02557.
[23] Z. Liu, Z. Ren, W. Zhu, Z. F. Wang, and J. Yang, arXiv:1912.01332.
[24] P. Werner and S. Hoshino, Phys. Rev. B **101**, 041104(R) (2020).
[25] B. Geisler and R. Pentcheva, arXiv:2001.03762.
[26] F. Bernardini and A. Cano, arXiv:2001.02133.
[27] M.-Y. Choi, K.-W. Lee, and W. E. Pickett, Phys. Rev. B **101**, 020503(R) (2020).
[28] One difference is that Nd has a $4f$ moment and La has not. However, because of the weak hybridization with the Ni-$3d_{x^2-y^2}$, one might expect these to order or undergo a Kondo screening only at prohibitively low temperatures.
[29] T. Katayama, A. Chikamatsu, K. Yamada, K. Shigematsu, T. Onozuka, M. Minohara, H. Kumigashira, E. Ikenaga, and T. Hasegawa, J. Appl. Phys. **120**, 085305 (2016).
[30] T. Onozuka, A. Chikamatsu, T. Katayama, T. Fukumura, and T. Hasegawa, Dalton Trans. **45**, 12114 (2016).
[31] P. Hohenberg and W. Kohn, Phys. Rev. **136**, B864 (1964).
[32] W. Kohn and L. J. Sham, Phys. Rev. **140**, A1133 (1965).
[33] R. M. Martin, *Electronic Structure: Basic Theory and Practical Methods* (Cambridge University Press, Cambridge, England, 2004).
[34] A. Georges, G. Kotliar, W. Krauth, and M. J. Rozenberg, Rev. Mod. Phys. **68**, 13 (1996).
[35] G. Kotliar and D. Vollhardt, Phys. Today No. 3 **57**, 53 (2004).
[36] W. Metzner and D. Vollhardt, Phys. Rev. Lett. **62**, 324 (1989).
[37] K. Held, Adv. Phys. **56**, 829 (2007).
[38] P. Blaha, K. Schwarz, G. Madsen, D. Kvasnicka, and J. Luitz, *An Augmented Plane Wave+Local Orbitals Program for Calculating Crystal Properties* (Technische Universitat Wien, Vienna, 2001).
[39] K. Schwarz, P. Blaha, and G. Madsen, Comput. Phys. Commun. **147**, 71 (2002).
[40] G. Kresse and J. Hafner, Phys. Rev. B **48**, 13115 (1993).
[41] J. P. Perdew, K. Burke, and M. Ernzerhof, Phys. Rev. Lett. **77**, 3865 (1996).
[42] J. P. Perdew, A. Ruzsinszky, G. I. Csonka, O. A. Vydrov, G. E. Scuseria, L. A. Constantin, X. Zhou, and K. Burke, Phys. Rev. Lett. **100**, 136406 (2008).
[43] G. H. Wannier, Phys. Rev. **52**, 191 (1937).
[44] N. Marzari, A. A. Mostofi, J. R. Yates, I. Souza, and D. Vanderbilt, Rev. Mod. Phys. **84**, 1419 (2012).
[45] A. A. Mostofi, J. R. Yates, Y.-S. Lee, I. Souza, D. Vanderbilt, and N. Marzari, Comput. Phys. Commun. **178**, 685 (2008).
[46] J. Kuneš, R. Arita, P. Wissgott, A. Toschi, H. Ikeda, and K. Held, Comput. Phys. Commun. **181**, 1888 (2010).
[47] V. I. Anisimov, J. Zaanen, and O. K. Andersen, Phys. Rev. B **44**, 943 (1991).
[48] See Supplemental Material at http://link.aps.org/supplemental/10.1103/PhysRevLett.124.166402 for additional DFT + U and DMFT results, supporting our conclusions.
[49] T. Miyake and F. Aryasetiawan, Phys. Rev. B **77**, 085122 (2008).
[50] I. A. Nekrasov, K. Held, G. Keller, D. E. Kondakov, T. Pruschke, M. Kollar, O. K. Andersen, V. I. Anisimov, and D. Vollhardt, Phys. Rev. B **73**, 155112 (2006).
[51] G. Lantz, M. Hajlaoui, E. Papalazarou, V. L. R. Jacques, A. Mazzotti, M. Marsi, S. Lupi, M. Amati, L. Gregoratti, L. Si, Z. Zhong, and K. Held, Phys. Rev. Lett. **115**, 236802 (2015).
[52] E. Gull, A. J. Millis, A. I. Lichtenstein, A. N. Rubtsov, M. Troyer, and P. Werner, Rev. Mod. Phys. **83**, 349 (2011).
[53] N. Parragh, A. Toschi, K. Held, and G. Sangiovanni, Phys. Rev. B **86**, 155158 (2012).
[54] M. Wallerberger, A. Hausoel, P. Gunacker, A. Kowalski, N. Parragh, F. Goth, K. Held, and G. Sangiovanni, Comput. Phys. Commun. **235**, 388 (2019).
[55] J. E. Gubernatis, M. Jarrell, R. N. Silver, and D. S. Sivia, Phys. Rev. B **44**, 6011 (1991).
[56] A. W. Sandvik, Phys. Rev. B **57**, 10287 (1998).
[57] T. U. Ito, A. Koda, K. Shimomura, W. Higemoto, T. Matsuzaki, Y. Kobayashi, and H. Kageyama, Phys. Rev. B **95**, 020301(R) (2017).
[58] T. Yajima, A. Kitada, Y. Kobayashi, T. Sakaguchi, G. Bouilly, S. Kasahara, T. Terashima, M. Takano, and H. Kageyama, J. Am. Chem. Soc. **134**, 8782 (2012).
[59] T. Yamamoto and H. Kageyama, Chem. Lett. **42**, 946 (2013).
[60] Hydrogen intercalation has also been reported when CaH_2 reducing further Ruddlesden-Popper oxides [61,62].
[61] L. Jin, M. Batuk, F. K. K. Kirschner, F. Lang, S. J. Blundell, J. Hadermann, and M. A. Hayward, Inorg. Chem. **58**, 14863 (2019).
[62] L. Jin and M. A. Hayward, Angew. Chem., Int. Ed. Engl. **59**, 2076 (2020).
[63] The entropy of $1/2$ H_2 at 500 K is $S = 7.5 \times 10^{-4}$ eV/K [64] corresponding to 0.38 eV. On the other hand, the reduction with CaH_2 might lead to a rather high H_2 pressure; and ABO_2H has a higher entropy than ABO_2. Its Mott insulating spin 1 (see below) yields

Die approbierte gedruckte Originalversion dieser Dissertation ist an der TU Wien Bibliothek verfügbar.
The approved original version of this doctoral thesis is available in print at TU Wien Bibliothek.
TU Bibliothek WIEN Your knowledge hub

$S = k_B \ln(3) = 1 \times 10^{-4}$ eV/K corresponding to 0.05 eV at 500 K; a prospective disorder entropy of say $ABO_2H_{0.5}$ would yield $S = k_B \ln(2) = 0.6 \times 10^{-4}$ eV/K or 0.03 eV at 500 K.

[64] M. W. Chase, *NIST-JANAF Themochemical Tables* (J. Phys. Chem. Ref. Data, Monograph, 1998).

[65] F. Denis Romero, A. Leach, J. S. Möller, F. Foronda, S. J. Blundell, and M. A. Hayward, Angew. Chem., Int. Ed. Engl. **53**, 7556 (2014).

[66] M. Amano Patino, D. Zeng, S. J. Blundell, J. E. McGrady, and M. A. Hayward, Inorg. Chem. **57**, 2890 (2018).

[67] T. Yamamoto, D. Zeng, T. Kawakami, V. Arcisauskaite, K. Yata, M. A. Patino, N. Izumo, J. E. McGrady, H. Kageyama, and M. A. Hayward, Nat. Commun. **8**, 1217 (2017).

[68] M. Hayward, E. Cussen, J. Claridge, M. Bieringer, M. Rosseinsky, C. Kiely, S. Blundell, I. Marshall, and F. Pratt, Science **295**, 1882 (2002).

[69] R. M. Helps, N. H. Rees, and M. A. Hayward, Inorg. Chem. **49**, 11062 (2010).

[70] T. Sakaguchi, Y. Kobayashi, T. Yajima, M. Ohkura, C. Tassel, F. Takeiri, S. Mitsuoka, H. Ohkubo, T. Yamamoto, J. e. Kim *et al.*, Inorg. Chem. **51**, 11371 (2012).

[71] Y. Kobayashi, O. J. Hernandez, T. Sakaguchi, T. Yajima, T. Roisnel, Y. Tsujimoto, M. Morita, Y. Noda, Y. Mogami, A. Kitada *et al.*, Nat. Mater. **11**, 507 (2012).

[72] For $(\mathrm{Sr,Nd})\mathrm{NiO}_2$, we perform (antiferro-)magnetic GGA + U calculations in vasp instead of the nonmagnetic calculations for other ABO_2 systems because (i) NdNiO_3 is experimentally determined to be an antiferromagnetic insulator [1] and (ii) nonmagnetic VASP calculations for $(\mathrm{Sr,Nd})\mathrm{NiO}_2$ hardly converge.

[73] V. I. Anisimov, J. Zaanen, and O. K. Andersen, Phys. Rev. B **44**, 943 (1991).

[74] A. Mercy, J. Bieder, J. Iniguez, and P. Ghosez, Nat. Commun. **8**, 1677 (2017).

[75] B. L. Gyorffy, A. J. Pindor, J. Staunton, G. M. Stocks, and H. Winter, J. Phys. F **15**, 1337 (1985).

[76] J. Varignon, M. N. Grisolia, J. Iniguez, A. Barthelemy, and M. Bibes, npj Quantum Mater. **2**, 21 (2017).

[77] G. Trimarchi, Z. Wang, and A. Zunger, Phys. Rev. B **97**, 035107 (2018).

[78] J. Varignon, M. Bibes, and A. Zunger, Nat. Commun. **10**, 1658 (2019).

[79] J. Varignon, M. Bibes, and A. Zunger, Phys. Rev. B **100**, 035119 (2019).

[80] Appropriate DFT or hybrid functionals may also open band gaps in strongly correlated systems, see, e.g., Refs. [81–87].

[81] J. P. Perdew and A. Zunger, Phys. Rev. B **23**, 5048 (1981).

[82] J. Heyd, G. E. Scuseria, and M. Ernzerhof, J. Chem. Phys. **118**, 8207 (2003).

[83] J. M. Tomczak, K. Haule, T. Miyake, A. Georges, and G. Kotliar, Phys. Rev. B **82**, 085104 (2010).

[84] F. Tran and P. Blaha, Phys. Rev. Lett. **102**, 226401 (2009).

[85] J. W. Furness, Y. Zhang, C. Lane, I. G. Buda, B. Barbiellini, R. S. Markiewicz, A. Bansil, and J. Sun, Commun. Phys. **1**, 11 (2018).

[86] Q. Liu, Q. Yao, Z. A. Kelly, C. M. Pasco, T. M. McQueen, S. Lany, and A. Zunger, Phys. Rev. Lett. **121**, 186402 (2018).

[87] C. Lane, J. W. Furness, I. G. Buda, Y. Zhang, R. S. Markiewicz, B. Barbiellini, J. Sun, and A. Bansil, Phys. Rev. B **98**, 125140 (2018).

[88] S. Ryee, H. Yoon, T. J. Kim, M. Y. Jeong, and M. J. Han, Phys. Rev. B **101**, 064513 (2020).

[89] F. Lechermann, Phys. Rev. B **101**, 081110(R) (2020).

[90] J. Karp, A. S. Botana, M. R. Norman, H. Park, M. Zingl, and A. Millis, arXiv:2001.06441.

[91] For a one- and two-band DMFT calculation, cf. [24,92], respectively.

[92] Y. Gu, S. Zhu, X. Wang, J. Hu, and H. Chen, arXiv:1911.00814.

[93] R. D. Sánchez, M. T. Causa, A. Caneiro, A. Butera, M. Vallet-Regí, M. J. Sayagués, J. González-Calbet, F. García-Sanz, and J. Rivas, Phys. Rev. B **54**, 16574 (1996).

[94] M. Abbate, G. Zampieri, F. Prado, A. Caneiro, J. M. Gonzalez-Calbet, and M. Vallet-Regi, Phys. Rev. B **65**, 155101 (2002).

[95] J. Alonso, M. Martínez-Lope, J. García-Muñoz, and M. Fernández-Díaz, J. Phys. **9**, 6417 (1997).

[96] Let us note that DMFT has been quite helpful for understanding the pnictide physics [97–103].

[97] K. Haule, J. H. Shim, and G. Kotliar, Phys. Rev. Lett. **100**, 226402 (2008).

[98] M. Aichhorn, L. Pourovskii, V. Vildosola, M. Ferrero, O. Parcollet, T. Miyake, A. Georges, and S. Biermann, Phys. Rev. B **80**, 085101 (2009).

[99] V. I. Anisimov, D. M. Korotin, M. A. Korotin, A. V. Kozhevnikov, J. Kuneš, A. O. Shorikov, S. L. Skornyakov, and S. V. Streltsov, J. Phys. Condens. Matter **21**, 075602 (2009).

[100] P. Hansmann, R. Arita, A. Toschi, S. Sakai, G. Sangiovanni, and K. Held, Phys. Rev. Lett. **104**, 197002 (2010).

[101] A. Toschi, R. Arita, P. Hansmann, G. Sangiovanni, and K. Held, Phys. Rev. B **86**, 064411 (2012).

[102] I. A. Nekrasov, N. S. Pavlov, and M. V. Sadovskii, JETP Lett. **102**, 26 (2015).

[103] D. Guterding, S. Backes, M. Tomi, H. O. Jeschke, and R. Valentí, Phys. Status Solidi (b) **254**, 1600164 (2017).

[104] S. Iimura, S. Matsuishi, H. Sato, T. Hanna, Y. Muraba, S. W. Kim, J. E. Kim, M. Takata, and H. Hosono, Nat. Commun. **3**, 943 (2012).

[105] J. Matsumoto, K. Hanzawa, M. Sasase, S. Haindl, T. Katase, H. Hiramatsu, and H. Hosono, Phys. Rev. Mater. **3**, 103401 (2019).

[106] J. Chaloupka and G. Khaliullin, Phys. Rev. Lett. **100**, 016404 (2008).

[107] P. Hansmann, X. Yang, A. Toschi, G. Khaliullin, O. K. Andersen, and K. Held, Phys. Rev. Lett. **103**, 016401 (2009).

[108] P. Hansmann, A. Toschi, X. Yang, O. K. Andersen, and K. Held, Phys. Rev. B **82**, 235123 (2010).

[109] X. Wang, M. J. Han, L. de' Medici, H. Park, C. A. Marianetti, and A. J. Millis, Phys. Rev. B **86**, 195136 (2012).

[110] A. Subedi, O. E. Peil, and A. Georges, Phys. Rev. B **91**, 075128 (2015).

Die approbierte gedruckte Originalversion dieser Dissertation ist an der TU Wien Bibliothek verfügbar.
The approved original version of this doctoral thesis is available in print at TU Wien Bibliothek.
TU Bibliothek WIEN Your knowledge hub

[111] O. Janson and K. Held, Phys. Rev. B **98**, 115118 (2018).
[112] Also in Ref. [9] it has been reported to be difficult to remove the excess oxygen.
[113] M. Hayward, M. Green, M. Rosseinsky, and J. Sloan, J. Am. Chem. Soc. **121**, 8843 (1999).
[114] The hydrogen surplus "fluorite peak" of Ref. [113] has not been detected for the superconducting nickelates in Ref. [1].
[115] K. Lee, B. H. Goodge, D. Li, M. Osada, B. Y. Wang, Y. Cui, L. F. Kourkoutis, and H. Y. Hwang, APL Mater. **8**, 041107 (2020).

Die approbierte gedruckte Originalversion dieser Dissertation ist an der TU Wien Bibliothek verfügbar.
The approved original version of this doctoral thesis is available in print at TU Wien Bibliothek.
TU Bibliothek WIEN Your knowledge hub

Computer Physics Communications 245 (2019) 106847

Contents lists available at ScienceDirect

Computer Physics Communications

journal homepage: www.elsevier.com/locate/cpc

The AbinitioDΓA Project v1.0: Non-local correlations beyond and susceptibilities within dynamical mean-field theory

Anna Galler [a,b,*], Patrik Thunström [a,c], Josef Kaufmann [a], Matthias Pickem [a,*], Jan M. Tomczak [a], Karsten Held [a]

[a] Institute of Solid State Physics, TU Wien, 1040 Vienna, Austria
[b] Centre de Physique Théorique, Ecole Polytechnique, 91128 Palaiseau, France
[c] Department of Physics and Astronomy, Materials Theory, Uppsala University, 75120 Uppsala, Sweden

ARTICLE INFO

Article history:
Received 10 January 2018
Received in revised form 16 July 2019
Accepted 24 July 2019
Available online 7 August 2019

Keywords:
Strongly correlated electron systems
Dynamical mean-field theory
Dynamical vertex approximation
Electronic structure calculations

ABSTRACT

The *ab initio* extension of the dynamical vertex approximation (DΓA) method allows for realistic materials calculations that include non-local correlations beyond *GW* and dynamical mean-field theory. Here, we discuss the AbinitioDΓA algorithm, its implementation and usage in detail, and make the program package available to the scientific community.

Program summary

Program Title: AbinitioDΓA
Program Files doi: `http://dx.doi.org/10.17632/h3k3fg6szb.1`
Licensing provisions: GNU General Public License v3
Programming language: `Fortran95` and `Python`
Required dependencies: `MPI`, `LAPACK`, `BLAS`, `HDF5` ($\geq$ 1.8.12), `Python` ($\geq$ 2.7), `h5py` ($\geq$ 2.5.0), `numpy` ($\geq$ 1.9.1)
Optional dependencies: `pip`, `matplotlib` ($\geq$ 1.5.1), `scipy` ($\geq$ 0.14.0)
Supplementary material: Test case files and step-by-step instructions.
Nature of problem: Realistic materials calculations including non-local correlations beyond dynamical mean-field theory (DMFT) as well as non-local interactions. Solving the Bethe–Salpeter equation for multiple orbitals. Determining momentum-resolved susceptibilities in DMFT.
Solution method:
Ab initio dynamical vertex approximation: starting from the local two-particle vertex and constructing from it the local DMFT correlations, the *GW* diagrams, and further non-local correlations, e.g., spin fluctuations. Efficient solution of the Bethe–Salpeter equation, avoiding divergencies in the irreducible vertex in the particle-hole channel by reformulating the problem in terms of the full vertex. Parallelization with respect to the bosonic frequency and transferred momentum.
Additional comments including restrictions and unusual features: As input, a Hamiltonian derived, e.g., from density functional theory and a DMFT solution thereof is needed including a local two-particle vertex calculated at DMFT self-consistency. Hitherto the AbinitioDΓA program package is restricted to SU(2) symmetric problems. A so-called λ correction or self-consistency is not yet implemented in the AbinitioDΓA code. Susceptibilities are so far only calculated within DMFT, not the dynamical vertex approximation.

© 2019 Elsevier B.V. All rights reserved.

1. Introduction

Dynamical mean-field theory (DMFT) [1,2] takes into account a major part of the electronic correlations, namely the local ones. It has been very successfully applied to models of strongly correlated electron system, see [3] for an early review and [4] for a series of lecture notes on the occasion of 25 years of DMFT. Its merger with density functional theory (DFT) [5,6] and *GW* [7,8] even allows for the realistic calculation of materials including strong electronic correlations, see [9–11] for reviews.

* Corresponding authors.
E-mail addresses: galler.anna@gmail.com (A. Galler), matthias.pickem@gmail.com (M. Pickem).

https://doi.org/10.1016/j.cpc.2019.07.012
0010-4655/© 2019 Elsevier B.V. All rights reserved.

Die approbierte gedruckte Originalversion dieser Dissertation ist an der TU Wien Bibliothek verfügbar.
The approved original version of this doctoral thesis is available in print at TU Wien Bibliothek.
TU Bibliothek WIEN Your knowledge hub

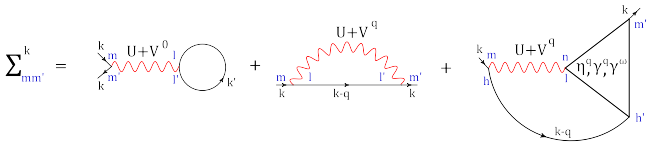

Fig. 1. Feynman-diagrammatic representation of the AbinitioDΓA equation of motion [Eq. (1)]: The self-energy is obtained from the three-leg vertices η^{q}, γ^{q} and γ^{ω}, which in turn are obtained from the full vertex F (see Fig. 3) that is determined via the Bethe–Salpeter equation. In addition, the Hartree and Fock contributions of Eq. (6) need to be added. Beside the momenta qkk′, orbital indices $lmm'l'$ are shown in blue . (For interpretation of the references to color in this figure legend, the reader is referred to the web version of this article.)

On the other hand, non-local correlations are at the heart of many fascinating phenomena of many-body physics. In the aforementioned *GW*+DMFT approach the screening of the bare interaction V to a screened W gives rise to non-local correlations in the self-energy. But there are important further effects of non-local correlations, e.g., spin fluctuations. Hence, extensions of DMFT that include the local DMFT correlations and additional non-local correlations are at the scientific frontier.

One main route to this end is cluster extensions of DMFT which consider a cluster of sites in a DMFT Weiss field. Two methods, the dynamical cluster approximation (DCA) [12] and the cellular DMFT [13,14], have been developed, see [15] for a review. Due to numerical limitations these approaches are restricted to short-range correlations and essentially a single interacting band. Realistic calculations are hardly possible or restricted to extremely small clusters [16,17].

Diagrammatic extensions of the DMFT on the other hand use a local two-particle vertex as a starting point and construct from it the local DMFT correlations as well as non-local correlations. These diagrammatic extensions are more suitable to deal with long-range correlations and realistic multi-orbital calculations. This more recent development started with the dynamical vertex approximation (DΓA) [18,19], subsequently followed by various other approaches such as the dual fermion (DF) approach [20], the one-particle irreducible (1PI) approach [21], the dynamical mean-field theory to functional renormalization group (DMF^{2}RG) approach [22], the triply-irreducible local expansion (TRILEX) [23] and the non-local expansion scheme [24]. These diagrammatic extensions of DMFT have been first applied to model systems, among others to calculate (quantum) critical exponents [25–28], see [29] for a review.

Most recently, these diagrammatic approaches have been extended to realistic multi-orbital *ab initio* DΓA calculations [30,31]. Using the local three-frequency and four-orbital vertex and on top of this the non-local bare interaction as a starting point, this approach not only includes the DMFT and *GW* Feynman diagrams but also many further non-local correlations. It is the aim of this paper to make the developed AbinitioDΓA program package available to the general scientific community.

The paper is organized as follows: In Section 2, we recapitulate the AbinitioDΓA formalism of Ref. [30] in the context of our implementation. Subsequently we explain the program from a user's point of view. Specifically, Section 3.1 shows the installation procedure, Section 3.2 makes the reader familiar with the necessary steps for a simple calculation, which is illustrated in Section 3.3 by an example case: $SrVO_3$. Further information for advanced users can be found in Section 4, where the parameters for the example case and the structure of the output file are discussed. Following this description for users we switch to a more technical description in Section 5 where we provide more details about the internal program flow and the implementation. We provide Appendix A where further user options are discussed; and Appendix B where results for a quick $SrVO_3$ test calculation with a small frequency box are presented. Finally, Section 6 provides a summary and recapitulates the approximations used when doing AbinitioDΓA calculations.

2. Implemented AbinitioDΓA equations

2.1. AbinitioDΓA self-energy

The main quantity, which is computed by the AbinitioDΓA algorithm, is the non-local (momentum-dependent) and dynamical (frequency-dependent) self-energy $\Sigma_{\mathrm{D\Gamma A}}$. We compute $\Sigma_{\mathrm{D\Gamma A}}$ in the ladder approximation of DΓA [32,33] which incorporates non-local ladder diagrams in both the particle-hole (ph) and transverse particle-hole ($\overline{ph}$) channels, starting from a local irreducible vertex in these channels. This way, among others, spin fluctuations are included, but one neglects the particle–particle (pp) channel which is, e.g., important for superconducting fluctuations.

In AbinitioDΓA the local irreducible vertex in the ph and $\overline{ph}$ channels is supplemented by the bare non-local Coulomb interaction $V^{\mathbf{q}}$. This generates additional diagrams and screening effects. If one included only the ph channel and the non-local Coulomb interaction, one would reproduce the *GW* approximation [34].

Let us here start the discussion of the AbinitioDΓA equations with the final quantity calculated in the code: the self-energy. Using the compound indices $\mathrm{k} = (\mathbf{k}, \nu)$ and $\mathrm{q} = (\mathbf{q}, \omega)$ for momenta $\mathbf{k}$, $\mathbf{q}$ and Matsubara frequencies ν, ω, the self-energy of the AbinitioDΓA is obtained from the Schwinger–Dyson equation as [30]

$$\begin{aligned}\Sigma^{\mathrm{k}}_{\mathrm{D\Gamma A}\,mm'} =& \Sigma^{\nu}_{\mathrm{DMFT}\,mm'} + \Sigma^{\mathbf{k}}_{\mathrm{HF}\,mm'} - \beta^{-1}\sum_{lnhh'\mathrm{q}}\left(U_{mlhn} + V^{\mathbf{q}}_{mlhn} - \frac{1}{2}\tilde{U}_{mlhn}\right)\eta^{\mathrm{q}\nu}_{d,nlh'm'}G^{\mathrm{k-q}}_{hh'} \\ &+ \beta^{-1}\sum_{lnhh'\mathrm{q}}\frac{3}{2}\tilde{U}_{mlhn}\eta^{\mathrm{q}\nu}_{m,nlh'm'}G^{\mathrm{k-q}}_{hh'} - \beta^{-1}\sum_{lnhh'\mathrm{q}}\left(V^{\mathbf{q}}_{mlhn}\gamma^{\omega\nu}_{d,nlh'm'} - U_{mlhn}\gamma^{\mathrm{q}\nu}_{d,nlh'm'}\right)G^{\mathrm{k-q}}_{hh'}.\end{aligned} \tag{1}$$

This expression for the AbinitioDΓA self-energy is depicted diagrammatically in Fig. 1. In the following we will introduce all quantities necessary for the evaluation of $\Sigma_{\mathrm{D\Gamma A}}$ in Eq. (1) and discuss how they are calculated. In particular, the non-local three-leg vertices $\gamma^{\mathrm{q}\nu}$ and $\eta^{\mathrm{q}\nu}$ are obtained in DΓA from the local irreducible vertex through the Bethe–Salpeter ladder. A brief description is given below, while a detailed derivation can be found in Ref. [30].

Die approbierte gedruckte Originalversion dieser Dissertation ist an der TU Wien Bibliothek verfügbar.
The approved original version of this doctoral thesis is available in print at TU Wien Bibliothek.
TU Bibliothek WIEN Your knowledge hub

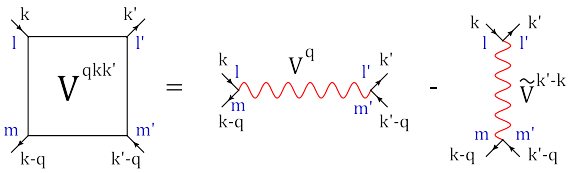

Fig. 2. The non-local Coulomb interaction $V^{\mathbf{q}\mathbf{k}\mathbf{k}'}$ consists of two terms: $V^{\mathbf{q}}$ and $V^{\mathbf{k}'-\mathbf{k}}$ (the latter is neglected in the AbinitioDΓA approach). The local Coulomb interaction U has the same structure, but without any momentum dependence so that both terms can be taken into account without effort.

One-particle Green's function. The one-particle Green's function $G^{\mathrm{k}-\mathrm{q}}$ appearing in the last three terms in Eq. (1) is the lattice Green's function, given by

$$G^{\mathrm{k}}_{hh'} = \left[i\nu + \mu - H^{\mathbf{k}}_{W} - \Sigma^{\nu} - \Sigma_{DC} \right]^{-1}_{hh'}. \tag{2}$$

Here, $H^{\mathbf{k}}_{W}$ is the material-dependent Hamiltonian obtained, e.g., from a DFT computation and a consecutive Wannier projection [35], Σ^{ν} is the dynamical but local DMFT self-energy, Σ_{DC} the double-counting correction, and μ the chemical potential of the DMFT calculation. Here, and in the following, Roman subscripts denote orbital indices, $\nu = (2n+1)\pi/\beta$ ($\omega = 2n\pi/\beta$) are fermionic (bosonic) Matsubara frequencies for an inverse temperature $\beta = 1/(k_B T)$.

From the products of two interacting one-particle Green's functions the unconnected (bare bubble) susceptibilities χ_0^{ω}, χ_0^{q} and $\chi_0^{nl,\mathrm{q}}$ are obtained. In order of increasing non-local character, these are defined as:

$$\chi^{\omega\nu\nu}_{0,lmm'l'} = -\beta G^{\nu}_{ll'} G^{\nu-\omega}_{m'm}, \tag{3}$$

$$\chi^{\mathrm{q}\nu\nu}_{0,lmm'l'} = -\beta \sum_{\mathbf{k}} G^{\mathrm{k}}_{ll'} G^{\mathrm{k}-\mathrm{q}}_{m'm}, \tag{4}$$

$$\chi^{\mathrm{nl},\mathrm{q}\nu\nu}_{0,lmm'l'} = \chi^{\mathrm{q}\nu\nu}_{0,lmm'l'} - \chi^{\omega\nu\nu}_{0,lmm'l'}. \tag{5}$$

Here, $\chi_0^{\omega\nu\nu}$ is a purely local bubble-term obtained by the product of two local one-particle DMFT Green's functions $G^{\nu}_{hh'} = \sum_{\mathbf{k}} G^{\mathrm{k}}_{hh'}$; $\chi_0^{\mathrm{q}\nu\nu}$ instead is the q-dependent product of two non-local DMFT Green's functions defined in Eq. (2). By subtracting Eq. (3) from Eq. (4) one finally obtains the purely non-local $\chi_0^{\mathrm{nl},\mathrm{q}\nu\nu}$.

Local and non-local Coulomb interaction. In the Wannier basis, local and non-local Coulomb interaction are four-index objects, denoted as $U_{lm'ml'}$ and $V^{\mathbf{q}}_{lm'ml'}$, respectively. The current implementation allows for an arbitrary orbital-dependence of the Coulomb interaction without any restriction in performance.

The $\tilde{U}$ in Eq. (1) is the local Coulomb interaction in the transverse particle-hole ($\overline{ph}$) channel and is related to U through $\tilde{U}_{lm'ml'} = U_{l\overline{m'}l'\overline{m}}$. The two channels are visualized in Fig. 2 for the non-local Coulomb interaction. However, the non-local component in the $\overline{ph}$-channel, $\tilde{V}^{\mathbf{k}'-\mathbf{k}}_{lm'l'm}$, is neglected in the AbinitioDΓA formalism (it would result in a $\mathbf{k}'$- and $\mathbf{k}$-dependence in the Bethe–Salpeter ladder equations, for details see Ref. [30,31]). This approximation is common practice: Indeed the *GW* [34] and *GW*+DMFT [7,8] approaches neglect both local and non-local interactions in the transverse channel.

DMFT and Hartree–Fock contribution. The first contribution to $\Sigma^{\mathrm{k}}_{\mathrm{D\Gamma A}}$ in Eq. (1) is the DMFT self-energy $\Sigma^{\nu}_{\mathrm{DMFT}}$ that contains all diagrams that can be build from the local Green's function $G^{\nu} = \sum_{\mathbf{k}} G^{\mathrm{k}}$ and the local interaction U. This contribution is the leading term to $\Sigma^{\mathrm{k}}_{\mathrm{D\Gamma A}}$ at large frequencies ν. $\Sigma^{\nu}_{\mathrm{DMFT}}$ includes the local and static Hartree–Fock term originating from the local Coulomb interaction U. However, AbinitioDΓA also contains the non-local Hartree–Fock term arising from the non-local Coulomb interaction $V^{\mathbf{q}}$. Indeed, the second term in Eq. (1), $\Sigma^{\mathbf{k}}_{\mathrm{HF}}$, is the non-local, static Hartree–Fock contribution and reads

$$\Sigma^{\mathbf{k}}_{\substack{\mathrm{HF}\\ mm'}} = 2 \sum_{ll'\mathbf{k}'} V^{\mathbf{q}=\mathbf{0}}_{mlm'l'} n^{\mathbf{k}'}_{l'l} - \sum_{ll'\mathbf{q}} V^{\mathbf{q}}_{mll'm'} n^{\mathbf{k}-\mathbf{q}}_{l'l}, \tag{6}$$

where $n^{\mathbf{k}} = 1/\beta \sum_{\nu} G^{\mathrm{k}}$ are the k-dependent occupancies.

Three-leg vertices. The quantities $\gamma_r^{\omega\nu}$, $\gamma_r^{\mathrm{q}\nu}$ and $\eta_r^{\mathrm{q}\nu}$ in Eq. (1) (with the index r referring to the (d)ensity or (m)agnetic channel) are three-leg vertices. Such three-leg vertices have been used in DΓA and dual fermion from the beginning, see, e.g., Ref. [32]; the TRILEX approach [23], which does not solve the non-local Bethe–Salpeter equation, is formulated entirely in terms of these three-leg vertices. They can be obtained from the full, four-leg vertex function F through a sum over the left fermionic frequency ν'. A diagrammatic representation of these three-leg vertices is shown in Fig. 3. With increasing order of non-locality the necessary three-leg vertices read

$$\gamma^{\omega\nu}_{r,lmm'l'} = \sum_{n'h'\nu'} \chi^{\omega\nu'\nu'}_{0,lmn'h'} F^{\omega\nu'\nu}_{r,h'n'm'l'}, \tag{7}$$

$$\gamma^{\mathrm{q}\nu}_{r,lmm'l'} = \sum_{n'h'\nu'} \chi^{\mathrm{nl},\mathrm{q}\nu'\nu'}_{0,lmn'h'} F^{\omega\nu'\nu}_{r,h'n'm'l'}, \tag{8}$$

$$\eta^{\mathrm{q}\nu}_{r,lmm'l'} = \sum_{n'h'\nu'} \chi^{\mathrm{q}\nu'\nu'}_{0,lmn'h'} F^{\mathrm{q}\nu'\nu}_{r,h'n'm'l'} - \gamma^{\omega\nu}_{r,lmm'l'}. \tag{9}$$

Thus, $\gamma^{\omega\nu}$ is a completely local three-leg vertex which can directly be extracted from the impurity solver [36,37]. If the DMFT impurity solver does not explicitly provide $\gamma^{\omega\nu}$, the latter is computed within the AbinitioDΓA program according to Eq. (7).

Die approbierte gedruckte Originalversion dieser Dissertation ist an der TU Wien Bibliothek verfügbar.
The approved original version of this doctoral thesis is available in print at TU Wien Bibliothek.
TU Bibliothek WIEN Your knowledge hub

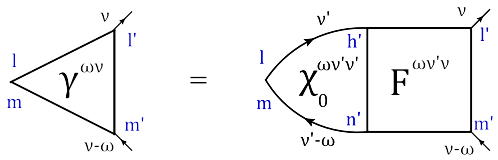

Fig. 3. The three-leg vertices are obtained from $\chi_0 F$ through a sum over the left fermionic frequency ν'. Here, exemplary, the relation for the purely local three-leg vertex $\gamma^{\omega\nu}$ in Eq. (7) is shown.

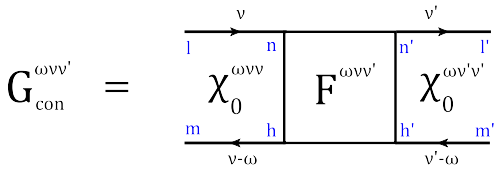

Fig. 4. The local vertex function $F^{\omega\nu\nu'}$ can be obtained from the connected part of the two-particle impurity Green's function $G^{\omega\nu\nu'}_{\text{con}}$ through an 'amputation' of the left and the right legs [see Eq. (11)].

The most complex ingredients of Eqs. (7)–(9) are the local four-leg vertex function $F_r^{\omega\nu'\nu}$ of the DMFT impurity and its non-local counterpart $F_r^{q\nu'\nu}$. The local four-leg vertex $F_r^{\omega\nu'\nu}$ is obtained from the connected part G_r^{con} of the DMFT two-particle Green's function. G_r^{con} can be computed by the DMFT impurity solver [38,39] and a subsequent combination of the spin components into channels $r = d, m$:

$$\begin{aligned} G_d^{\text{con}} &= G^{\text{con}}_{\uparrow\uparrow\uparrow\uparrow} + G^{\text{con}}_{\uparrow\uparrow\downarrow\downarrow}, \\ G_m^{\text{con}} &= G^{\text{con}}_{\uparrow\uparrow\uparrow\uparrow} - G^{\text{con}}_{\uparrow\uparrow\downarrow\downarrow}. \end{aligned} \tag{10}$$

The relation between G^{con} and F is visualized in Fig. 4 and explicitly reads

$$F^{\omega\nu\nu'}_{r,lmm'l'} = \sum_{nhn'h'} [(\chi_0^{\omega})^{-1}]^{\nu\nu}_{lmn'h'} G^{\text{con}\ \omega\nu\nu'}_{r,h'n'nh} [(\chi_0^{\omega})^{-1}]^{\nu'\nu'}_{hnm'l'}. \tag{11}$$

The non-local, full vertex function $F_r^{q\nu'\nu}$ in Eq. (9) instead is obtained through the non-local version of the Bethe–Salpeter equation.

Usually, the Bethe–Salpeter starts from the irreducible vertex in a given channel r and builds up ladder diagrams therefrom. This was also used in the first DΓA calculations [18,32], whereas the dual fermion approach employed the local full vertex as a starting point [20,40,41]. It turned out that the two approaches and the 1PI [21] actually construct the very same ladder diagrams, and only differ in how from this ladder, i.e., from the obtained $F_r^{q\nu'\nu}$, the self-energy is constructed, see e.g. Fig. 19 of [29]. Using the local full vertex as in DF instead of the irreducible vertex has the advantage that it does not suffer from vertex divergences [42], which is the reason why it is nowadays also employed in ladder DΓA and why we employ it in AbinitioDΓA.

Following Ref. [30], we hence rewrite Eq. (9) in the following compact form

$$\eta^{q\nu}_{r,lmm'l'} = \sum_{nh\nu'} (\vec{\mathbf{1}}_{lmhn} + \gamma^{\omega\nu'}_{r,lmhn}) \left\{ \left[\left(\mathbf{1} - \chi_0^{nl,q} F_r^{\omega} - 2\beta^{-2} \chi_0^{q} V^{\mathbf{q}} (\mathbf{1} + \gamma_r^{\omega}) \delta_{rd} \right)^{-1} \right]^{\nu'\nu}_{nhm'l'} - \mathbf{1}_{nhm'l'} \right\}, \tag{12}$$

where $\mathbf{1}_{lmhn} = \delta_{ln}\delta_{mh}\delta_{\nu\nu'}$ and $\vec{\mathbf{1}}_{lmhn} = \sum_{\nu'} \mathbf{1} = \delta_{ln}\delta_{mh}$. Thus, $\eta_r^{q\nu}$ can be computed efficiently through a single matrix inversion and a consecutive multiplication with the three-leg quantity $(\vec{\mathbf{1}} + \gamma_r^{\omega\nu'})$ from the left. Note that the matrix that is inverted has a compound index consisting of one fermionic frequency and two orbitals for both, row and column [cf. the indices $\{hn, \nu'\}$ and $\{m'l', \nu\}$ after the inversion in Eq. (12)]. In the expression that is inverted in Eq. (12), orbital and fermionic frequency indices have been omitted for clarity. For more details we refer the reader to Section 5.2.2 and Fig. 11 (F^{ω}), Fig. 12 ($\chi_0^{nl,q}$, χ_0^{q}), and Figs. 14, 15 (γ^{ω}, $V^{\mathbf{q}}$). Please also note that, by neglecting $\tilde{V}^{\mathbf{k}'-\mathbf{k}}$, the non-local Coulomb interaction $V^{\mathbf{q}}$ needs to be added only in the density channel.

2.2. Momentum-dependent susceptibilities

With the AbinitioDΓA program one can also compute momentum-dependent, physical susceptibilities. The susceptibilities χ_r^{q} in the density and magnetic channel $r \in \{d, m\}$ read

$$\chi^{q}_{r,lmm'l'} = \beta^{-2} \sum_{\nu\nu'} \chi^{q\nu\nu'}_{r,lmm'l'} = \chi^{q}_{0,lmm'l'} + \beta^{-2} \sum_{\nu\nu',nhh'n'} \chi^{q\nu\nu}_{0,lmhn} F^{q\nu\nu'}_{r,nhh'n'} \chi^{q\nu'\nu'}_{0,n'h'm'l'}. \tag{13}$$

Please note that the combined index q in Eq. (13) contains the momentum $\mathbf{q}$ and the bosonic frequency ω. We can now rewrite Eq. (13) by using the three-leg vertices in Eqs. (7) and (9), which yields

$$\chi^{q}_{r,lmm'l'} = \chi^{q}_{0,lmm'l'} + \beta^{-2} \sum_{\nu'h'n'} \eta^{q\nu'}_{r,lmh'n'} \chi^{q\nu'\nu'}_{0,n'h'm'l'} + \beta^{-2} \sum_{\nu'h'n'} \gamma^{\omega\nu'}_{r,lmh'n'} \chi^{q\nu'\nu'}_{0,n'h'm'l'}. \tag{14}$$

Die approbierte gedruckte Originalversion dieser Dissertation ist an der TU Wien Bibliothek verfügbar.
The approved original version of this doctoral thesis is available in print at TU Wien Bibliothek.
TU Bibliothek WIEN Your knowledge hub

In order to further split the susceptibility into local and non-local contributions, we insert Eq. (5) into Eq. (14) and obtain

$$\begin{aligned}\chi^{\mathrm{q}}_{r,lmm'l'} &= \left(\chi^{\omega}_{0,lmm'l'} + \chi^{\mathrm{nl,q}}_{0,lmm'l'}\right) + \beta^{-2}\sum_{\nu'h'n'}\eta^{\mathrm{q}\nu'}_{r,lmh'n'}\chi^{\mathrm{q}\nu'\nu'}_{0,n'h'm'l'} + \beta^{-2}\sum_{\nu'h'n'}\gamma^{\omega\nu'}_{r,lmh'n'}\left(\chi^{\omega\nu'\nu'}_{0,n'h'm'l'} + \chi^{\mathrm{nl,q}\nu'\nu'}_{0,n'h'm'l'}\right)\\ &= \chi^{\omega}_{r,lmm'l'} + \chi^{\mathrm{nl,q}}_{0,lmm'l'} + \beta^{-2}\sum_{\nu'h'n'}\eta^{\mathrm{q}\nu'}_{r,lmh'n'}\chi^{\mathrm{q}\nu'\nu'}_{0,n'h'm'l'} + \beta^{-2}\sum_{\nu'h'n'}\gamma^{\omega\nu'}_{r,lmh'n'}\chi^{\mathrm{nl,q}\nu'\nu'}_{0,n'h'm'l'},\end{aligned} \tag{15}$$

where in the last line we have used the purely local susceptibility, which reads

$$\chi^{\omega}_{r,lmm'l'} = \chi^{\omega}_{0,lmm'l'} + \beta^{-2}\sum_{\nu'h'n'}\gamma^{\omega\nu'}_{r,lmh'n'}\chi^{\omega\nu'\nu'}_{0,n'h'm'l'}. \tag{16}$$

Please note that a similar decomposition into local and non-local terms is also employed in the context of the dual boson approach and was shown to reduce statistical QMC-errors [40,41].

The usual magnetic and density susceptibilities are given by the spin–spin and charge–charge correlation functions

$$\chi_{m,ll'} = \left\langle \mathrm{T}_\tau \left(n_{l,\uparrow} - n_{l,\downarrow}\right)(\tau)\ \left(n_{l',\uparrow} - n_{l',\downarrow}\right)(0)\right\rangle \tag{17}$$

$$\chi_{d,ll'} = \left\langle \mathrm{T}_\tau \left(n_{l,\uparrow} + n_{l,\downarrow}\right)(\tau)\ \left(n_{l',\uparrow} + n_{l',\downarrow}\right)(0)\right\rangle \tag{18}$$

where T_τ denotes the time-ordering operator. These can be deduced from Eq. (13) by choosing the orbital combinations $\chi^{\mathrm{q}}_{r,lll'l'}$ and multiplying by a factor of 2. Finally, the physical susceptibilities, in units of μ_B^2/eV, can be readily obtained via an orbital summation:

$$\chi_r = 2\sum_{ll'}\chi^{\mathrm{q}}_{r,lll'l'} \tag{19}$$

Note that for $r = m$ the above coincides with the magnetic susceptibility defined by

$$\chi_m = g^2\sum_{ij} e^{i\mathbf{q}(\mathbf{R}_i-\mathbf{R}_j)}\int d\tau e^{i\omega\tau}\left\langle \mathrm{T}_\tau S^z_{il}(\tau)S^z_{jl'}(0)\right\rangle\ , \tag{20}$$

when assuming a Landé factor $g = 2$. Let us emphasize again that the thus calculated susceptibility is the q-dependent DMFT susceptibility. For calculating distinct DΓA susceptibilities a self-consistency or λ-correction [32] is needed.

3. Installation and first AbinitioDΓA run

3.1. Installation

In the following we assume that all necessary dependencies are installed, namely:

- `LAPACK` [43] library of version 3.8.0 and above.
- `HDF5` [44] library of version 1.8.12 and above.
- `h5py` [45] library of version 2.5.0 and above.
- `numpy` [46] library of version 1.9.1 and above.

One way to conveniently obtain the code is via github (`git` installation is required) or, alternatively, from the CPC repository:

```
$ git clone https://github.com/AbinitioDGA/ADGA.git
$ cd ADGA
```

This will create the code directory `ADGA` with all source files, documentation and test files included. Before the program can be compiled, a configuration file called `make_config` has to be created in the main `ADGA` folder. Here the necessary local path and environment variables are saved, on which the other Makefiles depend on. Since this is strongly system-dependent, we give only a generic example which can also be found in `make_configs/make_config_cpc`:

```
F90      = mpifort
FPPFLAGS  = -DMPI
FFLAGS    = -O3
FINCLUDE  = -I/opt/hdf5-1.8.16_gcc/include/

LD       = $(F90)
LDFLAGS   = -lhdf5_fortran -lhdf5hl_fortran -llapack -lblas
LDINCLUDE = -I/opt/hdf5-1.8.16_gcc/include/ -L/opt/hdf5-1.8.16_gcc/lib/
LDINCLUDE += -L/opt/lapack-3.8.0
```

The `F*` variables describe the dependencies necessary for the compilation of the Fortran object files (`*.o`) while the `LD*` variables describe the dependencies for the final linking process. The compilation with MPI support

(`FPPFLAGS = -DMPI`) and full optimization (`FFLAGS = -O3`) is strongly recommended. Compilation without MPI support however is still available by simply using a non-MPI compiler (e.g., `gfortran`) and leaving the `FPPFLAGS` variable empty. The rest of the variables contain absolute paths to the respective, mandatory libraries in combination with their standard linking variables (`-lhdf5_fortran` etc.).

Die approbierte gedruckte Originalversion dieser Dissertation ist an der TU Wien Bibliothek verfügbar.
The approved original version of this doctoral thesis is available in print at TU Wien Bibliothek.
TU Bibliothek WIEN Your knowledge hub

After successful creation of this file the AbinitioDΓA program can be compiled by simply executing

```
$ make
```

The compilation process automatically creates the subdirectory `bin` containing the executables `abinitiodga` and `setupvertex` (see Fig. 7).

3.2. Setting up a calculation

In this section we will illustrate the steps needed to perform an AbinitioDΓA calculation. The necessary input data, obtained from `w2dynamics` [47] and a Wannier90 Hamiltonian, is for this test case already included in the github repository (in the subfolder `srvo3-testdata`):

- `srvo3-1pg.hdf5` (`w2dynamics` DMFT output file)
- `srvo3-2pg.hdf5` (`w2dynamics` worm-sampling vertex output file)
- `srvo3_k20.hk` (`wien2wannier` Wannier Hamiltonian with 20x20x20 k-points)

The provided files contain only data within a reduced range of Matsubara frequencies (frequency box) to speed up the test calculation.

As mentioned in Section 2 we first have to symmetrize the spin-components of our vertex. Additionally, for the case of locally degenerate (equivalent) orbitals, also orbital-components can be symmetrized (option (o) below). This is done by executing the program `setupvertex` with the following user options:

```
$ cd srvo3-testdata
$ ../bin/setupvertex
Number of inequivalent atoms: 1
Vertex file: srvo3-2pg.hdf5
Number of correlated bands for inequivalent atom 1: 3
Outputfile for symmetrized Vertex: srvo3-2pg-symmetrized.hdf5

SU2 symmetry only (s) or SU2 AND orbital symmetry (o)?: o
```

This way, the symmetrized vertex has been saved under the specified file name `srvo3-2pg-symmetrized.hdf5`. Now all necessary input files are prepared and we are ready to use the main AbinitioDΓA program `abinitiodga`. For the latter we still need to setup a config file. For the sake of brevity in this section we use the provided config file listed in Appendix A.1 (which can also be found in `documentation/examples/config_example_eom`) and save it as `case.conf` (The configuration file will be explained in more detail in Section 4). The code can now be run by executing

```
$ mpirun -np $NCORES ../bin/abinitiodga case.conf
```

where `$NCORES` refers to the number of cores used. While running, the program writes runtime information into a log file called `out`. The output data instead is written into a custom HDF5 file. Depending on the run options the structure of the latter changes slightly. All possible output datasets are listed in detail in the provided `README.pdf`. The data of the HDF5 output file can be extracted via the h5py library in Python. We provide several scripts with a detailed documentation of all steps in `documenation/scripts`. The reference results (including prepared plot scripts) can be found in Appendix B.

Please note that the estimated run-time for the provided data is roughly 0.5s for each $\mathrm{q} = (\mathbf{q}, \omega)$ point. Thus the full self-energy calculation (8000 q-points $\times$ 61 ω-points) requires around 70 core hours [Intel Xeon E5-2650v2 (2.6 GHz, 16 cores per node)]. A calculation of static DMFT susceptibilities along the high-symmetry path instead (see Appendix A.2) requires just a few seconds (41 q-points $\times$ 1 ω-point).

3.3. $SrVO_3$ as test example

In this section we discuss the results of the previously set-up calculation for $SrVO_3$. The reduced range of Matsubara frequencies used in the previously set-up test calculation is too small to yield fully converged results. In the following sections we show the results calculated for much larger frequency box sized, and discuss their physical interpretation.

Our target material is a strongly correlated, metallic transition metal oxide with a cubic perovskite crystal structure whose low-energy physics is dominated by its degenerate vanadium t_{2g} states. Experimentally, several manifestations of electronic correlations have been observed in $SrVO_3$: photoemission spectroscopy [48] and specific heat measurements [49] find a mass enhancement of a factor of two compared to band-theory, the spectral function exhibits a satellite feature, i.e. a Hubbard band, below the quasiparticle peak [48,50,51], and at closer look a kink in the energy–momentum dispersion becomes visible [52–54]. Theoretically these phenomena have extensively been studied within various methods for strongly correlated electron systems. Indeed $SrVO_3$ has become a textbook example and testbed material in this field. Nonetheless, several physical aspects of this material are still under discussion and have recently been re-investigated with new, post-DMFT techniques. Calculations that include the dynamical nature of the screened Coulomb interaction suggest that a sizable part of the mass enhancement in $SrVO_3$ may originate from plasmon excitations [55–59]. Furthermore, screened exchange contributions to the self-energy – that are caused by non-local interactions $V^{\mathbf{q}}$ – have been shown to compete with the mass enhancement from dynamical correlations [58–60]. Besides this academic interest, $SrVO_3$ has potential for technological applications, e.g., as an electrode material [61], Mott transistor [62] or transparent conductor [63]. Hence, $SrVO_3$ is a suitable target material for illustrating the capabilities and usage of our new AbinitioDΓA algorithm.

Die approbierte gedruckte Originalversion dieser Dissertation ist an der TU Wien Bibliothek verfügbar.
The approved original version of this doctoral thesis is available in print at TU Wien Bibliothek.
TU Bibliothek WIEN Your knowledge hub

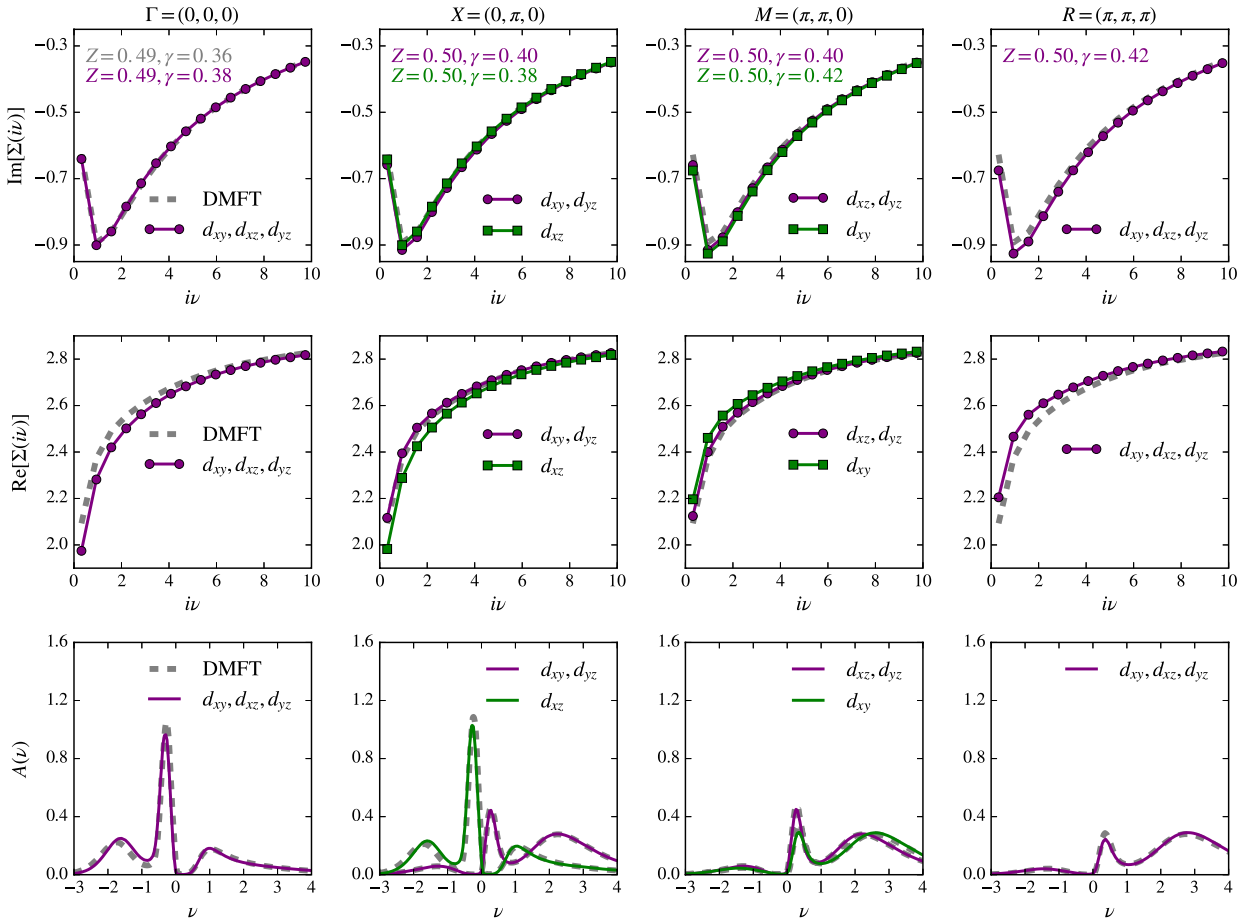

Fig. 5. AbinitioDΓA self-energies (top row: imaginary part, middle row: real part) and spectral functions (bottom row) for selected k-points in the Brillouin zone (Γ-point: first column, X-point: second column, M-point: third column, R-point: fourth column). In the two top panels, symbols indicate results for a small frequency box ($\#\omega/2 = 60$), while lines depict results for a large box ($\#\omega/2 = 200$): Congruence shows that the calculation is converged with respect to the number of frequencies . (For interpretation of the references to color in this figure legend, the reader is referred to the web version of this article.)

3.3.1. DFT+DMFT

For the present example case, the Wien2k program package [64,65] was used to perform the DFT computation, and the wien2wannier interface [66] and wannier90 [67] to construct the Wannier Hamiltonian $H_W^{\mathbf{k}}$. The subsequent DMFT calculation was done with w2dynamics [47,68,69] and its continuous-time quantum Monte Carlo (CTQMC) algorithm in the hybridization expansion (CT-HYB) [70–72]. The AbinitioDΓA program is adapted to the output formats of the described program packages. Let us mention here, however, that it is possible to reformat any DMFT code output to conform to the AbinitioDΓA input standards.

3.3.2. AbinitioDΓA self-energies

The results shown here, have been obtained [31] using only local Coulomb interactions in the Kanamori parametrization with $U = 5$ eV, $V = 3.5$ eV and $J = 0.75$ eV at an inverse temperature $\beta = 10$ eV^{-1}. The calculation was done on a k- and q-grid of $20 \times 20 \times 20$ points.

The AbinitioDΓA self-energies and corresponding spectral functions for four high-symmetry k-points are shown in Fig. 5. In the two top panels, the real and imaginary part of the self-energy are displayed in color (green and violet) while the momentum-independent DMFT self-energy is shown in gray. Beside its k-dependence, the AbinitioDΓA self-energy $\Sigma^{\mathbf{k}}_{mm'}$ is also orbital-dependent: Different colors (green and violet) in Fig. 5 refer to diagonal components Σ_{mm} of different orbitals $m = d_{xy}, d_{xz}, d_{yz}$. In general, also orbital-offdiagonal ($m \neq m'$) components of the self-energy can arise if allowed by symmetry. In this $SrVO_3$ example case however they are very small, so that we show only orbital-diagonal components. Please also note that due to the rather small non-local corrections to the self-energy no λ-correction [18,32] is needed in the AbinitioDΓA calculation for $SrVO_3$.

From a physical point of view, the top panel of Fig. 5 shows that at low energies the imaginary part of the self-energy on the Matsubara axis is – for all orbitals and k-points – very close to the DMFT result. As a result the scattering rate $\gamma = -\Im\Sigma(i\nu \to 0)$ and the quasi-particle weight $Z_{\mathbf{k}}$ do not depend significantly on the momentum, which is a quite common finding within post-DMFT methods [30,58,73–75]—at least in three spatial dimensions. The real-part of the self-energy instead shows larger deviations from the DMFT result. Indeed, at low energies the difference between AbinitioDΓA and DMFT reaches 200 meV.

The bottom panels of Fig. 5 show the AbinitioDΓA spectral functions. They were obtained by analytically continuing the Matsubara Green's function to the real-frequency axis, using the maximum entropy method [47,76,77]. As expected from the analysis of the self-energies, in the spectral functions we see signatures of reduced correlation effects compared to the DMFT results (in gray): the

Die approbierte gedruckte Originalversion dieser Dissertation ist an der TU Wien Bibliothek verfügbar.
The approved original version of this doctoral thesis is available in print at TU Wien Bibliothek.
TU Bibliothek WIEN Your knowledge hub

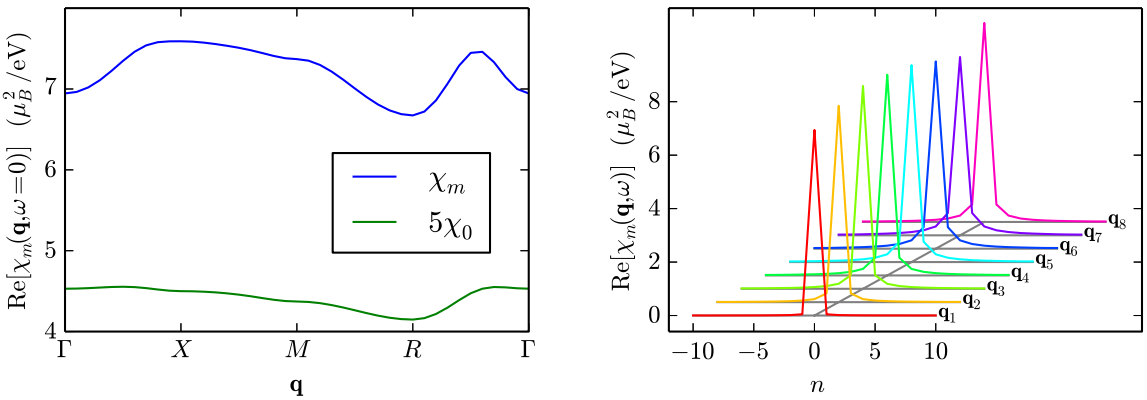

Fig. 6. Magnetic susceptibilities of $SrVO_3$. Left: real part of the magnetic susceptibility χ_m at zero frequency, along a q-path connecting high-symmetry points in momentum space. For comparison, we also show the particle-hole bubble, χ_0, scaled by a factor of 5. Right: real part of the dynamical magnetic susceptibility $\chi_m(i\omega_n)$ of Eq. (19) as a function of bosonic Matsubara frequencies $\omega_n = 2\pi n/\beta$ for 8 selected q-points: $\mathbf{q}_1 = (0,0,0)$, $\mathbf{q}_2 = (\pi/2,0,0)$, $\mathbf{q}_3 = (\pi,0,0)$, $\mathbf{q}_4 = (\pi, \pi/2,0)$, $\mathbf{q}_5 = (\pi, \pi,0)$, $\mathbf{q}_6 = (\pi, \pi, \pi/2)$, $\mathbf{q}_7 = (\pi, \pi, \pi)$, $\mathbf{q}_8 = (\pi/2, \pi/2, \pi/2)$. Please note that curves have been offset for better visibility.

quasi-particle peaks move very slightly away from the Fermi level while Hubbard bands are displaced towards it. For a more detailed discussion and physical interpretation of the results please refer to Ref. [31].

3.3.3. DMFT susceptibilities

Results for the *static* DMFT susceptibility of $SrVO_3$ are shown in the left panel of Fig. 6, summed over all orbital contributions ($\chi_r = 2\sum_{lm} \chi_{r,llmm}$). There is only a weak momentum-dependence of the magnetic susceptibility in the high-temperature paramagnetic phase of $SrVO_3$, but vertex corrections (susceptibilities beyond χ_0 of Eq. (4)) strongly enhance the susceptibility by a factor of seven.

Indeed only if vertex corrections are taken into account the susceptibility agrees with the experimental value [78,79]. For example, Ref. [78] reports $9.9\mu_B^2/\text{eV}^{-1}$ at 100 K and $8.7\mu_B^2/\text{eV}^{-1}$ at 300 K which, taken the temperature dependence into account, well agrees with our value of $\approx 7\mu_B^2/\text{eV}^{-1}$ at 1160 K (for the conversion of units note that $1\mu_B^2/\text{eV} = 3.2327 \times 10^{-5}$ emu/mol).

We are also able to produce the dynamical susceptibilities shown in the right panel of Fig. 6. These still need to be analytically continued to the physical (real frequency) dynamical susceptibilities. The susceptibilities on the Matsubara axis shown in Fig. 6 allow however for a better intercomparison and test case without the perils of analytical continuation, e.g., by the maximum entropy method.

4. Detailed user options

In this section we go into more detail regarding the program flow, run options and the effect of different parameters on the calculation (all from a user's point of view). The general program flow with its interfaces to other program packages is illustrated in Fig. 7.

4.1. DFT+DMFT input

The usual starting point of AbinitioDΓA is a converged DFT+DMFT calculation for the material under investigation. It provides the Wannier Hamiltonian $H_W^{\mathbf{k}}$ in the format of the current version of the `convham` program of Wien2k (version 18.2) and the local DMFT one-particle Green's function G^ν, self-energy Σ^ν and double counting Σ_{DC} as well as the chemical potential μ in an HDF5 file of the structure of the w2dynamics output format in its current version 1.0.0. For other DFT and DMFT programs this HDF5 file needs to be generated before using AbinitioDΓA

The local and non-local Coulomb interaction U and $V^{\mathbf{q}}$ can also be obtained *ab initio* by using the constrained random phase approximation (cRPA) [80,81].

The four-index U can either be stored in plain text file or be constructed directly by specifying the interaction parameters and interaction type in the config file of the main AbinitioDΓA program. The purely nonlocal interaction $V^{\mathbf{q}}$, on the other hand, is stored in a separate HDF5 file whose format is described in the file `README.pdf`.

After convergence of the DFT+DMFT cycle, the full DMFT two-particle Green's function $G^{(2)}$, or its connected part G^{con}, is computed. Since in a multi-orbital impurity the local interaction is usually not of density–density type, this requires a worm sampling technique [38,39].

Subsequently, the spin components of the two-particle Green's function are combined into the density (d) and magnetic (m) channel by using the program `setupvertex`, cf. Fig. 7.

4.2. Configuration file

The AbinitioDΓA program `abinitiodga` uses a free-format configuration file. A full documentation of the latter can be found in `documentation/configspec` and `documentation/README/README.pdf` in the code repository. Here we explain the most important parameters based on the config file corresponding to the example case in Section 3.3.

The config file is structured into several sections marked by square brackets. In the first section, the user needs to specify some general parameters:

Die approbierte gedruckte Originalversion dieser Dissertation ist an der TU Wien Bibliothek verfügbar.
The approved original version of this doctoral thesis is available in print at TU Wien Bibliothek.
TU Bibliothek WIEN Your knowledge hub

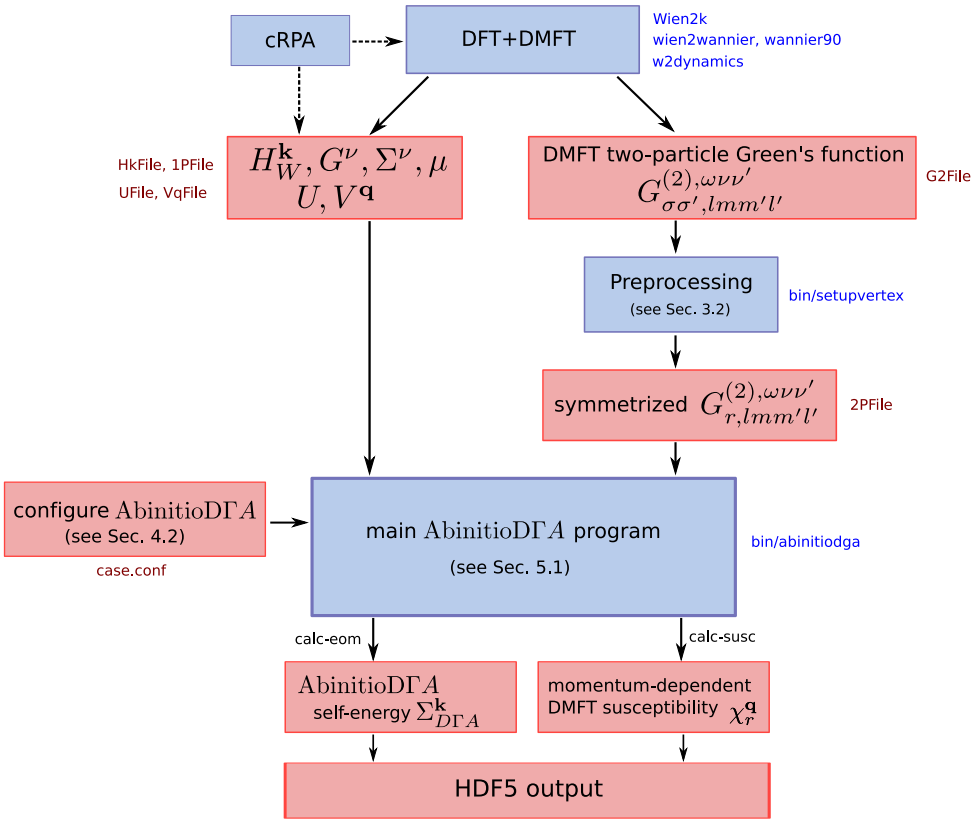

Fig. 7. Flow diagram of the AbinitioDΓA algorithm. Programs are indicated as blue boxes with the program names on the right. The input/output data files instead are indicated in red . (For interpretation of the references to color in this figure legend, the reader is referred to the web version of this article.)

```
[General]
calc-susc = T # calculate the momentum-dependent susceptibilities: (T)rue / (F)alse
calc-eom  = T # calculate the dga-selfenergy via the equation of motion: (T)rue / (F)alse

# number of positive f/b frequencies of the vertex
N4iwf = -1 # full box
N4iwb = -1 # full box

# Number of atoms
NAt = 1

# Wannier Hamiltonian
HkFile = srvo3_k20.hk

k-grid = 20 20 20 # Wannier Hamiltonian and eom momentum grid
q-grid = 20 20 20 # Grid for susc, and q-sum in eom
```

Here, we first specified that we want to calculate the DMFT susceptibility (`calc-susc`) and DΓA self-energies (`calc-eom`). The fermionic and bosonic frequency box sizes of the vertex are given by the parameters `N4iwf` and `N4iwb`. These two parameters can be used to check the convergence of the calculation with respect to the frequency box size: `N4iwf` $= -1$ employs the maximum frequency box (defined by the previous CT-QMC calculation), while one can also choose a smaller number of frequencies by explicitly setting, e.g., `N4iwf` $= 20$. The parameter `NAt` specifies the number of correlated atoms in the calculation and the Wannier Hamiltonian $H_W^{\mathbf{k}}$ in the reducible Brillouin zone (in the format of wien2wannier) is read from the file `HkFile`. `k-grid` specifies the number of k-points in each direction (the `k-grid` must coincide with the one of the Wannier Hamiltonian). `q-grid` instead controls the momentum grid convergence and only affects the self-energies due to the internal momentum sum (Please note that only an integer divisor for each direction is allowed, e.g., 4 5 10 in the case of a k-grid of 20 20 20).

Next, one needs to define, for each correlated atom `NAt`, the number of orbitals and the interaction type:

```
[Atoms]
[[1]]
Interaction = Kanamori # interaction type
Nd = 3 # number of d-orbitals
```

Die approbierte gedruckte Originalversion dieser Dissertation ist an der TU Wien Bibliothek verfügbar.
The approved original version of this doctoral thesis is available in print at TU Wien Bibliothek.
TU Bibliothek WIEN Your knowledge hub

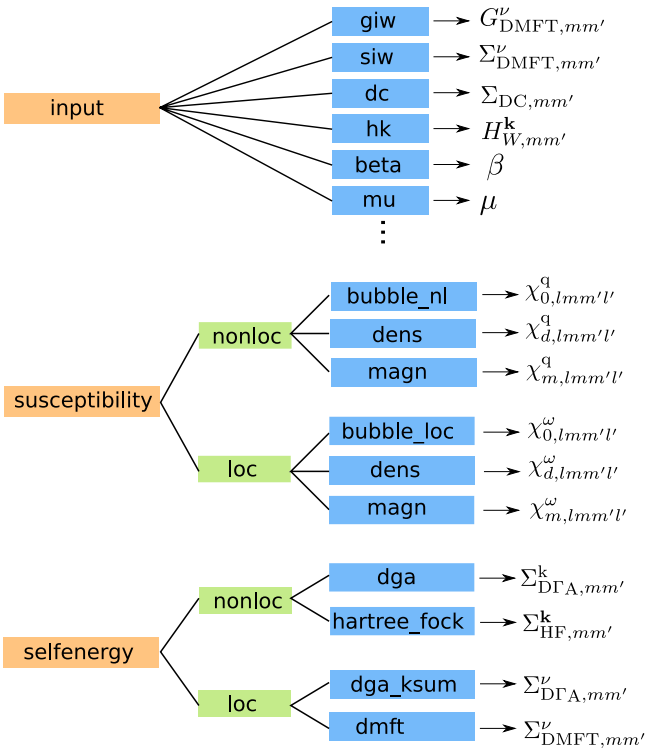

Fig. 8. Group structure of the AbinitioDΓA HDF5 output.

```
Np = 0 # number of p-orbitals
Udd = 5.0 # intra-orbital interaction
Vdd = 3.5 # inter-orbital interaction
Jdd = 0.75 # Hund's coupling
```

For this configuration, the program automatically generates a Kanamori interaction matrix with the given interaction parameters `Udd`, `Vdd` and `Jdd`. Alternatively, it is possible to provide a full four-index $U_{lm'ml'}$ in form of a plain text file `UFile` (examples are provided in `documentation/examples`). Besides the local interaction used in DMFT, a completely non-local interaction ($V^{\mathbf{q}}$, with $\sum_{\mathbf{q}} V^{\mathbf{q}} = 0$) can be specified in `VqFile`. The latter is a HDF5 file that contains only the non-zero spin–orbital components of $V^{\mathbf{q}}$ in the form of a lookup table.

Finally, we provide the one-particle data in the usual `w2dynamics` HDF5 output format. The two-particle data, on the other hand, uses a special HDF5 file format (described in Fig. 10) which is automatically generated by the program `setupvertex` described in Section 3.2.

```
[One-Particle]
# w2dynamics DMFT output file
1PFile = srvo3-1pg.hdf5

[Two-Particle]
# symmetrized vertex
2PFile = srvo3-2pg-symmetrized.hdf5
# legacy option
# 0: full two-particle Greens function, including disconnected parts
vertex-type = 0
```

4.3. Output

AbinitioDΓA uses HDF5 for its main output. The name of the output file is generated automatically and contains the time stamp of the start of the calculation in order to make its name unique and identifiable (example: `adga-20180904-022233.615-output.hdf5`).

At the top level, the file contains three groups (see Fig. 8):

1. `input` consists of several datasets, in which the DFT+DMFT input data (but not the two-particle Green's function) are stored. This is done merely for convenience, so as to simplify, e.g., comparisons of the DMFT self-energy (stored in `input/siw`) with the AbinitioDΓA self-energy.
2. `susceptibility` contains groups for both the local (`loc`) and non-local (`nonloc`) DMFT-susceptibility of Eqs. (13) and (16) in the density and magnetic channel.

Die approbierte gedruckte Originalversion dieser Dissertation ist an der TU Wien Bibliothek verfügbar.
The approved original version of this doctoral thesis is available in print at TU Wien Bibliothek.
TU Bibliothek WIEN Your knowledge hub

Table 1
Internal program flow of the AbinitioDΓA program. The first column lists, step-by-step, the instructions while the second and third columns show the corresponding functions and where to find them. An empty function name implicates that the task is performed in the main file (main.F90).

	function name	**file**
initialize MPI	mpi_initialize	mpi_org.F90
initialize HDF5 interface	init_h5	hdf5_module.f90
read & check config file	read_config	config_module.f90
	check_config	config_module.f90
read one-particle info	read_siw	hdf5_module.f90
	read_giw or create_giw	hdf5_module.f90
	...	
create interaction matrix U_{mlnh}	read_u or create_u	interaction_module.f90
calculate $n^{\mathbf{k}}$	get_nfock	one_particle_quant_module.f90
distribute MPI work load	mpi_distribute	mpi_org.F90
initialize HDF5 output file	init_h5_output	hdf5_module.f90
LOOP: bosonic frequency – $i\omega_n$		
calculate χ_0^{ω} (3)	get_chi0_loc	one_particle_quant_module.f90
read $i\omega_n$ slice of $G_r^{\mathrm{con}\ \omega\nu\nu'}$ (10)	read_vertex	hdf5_module.f90
calculate $\chi_0^{\omega} F_r^{\omega}$ (11)		
calculate γ_r^{ω} (7)		
calculate $\gamma_r^{\omega}\chi_0^{\omega}$ (13)	calc_chi_qw	susc_module.f90
calculate Σ^{DMFT} (for comparison)	calc_eom_dmft	eom_module.f90
LOOP: transferred momentum – q		
optional: read $V(\mathbf{q})$	read_vq	interaction_module.f90
calculate Σ^{HF} (6)	calc_eom_static	eom_module.f90
calculate χ_0^{q} (4)	accumulate_chi0	one_particle_quant_module.f90
calculate $\chi_0^{\mathrm{nl}} = \chi_0^{\mathrm{q}} - \chi_0^{\omega}$ (5)		
calculate $\gamma_r^{\omega}\chi_0^{\mathrm{nl}}$ (13)	calc_chi_qw	susc_module.f90
calculate γ_r^{q} (8)		
calculate η_r^{q} (9)		
calculate $\eta_r^{\mathrm{q}}\chi_0^{\mathrm{q}}$ (13)	calc_chi_qw	susc_module.f90
calculate $\Sigma^{\mathrm{D\Gamma A}}$ (1)	calc_eom_dynamic	eom_module.f90
gather (and/or sum) data from MPI processes		
output data to HDF5 output file	output_eom	hdf5_module.f90
	output_chi_loc	hdf5_module.f90
	output_chi_qw	hdf5_module.f90
	...	

3. `selfenergy` contains the AbinitioDΓA self-energy $\Sigma^{\mathrm{k}}_{\mathrm{D\Gamma A}}$ of Eq. (1) in the subgroup `nonloc/dga`. However, the latter does not contain the non-local Hartree–Fock term $\Sigma^{\mathbf{k}}_{\mathrm{HF}}$ of Eq. (6) which is stored separately in `nonloc/hartree_fock`. The subgroup `loc/dga_ksum` contains the local (**k**-summed) AbinitioDΓA self-energy $\Sigma^{\nu}_{\mathrm{D\Gamma A}} = \sum_{\mathbf{k}} \Sigma^{\mathrm{k}}_{\mathrm{D\Gamma A}}$. Furthermore, `loc/dmft` contains the DMFT self-energy obtained through the local version of the equation of motion, i.e. $\Sigma^{\nu}_{\mathrm{DMFT}} = -\beta^{-1}\sum_{\omega} U\gamma_d^{\omega\nu} G^{\boldsymbol{\nu}-\boldsymbol{\omega}} + \Sigma^{U}_{\mathrm{HF}}$ (with the local Hartree–Fock term Σ^{U}_{HF} included). Up to statistical fluctuations, the latter coincides with the 'original' DMFT self-energy stored in `input/siw`. A cross-check of `input/siw` with `selfenergy/loc/dmft` is always recommended.

The file `README.pdf` in the code repository contains a complete listing of all groups and datasets of the output file. Most conveniently they can be accessed and plotted in python by `h5py` and the `matplotlib`. Exemplary python scripts are provided in `documentation/scripts`.

5. Program structure and algorithmic details

In this section we are going to switch from the user's to the developer's point of view. We are first going to introduce the internal program flow in Section 5.1 and then go into detail about the internal storage layout and the resulting characteristics of the matrix operations in Section 5.2.

5.1. Program structure

The program is set up in three distinct steps shown in Table 1. First we initialize all the necessary interfaces and read in (or calculate) all the necessary variables which are needed throughout the program. After initializing the MPI and HDF5 interface we read and check the config file (described in detail in Section 4). Here we check for inconsistencies in the provided data and the provided run-options. If no errors are detected we read in the data necessary for the construction of the Green's function $G^{\mathrm{k}}_{hh'}$ (2) and the interaction matrix U_{mlnh}. At the end of this first step the work load is distributed to all the MPI processes (if compiled with MPI) and we can initialize the HDF5 output file.

In the second step we perform the two computationally heavy main loops (bosonic frequency $i\omega_n$ and transferred momentum **q**) where we calculate, step-by-step, the objects which are required for the momentum-dependent susceptibilities $\chi^{\mathrm{q}}_{r,lmm'l'}$ (13) and the DΓA self-energy $\Sigma^{\mathrm{k}}_{\substack{\mathrm{D\Gamma A}\\ mm'}}$ (1). Thirdly, we gather all the data, perform all necessary sums and write it to the HDF5 output file.

Die approbierte gedruckte Originalversion dieser Dissertation ist an der TU Wien Bibliothek verfügbar.
The approved original version of this doctoral thesis is available in print at TU Wien Bibliothek.
TU Bibliothek WIEN Your knowledge hub

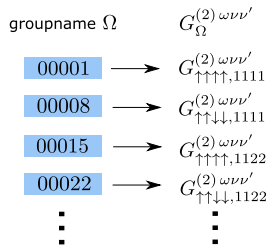

Fig. 9. Structure of the `G2File`, which contains the two-particle impurity Green's function $G^{(2)}$. Each group – named by the combined index Ω – contains the corresponding non-zero spin–orbital component of $G^{(2)}$. Shown are the first four groups in the $SrVO_3$ example file. Note that many spin–orbital combinations do not exist and are hence not stored, e.g., $\Omega = 2$ which corresponds to $G^{(2)\,\omega\nu\nu'}_{\uparrow\uparrow\uparrow\downarrow,1111}$.

5.2. Algorithmic details

5.2.1. Storage of the DMFT two-particle Green's function

The DMFT two-particle Green's function $G^{(2)}$, which can be measured in CT-HYB, is a very large quantity and needs a lot of storage capacity. In its most general form $G^{(2)}$ has four orbital indices $lmm'l'$ and four spin indices $\sigma_1\sigma_2\sigma_3\sigma_4$, and it depends on three Matsubara frequencies $\omega\nu\nu'$: $G^{(2)\,\omega\nu\nu'}_{\sigma_1\sigma_2\sigma_3\sigma_4,lmm'l'}$. However, the orbital and spin degrees of freedom are restricted by the symmetries of the local DMFT impurity problem. The Kanamori parametrization of interactions allows only for orbital combinations with pairwise identical orbitals: ($iijj$, $ijij$, $ijji$). Furthermore, in the SU(2)-symmetric and paramagnetic case, also the spin degrees of freedom are reduced. Hence, many spin–orbital components of $G^{(2)\,\omega\nu\nu'}_{\sigma_1\sigma_2\sigma_3\sigma_4,lmm'l'}$ are actually zero. Thus, the amount of storage for $G^{(2)}$ can be massively reduced by storing only its non-zero spin–orbital components in the file `G2File` (see Fig. 7). This reduces the required storage space by a factor of $\frac{[2(\#o)]^4}{6[3(\#o)^2-2(\#o)]} \approx 10$ for the example calculation in Section 3.3.

Group structure of the `g2file`. The non-zero spin–orbital components of $G^{(2)}$ are stored in the HDF5 file `G2File` in the form of a "lookup-table". This means that the band and spin indices of $G^{(2)\,\omega\nu\nu'}_{\sigma_1\sigma_2\sigma_3\sigma_4,lmm'l'}$ are translated into a single index Ω through a unique transformation:

$$\sigma_1\sigma_2\sigma_3\sigma_4,\, lmm'l' \leftrightarrow \Omega. \tag{21}$$

The index Ω is then used to store the non-zero spin–orbital components of $G^{(2)}$ in `G2file`. That is, the index Ω is the name of the groups in `G2File` containing the corresponding non-zero spin–orbital component of $G^{(2)}$. Thus, `G2File` contains as many groups as there are non-zero spin–orbital components in $G^{(2)}$. For example, for $SrVO_3$ in a paramagnetic t_{2g} setup the structure of the `G2File` is shown in Fig. 9. The number of non-zero elements in $G^{(2)}$ depends, in particular, on the type of interactions used. There is an increasing number of elements from density–density to Kanamori to full Coulomb interaction.

Group structure of the `2PFile`. The preprocessing program `setupvertex` symmetrizes the two-particle Green's function stored in `G2File` and transforms it into the density and magnetic channel $r \in \{d, m\}$ (see Section 3.2). The symmetrized $G^{(2)}_r$ is then written into the file `2PFile` (see Fig. 7 and Appendix A). The group structure of the latter is shown in Fig. 10. The file contains groups for inequivalent atoms, and subsequent groups for the density and the magnetic channel. As the AbinitioDΓA algorithm is parallelized over the bosonic Matsubara frequency, the data is further split in subgroups for each ω, allowing for an improved read-in of a given bosonic frequency slice of $G^{(2)}_r$ (see Table 1). Each bosonic frequency group finally contains subgroups with the non-zero orbital components of $G^{(2)\,\nu\nu'}_{r,lmm'l'}$. These orbital subgroups are labeled by the combined orbital index Ω_b. The latter is defined through a similar index transformation as in Eq. (21), but involving only the four orbital indices, i.e.,

$$lmm'l' \leftrightarrow \Omega_b. \tag{22}$$

Due to the mapping of six spin components into the two channels, the size of the `2PFile` is only about one third of the initial `G2File`.

5.2.2. Compound indices and matrix operations

In order to efficiently perform the orbital and frequency summations, we introduce compound indices so as to write the equations presented in Section 2 as matrix operations. The compound indices are obtained by transforming the four orbital and two fermionic frequency indices, e.g., of $F^{\omega\nu\nu'}_{lmm'l'}$, into two compound indices: the two left orbital indices lm and the left fermionic frequency index ν are combined into one compound index $\{ml, \nu\}$, while the two right orbital indices $m'l'$ and the right fermionic frequency index ν' form the second compound index $\{m'l', \nu'\}$.[1] This way, $F^{\omega\nu\nu'}_{lmm'l'}$ can be written in matrix form, $F^{\omega}_{\{ml,\nu'\}\{m'l',\nu\}}$, as illustrated in Fig. 11. Please note that in the local $F^{\omega\nu\nu'}_{lmm'l'}$ many matrix elements are zero, since the Kanamori interaction allows only for entries with pairwise matching orbitals. These zero matrix elements are exactly the orbital components not present in `2PFile`. However, in order to perform straightforward matrix operations, one needs to work with the whole matrix including all zero elements. Please note however that, despite this general implementation, due to the spin diagonalization into the density and magnetic channel a SU(2) symmetric interaction is still required.

Similar to the local, full vertex function $F^{\omega\nu'\nu}$, also the bubble terms $\chi_0^{ml,\mathrm{q}\nu\nu}$, $\chi_0^{\mathrm{q}\nu\nu}$ and $\chi_0^{\omega\nu\nu}$ can be written in matrix form with respect to the compound indices $\{ml, \nu\}$ and $\{m'l', \nu'\}$, as visualized in Fig. 12. Since the bubble terms are diagonal with respect to the fermionic frequency indices $\chi_0^{\nu\nu'} = \chi_0^{\nu\nu}\delta_{\nu\nu'}$, they have a block-diagonal structure in the compound basis.

[1] Note that the bosonic frequency ω does not enter the compound index; in fact, the AbinitioDΓA program is parallelized over the "external" index $\mathrm{q} = (\mathbf{q}, \omega)$.

Die approbierte gedruckte Originalversion dieser Dissertation ist an der TU Wien Bibliothek verfügbar.
The approved original version of this doctoral thesis is available in print at TU Wien Bibliothek.
TU Bibliothek Your knowledge hub WIEN

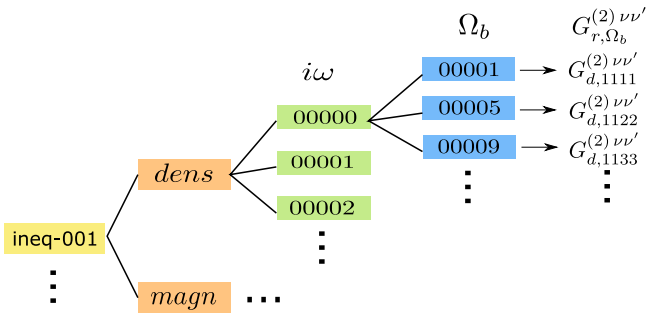

Fig. 10. Group structure of the `2PFile`, which contains the SU(2)- and orbital-symmetrized $G^{(2)}$ in the density and magnetic channel. $i\omega$ refers to the bosonic frequency index, while Ω_b is a combined index of the four orbital indices $lmm'l'$. Shown are the first few entries in the $SrVO_3$ file (three orbitals, Kanamori interaction).

$$
F^{\nu\nu'}_{lmm'l'} = \begin{array}{c|c}
 & \{m'l',\nu'\} \\
 & \begin{array}{cccccccccc} 11,\nu'_1 & 21,\nu'_1 & 12,\nu'_1 & 22,\nu'_1 & 11,\nu'_2 & 21,\nu'_2 & 12,\nu'_2 & 22,\nu'_2 & \cdots \end{array} \\
\{ml,\nu\} \begin{array}{c} 11,\nu_1 \\ 21,\nu_1 \\ 12,\nu_1 \\ 22,\nu_1 \\ 11,\nu_2 \\ 21,\nu_2 \\ 12,\nu_2 \\ 22,\nu_2 \\ \vdots \end{array} &
\left(\begin{array}{cccccccccc}
F^{\nu_1\nu'_1}_{1111} & F^{\nu_1\nu'_1}_{1121} & F^{\nu_1\nu'_1}_{1112} & F^{\nu_1\nu'_1}_{1122} & & & & & \\
F^{\nu_1\nu'_1}_{1211} & F^{\nu_1\nu'_1}_{1221} & F^{\nu_1\nu'_1}_{1212} & F^{\nu_1\nu'_1}_{1222} & & & \cdots & & \\
F^{\nu_1\nu'_1}_{2111} & F^{\nu_1\nu'_1}_{2121} & F^{\nu_1\nu'_1}_{2112} & F^{\nu_1\nu'_1}_{2122} & & & & & \\
F^{\nu_1\nu'_1}_{2211} & F^{\nu_1\nu'_1}_{2221} & F^{\nu_1\nu'_1}_{2212} & F^{\nu_1\nu'_1}_{2222} & & & & & \\
 & & & & F^{\nu_2\nu'_2}_{1111} & & & & \\
 & & \vdots & & & \ddots & & & \\
 & & & & & & & &
\end{array}\right)
\end{array}
$$

Fig. 11. By using compound indices $\{ml,\nu\}$ and $\{m'l',\nu'\}$, $F^{\omega\nu\nu'}_{lmm'l'}$ can be written in matrix form (in the graphics, the "external" bosonic frequency ω has been omitted for simplicity). Explicitly shown is the first orbital block ($\nu = \nu_1$, $\nu' = \nu'_1$) for the case of two orbitals. Please note that many entries are zero if density–density or Kanamori interactions are employed, e.g., $F^{\nu_1\nu'_1}_{1121} = 0$ and $F^{\nu_1\nu'_1}_{1112} = 0$.

$$
\chi^{\nu\nu'}_{0,lmm'l'} = \begin{array}{c|c}
 & \{m'l',\nu'\} \\
 & \begin{array}{cccccccccc} 11,\nu'_1 & 21,\nu'_1 & 12,\nu'_1 & 22,\nu'_1 & 11,\nu'_2 & 21,\nu'_2 & 12,\nu'_2 & 22,\nu'_2 & \cdots \end{array} \\
\{ml,\nu\} \begin{array}{c} 11,\nu_1 \\ 21,\nu_1 \\ 12,\nu_1 \\ 22,\nu_1 \\ 11,\nu_2 \\ 21,\nu_2 \\ 12,\nu_2 \\ 22,\nu_2 \\ \vdots \end{array} &
\left(\begin{array}{cccccccccc}
\chi^{\nu_1\nu'_1}_{0,1111} & \chi^{\nu_1\nu'_1}_{0,1121} & \chi^{\nu_1\nu'_1}_{0,1112} & \chi^{\nu_1\nu'_1}_{0,1122} & & & & & \\
\chi^{\nu_1\nu'_1}_{0,1211} & \chi^{\nu_1\nu'_1}_{0,1221} & \chi^{\nu_1\nu'_1}_{0,1212} & \chi^{\nu_1\nu'_1}_{0,1222} & & & 0 & & \\
\chi^{\nu_1\nu'_1}_{0,2111} & \chi^{\nu_1\nu'_1}_{0,2121} & \chi^{\nu_1\nu'_1}_{0,2112} & \chi^{\nu_1\nu'_1}_{0,2122} & & & & & \\
\chi^{\nu_1\nu'_1}_{0,2211} & \chi^{\nu_1\nu'_1}_{0,2221} & \chi^{\nu_1\nu'_1}_{0,2212} & \chi^{\nu_1\nu'_1}_{0,2222} & & & & & \\
 & & & & \chi^{\nu_2\nu'_2}_{0,1111} & \chi^{\nu_2\nu'_2}_{0,1121} & \chi^{\nu_2\nu'_2}_{0,1112} & \chi^{\nu_2\nu'_2}_{0,1122} & \\
 & & 0 & & \chi^{\nu_2\nu'_2}_{0,1211} & \chi^{\nu_2\nu'_2}_{0,1221} & \chi^{\nu_2\nu'_2}_{0,1212} & \chi^{\nu_2\nu'_2}_{0,1222} & \\
 & & & & \chi^{\nu_2\nu'_2}_{0,2111} & \chi^{\nu_2\nu'_2}_{0,2121} & \chi^{\nu_2\nu'_2}_{0,2112} & \chi^{\nu_2\nu'_2}_{0,2122} & \\
 & & & & \chi^{\nu_2\nu'_2}_{0,2211} & \chi^{\nu_2\nu'_2}_{0,2221} & \chi^{\nu_2\nu'_2}_{0,2212} & \chi^{\nu_2\nu'_2}_{0,2222} & \\
 & & & & & & & & \ddots
\end{array}\right)
\end{array}
$$

Fig. 12. Matrix structure of the bubble terms $\chi^{nl,\mathrm{q}\nu\nu}_{0,lmm'l'}$, $\chi^{\mathrm{q}\nu\nu}_{0,lmm'l'}$ and $\chi^{\omega\nu\nu}_{0,lmml}$ (in the graphics, the "external" bosonic index $\mathrm{q} = (\mathbf{q},\omega)$ has been omitted). Shown are the first two "orbital blocks" (in orange). The block-diagonal structure arises from the fact that the bubble terms are diagonal with respect to the fermionic frequency $\delta_{\nu\nu'}$. Here, the full structure is only shown for clarity, the main AbinitioDΓA program stores and works only with the non-zero orbital blocks . (For interpretation of the references to color in this figure legend, the reader is referred to the web version of this article.)

Simplified matrix operations. The computation of the three-leg vertices γ^{q} and η^{q} in Eqs. (8) and (12) involves a multiplication of $\chi_0^{nl,\mathrm{q}}$ with F^{ω}. This matrix multiplication can be simplified by exploiting the block-diagonal structure of $\chi_0^{nl,\mathrm{q}}$. In fact, by multiplying each

Die approbierte gedruckte Originalversion dieser Dissertation ist an der TU Wien Bibliothek verfügbar.
The approved original version of this doctoral thesis is available in print at TU Wien Bibliothek.
TU Bibliothek WIEN Your knowledge hub

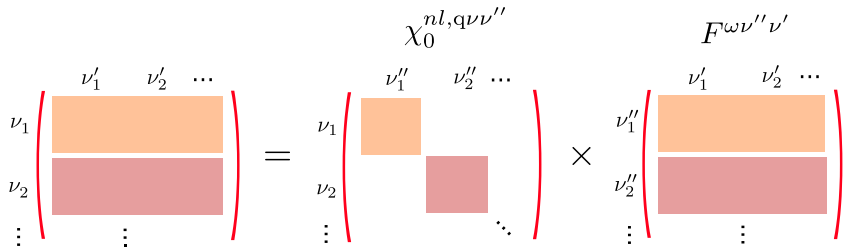

Fig. 13. The matrix multiplication of the block-diagonal $\chi_{0,lmm'l'}^{nl,\mathrm{q}\nu\nu}$ with the full $F_{r,lmm'l'}^{\omega\nu\nu'}$ in Eqs. (8) and (12) can be split into several smaller operations. By multiplying each orbital block of $\chi_{0,lmm'l'}^{nl,\mathrm{q}\nu\nu}$ with the corresponding slice of $F_{r,lmm'l'}^{\omega\nu\nu'}$ (marked with the same color), multiplications with entries that are zero by construction can be avoided . (For interpretation of the references to color in this figure legend, the reader is referred to the web version of this article.)

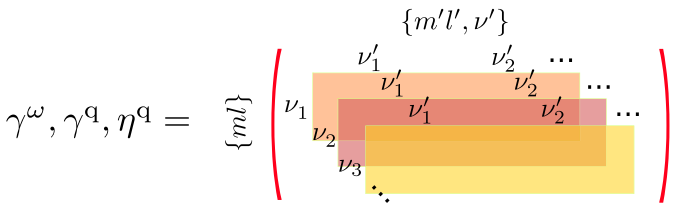

Fig. 14. Schematic representation of the sum over the left fermionic frequency needed to obtain the three-leg vertices γ^ω, γ^q and η^q in Eqs. (7)–(12). By summing over all stacked slices (different colors symbolize different left fermionic frequencies ν_i), the first dimension of the matrix is reduced to the orbital-only compound index $\{lm\}$. (For interpretation of the references to color in this figure legend, the reader is referred to the web version of this article.)

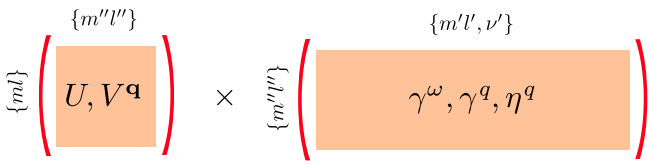

Fig. 15. Schematic representation of the matrix multiplication between the interaction matrices U and $V^\mathbf{q}$ and the three-leg vertices γ_r^ω, γ_r^q and η_r^q. This operation is part of the Schwinger–Dyson equation of motion (1).

orbital block of $\chi_0^{nl,\mathrm{q}}$ with the corresponding horizontal slice of F^ω, as shown in Fig. 13, one can avoid multiplications involving entries that are zero by construction.

The matrix inversion in the equation for η^q, Eq. (12), instead cannot make use of a block-diagonal structure so that the inversion of the full matrix is needed. From a numerical point of view, this matrix inversion is one of the most demanding operations in the main AbinitioDΓA program.

The calculation of the three-leg vertices in Eqs. (7)–(12) furthermore requires a sum over the left fermionic frequency. The summation over this left fermionic frequency makes them, diagrammatically, *three-leg* (electron-boson) vertices. In terms of compound matrices, this sum over the left fermionic frequency is visualized in Fig. 14. Through the sum, the left compound index is reduced to an orbital compound index $\{lm\}$ and the resulting matrix is not quadratic any more. Please note that this summation over the left fermionic frequency needs to be performed explicitly only in order to obtain γ^q and γ^ω.[2] The three-leg structure of η^q is actually obtained in a different way, namely by multiplying with $(\vec{\mathbf{1}} + \gamma^\omega)$ from the left, as can be seen in Eq. (12).

In the equation of motion (1), the three-leg vertices γ_r^ω, γ_r^q and η_r^q are multiplied with the corresponding local and non-local Coulomb interaction terms (U, $\tilde{U}$ and $V^\mathbf{q}$). In order to perform this operation in the basis of compound indices, the four-index $U_{lmm'l'}$ and $V_{lmm'l'}^\mathbf{q}$ are transformed to compound indices $\{ml\}$ and $\{m'l'\}$. Then, the multiplication of $V^\mathbf{q}$ and U times the three-leg γ's and η can be performed easily, as schematically depicted in Fig. 15. The final convolution with the non-local Green's function $G^{\mathrm{k}-\mathrm{q}}$ in the equation of motion (1) instead is more straightforward to perform by breaking up the compound indices into single orbital and frequency indices.

5.2.3. Numerical effort

Often the numerical effort for calculating the local vertex in CT-HYB is the computationally most demanding task of an AbinitioDΓA calculation. The calculation of the vertex scales as $\beta^5(\#o)^4$ with a large prefactor because of the Monte-Carlo sampling (let us remind the reader that $\#o$ is the number of orbitals and $\#\omega \sim \beta$ the number of Matsubara frequencies). This scaling can be understood from the fact that we need to calculate $(\#\omega)^3(\#o)^4$ different components of the local vertex, and the update of the CT-HYB hybridization matrix requires $\sim \beta^2$ operations because the mean expansion order and hybridization matrix dimension is $\sim \beta$. Since we eventually calculate the self-energy with only one frequency and two orbitals, a higher noise level can be tolerated if $\#\omega$ and $\#o$ are large. Hence, in practice a weaker dependence on $\#\omega$ and $\#o$ is possible. Calculating the vertex for $SrVO_3$ with $\#o = 3$, $\#\omega = 120$ and $\beta = 10\ \mathrm{eV}^{-1}$ took 150000 core hours on an Intel Xeon E5-2650v2 (2.6 GHz, 16 cores per node). One can also employ the asymptotic form [37,82,83] of the vertex for large frequencies. This asymptotic part depends on only two frequencies and thus scales as $\beta^4(\#o)^4$. This way the full

[2] If the purely local three-leg vertex γ^ω is directly computed in CT-HYB, the current sum over the left fermionic frequency to obtain γ^ω is redundant.

Die approbierte gedruckte Originalversion dieser Dissertation ist an der TU Wien Bibliothek verfügbar.
The approved original version of this doctoral thesis is available in print at TU Wien Bibliothek.
TU Bibliothek Your knowledge hub WIEN

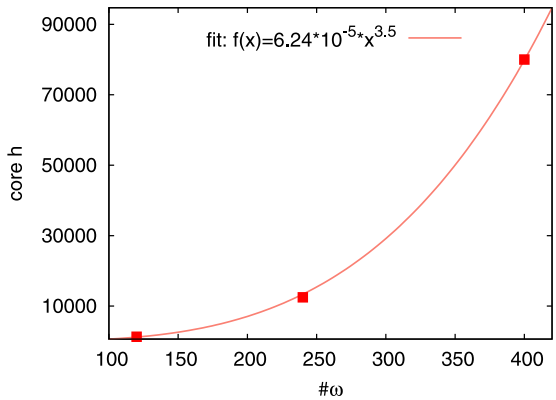

Fig. 16. Computational effort of the AbinitioDΓA program with respect to the number of involved Matsubara frequencies $\#\omega$.

CT-QMC calculation of the three-frequency vertex can be restricted to a small frequency box, and room temperature calculations are feasible.

Let us now turn to the main AbinitioDΓA program itself which is parallelized over the compound index $\mathrm{q} = (\mathbf{q}, \omega)$. This parallelization gives us a factor $\#q\ \#\omega$ for the numerical effort ($\#q$: number of $\mathbf{q}$-points). For each q-point, the numerically most costly task is the matrix inversion in Eq. (12). The dimension $\mathcal{N}$ of the matrix that needs to be inverted is $\mathcal{N} = \#\omega(\#o)^2$. While simple matrix inversions scale as $\mathcal{N}^3$ more efficient ones scale roughly as $\mathcal{N}^{2.5}$.[3] Hence, the overall effort is $\sim \#q\#\omega^{3.5}\#o^5$. The numerical effort for calculating the self-energy via the equation of motion (1), on the other hand, is $\sim \#q^2\#\omega^2\#o^6$ and only becomes the leading contribution at high temperatures and for a large number of q-points.

For the AbinitioDΓA computation of $SrVO_3$ with $\#o = 3$ and $\#q = 20^3$, the numerical effort with respect to the number of Matsubara frequencies $\#\omega$ has explicitly been tested by performing computations with three different frequency box sizes: $\#\omega = 120$, $\#\omega = 240$ and $\#\omega = 400$. Fig. 16 shows the respective numerical effort in core hours From Fig. 16 it can be seen that the main AbinitioDΓA program indeed roughly scales with $(\#\omega)^{3.5}$.

6. Conclusion and outlook

In this paper we have outlined the structure of the AbinitioDΓA program package and provided information on how to use it. While the numerical effort is considerably larger than for state-of-the-art DFT+DMFT calculations, our code makes realistic multi-orbital post-DMFT studies feasible. We expect AbinitioDΓA calculations to provide valuable insight into the physics of non-local correlations in strongly correlated materials. Besides studying, e.g., the nature of non-local spin-fluctuations, our methodology also allows to systematically assess the error made in DFT+DMFT calculations.

Approximations. Let us, at this point, reflect on the approximations involved in AbinitioDΓA. As a matter of course, any method aiming at an *ab initio* calculation of materials, requires approximations. First of all, there is the DΓA approximation which assumes the irreducible two-particle vertex to be local. In a more complete variant, this is the local two-particle fully irreducible vertex Λ and the parquet equations are employed to calculate the non-local full vertex and self-energy in parquet DΓA [82,84]. This approach is numerically too involved for realistic multi-orbital calculations. Instead AbinitioDΓA uses the Bethe–Salpeter ladder diagrams in both, the particle hole and transversal particle-hole channel, starting with the local irreducible vertex Γ in the respective channel (eventually the Bethe–Salpeter equations are reformulated in terms of the local full vertex F). That is, the particle–particle channel and with it superconducting fluctuations and weak localization effects are neglected, as is the feedback between the two particle-hole channels beyond the local level.

Second, while AbinitioDΓA includes all the DMFT diagrams, all the *GW* diagrams if the non-local Coulomb interaction is included in the AbinitioDΓA starting vertex Γ, as well as non-local spin fluctuations and further diagrams, we still need to supplement AbinitioDΓA with *GW* or DFT outside a low energy window of $\sim$ 10 orbitals. This bears the danger of a possible overscreening of the Coulomb interaction in the constrained random phase approximation as calculations for simple models suggest [85]. Further, so far only a non-local V^q is foreseen, not the k- and k'-dependence thereof (which would result in considerably more involved Bethe–Salpeter equations).

Third, if non-local correlations become truly large, actually two self-consistencies are needed: (i) the self-consistent calculation of the Green function lines connecting the vertex blocks and (ii) the self-consistent recalculation of the irreducible vertex. We plan these self-consistencies as additional scripts outside the core AbinitioDΓA code introduced in the present paper, in future versions of the code. A prospective alternative to mimic these self-consistencies is the so-called λ correction [18,32] or a $\mathcal{U}_\omega$ [86] correction, but for multi-orbital calculations this becomes cumbersome since many λ or $\mathcal{U}_\omega$ parameters need to be adjusted.

Outlook. Materials calculations with diagrammatic extensions of DMFT are just at the beginning. We believe that our code will contribute turning this route into a thriving research field, similar to what DFT+DMFT is today. We hope to foster this development by releasing the AbinitioDΓA program package under the terms of the GNU General Public License version 3.

[3] The matrix inversion in Eq. (12) is performed by using the `lapack` routines `zgetrf` and `zgetri`, which compute the inverse of a matrix by triangular decomposition.

Die approbierte gedruckte Originalversion dieser Dissertation ist an der TU Wien Bibliothek verfügbar.
The approved original version of this doctoral thesis is available in print at TU Wien Bibliothek.
TU Bibliothek WIEN Your knowledge hub

Acknowledgments

We are deeply indebted to Patrik Gunacker for furthering the w2dynamics code to calculate multi-orbital vertices, for fruitful discussions and the cooperation within the $SrVO_3$ project. This work has been financially supported by the European Research Council (ERC) under the European Union's Seventh Framework Program (FP/2007-2013) through ERC Grant Agreement No. 306447. Calculations have been done on the Vienna Scientific Cluster (VSC).

Appendix A. Exemplary config files

A.1. Config file for a self-energy calculation

In the following we show the config file, as used in the main text. Here we calculate both the self-energies (`calc-eom = T`) and the susceptibilities (`calc-susc = T`) on the largest possible momentum grid and the frequency box. The interaction is defined by providing Kanamori parameters (`Udd`, `Vdd` and `Jdd`).

```
[General]
calc-susc = T # calculate the momentum-dependent susceptibilities
calc-eom  = T # calculate the dga-selfenergy via the equation of motion

# number of positive f/b frequencies used from the vertex
N4iwf = -1 # full box
N4iwb = -1 # full box

NAt = 1 # Number of atoms

HkFile = srvo3_k20.hk # Wannier Hamiltonian

k-grid = 20 20 20 # Wannier Hamiltonian and eom momentum grid
q-grid = 20 20 20 # Grid for susc, and q-sum in eom

[Atoms]
[[1]]
Interaction = Kanamori # interaction type
Nd = 3 # number of d-bands
Np = 0 # number of p-bands
Udd = 5.0 # intra-orbital interaction
Vdd = 3.5 # inter-orbital interaction
Jdd = 0.75 # Hund's coupling

[One-Particle]
1PFile = srvo3-1pg.hdf5 # DMFT 1PG
orb-sym = T

[Two-Particle]
2PFile = srvo3-2pg-symmetrized.hdf5 # symmetrized vertex
vertex-type = 0
```

A.2. Config file for a susceptibility calculation

If one is only interested in susceptibilities, there are a few ways to save computational time. Since in this case it is not necessary to compute the equation of motion (which requires a momentum sum and a bosonic frequency sum (see Eq. (1)), the user has the freedom to reduce the number of bosonic frequencies ω and momenta $\mathbf{q}$.

In the following we show an example config file that contains the settings for calculating static susceptibilities on certain user-specified $\mathbf{q}$-points.

```
[General]
calc-susc = T # calculate the momentum-dependent susceptibilities
calc-eom  = F # calculate the dga-selfenergy via the equation of motion

# number of positive f/b frequencies used from the vertex
N4iwf = -1 # full fermionic box
N4iwb =  0 # only iwn = 0

NAt = 1 # Number of atoms
```

Die approbierte gedruckte Originalversion dieser Dissertation ist an der TU Wien Bibliothek verfügbar.
The approved original version of this doctoral thesis is available in print at TU Wien Bibliothek.
TU Bibliothek WIEN Your knowledge hub

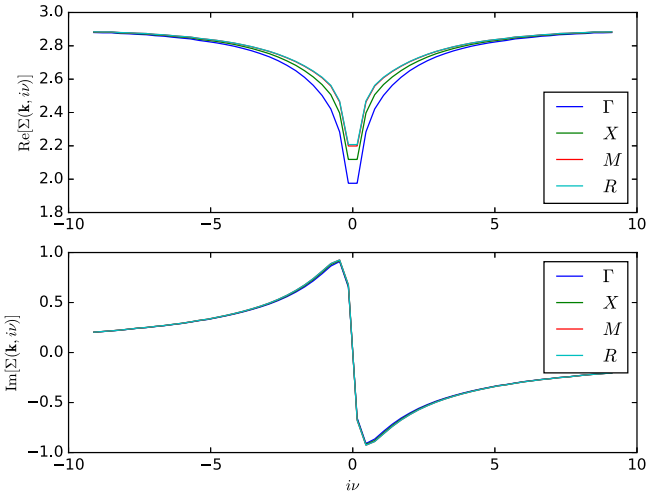

Fig. B.17. Self energy for a q-qrid calculation evaluated at the high-symmetry points Γ, X, M and R. The plot script can be found in documentation/scripts/1D_plot_selfenergy.py.

```
HkFile = srvo3_k20.hk # Wannier Hamiltonian

k-grid = 20 20 20 # Wannier Hamiltonian momentum grid
QDataFile = qpath

[Atoms]
[[1]]
Interaction = Kanamori # interaction type
Nd = 3 # number of d-bands
Np = 0 # number of p-bands
Udd = 5.0 # intra-orbital interaction
Vdd = 3.5 # inter-orbital interaction
Jdd = 0.75 # Hund's coupling

[One-Particle]
1PFile = srvo3-1pg.hdf5 # DMFT 1PG
orb-sym = T

[Two-Particle]
2PFile = srvo3-2pg-symmetrized.hdf5 # symmetrized vertex
vertex-type = 0
```

The file name provided in the `QDataFile` variable corresponds to a simple plain text file. The Bethe–Salpeter equations are then only solved for the given **q**-point(s) instead of a regular sized grid. Every line in the given file specifies a **q**-point by 3 integer numbers (please note that 0 corresponds to the first **q**-point). The `qpath` file may have the following contents:

```
0  0  0
0  10 0
10 10 0
10 10 10
```

Considering our example Hamiltonian, 0 0 0, 0 10 0, 10 10 0 and 10 10 10 refers to the Γ-, X-, M-point and R-point, respectively. Please note that if there is no `QDataFile` provided, the given **q**-mesh provided in `q-grid` is used instead.

Appendix B. Results with the provided data

Here we present the results for the test data from the repository (`srvo3-testdata/`). The data shown in Section 3.3 were calculated on a **k**-grid of $20 \times 20 \times 20$ with a frequency box of 200 positive fermionic and bosonic frequencies while the test data provided in the repository only has a frequency box of 30 positive fermionic and bosonic frequency. Using the same config file (see Appendix A.1), as well as the plot scripts found in `documentation/scripts/`, we obtain the self-energy displayed in Figs. B.17 and B.18. Note, that these results are not yet converged with respect to the size of the frequency box.

By using the second provided config file (see Appendix A.2) in combination with the provided qpath file in `documentation/examples/qpath` (containing 41 q-points running through the high-symmetry points $\Gamma \to X \to M \to R \to \Gamma$) we obtain the susceptibilities of Fig. B.19. Please keep in mind that the purpose of this test calculation is to provide a fast, computationally inexpensive

Die approbierte gedruckte Originalversion dieser Dissertation ist an der TU Wien Bibliothek verfügbar.
The approved original version of this doctoral thesis is available in print at TU Wien Bibliothek.
TU Bibliothek WIEN Your knowledge hub

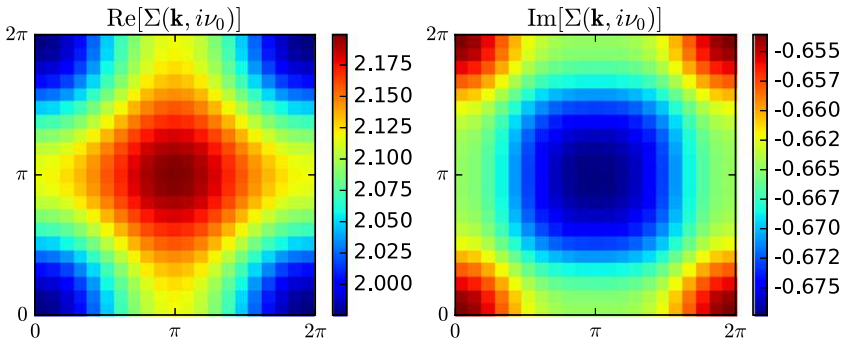

Fig. B.18. Self-energy for a q-qrid calculation in the $k_z = 0$ plane where we show the **k**-resolved value on the first Matsubara frequency $i\nu_0 = \frac{\pi}{\beta}$. Please note that here the Γ-point is located at the bottom left corner. The plot script can be found in documentation/scripts/2D_plot_selfenergy_plane.py.

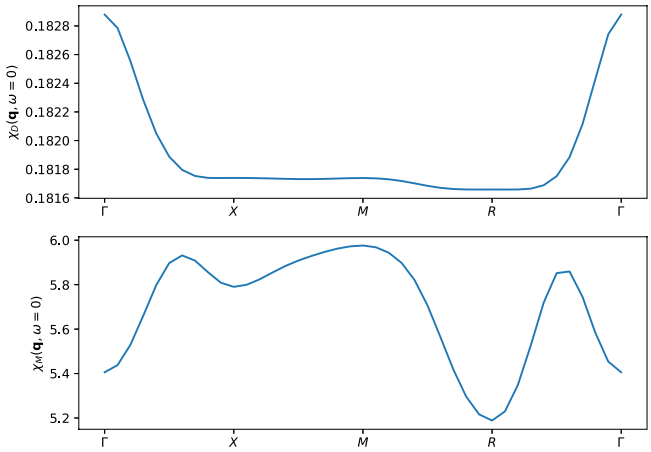

Fig. B.19. Susceptibility for a q-path calculation. The plot script can be found in documentation/scripts/1D_plot_qpath.py. Please note that the generally smaller susceptibilities (compared to Section 3.3) are caused by the much smaller box size.

check of the AbinitioDΓA code; 30 (positive) Matsubara frequencies are not enough to arrive at a result that is converged with respect to the frequency box. The effect of an insufficient number of Matsubara frequencies is most prominent in the frequency-summed susceptibility.

References

[1] W. Metzner, D. Vollhardt, Phys. Rev. Lett. 62 (1989) 324–327, http://dx.doi.org/10.1103/PhysRevLett.62.324.
[2] A. Georges, G. Kotliar, Phys. Rev. B 45 (1992) 6479–6483, http://dx.doi.org/10.1103/PhysRevB.45.6479.
[3] A. Georges, G. Kotliar, W. Krauth, M.J. Rozenberg, Rev. Modern Phys. 68 (1) (1996) 13, http://dx.doi.org/10.1103/RevModPhys.68.13.
[4] E. Pavarini, E. Koch, D. Vollhardt, A. Lichtenstein, DMFT At 25: Infinite Dimensions, in: Reihe Modeling and Simulation 4, Forschungszentrum Jülich Zentralbibliothek, vol. 4, Verlag (Jülich), Jülich, 2014, URL https://juser.fz-juelich.de/record/155829.
[5] V.I. Anisimov, A.I. Poteryaev, M.A. Korotin, A.O. Anokhin, G. Kotliar, J. Phys.: Condens. Matter 9 (1997) 7359–7367, URL http://stacks.iop.org/0953-8984/9/7359.
[6] A.I. Lichtenstein, M.I. Katsnelson, Phys. Rev. B 57 (1998) 6884–6895, http://dx.doi.org/10.1103/PhysRevB.57.6884.
[7] S. Biermann, F. Aryasetiawan, A. Georges, Phys. Rev. Lett. 90 (2003) 086402, http://dx.doi.org/10.1103/PhysRevLett.90.086402.
[8] P. Sun, G. Kotliar, Phys. Rev. B 66 (2002) 085120, http://dx.doi.org/10.1103/PhysRevB.66.085120.
[9] G. Kotliar, S.Y. Savrasov, K. Haule, V.S. Oudovenko, O. Parcollet, C.A. Marianetti, Rev. Modern Phys. 78 (2006) 865, http://dx.doi.org/10.1103/RevModPhys.78.865.
[10] K. Held, Adv. Phys. 56 (2007) 829–926, http://dx.doi.org/10.1080/00018730701619647.
[11] J.M. Tomczak, P. Liu, A. Toschi, G. Kresse, K. Held, Eur. Phys. J. Spec. Top. 226 (11) (2017) 2565–2590, http://dx.doi.org/10.1140/epjst/e2017-70053-1.
[12] M.H. Hettler, A.N. Tahvildar-Zadeh, M. Jarrell, T. Pruschke, H.R. Krishnamurthy, Phys. Rev. B 58 (1998) R7475–R7479, http://dx.doi.org/10.1103/PhysRevB.58.R7475.
[13] A.I. Lichtenstein, M.I. Katsnelson, Phys. Rev. B 62 (2000) R9283–R9286, http://dx.doi.org/10.1103/PhysRevB.62.R9283.
[14] G. Kotliar, S.Y. Savrasov, G. Pálsson, G. Biroli, Phys. Rev. Lett. 87 (2001) 186401, http://dx.doi.org/10.1103/PhysRevLett.87.186401.
[15] T. Maier, M. Jarrell, T. Pruschke, M.H. Hettler, Rev. Modern Phys. 77 (2005) 1027, http://dx.doi.org/10.1103/RevModPhys.77.1027.
[16] S. Biermann, A. Poteryaev, A. I.Lichtenstein, A. Georges, Phys. Rev. Lett. 94 (2005) 026404.
[17] H. Lee, K. Foyevtsova, J. Ferber, M. Aichhorn, H.O. Jeschke, R. Valentí, Phys. Rev. B 85 (2012) 165103, http://dx.doi.org/10.1103/PhysRevB.85.165103.
[18] A. Toschi, A.A. Katanin, K. Held, Phys. Rev. B 75 (2007) 045118, http://dx.doi.org/10.1103/PhysRevB.75.045118.
[19] H. Kusunose, J. Phys. Soc. Japan 75 (5) (2006) 054713, http://dx.doi.org/10.1143/JPSJ.75.054713, URL http://jpsj.ipap.jp/link?JPSJ/75/054713.
[20] A.N. Rubtsov, M.I. Katsnelson, A.I. Lichtenstein, Phys. Rev. B 77 (2008) 033101, http://dx.doi.org/10.1103/PhysRevB.77.033101.
[21] G. Rohringer, A. Toschi, H. Hafermann, K. Held, V.I. Anisimov, A.A. Katanin, Phys. Rev. B 88 (2013) 115112, http://dx.doi.org/10.1103/PhysRevB.88.115112.
[22] C. Taranto, S. Andergassen, J. Bauer, K. Held, A. Katanin, W. Metzner, G. Rohringer, A. Toschi, Phys. Rev. Lett. 112 (2014) 196402, http://dx.doi.org/10.1103/PhysRevLett.112.196402.
[23] T. Ayral, O. Parcollet, Phys. Rev. B 92 (2015) 115109, http://dx.doi.org/10.1103/PhysRevB.92.115109.
[24] G. Li, Phys. Rev. B 91 (2015) 165134, http://dx.doi.org/10.1103/PhysRevB.91.165134.
[25] G. Rohringer, A. Toschi, A. Katanin, K. Held, Phys. Rev. Lett. 107 (2011) 256402, http://dx.doi.org/10.1103/PhysRevLett.107.256402.

Die approbierte gedruckte Originalversion dieser Dissertation ist an der TU Wien Bibliothek verfügbar.
The approved original version of this doctoral thesis is available in print at TU Wien Bibliothek.
TU Bibliothek WIEN Your knowledge hub

[26] D. Hirschmeier, H. Hafermann, E. Gull, A.I. Lichtenstein, A.E. Antipov, Phys. Rev. B 92 (2015) 144409, http://dx.doi.org/10.1103/PhysRevB.92.144409.
[27] A.E. Antipov, E. Gull, S. Kirchner, Phys. Rev. Lett. 112 (2014) 226401, http://dx.doi.org/10.1103/PhysRevLett.112.226401.
[28] T. Schäfer, A.A. Katanin, K. Held, A. Toschi, Phys. Rev. Lett. 119 (2017) 046402, http://dx.doi.org/10.1103/PhysRevLett.119.046402.
[29] G. Rohringer, H. Hafermann, A. Toschi, A.A. Katanin, A.E. Antipov, M.I. Katsnelson, A.I. Lichtenstein, A.N. Rubtsov, K. Held, Rev. Modern Phys. 90 (2018) 025003, http://dx.doi.org/10.1103/RevModPhys.90.025003.
[30] A. Galler, P. Thunström, P. Gunacker, J.M. Tomczak, K. Held, Phys. Rev. B 95 (2017) 115107, http://dx.doi.org/10.1103/PhysRevB.95.115107.
[31] A. Galler, J. Kaufmann, P. Gunacker, M. Pickem, P. Thunström, J.M. Tomczak, K. Held, J. Phys. Soc. Japan 87 (4) (2018) 041004, http://dx.doi.org/10.7566/JPSJ.87.041004.
[32] A.A. Katanin, A. Toschi, K. Held, Phys. Rev. B 80 (2009) 075104, http://dx.doi.org/10.1103/PhysRevB.80.075104.
[33] G. Rohringer, A. Toschi, Phys. Rev. B 94 (2016) 125144, http://dx.doi.org/10.1103/PhysRevB.94.125144.
[34] L. Hedin, Phys. Rev. 139 (1965) A796–A823, http://dx.doi.org/10.1103/PhysRev.139.A796.
[35] J. Kuneš, R. Arita, P. Wissgott, A. Toschi, H. Ikeda, K. Held, Comput. Phys. Comm. 181 (2010) 1888.
[36] H. Hafermann, Phys. Rev. B 89 (2014) 235128, http://dx.doi.org/10.1103/PhysRevB.89.235128.
[37] J. Kaufmann, P. Gunacker, K. Held, Phys. Rev. B 96 (2017) 035114, http://dx.doi.org/10.1103/PhysRevB.96.035114.
[38] P. Gunacker, M. Wallerberger, E. Gull, A. Hausoel, G. Sangiovanni, K. Held, Phys. Rev. B 92 (2015) 155102, http://dx.doi.org/10.1103/PhysRevB.92.155102.
[39] P. Gunacker, M. Wallerberger, T. Ribic, A. Hausoel, G. Sangiovanni, K. Held, Phys. Rev. B 94 (2016) 125153, http://dx.doi.org/10.1103/PhysRevB.94.125153.
[40] H. Hafermann, E.G.C.P. van Loon, M.I. Katsnelson, A.I. Lichtenstein, O. Parcollet, Phys. Rev. B 90 (2014) 235105, http://dx.doi.org/10.1103/PhysRevB.90.235105.
[41] A.N. Rubtsov, M.I. Katsnelson, A.I. Lichtenstein, Ann. Phys. 327 (5) (2012) 1320, http://dx.doi.org/10.1016/j.aop.2012.01.002, URL http://www.sciencedirect.com/science/article/pii/S0003491612000164.
[42] T. Schäfer, G. Rohringer, O. Gunnarsson, S. Ciuchi, G. Sangiovanni, A. Toschi, Phys. Rev. Lett. 110 (2013) 246405, http://dx.doi.org/10.1103/PhysRevLett.110.246405.
[43] E. Anderson, Z. Bai, C. Bischof, S. Blackford, J. Demmel, J. Dongarra, J. Du Croz, A. Greenbaum, S. Hammarling, A. McKenney, D. Sorensen, LAPACK Users' Guide, third ed., Society for Industrial and Applied Mathematics, Philadelphia, PA, 1999.
[44] The HDF Group, Hierarchical Data Format, version 5, 1997–2019, http://www.hdfgroup.org/HDF5/.
[45] A. Collette, Python and HDF5, O'Reilly, 2013.
[46] T. Oliphant, NumPy: A Guide to NumPy, Trelgol Publishing, USA, 2006, URL http://www.numpy.org/.
[47] M. Wallerberger, A. Hausoel, P. Gunacker, A. Kowalski, N. Parragh, F. Goth, K. Held, G. Sangiovanni, Comput. Phys. Comm. 235 (2019) 388–399, http://dx.doi.org/10.1016/j.cpc.2018.09.007, URL http://www.sciencedirect.com/science/article/pii/S0010465518303217.
[48] A. Sekiyama, H. Fujiwara, S. Imada, S. Suga, H. Eisaki, S.I. Uchida, K. Takegahara, H. Harima, Y. Saitoh, I.A. Nekrasov, G. Keller, D.E. Kondakov, A.V. Kozhevnikov, T. Pruschke, K. Held, D. Vollhardt, V.I. Anisimov, Phys. Rev. Lett. 93 (15) (2004) 156402, http://dx.doi.org/10.1103/PhysRevLett.93.156402.
[49] I.H. Inoue, O. Goto, H. Makino, N.E. Hussey, M. Ishikawa, Phys. Rev. B 58 (1998) 4372–4383, http://dx.doi.org/10.1103/PhysRevB.58.4372.
[50] K. Morikawa, T. Mizokawa, K. Kobayashi, A. Fujimori, H. Eisaki, S. Uchida, F. Iga, Y. Nishihara, Phys. Rev. B 52 (1995) 13711–13714, http://dx.doi.org/10.1103/PhysRevB.52.13711.
[51] M. Takizawa, M. Minohara, H. Kumigashira, D. Toyota, M. Oshima, H. Wadati, T. Yoshida, A. Fujimori, M. Lippmaa, M. Kawasaki, H. Koinuma, G. Sordi, M. Rozenberg, Phys. Rev. B 80 (2009) 235104, http://dx.doi.org/10.1103/PhysRevB.80.235104.
[52] I.A. Nekrasov, K. Held, G. Keller, D.E. Kondakov, T. Pruschke, M. Kollar, O.K. Andersen, V.I. Anisimov, D. Vollhardt, Phys. Rev. B 73 (2006) 155112, http://dx.doi.org/10.1103/PhysRevB.73.155112.
[53] S. Aizaki, T. Yoshida, K. Yoshimatsu, M. Takizawa, M. Minohara, S. Ideta, A. Fujimori, K. Gupta, P. Mahadevan, K. Horiba, H. Kumigashira, M. Oshima, Phys. Rev. Lett. 109 (2012) 056401, http://dx.doi.org/10.1103/PhysRevLett.109.056401.
[54] K. Held, R. Peters, A. Toschi, Phys. Rev. Lett. 110 (2013) 246402, http://dx.doi.org/10.1103/PhysRevLett.110.246402.
[55] M. Casula, A. Rubtsov, S. Biermann, Phys. Rev. B 85 (2012) 035115, http://dx.doi.org/10.1103/PhysRevB.85.035115.
[56] J.M. Tomczak, M. Casula, T. Miyake, F. Aryasetiawan, S. Biermann, Europhys. Lett. 100 (6) (2012) 67001, URL http://stacks.iop.org/0295-5075/100/i=6/a=67001.
[57] R. Sakuma, P. Werner, F. Aryasetiawan, Phys. Rev. B 88 (2013) 235110, http://dx.doi.org/10.1103/PhysRevB.88.235110.
[58] J.M. Tomczak, M. Casula, T. Miyake, S. Biermann, Phys. Rev. B 90 (2014) 165138, http://dx.doi.org/10.1103/PhysRevB.90.165138.
[59] L. Boehnke, F. Nilsson, F. Aryasetiawan, P. Werner, Phys. Rev. B 94 (2016) 201106, http://dx.doi.org/10.1103/PhysRevB.94.201106.
[60] T. Miyake, C. Martins, R. Sakuma, F. Aryasetiawan, Phys. Rev. B 87 (2013) 115110, http://dx.doi.org/10.1103/PhysRevB.87.115110.
[61] J.A. Moyer, C. Eaton, R. Engel-Herbert, Adv. Mater. 25 (26) (2013) 3578–3582, http://dx.doi.org/10.1002/adma.201300900.
[62] Z. Zhong, M. Wallerberger, J.M. Tomczak, C. Taranto, N. Parragh, A. Toschi, G. Sangiovanni, K. Held, Phys. Rev. Lett. 114 (2015) 246401, http://dx.doi.org/10.1103/PhysRevLett.114.246401.
[63] L. Zhang, Y. Zhou, L. Guo, W. Zhao, A. Barnes, H.-T. Zhang, C. Eaton, Y. Zheng, M. Brahlek, H.F. Haneef, N.J. Podraza, M.H.W. Chan, V. Gopalan, K.M. Rabe, R. Engel-Herbert, Nat Mater 15 (2) (2016) 204–210, http://dx.doi.org/10.1038/nmat4493.
[64] P. Blaha, K. Schwarz, P. Sorantin, S.B. Trickey, Comput. Phys. Comm. 59 (2) (1990) 399–415, URL http://www.sciencedirect.com/science/article/pii/0010465590901876.
[65] K. Schwarz, P. Blaha, Comput. Mater. Sci. 28 (2003) 259.
[66] J. Kunes, R. Arita, P. Wissgott, A. Toschi, H. Ikeda, K. Held, Comput. Phys. Comm. 181 (11) (2010) 1888–1895, URL http://www.sciencedirect.com/science/article/pii/S0010465510002948.
[67] A.A. Mostofi, J.R. Yates, Y.S. Lee, I. Souza, D. Vanderbilt, N. Marzari, Comput. Phys. Comm. 178 (9) (2008) 685–699, URL http://www.sciencedirect.com/science/article/pii/S0010465507004936.
[68] N. Parragh, A. Toschi, K. Held, G. Sangiovanni, Phys. Rev. B 86 (2012) 155158, http://dx.doi.org/10.1103/PhysRevB.86.155158.
[69] M. Wallerberger, (Ph.D. thesis), TU Wien, 2016.
[70] P. Werner, A. Comanac, L. de' Medici, M. Troyer, A.J. Millis, Phys. Rev. Lett. 97 (2006) 076405, http://dx.doi.org/10.1103/PhysRevLett.97.076405.
[71] P. Werner, A.J. Millis, Phys. Rev. B 74 (2006) 155107, http://dx.doi.org/10.1103/PhysRevB.74.155107.
[72] E. Gull, A.J. Millis, A.I. Lichtenstein, A.N. Rubtsov, M. Troyer, P. Werner, Rev. Modern Phys. 83 (2) (2011) 349, http://dx.doi.org/10.1103/RevModPhys.83.349.
[73] J.M. Tomczak, M. van Schilfgaarde, G. Kotliar, Phys. Rev. Lett. 109 (2012) 237010, http://dx.doi.org/10.1103/PhysRevLett.109.237010.
[74] J.M. Tomczak, J. Phys. Conf. Ser. 592 (1) (2015) 012055, URL http://stacks.iop.org/1742-6596/592/i=1/a=012055.
[75] T. Schäfer, A. Toschi, J.M. Tomczak, Phys. Rev. B 91 (2015) 121107, http://dx.doi.org/10.1103/PhysRevB.91.121107.
[76] M. Jarrell, J.E. Gubernatis, Phys. Rep. 269 (3) (1996) 133–195, http://dx.doi.org/10.1016/0370-1573(95)00074-7, URL http://www.sciencedirect.com/science/article/B6TVP-3VTNGGS-3/2/5f7d5c3a6ee0870df8970b51e47592d2.
[77] A.W. Sandvik, Phys. Rev. B 57 (1998) 10287–10290, http://dx.doi.org/10.1103/PhysRevB.57.10287.
[78] Y. Lan, X. Chen, M. He, J. Alloys Compd. 354 (1) (2003) 95–98, http://dx.doi.org/10.1016/S0925-8388(02)01349-X, URL http://www.sciencedirect.com/science/article/pii/S092583880201349X.
[79] E. Burzo, 5.1.4.2 Magnetization and Magnetic Susceptibilities: Datasheet from Landolt-Börnstein - Group III Condensed Matter · Volume 27F1α: Perovskites I (Part a), springer-Verlag Berlin Heidelberg, 1996, http://dx.doi.org/10.1007/10037300_17, URL http://materials.springer.com/lb/docs/sm_lbs_978-3-540-46420-4_17.
[80] F. Aryasetiawan, M. Imada, A. Georges, G. Kotliar, S. Biermann, A.I. Lichtenstein, Phys. Rev. B 70 (2004) 195104, http://dx.doi.org/10.1103/PhysRevB.70.195104.
[81] T. Miyake, F. Aryasetiawan, Phys. Rev. B 77 (2008) 085122, http://dx.doi.org/10.1103/PhysRevB.77.085122.
[82] G. Li, N. Wentzell, P. Pudleiner, P. Thunström, K. Held, Phys. Rev. B 93 (2016) 165103, http://dx.doi.org/10.1103/PhysRevB.93.165103.
[83] N. Wentzell, G. Li, A. Tagliavini, C. Taranto, G. Rohringer, K. Held, A. Toschi, S. Andergassen, High-frequency asymptotics of the vertex function: diagrammatic parametrization and algorithmic implementation, URL arxiv:1610.06520.
[84] G. Li, A. Kauch, P. Pudleiner, K. Held, The.victory.project. v, Comput. Phys. Comm. 241 (2019) 146–154, http://dx.doi.org/10.1016/j.cpc.2019.03.008, URL http://www.sciencedirect.com/science/article/pii/S0010465519300864.
[85] C. Honerkamp, H. Shinaoka, F.F. Assaad, P. Werner, Phys. Rev. B 98 (2018) 235151, http://dx.doi.org/10.1103/PhysRevB.98.235151.
[86] F. Krien, Phys. Rev. B 99 (2019) 235106, http://dx.doi.org/10.1103/PhysRevB.99.235106.

Die approbierte gedruckte Originalversion dieser Dissertation ist an der TU Wien Bibliothek verfügbar.
The approved original version of this doctoral thesis is available in print at TU Wien Bibliothek.
TU Bibliothek WIEN Your knowledge hub

Die approbierte gedruckte Originalversion dieser Dissertation ist an der TU Wien Bibliothek verfügbar.
The approved original version of this doctoral thesis is available in print at TU Wien Bibliothek.

Statistical error estimates in dynamical mean-field theory and extensions thereof

Patrick Kappl, Markus Wallerberger, Josef Kaufmann, Matthias Pickem, and Karsten Held
Institute of Solid State Physics, TU Wien, 1040 Vienna, Austria

(Received 11 May 2020; accepted 22 July 2020; published 12 August 2020)

We employ the jackknife algorithm to analyze the propagation of the statistical quantum Monte Carlo error through the Bethe-Salpeter equation. This allows us to estimate the error of dynamical mean-field theory calculations of the susceptibility and of dynamical vertex approximation calculations of the self-energy. We find that the different frequency components of the susceptibility are uncorrelated, whereas those of the self-energy are correlated. For improving the quality of the correlation matrix taking sufficiently many jackknife bins is key, while for reducing the standard error of the mean sufficiently many Monte Carlo measurements are necessary. We furthermore show that even in the case of the self-energy, the finite covariance does not have a sizable influence on the analytic continuation.

DOI: 10.1103/PhysRevB.102.085124

Die approbierte gedruckte Originalversion dieser Dissertation ist an der TU Wien Bibliothek verfügbar.
The approved original version of this doctoral thesis is available in print at TU Wien Bibliothek.
TU Bibliothek WIEN Your knowledge hub

I. INTRODUCTION

Developing reliable theories for strong electronic correlation has proved a Herculean task. Three decades after its invention [1–3], dynamical mean-field theory (DMFT) has become state-of-the-art to calculate strongly correlated models [4] and materials [5–9]. Notwithstanding, one of the core scientific tasks, namely providing a proper error estimate for such calculations, is still in its infancy. Error estimates which directly follow from the quantum Monte Carlo (QMC) simulation of the (self-consistently determined) DMFT impurity problem, e.g., for the magnetization or compressibility, have been provided already from the beginning of DMFT, see, e.g., Refs. [3,10,11]. But as the focus of such calculations is nowadays more on the one-particle spectral function or two-particle susceptibility, error estimates are by and large missing.

This is because such an error estimate is nontrivial. First, calculating the spectrum or susceptibility requires complex, nonlinear post-processing routines such as a maximum entropy analytic continuation or the Bethe-Salpeter equation, respectively. Besides proper error propagation through these post-processing procedures, there is, secondly, the iteration error, i.e., the difference between the numerical solution and the exact (true) DMFT fixed point. Thirdly, DMFT is an approximation to the correlation problem itself, introducing a systematic error for finite dimensional systems.

The latter, i.e., the error of DMFT as an approximation, can be systematically improved upon by either cluster [12] or diagrammatic extensions [13]. Cluster extensions replace the single impurity site with a small cluster, thus interpolating between DMFT and the full lattice problem. Given proper finite size scaling, enlarging the cluster then yields an error estimate. The huge numerical effort essentially restricts such cluster extensions however to small clusters on one- and two-dimensional lattices.

Diagrammatic extensions, on the other hand, augment DMFT with a specific set of nonlocal Feynman diagrams. The dynamical vertex approximation (DΓA) [14,15], a prominent diagrammatic extension, generalizes the concept of a local one-particle vertex (self-energy) in DMFT systematically to the two-, three-, n-particle vertex. For $n \to \infty$ one recovers the full problem. The corrections on the two-particle vertex level provide an error estimate for the DMFT approximation, and similarly those of the three-particle level as an error estimate for the DΓA results on the two-particle vertex level. One can proceed in a similar fashion of approximating the error [16] in the dual Fermion approach [17]. Since both the size of the vertices and the effort of the associated diagrammatic equations grow strongly in n, one is restricted to small n.

In this paper, we focus on the error propagation through the post-processing procedure, specifically, the Bethe-Salpeter equation. This does not only involve the DMFT calculation of the susceptibility but also the DΓA calculation of the self-energy which employs the same Bethe-Salpeter equation and on top of that the Schwinger-Dyson equation. Input for both equations is the local two-particle Green's function and the properly converged DMFT one-particle Green's function. For multiorbital systems or at low temperatures the two-particle Green's function is only accessible using QMC techniques but requires quite some effort to calculate and hence has a substantial statistical QMC error. We employ the jackknife method [18,19] to analyze the propagation of the QMC error through the Bethe-Salpeter equation and to estimate the error of the final DMFT susceptibility and DΓA self-energy. Finally, we perform maximum entropy analytic continuations of the DΓA self-energy, using the jackknife estimates for error and covariance.

The remainder of the paper is organized as follows: Section II describes the methods employed: DMFT, continuous-time quantum Monte Carlo, *ab initio* DΓA, and jackknife resampling. The input to our calculations, the two-particle Green's function, is analyzed in Sec. III. The main results

 ©2020 American Physical Society

for the DΓA self-energy and the DMFT susceptibilities are presented in Secs. IV and V respectively, while an analytical continuation of the DΓA self-energy is done in Sec. VI. A discussion and conclusion can be found in Sec. VII.

II. METHODS

In the following, we briefly recapitulate the essential steps for calculating the DMFT susceptibility and DΓA self-energy, starting from the QMC calculation of the one- and two-particle Green's function. We restrict ourselves to the essential equations without discussing technical details such as reformulations of the equations or numerical efficiency. For these details we refer the reader to Ref. [20] as regards the QMC calculation with the w2dynamics package [20] and to Ref. [21] for a general review, to Refs. [22,23] as regards the calculation of the DMFT susceptibility and DΓA self-energy with the *ab initio dynamical vertex approximation* (ADGA) package, and to Ref. [13] for a review. Further, we discuss the essential idea of the jackknife algorithm, again referring the reader to the review Ref. [19] for a more detailed presentation.

A. Dynamical mean-field theory

In DMFT, we map the lattice model

$$H_{\text{lattice}} = U \sum_i \hat{c}^\dagger_{i\uparrow}\hat{c}^\dagger_{i\downarrow}\hat{c}_{i\downarrow}\hat{c}_{i\uparrow} + \sum_{\sigma,i,j} t_{ij}\hat{c}^\dagger_{i\sigma}\hat{c}_{j\sigma}, \tag{1}$$

where $\hat{c}_{i\sigma}$ annihilates a fermion of spin σ on site i, U is the onsite interaction, and t_{ij} is the hopping matrix, onto an Anderson impurity model (AIM) [2,3]:

$$\begin{aligned} H_{\text{AIM}} = {} & U\hat{c}^\dagger_\uparrow\hat{c}^\dagger_\downarrow\hat{c}_\downarrow\hat{c}_\uparrow + \sum_\sigma \tilde{\epsilon}_\sigma \hat{c}^\dagger_\sigma\hat{c}_\sigma \\ & + \underbrace{\sum_{\sigma,p}(V_p\hat{c}^\dagger_\sigma\hat{f}_{\sigma p} + V^*_p\hat{f}^\dagger_{\sigma p}\hat{c}_\sigma)}_{H_{\text{hyb}}} + \sum_p \epsilon_p \hat{f}^\dagger_{\sigma p}\hat{f}_{\sigma p}\,. \end{aligned} \tag{2}$$

Here U is the impurity interaction which is the same as that of the original lattice problem; V_p denotes the hybridization between the impurity (denoted by $\hat{c}^\dagger_\sigma$ and $\hat{c}_\sigma$ creation and annihilation operators for spin $\sigma \in \{\uparrow,\downarrow\}$) and bath site p (denoted by corresponding $\hat{f}^\dagger_{\sigma p}$ and $\hat{f}_{\sigma p}$ operators) at energy ϵ_p. In essence, DMFT determines an AIM that gives the same local one-particle physics as the lattice model where the corresponding parameters V_p and ϵ_p (or the hybridization function Δ) have to be determined self-consistently [2,3]. In what follows we assume that this DMFT self-consistency has been achieved to high accuracy. For the sake of simplicity, we have restricted the equations to the one-orbital problem, but the generalization to multiorbital models is straightforward.

B. Continuous-time quantum Monte Carlo

In order to obtain the one- and two-particle Green's function for the Anderson impurity model (2), we use continuous-time quantum Monte Carlo in the hybridization expansion (CT-HYB) [21,24] with worm sampling [25] as implemented in the w2dynamics package [20,26]. CT-HYB with worm sampling proceeds in a three-step fashion: First, one splits the Hamiltonian H into an interacting part, taken to be $H_I = H_{\text{hyb}}$, and the rest, H_0. Second, one expands both the partition function and the expectation value of some observable ("worm" $\mathcal{W}$) into a Dyson series with respect to H_I and uses Wick's theorem to group diagrams into determinants. For the partition functions, this yields:

$$\begin{aligned} \mathcal{Z} = {} & \sum_{n=0}^{\infty}\frac{(-1)^n}{n!}\sum_{\sigma_1,\sigma_1'}\cdots\sum_{\sigma_n,\sigma_n'}\int_0^\beta \mathrm{d}^n\tau\,\mathrm{d}^n\tau' \\ & \times \mathrm{Tr}\left[T_\tau \mathrm{e}^{-\beta H_{\text{loc}}}\prod_{i=1}^n \hat{c}^\dagger_{\sigma_i}(\tau_i)\,\hat{c}_{\sigma_i'}(\tau_i')\right]\det\mathbf{\Delta}, \end{aligned} \tag{3}$$

where T_τ denotes time ordering. The elements of the hybridization matrix $\mathbf{\Delta}$ are given by $\mathbf{\Delta}_{ij} = \Delta_{\sigma_i\sigma_j'}(\tau_i - \tau_j')$ with the hybridization function $\Delta_{\sigma\sigma'}(\tau) = \delta_{\sigma\sigma'}\sum_p V_p(\partial_\tau - \epsilon_p)^{-1}V_p^*$.

Similarly, we write down the hybridization expansion for the "worm" operator $\mathcal{W}(\{\tilde{\tau}\})$. It can consist of several creation and annihilation operators with various number of time arguments. Most important examples are the one- and two-particle Green's function, where $\mathcal{W}(\{\tilde{\tau}\})$ stands for $T_\tau\hat{c}_\sigma(\tau)\hat{c}^\dagger_\sigma(\tau')$ and $T_\tau\hat{c}_\sigma(\tau_1)\hat{c}^\dagger_\sigma(\tau_2)\hat{c}_\sigma(\tau_3)\hat{c}^\dagger_\sigma(\tau_4)$, respectively. Other worm operators have been introduced in Refs. [27–29]. For the sampling space of $\mathcal{W}(\{\tilde{\tau}\})$, we thus get:

$$\begin{aligned} \mathcal{Z}_{\mathcal{W}} = {} & \sum_{n=0}^{\infty}\frac{(-1)^n}{n!}\sum_{\sigma_1,\sigma_1'}\cdots\sum_{\sigma_n,\sigma_n'}\int_0^\beta \mathrm{d}^n\tau\,\mathrm{d}^n\tau'\,\mathrm{d}\{\tilde{\tau}\} \\ & \times \mathrm{Tr}\left[T_\tau \mathrm{e}^{-\beta H_{\text{loc}}}\mathcal{W}(\{\tilde{\tau}\})\prod_{i=1}^n \hat{c}^\dagger_{\sigma_i}(\tau_i)\,\hat{c}_{\sigma_i'}(\tau_i')\right]\det\mathbf{\Delta}. \end{aligned} \tag{4}$$

Third, we combine both sampling spaces by taking the abstract sum $\mathcal{Z} + \eta\mathcal{Z}_{\mathcal{W}}$, where η is a balancing parameter. The resulting space is sampled using Markov chain Monte Carlo.

An estimator for the worm operator $\mathcal{W}(\{\tilde{\tau}\})$ is then simply given by:

$$\langle\mathcal{W}(\{\tilde{\tau}\})\rangle = \frac{\mathcal{Z}_{\mathcal{W}}}{\mathcal{Z}}\langle\sigma(\{\tilde{\tau}\})\rangle\,, \tag{5}$$

where $\sigma(\{\tau_i\})$ is the indicator function of a configuration in $\mathcal{Z}_{\mathcal{W}}$ with the matching times, $\mathcal{Z}_{\mathcal{W}}/\mathcal{Z}$ is the ratio of volumes between the two spaces. Let us note that in the case of the one- or two-particle Green's function one worm measurement is computationally cheaper than one measurement of the removal estimator in Z sampling, but it also yields less information.

C. DMFT susceptibility

In the following, we will make the transition from imaginary time to Matsubara frequencies, where the one-particle Green's function is

$$G^\nu_\sigma = \int_0^\beta \mathrm{d}\tau e^{i\nu(\tau)}\langle T_\tau\hat{c}_\sigma(\tau)\hat{c}^\dagger_\sigma(0)\rangle \tag{6}$$

Die approbierte gedruckte Originalversion dieser Dissertation ist an der TU Wien Bibliothek verfügbar.
The approved original version of this doctoral thesis is available in print at TU Wien Bibliothek.
TU Bibliothek WIEN Your knowledge hub

and the two-particle Green's function is

$$G^{(2),\nu\nu'\omega}_{\sigma\sigma'} = \frac{1}{\beta}\int_0^\beta \mathrm{d}\tau_1\,\mathrm{d}\tau_2\,\mathrm{d}\tau_3 e^{i[\nu\tau_1-(\nu+\omega)\tau_2+(\nu'+\omega)\tau_3]} \times \langle T_\tau \hat{c}_\sigma(\tau_1)\hat{c}^\dagger_\sigma(\tau_2)\hat{c}_{\sigma'}(\tau_3)\hat{c}^\dagger_{\sigma'}(0)\rangle\,. \tag{7}$$

Note that here and in the following we use the notation of the w2dynamics code [20] which has the extra $1/\beta$ factor in the definition of the two-particle Green's function (7) compared to Ref. [13]. From these Green's functions, we can calculate the generalized local susceptibility

$$\chi^{\nu\nu'\omega}_{\sigma\sigma'} = \beta G^{(2),\nu\nu'\omega}_{\sigma\sigma'} - \beta G_\nu G_{\nu'}\delta_{\omega 0}. \tag{8}$$

Diagrammatically, the above equation means that we remove one disconnected contribution from $G^{(2)}$. In the presence of SU(2) symmetry, i.e., in the paramagnetic phase, one can further restrict oneself to the following two spin combinations, also referred to as density (d) and magnetic (m) channel.

$$\chi^{\nu\nu'\omega}_{d/m,} = \chi^{\nu\nu'\omega}_{\uparrow\uparrow} \pm \chi^{\nu\nu'\omega}_{\uparrow\downarrow}\,. \tag{9}$$

From the local susceptibility $\chi^{\nu\nu'\omega}_r$ with $r \in \{d, m\}$ and the local bare bubble susceptibility $\chi^{\nu\nu'\omega}_0 = -\beta G_\nu G_{(\nu+\omega)}\delta_{\nu\nu'}$, we can determine the local irreducible vertex through an inversion of the local Bethe-Salpeter equation

$$\Gamma_r = \chi_r^{-1} - \chi_0^{-1}\,. \tag{10}$$

This equation is diagonal with respect to each bosonic frequency ω while the inversion itself is performed in the implicit matrix notation ν and ν'. From Γ and the local particle-hole bubble $\chi^{\nu\nu'\omega}_{0,\mathbf{kk'q}} = -\beta G_{\mathbf{k}\nu} G_{(\mathbf{k+q})(\nu+\omega)}\delta_{\nu\nu'}\delta_{\mathbf{kk'}}$ the lattice Bethe-Salpeter equation now allows us to calculate the generalized DMFT lattice susceptibility

$$\chi^{\nu\nu'\omega}_{r,\mathbf{kk'q}} = \chi^{\nu\nu'\omega}_{0,\mathbf{kk'q}} - \sum_{\substack{\nu_1\nu_2\\ \mathbf{k_1k_2}}} \chi^{\nu\nu_1\omega}_{0,\mathbf{kk_1q}}\Gamma^{\nu_1\nu_2\omega}_r \chi^{\nu_2\nu'\omega}_{r,\mathbf{k_2k'q}}. \tag{11}$$

Here and in the following, we distinguish lattice and local quantities through the additional momentum indices $\mathbf{k}$, $\mathbf{k}'$, $\mathbf{q}$; and implicitly assume a factor $1/\beta$ for each Matsubara frequency sum, as in Ref. [13]. That is, $\sum_{\nu_1}$ actually means $\frac{1}{\beta}\sum_{\nu_1}$. From these, physical susceptibilities at frequency ω and momentum $\mathbf{q}$ can be calculated through summing over ν, ν', $\mathbf{k}$, $\mathbf{k}'$.

D. *Ab initio* DΓA self-energy

Similar to Eq. (11), we can also calculate the full vertex F through the Bethe-Salpeter equation

$$F^{\nu\nu'\omega}_{r,\mathbf{kk'q}} = \Gamma^{\nu\nu'\omega}_r + \sum_{\substack{\nu_1\nu_2\\ \mathbf{k_1k_2}}} \Gamma^{\nu\nu_1\omega}_r \chi^{\nu_1\nu_2\omega}_{0,\mathbf{k_1k_2q}} F^{\nu_2\nu'\omega}_{r,\mathbf{k_2k'q}}. \tag{12}$$

However in the ladder approximation the resulting F from Eq. (12) simplifies further and does not have an explicit dependence on $\mathbf{k}$ and $\mathbf{k}'$:

$$F^{\nu\nu'\omega}_{r,\mathbf{q}} = \Gamma^{\nu\nu'\omega}_r + \sum_{\nu_1\nu_2} \Gamma^{\nu\nu_1\omega}_r \chi^{\nu_1\nu_2\omega}_{0,\mathbf{q}} F^{\nu_2\nu'\omega}_{r,\mathbf{q}}. \tag{13}$$

Here we defined $\chi^{\nu\nu'\omega}_{0,\mathbf{q}} = \sum_{\mathbf{k},\mathbf{k}'}\chi^{\nu\nu'\omega}_{0,\mathbf{kk'q}}$. Please note that the generated nonlocal full vertices F in Eq. (13) are no longer crossing symmetric. By taking into account the corresponding diagrams in the transversal particle-hole channel we get for the density component

$$F^{\nu\nu'\omega}_{d,\mathbf{kk'q}} = F^{\nu\nu'\omega}_{d,\mathbf{q}} + \tfrac{1}{2}F^{\mathrm{nl}\,(\nu'-\nu)(\nu'-\omega)\nu'}_{d,\mathbf{k'-k}} + \tfrac{3}{2}F^{\mathrm{nl}\,(\nu'-\nu)(\nu'-\omega)\nu'}_{m,\mathbf{k'-k}} \tag{14}$$

where we defined $F^{\mathrm{nl}\,\nu\nu'\omega}_{r,\mathbf{q}} = F^{\nu\nu'\omega}_{r,\mathbf{q}} - F^{\nu\nu'\omega}_r$. From this vertex we can calculate the DΓA self-energy

$$\Sigma_{\mathbf{k}\nu} = \frac{Un}{2} - U\sum_{\nu'\omega\mathbf{k'q}} F^{\nu\nu'\omega}_{d,\mathbf{kk'q}} G_{\mathbf{k}'\nu'} G_{(\mathbf{k'+q})(\nu'+\omega)}\, G_{(\mathbf{k+q})(\nu+\omega)}, \tag{15}$$

where n is the electron density entering in the Hartree term. The actual calculations for both the DMFT susceptibility and the DΓA self-energy are done using the ADGA program package which together with further computational details is discussed in Refs. [22,23].

E. Jackknife

The jackknife is a resampling method, used for bias reduction and error estimation. It is a versatile method for a range of problems, hence the name [18,19].

Before we describe the jackknife in detail, let us recapitulate some statistical terms that we will need later on. Let θ be the true, yet unknown, value of some quantity. To access θ we construct an estimator, $\hat{\theta}$, which is a function of n random variables, $X_1, \ldots, X_n$. In our case X_i are just Monte Carlo measurements. The bias of the estimator $\hat{\theta}$ is then given by the difference between its expectation value $\mathrm{E}[\hat{\theta}]$ and the true value θ,

$$\mathrm{bias}[\hat{\theta}] := E[\hat{\theta}] - \theta. \tag{16}$$

For $\hat{\theta}$ to be useful, its bias must be systematically improvable by increasing the sample size n. More specifically, a sequence of estimators $\{\hat{\theta}_n(X_1, \ldots, X_n)\}$ is called *consistent* with θ if and only if the probability of deviating from θ goes to zero with n, i.e.,

$$\lim_{n\to\infty} \Pr(|\hat{\theta}_n(X_1, \ldots, X_n) - \theta| > \epsilon) = 0, \quad \forall\epsilon > 0. \tag{17}$$

Now let us explain jackknife resampling based on the following general problem. Assume we want to calculate some quantity $y = f(x)$, where f is some arbitrary, known function. If we knew the true value of x the task would be trivial. In our case, however, x is a random variable and we only have access to a sample $\{x_i\}$ of size n. Therefore we need to find a good estimator $\hat{y}$ and be able to quantify its error. In Secs. IV and V the input samples x_i are the two-particle Green's functions from QMC calculations, y is either the DΓA self-energy or the DMFT susceptibility, f is given by the Bethe-Salpeter equation and in case of the self-energy also by the Schwinger-Dyson equation.

Die approbierte gedruckte Originalversion dieser Dissertation ist an der TU Wien Bibliothek verfügbar.
The approved original version of this doctoral thesis is available in print at TU Wien Bibliothek.
TU Bibliothek WIEN Your knowledge hub

For simplicity, we only propagate the error in the two-particle Green's function. This is justified, because the one-particle Green's function is calculated by symmetric improved estimators and thus its error is smaller by several orders of magnitude [29].

The general strategy of resampling techniques is to generate subsamples from the initial one which are preferably independent and identically distributed (iid). With this, one can then estimate certain statistics of the sample like its mean or variance. In case of the jackknife a bias estimation and reduction is also possible. To show this, let $\hat{y}_n$ be a consistent estimator function for y. A common choice that we used for all calculations in this paper is

$$\hat{y}_n(x_1, \ldots, x_n) = f(\bar{x}), \tag{18}$$

where f is the function from the original problem and $\bar{x}$ is the input sample mean. The latter is an unbiased, consistent estimator for x. If f is a continuous function, it is easy to see that $f(\bar{x})$ is a consistent estimator for y. We note that if f is linear, then $f(\bar{x})$ is already unbiased.

After choosing $\hat{y}_n$ we generate n leave-one-out samples

$$y_{-i} = \hat{y}_{n-1}(x_1, \ldots, x_{i-1}, x_{i+1}, \ldots, x_n). \tag{19}$$

Note that this simple choice of resampling implies that the leave-one-out samples are also consistent estimators for y and carry a different but similar bias. The reason why this is important for obtaining a bias-corrected estimator will become clearer in the following. Consistency requires the bias to vanish in the limit of $n \to \infty$. Thus, if f is not only continuous but also analytic around the true value x, we can expand the bias of $\hat{y}_n$ in powers of $1/n$ and write

$$\text{bias}[\hat{y}_n] = \frac{a}{n} + \frac{b}{n^2} + O(n^{-3}), \tag{20}$$

$$\text{bias}[y_{-i}] = \text{bias}[\hat{y}_{n-1}] = \frac{a}{n-1} + \frac{b}{(n-1)^2} + O(n^{-3}), \tag{21}$$

with some a and b. The expectation value as well as the bias are linear operators [see Eq. (16)]. It is therefore easy to construct new samples y_i' in such a way that we get rid of the leading $O(1/n)$ term in the bias

$$y_i' = n\hat{y}_n - (n-1)y_{-i}, \tag{22}$$

$$\begin{aligned}\text{bias}[y_i'] &= n\,\text{bias}[\hat{y}_n] - (n-1)\,\text{bias}[y_{-i}] \\ &= \left(a + \frac{b}{n}\right) - \left(a + \frac{b}{n-1}\right) + O(n^{-3}) \\ &= -\frac{b}{n(n-1)} + O(n^{-3}) = O(n^{-2}).\end{aligned} \tag{23}$$

By calculating the sample mean of the y_i' we finally arrive at the bias-corrected jackknife estimator

$$\hat{y}_{\text{JK}} = \bar{y}' = \frac{1}{n}\sum_{i=1}^{n} y_i'. \tag{24}$$

Its expectation value is given by

$$\begin{aligned}\text{E}[\hat{y}_{\text{JK}}] &= \frac{1}{n}\sum_{i=1}^{n}(\text{E}[y_i']) = \frac{1}{n}\sum_{i=1}^{n}(n\,\text{E}[\hat{y}_n] - (n-1)\,\text{E}[y_{-i}]) \\ &= \frac{1}{n}\sum_{i=1}^{n}(n(y + \text{bias}[\hat{y}_n]) - (n-1)(y + \text{bias}[y_{-i}])) \\ &= \frac{1}{n}\sum_{i=1}^{n}(y + \text{bias}[y_i']) = y + O(n^{-2}),\end{aligned} \tag{25}$$

where Eq. (23) was used in the last step. This shows that $\hat{y}_{\text{JK}}$ is a consistent estimator for y with a reduced bias of $O(1/n^2)$.

Without proof, consistent estimators for the variance, standard deviation, covariance, etc. of y can also be obtained by calculating the corresponding sample estimates of $\{y_i'\}$ [30]. In Secs. III–V we are specifically interested in the standard error of the mean (SEM) and the linear correlation, corr[·, ·]. The latter is estimated by the sample Pearson correlation coefficients r. For scalar random variables p and q with samples $\{p_i\}$ and $\{q_i\}$ of size n the following holds

$$\text{SEM}_p := \frac{s_p}{\sqrt{n}} = \sqrt{\frac{1}{n(n-1)}\sum_{i=1}^{n}|p_i - \bar{p}|^2} \tag{26}$$

$$\widehat{\text{corr}}[p, q] = r_{pq} = \frac{\sum_{i=1}^{n}(p_i - \bar{p})(q_i - \bar{q})^*}{\sqrt{\sum_{i=1}^{n}|p_i - \bar{p}|^2}\sqrt{\sum_{i=1}^{n}|q_i - \bar{q}|^2}}. \tag{27}$$

Here s denotes the corrected sample standard deviation, $\bar{p}$ the sample mean of the p_i, and $\widehat{\text{corr}}$ the estimated correlation. The generalization to random vectors and objects of higher rank is straightforward by componentwise application of the above formulas. In the following, p_i is a scalar component of the ith sample x_i or y_i, e.g., $p_i = (\Sigma_{\text{D}\Gamma\text{A},\mathbf{k}=(0,0),\nu=\pi/\beta})_i$ might be the ith measurement of the self-energy at a fixed momentum $\mathbf{k}$ and frequency ν.

Let us note an important caveat in using Eq. (27) as estimator for a $k \times k$ correlation matrix r_{pq} with a large number of features k: While each component of the covariance converges as $1/\sqrt{n}$ regardless of k, the eigenvalues of the covariance matrix, which are used to construct independent errors, converge only as a function of n/k. In particular, the estimator yields a singular correlation matrix for any $n < k$.

For practical use, the whole derivation and discussion of the jackknife above can be condensed into three simple steps:

(1) Resample

$$x_i \to x_i' = \frac{1}{n-1}\sum_{j\neq i} x_j = \frac{n\bar{x} - x_i}{n-1} \tag{28}$$

(2) Transform

$$y_i' = nf(\bar{x}) - (n-1)f(x_i') \tag{29}$$

(3) Calculate sample statistics of $\{y_i'\}$, e.g., Eqs. (24), (26), and (27)

Another statistical method, similar to the jackknife, is the bootstrap. It is more powerful but usually requires a greater number of resamples to take advantage of that [31]. Depending on the specific problem, at least hundreds or

Die approbierte gedruckte Originalversion dieser Dissertation ist an der TU Wien Bibliothek verfügbar.
The approved original version of this doctoral thesis is available in print at TU Wien Bibliothek.
TU Bibliothek WIEN Your knowledge hub

thousands of new samples are drawn for the bootstrap method [30,32] as opposed to the 16 to 256 jackknife samples that are used in Secs. IV and V. Since each resample requires a full DΓA calculation, the jackknife is computationally cheaper and therefore the method of choice.

F. Parallel implementation

The main focus of this paper is on the jackknife estimates of the self-energy and susceptibilities calculated within ADGA. In this case the parallelization is simple, because the ADGA calculation is by far the most computationally intensive task and already implemented in a parallel way. Therefore the actual jackknife part is programmed in serial and only the calls to the ADGA code are done in parallel.

III. STATISTICAL ANALYSIS OF THE INPUT: TWO-PARTICLE GREEN'S FUNCTION

Before we analyze the DΓA self-energy and DMFT susceptibilities, let us take a closer look at the input of the DMFT and DΓA calculations, namely the two-particle Green's function $G^{(2),\nu\nu'\omega}$. In particular we want to check if the correlations of the self-energy and susceptibilities are completely intrinsic or if they originate at least in part from the input. For this reason we estimate $\mathrm{corr}[G^{(2),\nu_1\nu_1'\omega_1}_{\uparrow\uparrow}, G^{(2),\nu_2\nu_2'\omega_2}_{\uparrow\uparrow}]$ for various frequency combinations, and plot two-dimensional cuts of this high-dimensional quantity.

All QMC simulations were done for the 2D square lattice Hubbard model at half-filling using the following parameters: $U = 4t$, $\beta = \{2/t, 4/t\}$, where the hopping amplitude $t = 1$ serves as our energy unit. The hopping matrix in Eq. (1) is taken to permit only nearest-neighbor hopping. The number of fermionic frequencies is 40 for $\beta = 2$ and 80 for $\beta = 4$. Due to the imposed particle-hole symmetry, the two-particle Green's function and therefore also its correlation matrix is purely real. Before the latter was estimated, the total number of n_t QMC measurements were divided equally into n_b bins. The $n_m = n_t/n_b$ measurements in each bin were then averaged and used as the samples for the estimations. All results in this section were obtained with $n_m = 2.4 \times 10^6$.

In Fig. 1 the estimated correlation of

$$G^{(2)}_{\mathrm{cut1}}(\nu_1) := G^{(2),\nu=\nu_1,\nu'=\nu_1,\omega=0}_{\uparrow\uparrow} \tag{30}$$

with itself is shown for two temperatures $\beta = 2$ (top) and $\beta = 4$ (bottom) and two numbers of bins $n_b = 16$ (left) and $n_b = 256$ (right). Although there is quite some noise in the plots with fewer bins, the diagonal matrix structure is evident in all four graphs (note the sign of the y axis resembling the typical arrangement in a matrix). This suggests that the two-particle Green's function is uncorrelated at different frequencies, at least along the cut.

To further test this, we next consider the estimated correlation between

$$G^{(2)}_{\mathrm{cut2}}(\omega_1) := G^{(2),\nu=0,\nu'=0,\omega=\omega_1}_{\uparrow\uparrow} \tag{31}$$

and $G^{(2)}_{\mathrm{cut1}}$ which is shown for $\beta = 2$ in Fig. 2 and for $\beta = 4$ in Fig. 3. The same numbers of bins are used as before. Apart from the noise, the correlation vanishes again.

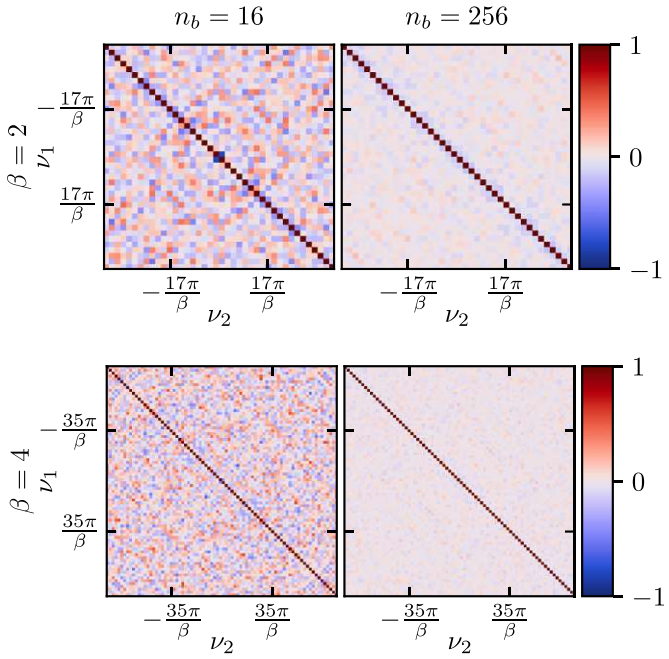

FIG. 1. Estimated correlation matrix $\widehat{\mathrm{corr}}[G^{(2)}_{\mathrm{cut1}}(\nu_1), G^{(2)}_{\mathrm{cut1}}(\nu_2)]$ for the two-particle Green's function at the cut $\nu = \nu' = \nu_i$, $\omega = 0$ comparing different temperatures and numbers of bins. The 40×40 matrices in the top row and the 80×80 matrices in the bottom row correspond to 40 and 80 fermionic frequencies, respectively.

Altogether, this suggests that it is reasonable to assume that the two-particle Green's function at different frequencies as calculated with QMC is uncorrelated. Since this is the input to the subsequent DMFT or DΓA calculations, any correlations of the output data must emerge through the post-processing.

IV. SELF-ENERGY

From the local two-particle Green's function as well as the local one-particle Green's function as an input, the self-energy $\Sigma_{\mathrm{D\Gamma A},\nu\mathbf{k}}$ of the 2D square lattice Hubbard model at

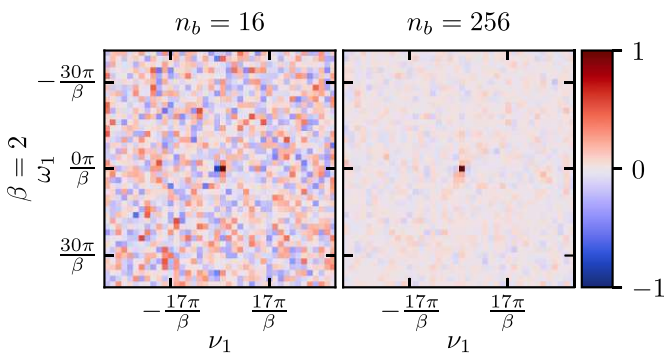

FIG. 2. Same as Fig. 1 (top) but now for the estimated correlation matrix $\widehat{\mathrm{corr}}[G^{(2)}_{\mathrm{cut2}}(\omega_1), G^{(2)}_{\mathrm{cut1}}(\nu_1)]$, i.e., the correlation between cut2 with ω_1, $\nu' = \nu = 0$ and cut1 with $\omega = 0$, $\nu' = \nu = \nu_1$. The 41×40 correlation matrices correspond to 41 bosonic and 40 fermionic frequencies. As in Fig. 1, for sufficiently many bins (right) the off-diagonal components of the correlation matrix vanish. (Note that in this figure there are no diagonal components, since there are different frequencies on the axes.)

Die approbierte gedruckte Originalversion dieser Dissertation ist an der TU Wien Bibliothek verfügbar.
The approved original version of this doctoral thesis is available in print at TU Wien Bibliothek.
TU Bibliothek WIEN Your knowledge hub

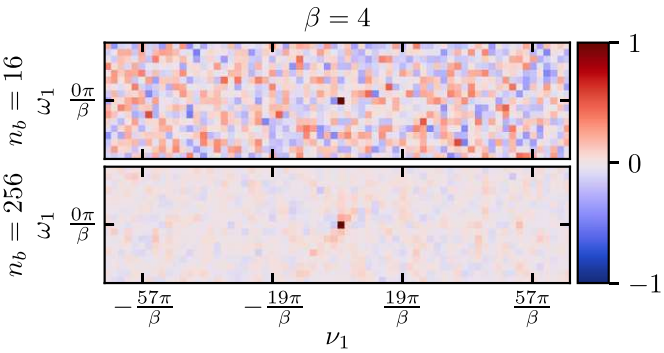

FIG. 3. Same as Fig. 2 but now at $\beta = 4$. The 17×70 matrices correspond to 70 fermionic and 17 bosonic frequencies (which we reduced to save computational time as there was no measurable change in the self-energy).

half-filling is calculated in DΓA. All results in this section are generated using the same parameters as in Sec. III: $U = 4t$, $\beta = \{2/t, 4/t\}$, $t = 1$, $t' = 0$, i.e., only nearest neighbor hopping is considered. The DΓA calculations use nine bosonic as well as 40 and 80 fermionic frequencies for $\beta = 2$ and $\beta = 4$, respectively. The inner momentum-(**k**-)grid is 48×48 and the transfer momentum-(**q**-)grid is 12×12 for $\beta = 2$ and 24×24 for $\beta = 4$. Before jackknife resampling is applied, the total number n_t of QMC measurements of the two-particle Green's function is divided equally into n_b bins with $n_m = n_t/n_b$ measurements per bin which are averaged for each bin. These n_b averages are then used as the input samples for the jackknife. For a more compact notation and easier comparison of the multipanel figures in this section it is convenient to give the number of measurements as a multiple of $n_0 = 2.4 \times 10^6$.

A. Standard error of the mean (SEM)

Figure 4 shows the imaginary part of the DΓA self-energy at $\beta = 2$ and $\beta = 4$ using 256 bins with n_0 QMC measurements each. Note that the error bars are enlarged by a factor of 500 for the left and 50 for the right plot. Taking this rescaling of the error into account, the SEM for $\beta = 4$ (right) is about 10 times higher than for $\beta = 2$ (left) but still very small. We do not plot the real part of the self-energy because on the Fermi surface at half-filling it is just a constant.

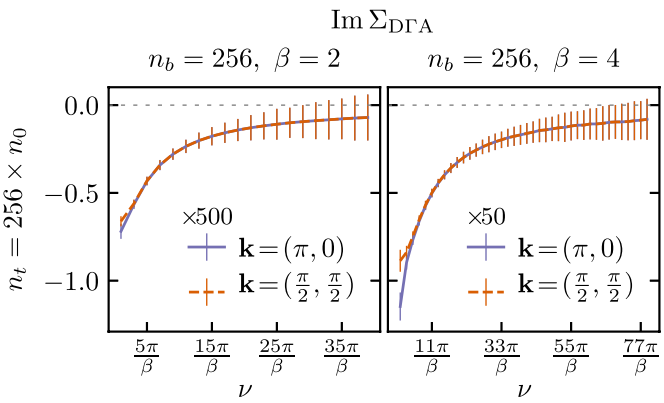

FIG. 4. Imaginary part and jackknife SEM of the DΓA self-energy at different temperatures. For better visibility, the errors bars are enlarged by a factor of 500 on the left and by 50 on the right.

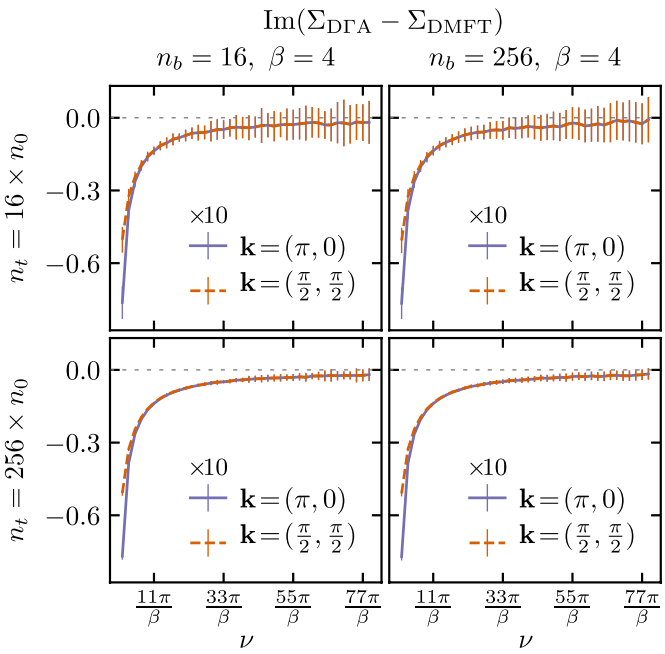

FIG. 5. Imaginary part and jackknife SEM of the difference between the DMFT and DΓA self-energy, $\Sigma_{\mathrm{D\Gamma A},\mathbf{k}\nu} - \Sigma_{\mathrm{DMFT},\nu}$, at $\beta = 4$. Different numbers of bins and total measurements are compared. For better visibility the error bars are enlarged by a factor of 10.

Since ADGA actually calculates two-particle corrections to the DMFT self-energy it is more reasonable to plot the error bars of the difference between the DMFT and DΓA self-energy, $\Sigma_{\mathrm{D\Gamma A},\mathbf{k}\nu} - \Sigma_{\mathrm{DMFT},\nu}$. In Fig. 5 the imaginary part of this DΓA self-energy correction is plotted for $\beta = 4$ and various combinations of the total number of QMC measurements n_t and number of bins n_b. In the top (bottom) row $n_t = 16 \times n_0$ ($256 \times n_0$); in the left (right) column $n_b = 16$ (256) bins. It is obvious that the SEM scales with n_t. That is, the error for the larger number of measurements n_t (bottom row in Fig. 5) is smaller than for a smaller n_t (top row in Fig. 5), just as expected. However, there is practically no dependence of the error on the number of bins n_b (left vs right column of Fig. 5). One can also see that even only $16 \times n_0 \approx 4 \times 10^7$ total measurements (top row in Fig. 5) lead to still acceptable sizes of the error bars (note they are resized by a factor of ten).

B. Correlation matrix

Let us now turn to the correlation of the different frequency components of the DΓA self-energy. Figure 6 shows the real part of the estimate for the correlation of $\Sigma_{\mathrm{D\Gamma A},\mathbf{k}\nu}$ with $\Sigma_{\mathrm{D\Gamma A},\mathbf{k}\nu'}$ for $\beta = 4$ and $\mathbf{k} = (\pi, 0)$. (For the statistical analysis of the input data, we refer the reader to Sec. III.) It uses the same layout as Fig. 5, i.e., $n_t = 16 \times n_0$ in the top row and $n_t = 256 \times n_0$ in the bottom one, with $n_b = 16$ on the left and $n_b = 256$ on the right. Contrary to the SEM, the estimated correlation matrix strongly depends on n_b as the comparison between the left and right column in Fig. 6 shows. While increasing n_t does improve the noise slightly, a large number of jackknife samples is crucial for an acceptable noise level. It is evident in all four plots that the largest correlations appear in the low-frequency region. Disregarding noise, the

Die approbierte gedruckte Originalversion dieser Dissertation ist an der TU Wien Bibliothek verfügbar.
The approved original version of this doctoral thesis is available in print at TU Wien Bibliothek.
TU Bibliothek WIEN Your knowledge hub

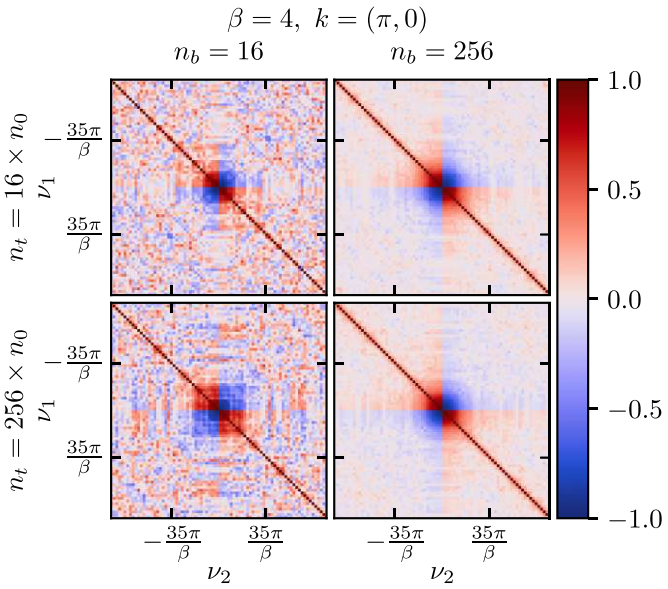

FIG. 6. Real part of the estimated correlation matrix $\widehat{\mathrm{corr}}[\Sigma_{\mathrm{D\Gamma A},\mathbf{k}\nu_1}, \Sigma_{\mathrm{D\Gamma A},\mathbf{k}\nu_2}]$. As in Fig. 5 different numbers of bins and total measurements are compared. The 80×80 matrices correspond to 80 fermionic frequencies.

only correlations outside of this area are those between low and high frequencies.

Figure 7 shows the dependence of the real part of the estimated correlation matrix on β (from the top to the bottom of Fig. 7) and $\mathbf{k}$ (from left to right). One can see that the correlation increases slightly with increasing β (or decreasing temperature) and is also more pronounced for $\mathbf{k} = (\pi, 0)$

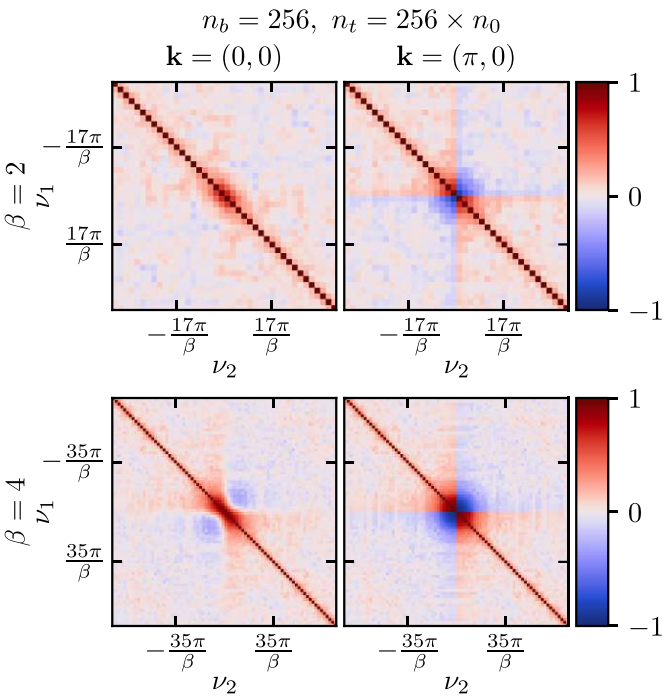

FIG. 7. Real part of the estimated correlation matrix $\widehat{\mathrm{corr}}[\Sigma_{\mathrm{D\Gamma A},\mathbf{k}\nu_1}, \Sigma_{\mathrm{D\Gamma A},\mathbf{k}\nu_2}]$ at different temperatures and $\mathbf{k}$ points. The 40×40 (top) and 80×80 matrices (bottom) correspond to 40 and 80 fermionic frequencies, respectively.

(right) than for $\mathbf{k} = (0, 0)$ (left). However, the general structure of the matrix—high correlation at low frequencies, very low correlation otherwise—is similar in all cases. We do not plot the imaginary part of the estimated correlation matrix because with the chosen parameters (half-filling and $\mathbf{k}$-points on Fermi surface) it vanishes and shows only noise.

The cross correlation between frequencies of the DΓA self-energy can be understood from Eq. (15). It can be rewritten, such that we have the DMFT self-energy plus nonlocal corrections arising from the two-particle Green's function [22]. Both DMFT and DΓA self-energy have the same asymptotic behavior, thus nonlocal corrections have to be restricted to the lower Matsubara frequencies. Since here we consider the correlation arising from the two-particle Green's function, we can conclude that they mainly influence the low-frequency region. Furthermore, in the model under consideration vertex corrections increase with lower temperatures, and the largest influence is to be expected at $\mathbf{k} = (\pi, 0)$, where the formation of a pseudogap can be observed.

The symmetries in Figs. 6 and 7 can be explained by the definition of the estimated correlation coefficients and properties of the self-energy. Using Eq. (27) and $\Sigma(\nu)^* = \Sigma(-\nu)$ yields

$$\begin{aligned}\widehat{\mathrm{corr}}[\Sigma(\nu_1), \Sigma(\nu_2)] &= \widehat{\mathrm{corr}}[\Sigma(\nu_2), \Sigma(\nu_1)]^* \\ &= \widehat{\mathrm{corr}}[\Sigma(\nu_2)^*, \Sigma(\nu_1)^*] \\ &= \widehat{\mathrm{corr}}[\Sigma(-\nu_2), \Sigma(-\nu_1)].\end{aligned} \tag{32}$$

Therefore the real part of the correlation matrices is symmetric around the main- and antidiagonal.

V. SUSCEPTIBILITIES

For periodic systems, the density and magnetic DMFT susceptibilities $\chi_d(\mathrm{i}\omega, \mathbf{q})$ and $\chi_m(\mathrm{i}\omega, \mathbf{q})$ are the Fourier transform of the following imaginary time expectation values:

$$\chi_d(\tau, l - l') = \langle T_\tau (n_{l\uparrow} + n_{l\downarrow})(\tau)(n_{l'\uparrow} + n_{l'\downarrow})(0)\rangle\,, \tag{33}$$

$$\chi_m(\tau, l - l') = \langle T_\tau (n_{l\uparrow} - n_{l\downarrow})(\tau)(n_{l'\uparrow} - n_{l'\downarrow})(0)\rangle\,. \tag{34}$$

Here l and l' are lattice site indices, T_τ is the time-ordering operator, and $n_{l\sigma}$ is the electron density at site l with spin $\sigma \in \{\uparrow, \downarrow\}$. In DMFT, they are calculated in momentum space for the square-lattice Hubbard model at half-filling, using the Bethe-Salpeter equations discussed in Sec. II A. All results in this section are generated using the same parameters as in Sec. III: $U = 4t$, $\beta = \{2/t, 4/t\}$, where $t = 1$ sets the energy unit, and only nearest-neighbor hopping is considered. Again, we use nine bosonic as well as 40 and 80 fermionic frequencies for $\beta = 2$ and $\beta = 4$, respectively. The inner momentum- or $\mathbf{k}$-grid (for the one-particle quantities and χ_0) is 48×48, whereas the transfer momentum- or $\mathbf{q}$-grid is 12×12 for $\beta = 2$ and 24×24 for $\beta = 4$. As before, the total number of QMC measurements n_t for the two-particle Green's function is given in multiples of $n_0 = 2.4 \times 10^6$ and divided into n_b bins, with $n_m = n_t/n_b$ measurements averaged per bin. These averages are then used as the input samples for the jackknife. Note that at half-filling, the susceptibilities and therefore also their correlation matrices are purely real.

Die approbierte gedruckte Originalversion dieser Dissertation ist an der TU Wien Bibliothek verfügbar.
The approved original version of this doctoral thesis is available in print at TU Wien Bibliothek.
TU Bibliothek WIEN Your knowledge hub

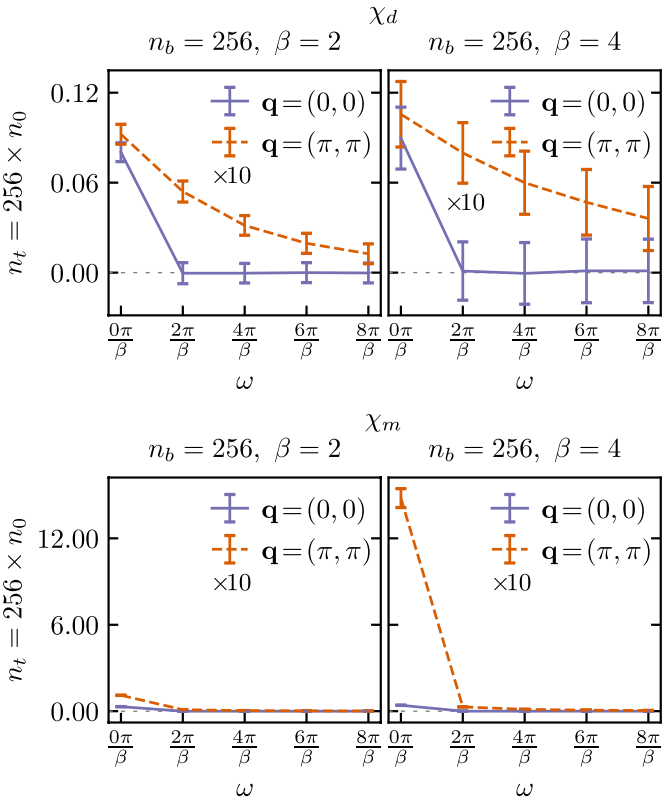

FIG. 8. Density and magnetic DMFT susceptibility, χ_d and χ_m, at different temperatures and momenta. For better visibility the error bars are enlarged by a factor of 10.

A. Standard error of the mean (SEM)

Figure 8 shows the density and magnetic susceptibilities at $\beta = 2$ and $\beta = 4$, where $n_t = 256 \times n_0$ measurements are divided into $n_b = 256$ bins. Since there is a transition to an antiferromagnetic phase at $\beta = 4.3$ [33], $\chi_m(\mathbf{q} = (\pi, \pi))$ as well as its error are dominated by the contributions at $\omega = 0$. This makes it harder to compare the plots of the two susceptibilities but one can still see that the SEM increases with β (left vs right panels) for both quantities, just like in the case of the DΓA self-energy.

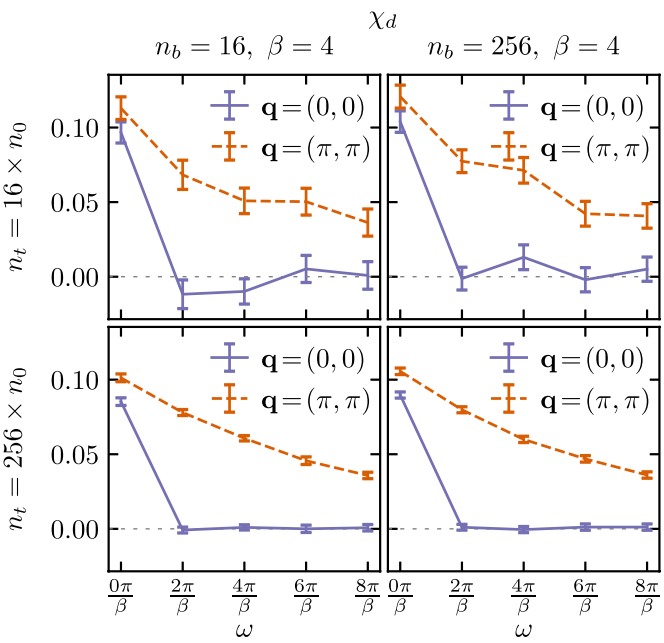

FIG. 9. DMFT density susceptibility χ_d at $\beta = 4$ for two different momenta $\mathbf{q}$, comparing different numbers of bins and total measurements.

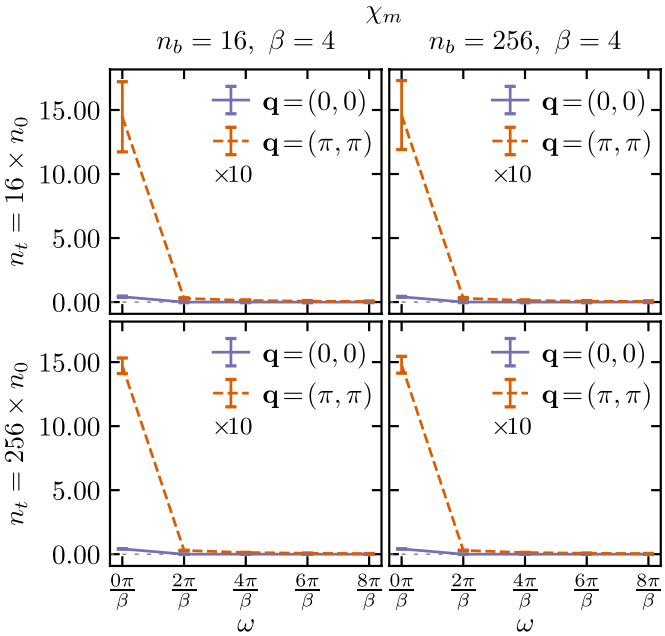

FIG. 10. Same as Fig. 9 but for the magnetic susceptibility χ_m. For better visibility the error bars are enlarged by a factor of 10.

The dependence on the total number of measurements n_t and the number of bins n_b is shown in Fig. 9 for χ_d and in Fig. 10 for χ_m; both at $\beta = 4$. They use the same layout as Fig. 5, i.e., $n_t = 16 \times n_0$ in the top rows and $256 \times n_0$ in the bottom ones, with $n_b = 16$ on the left and 256 on the right. Only the error bars of χ_m are enlarged by a factor of 10. Similar to Sec. IV the SEM scales with the total number of measurements (top vs bottom panels), but it does not depend on the number of jackknife samples n_b (left vs right panels). Contrary to the results of the self-energy, even using a total of $256 \times n_0 \approx 6 \times 10^8$ measurements only yields borderline acceptable error bars. This means the main features of the χ_d curve are still recognizable but larger error bars would render the signal statistically insignificant. Therefore one should aim for at least $O(10^9)$ total measurements in this case.

B. Correlation matrix

The estimate for the correlation of the susceptibilities with themselves is shown in Fig. 11. Both χ_d and χ_m are uncorrelated for both temperatures ($\beta = 2$ and $\beta = 4$) and for both momenta [$\mathbf{q} = (0, 0)$ and $\mathbf{q} = (\pi, \pi)$]. The same is true for $\mathbf{q} = (\pi, 0)$, shown in Fig. 12, which studies the effects of using more jackknife bins. Clearly, a good estimate of the correlation matrix of the susceptibility requires more than $O(10)$ bins.

The symmetries of the correlation matrices in Figs. 11 and 12 are the same as those in Sec. IV B. They are

Die approbierte gedruckte Originalversion dieser Dissertation ist an der TU Wien Bibliothek verfügbar.
The approved original version of this doctoral thesis is available in print at TU Wien Bibliothek.
TU Bibliothek WIEN Your knowledge hub

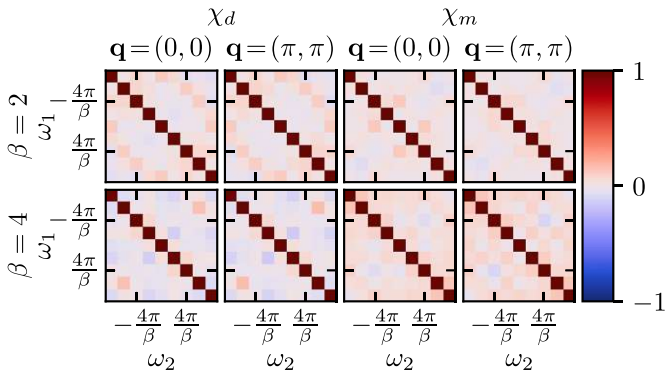

FIG. 11. Estimated correlation matrix of the DMFT susceptibilities $\widehat{\mathrm{corr}}[\chi_r(\omega_1), \chi_r(\omega_2)]$, $r \in \{m, d\}$ at different temperatures and momenta. A total number of $256 \times n_0$ measurements are binned into 256 jackknife samples. The 9×9 matrices correspond to nine bosonic frequencies.

symmetric around the main- and antidiagonal because $\chi_{m,d}(\omega) = \chi_{m,d}(-\omega)$, which is the same property as that of the self-energy considering that the susceptibilities are also real.

VI. MAXIMUM ENTROPY ANALYTIC CONTINUATION

Extracting real-frequency information, $A(\omega)$, out of Matsubara-frequency data, $y(\nu)$, amounts to solving the following fitting problem:

$$\min_A \left\| y(\nu) - \int \mathrm{d}\omega K(\nu,\omega) A(\omega) \right\| = \min_{\mathbf{A}} ||\mathbf{y} - K\mathbf{A}||, \quad (35)$$

where K is an integral kernel which is different for bosonic or fermionic functions. $\mathbf{y}$ and $\mathbf{A}$ are the Fourier coefficients of $y(\nu)$ and $A(\omega)$ in an appropriate basis. Eq. (35) is minimal if and only if the log-likelihood

$$L[\mathbf{A}] = -\tfrac{1}{2}(\mathbf{y} - K\mathbf{A})^\dagger C^{-1}(\mathbf{y} - K\mathbf{A}), \quad (36)$$

is maximal, where C is the covariance matrix (a positive definite symmetric matrix). Equations (35) and (36) are ill posed on numerical data as the singular values of K drop superexponentially.

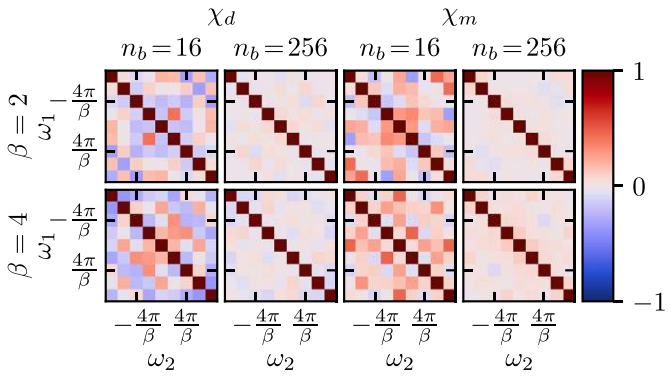

FIG. 12. Same as Fig. 11 but now at $\mathbf{q} = (\pi, 0)$ and comparing different numbers of jackknife bins n_b for a total number of $16 \times n_0$ measurements.

The maximum entropy method (MEM) [34] is a widely employed method to regularize this problem. Briefly, instead of Eq. (35), we maximize an augmented functional:

$$Q_\alpha[\mathbf{A}] = L[\mathbf{A}] + \alpha S[\mathbf{A}|\mathbf{A}_0], \quad (37)$$

where $S[\mathbf{A}|\mathbf{A}_0]$ is the relative (information) entropy with respect to an *a priori* default model $\mathbf{A}_0$. This term regularizes the optimization and has to be scaled by a hyperparameter α. Equation (37) can be used on numerical data: $\mathbf{y}$ is now the sample mean and C is the sample covariance matrix in Eq. (36).

Equation (36) can be evaluated much more efficiently if the covariance matrix is diagonal. However, if that is not the case, we may still perform the transformation $C = \mathcal{U}^\dagger V \mathcal{U}$, where $\mathcal{U}$ is unitary and V is a positive definite diagonal matrix. Equation (36) then acquires the simpler form

$$L[\mathbf{A}] = -\frac{1}{2}\sum_j \frac{|\tilde{\mathbf{y}}_j - (\tilde{K}\mathbf{A})_j|^2}{V_j} \quad (38)$$

with $\tilde{\mathbf{y}} = \mathcal{U}\mathbf{y}$ and $\tilde{K} = \mathcal{U}K$.

If this rotation of the data and the kernel is done as a preprocessing step, then the remaining problem is identical to the case where the covariance matrix is diagonal. In particular, it is still possible to treat real and imaginary part as separate variables by stacking $\tilde{\mathbf{y}} \to [\mathrm{Re}\,\tilde{\mathbf{y}}, \mathrm{Im}\,\tilde{\mathbf{y}}]$ and $\tilde{K} \to [\mathrm{Re}\,\tilde{K}, \mathrm{Im}\,\tilde{K}]$. We use the `ana_cont` library [35,36] to perform analytic continuations of the DΓA self-energy at $\beta = 4$. To this end, we have to subtract the Hartree energy $U/2$, such that asymptotically also the real part approaches zero. Then the standard kernel for fermionic Green's functions can be used [37] and we obtain a function $A_\Sigma(\omega)$ which is

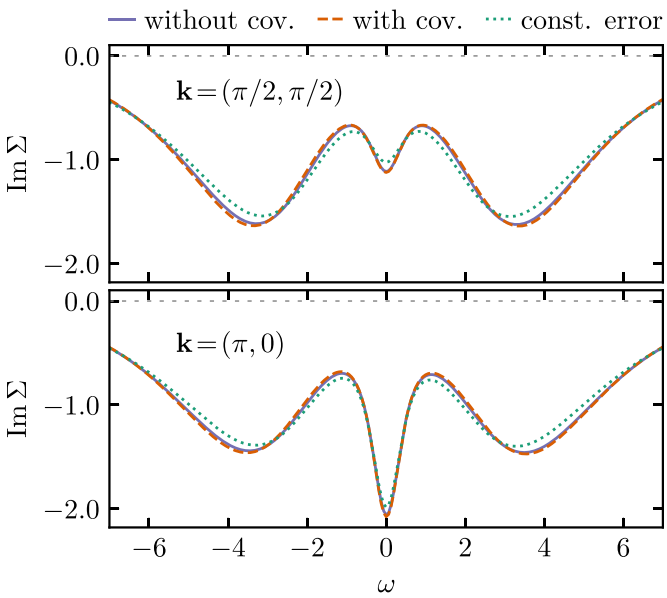

FIG. 13. Imaginary part of the self-energy on the real-frequency axis at different momenta $\mathbf{k}$, comparing the analytic continuation without covariance matrix, with the proper covariance matrix, and with a constant error.

Die approbierte gedruckte Originalversion dieser Dissertation ist an der TU Wien Bibliothek verfügbar.
The approved original version of this doctoral thesis is available in print at TU Wien Bibliothek.
TU Bibliothek WIEN Your knowledge hub

related to the imaginary part of the self-energy by

$$A_\Sigma(\omega) = -\frac{1}{\pi}\,\mathrm{Im}\,\Sigma(\omega + \mathrm{i}0^+). \tag{39}$$

In Fig. 13 we see that in this case the correlations are not strong enough to make the analytic continuation instable. However, using a constant error rather the one calculated by the jackknife method leads to a slightly different result.

VII. CONCLUSION AND DISCUSSION

We have implemented and studied a jackknife error estimate for typical DMFT and DΓA post-processing calculations after a QMC solution of the Anderson impurity problem. While mere QMC error bars have been analyzed before (also employing the jackknife [38,39]), the error of the post-processed quantities such as the DMFT susceptibilities and the DΓA self-energies has not been systematically studied. Here, the QMC statistical error is propagated through nonlinear equations, namely the Bethe-Salpeter equation. In such a situation the jackknife method is the method of choice, and we make our routines that have been tested with QMC input from w2dynamics [20] available at Ref. [40].

From a statistical point of view, our study reveals that the different components of the two-particle Green's function, which is the CT-HYB QMC output and main jackknife input, are uncorrelated. But a binning into $O(100)$ bins is necessary to remove the spurious off-diagonal components of the correlation matrix. The same holds for the DMFT susceptibility which is calculated through the Bethe-Salpeter equation. Because of the vanishing off-diagonal elements of the correlation (or covariance) matrix, an analytical continuation without covariance is possible.

The DΓA self-energy on the other hand has a nondiagonal correlation matrix. Its calculation consists of the Bethe-Salpeter equation, as in DMFT, and additionally the Schwinger-Dyson equation. We conclude that the latter leads to the correlations between the DΓA self-energy at different frequencies. This is also quite intuitive since the same (bosonic) frequency component of the susceptibility contributes to the DΓA self-energy at different fermionic frequencies. However, we have shown that the results of analytic continuation of the self-energy are hardly influenced by this. We thus conclude that the correlations introduced by two-particle corrections are still small enough to allow for a reliable interpretation of the results. Still one should keep in mind that using the actual jackknife error, as opposed to a constant, does have a small influence on the analytic continuation.

We have further studied the standard error of the mean (SEM) and observe that it hardly depends on the number of bins n_b into which the total number of measurements n_t is divided. However as a matter of course the SEM depends strongly on n_t. Depending on the physical quantity studied and the required accuracy, a total number of measurements n_t of $O(10^7)$ to $O(10^9)$ is needed. Here, the error bars of the DMFT susceptibilities are somewhat larger than for the DΓA self-energy. The error also increases with decreasing temperature or larger interval $[0, \beta]$, as this interval is sampled less accurately if n_t is kept fixed.

Our paper has shown that the jackknife method is a valuable tool for calculating DMFT and DΓA error bars. Beyond the present paper, the statistical error of the one-particle Green's function can be included. However, with the use of symmetric improved estimators the errors of the one-particle Green's function are practically nonexistent. A further extension would be to consider the error of the DMFT self-consistency loop itself by drawing bins from statistically independent DMFT solutions. The latter can be achieved either by completely independent DMFT calculations or by determining the auto-correlation time of the DMFT loop and adjusting the binning to it. Our approach can be combined with various other methods to reduce the Monte Carlo noise [27,29,41] or the cutoff error of the frequency box [28,42–45] as well as with compactifications of the vertex [46–48]. We hope that our paper will spread the seed for a proper error estimate in future DMFT calculations and diagrammatic extensions thereof.

ACKNOWLEDGMENTS

The present research was supported by the Austrian Science Fund (FWF) through the Doctoral School W1243 Building Solids for Function (P. K.) as well as projects P32044 and P30997. Calculations were done on the Vienna Scientific Cluster (VSC).

[1] W. Metzner and D. Vollhardt, Phys. Rev. Lett. **62**, 324 (1989).
[2] A. Georges and G. Kotliar, Phys. Rev. B **45**, 6479 (1992).
[3] M. Jarrell, Phys. Rev. Lett. **69**, 168 (1992).
[4] A. Georges, G. Kotliar, W. Krauth, and M. J. Rozenberg, Rev. Mod. Phys. **68**, 13 (1996).
[5] V. I. Anisimov, A. I. Poteryaev, M. A. Korotin, A. O. Anokhin, and G. Kotliar, J. Phys.: Condens. Matter **9**, 7359 (1997).
[6] A. I. Lichtenstein and M. I. Katsnelson, Phys. Rev. B **57**, 6884 (1998).
[7] K. Held, I. A. Nekrasov, G. Keller, V. Eyert, N. Blümer, A. K. McMahan, R. T. Scalettar, T. Pruschke, V. I. Anisimov, and D. Vollhardt, Phys. Status Solidi B **243**, 2599 (2006), previously appeared as Psi-k Newsletter No. 56 (April 2003).
[8] G. Kotliar, S. Y. Savrasov, K. Haule, V. S. Oudovenko, O. Parcollet, and C. A. Marianetti, Rev. Mod. Phys. **78**, 865 (2006).
[9] K. Held, Adv. Phys. **56**, 829 (2007).
[10] M. Ulmke, V. Janiš, and D. Vollhardt, Phys. Rev. B **51**, 10411 (1995).
[11] K. Held, M. Ulmke, N. Blümer, and D. Vollhardt, Phys. Rev. B **56**, 14469 (1997).
[12] M. H. Hettler, M. Mukherjee, M. Jarrell, and H. R. Krishnamurthy, Phys. Rev. B **61**, 12739 (2000).
[13] G. Rohringer, H. Hafermann, A. Toschi, A. A. Katanin, A. E. Antipov, M. I. Katsnelson, A. I. Lichtenstein, A. N. Rubtsov, and K. Held, Rev. Mod. Phys. **90**, 025003 (2018).
[14] A. Toschi, A. A. Katanin, and K. Held, Phys. Rev. B **75**, 045118 (2007).

Die approbierte gedruckte Originalversion dieser Dissertation ist an der TU Wien Bibliothek verfügbar.
The approved original version of this doctoral thesis is available in print at TU Wien Bibliothek.
TU Bibliothek WIEN Your knowledge hub

[15] A. A. Katanin, A. Toschi, and K. Held, Phys. Rev. B **80**, 075104 (2009).
[16] T. Ribic, P. Gunacker, S. Iskakov, M. Wallerberger, G. Rohringer, A. N. Rubtsov, E. Gull, and K. Held, Phys. Rev. B **96**, 235127 (2017).
[17] A. N. Rubtsov, M. I. Katsnelson, and A. I. Lichtenstein, Phys. Rev. B **77**, 033101 (2008).
[18] R. G. Miller, Ann. Math. Statist. **35**, 1594 (1964).
[19] R. G. Miller, Biometrika **61**, 1 (1974)
[20] M. Wallerberger, A. Hausoel, P. Gunacker, A. Kowalski, N. Parragh, F. Goth, K. Held, and G. Sangiovanni, Comput. Phys. Commun. **235**, 388 (2019).
[21] E. Gull, A. J. Millis, A. I. Lichtenstein, A. N. Rubtsov, M. Troyer, and P. Werner, Rev. Mod. Phys. **83**, 349 (2011).
[22] A. Galler, P. Thunström, P. Gunacker, J. M. Tomczak, and K. Held, Phys. Rev. B **95**, 115107 (2017).
[23] A. Galler, P. Thunström, J. Kaufmann, M. Pickem, J. M. Tomczak, and K. Held, Comput. Phys. Commun. **245**, 106847 (2019).
[24] P. Werner, A. Comanac, L. de' Medici, M. Troyer, and A. J. Millis, Phys. Rev. Lett. **97**, 076405 (2006).
[25] P. Gunacker, M. Wallerberger, E. Gull, A. Hausoel, G. Sangiovanni, and K. Held, Phys. Rev. B **92**, 155102 (2015).
[26] N. Parragh, A. Toschi, K. Held, and G. Sangiovanni, Phys. Rev. B **86**, 155158 (2012).
[27] P. Gunacker, M. Wallerberger, T. Ribic, A. Hausoel, G. Sangiovanni, and K. Held, Phys. Rev. B **94**, 125153 (2016).
[28] J. Kaufmann, P. Gunacker, and K. Held, Phys. Rev. B **96**, 035114 (2017).
[29] J. Kaufmann, P. Gunacker, A. Kowalski, G. Sangiovanni, and K. Held, Phys. Rev. B **100**, 075119 (2019).
[30] B. Efron, *The Jackknife, the Bootstrap and Other Resampling Plans* (Society for Industrial and Applied Mathematics, Philadelphia, Pennsylvania, 1982).
[31] B. Efron, Ann. Statist. **7**, 1 (1979).
[32] R. Wilcox, *Fundamentals of Modern Statistical Methods: Substantially Improving Power and Accuracy* (Springer, New York, 2010).
[33] J. Kuneš, Phys. Rev. B **83**, 085102 (2011).
[34] M. Jarrell and J. E. Gubernatis, Phys. Rep. **269**, 133 (1996).
[35] D. Geffroy, J. Kaufmann, A. Hariki, P. Gunacker, A. Hausoel, and J. Kuneš, Phys. Rev. Lett. **122**, 127601 (2019).
[36] J. Kaufmann, Ana-cont, https://github.com/josefkaufmann/ana_cont (2019).
[37] J. M. Luttinger, Phys. Rev. **121**, 942 (1961).
[38] E. Pavarini, E. Koch, D. Vollhardt, and A. Lichtenstein, *DMFT at 25: Infinite Dimensions*, Reihe Modeling and Simulation 4 Vol. 4 (Forschungszentrum Jülich Zentralbibliothek, Verlag (Jülich), Jülich, 2014).
[39] M. Bercx, F. Goth, J. S. Hofmann, and F. F. Assaad, SciPost Phys. **3**, 013 (2017).
[40] P. Kappl, jackknife, https://gitlab.com/PatrickKappl/jackknife (2019).
[41] H. Hafermann, K. R. Patton, and P. Werner, Phys. Rev. B **85**, 205106 (2012).
[42] N. Wentzell, G. Li, A. Tagliavini, C. Taranto, G. Rohringer, K. Held, A. Toschi, and S. Andergassen, Phys. Rev. B **102**, 085106 (2020).
[43] M. Kitatani, T. Schäfer, H. Aoki, and K. Held, Phys. Rev. B **99**, 041115(R) (2019).
[44] F. Krien, Phys. Rev. B **99**, 235106 (2019).
[45] A. Katanin, Phys. Rev. B **101**, 035110 (2020).
[46] L. Boehnke, H. Hafermann, M. Ferrero, F. Lechermann, and O. Parcollet, Phys. Rev. B **84**, 075145 (2011).
[47] H. Shinaoka, J. Otsuki, K. Haule, M. Wallerberger, E. Gull, K. Yoshimi, and M. Ohzeki, Phys. Rev. B **97**, 205111 (2018).
[48] H. Shinaoka, D. Geffroy, M. Wallerberger, J. Otsuki, K. Yoshimi, E. Gull, and J. Kuneš, SciPost Phys. **8**, 12 (2020).

Die approbierte gedruckte Originalversion dieser Dissertation ist an der TU Wien Bibliothek verfügbar.
The approved original version of this doctoral thesis is available in print at TU Wien Bibliothek.
TU Bibliothek WIEN Your knowledge hub